Gravitational and electromagnetic signatures of massive relics in Cosmology

Vivian Poulin

Communauté
UNIVERSITÉ Grenoble Alpes

THÈSE

Pour obtenir le grade de

Docteur de la Communauté Université Grenoble Alpes

Spécialité : **Physique Théorique**

Arrêté ministériel : 7 Août 2006

Présentée par

Vivian Poulin

Thèse dirigée par **Pasquale D. Serpico**
et codirigée par **Julien Lesgourgues**

Préparée au sein du **Laboratoire d'Annecy-le-Vieux de Physique Théorique** et de l'**École doctorale de physique de Grenoble** en cotutelle avec l'**Université RWTH d'Aachen**

Gravitational and electromagnetic signatures of massive relics in Cosmology

Thèse soutenue publiquement le **03 Juillet 2017**,
devant le jury composé de :

Pierre Salati
USMB/LAPTh, Président

Tracy Slatyer
MIT, Rapporteur

Jens Chluba
University of Manchester, Rapporteur

Michael Kramer
RWTH Aachen, Examinateur

Laura Lopez-Honorez
ULB, Examinateur

Pasquale D. Serpico
LAPTh, Directeur de thèse

Julien Lesgourgues
RWTH Aachen, Co-Directeur de thèse

ABSTRACT

Despite their great successes, cosmology and particle physics are facing deep issues that have been puzzling physicists for a long time. In particular, 85% of the matter content in our Universe is in the form of a cold, non-interacting component, whose impacts have only been probed through gravity. On the other hand, the discovery of neutrino oscillations points towards the existence of tiny but non-vanishing neutrino masses, a phenomenon that cannot be successfully explained within the Standard Model of Particle Physics. This work tries to tackle the dark matter and neutrino masses conundrums by looking for electromagnetic and gravitational signatures of peculiar massive relics in cosmological probes. In particular, we study the impacts on i) CMB temperature and polarization anisotropies; ii) Large Scale Structure surveys; iii) Spectral distortions of the CMB blackbody spectrum; iv) and Big Bang Nucleosynthesis (BBN).

After a thorough review of all necessary tools to compute these observables, we make use of the latest data from present experiments, and forecast the potential for detection of future ones. We firstly focus on the purely gravitational effects of decaying massive relics, deriving the strongest constraints to date and extending the phenomenology to multicomponent models with very high decay rate. These constraints represent robust, largely model independent bounds that any massive relic has to satisfy.

In a second step, we switch to electromagnetic channels and compare the relative constraining power of non-thermal BBN, CMB spectral distortions and statistics of CMB anisotropies. As an example, we apply our methods to specific models taken from the literature, including exotic particle physics models and astrophysical candidates such as Primordial Black Holes. Moreover, we show that a loophole to the standard theory of e.m. cascade may allow one to solve the cosmological Lithium problem thanks to photon injection. We then study the impact of annihilating relics, with a special emphasis on annihilations in halos and their interplay with stars in reionizing our Universe.

The last part of this work is devoted to the cosmological determination of neutrino properties with current and future data. We demonstrate that: i) it is possible to make a robust statement about the detection of the cosmic neutrino background by CMB experiments; ii) the joint analysis of future CMB and Large Scale Structure data should allow the first $5\,\sigma$ cosmological detection of neutrino masses. Our results emphasize the complementarity of the different probes, and the need for combined analyses when looking for new physics, especially in the era of precision cosmology.

Est-ce que tu vois le printemps? Celui qui met nos terres au soleil.
Dis moi, est-ce que tu l'entends? De la fleur y'a l'épine qui sommeille.
Est-ce que tu vois le printemps? Celui qui fait couler les ruisseaux,
Entre les doigts des torrents, oui c'est sûr qu'ils sont ivres nos bateaux.
Est-ce que tu vois le printemps? Nos amours que l'on jette en patûre.
Dans les flots des océans, les lettres restent mortes, littérature.

.

— **Damien Saez, *Les Printemps.***

ACKNOWLEDGEMENTS

Cette thèse faisant déjà près de 400 pages, je vais m'efforcer de garder la longueur de mes remerciements raisonnables. Après tout, je suis réputé pour garder mes discours clairs et concis.... ou est-ce le contraitre? Cependant, il m'est impossible de ne pas prendre les quelques paragraphes nécessaires pour exprimer ma gratitude aux gens qui m'ont entourés pendant ces trois années, et parfois pendant bien plus longtemps.

Je vais commencer par remercier mes directeurs de thèses, par ordre alphabetique Julien Lesgourgues et Pasquale D. Serpico, pour m'avoir offert la possibilité de rentrer dans le monde de la physique, tout en ayant été des guides attentifs et passionnants. Ils resteront des modèles à suivre durant ma carrière, mais aussi sur le plan humain. Je voudrais également les remercier pour les multiples voyages auxquels j'ai pu participer grâce à leur support, ainsi que pour les divers moments partagés, depuis les parties de croquet suivies d'une raclette en plein été, aux soirées salsas dans les rues de Rio et Sao Paulo, en passant par les matches de ping-pong aux Houches ou encore les longues heures d'égarements dans Tokyo.

Je tiens évidemment à remercier tous les collègues, copains, amis avec lesquels j'ai partagé une grande partie de ces années, en tout premier lieu mes colocataires d'enfer, Cécile et Yoann, qui auront été au plus près dans les meilleurs comme dans les pires moments. J'ai une très grosse pensée pour tous les autres doctorants et postdocs du labo avec qui j'ai pu évacuer toute la pression d'une thèse à coup de pressions, Vincent ($\times$ 2), Romain, Méril, Thibault, Mathieu ($\times$ 2), Matthieu, Sami, Philippe, Marine, Daniele ($\times$ 2), Thomas, Alberto, Léo, Angela, Anne, Jill, Nina, Jordan, Cailey, Laura, Bryan, Kengo, Shankha. Un sincère et profond merci à Lena qui m'aura tant apporté durant ma difficile dernière année. Et un hommage tout particulier à notre éphémère (mais intense!) groupe de rock, les Dock'ers. Enfin, un grand merci aux cracs de l'informatique Mathieu et Pierre qui m'auront évité de vivre un enfer durant ma thèse.

I also want to thank deeply my non-German friends from Germany Thejs, Deanna, Christian, Anagha as well as the German ones, Jan, Patrick, Lukas, Benjamin, Max, Sebastian who gave a wonderful color to the time I spent in Germany. Good luck to all of you guys !

Je ne serais pas où j'en suis sans les rencontres et les amitiés que j'ai développées pendant mes années grenobloises, en particulier les membres du plus grand groupe de Rock de tous les temps, *les Wookies* devenu *Vertige*, Anaël, Clémence et Kévin, mais aussi celui qui m'aura suivi pendant de longs périples en Allemagne et en Belgique, Séverin. Je dois beaucoup aussi à mes amis de promos Boris, Killian, Marine, Will, Thomas, Simon, Valentin et je leur souhaite à tous le meilleur et la réussite dans leur

projet. Un très grand et sincère merci à Susanne qui m'aura accompagné et soutenue intensément pendant mes deux premières années de thèse et à qui je souhaite également de s'épanouir dans son travail de chercheuse.
J'ai eu la chance de côtoyer des collègues incroyables durant ces années, qui font du LAPTh un endroit à part dans le monde universitaire et de la recherche, un grand merci à eux tous, Geneviève, Laurent, Eric (× 2), Björn, Diego, Franck, Cédric, Jean-Pierre, Patrick, Paul, Pascal, Francesca, les anciens et actuels directeurs Fawzi et Luc. Je remercie aussi sincèrement nos trois secrétaires exceptionnelles, Dominique, Virginie et Véronique pour leur aide infiniment précieuse et leur patience à mon égard.
Je voudrais remercier tout particulièrement mon directeur de thèse non-officiel, ancien professeur de master, président de Jury et avant tout une personne incroyable, Pierre Salati, qui m'aura beaucoup appris sur tous les plans, de la recherche, de l'enseignement et des qualités humaines de persévérance et d'humilité. Un très grand merci également à Aurélien Barrau, qui m'aura énormément soutenu et apporté durant mes années d'étudiant et auprès au duquel je continue à apprendre quotidiennement sur des sujets aussi variés que la philosophie de Deuleze ou les soutiens aux réfugiés de tous horizons.
Durant ces trois années j'ai eu l'opportunité de donner des cours en Licence de Physique à l'université de Savoie et je voudrais remercier chaleureusement l'équipe pédagogique exceptionnelle qui m'a encadré, en particulier Richard Taillet, dont le niveau de qualité et d'exigeance des cours restera un exemple à suivre pour moi tout au long de ma carrière, ainsi que Gilles Maurin et Damir Buskulic, pour les discussions très intéressantes que nous avons eues.
Je tiens aussi à dire un grand merci à toute les membres de la collaboration CRAC, avec lesquels j'ai partagé des moments de recherche intenses et passionnants, Marco Cirelli, Manuella Vecchi, David Maurin, Julien Lavalle, Vincent Poireau, Sylvie Lees-Rosier, Laurent Derôme.
Let me thank warmly my Jury members, Laura Lopez-Honorez, Michaël Krämer and my two referees Tracy Slatyer and Jens Chluba for their careful reading of the manuscript as well as their very constructive comments. It has been an honor to defend my Thesis before them.
Enfin, je tiens à remercier toute ma famille pour leur soutien constant depuis le début de mes études (et même bien avant l'université), en particulier mon père et ma mère, que je suis heureux de rendre fier par mon travail. Ce document est aussi une manière de leur faire partager ma passion et mon quotidien. Merci à mon cousin Antoine, à son amie Laura et à mon frère Damien d'être venus me soutenir le jour de ma soutenance, ainsi qu'à tous les autres pour leur message de soutien, Nanoue, Simon, Martina, Jo, Véro, Nathalie, Annick, Alain. J'ai une pensée émue pour les absents, partis vers d'autres horizons, qui m'ont tout autant soutenus tout au long de leur vie, Papily, Gepeto et Maya. Enfin, un grand merci à mes amis du Lycée pour m'avoir accompagné avant, pendant et après cette évènement, Charlotte, Baptiste, Thomas, Simon, Estelle, Valentine. Je vous souhaite à tous de continuer à rester au top et je suis fier de vous compter dans ma famille ou comme ami.
Ce manuscript de thèse marque la fin d'une époque formidable de ma vie, mais aussi une transition vers ce métier de chercheur en Physique qui est plus que jamais ma passion, que j'espère transmettre à travers l'enseignement, et exercer au quotidien aussi longtemps qu'il me le sera permis. Comme le dit cette citation attribuée à Niels Bohr, "*les prédictions sont très difficiles, en particulier lorsqu'elles concernent le futur*", mais si je dois avoir une pensée egocentrée, je me souhaite un futur aussi riche de rencontres, de partages et d'émotions que ceux que j'ai pu vivre durant ces dernières années.

À Annecy, le 03 octobre 2017,

Vivian Poulin

CONTENTS

GENERAL INTRODUCTION

Cosmology, which literally means *the study of the world* in Greek, is probably one of the biggest endeavors of humanity. Historically, it was associated to the deepest questions such as "why and how are we here?". Thus, before being a science, this subject was the realm of faith and religions, with many Cosmologies and Cosmogonies (*the creation of the world* in Greek) being built throughout the history of our species. Physical Cosmology, more modestly, consists of the study of the large-scale properties of the universe as a whole, such as its global composition, its dynamics, or the clustering and formation of structures in which galaxies, stars, and ultimately life appear. The transition from meta-physics to physics was made possible thanks to Albert Einstein and his theory of General Relativity [228]. However, as could be said for any branch of Physics, its evolution has known many major contributors and would deserve an entire book (at least, if not many) to be covered in a fair way. Here, rather, I want to briefly recap some key parts of this history, in order to incorporate this work also, at a very modest level, in a more global picture that started about a century ago and shall continue into the far future.

The history of Cosmology is also interesting in that it shows nicely the great synergy between theoretical and observational advances. Soon after Einstein published his theory, attempts at finding solutions to what he thought was an unsolvable equation began. In 1917, the classic work by Schwarzschild led him to the discovery of the black hole solution. The same year, in the cosmological context, De Sitter found the solution to Einstein's field equations in a Universe filled with a cosmological constant Λ and in the absence of matter $\rho = p = 0$ (today known as the De Sitter space). Friedmann in 1922 and 1924, Lemaître in 1927, with extensions by Robertson and Walker independently in 1935, reported a solution that is of most importance for us, as it is the metric solution to an homogeneous and isotropic Universe, dubbed "FLRW metric" hereafter.

At the same time, much technological progress was made, such as the development of photography and reflecting telescopes. Those allowed Hubble in 1925 to answer the big question about the extra-galactic nature of the "spiral nebulae". Improvements in spectrometric survey by Vesto M. Slipher (1917) enabled the inference of velocities of the galaxies from the Doppler shifts of their absorption lines. His major finding was that they were i) much faster than any known objects; ii) moving away from the Solar System, since their lines were *redshifted* to longer wavelengths, with stretching factor at a redshift z defined as

$$1 + z \equiv \frac{\lambda_{\rm obs}}{\lambda_{\rm emit}} \, .$$

Still, at that time people were not yet convinced that the Universe was expanding. As it is well known, Einstein himself was convinced that the Universe was static, which led him to introduce the cosmological constant in order to counteract the natural expansion dynamic encoded in his equation. A milestone was set in 1929 by Hubble: using distance measurements of 24 galaxies (notably thanks to Cepheid variability, absolute magnitude of the brightest stars and the mean luminosities of nebulae in the Virgo cluster), he established his famous relation encoding the fact that galaxies are recessing faster the further away from us they are,

$$v \equiv H_0 d \, ,$$

with H_0's original value of about 500 km/s/Mpc. This was considered as the first convincing proof of the Universe expansion, leading Einstein to call the introduction of the cosmological constant "his biggest blunder" according to Gamow (1970).
The first evidence for Dark Matter in our Universe came soon. This term was introduced already in 1922 by J. Kapteyn in his paper *First attempt at a theory of the arrangement and motion of the sidereal system* [359], in which he understood that inclusion of dark matter was necessary in order to explain the rotating motions of stars. However, he thought at that time that this dark matter would represent a subdominant fraction of the total mass. What is commonly presented as the first convincing evidence for Dark Matter was introduced shortly after. In his seminal papers of 1933, *Die rotverschiebung von extragalaktischen Nebeln* [610] and 1937, *On the Masses of Nebulae and of Clusters of Nebulae* [611], Fritz Zwicky estimated the total mass of the Coma cluster assuming it to be mechanically stable such that the virial theorem holds. The theorem relates the time-averaged total internal kinetic energy of the galaxies in a cluster to its self-gravitational potential energy. Assuming the galaxies within the cluster to be distributed homogeneously inside a sphere of radius R, he found

$$M = \frac{5R\langle v^2\rangle}{3G}$$

where $G = 6.708 \cdot 10^{-45}\text{MeV}^{-2}$.

Measuring the velocity dispersion of the galaxies in the Coma cluster, Zwicky established that the ratio of the cluster mass extracted from virial theorem to the luminous mass was about 500, whereas in a typical galaxy like ours J. Kapteyn found this value to be closer to 3. These results led him to conclude that there could be about 100 times more dark or hidden matter as compared to visible matter in the cluster. With time, this number has been decreased by about one order of magnitude, but still, all studied clusters have led to the similar conclusion that most of the matter in the Universe must be invisible. Other probes, such as gravitational lensing, galaxy rotation curves, cosmological structure formation and the cosmic microwave background have brought a wealth of convincing evidence for this dark matter on very different scales, from galaxies to the whole observable Universe.
In the 30's, it was realised that the abundances of cosmic light elements could not be explained by star nucleosynthesis. In 1931, Lemaître suggested the existence of a very hot phase at the beginning of the Universe, which he named "primaeval atom". Shortly after, George Gamow's extended upon his idea and, extrapolating Friedman's universe to very early times, found that: i) densities and temperature were sufficient for nucleosynthesis to happen; ii) the time scale for reaching equilibrium was such that formation of a relic abundance of primordial nuclei would occur. The first computation of this relic abundance was done by Alpher, Bethe and Gamow - the $\alpha\beta\gamma$ paper of 1948 [44]. Alpher and Hermann in 1948 [45] improved upon this computation by taking into account the Universe expansion, finding that at that epoch the Universe must have been radiation - and not matter - dominated. They predicted the presence of a thermal blackbody spectrum of photons as a remnant of the early hot phases of the universe, at a temperature of about 5 K.
At that time, the expanding Universe picture had many detractors. Hermann Bondi, Thomas Gold and Fred Hoyle in 1948 pioneered steady state cosmology by extending the cosmological principle of spatial homogeneity and isotropy to the *perfect cosmological principle*, stating that all observers should observe the same large-scale Universe *at all time* [113], [318]. Fred Hoyle in the late 1940's during a radio show introduced the term "Big Bang" to denigrate the evolving Universe model, which has the serious issue of having a singularity at the origin, absent in his steady-state model. In 1965, the accidental discovery of the remnant radiation - the so-called *Cosmic Microwave Background* - by

Penzias and Wilson [476] provided strong evidence for what is now known as the Big Bang cosmology. They were awarded the Nobel prize in 1978 for this discovery. This radiation has been studied intensively afterwards. The most recent measurement of its energy spectrum has been performed thanks to the Firas instrument, onboard the COBE satellite in 1996 [246]. It is the most perfect blackbody ever detected with a temperature of $T_0 = 2.7255 \pm 0.0006$ K, in every direction of the sky. For this outstanding measurement, George F. Smoot and John C. Mather received the Nobel prize in 2006. Quickly, it was understood that tiny deviations from a perfect blackbody are actually expected even within Big Bang cosmology [606], leading to the development of the physics of spectral distortions of the CMB blackbody spectrum, that will be detailed later in this work.

However, the temperature of the blackbody turned out to show very slight anisotropies depending on the direction of the sky at which one looks, at the level of $\Delta T/T \sim 10^{-5}$. These small deviations from perfect isotropy, believed to be the seeds of galaxies, have been measured with increasing precision up to very small angular scales since COBE by balloon experiments BOOMERANG [450] and MAXIMA [289], followed by the *WMAP* satellite (first data release in 2003 [562]) and in the very last years by the *Planck* satellite (first data release in 2013 [17]). The link between temperature fluctuations and galaxy seeds has been proved very recently with the measurements of the *Baryonic Acoustic Oscillation* by the Sloan Digital Sky Survey (SDSS) [229]. The physics of these temperature fluctuations and density perturbations is now very well understood and will be discussed in great details in this work as well.

The most recent history is also made of other major discoveries. In 1998, by analyzing supernovae Ia data, which are thought to be good "standard candles" for measuring distances in our Universe, the Supernova Cosmology Project led by Saul Perlmutter, and the Supernova Search Team led by Adam Riess and Brian Schmidt found that the cosmic expansion was currently accelerating; usually attributed to a non-zero cosmological constant that one can also interpret dynamically as a so-called "Dark Energy" component with a negative equation of state. For this finding, later corroborated by LSS and CMB experiments, they received the Nobel prize in 2012.

However, Cosmology is not the only field of Physics with such an amount of enigmas. For instance, we know since the turn of the century and the SuperKamionkande and SNO oscillation experiments that neutrinos are not massless as it was expected, but carry a very tiny mass, with mass splittings of the order of $\sim \mathcal{O}(10 - 100)$ meV. This observation has tremendous consequences as it cannot be satisfactorily explained within the Standard Model of particle physics either. Interestingly, it is even possible to link neutrino masses to the very existence of Dark Matter. Cosmology is currently the most powerful probe of the neutrino mass. The discovery of the neutrino oscillation led Arthur. B. MacDonald and Takaaki Kajita to receive the Nobel prize in 2015.

This work tries to tackle the Dark Matter and neutrino masses puzzles, by looking for electromagnetic and gravitational signatures of peculiar massive relics in Cosmological probes that have been developed over the years. In particular, we will study the impact on i) CMB temperature and polarization anisotropies; ii) Large Scale Structure surveys; iii) Spectral distortions of the CMB blackbody spectrum; iv) and Big Bang Nucleosynthesis. After a thorough review of all necessary tools to compute those observables in chapter 1 to 3, we make use of the latest data from present experiments, and forecast the potential for detection of future ones. We focus on the purely gravitational effects of decaying massive relics in chapter 4 before switching to electromagnetic (e.m.) channels. Chapter 5 is devoted to early-time constraints due to non-thermal Big Bang nucleosynthesis induced by e.m. energy injections, while chapter 6 focuses on CMB constraints. A detailed comparison of spectral distortions, BBN, and anisotropies constraints is performed. As an example, we apply our methods to

specific models taken from the literature, including exotic particle physics models and astrophysical candidates such as Primordial Black Holes. We then study the impact of annihilating relics, with a special emphasis on annihilations in halos and its synergy with stars in reionizing our Universe. The last part of this work is devoted to the cosmological determination of neutrino properties with current and future data. Our results emphasize the complementarity of the different probes, and the need for combined analyses when looking for new physics, especially in the era of precision Cosmology.

Part I

INTRODUCTION TO PARTICLE COSMOLOGY

The first part of this Thesis is devoted to a presentation of the general features of the concordance model of cosmology, introducing all necessary tools for our studies. In chapter 1 we discuss the homogeneous and isotropic Universe, including an extended description of the process of $e^- - p$ recombination, a key era in this work. Chapter 2 is devoted to a thorough description of the evolution of small perturbations on top of this background, as well as the computation of the cosmic microwave background and matter power spectrum. Our discussion is limited to linear regime but comments on the important higher-order contributions are made, and relevant references introduced. Finally, chapter 3 introduces the broad lines of the particle physics models that are studied, i.e. models incorporating massive relics that can constitute Dark Matter and/or related to neutrino masses. A discussion on the physics of electromagnetic cascades, a fundamental process at play in many of the studied scenarii, is also developed.

1

THE STANDARD COSMOLOGICAL MODEL

1.1 General Relativity in a homogeneous and isotropic Universe

The cornerstone of the standard model of Cosmology is the so-called "Cosmological Principle": it is the assumption that the Universe is homogeneous and isotropic on sufficiently large scales, in such a way that its metric is the standard "Friedmann-Lemaitre-Robertson-Walker" one. This is illustrated in Fig. 1, where we show the temperature map of the Cosmic Microwave Background radiation as seen by the *Planck* satellite, corresponding to the largest scales we can observe. Deviations from perfect isotropy only appear at the level of 10^{-5}!

Given a certain energy-matter content, and together with the the Einstein equations, the Cosmological Principle allows one to derive how the entire Universe has evolved and will be evolving in the future. However, the homogeneous picture has its obvious limitations since it does not allow to describe both i) the formation of galaxy and galaxy clusters as well as their structures in filaments, illustrated in fig 2, and more generally the matter perturbations: in a perfectly homogeneous and isotropic universe, we would not even be here to discuss it; ii) the small temperature and polarization anisotropies of the cosmic microwave background (CMB) photons. Given a homogeneous and isotropic energy-matter field with FLRW metric, it is possible to compute perturbatively the evolution of small inhomogeneties and isotropies that live on top of this background. One first solves for the evolution of the background quantities, as we shall see in this section, neglecting back-reaction of the density and metric perturbations.

Once background quantities are known, one can solve the equations governing the evolution of the

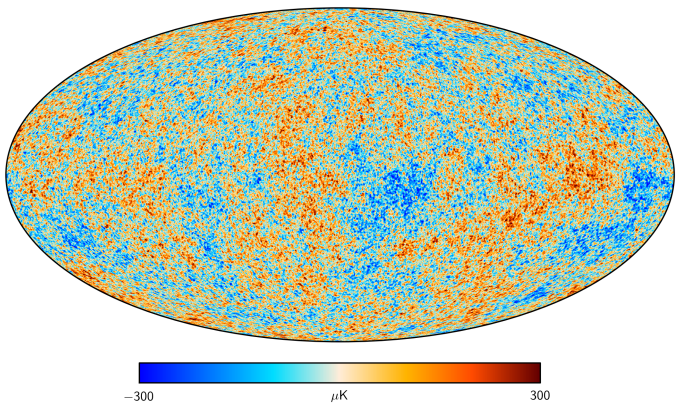

Figure 1: The CMB temperature map as it is seen by *Planck*. Taken from ESA website: *https://www.cosmos.esa.int.*

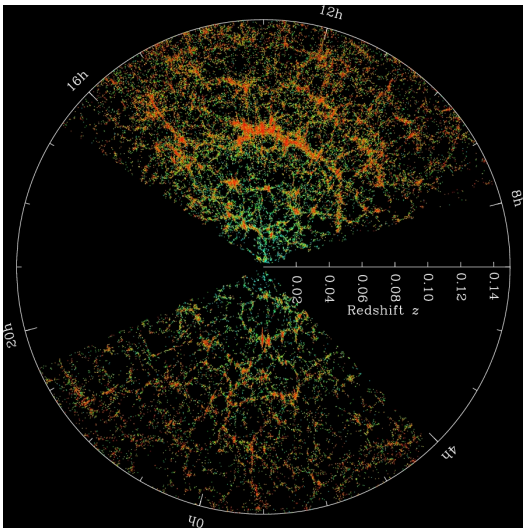

Figure 2: The SDSS's map of the Universe. Each dot is a galaxy; the color bar shows the local density. Taken from SDSS website: *http://www.sdss.org.*

perturbations, which will be introduced in sec. 2.1. We shall do it starting either from the Einstein equations and the stress-energy tensor conservation, or from the full perturbed Boltzmann equations for the phase-space density, as required for non-perfect fluids. This perturbative approach also has limitations. A standard result is that density perturbations during matter domination grow like the scale factor and eventually

$$\frac{\delta\rho}{\rho} \equiv \frac{\bar{\rho}-\rho}{\rho} > 1\,. \tag{1.1.1}$$

Hence, our assumption of small density perturbations breaks down when structure formation starts to be efficient: one needs to go to the so-called "non-linear" perturbation theory, which is, however, beyond the scope of this work, although we will comment on it. One might wonder about the importance of neglecting back-reaction in that case. This is indeed still an open problem, some authors arguing that this could even be responsible for (at least part of) the accelerated expansion in our Universe (e.g. [130] for a review). However, staying at the linear level, we shall see that the studies of matter perturbations and CMB anisotropies are still a very powerful tool in our quest for understanding the nature of DM, which shows a nice complementarity with the study of Big Bang nucleosynthesis and spectral distortions of the CMB blackbody distribution.
This recap is based on textbooks [90], [217], [389], [391], [412] and references therein, to which the reader is referred for more details. We will use *Planck* units $\hbar = c = 1$ in this work, so for brevity, those factors will not always be explicitly mentioned.

1.1.1 *Geometry of the expanding Universe*

The brilliant intuition of Einstein was to understand that gravity is not a force, in the common "Newtonian" sense, acting to modify trajectory of particles moving in flat space. On the contrary, he understood that particles are traveling freely in *curved space*, the exact geometry of which is determined by the influence of the energy density of the particles themselves. The key equation from which everything starts is the famous Einstein equation, relating the content in matter-energy at one

point of the Universe $x^\mu = (ct, x^i)$ through the tensor $T_{\mu\nu}$, to its geometrical properties at the same point encoded in the so-called Einstein tensor $G_{\mu\nu}$:

$$G_{\mu\nu} \equiv R_{\mu\nu} - \frac{1}{2}\mathcal{R}g_{\mu\nu} - \Lambda g_{\mu\nu} = 8\pi G T_{\mu\nu}\,. \tag{1.1.2}$$

This is a non-linear equation for the metric $g_{\mu\nu}$, which relates the invariant space-time interval ds^2 and the coordinates dx^μ:

$$ds^2 = g_{\mu\nu}dx^\mu dx^\nu \tag{1.1.3}$$

where Einstein's implicit sum convention has been used. The *Ricci tensor* $R_{\mu\nu}$ depends on the metric and its derivatives; as well as the *Ricci scalar* $\mathcal{R} \equiv g^{\mu\nu}R_{\mu\nu}$.
The Ricci tensor is usually expressed in terms of the *Christoffel symbol* $\Gamma^\mu_{\alpha\beta}$ as,

$$R_{\mu\nu} = \Gamma^\alpha_{\mu\nu,\alpha} - \Gamma^\alpha_{\mu\alpha,\nu} + \Gamma^\alpha_{\beta\alpha}\Gamma^\beta_{\mu\nu} - \Gamma^\alpha_{\beta\nu}\Gamma^\beta_{\mu\alpha} \quad , \tag{1.1.4}$$

where the Christoffel symbols $\Gamma^\mu_{\alpha\beta}$ are related to derivatives of the metric through the identity,

$$\Gamma^\mu_{\alpha\beta} = \frac{g^{\mu\nu}}{2}\left[g_{\alpha\nu,\beta} + g_{\beta\nu,\alpha} - g_{\alpha\beta,\nu}\right]. \tag{1.1.5}$$

Here, commas mean derivatives with respect to x.
The question now is: what is the metric of our Universe? Following the cosmological principal means that our Universe can be represented by a time-ordered sequence of three-dimensional spatial slices, each of which is homogeneous and isotropic. In this case, the most general form of the metric is the FLRW solution that can be expressed in polar comoving coordinates and physical time:

$$ds^2 = g_{\mu\nu}dx^\mu dx^\nu = dt^2 - a(t)^2\left[\frac{dr^2}{1-kr^2} + r^2 d\theta^2 + r^2\sin^2\theta d\phi^2\right]. \tag{1.1.6}$$

Remarkably, the metric depends only on one time-dependent parameter, namely the *scale factor* $a(t)$, and a normalized constant spatial 3-curvature k, which can only take values 1,-1 or 0 for elliptical, hyperbolic and euclidian (sometimes loosely dubbed *flat*) geometry respectively, as enforced by the homogeneous and isotropic 3-spaces.
The physical coordinates $x^i_{\rm phys}$ are related to the comoving ones via $x^i_{\rm phys} = a(t)x^i$, and the physical velocities are thus:

$$v^i_{\rm phys} \equiv \frac{dx^i_{\rm phys}}{dt} = v^i_{\rm pec} + Hx^i_{\rm phys}\,. \tag{1.1.7}$$

It has two parts: the peculiar velocity $v^i_{\rm pec}$ and the *Hubble flow* $Hx^i_{\rm phys}$, where H is the usual Hubble parameter defined as $H \equiv \dot{a}/a$. One can see that we simply find again the law already introduced by Hubble in 1929. Similarly, if we arbitrarily normalize the scale factor to 1 at present time, we can re-introduce the redshift as

$$1 + z \equiv \frac{\{a(t_0) = 1\}}{a} \tag{1.1.8}$$

since wavelengths are stretched with the Universe's expansion as well. Introducing conformal time

$$\tau = \int \frac{dt}{a(t)} \tag{1.1.9}$$

to which we shall give some meaningful sense later, one can rewrite the former metric in the nice way:

$$ds^2 = a(t)^2\left(d\tau^2 - \left[\frac{dr^2}{1-kr^2} + r^2 d\Theta^2 + r^2\sin^2\Theta d\phi^2\right]\right). \tag{1.1.10}$$

The second key equation, equivalent to "$F = ma$" in Newtonian physics, is the *geodesic equation*. The starting point is to impose the parallel transport of a freely falling partice in a given spacetime metric with four velocity

$$U^\mu = \frac{dx^\mu}{d\lambda} \tag{1.1.11}$$

where λ is a monotonically increasing variable along the particle's path.
It yields the following equation:

$$\frac{dU^\mu}{d\lambda} + \Gamma^\mu_{\alpha\beta} U^\alpha U^\beta = 0\,. \tag{1.1.12}$$

Note that it is possible to rewrite this equation in a more practical way since:

$$\frac{d}{d\lambda} U^\mu(x^\alpha(\lambda)) = U^\alpha \frac{\partial U^\mu}{\partial x^\alpha} \Rightarrow U^\alpha \left(\frac{\partial U^\mu}{\partial x^\alpha} + \Gamma^\mu_{\alpha\beta} U^\alpha U^\beta \right) = 0 \tag{1.1.13}$$

It is standard to introduce the energy-momentum 4-vector $P^\mu = mU^\mu$, which verifies the "on-shell" condition $P^2 \equiv g_{\mu\nu} P^\mu P^\nu = m^2$ for a massive particle (0 for a massless one with energy-momentum 4-vector now defined as $P^\mu = (E, P^i)$). One can thus rewrite eq. (1.1.12):

$$P^\alpha \frac{\partial P^\mu}{\partial x^\alpha} + \Gamma^\mu_{\alpha\beta} P^\alpha P^\beta = 0\,. \tag{1.1.14}$$

Furthermore, for a homogeneous FLRW background, $\partial_i P^\mu = 0$ hence one finds that P^μ satisfies the following geodesic equation:

$$P^0 \frac{dP^\mu}{dt} + \Gamma^\mu_{\alpha\beta} P^\alpha P^\beta = 0\,. \tag{1.1.15}$$

For a homogeneous and isotropic fluid, described by the FLRW metric, the physical energy and momentum measured by comoving observers are

$$E = P^0, \quad p^i = aP^i \quad , \tag{1.1.16}$$

Combining the geodesic equation and the on-shell condition leads to the standard result that:

- For massless particles, $p = E \propto \frac{1}{a}$,
- For massive particles, $p = \frac{mv}{\sqrt{1-v^2}} \propto \frac{1}{a}$,

where v^2 is the magnitude of the physical peculiar velocity.

1.1.2 *Dynamics of the expanding Universe*

1.1.2.1 *The continuity equation*

The last fundamental quantity that has not been developed further is the stress-energy tensor on the right-hand side (RHS) of eq. (1.1.2). Before considering perturbations with it, we will assume that each species can be described as a perfect isotropic fluid. For such a species, the stress-energy tensor is given by

$$T^\mu_{\ \nu} = (\rho + \mathcal{P}) U^\mu U_\nu - \mathcal{P} g^\mu_{\ \nu}\,, \tag{1.1.17}$$

where ρ is the density of the fluid and $\mathcal{P}$ its pressure. If the fluid has 0 velocity in the comoving frame, $U_\mu = dx^\mu/dt = (1, \vec{0}) = \delta^0{}_\mu$ or in conformal time $U_\mu = a^{-1}\delta^0{}_\mu$, the stress-energy tensor is also commonly written as:

$$T^\mu{}_\nu = \mathrm{diag}(\rho, -\mathcal{P}, -\mathcal{P}, -\mathcal{P})\,. \tag{1.1.18}$$

Quite interestingly, it is possible to add the cosmological constant directly inside the stress energy-tensor as

$$T^\lambda_{\mu\nu} = \frac{\Lambda}{8\pi G} g_{\mu\nu}\,, \tag{1.1.19}$$

where it is now interpreted as a new *dark energy* fluid with $\rho_\Lambda = \Lambda 8\pi G = -\mathcal{P}_\Lambda$. Historically, it was understood as a the energy/pressure of the vacuum itself, as predicted by quantum field theory. However, the predicted vacuum energy density is off by about 120 orders of magnitude!! Such a discrepancy still remains to be solved, and it could point to exotic physics or modifications of GR.
The conservation criterion in a expanding universe, following Bianchi identities, implies the vanishing of the *covariant* derivative,

$$T^\mu_{\nu;\mu} \equiv T^\mu_{\nu,\mu} + \Gamma^\mu_{\alpha\mu} T^\alpha{}_\nu - \Gamma^\alpha_{\nu\mu} T^\mu{}_\alpha \quad . \tag{1.1.20}$$

It is four separate equations which for $\nu = 0$ yields the continuity equation,

$$\frac{\partial\rho}{\partial t} + 3\frac{\dot{a}}{a}[\rho + \mathcal{P}] = 0 \tag{1.1.21}$$

$$\Leftrightarrow a^{-3}\frac{\partial[\rho a^3]}{\partial t} = -3\frac{\dot{a}}{a}\mathcal{P} \tag{1.1.22}$$

and for $\nu = i$ the Euler equation (conservation of momentum, vanishing at zeroth order for a homogeneous background). We shall see a more general form of the stress-energy tensor in sec. 1.3.
In order to close the system of equations, one needs to postulate an equation of state, i.e. an equation relating the "state variables" pressure and density, which in the case of a perfect fluid can be written as:

$$\mathcal{P} = w\rho. \tag{1.1.23}$$

From eq. (B.1.64), this means that

$$a^{-3}\frac{\partial[\rho a^3]}{\partial t} = -3\frac{\dot{a}}{a}\omega\rho \quad \Rightarrow \rho \propto a^{-3(1+\omega)}\,. \tag{1.1.24}$$

Typically, non-relativistic particles (i.e. particles whose energy density is dominated by their mass) such as baryons and dark matter have negligible pressure, $w \simeq 0$, meaning $\rho \propto a^{-3}$. On the other hand, relativistic species such as photons and neutrinos before their non-relativistic transition have $w \simeq 1/3$, leading to $\rho \propto a^{-4}$. Finally, by comparing $T^\Lambda_{\mu\nu}$ and eq. (1.1.18), one can see that the equation of state for vacuum energy is $w = -1$, yielding indeed $\rho = \text{const}$. More exotic physics, for instance a scalar field evolution, could result in a time-varying equation of state. This will be extensively studied by the next generation LSS such as Euclid and LSST.

1.1.2.2 *Friedmann-Lemaître equations*

We now want an equation for the evolution of the scale factor. This is obtained by considering the only non-zero components of the Einstein eq. (1.1.2), namely $\mu = \nu = 0$ and $\mu = \nu = i$. The (00) component is:

$$G_{00} \equiv 3\left[\frac{k}{a^2} + \left(\frac{\dot{a}}{a}\right)^2\right] = 8\pi G\Big\{T_{00} = \rho + \rho_\Lambda\Big\}\,, \tag{1.1.25}$$

which can be rewritten as

$$H^2 \equiv \left(\frac{\dot{a}}{a}\right)^2 = \frac{8\pi G}{3}\rho - \frac{k}{a^2} + \frac{\Lambda}{3} \quad .$$

where, from now on, $\cdot$ represents derivatives with respect to proper time t and $'$ will denote derivatives with respect to conformal time η defined in eq. (1.1.9). It is common to express this in terms of the *critical density today*, i.e. the density of a flat universe ($k = 0$) today

$$\rho_{\text{crit},0} = \frac{3H_0^2}{8\pi G} = 1.9 \times 10^{-29} h^2 \text{ g cm}^{-3} \tag{1.1.26}$$

where the dimensionless parameter h has been introduced as

$$H_0 \equiv 100\ h \text{ km sec}^{-1} \text{ Mpc}^{-1}\,. \tag{1.1.27}$$

The reduced Hubble parameter h is nowadays measured to be very close to 0.7. We define the dimensionless density parameters

$$\Omega_I \equiv \frac{\rho_{I,0}}{\rho_{\text{crit},0}} \qquad \Omega_\Lambda \equiv \frac{\Lambda}{3H_0^2} \qquad \Omega_k \equiv -\frac{k}{H_0^2 a^2} \tag{1.1.28}$$

which verify

$$\Omega_{\text{tot}} \equiv \{\Omega_r \equiv \Omega_\gamma + \Omega_\nu\} + \{\Omega_M \equiv \Omega_b + \Omega_{\text{cdm}}\} + \Omega_\Lambda = 1 - \Omega_k\,. \tag{1.1.29}$$

This parametrization allows one to write eq. (1.1.26) as

$$H^2(a) = H_0^2\left[\Omega_r a^{-4} + \Omega_M a^{-3} + \Omega_k a^{-2} + \Omega_\Lambda\right]. \tag{1.1.30}$$

For a Universe dominated by one of its components this equation can be readily integrated to give:

$$a(t) \propto \begin{cases} t^{\frac{2}{3(1+w)}} & w \neq -1 \\ e^{Ht} & w = -1 \end{cases} \tag{1.1.31}$$

Capital Ω's represent the relative abundance of each fluid in the universe today. The physical density of each species s, in units of the critical density today, is usually defined in the following way

$$\omega_{\text{s}} \equiv \Omega_{\text{s}} h^2\,, \tag{1.1.32}$$

which allows one to rewrite eq. (1.1.26) in yet another form:

$$H^2(a) = 100\left[\omega_r a^{-4} + \omega_M a^{-3} + \omega_k a^{-2} + \omega_\Lambda\right]. \tag{1.1.33}$$

Anticipating a bit for the next chapter, we mention that the proportion of each fluid in our Universe has been measured very precisely nowadays. They have been found to be:

$$\Omega_\Lambda = 0.69, \quad \Omega_M = 0.31, \quad \Omega_b = 0.05, \quad \Omega_\gamma = 5.38 \times 10^{-5}, \quad \Omega_\nu \leq 0.016, \quad \Omega_k \leq 0.021\,. \tag{1.1.34}$$

From the measurement of Ω_M and Ω_b it is possible to deduce that about 90% of the matter content today is in the form of cold dark matter (CDM). Cosmology thus constitutes one of the best indicators for the presence of CDM. We develop on this measurement in chapter 2 and in chapter 3.
Two very important eras in this study are the time of *matter-radiation* and *matter*-Λ equality. As we

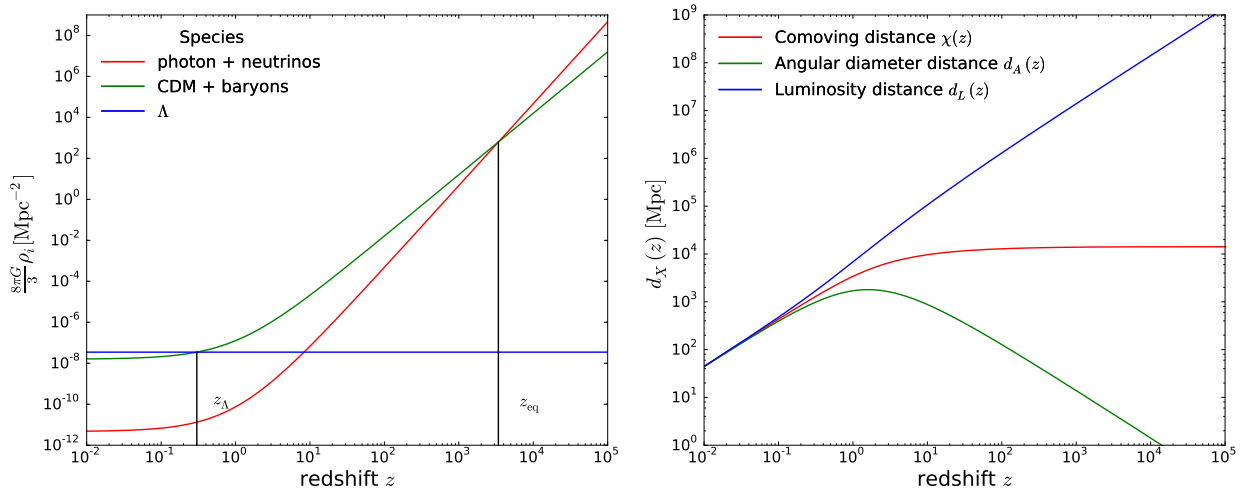

Figure 3: The evolution of the species densities (left panel) and distances (right panel) in the Universe using the best-fit parameters from *Planck* [19]. The redshifts of matter-radiation equality and Λ-matter equality are also shown.

will see later, the change in the time-evolution of the expansion rate will induce a time-evolution of the gravitational potential wells which are of utmost importance for the generation of CMB temperature anisotropies. Matter-radiation equality happened at:

$$\Omega_r h^2 a_{\rm eq}^{-4} \stackrel{!}{=} \Omega_M h^2 a_{\rm eq}^{-3} \;\Leftrightarrow a_{\rm eq}^{-1} = \frac{\Omega_M}{\Omega_r} \;\Leftrightarrow 1 + z_{\rm eq} = 2.4 \times 10^4 \Omega_M h^2 \simeq 3440\,, \tag{1.1.35}$$

whereas matter-Λ equality occurred around:

$$\Omega_M h^2 a_\Lambda^{-3} = \Omega_\Lambda h^2 \;\Leftrightarrow a_\Lambda^{-1} = \left(\frac{\Omega_\Lambda}{\Omega_M}\right)^{1/3} \;\Leftrightarrow 1 + z_\Lambda \simeq 1.3\,. \tag{1.1.36}$$

The (ii) component of the Einstein equation, combined with the continuity eq. (B.1.64), leads to the "acceleration equation":

$$\begin{aligned} G_{ii} = \left[2\frac{\ddot{a}}{a} + \left(\frac{\dot{a}}{a}\right)^2 + \frac{k}{a^2}\right] &= 8\pi G\Big\{T_{ii} = -\mathcal{P} + \Lambda\Big\} \\ \Leftrightarrow \frac{\ddot{a}}{a} &= -\frac{4\pi G}{3}[\rho - 3\mathcal{P}] + \frac{\Lambda}{3} \quad . \end{aligned} \tag{1.1.37}$$

This equation indicates that the Universe's expansion is adiabatic, i.e. that the total entropy is constant, and we shall come back to that later. Introducing the *deceleration parameter* q as:

$$q = -\frac{\ddot{a}}{a}\frac{1}{H_0^2}\,, \tag{1.1.38}$$

one can write former equation as

$$q = \frac{\Omega_{\rm tot}}{2}\Big(1 + 3w_{\rm tot}\Big)\,, \tag{1.1.39}$$

where $w_{\rm tot} \equiv \sum_s P_s / \sum_s \rho_s$. Those constitute the well-known Friedmann-Lemaître equations governing the expansion of the Universe.

1.1.3 *Distances in our Universe*

In an expanding Universe, such as the one of GR, the notion of distance can be somewhat trickier than the everyday life definition. The first distance that one can introduce is the *comoving distance* traveled by photons between a distant object emitting them from $(t_e, r_e, \theta_e, \phi_e)$ and us, which remains fixed as the universe expands. It has the form:

$$\chi(r) = \int_0^{r_e} \frac{dr}{\sqrt{1-kr^2}} \tag{1.1.40}$$

which can readily be integrated to give

$$\chi(r) = \begin{cases} \sin^{-1}(r) & \text{if} \quad k=1 \\ r & \text{if} \quad k=0 \\ \sinh^{-1}(r) & \text{if} \quad k=-1 \end{cases} \tag{1.1.41}$$

Note that by using $ds^2 = 0$ for photons, one can rewrite it as

$$\chi(z) = \int_{t_e}^{t_0} \frac{dt}{a(t)} = \int_{a(t_e)}^{a(t_0)} \frac{da}{a^2 H(a)} = \int_0^{z(t_e)} \frac{dz}{H(z)} \tag{1.1.42}$$

and we can relate it to eq. (1.1.9) for $t_e = 0$, in which case it has been dubbed conformal time. The evolution of the Hubble rate with redshift $H(z)$ is related to the matter content of the Universe through Friedmann eq. (1.1.30). This is a fundamental distance, as it is the maximum distance that can have been crossed since the beginning of time, and thus plays the role of a *comoving horizon*. For geodesics corresponding to propagation along the radial direction (i.e. fixed ϕ and θ) we have $d\chi = dr/\sqrt{1-kr^2}$, and it is useful to rewrite the FLRW metric as

$$ds^2 = g_\mu \nu dx^\mu dx^\nu = dt^2 - a^2(t)\left[d\chi^2 + r^2(\chi)(d\theta^2 + sin^2\theta d\phi^2\right] \tag{1.1.43}$$

where the function $r^2(\chi)$ is

$$r^2(\chi) = \begin{cases} \sinh^2\chi & \text{if} \quad k=1 \\ \chi^2 & \text{if} \quad k=0 \\ \sin^2\chi & \text{if} \quad k=-1 \end{cases} \tag{1.1.44}$$

A second very important distance enters the definition of the observed flux F emitted by an object with known luminosity L (or "standard candle") at a comoving distance χ. Assuming isotropy, from conservation of the luminosity passing through a spherical shell of radius d_L, one simply gets that the flux is given by:

$$F = \frac{L}{4\pi d_L(a)^2} \tag{1.1.45}$$

Considering now that the Universe's expansion will affect both the wavelength (or energy) of the emitted photons and the distance that they have to cross by a factor a, the observed flux will thus be:

$$F = \frac{La^2}{4\pi\chi(a)^2}\,. \tag{1.1.46}$$

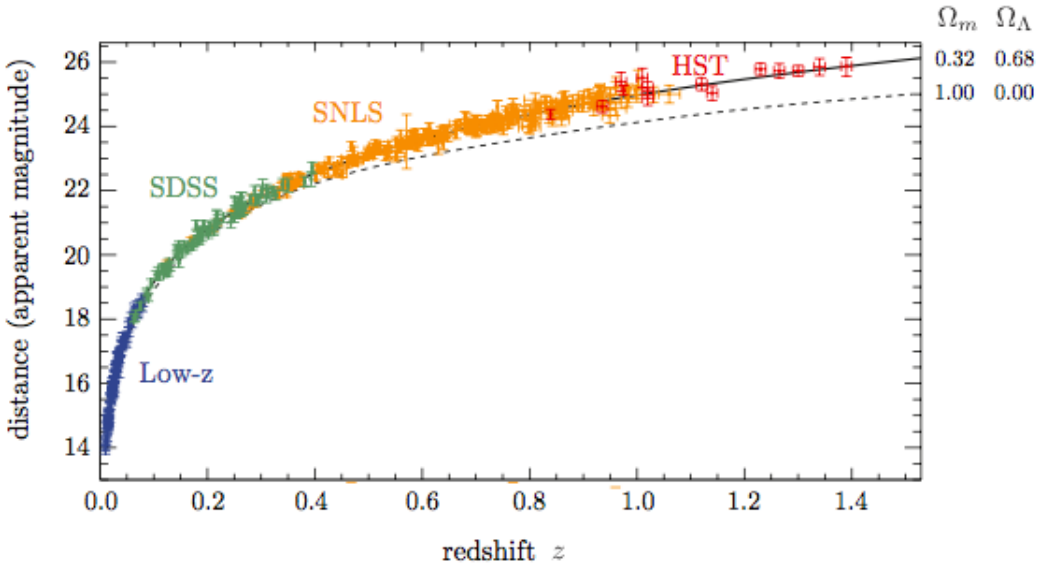

Figure 4: The Hubble diagram constructed from the observations of SNIa. The unit on the left axis is directly related to the measured flux, and thus to the luminosity distance assuming the intrinsic luminosity of the source is known. Taken from ref. [90].

Hence, the *luminosity distance* d_L is defined as:

$$d_L = \frac{\chi(a)}{a} = \chi(z)(1+z)\,. \tag{1.1.47}$$

Supernovae Ia (SNIa) are, for instance, such standard candles. If on top of the luminosity distance, the redshift of the source is known (e.g. from spectral lines or information on the host of the SNIa), one can construct a SNIa *Hubble diagram* (d_L vs z), as represented in fig. 4, and try to adjust this relation assuming a given energy content. It is possible to extract the expansion rate and the proportion of the different species today from such analysis. As mentioned in the introduction, it is the study of such a diagram that has led to the discovery of the accelerated expansion in our Universe.

A last distance we need to introduce is very useful when one disposes of a "standard ruler", i.e. an object of known intrinsic size D. One can decide to measure its angular size $\delta\theta$, and assuming it to fulfill $\delta\theta \ll 1$, we can introduce the angular diameter distance of that object as

$$d_A = \frac{D}{\delta\theta}\,. \tag{1.1.48}$$

The comoving size of the object is simply D/a, so the comoving distance to the object is $\chi(a) = D/(a\delta\theta)$. Thus, the angular diameter distance can be related to the comoving distance by:

$$d_A = a\chi(a) = \frac{\chi(z)}{(1+z)} \tag{1.1.49}$$

which also implies the relation $d_A = a^2 d_L$. This distance will be of major interest in this work, as the typical size of CMB fluctuations (also known as sound horizon at decoupling) can be computed from first principles.

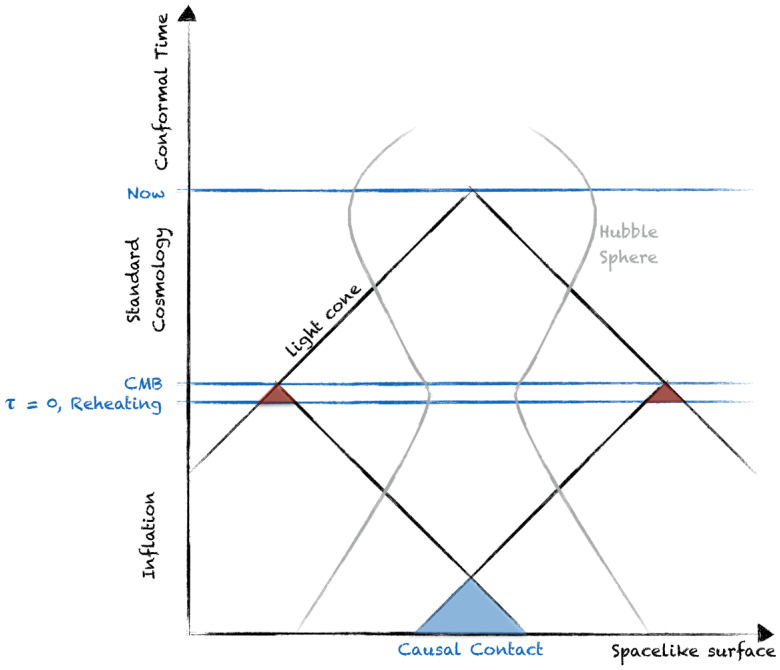

Figure 5: Illustration of the *Horizon Problem* in standard cosmology and its inflationary solution. Adapted from Ref. [90].

1.2 Inflation in a nutshell

We now wish to introduce the *Inflation mechanism*, i.e. a phase of accelerated expansion in the early universe, necessary to solve several puzzles of the standard cosmological models, and able to explain the origin of fluctuations that we shall describe later on. This section is mostly based on lectures notes [89], [90].

1.2.1 *Original motivations for Inflation*

1.2.1.1 *The Horizon Problem*

It was soon realized that the FLRW Cosmology could not be complete. Indeed, it is based on the hypothesis of isotropy and homogeneity of the Universe on large scales, which is well confirmed by observations (for instance, the temperature varies only at the $\mathcal{O}(10^{-5})$ level everywhere in the sky). However, it is necessary to make sure that different parts of the sky could have been in causal contact far in the past in order to thermalize, which raises a conceptual problem: the size of a causal patch is nothing but the distance that light can travel in a certain amount of time. It is given by eq. (1.1.42). The maximum distance that can be traveled by light since the beginning of time has already been introduced before: it is nothing but the definition of conformal time (in units with $c = 1$), sometimes dubbed (comoving) *particle horizon*. The size of the causal region at a given time τ is thus given by the intersection of the past light cone of a given observer with the spacelike surface $\tau = \tau_i$. This leads to a fundamental problem in the standard model, which is known as the *Horizon problem*, represented in fig. 5: The finiteness of the conformal time between $t_i = 0$ and the time of CMB decoupling $t_{\rm dec}$

implies that most spots in the CMB *cannot* be in thermal contact. Indeed, light cones of distant points in space (straight 45° line in the space-time diagram) do not cross, and their causal regions, represented in red in fig. 5 in the context of standard cosmology, do not overlap. Let us now see how one can solve this puzzle with inflation.
It is possible to rewrite eq. (1.1.9) in an illuminating way

$$\tau = \int_0^t \frac{dt}{a(t)} = \int_{a_i \equiv 0}^{a} \frac{da}{a\dot{a}} = \int_{\ln a_i}^{\ln a} \mathcal{H}^{-1} d\ln a \,. \tag{1.2.1}$$

In other words, the causal structure of spacetime can be related to $\mathcal{H}^{-1} = (aH)^{-1}$, the comoving Hubble radius. As before, we consider a Universe dominated by a given fluid with constant equation of state $w \equiv \mathcal{P}/\rho$. Hence,

$$\mathcal{H}^{-1} = H_0^{-1} a^{\frac{1}{2}(1+3w)} \,. \tag{1.2.2}$$

All standard forms of matter satisfy the *strong energy condition* (SEC), $1 + 3w > 0$, which results in an *increasing* comoving Hubble radius as the universe expands, and conversely if we go back in time, the comoving Hubble radius was smaller and smaller [1]. To solve the issue we need to postulate a phase of *decreasing Hubble radius* in the early universe

$$\frac{d}{dt}\mathcal{H}^{-1} < 0 \,, \tag{1.2.3}$$

which can be obtained only if the SEC is violated, $1 + 3w < 0$. Now comes an important point: In writing eq. (1.2.1), we have implicitly assumed that at $a_i = 0$ (or $t_i = 0$), conformal time τ_i goes to 0 as well. It can be easily checked that this is indeed the case as long as the SEC is verified, by slightly generalizing eq. (1.2.1) in trading the lower integration bound for τ_i defined as

$$\tau_i \equiv \frac{2H_0^{-1}}{(1+3w)} a_i^{\frac{1}{2}(1+3w)} \to 0 \qquad \text{if } a_i \to 0,\ w > -\frac{1}{3} \,. \tag{1.2.4}$$

However, once the SEC is violated, one can quickly realize that the Big Bang singularity is pushed to negative conformal time

$$\tau_i \equiv \frac{2H_0^{-1}}{(1+3w)} a_i^{\frac{1}{2}(1+3w)} \to -\infty \qquad \text{if } a_i \to 0,\ w < -\frac{1}{3} \,. \tag{1.2.5}$$

In practice, there is much more conformal time than previously thought between the singularity and decoupling, as illustrated in fig. 5. The point $\tau = 0$ has now become a transition point between inflation and the standard Big Bang evolution, which corresponds to the phase of "reheating", as we will see. We can now give more sense to fig. 25. At early times, before inflation, all scales of interest were deep inside the Hubble radius, and therefore able to interact. During inflation, the Hubble radius decreases. Hence, scales exit the Hubble radius, meaning that they cannot communicate. When standard cosmology takes over, the Hubble radius increases again, and modes can reenter it.

1.2.1.2 *The flatness problem*

Another historical problem associated to the standard Big Bang model is related to the smallness of the spatial curvature Ω_k. The *Planck* satellite, for instance, indicates that $|1 - \Omega_k| < 10^{-2}$ [19]. Should

1 We can readily perform integration of eq. (1.2.1) to get $\tau = \frac{2}{(1+3w)}\mathcal{H}^{-1}$. In standard cosmology, it is common to trade the word "particle Horizon" for "Hubble radius", although their rigorous equality is only true for photons.

we be surprised by this very small value? Let us consider the Friedmann equation with curvature but no cosmological constant, eq. (1.1.30). Dividing both sides by the Hubble parameter, we can write

$$\Omega(a) = 1 - \Omega_k(a) \qquad \text{with} \qquad \Omega(a) \equiv \frac{\rho(a)}{\rho_{\rm crit}}\,, \quad \Omega_k(a) \equiv -\frac{k}{a^2H^2}\,. \tag{1.2.6}$$

This implies

$$\frac{d\Omega}{dt} = -2\frac{k}{a^2H^2}\left\{\frac{\dot a}{a} + \frac{\dot H}{H}\right\} = -2\Omega_k H\left\{1 + \frac{\dot H}{H^2}\right\} = -2\Omega_k H(1-\varepsilon) \tag{1.2.7}$$

where the parameter $\varepsilon \equiv -\frac{\dot H}{H^2}$ has been defined.The Friedmann equation (1.1.26) and the continuity equation (B.1.64) can be combined to obtain

$$\varepsilon = -\frac{\dot H}{H^2} = \frac{3}{2}\left(1 + \frac{\mathcal{P}}{\rho}\right) = \frac{3}{2}\left(1 + w\right) \tag{1.2.8}$$

For standard matter $w > 0$ and therefore $\varepsilon > 1$, as we have already stated. This implies that $d\Omega_k/dt > 0$. Therefore, *if we start away from null curvature, it will increase with time*! To get such a tiny fraction of curvature, one would need to start at early times with $|1 - \Omega_k| < 10^{-55}$. It is really hard to believe that this was the case by the virtue of initial conditions. However, we see that when $w < 1/3$, i.e. when the SEC is violated, $\frac{d\Omega}{dt}$ becomes negative: the solution with null curvature at late time is an attractor, which is much more satisfying form the conceptual point of view.

1.2.1.3 *Conditions for successful Inflation*

The first important comment to make is that the shrinking Hubble sphere implies *accelerated expansion*:

$$\frac{d}{dt}\mathcal{H}^{-1} = \frac{d}{dt}(aH)^{-1} = \frac{d}{dt}(\dot a)^{-1} = \frac{\ddot a}{\dot a^2} \tag{1.2.9}$$

$$\frac{d}{dt}\mathcal{H}^{-1} < 0 \qquad \Rightarrow \qquad \ddot a > 0\,. \tag{1.2.10}$$

We have already stated that it corresponds to a situation where $\varepsilon = -\dot H/H^2 < 1$, which requires a small value of $\dot H$ or a *slowly varying Hubble parameter*. Perfect inflation corresponds to $\varepsilon = 0$, in which case the spacetime metric becomes the historical *De Sitter space*

$$ds^2 = dt^2 - e^{2Ht}d\vec{x}^2 \tag{1.2.11}$$

where $H = const.$ A small but finite $\varepsilon \neq 0$ is required in order for inflation to end. However, this line element is still a good approximation, which is why inflation is often dubbed *quasi-de Sitter period*. The parameter ε is often rewritten as

$$\varepsilon = \frac{\dot H}{H^2} = -\frac{d\ln H}{dN} \qquad \text{where} \quad dN \equiv d\ln a = Hdt\,. \tag{1.2.12}$$

N measures the number of e-folds of inflation, i.e. the number of times a increase by a factor e. How many e-folds of inflation do we need? At the very least, modes that are observable today should fit inside the comoving Hubble radius at the beginning of inflation, i.e.

$$\mathcal{H}_0^{-1} < \mathcal{H}_I^{-1}\,. \tag{1.2.13}$$

Assuming a radiation dominated universe ($\mathcal{H} = aH \propto a^{-1}$) since the end of inflation for a simple estimate, one obtains

$$\frac{\mathcal{H}_0}{\mathcal{H}_E} = \frac{a_E}{a_0} \sim \frac{T_0}{T_E}\,. \tag{1.2.14}$$

The temperature at the end of inflation T_E is unknown. Historically, values considered were of order $T_E \sim 10^{15}$ GeV, which corresponds to the energy scale of Grand Unified Theory (we comment a bit on this in chapter 3). However, the only real lower constraints come from the requirement of a successful BBN i.e. $T_E > \mathcal{O}(10)$ MeV. Sticking to the historical estimate $T_E \sim 10^{15}$ GeV, while $T_0 \sim 10^{-4}$ eV, we can write

$$\mathcal{H}_I^{-1} > \mathcal{H}_E^{-1} \sim 10^{28}\mathcal{H}_E^{-1}\,. \tag{1.2.15}$$

We thus need the comoving Hubble radius to shrink by a factor 10^{28}, or in other words assuming $H \sim const.$ During inflation

$$\frac{a_E}{a_I} > 10^{28} \qquad \Rightarrow \qquad \ln\left(\frac{a_E}{a_I}\right) > 64\,, \tag{1.2.16}$$

which leads to the famous result that a successful solution to the horizon problem requires about $N = 60$ e-folds of inflation.
The duration of inflation is measured by a second parameter

$$\eta \equiv \frac{d\ln\varepsilon}{dN} = \frac{\dot{\varepsilon}}{H\varepsilon}\,. \tag{1.2.17}$$

If $|\eta| < 1$, the fractional change of ε per Hubble time is small and inflation persists.
For inflation to be realized, it is required to have a violation of the SEC, $w = \mathcal{P}/\rho < 1/3$. This means that *inflation requires negative pressure*, and we will see how this can be realized thanks to a scalar field. Note also that the condition on ε implies (via the continuity equation (B.1.64))

$$\left|\frac{d\ln\rho}{d\ln a}\right| = 2\varepsilon < 2\,, \tag{1.2.18}$$

which means that, for small ε, the energy density is roughly constant with the expansion instead of diluting.

1.2.2 *Scalar field inflation and slow-roll conditions*

1.2.2.1 *Scalar field dynamics*

The simplest inflation model invokes a single scalar field $\phi(t,\vec{x})$, the *inflaton*, minimally coupled to Einstein gravity

$$S = \int d^4x\sqrt{-g}\Big[\underbrace{\frac{M_{\rm pl}^2}{2}\mathcal{R}}_{S_{\rm EH}} - \underbrace{\frac{1}{2}g^{\mu\nu}\partial_\mu\phi\partial_\nu\phi - V(\phi)}_{S_\phi}\Big]\,, \tag{1.2.19}$$

where $g \equiv \det(g_{\mu\nu})$ and we have defined the (reduced) Planck mass

$$M_{\rm pl} = \sqrt{\frac{\hbar c}{8\pi G}} = 2.4\times 10^{18}\ \text{GeV}\,. \tag{1.2.20}$$

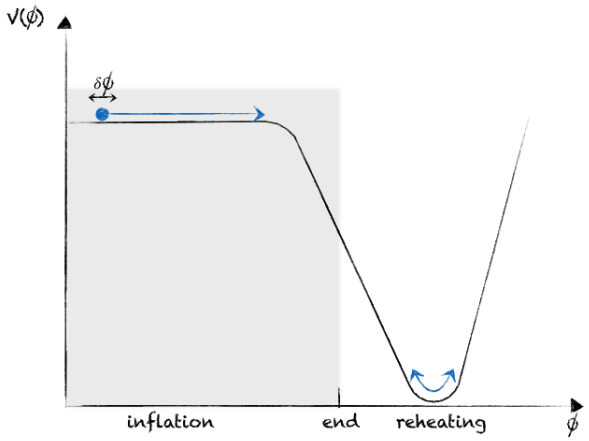

Figure 6: An arbitrary slow-roll potential. Adapted from Ref. [90].

The action eq. 1.2.19 is the sum of the Einstein-Hilbert action $S_{\rm EH}$ and a scalar field S_ϕ with canonical kinetic term and potential term $V(\phi)$, whose shape we will choose to be similar to fig. 6. The stress-energy tensor for a scalar field is

$$T^{\phi}_{\mu\nu} \equiv -\frac{2}{\sqrt{-g}}\frac{\delta S_\phi}{\delta g^{\mu\nu}} = \partial_\mu\phi\partial_\nu\phi - g_{\mu\nu}\left(\frac{1}{2}g^{\alpha\beta}\partial_\alpha\phi\partial_\beta\phi - V(\phi)\right) \tag{1.2.21}$$

while the least action principle applied to S_ϕ leads to the standard Klein-Gordon equation of motion

$$\frac{\partial S_\phi}{\partial\phi} = \frac{1}{\sqrt{-g}}\partial_\mu(\sqrt{-g}\partial^\mu\phi) + V_{,\phi} = 0\,. \tag{1.2.22}$$

where $V_{,\phi} \equiv dV/d\phi$. We now restrict the study to the FLRW metric. The symmetries of the FLRW spacetime require $\phi = \phi(t)$ while $\det(g^{\mu\nu}) = -a^8$. Thus we infer

$$T^0_0 = \rho_\phi = \frac{1}{2}\dot\phi + V(\phi)\,, \tag{1.2.23a}$$

$$T^i_j = -P_\phi\delta^i_j = -\left(\frac{1}{2}\dot\phi^2 - V(\phi)\right)\delta^i_j\,, \tag{1.2.23b}$$

$$\ddot\phi + 3H\dot\phi + V_{,\phi} = 0. \tag{1.2.23c}$$

Furthermore, the Friedmann equations reduce to

$$H^2 = \frac{1}{3M^2_{\rm pl}}\left[\frac{1}{2}\dot\phi^2 + V\right]\,, \tag{1.2.24a}$$

$$\dot H = -\frac{(\rho_\phi + \mathcal{P}_\phi)}{2M^2_{\rm pl}} = \frac{1}{2}\frac{\dot\phi^2}{M^2_{\rm pl}}\,. \tag{1.2.24b}$$

This allows one to determine the ε and η parameters

$$\varepsilon = -\frac{\dot{H}}{H^2} = \frac{\dot{\phi}^2/2}{M_{\rm pl}^2 H^2} \tag{1.2.25}$$

$$\begin{aligned}\eta &= \frac{\dot{\varepsilon}}{H\varepsilon} = \frac{1}{H\varepsilon}\left\{\frac{1}{M_{\rm pl}^2 H^2}\left[\ddot{\phi}\dot{\phi} + \frac{\dot{\phi}^2\dot{H}}{H^2}\right]\right\} \\ &= 2\left[\frac{\ddot{\phi}}{H\dot{\phi}} - \frac{\dot{H}}{H^2}\right] \\ &= 2(\varepsilon - \delta)\,,\end{aligned} \tag{1.2.26}$$

where the dimensionless acceleration per Hubble time $\delta \equiv -\ddot{\phi}/(H\dot{\phi})$ has been introduced. The conditions for inflation $\{\varepsilon, |\eta|\} < 1 \Leftrightarrow \{\varepsilon, |\delta|\} < 1$ imply that the kinetic energy $\dot{\phi}^2/2$ must make a small contribution to the total energy density $\rho_\phi = 3M_{\rm pl}^2 H^2$. This is known as *slow-roll inflation*. Under the assumption that slow-roll is verified $\varepsilon \ll 1 \Rightarrow \dot{\phi}^2/2 \ll V$, it is possible to write the Friedmann equation (1.2.24a)

$$H^2 \sim \frac{V}{3M_{\rm pl}^2}\,, \tag{1.2.27}$$

while $\delta \ll 1$ allows to write the KG equation (1.2.23c) as

$$3H\dot{\phi} \sim -V_{,\phi}\,. \tag{1.2.28}$$

Taking the time derivative of eq. (1.2.28) combined with eq. (1.2.27) allows one to rewrite the slow-roll parameters as function of the potential $V(\phi)$ and its derivative; these new parameters are dubbed *potential slow-roll parameters*

$$\epsilon_V \equiv \frac{M_{\rm pl}^2}{2}\left(\frac{V_{,\phi}}{V}\right)^2, \qquad |\eta_V| \equiv M_{\rm pl}^2\frac{|V_{,\phi\phi}|}{V}\,. \tag{1.2.29}$$

One can thus check whether slow-roll is verified, $\{\epsilon_V, |\eta_V|\} \ll 1$, directly from the inflaton potential. For instance, a toy model for inflation is

$$V(\phi) = \frac{1}{2}m^2\phi^2\,. \tag{1.2.30}$$

We can readily obtain the slow-roll parameters as $V_{,\phi} = m^2\phi$ and $V_{,\phi\phi} = m^2$. Those are

$$\eta_V(\phi) = \eta_V(\phi) = 2\left(\frac{M_{\rm pl}}{\phi}\right)^2. \tag{1.2.31}$$

Therefore, in this toy model, slow-roll is satisfied only for super-Planckian values of the inflaton $\phi > \sqrt{2}M_{\rm pl}$.

1.2.2.2 *Reheating*

In order for standard cosmology to start, we need inflation to end. This is achieved when the potential steepens and the inflaton field gets kinetic energy. After inflation, the inflaton field begins to oscillate at the bottom of the potential $V(\phi)$, and the amplitude of ϕ is small. If we assume that it can be locally approximated by $V(\phi) = \frac{1}{2}m^2\phi^2$, then the equation of motion is given by

$$\ddot{\phi} + 3H\dot{\phi} = -m^2\phi\,. \tag{1.2.32}$$

Both $V(\phi)$ and $\dot{\phi}$ are small, such that the expansion time scale, given by eq. (1.2.24a), has become much longer than the oscillation period $H^{-1} \gg m^{-1}$, and the friction term is negligible. We thus can integrate

$$\ddot{\phi} = -m^2\phi \Rightarrow d\dot{\phi} = -m^2\phi\frac{dt}{d\phi}d\phi \Rightarrow d\dot{\phi}\dot{\phi} = -m^2\phi d\phi \Rightarrow \dot{\phi}^2 = -m^2\phi^2 \tag{1.2.33}$$

The continuity equation, combined with eqs. (1.2.23a), yields

$$\dot{\rho}_\phi + 3H\rho_\phi = -3H\mathcal{P}_\phi = -\frac{3}{2}H\underbrace{(m^2\phi^2 - \dot{\phi}^2)}_{\text{time average } \to 0} \tag{1.2.34}$$

Hence, we see that the oscillating field behaves like pressureless matter, with $\rho_\phi \propto a^{-3}$. However, if we don't want to end up with an empty universe, the energy of the inflaton has to be transferred to standard model (SM) particles: this is the *reheating* phase. We assume that eventually the inflaton is coupled to SM particles such that it will experiences decay at a constant rate Γ_ϕ. Hence, the energy density follows the equation

$$\dot{\rho_\phi} + 3H\rho_\phi = -\Gamma_\phi\rho_\phi\,. \tag{1.2.35}$$

The physics entering the computation of Γ_ϕ can be extremely involved, and while we will not detail anything here, an interested reader can have a look at the review [87]. Let us just mention that if the decay occurs into fermions, the decay is usually slow and our equation is valid.
The generic pictures however, is that particles will quickly be created by interactions with each other, and the plasma will reach an equilibrium with some *reheating temperature* $T_{\rm rh}$, fixed by the energy density of the inflaton at the end of the preheating epoch. It can eventually be much smaller than the energy density at the end of inflation if the reheating phase is long. After the thermalization of the standard model particles is complete, the hot Big Bang Cosmological model begins.

1.3 Thermal history of the Universe

In this section I would like to give an overview of the thermal history of the Universe, i.e. how the thermodynamical properties and the particle content of the Universe evolved over time. Indeed, typically any kind of electromagnetic energy injection can potentially lead to a modification of this history and thus can leave traces in the observables that we have at hand.

1.3.1 *From equilibrium to freeze-out*

At some point after the end of inflation—that we shall describe a bit further on in this work as the mechanism generating primordial fluctuations—baryogenesis and dark matter generation take place. These topics are research fields of their own, so we will not enter in details. In particular, baryogenesis is associated to the great mystery of "why is there more matter than anti-matter in the Universe?". Indeed, if the universe was initially filled with an equal amount of particles and antiparticles, it turns out to be non-trivial to explain the observed asymmetry between baryons and antibaryons dynamically. This asymmetry can be related to the inferred photon-baryon ratio η:

$$\eta = \frac{n_b}{n_\gamma} \sim 10^{-10} \quad , \tag{1.3.1}$$

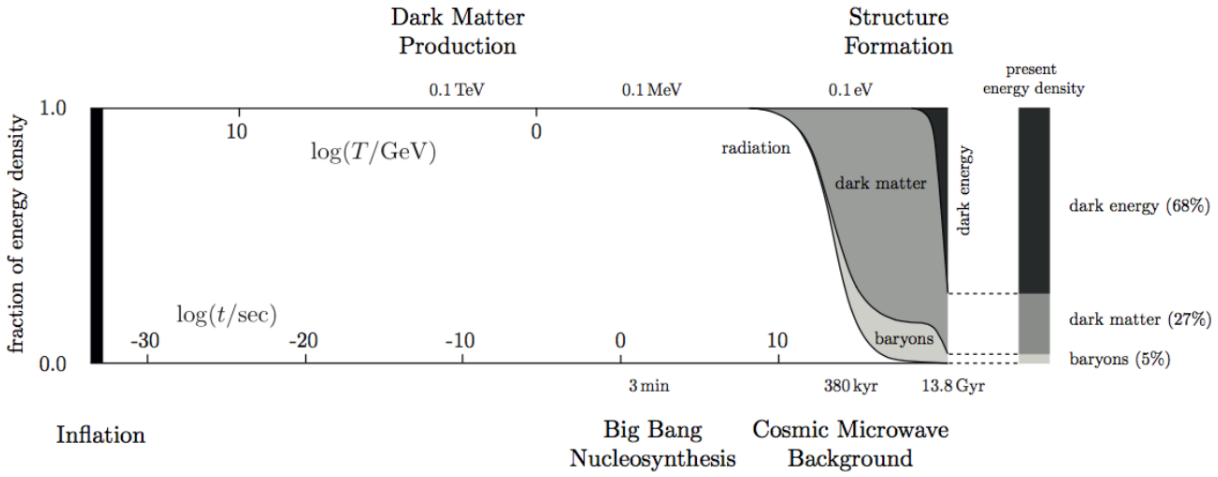

Figure 7: A sketch of our Universe History from the Big Bang until today. Taken from Ref. [90].

which can also be re-expressed in terms of the baryon fraction as

$$\Omega_b = \frac{\rho_b}{\rho_{\rm crit}} = \frac{m_b \eta n_\gamma}{\rho_{\rm crit}} = \eta \frac{m_b}{\rho_{\rm crit}} \frac{2\zeta(3)}{\pi^2} T_0^3 \tag{1.3.2}$$

where m_b is the sum of the masses of the different baryonic components weighted by their relative abundance.

It is customary to write

$$\eta \cdot 10^{10} = \frac{273.49 \Omega_b h^2}{1 - 0.007 Y_p} \left(\frac{2.725 \text{ K}}{T_0} \right)^3 \left(\frac{6.708 \cdot 10^{-45} \text{MeV}^{-2}}{G} \right). \tag{1.3.3}$$

where the primordial Helium mass fraction $Y_p \equiv 4 n_{^4\text{He}}/n_b$ has been introduced. We will take η or Ω_b as a fitted parameter in the following, just like we have done with the dark matter abundance till now. In the following chapter we will at least provide some basic ideas on the favored dynamical processes for generating DM.

At least at sub-TeV temperatures corresponding to energies explored by known standard model processes, for most considerations the primordial (or "primeval") plasma can be thought to be constituted of free elementary particles that can be described as an ideal gas, given that their kinetic energy is much bigger than the potential energy due to mutual interactions. In practice, this is not always a good approximation. For instance, it does not allow to describe the QCD phase transition, when the strong interaction confines quarks in bound hadrons such as protons, neutrons and pions.

1.3.1.1 *Equilibrium distribution, number density, energy density and pressure*

During the first second following reheating, the temperature in the Universe is huge and collision rates are so high that all SM particles follow Boltzmann distributions at the same temperature T and zero chemical potential. Kinetic equilibrium will be achieved through processes such as

$$e^\pm \gamma \leftrightarrow e^\pm \gamma \qquad \nu_e e \leftrightarrow \nu_e e \qquad p e^\pm \leftrightarrow p e^\pm \tag{1.3.4}$$

Moreover, the chemical potential μ of any species whose production is not constrained by some quantum number conservation is driven to 0 at equilibrium through number changing processes such as:

$$e^- p \leftrightarrow e^- p\gamma \qquad \Rightarrow \mu_\gamma = 0 \tag{1.3.5}$$

Similarly, any particle x at equilibrium with its antiparticles verifies $\mu_x = -\mu_{\bar{x}}$. For instance,

$$e^+ e^- \rightarrow \gamma\gamma \qquad \Rightarrow \mu_{e^-} = -\mu_{e^+}. \tag{1.3.6}$$

For a more quantitative description, it is worth introducing the phase-space distribution of any species:

$$F(\overrightarrow{r}, \overrightarrow{p}, t) = \frac{dN}{d^3 r d^3 p}\,, \tag{1.3.7}$$

which is also written in a dimensionless way as:

$$f(\overrightarrow{r}, \overrightarrow{p}, t) = \frac{F}{g/(2\pi\hbar)^3}, \tag{1.3.8}$$

where g is the number of spin states for a species and $(2\pi\hbar)^3$ is the volume of a phase-space cell. The well-known thermal equilibrium distributions at temperature T and with chemical potential μ are either the Fermi-Dirac one (+) or the Bose-Einstein (-) one

$$f_\pm = \frac{1}{e^{(E-\mu)/T} \pm 1} \quad , \tag{1.3.9}$$

which only depend on the modulus p.

One can express the stress-energy tensor as well as the particle current density n^μ in terms of the phase-space distribution by:

$$T^\mu_\nu(\vec{x}, t) = g \int \frac{d^3 P}{(2\pi)^3} (-\det[g_{\alpha\beta}])^{-1/2} \frac{P^\mu P_\nu}{P^0} f(\vec{x}, P, t) \quad , \tag{1.3.10}$$

$$n^\mu = g \int \frac{d^3 P}{(2\pi)^3} (-\det[g_{\alpha\beta}])^{-1/2} \frac{P^\mu}{P^0} f(\vec{x}, P, t) \quad , \tag{1.3.11}$$

where $(-\det[g_{\alpha\beta}])^{-1/2} = a^{-3}$. The only non-zero components of these tensors give the number density n, the energy density ρ and the pressure $\mathcal{P}$:

$$n^0 = n(t) = \frac{g}{(2\pi)^3} \int d^3 p f_s(t, p) \quad , \tag{1.3.12}$$

$$T^0_0 = \rho(t) = \frac{g}{(2\pi)^3} \int d^3 p E_s f_s(t, p) \quad , \tag{1.3.13}$$

$$T^i_j = -\mathcal{P}(t)\delta^i_j = -\delta^i_j \frac{g}{(2\pi)^3} \int d^3 p \frac{p^2}{3E_s} f_s(t, p) \quad . \tag{1.3.14}$$

Note that in the previous equations, the phase-space distribution does not depend on $\vec{x}$ (as a consequence of homogeneity) and only on the modulus of $\vec{p}$ (as a consequence of isotropy). The ultra-relativistic limit $T \gg m$, which will be useful in this work, gives the explicit expressions:

$$n = \frac{g\zeta(3)}{\pi^2} T^3 \times \begin{cases} 1 & \text{bosons} \\ 3/4 & \text{fermions} \end{cases} \tag{1.3.15}$$

$$\rho = \frac{\pi^2}{15} g T^4 \times \begin{cases} 1 & \text{bosons} \\ \frac{7}{8} & \text{fermions} \end{cases} \tag{1.3.16}$$

$$\mathcal{P} = \frac{1}{3}\rho \tag{1.3.17}$$

We thus find the typical behavior $n \propto T^3$, $\rho \propto T^4$ and $w = 1/3$ for relativistic particles. Similarly, the non-relativistic limit leads to:

$$n = g\left(\frac{mT}{2\pi}\right)^{\frac{3}{2}} e^{-m/T} \tag{1.3.18}$$

$$\rho = mn + \frac{3}{2}nT \underset{T\ll m}{\simeq} mn \tag{1.3.19}$$

$$\mathcal{P} = nT \ll \rho \tag{1.3.20}$$

In the non-relativistic case, a Boltzmann factor $\exp(-m/T)$ suppresses particle distributions: particles and antiparticles tend to annihilate but the bath does not have enough energy to recreate them.

1.3.1.2 *Effective number of relativistic degrees of freedom*

The total radiation density is the sum over the energy densities of all relativistic species:

$$\rho_r = \sum_i \rho_i = \frac{\pi^2}{30} g_{\text{eff}}(T) T^4 \,. \tag{1.3.21}$$

The g_{eff} factor is the effective number of relativistic degrees of freedom at the temperature T. A relativistic species i contributes to the number of degrees of freedom even if it is decoupled with a different temperature from the thermal bath:

$$g_{\text{eff}}(T) \simeq \sum_{\text{bosons}} g_i \left(\frac{T_i}{T}\right)^4 \Theta(T - m_i) + (7/8) \sum_{\text{fermions}} g_i \left(\frac{T_i}{T}\right)^4 \Theta(T - m_i) \,. \tag{1.3.22}$$

The second Friedmann-Lemaître law encodes the fact that the total entropy of the Universe is conserved. From the second law of thermodynamics, $TdS = dU + \mathcal{P}dV - \mu N$, we can express the *entropy density* $s \equiv S/V$ of a given species as

$$s_i(T, \mu) = \frac{\rho_i + \mathcal{P}_i - \mu n_i}{T} \,. \tag{1.3.23}$$

From eq. (1.3.12), one can compute the total entropy of the primordial plasma:

$$s = \sum_i s_i = h_{\text{eff}}(T) \frac{2\pi^2}{45} T^3 \,. \tag{1.3.24}$$

Again, this quantity is dominated by relativistic species, that do not receive a Bolzmann suppression. Hence, h_{eff} is the effective number of degrees of freedom in entropy, which can be written as:

$$h_{\text{eff}}(T) \simeq \sum_{\text{bosons}} g_i \left(\frac{T_i}{T}\right)^3 \Theta(T - m_i) + (7/8) \sum_{\text{fermions}} g_i \left(\frac{T_i}{T}\right)^3 \Theta(T - m_i) \,. \tag{1.3.25}$$

The evolution of g_{eff} and h_{eff} with time, which roughly corresponds to the evolution of the particle contents of the cosmic plasma , is shown in Fig. 8. One can see the most important events happening in the universe: i) The electroweak phase transition around 100 GeV, when particles acquire their masses through the Higgs mechanism; ii) The QCD phase transition, around 150 MeV, when the strong interaction mediated by gluons binds quarks together inside baryons (protons, neutrons ...)

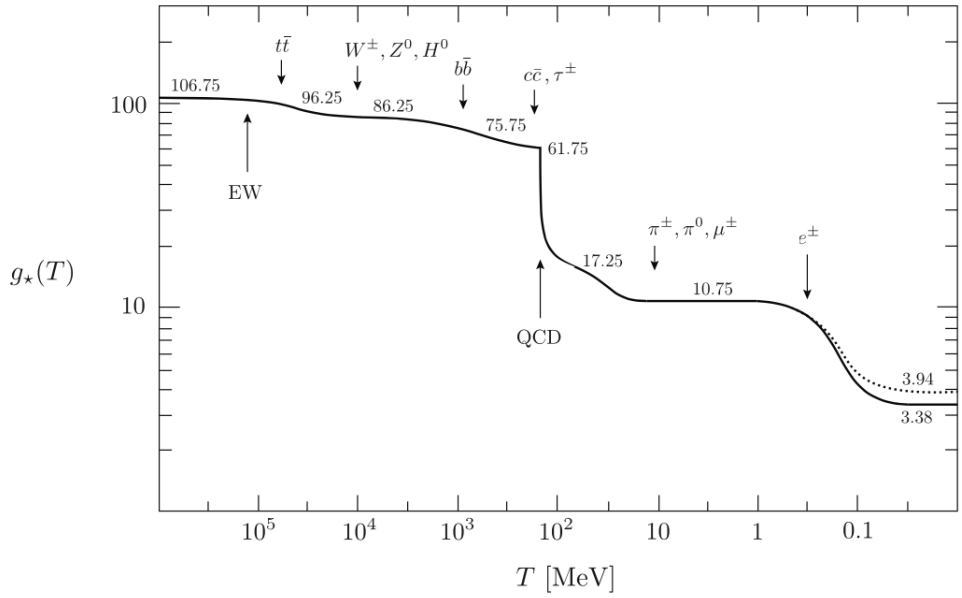

Figure 8: Evolution of relativistic degrees of freedom $g_{\rm eff}(T)$ (full line) and effective degrees of freedom in entropy $h_{\rm eff}(T)$ assuming the Standard Model particle content. Figure taken from ref. [90].

and mesons (pions,...); iii) e^+e^- annihilations, which lead to a slight reheating of the photons with respect to neutrinos, that decoupled from the thermal bath around MeV temperatures (see below) Entropy conservation leads to $d(sa^3) = 0$ i.e. $s \propto a^{-3}$. Hence we get

$$\begin{aligned} s(T)a^3 &\propto h_{\rm eff}(T)T^3a^3 = \text{const.} \\ \Rightarrow T &\propto h_{\rm eff}^{-1/3}a^{-1}\,. \end{aligned}$$

Thus, $T \propto a^{-1}$, except when a particle annihilates, leading to a decrease in $h_{\rm eff}$ and thus a heating of photons with respect to decoupled species.

1.3.1.3 *Equilibrium and departure from equilibrium: The case of neutrino decoupling*

The formal tool to describe departures from equilibrium is the Boltzmann equation, which is introduced in appendix A.1.

We can quickly verify that the plasma is indeed locally at thermal equilibrium (i.e kinetic and chemical equilibria are realized). The rationale for this lies in the comparison between the expansion rate of the Universe, or Hubble rate H, and the interaction rate of a given particle Γ with the thermal bath. If $\Gamma \gg H$, or equivalently $\{\tau_\Gamma \equiv \Gamma^{-1}\} \ll \{\tau_H = H^{-1}\}$ then particles attain equilibrium with the thermal bath. According to *Gamow criterion*, when $\Gamma = H$, the processes becomes inefficient and the particles decouple from the thermal bath. At temperature $T \geq \mathcal{O}(100)$ GeV, all standard model particles are relativistic. In that case,

$$\Gamma = n\sigma v \sim \alpha_A^2 T \tag{1.3.26}$$

where $n \propto T^3$ is the number density of particles, $v \simeq c$ their average relative velocity, σ the cross section (proportional to the fourth power of the coupling with the gauge boson A, g_A^4, for a diagram with two vertices) and $\alpha_A \equiv g_A^2/4\pi$ is a generalized "fine-structure" constant. In the relativistic limit, the mass

of particles is irrelevant and, on a dimensional basis, one also has $[\sigma] = [E]^{-2}$, hence $\sigma \propto \alpha_A^2/T^2$ since T is the only energy scale available. Given that during radiation domination

$$H^2 \simeq \frac{\rho}{3M_{\rm pl}^2} \sim \frac{T^4}{M_{\rm pl}^2}\,, \tag{1.3.27}$$

one typically gets a ratio

$$\frac{\Gamma}{H} \sim \frac{M_{\rm pl}\alpha_A^2}{T} \sim \frac{10^{16}\ \text{GeV}}{T} \tag{1.3.28}$$

when $\alpha_A \sim 0.01$ is used. Thus, we can safely assume that as long as 100 GeV $\leq T \leq 10^{16}$ GeV, our assumption of local thermal equilibrium is satisfied.

Once particles become non-relativistic and start to annihilate, their abundance does not asymptotically go to zero. In practice, the assumption of local thermal equilibrium is not always fulfilled because of the Universe's expansion. The Gamow criterion for the annihilation rate is eventually matched, processes start to be inefficient and the abundance of a given species is said to *freeze-out*.
A textbook case for this are neutrinos. Neutrinos are coupled to the thermal bath via the weak interaction, inducing elastic and inelastic scattering processes of the type:

$$\nu_i + \bar{\nu}_i \leftrightarrow i + \bar{i} \tag{1.3.29}$$

$$\nu_i + i \leftrightarrow \nu_i + i \tag{1.3.30}$$

where $i = e, \mu, \tau$. The typical collision rate for a Fermi-type of interaction is given by

$$\Gamma_F \simeq \langle \sigma v \rangle n \sim G_F^2 T^5\,, \tag{1.3.31}$$

where $G_F \simeq 1.166 \times 10^{-5}$ GeV^{-2} is the Fermi constant. The Hubble rate is $H \sim T^2/M_{\rm pl}^2$, thus, the Gamow criterion gives

$$\frac{\Gamma_F}{H} \simeq G_F^2 M_{\rm pl}^2 T^3 \sim \left(\frac{T}{1\text{MeV}}\right)^3. \tag{1.3.32}$$

Neutrino decoupling roughly happens at $T_{\nu,\rm dec} \sim 1$ MeV. Afterwards, they propagate freely following geodesics and their distribution remains frozen with

$$f_\nu(p) = \frac{1}{\exp\left(\frac{p}{T_\nu}\right) + 1}\,. \tag{1.3.33}$$

The geodesic equation implies $p \propto a^{-1}$, thus the fact that the distribution remains frozen implies $T_\nu \propto a^{-1}$ at all time. Before neutrinos become non-relativistic, their number density, energy density and pressure is simply given by eq. (1.3.15). After neutrinos decoupling, the entropy of the universe receives contributions from photons (2), electrons ($4 \times 7/8$) and neutrinos ($6 \times 7/8 \times (T/T_\nu)^3$):

$$h_{\rm eff} = h_{\rm eff}\Big|_{\rm plasma} + h_{\rm eff}\Big|_{\nu} = \left[2 + \frac{7}{8} \times 4\right] + \left[6 \times \frac{7}{8} \times \left(\frac{T_\nu}{T}\right)^3\right] = \frac{11}{2} + \left[\frac{42}{8} \times \left(\frac{T_\nu}{T}\right)^3\right] \tag{1.3.34}$$

As long as $T = T_\nu$, nothing special happens for the plasma with respect to neutrinos and $h_{\rm eff} = 10.75$. However at $T \sim m_e$, $e^\pm$ annihilate, reheating the plasma with respect to neutrinos. Entropy conservation applies separately to neutrinos and the plasma. For the plasma, it leads to

$$\begin{aligned} h_{\rm eff}(T_{\rm before})\Big|_{\rm plasma} T_{\rm before}^3 a^3 &= h_{\rm eff}(T_{\rm after})\Big|_{\rm plasma} T_{\rm after}^3 a^3 \\ \Leftrightarrow T_{\rm after} &= T_{\rm before} \times \left(\frac{h_{\rm eff}(T_{\rm before}) = 11/2}{h_{\rm eff}(T_{\rm after}) = 2}\right)^{1/3}\Bigg|_{\rm plasma} \\ \Leftrightarrow T_{\rm after} &= T_{\rm before} \times \left(\frac{11}{4}\right)^{1/3}\Bigg|_{\rm plasma} \end{aligned} \tag{1.3.35}$$

At zero-th order, we can assume that neutrino decoupling is instantaneous, hence for neutrinos entropy conservation simply gives $T_{\nu,\rm after} = T_{\nu,\rm before}$. Thus, we conclude that the temperature of the thermal bath gets reheated with respect to neutrinos by a factor $(11/4)^{1/3}$. This relation still holds today, and the photon temperature has been measured very precisely. We can infer the neutrino temperature and number density (for 3 neutrino families):

$$T_{\gamma 0} = 2.7255 \text{ K}\,, \qquad T_{\nu 0} = 1.946 \text{ K}\,, \tag{1.3.36}$$

$$n_{\gamma 0} = 410 \text{ cm}^3\,, \qquad n_{\nu 0} = 112 \text{ cm}^3\,. \tag{1.3.37}$$

After $e^\pm$ annihilation, the relativistic degrees of freedom populating the universe are photons and neutrinos only. It is common to introduce the *effective number of relativistic species* $N_{\rm eff}$ in the following way:

$$\rho_r = \rho_\gamma \left(1 + \frac{7}{8}\left(\frac{11}{4}\right)^{4/3} N_{\rm eff}\right). \tag{1.3.38}$$

$N_{\rm eff}$ is equal to three if three conditions are fulfilled: i) There are no other relativistic particles than the three neutrino species; ii) Neutrinos follow Fermi-Dirac distribution with vanishing chemical potential; iii) The instantaneous decoupling limit is verified. In practice, we already know that iii) is not realized: the standard model prediction for $N_{\rm eff}$ is thus 3.046 instead of 3. As we will see further in this work, cosmology, via measurements of CMB temperature and polarization anisotropies and BBN, is a very powerful too to constrain any deviation from the standard value of $N_{\rm eff}$.
Given that neutrinos are non-relativistic today, we can express their relic density $\rho_{\nu 0} = \sum_i m_{\nu,i} n_{\nu 0}$ as

$$\Omega_\nu = \frac{\rho_{\nu 0}}{\rho_{\rm crit,0}} \simeq \frac{\sum_i m_{\nu,i}}{94 \text{ eV} h^2}\,. \tag{1.3.39}$$

The overclosure relation $\Omega_M < 1$ gave historically [198] the best bound on neutrino masses:

$$\sum_i m_{\nu,i} < 94 \text{ eV} h^2\,. \tag{1.3.40}$$

Currently, significantly more stringent bounds can be derived from a detailed study of structure formation in the presence of massive neutrinos, as we will see later on.

1.3.2 *Big Bang Nucleosynthesis*

Big Bang Nucleosynthesis (BBN) is one of the "observational pillars" of the hot Big Bang model, allowing us to constrain properties of the Universe back to when it was a few seconds old, or equivalently

at the MeV temperature scale. Thus, it corresponds currently to the earliest direct cosmological probe available, although this might change if primordial B-mode polarization induced by inflation were to be discovered by the next generation CMB experiments.

1.3.2.1 *Theoretical basics*

The theory of primordial nucleosynthesis, in its simplest scenario, only contains one free parameter: the photon-to-baryon ratio η. Until the era of precision CMB physics, measurements of the observational abundance of deuterium yielded the most precise determination of η. Historically, it was the first very compelling argument corroborating the non-baryonic nature of the dark matter invoked for astrophysical dynamics.

BBN is in principle a complicated process of departure from equilibrium, that requires following many coupled Boltzmann equations governing the evolution of all nuclear abundances, see below. Its main results can, however, be understood with limited effort, and we shall describe them in the following. First, it is worth summarizing BBN as the process of incorporation of neutrons inside nuclei, whose dominant outcome is the production of 4-Helium, which is in fact to a large extent insensitive to the exact BBN reaction network. Due to the low density, the main processes of neutron incorporation inside nuclei are a sequence of two-body reactions

$$n\,p \to {}^2\mathrm{H}\,\gamma$$

$${}^2\mathrm{H}\,{}^2\mathrm{H} \to {}^3\mathrm{He}\,n \qquad {}^2\mathrm{H}\,{}^2\mathrm{H} \to {}^3\mathrm{H}\,p$$

$${}^3\mathrm{He}\,{}^2\mathrm{H} \to {}^4\mathrm{He}\,p \qquad {}^3\mathrm{H}\,{}^2\mathrm{H} \to {}^4\mathrm{He}\,n \qquad {}^2\mathrm{H}\,{}^2\mathrm{H} \to {}^4\mathrm{He}\,\gamma$$

The most important quantity, beside η, is the initial n/p ratio. At temperatures above few MeV, neutrons and protons are in thermal equilibrium via reactions such as,

$$\nu_e n \leftrightarrow e^- p \qquad \bar{\nu}_e p \leftrightarrow e^+ n \qquad n \leftrightarrow p + e^- + \bar{\nu}_e$$

We have already seen, when talking about neutrino decoupling, that the weak interaction becomes inefficient around $T_{\nu,\mathrm{dec}} \sim 1$ MeV. At that time, neutrons and protons are non-relativistic, thus their ratio is given by:

$$\frac{n_n}{n_p} \sim \exp(-\Delta m/T_{\nu,\mathrm{dec}}) \sim 0.2 \qquad \text{with} \quad \Delta m = m_n - m_p = 1.29\,\mathrm{MeV}\,. \tag{1.3.41}$$

However, this ratio will not stay constant; neutrons start to decay when $t \sim \tau_n = 886.7 \pm 0.8\,\mathrm{s}$. Thus, we get

$$\frac{n_n}{n_p} \sim \exp(-\Delta m/T_{\nu,\mathrm{dec}})\exp(-t/\tau_n)\,. \tag{1.3.42}$$

This gives the value of the n/p ratio when BBN starts. One might expect nucleosynthesis to start when the mean energy of the CMB photons is below the binding energy of the lightest nuclei ${}^2\mathrm{H}$, i.e. $B_{2\mathrm{H}} = 2.22$ MeV. However, at $T \sim$ MeV, the reaction rate is still much bigger than the Hubble rate, given the very high number of high energy photons in the tail of the photon Boltzmann distribution. Thus, the reaction $n + p \leftrightarrow {}^2\mathrm{H} + \gamma$ is at equilibrium and the vanishing photon chemical potential

implies $\mu_n + \mu_p = \mu_{^2\mathrm{H}}$. Using the expression of the non-relativistic distribution, one can trade this equality for the following equation:

$$\begin{aligned}
\left.\frac{n_{^2\mathrm{H}}}{n_n n_p}\right|_{\mathrm{eq}} &= \frac{3}{4}\left(\frac{m_{^2\mathrm{H}}}{m_n m_p}\frac{2\pi}{T}\right)^{3/2}\exp(B_{^2\mathrm{H}}/T) \\
\Leftrightarrow \left.\frac{n_{^2\mathrm{H}}}{n_p}\right|_{\mathrm{eq}} &= \frac{3}{4}n_n|_{\mathrm{eq}}\left(\frac{4\pi}{m_p T}\right)^{3/2}\exp(B_{^2\mathrm{H}}/T) \qquad \text{with} \quad m_{^2\mathrm{H}} \simeq 2m_n \simeq 2m_p \\
\Leftrightarrow \left.\frac{n_{^2\mathrm{H}}}{n_p}\right|_{\mathrm{eq}} &\simeq \eta\left(\frac{T}{m_p}\right)^{3/2}\exp(B_{^2\mathrm{H}}/T) \qquad \text{with} \quad n_n \sim n_b = \eta n_\gamma = \eta \times \frac{2\zeta(3)}{\pi^2}T^3\,. \quad (1.3.43)
\end{aligned}$$

Hence, the creation of a significant fraction of deuterium is prohibited by the very small baryon-to-photon ratio η until the term $\exp(B_{^2\mathrm{H}}/T)$ compensates, i.e. for $T \sim 70$ keV. At that time, deuterium is not destroyed efficiently anymore and BBN can start. This delay of the beginning of the BBN is known as the *deuterium bottleneck*.

To get an estimate of the main BBN outcome, namely the amount of 4-Helium, one can simply assume that all neutrons will be incorporated inside ^{4}He. Hence, the number of Helium nuclei is $n_{^4\mathrm{He}} = n_n/2$ and the hydrogen one $n_{\mathrm{H}} = n_p - n_n$. Introducing the primordial Helium mass fraction Y_p leads to the famous result:

$$Y_p = 4 \times \frac{n_n/2}{n_p - n_n} = \frac{2n_n/n_p}{1 - n_n/n_p} \sim \frac{2}{1 + \exp(\Delta m/T_{\nu,\mathrm{dec}})\exp(-t/\tau_n)} \sim 0.25 \qquad (\eta \sim 6 \times 10^{-10}).$$

BBN is not limited to 4-Helium formation. The isotopes ^{2}H, ^{3}H (eventually β-decaying into ^{3}He) and ^{3}He also survive at the level of 10^{-5} number fraction as ashes of the chains leading to 4-Helium. On the other hand, the main reactions beyond 4-Helium are:

$$^3\mathrm{H}\,^4\mathrm{He} \to {}^7\mathrm{Li}\,\gamma \qquad {}^4\mathrm{He}\,^3\mathrm{He} \to {}^7\mathrm{Be}\,\gamma \qquad {}^7\mathrm{Be}\,e^- \to {}^7\mathrm{Li}\,\nu_e\,,$$

which only yield 7-Lithium traces at the 10^{-10} level (number fraction). BBN stops quickly at $A = 7$ since there are no stable elements with $A = 5$ or $A = 8$, although BBN studies typically follow up to the Oxygen isotopes to achieve sufficient precision. Furthermore, the Coulomb barrier between charged nuclei highly suppresses production cross section for $T < 60$ keV. BBN stops around $T \sim 30$ keV with a relic density of nuclei that are in kinetic, but *not* in chemical (hence thermal) equilibrium with the plasma. No heavy nuclei are produced during BBN and one has to wait for stellar nucleosynthesis, in stellar cores or supernovae explosion, to produce all of the other chemical elements.

The typical set of differential equations ruling primordial nucleosynthesis is made of [339] i) the Friedmann equation (1.1.26); ii) the continuity equation (B.1.64) for the sum of all species involved in BBN, i.e. photons, electrons, neutrinos and baryons ; iii) a set of N_{nuc} Boltzmann equations for $X_i \equiv n_i/n_b$ of the form

$$\dot{X}_i = \sum_{j,k,l} N_I\left(\Gamma_{kl\to ij}\frac{X_k^{N_k}X_l^{N_l}}{N_k!N_l!} - \Gamma_{ij\to kl}\frac{X_i^{N_i}X_j^{N_j}}{N_i!N_j!}\right) \equiv \Gamma_i\,, \qquad (1.3.44)$$

which describe the density evolution of each nuclide species; iv) an equation stating the universe charge neutrality in terms of the electron chemical potential,

$$n_B\sum_j Z_j X_j = n_{e^-} - n_{e^+} \equiv L\big(\frac{m_e}{T},\phi_e\big) \equiv T^3\hat{L}\big(\frac{m_e}{T},\phi_e\big)\,, \qquad (1.3.45)$$

with $L(m_e/T, \phi_e)$ the charge density in the lepton sector in unit of the electron charge; v) the Boltzmann equations for neutrinos species ν_α

$$\frac{d}{dt} f_{\nu_\alpha}(|\vec{p}|, t) = \mathcal{C}_{\nu_\alpha}[f_{\nu_x}, f_{\bar{\nu}_x}, f_{e^-}, f_{e^+}] \tag{1.3.46}$$

where $\mathcal{C}_{\nu_\alpha}[f_{\nu_x}, f_{\bar{\nu}_x}, f_{e^-}, f_{e^+}]$ stands for the collisional integral which contains all microscopic processes creating or destroying the species ν_α. This set of equations is usually solved using numerical codes such as PArthENoPE [481], and we make use of the outcome of this code (typically fitting functions depending on the neutron lifetime, the effective number of relativistic species, the density of baryons and the expansion rate today) for our studies.

1.3.2.2 *Beyond standard model*

The result of BBN depends on a number of input parameters (only η in the minimal model) and assumptions, which allow to test modifications to the standard model. For instance

- Increasing η increases the number of baryons and therefore makes BBN happen earlier. This will lead to a larger number of ^{4}He, and therefore to lower number of ^{2}H and ^{3}He.
- $N_{\rm eff}$ affects the expansion history of the universe and hence the freeze-out temperature $T_{\nu,\rm dec}$. If $N_{\rm eff}$ increases, the freeze out temperature does as well, which in turn increases the n/p ratio and the final 4-Helium abundance, while decreasing ^{2}H and ^{3}He. This fact is illustrated with the red dot-dashed lines in fig. 9.
- A larger neutron lifetime τ_n reduces the amount of neutron decay after freeze-out and therefore increases the final 4-Helium abundance.
- A larger mass difference between neutrons and protons would decrease the n/p ratio at freeze-out and thus decrease the final 4-Helium abundance.
- The strength of gravity G enters the freeze-out temperature. Increasing it would also increase $T_{\nu,\rm dec}$ and in turn the final 4-Helium abundance.
- On the other hand, increasing the weak force G_F would decrease the freeze-out temperature and therefore the ^{4}He abundance.
- It is possible to constrain exotic neutrino physics because BBN is a very good probe of the neutrino sector. They can affect the BBN yields typically in two ways: i) the $n-p$ conversion rate; ii) the overall expansion rate. Electromagnetic (or more exotic) interaction would for instance modify i). We refer to [339] for a review of the constraints.
- Electromagnetic energy injections in the form of $e^\pm$ and γ can destroy nuclei through photodissociation reactions, while producing others as a product of the reaction. We will make use of this important effect in chapter 5.
- Hadronic energy injections can affect the $n-p$ conversion rate through charge exchange reactions and the n/p ratio by (mostly) annihilating protons. Studies of these effects can be found in refs. [349], [364].

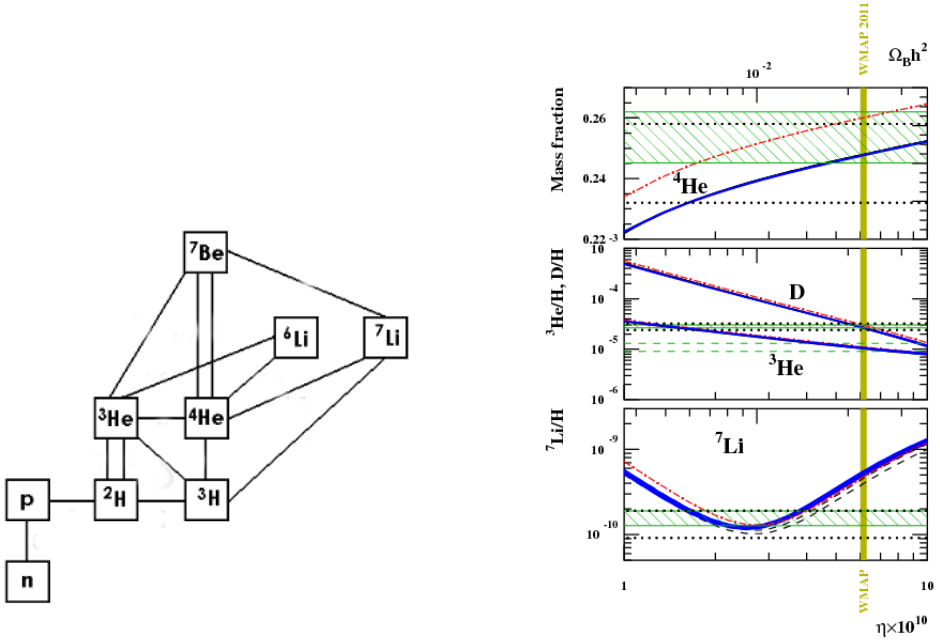

Figure 9: *Left panel* - The principal network of reaction happening during BBN [339]. *Right panel* - The most recent estimates of ^{4}He, D, ^{3}He and ^{7}Li abundances as a function of η calculated with the reduced network presented on the left panel (light blue dashed) or with an extended one including C, N, O nuclei (dark blue). The vertical areas correspond to the *WMAP* (dot, black) and *Planck* (solid, yellow) baryonic densities. The horizontal areas (hatched a) represent the most recent observational abundances while the horizontal dotted lines correspond to former estimates. The red dash-dotted lines correspond to a primordial Helium fraction computed with a different value of the effective number of relativistic species $N_{\rm eff} = 3.30 \pm 0.27$ derived from *Planck* 2013 data. Figure taken from Ref. [196].

1.3.2.3 *Observational determination of BBN yields*

The observational determination of these abundances is very involved. As the Universe is no longer in the same state as after BBN, efforts devoted to measuring primordial yields are focused on very old regions, believed to have experienced only little astrophysical evolution, or attempts to model the influence of stars and astrophysical phenomena on these abundances.

Deuterium

The particularity of Deuterium is that stars only destroy it during stellar evolution and produce negligible amounts of it. Thus, any astrophysical measurement can in principle produce a lower bound on the amount of primordial deuterium. Historically, measurements of the local ISM in the Milky Way have given by far the biggest numbers of measurements. However, the scattering in the value of ^{2}H/H pointed towards stellar reprocessing of the pristine value due to astration. It is possible to get a much less contaminated estimate of the amount of primordial deuterium using the Lyman-α forest: the presence of a hydrogen rich gas cloud crossed by photons emitted by a distant quasar

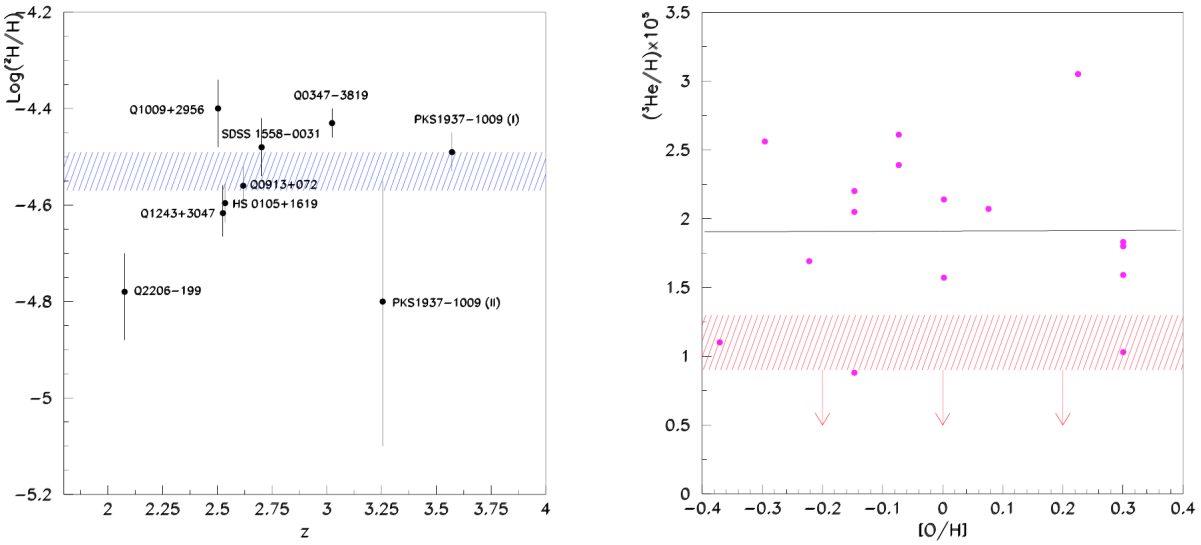

Figure 10: *Left panel* - A compilation of nine measurements of ^{2}H/H via Lymanα absorption along QSOs lines of sight used in the analysis of Ref. [339]. The horizontal band represents their value of ^{2}H/H, very similar to the one used in this work taken from Ref. [455]. *Right panel* - Compilation of ^{3}He/H measurements from *HII* region as a function of the metallicity O/H, together with the two determination from PSM and LISM (taken from Ref. [339], original measurements are from Ref. [78]).

induces absorption at the Ly-α frequency at the epoch of the cloud crossing, being thus observed at a wavelength λ_1

$$\lambda_1/\lambda_{Ly\alpha} = (z_{\rm cloud}+1)/(z_{\rm quasar}+1)\,.$$

The amount of deuterium relative to the one of hydrogen is determined from the detailed study of the line profile, close to its edge (due to the isotopic shift). In practice, a handful of measurements are available as it is necessary to find clouds in a narrow range of optical depth such that the hydrogen line absorption is not overwhelming and the effect of deuterium sufficiently strong to be detectable. A compilation of QSOs estimates taken from Ref. [339] is shown in Fig. 10.
From these measurements, the ratio ^{2}H/^{1}H has been determined, and thus the value of η and Ω_b could be inferred. For ^{2}H we adopt the 2-σ limit $2.56\times10^{-5} < {}^2{\rm H/H} < 3.48\times10^{-5}$ from Ref. [455]; similar results would follow by adopting the combination value compiled in Ref. [339], namely $2.45\times10^{-5} < {}^2{\rm H/H} < 3.31\times10^{-5}$, which is also closer to the results of Ref. [480]; our interval also overlaps with the recent determination in Ref. [507].

Helium

Two Helium isotopes are produced during BBN. The first and most important, as we have seen, is ^{4}He. The difficulty is that Helium is produced inside stars at the same time as heavier elements. However, a linear correlation between the amount of Helium and the metallicity has been observed, and the extrapolation to "zero-metallicity" is thought as beeing a good estimator of the primordial abundance (historically proposed in [473], [474]), although affected by systematic uncertainties such as plasma temperature or stellar absorption [73], [344]. The abundance of ^{4}He can be measured

through recombination lines in low-metallicity extragalactic HII regions. This has been done for various samples of Dwarf Irregular (DIrrs) and Blue Compact Galaxies (BCGs) [343], [346].

The most recent measurement comes from [74] and yields a 4-Helium mass fraction of $^4\mathrm{He/H} \sim 0.2465 \pm 0.0097$. Given that Helium is only produced by stars, it is safer to only use a lower limit on its abundance, as we shall do later in this work.
Note that in principle the study of CMB anisotropies, sensitive to the Helium fraction, could give an estimate of the primordial value. However, *Planck* data do not allow to get a measurement competitive with direct measurements.

The second Helium isotope is ^{3}He. It is a nucleus of utmost importance for BBN test as its abundance, like deuterium, is extremely sensitive to the baryon density. The difficulty regarding this nucleus is that it can be both produced or destroyed during stellar nucleosynthesis. It is possible to determine the abundance of ^{3}He in our solar system via meteorites and solar winds [273], although the most accurate measurement was done in Jupiter's atmosphere by the Galileo Probe [415] which allowed researchers to deduce the amount of ^{3}He in the proto-stellar material (PSM) out of which our Sun formed, but it is clear that amount of ^{3}He in the local environment has been modified by its influence. Another measurement was obtained in the Local InterStellar Medium (LISM) thanks to the Ulysses spacecraft [273]. However, the best observation of primordial ^{3}He are done via the hyperfine transition in the radio band at 3.46 cm. These very weak emissions is more easily observed in HII region or in Planetary Nebulae within the Galaxy. Fig.10 - right panel reports these data as a function of the metallicity O/H together with the two determination from PSM and LISM (taken from Ref. [339], original measurements are from Ref. [78]). Contrarily to 4-Helium, a dependence on the medium metallicity has not been observed, albeit it was originally predicted by models of stellar and galactic evolution. Although more involved 3D-models are now consistent with observations, the safest approach is to consider only an upper limit on the ^{3}He primordial abundance from Ref. [78] $^3\mathrm{He/H} < (1.1 \pm 0.2) \times 10^{-5}$. This upper limit is also represented in Fig. 10, right panel.

Lithium and the "lithium problems"

Like in the case of Helium, two isotopes can potentially be produced during BBN: ^{7}Li and ^{6}Li. Let us first consider ^{7}Li. It is produced either *directly*, by fusion of 4-Helium and tritium nuclei, or *indirectly*, by Beryllium production followed by decay through electronic capture. The production branching ratios are highly dependent on the baryon-to-photon ratio η, and for $\eta \sim 6 \cdot 10^{-10}$, the production turns out to be dominated by the *indirect* channel. Now, the lifetime of Beryllium is rather long (53,12 days $\sim 4.58 \cdot 10^6$ s). Thus, the electronic capture occurs well *after* the end of BBN. An accurate computation, taking into account the high density of background photons and, therefore, the high probability for high-energy photon to destroy Beryllium atoms before the electronic capture, allows one to determine the temperature at which 50% of Beryllium has decayed. It is similar to the computation of deuterium formation and it yields $T = 8.83\,\mathrm{eV} \Leftrightarrow 1.2 \cdot 10^{10}\,\mathrm{s}$ [367].
Many astrophysical processes have been proposed as possible sources of non-primordial Lithium. For instance, Cosmic-rays by interacting with the ISM could produce both isotopes through spallation or fusion reactions [243], whereas neutrino spallation in supernova could trigger formation of ^{7}Li [301]. Finally, ^{7}Li could even be produced in low mass stars, depending on their stellar evolution [139].

The abundance of 7-Lithium is estimated from absorption lines in metal-poor population II stars. Spite and Spite [564] performed such observations in stars surrounded by a rather hot halos ($T \geq 6000$

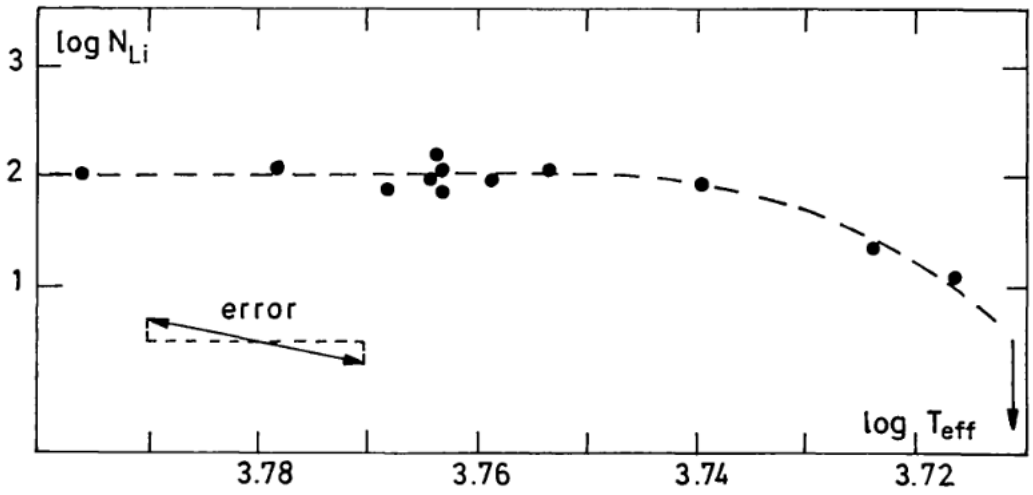

Figure 11: The original *Spite Plateau* as measured by Spite and Spite [564]. The abscissa stands for the effective temperature of the atmosphere surrounding the stars.

K). These stars have a thin convection zones avoiding the Li to be brought to regions hot enough to destroy it. They exhibit two remarkable features: i) a substantially lower Li content than solar metallicity stars; ii) a Li abundance that does not vary with metallicity. This constant value, nowadays called *Spite plateau* was supposed to be the primordial one, under the assumption that the host stars had not destroyed any of their primordial lithium. Up to hundreds of these metal-poor stars have been observed and this Spite plateau was thought to be very robust, until recently, when observations of stars with even lower metallicity revealed a lowering of the plateau (see e.g. [203] for a recent review).

Today, it is still debated to which extent this plateau reflects a primordial value, but it seems that at least some halo stars have destroyed their Li. If interpreted as primordial, recent analyses yield $^7\mathrm{Li/H} \sim (1.6 \pm 0.3) \times 10^{-10}$ [527].

On the other hand, measurements of the very fragile isotope^{6}Li are very involved. Abundances are deduced from star halos that contain primordial ^{7}Li: by looking very precisely at the λ 6.708 nm resonance line, one can detect the presence of ^{6}Li as a slight modification of the width and asymmetry of the line profile (e.g. [66]). These are measurements at the edge of sensitivity, with limits at the $^6\mathrm{Li}/^7\mathrm{Li} < 0.1$ level and some tentative detections around $^6\mathrm{Li}/^7\mathrm{Li} \sim 0.05$ which have been claimed. Of course, if stellar destruction affects ^{7}Li, *a fortiori* it will affect the more fragile ^{6}Li. A further complication is that 6-Lithium is also produced by fusions of helium nuclei $\alpha\alpha \rightarrow {}^6\mathrm{Li} + ...$, which is certainly not primordial but comes from cosmic ray interacting with the ISM. What could be a few percent astrophysical contribution via the $\alpha\alpha$ channel to the measured ^{7}Li might completely dominate the observed value of ^{6}Li.Thus, the determination of the ^{6}Li abundance allows one at best to put an upper limit on the primordial ^{6}Li.

Hence, the comparisons of theory and observation for both Lithium isotopes is puzzling: for sure, inferred values are statistically very different from standard BBN predictions. For instance, the ^{7}Li fraction predicted by a code like PArthENoPE, obtained assuming values of $\Omega_b h$ measured by *WMAP* and *Planck*, is [339] $^7\mathrm{Li}/^1\mathrm{H} \sim (4.57 \pm 0.4) \times 10^{-10}$, a factor ~ 4 above measurements. For 6-Lithium, the observed ratio is three orders of magnitude above the value expected from standard BBN, where the suppressed channel $^4\mathrm{He}\,^2\mathrm{H} \rightarrow {}^6\mathrm{Li}\,\gamma$ dominates the production. Yet, this tension may be mostly

attributed to observational issues, according to recent studies [406].
Those discrepancies, still under inspection nowadays, are known as "lithium problems". We will ignore ^{6}Li in this work, given recent indications of spurious detections in the direction of solving the discrepancy, but we mention that using observations as an upper limit to its primordial value would provide very powerful constraints to some regions of parameter space for exotic models.
Regarding ^{7}Li, the situation is less clear. Many solutions for solving the tension have been proposed, for a recent review on the subject one can look at ref. [242]. We can, however, say that reasons for the difference are unlikely to originate from unresolved systematic errors, whereas underestimated errors in the adopted nuclear reaction rates are now excluded (e.g. Ref. [129]). Hence, it seems that the discrepancy comes from: i) either some modification to the BBN scenario (with e.g. some decaying exotic particles as we shall explore further); ii) or, perhaps more likely, a reprocessing of the lithium abundance in very metal-poor stars, contrary to what is commonly believed.

1.3.3 *Recombination*

When the temperature of the cosmic plasma is high enough, electrons and photons are tightly coupled due to efficient Thomson scattering between them. As we have seen already, the Hubble expansion tends to cool down the plasma, allowing BBN to happen. Eventually, the plasma temperature and density will lower enough for Hydrogen to efficiently form, allowing at the same time photons to propagate freely, causing the end of the "primordial plasma epoch". CMB anisotropies that we observe today, as we shall discuss later, are nothing but a "snapshot" of the universe at photon decoupling, also called *last scattering surface*. The recombination era, which encodes the dynamics of the Thomson scattering and especially of the photon freeze-out, is, therefore, a key era one has to understand in order to compute meaningful CMB observables. As we will see later, the precision of an experiment like *Planck* requires a theoretical knowledge of this era better than the per-mille level! This challenge has been successfully taken on in the last ten years, and now we shall briefly describe the physics at play. Furthermore, the recombination history in its whole will be of utmost importance in our study of the impact of e.m. energy injection, as its modification with respect to the standard behavior will lead to the biggest phenomenological impact.
This recap is based on ref. [90], [308].

1.3.3.1 *Saha recombination and the redshift of decoupling*

The key process to follow is the combination of protons and electrons into Hydrogen accompanied by high energy photon emission. At sufficiently high temperature, or early times, the following "recombination process" is at equilibrium:

$$p^+ + e^- \leftrightarrow \mathrm{H} + \gamma\,. \tag{1.3.47}$$

Since the photon chemical potential is null, chemical equilibrium ensures that

$$\mu_p + \mu_e = \mu_{\mathrm{H}}\,. \tag{1.3.48}$$

Thus, we can invert this equation to get a relation between the number density of particles at chemical equilibrium, the so-called *Saha equation*:

$$\frac{n_p n_e}{n_H} = \left(\frac{m_e T}{2\pi}\right)^{3/2} e^{-\epsilon_0/T}\,, \tag{1.3.49}$$

where $\epsilon_0 = m_p + m_e - m_{\rm H} = 13.6$ eV and $g_p = g_e = 2$ and $g_H = 4$ has been used. The difference between m_p and $m_{\rm H}$ is ignored, except in the exponential function. This very generic equation does not only apply to cosmology, however in this context global neutrality ensures $n_p = n_e$. It is common to introduce the *free electron fraction* x_e, i.e. the fraction of electrons that are not bound inside atoms, as:

$$x_e \equiv \frac{n_e}{n_{\rm H}} \,. \tag{1.3.50}$$

Note that the number of electrons bound inside Helium is not taken into account, leading to a free electron fraction bigger than one in a fully ionized universe. From previous BBN computations, we know that (in mass fraction) ^{4}He $\simeq 25\%$ H so x_e can be as high as ~ 1.16 when Helium is doubly ionized. With this definition, the Saha equation becomes:

$$\frac{x_e^2}{1-x_e} = \frac{1}{n_{\rm H}} \left(\frac{m_e T}{2\pi} \right)^{3/2} e^{-\epsilon_0/T} \,. \tag{1.3.51}$$

Similarly to the BBN computation, the huge number of photons significantly delays recombination: one can estimate that when $T \sim \epsilon_0 \simeq 1.6 \times 10^5$ K, the RHS is of order 10^{15}! If the reaction were always at equilibrium, this would allow us to estimate that one has to wait for $T \simeq 3100$ K$= 0.3$ eV or $z = 1140$ to have 99% of Hydrogen recombined ($x_e \sim 10^{-2}$).
From this simple calculation it is possible to estimate the redshift of photon decoupling. Compton scattering is a key process to understand CMB physics as it rules coupling between photons and baryons. It corresponds to the following process:

$$e^\pm + \gamma \leftrightarrow e^\pm + \gamma \,. \tag{1.3.52}$$

with the (non-relativistic) interaction rate given by

$$\Gamma_\gamma \simeq n_e \sigma_T \,, \tag{1.3.53}$$

where $\sigma_T \simeq 2 \times 10^{-3}$ MeV^{-2} is the Thomson cross section, valid as the mean photon energy $\sim T$ is very small compared to the electron rest mass $m_e \sim 511$ keV at the time of interest. As recombination progresses, the density of free electrons drops and eventually the interaction rate becomes smaller than the expansion rate. We can determine when decoupling approximately happens:

$$\begin{aligned}
\Gamma_\gamma(T_{\rm dec}) &\sim H(T_{\rm dec}) \\
\Leftrightarrow n_{\rm H} x_e(T_{\rm dec}) \sigma_T &= H(T_{\rm dec}) \\
\Leftrightarrow \eta \frac{2\zeta(3)}{\pi^2} T_{\rm dec}^3 x_e(T_{\rm dec}) \sigma_T &= H_0 \sqrt{\Omega_m} \left(\frac{T_{\rm dec}}{T_0} \right)^{3/2} \\
\Leftrightarrow x_e(T_{\rm dec}) T_{\rm dec}^{3/2} &= \frac{\pi^2 H_0 \sqrt{\Omega_m}}{2\zeta(3) \eta \sigma_T T_0^{3/2}} \,.
\end{aligned} \tag{1.3.54}$$

Taking the Saha approximation for $x_e(T_{\rm dec})$, it is found

$$z_{\rm dec} \sim 1320 \qquad \Leftrightarrow t_{\rm dec} \sim 290\ 000 \text{ yrs} \,. \tag{1.3.55}$$

More advanced calculations within the concordance ΛCDM model find $z_{\rm dec} \sim 1090$. It is common to introduce the *optical depth* $\tau(z)$ and the *visibility function* $g(z)$ as

$$\tau_{\rm depth}(z) \equiv \int_0^z n_e(z) \sigma_T \frac{dt}{dz'} dz' \,, \tag{1.3.56}$$

$$g(z) \equiv e^{-\tau} \frac{d\tau_{\rm depth}}{dz} \,, \tag{1.3.57}$$

as those are key functions entering the computation of CMB anisotropies. Typically, $\tau(z)$ represents the opacity of the universe at a given time, when seen from today ($z_0 = 0$). It tends to infinity in the far past, falls below one at recombination and stabilizes at around 0.1, before the reionization of our Universe, which we shall describe later. After reionization, it decreases smoothly and reaches 0 today by definition. $g(z)$ also has a very clear meaning, giving the probability that a CMB photon seen today experienced its last scattering at redshift (z). In standard cosmology, it is exponentially suppressed in the primordial universe, reaches its maximum with a very narrow peak around decoupling and then falls again as the universe is mostly neutral. When reionization happens, g develops a second smaller and broader peak. The width of the first peak corresponds to the so-called *last scattering surface* while the maximum of the visibility function is usually used to define the time of photon decoupling.
A very high precision in the computation of these functions is necessary in order to get meaningful CMB observables. Unfortunately, there are several important issues with the simple Saha result. Firstly, as the universe expands, the rate for recombination falls, so that equilibrium becomes difficult to maintain. In practice, a relic abundance of electrons will freeze-out. Modification of this freeze-out plateau in the case of e.m. energy injection around and after recombination will have important consequences, as we explain later on. Using the Saha equation, we can write the Boltzmann equation for the electron density, including Universe's expansion and the process (1.3.47), as (see appendix A.1 for derivation):

$$a^{-3}\frac{d(n_e a^3)}{dt} = -n_e^{\rm eq} n_p^{\rm eq}\langle\sigma v\rangle\left[\frac{n_{\rm H}}{n_{\rm H}^{\rm eq}} - \frac{n_e^2}{n_e^{\rm eq} n_p^{\rm eq}}\right]. \tag{1.3.58}$$

We can rewrite this equation in terms of the free electron fraction using the Saha eq. (1.3.51) valid at equilibrium, in order to remove Hubble expansion

$$\frac{dx_e}{dt} = \left[(1-x_e)\beta - x_e^2 n_{\rm H}\alpha\right], \tag{1.3.59}$$

where the ionization rate β has been introduced as

$$\beta \equiv \left(\frac{m_e T}{2\pi}\right)^{3/2} e^{-\epsilon_0/T}, \tag{1.3.60}$$

and the recombination rate α is

$$\alpha \equiv \langle\sigma v\rangle. \tag{1.3.61}$$

This is the standard form of the recombination equation. When β and α drop, x_e freezes-out, leading to departure from the Saha equation. There is, however, an important issue with this model: indeed, if one considers recombination happening directly to the ground state, the emitted photon has enough energy to reionize a neighbouring neutral hydrogen atom. A quick computation shows that the mean free path of photon with energy just above 13.6 eV is

$$L_0 \sim \frac{1}{x_{1s} n_{\rm H} \sigma_{H(1s)\gamma\leftrightarrow pe}} \sim 4\times 10^{14} x_{1s}^{-1}{\rm cm} \tag{1.3.62}$$

where x_{1s} is the fraction of atom recombined in the ground ($1s$) state, $n_H \sim 200[(1+z)/1000]^3$ cm^{-3} and $\sigma_{H(1s)\gamma\leftrightarrow pe} \sim 6\times 10^{-18}$ cm^2. The rate at which photons are reabsorbed is

$$\frac{c}{L_0} \sim 10^{-4} x_{1s}\ {\rm s}^{-1}. \tag{1.3.63}$$

Since around recombination $H \sim 10^{-18}(1+z)^{3/2}$ s^{-1} $\sim 10^{-14}$ s^{-1}, if $x_1 > 10^{-9}$, ionization is much faster than the Hubble expansion and recombination cannot happen efficiently. It is, therefore, necessary to consider recombination in an *excited state* in order to understand the dynamics of this era.

1.3.3.2 *Helium recombination*

Before going to a more involved picture of recombination, it is mandatory to discuss the case of heavier nuclei produce during BBN. In practice however, all species but Helium are irrelevant for understanding CMB anisotropies as they represent only a very tiny fraction of the baryons. We shall therefore ignore their recombination for simplicity. Helium abundance being about a quarter of that of hydrogen, CMB anisotropies are sensitive at the % level (increasing with higher peaks) to modifications of the free electron fraction due to their recombination. It is, therefore, crucial to model Helium recombination in an accurate way for CMB anisotropy studies.

Helium has two electrons and therefore experiences a recombination in two steps: $He^{2+} \rightarrow He^{+}$ followed by $He^{+} \rightarrow He$, with ionization energy respectively given by $\epsilon_{He^{2+}} = 54.4$ eV and $\epsilon_{He^{+}} = 24.6$ eV. Given that those energies are larger than H ionization energy, He will recombine first. Assuming that recombination proceeds at equilibrium leads to the Saha equations for He^{+} and He^{2+}. They are respectively

$$n_{\rm H}\frac{x_e x(\mathrm{He}^{+})}{x(\mathrm{He}^{0})} = \left(\frac{m_e T}{2\pi}\right)^{3/2} e^{-\epsilon_{\mathrm{He}^{2+}}/T}\,, \tag{1.3.64}$$

$$n_{\rm H}\frac{x_e x(\mathrm{He}^{2+})}{x(\mathrm{He}^{+})} = 4\left(\frac{m_e T}{2\pi}\right)^{3/2} e^{-\epsilon_{\mathrm{He}^{+}}/T}\,. \tag{1.3.65}$$

The factor 4 in the second equation comes from statistical spin weight.

Although HeIII $\rightarrow$ HeII recombination can be understood as a generalization of HI recombination, a key complication arises in HeII $\rightarrow$ HeI recombination due to the non-hydrogenic nature of the Helium atom: the three-body (two electrons one nucleus) problem does not have analytical solutions. More involved computations, following singlet and triplet states have been developed in the last decade [310], [532], [574], [575]. We will describe them in more details in the next section, but we can already anticipate that the first helium recombination is accurately described by Saha's equation, since reaction rates are fast enough for it to proceed in equilibrium. It teaches us that 50 % of the He^{2+} atoms have recombined by $z \sim 5800$. However, important differences appear for the second helium recombination, which can be significantly delayed with respect to Saha's equation, predicting that half of the He^{+} has recombined by $z \sim 2500$.

1.3.3.3 *The three level atoms*

The first realistic model for the recombination was developed first by Zeldovich, Kurt and Sunyaev [605], [607], soon followed by Peebles [472] and is known as the *three-level atom* (TLA). Its schematic representation can be found on the left panel of fig. 12. In this model, Hydrogen can be in the ground state ($1s$), an excited state (mostly $2s$ and $2p$) or ionized, i.e. $H^{+}+e^{-}$. Recombination occurs primarily through formation of an excited state $\mathrm{H}(nl, n \geq 2)$, i.e. via the reaction

$$p^{+} + e^{-} \leftrightarrow \mathrm{H}(nl, n \geq 2) + \gamma\,. \tag{1.3.66}$$

followed by a very fast radiative cascade until $n = 2$. The subscript nl refers to the bound state with principal quantum number n and angular momentum quantum number l. Assuming that all collision rates and radiative transfers between level are sufficiently fast allows one to consider thermal equilibrium between excitation states. Thus, the hydrogen density in the state nl is simply given by:

$$n_{nl} = (2l+1) n_{2s} e^{\frac{\epsilon_2 - \epsilon_n}{T}} \quad , \tag{1.3.67}$$

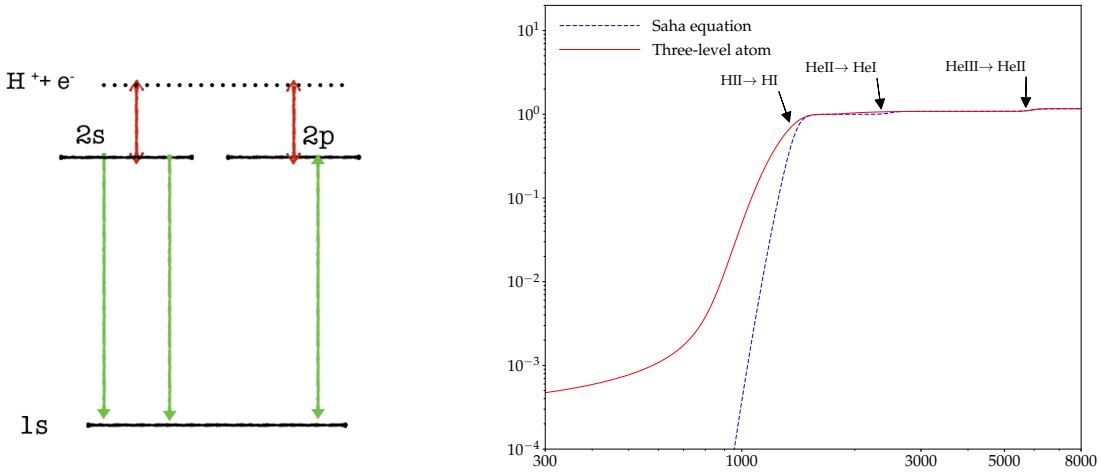

Figure 12: *Right panel* – A schematic picture of the *three-level atom*. *Left panel* – Comparison of the ionization fraction x_e assuming, for both Helium and Hydrogen, that Saha equation is valid (i.e. Boltzmann equilibrium is verified) or the "three-level atoms".

where $\epsilon_n = \{\epsilon_0 = 13.6 \text{ eV}\}/n^2$ and n_{2s} is the atomic density in state $2s$. For instance, the $2p$ ($l = 1$) and $2s$ ($l = 0$) states verify $n_{2p} = 3n_{2s}$.
The production rate of a hydrogen atom in an excited state is given by $\alpha_{\rm B}(T) n_e n_p$, where

$$\alpha_{\rm B} = \sum_{n=2}^{\infty} \sum_{l=0}^{n-1} \langle \sigma[p^+ + e^- \rightarrow {\rm H}(nl) + \gamma] v \rangle \quad . \tag{1.3.68}$$

This number is called *Case B recombination coefficient*, where case A includes the ground states. Once the atom is in an excited state, we assume that it rapidly decays to $n = 2$, whereas the decay to the ground state takes much longer. Ignoring it in a first step, the evolution of the number of atoms in the $n = 2$ states is simply

$$\frac{dx_2}{dt} \equiv \frac{d}{dt}\left(\frac{n_2}{n_{\rm H}}\right) = \alpha_{\rm B} x_e^2 (n_{\rm H}) - \beta_{\rm B} x_2 \quad . \tag{1.3.69}$$

The coefficient $\beta_{\rm B}$ is the (Boltzmann averaged) thermal coefficient of photoionization from an excited state. It can be determined by assuming detailed balance

$$\beta_{\rm B}/\alpha_{\rm B} = \left(\frac{x_e^2 n_{\rm H}}{x_2}\right)_{\rm eq.} = \frac{1}{4}\left(\frac{m_e T}{2\pi}\right)^{3/2} e^{-\epsilon_2/T} \quad . \tag{1.3.70}$$

The factor 4 comes from the different spin statistics. In practice, an atom in the $n = 2$ state can also decay through

$$H(2s) \quad \leftrightarrow \quad H(1s) + \gamma + \gamma \,, \tag{1.3.71}$$

$$H(2s) \quad \leftrightarrow \quad H(1s) + \gamma_{{\rm Ly}\alpha} \,, \tag{1.3.72}$$

One might want to add those as simplest decay processes

$$\frac{dx_2}{dt} = \alpha_{\rm B} x_e^2 n_{\rm H} - \beta_{\rm B} x_2 - A_{2s1s}\{x_{2s} = x_2/4\} - A_{2p1s}\{x_{2p} = 3x_2/4\} \,, \tag{1.3.73}$$

with Einstein coefficients $A_{2s1s} \simeq 8.2\ \mathrm{s}^{-1}$ and $A_{2p1s} = 6.2 \times 10^8\ \mathrm{s}^{-1}$. However, this would be missing important physics: the fact that part of the $Ly\alpha$ photons emitted will quickly be reabsorbed with probability P, which we can relate to the optical depth:

$$\tau = \int n_{1s}\sigma dt = \int n_{1s}\sigma \frac{d\omega}{|\dot{\omega}|} = \int n_{1s}\sigma \frac{d\omega}{H\omega}\,. \tag{1.3.74}$$

Under the narrow width assumption (i.e. $\sigma \propto \delta(\omega - \omega_{Ly\alpha})$) and detailed balance for the reaction $2p \leftrightarrow 1s$, one obtains (e.g. [308]):

$$\tau_{\rm Sob} = \frac{3\pi^2 A_{2p1s} n_H x_{1s}}{H\omega^3_{\rm Ly\alpha}}\,. \tag{1.3.75}$$

This is the so-called *Sobolev optical depth*. Plugging some numbers give $\tau \sim 10^8$ during recombination. For such optical thick line the probability for a Lyman-α to be reabsorbed is given by $P \simeq 1/\tau_{\rm Sob}$. It is remarkable that, although the forbidden transition is so slow, $A_{2s1s} \sim 10^{-8} \times A_{2p1s}$, the high probability for a Lyman-α to be re-absorbed before redshifting away from the line make the two processes contribute in an almost equal way to the recombination of our Universe. A more careful computation shows that it even dominates, at 57% against 43%.

Finally, it is necessary to add a correction for thermal excitation of atoms in the $(1s)$ state by CMB photons that redshift into the Lyman-α resonance, which we do assuming detailed balance between excitation and decay. Since we neglect direct recombination to the ground state, the evolution equation of the $1s$ state is simply obtained by considering the same decay/excitation processes with opposite sign. The final set of equations is thus:

$$\begin{aligned}
\frac{dx_2}{dt} &= \alpha x_e^2 n_{\rm H} - \beta x_2 - \frac{A_{2s1s}x_2}{4} - \frac{3A_{2p1s}Px_2}{4} + \big(3A_{2p1s}P + A_{2s1s}\big)x_1 e^{-\nu_{\rm Ly\alpha}/T} \\
&= \alpha x_e^2 n_{\rm H} - \beta x_2 - \Big(A_{2s1s} + 3A_{2p1s}P\Big)\left(\frac{x_2}{4} - x_1 e^{-\nu_{\rm Ly\alpha}/T}\right) \quad , \qquad (1.3.76)\\
\frac{dx_1}{dt} &= \Big(A_{2s1s} + 3A_{2p1s}P\Big)\left(\frac{x_2}{4} - x_1 e^{-\nu_{\rm Ly\alpha}/T}\right) \qquad (1.3.77)
\end{aligned}$$

To solve this coupled system of equation, we assume that $\dot{x}_2 \simeq 0$ so that:

$$x_2 = 4\frac{\alpha_{\rm B} n_{\rm H} x_e^2 + (A_{2s1s} + 3A_{2p1s}P)x_1 e^{-\nu_{\rm Ly\alpha}/T}}{A_{2s1s} + 3A_{2p1s}P + 4\beta_{\rm B}}\,. \tag{1.3.78}$$

Plugging into x_1, we find that the net evolution of free electrons $\dot{x}_e = -\dot{x}_2^{\rm rec} \simeq -\dot{x}_1$ is simply given by:

$$\frac{dx_e}{dt} = -C\left(\alpha_{\rm B} n_{\rm H} x_e^2 - 4\beta_{\rm B} x_1 e^{-\nu_{\rm Ly\alpha}/T}\right). \tag{1.3.79}$$

with

$$C \equiv \frac{A_{2s1s} + 3A_{2p1s}P}{A_{2s1s} + 3A_{2p1s}P + 4\beta_{\rm B}}\,. \tag{1.3.80}$$

Introduced by Peebles, this factor represents the probability that an electron in the $n = 2$ shells reaches the ground state before being photoionized. Eq. (1.3.79) is the *three-level atom* equation, which predicts that recombination is delayed with respect to the Saha equation, and that the free electron fraction freezes-out with non-zero value due to the Universe's expansion. Typically, 99% of the hydrogen recombines around $z \sim 820$ instead of 1140 with Saha's equation, while $x_e^{\rm f.o.} \sim 10^{-4}$. Differences with the Saha equation are illustrated in fig. 12, right panel.

The three-level atom can be generalized to singly ionized Helium including the ground state, $n = 2$ singlet states and the continuum, showing as well delayed recombinaison [532]. Since the 1970's, there have been many improvements allowing an increase in the precision of the recombination physics up to the per-mille level around the peak of the visibility function, as it is necessary with *Planck*, and we shall give an overview of these improvements later on.

1.3.3.4 *The matter temperature evolution*

Recombination physics requires to follow not only the evolution of the free electron fraction but also the matter temperature, as it enters in several places in eq. (1.3.79). The assumption $T_{\rm M} = T_\gamma$ is true in the early universe, but certainly not later. The main processes that determine the gas temperature are:

- *adiabatic expansion*, which tend to cool down matter and CMB photon at different rates. For a massive non-relativistic particle the kinetic energy $E_k = p^2/2m \propto a^{-2}$ and can be related to the averaged energy of individual particles in a monoatomic gas $E_k = 3/2 k_b T$ implying

$$\left.\frac{dT_{\rm M}}{dt}\right|_{\rm adia} = -2\frac{\dot{a}}{a}T_{\rm M} = -2HT_{\rm M}\,. \tag{1.3.81}$$

- *Compton interaction* between CMB photons and the gas. It is a textbook calculation to show that (see e.g. [308])

$$\left.\frac{dT_{\rm M}}{dt}\right|_{\rm Compton} = H\gamma(T_\gamma - T_{\rm M}) \tag{1.3.82}$$

  where the dimensionless parameter γ, also called opacity of the gas, is defined as :

$$\gamma \equiv \frac{8\sigma_T a_r T_{\rm CMB}^4}{3Hm_e c}\frac{x_e}{1+f_{He}+x_e} \tag{1.3.83}$$

  with a_r the radiation constant.

The evolution of the matter temperature is thus ruled by the equation:

$$\frac{dT_{\rm M}}{dz} = -\frac{1}{(1+z)H(z)}\left[\left.\frac{dT_{\rm M}}{dt}\right|_{\rm adia} + \left.\frac{dT_{\rm M}}{dt}\right|_{\rm Compton}\right] = \frac{1}{1+z}\left[2T_{\rm M} + \gamma(T_{\rm M} - T_\gamma)\right]. \tag{1.3.84}$$

The evolution of $T_{\rm M}$, therefore, mainly depends on the second term, with the sign of the difference $T_{\rm M} - T_\gamma$ determining whether collisions heat or cool down the gas, and the value of γ is responsible for the coupling strength: If $\gamma \gg 1$, the second term dominates and Compton scatterings thermally couple CMB photons and baryons ($T_{\rm M} \propto T_\gamma \propto (1+z)$), whereas $T_{\rm M}$ adiabatically decays as $T_{\rm M} \propto (1+z)^2$ when $\gamma \ll 1$. This transition typically occurs around $z \sim 150$ when $T_{\rm M} \sim 400$ K.
Those two processes are the dominant ones at high redshift (typically above $z \geq 50$). Other processes that can play a role depending on the physical context include *bremsstrahlung*, *Photoionization heating*, *Photorecombination cooling*, *Collisional ionization cooling*, *Collisionial recombination heating*, *Shocks* and *Line cooling*. Standard CMB codes usually ignore those processes since they impact the ionization fraction only at the 10^{-3}% level [532]. Electromagnetic energy injection can lead to important heating as well, and we shall include this process later in this work.

1.3.3.5 *Beyond the first realistic model: numerical resolutions*

In the late 1990's and the beginning of this millenium, it was realized that correct interpretation of the results from *WMAP*, and later *Planck* experiments would require percent and permille precision respectively around the peak of the visibility function, i.e. the time of last scattering [327], [403], [515], [532]. In order to overcome this challenge, the physics of recombination has been extensively complexified, and numerical codes developed for solving the relevant sets of equations. In general, an accurate recombination code should solve a very involved system of equations that couples: i) a virtually infinite number of levels of the hydrogen atoms, including angular momentum substates; ii) a virtually infinite number of levels of the Helium atoms singly and doubly ionized; iii) the photons field through the radiative transfer equation; iv) the matter temperature. Entering in a full description of the relevant physics, which took about a decade of hard work at the start of the millennium, goes well beyond the scope of this work. It is, however, necessary to introduce the different recombination codes used, namely Recfast [531], [532], HyRec [38] and CosmoRec [165], and to sketch the main differences between them. This short review is mainly based on Refs. [38], [165], who introduced the two most precise recombination codes available today. The main goal of these codes is to solve a generalized version of eq. (1.3.79) under a certain number of assumptions (preferably as least as possible) (see e.g. ref [38]), taking into account "bound-free", "bound-bound" and ground state transitions. The standard "multilevel atoms " set of equation is

$$\dot{x}_{nl} = \dot{x}_{nl}^{\rm rec} + \sum_{n'\geq 2,l'} \dot{x}_{nl\leftrightarrow n'l'} + \dot{x}_{nl\leftrightarrow 1s} \tag{1.3.85}$$

with $\dot{x}_{nl}^{\rm rec}$ the contributions from "bound-free" transitions given by

$$\dot{x}_{nl}^{\rm rec} = n_{\rm H} x_e^2 \alpha_{nl}(T_m, T_r) - x_{nl}\beta_{nl}(T_r) \tag{1.3.86}$$

where $\alpha_{nl}(T_m, T_r)$ is the recombination coefficient to the excited state nl, including stimulated recombinations, and $\beta_{nl}(T_r)$ is the rate of photoionizations from nl by blackbody photons. As in the TLA, the photoionization rate is related to the recombination rate assuming detailed balanced is satisfied. They are typically given by [38], [133], [532]

$$\alpha_{nl}(T_m, T_r) = \frac{h^3}{(2\pi\mu_e T_m)^{3/2}} \int_0^{+\infty} e^{-\epsilon_0\kappa^2/T_m} \gamma_{nl}(\kappa)[1 + f^{\rm bb}(E_{\kappa n}, T_r)] d(\kappa^2) \tag{1.3.87}$$

$$\beta_{nl}(T_r) = \frac{(2\pi\mu_e T_m)^{3/2}}{(2l+1)h^3} e^{\epsilon_n/T_r} \alpha_{nl}(T_m = T_r, T_r)\,. \tag{1.3.88}$$

with $\mu_e \equiv m_e m_p/(m_e + m_p)$ the reduced mass of the electron-proton system, κ the momentum of the outgoing electron in units of $h/2\pi a_0$ with a_0 the reduced-mass Bohr radius and $\epsilon_{kn} \equiv \epsilon(\kappa^2 + n^{-2}) = h\nu$ according to the energy conservation law. The coefficient $\gamma_{nl}(\kappa)$ encodes the transition probability from bound state nl to free state with momentum κ (summing over momentum substates $l' = l \pm 1$) and is given in Refs. [38], [133].

The contributions from bound-bound transition is [38]

$$\dot{x}_{nl\leftrightarrow n'l'} = -\dot{x}_{n'l'\leftrightarrow nl} = x_{n'l'} R_{n'l'\to nl}(T_r) - x_{nl} R_{nl\to n'l'}(T_r) \tag{1.3.89}$$

where $R_{nl\to n'l'}$ is the transition rate from state nl to $n'l'$. In general it is given by the sum between radiative and collisional processes:

$$R_{nl\to n'l'} = R^{\rm rad}_{nl\to n'l'}(T_r) + R^{\rm coll}_{nl\to n'l'}(T_m, n_e)\,, \tag{1.3.90}$$

However, collisionial excitations are usually negligible in the cosmological context. $R^{\rm rad}_{nl\rightarrow n'l'}(T_r)$ is either the rate of absorption of blackbody photons resonant with the transition if $n' < n$, or the rate of spontaneous and stimulated decays if $n' > n$. It is given by

$$R^{\rm rad}_{nl\rightarrow n'l'}(T_r) = \begin{cases} A_{n'l'\rightarrow n'l'}[1 + f_{\rm bb}(\epsilon_n - \epsilon_{n'}, T_r)] & \text{if} \quad n > n' \\ \frac{g_{l'}}{g_l} e^{(\epsilon'_n - \epsilon_n)/T_r} R^{\rm rad}_{n'l'\rightarrow nl} & \text{if} \quad n < n' \end{cases} \tag{1.3.91}$$

where, as usual, $A_{n'l'\rightarrow n'l'}$ is the Einstein A-coefficient for spontaneous emission. Stimulated emission, accounted for via the term proportional to f_{bb}, is an important process in our Universe, in particular for the highly excited states.

Finally the transition to the ground states are accounted for by the $\dot{x}_{nl\leftrightarrow 1s}$ term. However, a large number of transition are forbidden. At first sight, only the $2s$ and np ($n \geq 2$) are relevant, given that two-photons transitions from higher energy states are dominated by the so-called "1+1" photon decays (i.e. cascade process), already accounted for in this treatment. They are given by :

$$\dot{x}_{2s\leftrightarrow 1s} = -A_{2s1s}(x_{2s} - x_{1s} e^{-E_{21}/T_r}) \tag{1.3.92}$$

$$\dot{x}_{np\leftrightarrow 1s} = A_{np1s}(1 + f^{\rm bb}_{np1s})\left[x_{np} - 3x_{1s} f^{+}_{np}\right] \tag{1.3.93}$$

We have already encountered the first equation in the TLA model and we had introduced A_{2s1s} as the (forbidden) $2-\gamma$ decay rate from the $2s$ state to the ground state. In a similar fashion, A_{np1s} stands for the spontaneous Lyman$-n$ emission rate, $f^{\rm bb}_{np1s}$ the blackbody photon occupation number and f^{+}_{np} is the photon occupation number with frequency higher than the Lyman$-n$ one. Note that, like in the TLA model, Lyman$-n$ photons are very likely to be reabsorbed given the high optical depth of those lines. Working in the Sobolev approximation allows to multiply each A_{np1s} coefficient by the absorption probability $P_{np1s} = 1/\tau_{np1s}$, which is just a generalization of our eq. (1.3.75), replacing the Lyman$-\alpha$ wavelength by the Lyman$-n$ one.

The number of free electrons, assuming that the number of electrons in excited states of hydrogen or helium is negligible and that helium is singly ionized, is simply

$$x_e \simeq 1 - x_{1s} + f_{\rm He} - x^{\rm He}_{1s}\,, \tag{1.3.94}$$

where $f_{\rm He} \equiv Y_p/(4(1-Y_p))$ represents the fraction of helium nuclei. Thus, ignoring here the contribution from Helium, we simply get [2]

$$\dot{x}_e = -\dot{x}_{1s} = \dot{x}_{2s\leftrightarrow 1s} + \sum_{n\geq 2,} \dot{x}_{np\leftrightarrow 1s}\,. \tag{1.3.95}$$

Transition rates involve integration over the photon number density and thus require to follow the evolution of the background radiation with a radiative transfer equation. This will lead to departures (or spectral distortions) from the standard blackbody distribution. Introducing $\Delta f(\nu, t) = f(\nu, t) - f_{\rm bb}(\nu, t)$, one can write the partial differential equation governing the evolution of the distortion as [161], [165]:

$$\frac{1}{c}\frac{d\Delta f(\nu,t)}{dt} = \frac{1}{c}\left[\frac{\partial \Delta f(\nu,t)}{\partial t} - \nu H(t)\frac{\partial \Delta f(\nu,t)}{\partial \nu}\right] = \mathcal{C}[\Delta f(\nu,t)]_{\rm em/abs} + \mathcal{C}[\Delta f(\nu,t)]_{\rm scat}\,, \tag{1.3.96}$$

2 Hydrogenic (monoelectronic) Helium can be treated with the same set of equations and rescaled transition rates by $Z^4\mu$, where μ is the helium nuclei-electron reduced mass. For a detailed multi-level treatment of HeI, see Ref. [163], [574]. Some complication arises due to the necessity of distinguishing singlet spin state and triplet spin state.

where, in general, it is necessary to distinguish emission and absorption processes, taken into account via $\mathcal{C}[\Delta f(\nu,t)]_{\rm em/abs}$ and real scattering ones accounted for by $\mathcal{C}[\Delta f(\nu,t)]_{\rm scat}$.

The Recfast code

One of the first codes attempting to solve the full recombination problem is the *Recfast* code [531], [532]. However, it makes use of a simplified version of the multi-level equations assuming: i) statistical equilibrium among l substates; ii) that the photon field can be described by a blackbody distribution expect near the Ly-α line. The first simplification is a major computational gain, as the number of equations scales like $\sim n$ instead of $\sim n^2$. The nl substates are simply related by a generalization of eq. (1.3.67):

$$n_{nl} = \frac{(2l+1)}{n^2} n_n \tag{1.3.97}$$

with n_n the total number of H atoms in a excited state with principal quantum number n. In practice, their computation amounts to rescaling the equilibrium photoionization and recombination coefficient of each state by the exact number density of the corresponding state. In its original version, the code allows to describe recombination physics at the $\pm 1.5\%$ accuracy level. At the % level percent precision, $\mathrm{He}^{2+} \rightarrow \mathrm{He}^{+}$ recombination is shown to be well described by an effective three-level atom, whereas equilibrium is shown to be valid for He^{2+}. However, this computation leads to an overlaping of the recombination of hydrogen and helium. This is not correct and comes from neglecting HI absorption process and spin-forbidden transition of helium, leading to $\sim$3% difference at helium recombination. Their main result is that hydrogen recombination happens *faster* and the freeze-out fraction is lower than in the standard case. This is due to the fact that the typical photoionization and recombination rates are bigger than in the 'case B'. Remarkably, most of the effects of the complicated calculations can be captured by a *single fudge factor* $F = 1.14$, rescaling ionization and recombination coefficient entering the TLA from the 1960's! This allows to speed up the computation greatly with respect to the multi-level case, without losing the required precision at that time.
Even nowadays, this code is still by far the most used one despite its (original) limited precision. Indeed, it is possible to mimick the lacking physics by upgrading the fudge factors to *fudge functions* [515], in order to get per-mille precision if the ionization history does not vary too much from the referenced one [541]. Thus, it is possible to get accurate ionization history in a runtime of a fraction of seconds, which makes it very interesting in the perspective of statistical analysis using Monte Carlo Markov Chains.

HyRec and CosmoRec: towards a complete treatment of cosmological recombination

With the increasing precision of experiments, several groups have pointed out that early calculations using original Recfast are not sufficently accurate for an unbiased estimate of cosmological parameters [403], [515]. The main parameters affected being the amplitude A_s and tilt n_s of the primordial power spectrum, ultimately related to inflation modeling, and the density of baryons ω_b. To summarize, a nice quote attributed to D. Scott states that "getting 10^{16} GeV physics right means we have to understand eV physics with high precision". The significant physical effects that need to be included beyond Recfast are:

- The computation of the non-equilibrium angular momentum substates of each level, relevant at late times, which amounts to solving eqs. (1.3.85) and (1.3.95). It was first shown in Refs. [167], [285] that it was necessary to go beyond equilibrium assumption as collisions are too little to

smear out the electrons and distribute them in each angular momentum substate. Although conceptually simple, this improvement is extremely demanding computationally as now the number of equations scales like $\sim n^2$. To get results at the required accuracy, up to 500 levels need to be followed, meaning about 250 000 equations need to be solved simultaneously! It was made possible, however, to get runtime of the order of ~ 2 seconds thanks to the "effective" multilevel atom method introduce in Ref. [37]. The main idea is that one can solve eqs. (1.3.85) and (1.3.95) only for a population of a few excited states (typically $2s$ and the lowest p levels) and make use of precomputed transition tables for higher excited states, which are mediated by CMB blackbody photons and therefore only depends on the photon and matter temperature, independently of the Cosmology. Illustration of the modification in Hydrogen recombination with 20, 50, 500 Hydrogen shells are plotted in fig. 13, left panel.

- Many subtle physical effects of the Lyman$-\alpha$ turns out to be important, which require solving the full radiative transfer in the vicinity of the line. As we have seen, the most important channels for hydrogen recombination are the $2p \rightarrow 1s$, controlled by the slow escape from the line via redshifting of photon and the $2s \rightarrow 1s$, for which computation of the two-photons absorption rate receives many corrections. In the historical TLA, the Sobolev approximation was used to compute escape from the center of the resonnance, further implemented in the Recfast code. The Sobolev approximation, introduced in the context of stars in order to describe the probability of photons to escape the expanding envelopes [560], greatly simplifies the problem, as it enables to separate the problem of the evolution of the photon field and the populations of the hydrogen atom. It assumes that i) the populations of the levels and the radiation field are quasi-stationary; ii) Each scattering leads to a complete redistribution of photons over the whole line profile. However, computations beyond this approximation are required to get accurate results. Indeed, time-dependent effects in the escape problem due to the evolution of the properties of the medium (especially the ionization degree) can induce a 1.6-1.8% correction to x_e around $z_{\rm rec}$ [162]. Atomic recoil, doppler boosting and broadening (as encoded in the Kompaneets equation for Compton scattering) affect the frequency redistribution of the resonnant scattering, which leads to partial redistribution of photons over the line profile. Meanwhile, a correct application of detailed balance show a frequency-dependent asymmetry between the emission and absorption profile. All these effect generate in turn important corrections to the Sobolev optical depth [162], [281], [307].

- Moreover the $2s \rightarrow 1s$ absorption rate is also affected by subtle physics. The stimulated emission due to ambient CMB photons slightly increases the total transition rate, leading to more than 1% difference of x_e around recombination [180]. Soon after, it was realized that the excess of non-thermal photons can also affect the $2s \rightarrow 1s$ process, as their absorption delay recombination and introduce percent-level corrections [309], [369]. Sub-percent correction comes from considering the feedback of Lyman$-n$ photons [181]. Modifications to Hydrogen recombination by including feedback and induced $2s1s$ transitions are shown in fig. 13, right panel.

- Two-photon decays from higher levels, initially neglected in the treatment of eq. (1.3.92), were shown to have an important effect in Ref. [221], [597], with a treatment improved later on by Refs. [160], [306]. The inclusion of possible Raman scattering tends to increase the number of photons on the blue side of the Lyman$-\alpha$ line, in turn increasing the impact of Lyman$-\beta$

feedback, while decreasing the Lyman$-n$ one [165], [306]. All these effects must be included as well in order to have reliable results.

- Helium HeII$\rightarrow$ HeI recombination must also be extended, taking into account singlet and triplet spin states, while corrections to HeIII $\rightarrow$ HeI Saha equilibrium recombination are negligeable. It is usually solved in a standard multilevel atoms for up to few hundred levels and resolution of the l substates up to $n = 10$ [310], [532]. Typically, a similar list of processes as the one of hydrogen enters the problem, with further complications given that HeI is non-hydrogenic [163], [310], [574], [575]. The effects of semi-forbidden transitions (i.e. spin-changing transitions) are important for HeI recombination [221], [370], [574], [596]. The detailed feedback of Helium photons has to be taken into account [163], [174], [574]. Furthermore, although the number of neutral H during HeI recombination is tiny, the opacity of the HI continuum is very high. This leads to the absorption of part of the photons emitted by Helium and thus decreases the level of HeI feedback onto itself. HeI recombination is pushed closer to Saha equilibrium, henceforth accelerating it with respect to the Recfast result [174], [310], [370], [520]. Effects of Helium photon feedbacks when switching on/off HI continuum absorption are illustrated in fig. 14, left panel. On the right panel of the same figure, we illustrate the impact of switching on/off the spin semi-forbidden transition and HI continuum absorption of the $2^1P \rightarrow 1s$ and $2^3P \rightarrow 1s$ photons.

HyRec and CosmoRec are the most precise codes, both based on the "effective" multi level approach, although the later one includes more physical effects in particular related to Helium recombination and radiative transfer [174], [541], which are especially relevant for the studies of spectral distortions [173]. Differences in the code also arise at the level of the resolution scheme. While CosmoRec solves iteratively the coupled system of equations "recombination+radiative transfer", HyRec simultaneously solves for the radiation field and the recombination history thanks to validated analytic approximations.
All three codes are now implemented in the Boltzmann code CLASS, allowing to perform a detailed comparison of these codes at the level of the ionization histories, illustrated here in Fig. 15 left panel and later on at the level of the CMB power spectra. The difference with the improved treatments are clearly visible as few percent corrections to the original Recfast. The most important corrections are the ones arising around the peak of the visibility functions, namely the improved treatment of the radiative transfer of Lyman$-n$ lines. However, the main modifications to HeI recombination due to HI continuum absorption are also important. The differences between HyRec, Recfast with fudge functions and CosmoRec are further illustrated in the right panel of Fig. 15, and mainly consist in the improved treatment of HeI recombination in CosmoRec, as well as a higher number of levels considered in the 2γ and Raman processes. However, these differences will stay below cosmic variance in the multipole range of the CMB power spectra probed by *Planck* and, although CosmoRec includes more physical effects, it is safe to use HyRec or a fudged version of Recfast for cosmological parameter extraction [541].

1.3.3.6 *Recombination as a tool for new physics: a first comment*

It is remarkable that such a high precision on recombination physics has been achieved during the last decade, while current cosmological data indicate an excellent agreement with standard physics expectations. Interesting consequences of such hard work is the possibility of constraining non-standard scenario as we shall explore in this work, especially in the case of *exotic electromagnetic energy injec-*

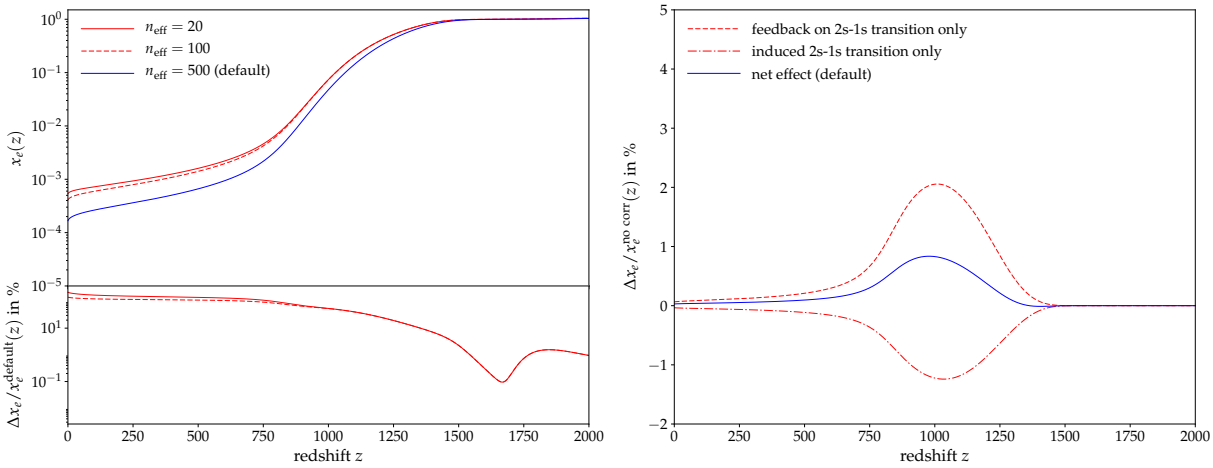

Figure 13: Comparison of some standard feature of CosmoRec in the Hydrogen physics. *Left panel* – Increasing the number of Hydrogen shells. *Right panel*– Switching on feedback onto the 2s1s transition (red dashed line) delays recombination while the induced 2s1s transition (red dashed-dotted line) accelerates it. The net effect is acceleration (blue curve).

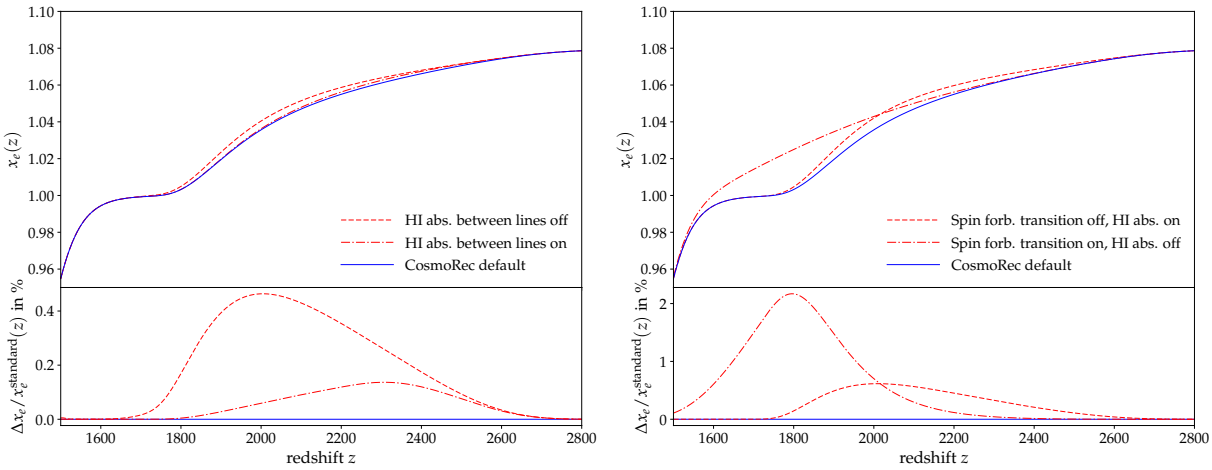

Figure 14: Comparison of some standard feature of CosmoRec in the Helium physics. *Left panel* – Switching off semi-forbidden spin transition (red dashed curve) or HI continuum absorption (red dashed-dotted curve) tend to delay recobmination with respect to defaut case (blue curve). *Right panel* – Switching on HeI feedback delay recombination (red dashed curve), however taking into account absorption from HI continuum between lines tend to accelerate it again, with a net effect that is usually neglected in standard recombination (blue curve).

tion, which can follow from particle decays or annihilations. Another nice repercussion is the possibility of testing *variations of fundamental constants*, as has been done extensively in the past [72], [88], [260], [292], [358], [424], [513], [530].

Recombination physics, as we have already argued, has a major impact on the studies of CMB anisotropies, and it is through modifications of the CMB TT, EE and TE power spectrum that most of the constraints come from. The impact of varying some cosmological parameters inside their current (roughly) 1σ uncertainty as measured by *Planck* [19] is illustrated in Fig. 16. The degeneracy between parameters in CMB power spectra analysis degrade the possible sensitivity that one could

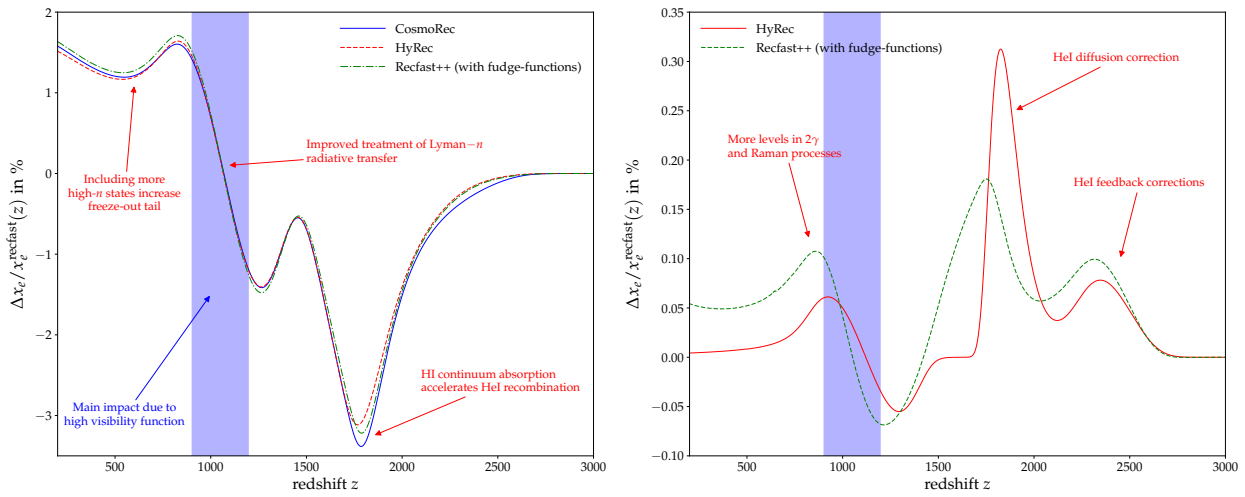

Figure 15: *Left panel* – Comparison of the recombination history from the CosmoRec, HyRec and Recfast v1.5 (with fudge-functions) codes in their default setting with respect to original Recfast. *Right panel* – Further comparison of the recombination history from HyRec and Recfast v1.5 (with fudge-functions) codes in their default setting with respect to CosmoRec. Adapted from Ref. [541]..

hope to have thanks to the subpercent precision on the recombination physics.

It is, however, important to recall that recombination physics is intrinsically linked to another observables, namely the spectral distortions from a perfect blackbody of the CMB. Indeed, we have seen that solving the recombination problem in practice amounts to solving the coupled system of equations "recombination physics + radiative transfer", which means that an accurate code is able to follow those distortions and predict the amount expected today due to both *purely standard and non-standard physics*. A recent review of all standard processes leading to spectral distortions can be found in Ref. [172]. Nowadays, simple analytical estimate as well as accurate numerical codes are available to compute spectral distortions, and we discuss those in more details in sec. 3.6. However, in the context of standard recombination physics, it is necessary to mention the most important ones, namely the *cosmological recombination lines* (CRR), created by the large emissions of photons in bound-bound and bound-free transitions. Many calculations have been carried out over the years [163], [167], [178], [179], [222], [223], [368], [516], [520], [522], and it is nowadays possible to get % level prediction in a few seconds runtime, thanks to the most recent one, namely the CosmoSpec code [173]. These tiny distortions, at the nK-μK level, which should today be present at mm to dm wavelength, are sensitive to the finest details of the recombination history. They represent a *fingerprint* from the recombination era, encoding very distinct spectral features of the recombination processes. Their amplitude typically depends on the number density of baryons in the Universe, while the detailed shapes of the CRR is affected by Helium recombination. Moreover, the positions and width of the line depends on both *when* and *how fast* recombination occurs, thereby giving a tremendous leverage on recombination physics, while providing us with an independent way of measuring cosmological parameters [159]. Unfortunately, in its current proposal to NASA, the *PIXIE* experiment lacks sensitivity by a factor of a few [172], [209]. One needs to go for space experiments such as *PRISM* [48] and *Millimetron* [556], or ground-based experiment in the cm to dm wavelength range [501] to measure these distortions.

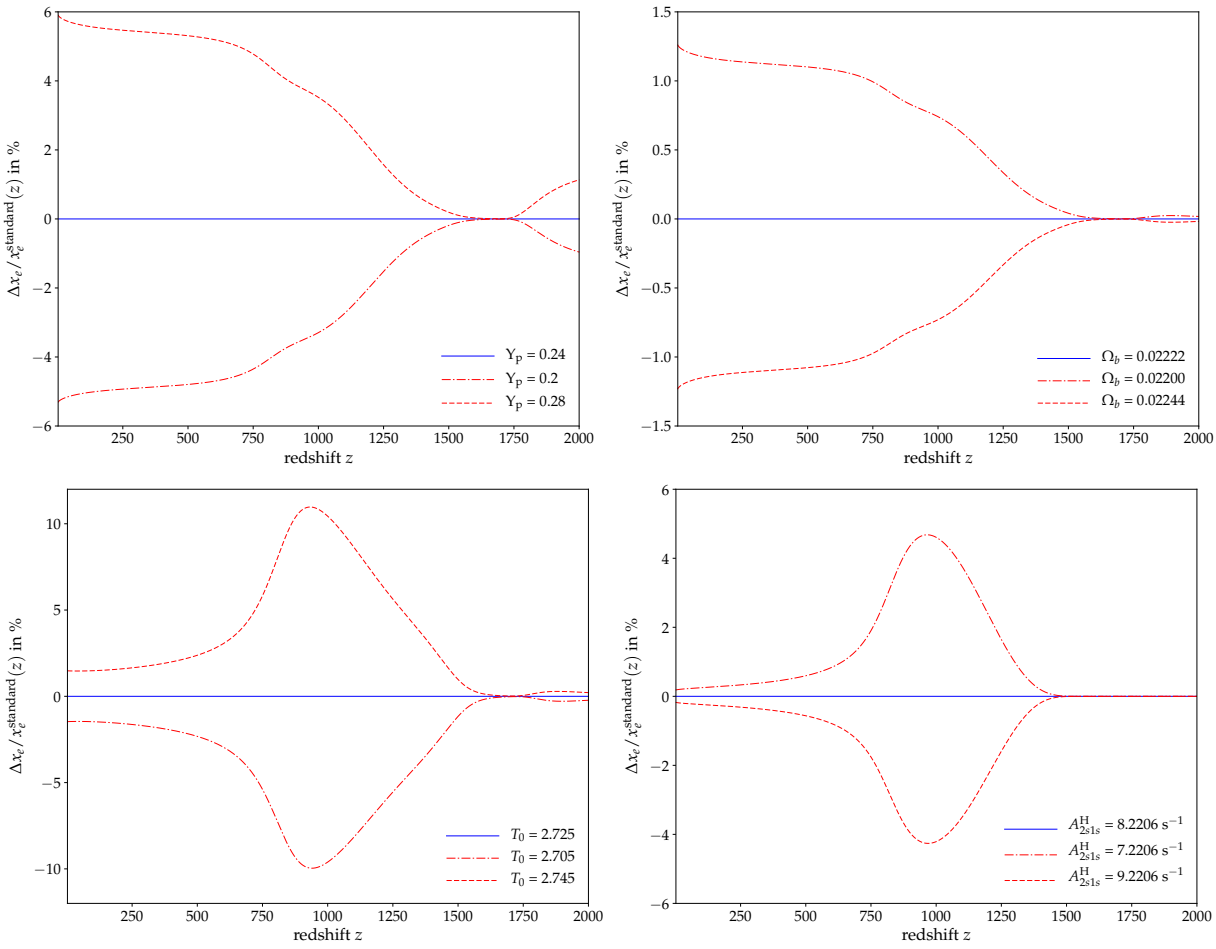

Figure 16: Impact of varying some cosmological parameters on the recombination history inside their current (roughly) 1σ uncertainty as measured by *Planck* [19].

1.3.4 *Reionization*

1.3.4.1 *General considerations*

Although the recombination era is well under control from both the theoretical and the observational point of view, the low-redshift evolution of the ionization fraction is affected by a major unknown: the onset of star formation, which triggers the beginning of the so-called *Epoch of reionization* (EoR). The EOR of the Universe, namely the era at which the cosmic gas mainly made of Hydrogen and Helium atoms goes from (almost) fully neutral to fully reionized, is still largely unknown nowadays. Currently, the best observation of this transition of the Universe is the so-called Gunn-Peterson trough: the observation of redshifted Lyman-α absorption lines in quasar spectra is a very sensitive probe of the presence of neutral hydrogen along the line of sight. Even a small fraction of neutral hydrogen leads to a clear signature, and we expect quasars spectra to show a very small level of Lyman-α absorption at redshift for which the Universe is reionized. Predicted in 1965 [286] and observed in Quasar spectra much more recently (Fig. 17 shows the historical first measurement of the GP trough) [92], [94], [238], [239], [585], it teaches us that the Hydrogen was almost fully reionized by $z \simeq 6$. Hence, in the standard picture, Hydrogen reionization occurs across the entire Universe between $z \simeq 12$ to $z \simeq 6$, typically

because of ionizing photons emmited by early star-forming galaxies. Quasars are then believed to be responsible for Helium reionization from $z \simeq 6$ to $z \simeq 2$ (see e.g. [425] for a recent review).

Details of the EoR are strongly connected to many fundamental questions in cosmology and astrophysics. It could teach us about many properties of the first galaxies and quasars, such as the time at which they form and how the formation of very metal-poor stars proceeded, but we could also learn about more exotic processes such as the nature of DM itself. It is usually accepted that a dominant source of reionization would be given by Lyman continuum photons from UV sources in pristine star-forming galaxies, but the fraction of photons produced by stellar populations that can escape to ionize the IGM, or the efficiency of the stellar population to produce Lyman continuum photons, two key quantities of our current reionization models, are still suffering orders of magnitude uncertainties.
Another question that has also puzzled the community is whether early galaxies were the only source of reionization in the Universe. A key quantity measured by CMB experiments is the so called *optical depth to reionization* $\tau_{\rm reio}$, quantifying the amount of Thomson scattering between CMB photons and free electrons in the IGM. From eq. (1.3.56), one defines

$$\tau_{\rm reio}(z) \equiv \int_0^{z_{\rm beg,\ reio}} n_e(z)\sigma_T \frac{dt}{dz'} dz' \ . \tag{1.3.98}$$

with $z_{\rm beg,\ reio}$ the redshift of the beginning of reionization[3], $n_e(z)$ the number density of free electrons and σ_T the Thomson cross-section. Measurements of the Gunn-Peterson trough seem to require reionization to be centered around $z\ 6-7$, thus hinting to rather small optical depth to reionization τ. However, this bound was in tension with the very high measurements of $\tau_{\rm reio} = 0.17 \pm 0.04$ based on the temperature-polarization TE cross-power spectrum of *WMAP* after 1 year of data taking [373], requiring reionization to be centered somewhere in between $11 < z_{\rm reio} < 30$ (95% CL). Several solutions to the problem have been invoked: i) One might need to reinterpret the Gunn-Peterson bound, since they are model-dependent. In practice, they rely on a modelling of the IGM density and temperature, the UV background from stars and some assumption about the homogeneity of the reionization. Release of the tension has been achieved by questioning these modelisations [93], [421]. ii) This discrepancy could also indicate the need for a complexified star reionization picture (invoking e.g several population of stars [153], [598]). iii) Finally, it was suggested that this could be a hint for DM annihilations in halos or decay, since these processes would typically enhance the optical depth. One of the first proposals was, for instance, the presence of decaying massive sterile neutrinos [294]. Over the years, this discrepancy has systematically decreased, and finally disappeared with *Planck* measurements, but still improving our knowledge of this epoch could lead to unexpected discoveries, while at the same time helping us to constrain exotic reionization models, as we shall do in this work. In the near future, many experimental efforts will be devoted to measuring this era precisely, mostly through the 21 cm line created by the hyperfine transition of the Hydrogen atom. Tomographic surveys of the cosmological 21cm observable, sensitive both to $x_e(z)$ and $T_{\rm M}(z)$, are certainly the most promising avenue to progress in the knowledge of these redshift epochs. Experiments such as PAPER

3 In CAMB it is hardly coded at 50. In CLASS it can be set by the user. In our studies, we define it as the minimum of the visibility function $g(z)$ since in the absence of reionization it is a decreasing function of redshift. We comment on this issue in appendix D.3.

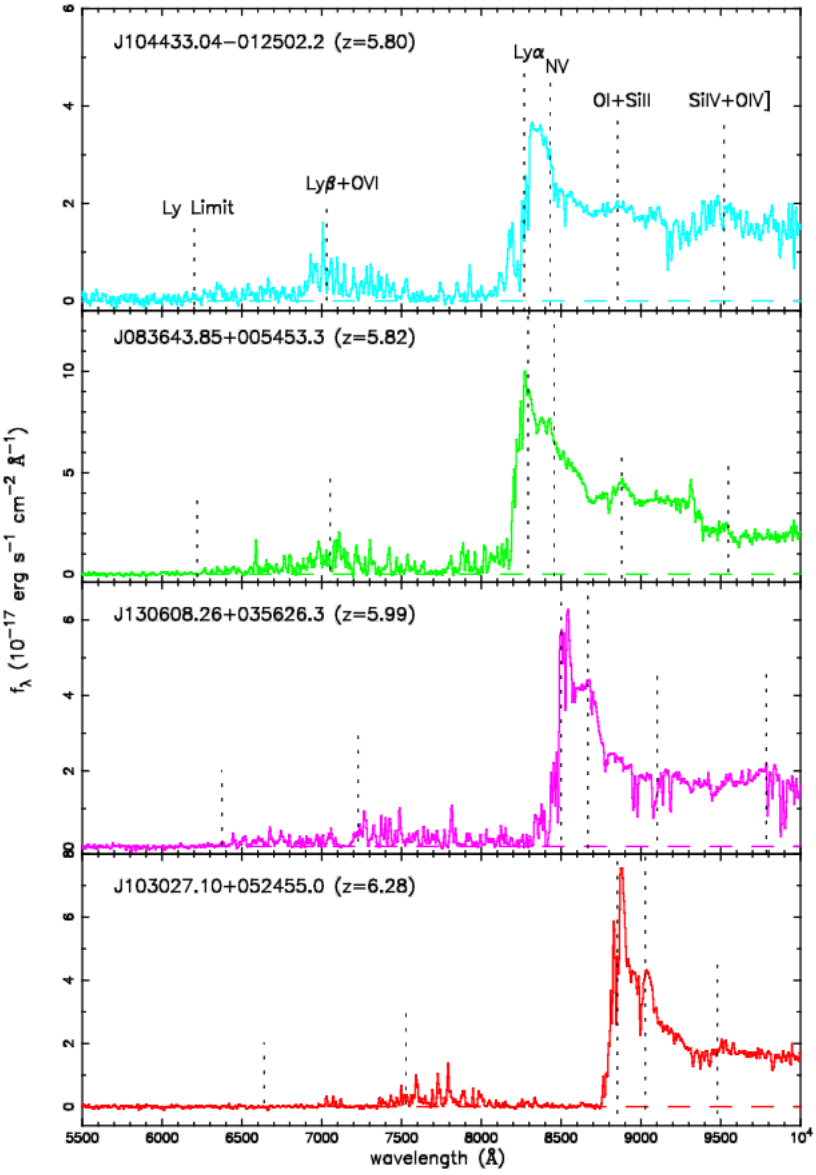

Figure 17: Optical spectra of $z \geq 5.8$ quasars observed with Keck/ESI, in the observed frame. In each spectrum, the expected wavelengths of prominent emission lines, as well as the Lyman limit, are indicated by the dashed lines. The quasar spectrum at $z = 6.28$ is historically the first spectrum ever measured exhibiting the Gunn-Peterson trough: its average transmitted flux in the band $8450 < \lambda < 8710$ (Lyman-α forest region) is consistent with zero flux. Figure taken from ref. [94].

64 [4], 21CMA [5], MWA [6], LOFAR [7], HERA [8] or SKA [9], are now, or will be, attempting at measuring the 21 cm signal. Although pathfinders and first generation instruments have given a few results [40], [485], experiments having the good accuracy level in the redshift range of interest are not yet built, and therefore far from shedding light on the EoR.

On the other hand, CMB experiments are also sensitive to the EoR. Indeed, the increase of free electrons at low-z enhancing the Compton scattering rate of CMB photons off these free electrons will lead to very peculiar pattern in the power spectra. The most characteristic ones, which we shall describe in this section, are the step-like suppression of CMB TT modes inside hubble horizon at reionization, typically above $\ell \sim 20$, accompanied by the big regeneration of power in the same multipole range of the EE spectrum, the so-called *reionization bump*. Many studies in the past have tried to assess more carefully what amount of information could be extracted from CMB power spectra (see e.g. [326], [356], [403], [435] for more detailed studies). The CMB is mostly sensitive to the column density of electrons along each line-of-sight[10] and therefore to the Thomson optical depth to reionization τ. There are well known degeneracies between τ and other cosmological parameters, e.g., when using temperature data alone, with the amplitude of the primordial scalar perturbations[11] A_s and the spectral index n_s. Moreover, in extensions of the ΛCDM model, there exists a degeneracy between τ and the sum of neutrino masses $\sum m_\nu$, which gets *strengthened* by the addition of external datasets such as BAO measurements [42], [407]. Thus, an accurate measurement of τ through the reionization bump at large scales is essential for the determination of other cosmological parameters as well.

Let us also mention that different reionization histories do lead to differences in the low-ℓ part of the EE spectrum that can potentially give more insight on this epoch. Unfortunately, principal component analysis (PCA) have revealed that CMB experiments, limited by cosmic variance in this multipole range, would not be the best probe of this era although it can have some handle on the first five eigenmodes [435].

1.3.4.2 *Implementation in Boltzmann codes*

In principle, in order to account for the reionization in our universe, one needs to modify the coupled recombination equations by adding a source term quantifying the impact of stars (typically UV photons background). This is, however, not the strategy that has been adopted until now by Boltzmann codes, based on the fact that: i) There are order of magnitudes uncertainties on the paramaters quantifying the impact of stars; ii) The CMB is not so sensitive to the exact details of reionization, affecting multipoles that are cosmic variance limited; iii) Although stellar reionization is believed to have happened in "bubbles" embedded in neutral surroundings, and thus to be very inhomogenous, the CMB is sensitive to the average over all sky directions of $x_e(1+\delta_b)$ and this complication only affects the determination of cosmological parameters at a negligeable level [15]. Thus, simple prescriptions

4 http://eor.berkeley.edu
5 http://21cma.bao.ac.cn
6 http://www.mwatelescope.org
7 http://www.lofar.org
8 http://reionization.org
9 http://www.skatelescope.org
10 Note that potentially, the CMB is sensitive to *inhomogeneous* (or patchy) reionization. Measuring such traces would also help in constraining models of reionization. It has been found, however, that the effect of patchy reionization, leading to non-gaussianity at small scales, would be very challenging to detect with next-generation CMB experiments [444], [557], [569].
11 The normalization of the $\ell > 20$ part of the spectrum is mostly controlled by the product $A_s \exp^{-2\tau}$.

have been used to model the impact of stars, simply interpolating between a vanishing free electron fractions at high-z to a fully reionized medium at low-z. Usually, reionization occurs in two steps: the first step corresponds to the Hydrogen reionization and the first ionization of the Helium, while the second, much smaller, corresponds to the Helium second reionization.
The most common parametrization of this first step is the so-called instantaneous ("camb-like") reionization, parametrized as [398]:

$$x_e(z) = \frac{f}{2}\left[1 + \tanh\left(\frac{y - y_{\rm re}}{\Delta y}\right)\right] \tag{1.3.99}$$

with $f = 1 + n_{\rm He}/n_{\rm H}$, $y = (1+z)^{3/2}$ and $\Delta y = 3(1+z)^{1/2}\Delta z$. The reionization is, therefore, redshift-symmetric, centered around the key parameter $z_{\rm re}$ with a width given by Δz, both parameters being free to vary. This parametrization has been used, for instance, by the *Planck* collaboration in their recent data release in 2013 and 2015.
However, this redshift-symmetric behaviour is in tension with constraints from ionizing background measurements of star-forming galaxies and from low-redshift line-of-sight probes such as quasars, Lyman-α emitters, or γ-ray bursts [185], [237], [342], [511]. Thus, people have been investigating redshift-asymmetric parametrization, the simplest ones being exponential or power-law functions. An example of the latter one is given by [220] [12]:

$$x_e(z) = f \times \begin{cases} \frac{1-Q_{\rm p}}{(1+z_{\rm p})^3-1}\left((1+z_{\rm p})^3 - (1+z)^3\right) + Q_{\rm p} & {\rm for} z < z_{\rm p} \\ Q_{\rm p}\exp\left(-\lambda(z - z_{\rm p})\right) & {\rm for} z \geq z_{\rm p}. \end{cases} \tag{1.3.100}$$

The parameters of the second model have been estimated to be close to $z_{\rm p} = 6.1$, $Q_{\rm p} \equiv Q_{\rm HII}(z_{\rm p}) = 0.99986$ and $\lambda = 0.73$ by direct observations of the ionized hydrogen fraction $Q_{\rm HII}(z)$. Similarly to Ref. [453], we fix $z_{\rm p}$ and $Q_{\rm p}$ to their best-fit values, and we let the evolution rate λ free to vary in order to cover a large range of possible ionization histories.
For comparaison, it is possible to use the power-law asymmetric reionization suggested by Ref. [15]:

$$x_e(z) = \begin{cases} f & \text{for } z < z_{\rm end}, \\ f \times \left(\frac{z_{\rm early} - z}{z_{\rm early} - z_{\rm end}}\right)^{\alpha} & \text{for } z \geq z_{\rm end}, \end{cases} \tag{1.3.101}$$

where $f = 1 + f_{\rm He} = 1 + n_{\rm He}/n_{\rm H}$ and we have checked explicitly that differences between the two parameterizations are not visible at the current sensitivity level, and most probably even for future CMB experiments.
Non-parametric reionization have also been proposed, with the ionization fraction let free to vary in a given redshift bin [403], allowing to test exotic reionization scenarios happening in several steps, as it could happen if several sources of reionization were around.
In all cases, helium second ionization is treated as a hyperbolic tangeant centered around $z = 3.5$ with width $\delta_z = 0.5$. Changing the helium reionization redshift between 2.5 and 4.5 is known to change the total optical depth by less than 1 % [15].

Finally, we shall develop a new strategy in the following based on a somewhat important point:

12 Like the authors of Ref. [453], we replaced the argument of the exponent by $-\lambda\frac{(z-z_{\rm p})^3}{(z-z_{\rm p})^2+0.2}$ in order to improve the smoothness of the transition.

All these parametrizations neglect the fact that stars, while reionizing, also reheat the IGM. We shall therefore explicitly check that this is safe when computing the CMB and matter power spectrum, however this is of major importance for observables based on the temperature of the IGM, such as the 21cm signal.

To account for Lyman continuum photons from UV sources in early star-forming galaxies, we add a source term taken from [511], [512] of the form of Eq. (6.2.3) to the evolution equation of x_e:

$$\left.\frac{1}{E}\frac{dE}{dV\,dt}\right|_{\rm dep} = A_*\, f_{\rm esc}\xi_{\rm ion}\rho_{\rm SFR}(z)(1+z)^3 \tag{1.3.102}$$

where $f_{\rm esc}$ is the fraction of photons produced by stellar populations that escape to ionize the IGM, $\xi_{\rm ion}$ is the Lyman continuum photon production efficiency of the stellar population and $\rho_{\rm SFR}$ is the comoving star formation rate density. The fiducial values for these parameters are taken from Ref. [511], namely $f_{\rm esc} = 0.2$, $\xi_{\rm ion} = 10^{53.14}$ s^{-1}M$_\odot^{-1}$yr. We also use the functional form for the star formation density rate provided in Ref. [511],

$$\rho_{\rm SFR} = a_p \frac{(1+z)^{b_p}}{1+[(1+z)/c_p]^{d_p}} \tag{1.3.103}$$

with fit parameters $a_p = 0.01376 \pm 0.001$ M$_\odot$yr^{-1}Mpc^{-3}, $b_p = 3.26 \pm 0.21$, $c_p = 2.59 \pm 0.14$ and $d_p = 5.68 \pm 0.19$ [511]. Given that we do not have the correlation matrix of the fitted parameters, it is dangerous to vary more than one parameter at the same time within its confidence level. We thus simply leave an overall fudge factor A_* (expected to be of order one) free to match the measured optical depth.

Anticipating a bit over chapter 6, we mention that a consistent treatment of such a source term requires to specify *energy repartition functions* χ's encoding how the power is distributed among heating, ionization and excitation of the IGM. We follow the prescription of Refs. [155], [270] in which $\chi_i = \chi_\alpha = (1-x_e)/3$. To motivate this choice, we remind the reader that in the simple estimate provided by Shull and Van Steenberg [548] approximatively $1/3$ of the energy is effectively available for ionization in a neutral gas ($x_e = 0$). The adopted expression also fulfills the obvious physical criterion that no energy is available to ionize (or excite) an already fully ionized gas ($x_e = 1$). A linear interpolation is used for values in between, which corresponds to the reasonable Ansatz that the rate of ionization is proportional to the abundance of neutral hydrogen. The equality $\chi_i = \chi_\alpha$ has been checked to be approximately true by Ref. [155]. Qualitatively, stellar phenomena should also contribute to the heating of the IGM. In principle, one might expect this phenomenon to be captured by a term similar to the one introduced above, modulo a different energy repartition fraction function. However, it is sometimes argued that heating is most efficiently achieved thanks to harder photons (X-ray band), see e.g. Ref. [485]. To account for this, we introduce a source term in the brackets at the RHS of Eq. (1.3.84) with a *different* normalization, taken from Ref. [485],

$$\left.\frac{dE}{dV\,dt}\right|_{\rm dep} = 3.4\times 10^{40} f_X \rho_{\rm SFR}(z)(1+z)^3\,{\rm erg\,s^{-1}M_\odot^{-1}\,yr}. \tag{1.3.104}$$

The X-ray efficiency fudge factor f_X rescales the star formation rate/X-ray luminosity correlation and it thus expected to be of order $\mathcal{O}(1)$. Recent studies have suggested that it could vary up to 1 order of magnitude in the range $[0.2-2]$ [216], [252], [388], [428]–[430], and we thus set it to the benchmark value $f_X = 0.2$. Concerning the heating repartition function, for consistency with the approximation

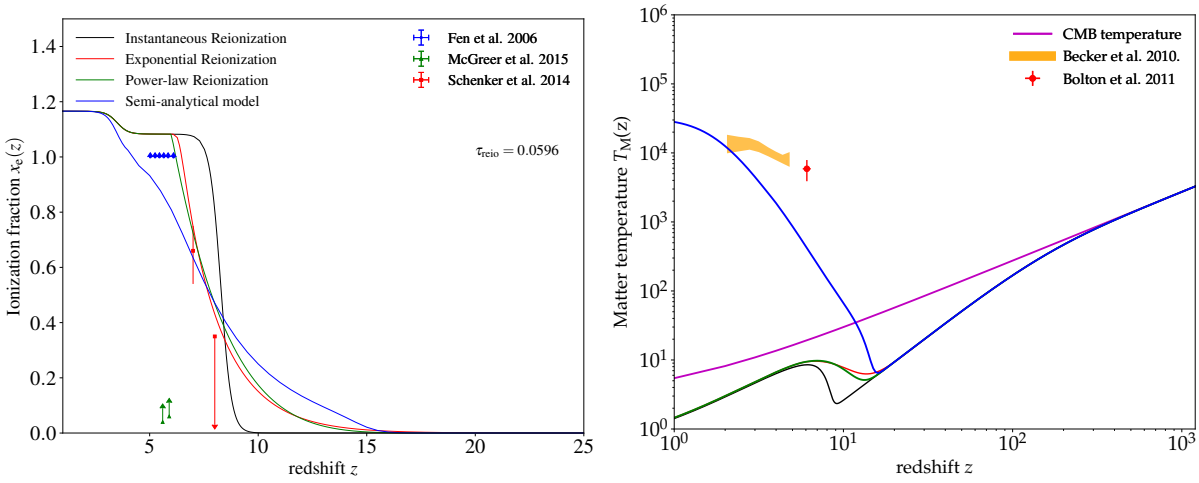

Figure 18: A comparison of the reionization and thermal history in each model used in this work. All models share the same reionization optical depth $\tau_{\rm reio} \simeq 0.0596$, corresponding to *Planck* TTTTTE + SIMlow bestfit [15].

used above for χ_i and χ_α we adopt $\chi_h = (1 + 2x_e)/3$ as suggested by [155], [270]. To our knowledge, it is the first time that a stellar heating term like this one is accounted for in a study of cosmological sensitivity to DM effects.

Let us note that similar modifications could also be done to the equations describing helium reionization, but we leave that for future works since neither HyRec nor Recfast can be used in their current form to model such subleading effects[13]. Throughout this thesis, we keep using a phenomenological hyperbolic tangent function to describe helium reionization.

Fig. 18 illustrates the differences between reionization and thermal history in all models used in this work. All models share the same reionization optical depth $\tau_{\rm reio} \simeq 0.0596$, corresponding to *Planck* TTTTTE + SIMlow bestfit [15]. The exponential reionization is very similar to the power-law as expected, both giving a free-electron fractions evolution rather close to the semi-analytical resolution. However, none of the simple parametrizations encode the corresponding reheating that one can see for the semi-analytical model.

13 CosmoRec could be used but it was not implemented in CLASS by the time the studies were done and therefore deserve further work.

2

FROM PERTURBATIONS TO OBSERVABLES: CMB AND MATTER POWER SPECTRUM

2.1 Cosmological perturbation theory at first order

We now want to describe the evolution of *small* (typically $\mathcal{O}(10^5)$ times smaller than background quantities) inhomogeneities and anisotropies in the Universe. Those will lead to fluctuations of the temperature and polarization of the CMB accross the sky, providing the seeds of galaxies and galaxy cluster nowadays.
The basic idea is to consider small perturbations $\delta g_{\mu\nu}$ and $\delta T_{\mu\nu}$ around the FLRW metric $\bar{g}_{\mu\nu}$ and the smooth background stress-energy tensor $\bar{T}_{\mu\nu}$,

$$g_{\mu\nu} = \bar{g}_{\mu\nu} + \delta g_{\mu\nu}, \quad T_{\mu\nu} = \bar{T}_{\mu\nu} + \delta T_{\mu\nu} \quad . \tag{2.1.1}$$

The Einstein equations will do the job of coupling metric perturbations to matter ones. We will limit our computation to the linear regime, meaning that we will drop all second order terms in perturbed quantities. This is a safe move for CMB physics, for which most of the relevant physics occur during the early universe at a time where over-densities are small. However, we shall comment on non-linearities (including second order corrections) in a later section. We will also go from real space to Fourier space, in order to trade one equation with partial spatial derivatives against a set of equations with "k" factors. The great advantage of linear theory is to obtain independent equations of evolution for each Fourier mode. This is of course related to the fact that in flat space, plane waves are eigenfunctions of the Laplacian operator, with eigenvalue given by the Fourier mode k. Our assumption of flat space is justified a posteriori by *Planck* measurement of $\Omega_k \simeq 0$. From a continuous density distribution of a given species s, we define

$$\bar{\rho}_s(t) = \langle \rho_s(\vec{x}, t) \rangle_{\vec{x}} \tag{2.1.2}$$

$$\delta\rho_s(\vec{x}, t) = \rho_s(\vec{x}, t) - \bar{\rho}_s(t) \tag{2.1.3}$$

$$\delta_s(\vec{x}, t) = \frac{\delta\rho_s(\vec{x}, t)}{\bar{\rho}_s(t)} \tag{2.1.4}$$

$$\delta_s(\vec{k}, t) = \int \delta_s e^{i\vec{k}\vec{x}} \frac{d^3\vec{x}}{(2\pi)^{3/2}} \tag{2.1.5}$$

In an expanding space, k refers to a comoving wavelength, and the associated physical wavelength is simply obtained by

$$\lambda(t) = a(t)\frac{2\pi}{|\vec{k}|} \tag{2.1.6}$$

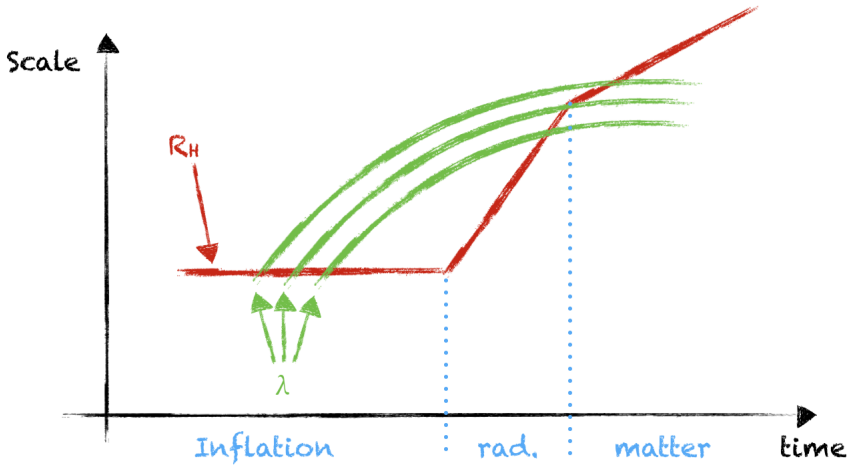

Figure 19: A schematic pictures of three wavelengths initially in causal contact, exiting the Hubble radius during inflation and entering it again during radiation or matter domination.

A key criterion comes from the comparison of a given wavelength with the Hubble radius $R_H(t) = H(t)^{-1}$. The ratio $\lambda/R_H \propto \dot{a}$. Hence, when the Universe expansion is accelerated (during Λ domination, or inflation), modes "exit" the Hubble radius (which is very close to the photon horizon), while they "enter" the Hubble radius when expansion is decelerated (during radiation/ matter domination). We have already mentioned this key observation as a motivation for an inflation phase in order to explain causal contact between different points in space. This is illustrated in Fig. 19. This section is based on many textbooks [90], [217], [392] and seminal papers [353], [412], [534], to which the reader is referred for further details. In this work, we will make use of the Boltzmann code CLASS [1] [390] to numerically solve the relevant evolution equations and compute the important statistical quantities introduced in next section.

2.1.1 *Perturbed Einstein equations*

2.1.1.1 *Perturbations of the metric*

A perturbed flat FLRW metric can be written in general as (careful we use from here on conformal time):

$$\begin{aligned} g_{00} &= a^2(\tau)(1+2\phi) \\ g_{0i} &= -a^2(\tau)B_i \\ g_{ij} &= -a^2(\tau)(\delta_{ij}+H_{ij}) \end{aligned} \tag{2.1.7}$$

where ϕ, B_i and H_{ij} are functions of space and time.

1 http://class-code.net

Scalar, Vector and Tensor decomposition

Since the metric is symmetric, this object contains ten degrees of freedom (d.o.f.). It is extremely useful to decompose these quantities into scalar, vector and tensor (with respect to spatial rotation SO(3)) sectors. In fact, what makes this decomposition so powerful is that at linear order all sectors do not mix and can therefore be treated separately.

We start by splitting B_i into its longitudinal and transverse part (it is called the *Helmholtz decomposition*):

$$B_i = \vec{\nabla}\zeta + \vec{\nabla} \times \vec{b} \quad , \tag{2.1.8}$$

where $\vec{b}$ is a transverse 3-vector, meaning that it obeys $\mathrm{div}(\vec{b}) = \partial^i b_i = 0$. Similarly, any rank-2 symmetric tensor can be written as

$$\begin{aligned} H_{ij} &= -2\psi\delta_{ij} + 2\big(\partial_i\partial_j - \frac{1}{3}\delta_{ij}\nabla^2\big)\mu \\ &+ (\partial_i a_j + \partial_j a_i) \qquad \text{with } \partial^i a_i = 0 \\ &+ 2h_{ij} \qquad\quad \text{with } \partial^i h_{ij} = 0 \text{ and } h^i{}_i = 0 \quad . \end{aligned} \tag{2.1.9}$$

The 10 d.o.f. are now split between:

- scalars: ϕ,ζ,ψ,μ
- vectors: $\vec{a}$ and $\vec{b}$
- tensors: h_{ij} .

In this manuscript, I will mostly describe scalar modes as they are the relevant degrees of freedom to study the evolution of density perturbations. They generalize the notion of gravitational potential, related to density perturbations through Poisson equation. Vector perturbations represent gravitational effects generated by the vorticity of the field. They are often called "gravito-magnetism" effect by analogy. They can be important in astrophysics, for instance in the context of Black Hole merging, but in Cosmology they are usually neglected, given that they quickly decay with the Universe expansion. On the other hand, tensor perturbations, which represent what is usually called *gravitational waves* are very important in Cosmology. Indeed, they are predicted by inflation theories, and although it is not the main topic of this work, some comments will be given in a further section.

The Gauge Freedom

Cosmological perturbation theory (like GR itself) is a *gauge* theory, in the mathematical sense that one needs to choose a reference frame (in a so-called *fiber bundle*) in which to describe the perturbations, i.e. a way to slice the space-time in equal-time hyper-surfaces and a specific spatial coordinate choice on these hyper-surfaces. Physical quantities do not depend on the gauge choice, but intermediate quantities in this calculation constructed from the perturbations do! A clever gauge choice thus usually aims at simplifying computations depending on the problem to solve. On the other hand, it is easily possible to create "fictitious perturbations" from a unperturbed distribution with an inconvenient gauge choice. One very common way of creating perturbations is "the time shifting" $\tau \to \tau + \xi^0(\tau, \vec{x})$, with $\xi^0(\tau, \vec{x})$ being very small. The homogeneous density of the Universe then gets perturbed, $\rho(\tau) \to \rho(\tau + \xi^0(\tau, \vec{x})) = \bar{\rho}(\tau) + \big\{\delta\rho \equiv \bar{\rho}'\xi^0(\tau, \vec{x})\big\}$. A change of the time coordinate can therefore introduce such fake density perturbations.

In practice, they are two ways of dealing with the gauge freedom:

- one choose (or fix) the gauge, i.e. introduce a condition that completely defines the space-time reference frame. In any case, this is safe as the physical quantities are always independent of the gauge choice.
- one can work with gauge-invariant quantities (i.e. non trivial integro-differential combinations of the metric and stress-energy tensor components left invariant by a gauge transformation) and derive gauge-invariant equations of motions for these quantities.

Gauge fixing

- *Synchronous gauge:* Historically, this gauge choice was first introduced by Lifshitz [405] and is defined by the prescription $\phi = 0$ and $B_i = 0$. This gauge allows a description simultaneously of scalars, vectors and tensors as μ, ψ, $\vec{a}$ and h_{ij} are free. For scalar perturbations, we further restrict the degrees of freedom to μ and ψ only. Traditionally, one introduces the function η and h such that :

$$2\nabla^2\mu = 6\eta + h \tag{2.1.10}$$

with h being defined as the trace of H_{ij} : $H^i{}_i = -6\psi \equiv h$. This gives in Fourier space :

$$-2k^2\mu = 6\eta + h \tag{2.1.11}$$

$$H_{ij} = \frac{h}{3}\delta_{ij} - 2\big(k_ik_j - \frac{1}{3}\delta_{ij}k^2\big)\mu = \hat{k_i}\hat{k_j}h + (\hat{k_i}\hat{k_j} - \frac{1}{3}\delta_{ij})6\eta \tag{2.1.12}$$

In this gauge, a convenient way of writing the metric is therefore :

$$ds^2 = a^2(\tau)\big\{d\tau^2 - (\delta_{ij} + H_{ij})dx^i dx^j\big\} \quad . \tag{2.1.13}$$

There is a complication associated to this gauge. Indeed, all the d.o.f. have not been fixed, as the prescription fixes the hyper-surfaces of simultaneity relative to each other, with a remaining freedom to choose their origin. It is still possible to perform a gauge transformation, leaving ϕ and B_i equal to zero, to define a new coordinate frame as we will see in the next part.

- *Newtonian gauge:* It is defined by $\mu = 0$, $B_i = a_i = 0$ and $h_{ij} = 0$. In this gauge, the world-line of an observer at rest is simply orthogonal to hyper-surfaces of simultaneity (since B_i is 0), those hyper-surfaces of constant time having furthermore isotropic induced geometries (since h_{ij}, a_i and μ are 0). This gives for the metric :

$$ds^2 = a^2(\tau)\big\{d\tau^2(1 + 2\phi) - (1 - 2\psi)\delta_{ij}dx^i dx^j\big\} \quad . \tag{2.1.14}$$

Note that it is only suitable to describe scalar modes, but can be generalized to describe vectors and tensors. In the Newtonian (or weak-field) limit, for sub-horizon scales, ϕ coincides with the Newtonian gravitational potential (hence the name).

Other gauges exist in the literature, that can be more practical depending on the computation, but those two gauges are the ones we have been working with in this study. Since observables do not depend on the gauge, having a code that work in both gauges allow to consistently check the result of a computation. In order to go from one gauge to another, one needs to perform a gauge transformation. Let see now how this is done.

Gauge Transformation

As already explained, a gauge is nothing but a specific time slicing of the space-time of General Relativity, with a specific choice of spatial coordinates on these time slices. Therefore, a gauge transformation will corresponds to a coordinate transformations, although very small since we deal with perturbations, and with a certain subtlety compared to standard coordinate transformations. Let see why.

We want to study the space-time U (a Lorentzian manifold in geometric terms which represents the base of a fiber bundle, while the fibers are simply the tangent spaces), supplied with a map F on $\mathbb{R}$:

$$\begin{aligned} F : \mathbb{R}^4 &\rightarrow U \\ x &\rightarrow X \end{aligned}$$

To linearize Einstein equation, we compare the physical space-time U to a "fake" reference space-time $\bar{U}$, homogeneous and isotropic, supplied with a map f on $\mathbb{R}^4$ together with a FLRW metric. We decompose the map $F = j \circ f$, where j is a diffeomorphism between U and $\bar{U}$, to compare physical quantities to the background ones and hence to define the perturbations.

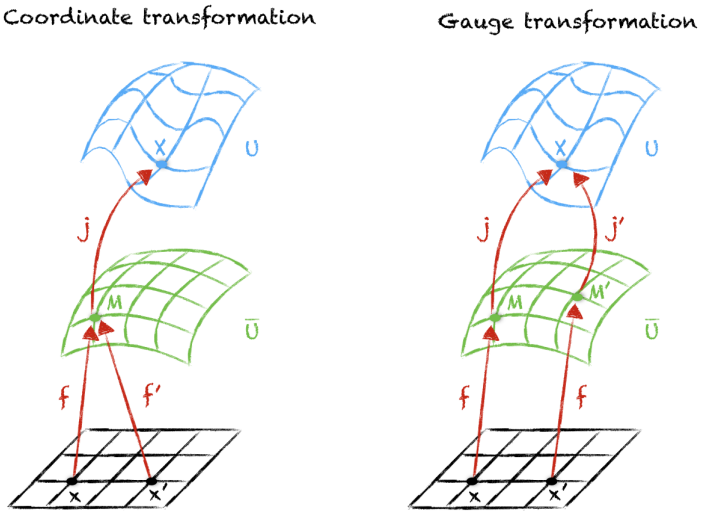

Figure 20: left panel: coordinate transformation, right panel: gauge transformation. Adapted from Julien Lesgourgues's master course.

The usual coordinate change means changing the map f; all quantities on U and $\bar{U}$ would change under the Lorentz group and this would not have any interest, as it could destroy homogeneity and isotropy of the "background" Universe (see fig. 20, left panel). Rather, we would like to change the coordinate frame without destroying these properties of the background Universe. This means changing the map j between $\bar{U}$ and U. In other words, by choosing another diffeomorphism j', we change the coordinate frame on U (with new map $j' \circ f$) without changing the one on $\bar{U}$ (fig 20, right panel). After this transformation, the quantities in X correspond to the coordinate x' instead of x and are not compared to the homogeneous quantities in M but in M'.

Now, let see how this is done mathematically. We consider the coordinate transformation

$$X^\mu \rightarrow \tilde{X}^\mu \equiv X^\mu + \xi^\mu(\tau, \vec{x}), \quad \text{where} \quad \xi^0 \equiv T, \; \xi^i \equiv S^i = \partial^i S + \hat{S}^i \; . \tag{2.1.15}$$

The spatial shift S^i has been split again into a scalar, S, and a divergenceless vector, $\hat{S}^i$. We now want to know how the metric transforms under this change of coordinates. Using the invariance of ds^2 under a coordinate transformation, we can write :

$$ds^2 = g_{\mu\nu}(X)dX^\mu dX^\nu = \tilde{g}_{\alpha\beta}(\tilde{X})d\tilde{X}^\alpha d\tilde{X}^\beta \quad . \tag{2.1.16}$$

Using $dX^\alpha = \left(\frac{\partial \tilde{X}^\alpha}{\partial X^\mu}\right)dX^\mu$ one relats old and new metrics via

$$g_{\mu\nu}(X) = \frac{\partial \tilde{X}^\alpha}{\partial X^\mu}\frac{\partial \tilde{X}^\beta}{\partial X^\nu}\tilde{g}_{\alpha\beta}(\tilde{X}) \tag{2.1.17}$$

The explicit computation is done in appendix B.1.1. The result is that metric variables transform as:

$$\phi \to \tilde{\phi} = \phi - T' - \mathcal{H}T \tag{2.1.18}$$
$$B_i \to \tilde{B}_i = B_i + \partial_i T - S_i' \tag{2.1.19}$$
$$H_{ij} \to \tilde{H}_{ij} = H_{ij} - 2\mathcal{H}T - \left\{\partial_i S_j + \partial_j S_i\right\}. \tag{2.1.20}$$

where $\mathcal{H} \equiv a'/a = aH$ is the Hubble parameter in conformal time. In terms of the SVT-decomposition, we have

$$\phi \to \phi - T' - \mathcal{H}T \tag{2.1.21}$$
$$\zeta \to \zeta + T - S', \qquad b_i \to b_i - \hat{S}_i', \tag{2.1.22}$$
$$\psi \to \psi - \mathcal{H}T - \frac{1}{3}\nabla^2 S, \tag{2.1.23}$$
$$\mu \to \mu - S, \qquad a_i \to a_i - \hat{S}_i, \qquad h_{ij} \to h_{ij}. \tag{2.1.24}$$

Gauge-invariant perturbations

As already explained, to avoid the gauge problem, it is possible to define special combinations of metric perturbations that do not transform under a change of coordinates. These are the *Bardeen variables* [79]:

$$\Psi \equiv \phi + \mathcal{H}(\zeta - \mu') + (\zeta - \mu')' \qquad \Phi \equiv -\psi - \mathcal{H}(\zeta - \mu') + \frac{1}{3}\nabla^2\mu \tag{2.1.25}$$
$$\hat{\Phi}_i \equiv a_i' - b_i \qquad h_{ij} \tag{2.1.26}$$

Indeed, if we perform a gauge transformation on Ψ we have :

$$\begin{aligned}\Psi \to \tilde{\Psi} &= \tilde{\phi} + \mathcal{H}(\tilde{\zeta} - \tilde{\mu}') + (\tilde{\zeta} - \tilde{\mu}')' \\ &= \phi - T' - \mathcal{H}T + \mathcal{H}(\zeta + T - S' - \mu' + S') + (\zeta + T - S' - \mu' + S')' \\ &= \underbrace{\phi + \mathcal{H}(\zeta - \mu') + (\zeta - \mu')'}_{\Psi} - T' - \mathcal{H}T + \mathcal{H}T + T' \\ &= \Psi\end{aligned} \tag{2.1.27}$$

and the same calculations can be easily performed on other variables to show their invariance under gauge transformations.

They can be considered as being the "physical" spacetime perturbations since they cannot be removed

by a gauge transformation. Unfortunately, the equations in these variables can be quite tricky. Thus, it is usual to perform computation in a special gauge that makes it easier, then form the gauge-invariant variables and finally, if needed, turn these into the perturbations in any other gauges. The question is now, what are their expressions in the two special gauges we saw before, namely the synchronous and newtonian gauges.
Using the prescriptions defined above, restricted to scalar modes, it is immediate to show:

- *synchronous gauge:*

$$\begin{aligned}\Psi &= -\mu'' - \mathcal{H}\mu' \\ &\overset{\text{FS}}{=} \mathcal{H}\frac{(6\eta+h)'}{2k^2} + \frac{(6\eta+h)''}{2k^2} \qquad (2.1.28)\\ \Phi &= \frac{h}{6} - \frac{1}{3}\nabla^2\mu - \mathcal{H}\mu' \\ &\overset{\text{FS}}{=} -\eta + \mathcal{H}\frac{(6\eta+h)'}{2k^2} \qquad (2.1.29)\end{aligned}$$

- *newtonian gauge:*

$$\Psi = \phi \qquad\qquad \Phi = -\psi \qquad (2.1.30)$$

  This makes the newtonian gauge so useful: the perturbation variables are identical to the gauge-invariant variables up to a minus sign ! Equating variables in both gauges yields the way to go from one to the other very quickly.

2.1.1.2 *Perturbations of the stress-energy tensor*

We start from the background, homogeneous and isotropic stress-energy tensor of the Universe $\bar{T}^\mu_{\ \nu}$, which takes the form a perfect fluid as given by (1.1.17) and consider small perturbations $\delta T^\mu_{\ \nu}$. Using the notation $\rho = \bar{\rho} + \delta\rho$, $\mathcal{P} = \bar{\mathcal{P}} + \delta\mathcal{P}$, $U^\mu = \bar{U}^\mu + \delta U^\mu$ and introducing the anisotropic stress tensor $\Pi^\mu_{\ \nu}$, we develop equation (1.1.17) keeping only first order terms. It reads

$$\delta T^\mu_{\ \nu} = (\delta\rho + \delta\mathcal{P})\bar{U}^\mu\bar{U}_\nu + (\bar{\rho}+\bar{\mathcal{P}})(\delta U^\mu\bar{U}_\nu + \bar{U}^\mu\delta U_\nu) - \delta\mathcal{P}\delta^\mu_{\ \nu} - \Pi^\mu_{\ \nu} \qquad (2.1.31)$$

In appendix B.1.2, the 4-vector velocity is shown to be given by $U_\mu = a\big[1+\phi, -(v_i+B_i)\big]$. The velocity v_i will couple through Einstein equations to both scalar and vectorial perturbations. It could be useful to perform the scalar-vector-tensor decomposition also for the stress-energy tensor variables, as it is defined by equation (2.1.8) and (2.1.9). However, only the longitudinal part of v_i will be involved in the scalar sector, which we usually write : $v_i^{\parallel} = \partial_i v$. Traditionally, we prefer to take as scalar degrees of freedom the divergence θ:

$$\theta \equiv \partial^i v_i = \nabla^2 v \qquad (2.1.32)$$

where the last equality holds since the orthogonal part is, by definition, divergenceless.
In the same way, instead of introducing a potential through the longitudinal part of Π^i_j as $\Pi^{i\parallel}_{\ \ j} = (\partial_i\partial_j - \frac{1}{3}\nabla^2\delta_{ij})\tilde{\sigma}$, it is common to define the scalar degrees of freedom σ (called *shear* or *anisotropic stress*) by

$$(\bar{\rho}+\bar{\mathcal{P}})\nabla^2\sigma = -(\partial_i\partial_j - \frac{1}{3}\nabla^2\delta_{ij})\Pi^i_{\ j} = -\partial_i\partial_j\Pi^i_{\ j} \qquad (2.1.33)$$

So, together with $\delta \equiv \delta\rho/\bar{\rho}$, it is shown also in appendix B.1.2 that the scalar degrees of freedom of the stress-energy tensor are

$$\begin{aligned} T^0_{\ 0} &= \bar{\rho}(1+\delta) \quad , & (2.1.34)\\ \partial_i T^i_{\ 0} &= (\bar{\rho}+\bar{\mathcal{P}})\theta \quad , & (2.1.35)\\ T^i_{\ i} &= -3(\bar{\mathcal{P}}+\delta\mathcal{P}) \quad , & (2.1.36)\\ (\partial_i\partial_j - \frac{1}{3}\nabla^2\delta_{ij})T^i_{\ j} &= (\bar{\rho}+\bar{\mathcal{P}})\nabla^2\sigma \quad . & (2.1.37) \end{aligned}$$

If there are several species in the Universe, hence several contributions to the stress-energy tensor, they are added such that $T_{\mu\nu} = \sum_s T^s_{\mu\nu}$. This implies

$$\delta\rho = \sum_s \delta\rho_s\,, \quad \delta\mathcal{P} = \sum_s \delta\mathcal{P}_s\,, \quad q^i = \sum_s q^i_s\,, \quad \Pi^{ij} = \sum_s \Pi^{ij}_s\,. \tag{2.1.38}$$

where the *momentum density* $q^i \equiv (\bar{\rho}+\bar{\mathcal{P}})v^i$ has been introduced. Density perturbations, pressure perturbations and anisotropic stress simply add. It is the momentum densities that add, and not the velocities though.
Adiabatic pressure perturbations are defined as

$$\delta\mathcal{P}_{\rm ad} \equiv \frac{\dot{\bar{\mathcal{P}}}}{\dot{\bar{\rho}}}\delta\rho \tag{2.1.39}$$

while the non-adiabatic, or entropic, pressure perturbations are simply

$$\delta\mathcal{P}_{\rm en} \equiv \delta\mathcal{P} - \delta\mathcal{P}_{\rm ad}\,. \tag{2.1.40}$$

Gauge freedom, gauge transformations and gauge invariant variables

Just as for the metric perturbations, the gauge freedom can be used to simplify calculations in the matter sector. Very common gauges are

- *Uniform density gauge :* It is define by setting $\delta\rho = 0$. Therefore it is a gauge choice in which there is no density perturbation.
- *Comoving gauge :* It is the gauge comoving with a given fluid. For a given species, the scalar momentum density q, or equivalently the divergence θ is asked to vanish $q = \theta = 0$.

There are several ways of defining these gauges, depending on how degrees of freedom are kept or killed in the metric sector. One common way is to combine synchronous and comoving gauges as we will do later on. In CLASS, the synchronous gauge is written in the gauge comoving with the DM. To motivate this choice, we will see in chapter 4, that this will lead to very simple equations for the decaying DM and its daughter particle.

Relevant d.o.f. inside the stress-energy tensor transforms under a gauge-transformation as (see appendix B.1.2):

$$\begin{aligned}
\delta \to \tilde{\delta} &= \delta - \frac{\bar{\rho}'}{\bar{\rho}} T && (2.1.41)\\
\delta\mathcal{P} \to \delta\tilde{\mathcal{P}} &= \delta\mathcal{P} - T\bar{\mathcal{P}}' && (2.1.42)\\
q_i \to \tilde{q}_i &= q_i + \left(\bar{\rho} + \bar{\mathcal{P}}\right) S'_i && (2.1.43)\\
\Leftrightarrow \theta \to \tilde{\theta} &= \theta + \partial^i S'_i && (2.1.44)\\
\Leftrightarrow v \to \tilde{v} &= v + S' && (2.1.45)\\
\Pi_{ij} &\to \Pi_{ij} && (2.1.46)
\end{aligned}$$

Like for the metric, one can build gauge-invariant combination of previous variables. For instance, the *comoving-gauge density perturbation* Δ (called like that since it is equal to the density perturbation in the gauge comoving with the fluid) is defined as

$$\Delta \equiv \delta + \frac{\bar{\rho}'}{\bar{\rho}}(v + \zeta) \quad . \tag{2.1.47}$$

We prove in appendix B.1.2 that it is indeed gauge invariant. Its interest lies in the fact that the Poisson equation will take a trivial form thanks to it. This is however not the most used variable.
The usual matter gauge-invariant variables can be constructed from relations (2.1.21), (B.1.28-B.1.31) and are :

$$\begin{aligned}
\delta^{gi} &= \delta - \frac{\bar{\rho}'}{\bar{\rho}}(\mu' - \zeta)\\
\theta^{gi} &= \theta + \nabla^2(\mu' - \zeta)\\
\delta\mathcal{P}^{gi} &= \delta\mathcal{P} - \bar{\mathcal{P}}'(\mu' - \zeta) && (2.1.48)
\end{aligned}$$

where the second equality holds since, at first order $\partial_i T = S'_i$. Note that by construction $\delta\mathcal{P}_{\rm en}$ is gauge invariant.

From gauge to gauge

Using the gauge-invariant variables, we can now immediately go from the newtonian to the synchronous gauge and vice versa. In fact, all newtonian variables are identical to the invariant ones since $\zeta = \mu = 0$ in this gauge. We only need to express them in synchronous gauge to have our relations. Setting $\zeta = 0$ and $\mu = -(6\eta + h)/(2k^2)$ (in Fourier space) we have

$$\begin{aligned}
\delta(new) &= \delta(syn) + \tfrac{\bar{\rho}'}{\bar{\rho}} \tfrac{6\eta' + h'}{2k^2} && (2.1.49)\\
\theta(new) &= \theta(syn) + \tfrac{1}{2}(6\eta' + h') && (2.1.50)\\
\delta\mathcal{P}(new) &= \delta\mathcal{P}(syn) + \bar{\mathcal{P}}' \tfrac{6\eta' + h'}{2k^2} && (2.1.51)
\end{aligned}$$

2.1.1.3 *Summary of the important relations in newtonian and synchronous gauge*

In appendix B.1.3, we explicitly relate, at first order, metric perturbations to matter ones by means of i) Einstein equations (1.1.2); ii) the conservation of the stress-energy tensor. To do so, one needs to perturb the Christoffels $\Gamma^{\mu}_{\alpha\beta}$, the Ricci tensor $R_{\mu\nu}$ and Ricci scalar $\mathcal{R}$. The strategy adopted is to work in the newtonian gauge restricted to scalar modes given by eq. (2.1.14), and then form the Bardeen

variables to be able to change the gauge easily. Using Einstein equations, one finds four relations between the two metric variables ϕ and ψ, and the two matter variables δ and θ. These four equations are (in Fourier space)

$$\boxed{\begin{aligned} k^2\psi + 3\mathcal{H}(\mathcal{H}\phi + \psi') &= -4\pi G a^2 \bar{\rho}\delta \qquad (00) \\ -k^2(\psi' + \mathcal{H}\phi) &= 4\pi G a^2(\bar{\rho} + \bar{\mathcal{P}})\theta \qquad (0i) \\ \psi'' + (2\mathcal{H}' + \mathcal{H}^2)\phi + \mathcal{H}\phi' + 2\mathcal{H}\psi' - \frac{1}{3}k^2(\phi - \psi) &= 4\pi G a^2 \delta\mathcal{P} \qquad (ii) \\ k^2(\phi - \psi) &= 12\pi G a^2(\bar{\rho} + \bar{\mathcal{P}})\sigma \qquad (ij) \end{aligned}} \tag{2.1.52a–d}$$

The Poisson equation (B.1.55) can be rewritten in a particularly simple form by introducing the comoving gauge density contrast

$$-k^2\psi = 4\pi G a^2 \bar{\rho}\Delta\,. \tag{2.1.53}$$

In some cases, it might be easier to use the conservation of the stress-energy tensor, which yields two other equations (redundant with previous ones)

$$\boxed{\begin{aligned} \delta' &= 3\mathcal{H}\delta\Big(\omega - \frac{\delta\mathcal{P}}{\delta\rho}\Big) + (3\psi' - \theta)(1+\omega) \qquad \text{Continuity equation} \\ \theta' &= (3\omega - 1)\mathcal{H}\theta - \left(\frac{\omega'}{1+\omega}\right)\theta + \frac{k^2}{1+\omega}\frac{\delta\mathcal{P}}{\delta\rho}\delta + k^2\phi - k^2\sigma \qquad \text{Euler equation} \end{aligned}} \tag{2.1.54a–b}$$

Here we have made use of the *equation of state* $\bar{\mathcal{P}} = \omega\bar{\rho}$.

All these relations can be rewritten in other gauges by means of the gauge invariant variables Φ, Ψ, δ^{gi}, θ^{gi}, $\delta\mathcal{P}^{gi}$ through the relations

$$\boxed{\begin{aligned} \Psi &= \phi + \mathcal{H}(\zeta - \mu') + (\zeta - \mu')' \qquad \Phi = -\psi - \mathcal{H}(\zeta - \mu') + \frac{1}{3}\nabla^2 \qquad (2.1.55a) \\ \delta^{gi} &= \delta - \frac{\bar{\rho}'}{\bar{\rho}}(\dot{\mu} - \zeta) \qquad \theta^{gi} = \theta + \nabla^2(\dot{\mu} - \zeta) \qquad \delta\mathcal{P}^{gi} = \delta\mathcal{P} - \bar{\mathcal{P}}'(\dot{\mu} - \zeta) \qquad (2.1.55b) \end{aligned}}$$

Recalling that the metric in the synchronous gauge is given by eq. (2.1.13), we have for the particular example of switching between newtonian and synchronous gauges, in Fourier space,

$$\boxed{\begin{aligned} \phi &= \mathcal{H}\frac{(6\eta + h)'}{2k^2} + \frac{(6\eta + h)''}{2k^2} \qquad (2.1.56a) \\ \psi &= \eta - \mathcal{H}\frac{(6\eta + h)'}{2k^2} \qquad (2.1.56b) \\ \delta(new) &= \delta(syn) + \frac{\bar{\rho}'}{\bar{\rho}}\frac{6\eta' + h'}{2k^2} \qquad (2.1.56c) \\ \theta(new) &= \theta(syn) + \frac{1}{2}(6\eta' + h') \qquad (2.1.56d) \\ \delta\mathcal{P}(new) &= \delta\mathcal{P}(syn) + \bar{\mathcal{P}}'\frac{6\eta' + h'}{2k^2} \qquad (2.1.56e) \end{aligned}}$$

This enables us to obtain Einstein equations as well as the Euler and continuity equations in the synchronous gauge:

$$k^2\eta - \frac{1}{2}\mathcal{H}h' = -4\pi G a^2 \bar{\rho}\delta \qquad (00) \tag{2.1.57a}$$

$$-k^2\eta' = 4\pi G a^2(\bar{\rho} + \bar{\mathcal{P}})\theta \qquad (0i) \tag{2.1.57b}$$

$$-\frac{1}{2}h'' - \mathcal{H}h' + k^2\eta = 12\pi G a^2 \delta\mathcal{P} \qquad (ii) \tag{2.1.57c}$$

$$\frac{1}{2}(6\eta'' + h'') + \mathcal{H}(6\eta' + h') - k^2\eta = 12\pi G a^2(\bar{\rho} + \bar{\mathcal{P}})\sigma \qquad (ij) \tag{2.1.57d}$$

$$\delta' = 3\mathcal{H}\delta\left(\omega - \frac{\delta\mathcal{P}}{\delta\rho}\right) - (\theta + \frac{h'}{2})(1+\omega) \qquad \text{Continuity equation} \tag{2.1.58a}$$

$$\theta' = (3\omega - 1)\mathcal{H}\theta - \left(\frac{\omega'}{1+\omega}\right)\theta - \frac{k^2}{1+\omega}\frac{\delta\mathcal{P}}{\delta\rho}\delta - k^2\sigma \qquad \text{Euler equation} \tag{2.1.58b}$$

2.1.2 *Perturbed collisionless Boltzmann equations*

In previous section, we have determined evolution equations for the global cosmic fluid perturbations. They can be used to describe separate fluids if they are uncoupled by simply summing every components. However, in the Universe all species are not isolated and therefore does not participate to the

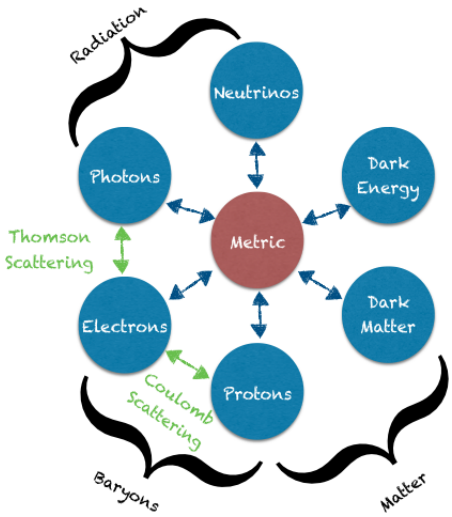

Figure 21: A schematic picture of the interactions between the different component of the universe. Adapted from [90].

evolution of perturbations in the same way. The only common point is that *all* species are affected by gravity, i.e. they are all coupled to each other through their influence on the spacetime metric. Photons and baryons are also strongly coupled together through Compton and Coulomb scattering, whereas neutrinos are only collisionally coupled (through weak interactions) very early in the history of the Universe. Dark Matter in the standard picture is never collisionally coupled to other species, even though in principle it could have very tiny interactions with them. In chapter 4, we will play the

game of adding a decaying term in its evolution equation. Figure 21 sums up the way in which the different components of the Universe interact with each other.
To describe all these coupling, one needs to write down a Boltzmann equation for each species in the Universe, similar to the one introduced in sec. A.1. We recall that it takes the schematic form

$$\frac{df}{dt} = \mathcal{C}[f]\,. \tag{2.1.59}$$

where the LHS is the Liouville operator, while the RHS is the collision operator, containing all possible interactions terms. We now aim at developing the total derivative in terms of partial ones, in order to derive (in a first step) the collisionless Boltzmann equation $df/dt = 0$.

2.1.2.1 *The general collisionless Boltzmann equation*

In principle the distribution f lives in a 8 dimensional space $f(x^\mu, P^\mu)$. However, we can use some constraints to reduce the dimension. Indeed, imposing $P^2 = g_{\mu\nu}P^\mu P^\nu = m^2$, where P^μ is define in eq. (1.1.16), allows to express one of the 4-momentum component as a function of the others. Since $g_{\mu\nu}$ appears here, we will need to work in a given gauge. In this section for simplicity we shall make use of the Newtonian gauge *in cosmic time*. Practically, it means that there are no more a^2 term in g_{00} (see eq. (2.1.7)) and that $\tau \to t$. The generalization of eq. (1.1.16) in presence of perturbations in the metric is therefore (in cosmic time)

$$P^\mu = \left(E(1-\phi), \frac{pn^i}{a}(1+\psi)\right) \Leftrightarrow P_\mu = \left(E(1+\phi), -apn_i(1-\psi)\right) \tag{2.1.60}$$

Thanks to the mass-shell constraint, we only need to include a term proportional to $\partial f/\partial\vec{p}$, which we usually split between the magnitude p and the direction n^i. We thus have

$$\frac{df}{dt} = \frac{\partial f}{\partial t} + \frac{\partial f}{\partial x^i}\frac{dx^i}{dt} + \frac{\partial f}{\partial p}\frac{dp}{dt} + \frac{\partial f}{\partial n^i}\frac{dn^i}{dt} \tag{2.1.61}$$

or in term of the energy E

$$\frac{df}{dt} = \frac{\partial f}{\partial t} + \frac{\partial f}{\partial x^i}\frac{dx^i}{dt} + \frac{\partial f}{\partial E}\frac{dE}{dt} + \frac{\partial f}{\partial n^i}\frac{dn^i}{dt} \tag{2.1.62}$$

We prove in appendix B.2.1.1, by using properties of the isotropic zero-order distribution and the geodesic equation (1.1.12), that the collisionless Boltzmann equation can be rewritten as

$$\boxed{\frac{df}{dt} = \frac{\partial f}{\partial t} + \frac{\partial f}{\partial x^i}\frac{p}{E}\frac{n^i}{a} - \frac{\partial f}{\partial E}\left[\frac{\partial\phi}{\partial x^i}\frac{pn^i}{a} + \left[H - \frac{\partial\psi}{\partial t}\right]\frac{p^2}{E}\right]} \tag{2.1.63a}$$

$$\boxed{\stackrel{!}{=} 0 \quad \text{collisionless}} \tag{2.1.63b}$$

Up to this point we have made no simplifications about the nature of the species, apart that it is collisionless. To include collisions will be our task in section 2.1.3, while a decay term will be considered in chapter 4. First of all, let's see what are the perturbation equations for collisionless species.

2.1.2.2 *Cold Dark Matter*

To describe collisionless cold Dark Matter (CDM) (or non-interacting baryons), we neither needed such a careful treatment of the distribution, nor to include a collision term, since by definition i) it is cold so it has virtually no phase space distribution, ii) it is collisionless. For the moment we can either integrate over f in previous equations (a bit lengthy, see [217] for instance), or directly use the perturbed continuity and Euler equations (2.1.54) and (2.1.58), to obtain the evolution of the perturbation in the CDM fluid in both newtonian and synchronous gauges (here again in conformal time).

- *Newtonian gauge* : We only need to set $\omega = \omega' = 0$, $\sigma = 0$ and $\delta\mathcal{P}/\delta\rho = 0$

$$\boxed{\delta'_{CDM} = -\theta_{CDM} + 3\psi' \,, \quad \theta'_{CDM} = -\mathcal{H}\theta_{CDM} + k^2\phi} \tag{2.1.64a}$$

- *Synchronous gauge* : If we use the CDM particles to define the synchronous coordinates we can even set $\theta = 0$

$$\boxed{\delta'_{CDM} = -\frac{1}{2}h'} \tag{2.1.65a}$$

2.1.2.3 *Relativistic-massless species*

Photons and massless neutrinos for instance enter this category.[2] However, given that we do not have yet switched on the collision term, the set of equations we will derive only apply to massless neutrinos. In this case, the phase-space distribution is non-zero and the degrees of freedom δ, θ and σ aren't enough to describe the full distribution. To go further, we expand the photon distribution f about its zero-order value. We first write

$$f(\vec{x}, p, \vec{n}, t) = \left[\exp\left\{ \frac{E(p)}{T(t)[1 + \Theta(\vec{x}, \vec{n}, t)]} \right\} - 1 \right]^{-1} \quad , \tag{2.1.66}$$

with $E(p) = p$ in the massless case. The zero-order temperature T is a function of time only and neither of space nor of p and $\vec{n}$. $\Theta \equiv \delta T/T$ is a inhomogeneous and anistropic perturbation to the distribution function. We simply assume that it doesn't depend on the magnitude p of the momentum, which follows from the fact that the magnitude of the photon momentum is virtually unchanged during a Compton scatter at low energies. Under the massless condition $E(p) = p$, eq. (2.1.63) simplifies greatly and becomes

$$\frac{df}{dt} = \frac{\partial f}{\partial t} + \frac{\partial f}{\partial x^i}\frac{n^i}{a} - p\frac{\partial f}{\partial p}\left[\frac{\partial \phi}{\partial x^i}\frac{n^i}{a} - \frac{\partial \psi}{\partial t} + H \right] \quad . \tag{2.1.67}$$

We can then split between zero and first order. It is shown in appendix B.2.1.2 that the zero-order equation is

$$\boxed{\left.\frac{df}{dt}\right|_{\text{zero-order}} = \frac{\partial f^{(0)}}{\partial t} - Hp\frac{\partial f^{(0)}}{\partial p} \stackrel{!}{=} 0 \,,} \tag{2.1.68}$$

which leads to the famous result

$$T \;\propto\; \frac{1}{a} \quad . \tag{2.1.69}$$

2 Massive neutrinos will get a slight complication due to their mass. We will treat them just after.

The first order equation on the other hand is

$$\left.\frac{df}{dt}\right|_{\rm first-order} = -p\frac{\partial f^{(0)}}{\partial p}\left[\frac{\partial\Theta}{\partial t}+\frac{\partial\phi}{\partial x^i}\frac{n^i}{a}-\frac{\partial\psi}{\partial t}+\frac{\partial\Theta}{\partial x^i}\frac{n^i}{a}\right], \tag{2.1.70}$$

and assuming collisionless species

$$\boxed{\frac{\partial\Theta}{\partial t}+\frac{\partial\phi}{\partial x^i}\frac{n^i}{a}-\frac{\partial\psi}{\partial t}+\frac{\partial\Theta}{\partial x^i}\frac{n^i}{a}=0\,.} \tag{2.1.71}$$

Using the definition of the stress-energy tensor (1.1.18) and that in the newtonian gauge $(-\det[g_{\alpha\beta}]^{-1/2}) = a^{-3}(1-\phi+3\psi)$ and $d^3P = a^3(1-3\psi)p^2dpd\Omega$, we can relate the distribution to the degrees of freedom we have defined previously :

$$T^0_{\ 0} = \bar\rho(1+\delta) = g_s\int\frac{p^2dpd\Omega}{(2\pi)^3}p\left[f^{(0)}-p\frac{\partial f^{(0)}}{\partial p}\Theta\right] \quad , \tag{2.1.72}$$

$$\partial^i T^0_{\ i} = -(\bar\rho+\bar{\mathcal{P}})\theta = \partial^i\left\{-g_s\int\frac{p^2dpd\Omega}{(2\pi)^3}pn_i\left[f^{(0)}-p\frac{\partial f^{(0)}}{\partial p}\Theta\right]\right\} \quad , \tag{2.1.73}$$

$$T^i_{\ i} = -3(\bar{\mathcal{P}}+\delta\mathcal{P}) = -g_s\int\frac{p^2dpd\Omega}{(2\pi)^3}p\left[f^{(0)}-p\frac{\partial f^{(0)}}{\partial p}\Theta\right] \quad , \tag{2.1.74}$$

$$(\partial_i\partial_j-\frac{1}{3}\nabla^2\delta_{ij})T^i_{\ j} = (\bar\rho+\bar{\mathcal{P}})\nabla^2\sigma = (\partial_i\partial_j-\frac{1}{3}\nabla^2\delta_{ij})\left\{-g_s\int\frac{p^2dpd\Omega}{(2\pi)^3}p^2n^in_j\left[f^{(0)}-p\frac{\partial f^{(0)}}{\partial p}\Theta\right]\right\} \quad . \tag{2.1.75}$$

To go further, it is common to reduce the number of variables by integrating out the $p-$dependence in the distribution and to expand the angular dependence of the perturbations in a series of Legendre polynomials $\mathcal{P}_\ell(\mu)$, with $\mu\equiv\vec k\cdot\vec n/\|\vec k\|$:

$$\Theta(\vec k,\mu,t) = \sum_\ell(-i)^\ell(2\ell+1)\Theta_\ell(t,\vec k)\mathcal{P}_\ell(\mu)\,, \tag{2.1.76}$$

$$\Theta_\ell(t,\vec k) = \frac{1}{(-i)^\ell}\int_{-1}^{1}\frac{d\mu}{2}\Theta(\vec k,\mu,t)\mathcal{P}_\ell(\mu)\,. \tag{2.1.77}$$

We show explicitly in appendix B.2.1.2 that splitting between $\ell=0$, $\ell=1$ and $\ell\geq 2$ gives the following hierarchy of moments for Θ

$$\dot\Theta_0 = -k\Theta_1+\dot\psi \tag{2.1.78a}$$

$$\dot\Theta_1 = \frac{k}{3a}\left[\Theta_0-2\Theta_2+\phi\right] \tag{2.1.78b}$$

$$\dot\Theta_\ell = \frac{k}{(2\ell+1)a}\left[\ell\Theta_{\ell-1}-(\ell+1)\Theta_{\ell+1}\right], \qquad \ell\geq 2\,, \tag{2.1.78c}$$

which we can immediately relate to the scalar degrees of freedom introduced in previous section through (proof is in appendix B.2.1.2)

$$\delta = 4\Theta_0\,, \qquad \theta = 3k\Theta_1\,, \qquad \sigma = 2\Theta_2\,. \tag{2.1.79}$$

The equations now in conformal time $dt = ad\tau$ read

- *Newtonian gauge:*

$$\delta' = -\frac{4}{3}\theta + 4\psi' \tag{2.1.80a}$$
$$\theta' = k^2\left[\frac{\delta}{4} - \sigma + \phi\right] \tag{2.1.80b}$$
$$\Theta'_\ell = \frac{k}{(2\ell+1)}\left[l\Theta_{\ell-1} - (l+1)\Theta_{l+1}\right] \qquad l \geq 2\,. \tag{2.1.80c}$$

- *Synchronous gauge:* It is straight forward to obtain the same set of equations in synchronous gauge using eq. (2.1.56).

$$\delta' = -\frac{4}{3}\theta - \frac{2}{3}h' \tag{2.1.81a}$$
$$\theta' = k^2\left[\frac{\delta}{4} - \sigma\right] \tag{2.1.81b}$$
$$\sigma' = \frac{16}{15}\theta - \frac{6}{5}k\Theta_3 + \frac{8}{15}h' + \frac{16}{5}\eta' \tag{2.1.81c}$$
$$\Theta'_\ell = \frac{k}{(2\ell+1)}\left[l\Theta_{\ell-1} - (\ell+1)\Theta_{\ell+1}\right] \qquad l \geq 3\,. \tag{2.1.81d}$$

Truncation Scheme

Of course, we cannot follow an infinite number of equations. Hence, these sets of equations need to be truncated at some maximum multipole $\ell_{\rm max}$. For understanding CMB temperature and polarisation anisotropies, we will see that only the first few multipoles enter the relevant quantities. For a perfect fluid, which does not develop any shear, nor higher momenta, it could be sufficient to cut at $\ell_{\rm max} = 2$. However, this wouldn't be accurate for a species such as neutrinos. Typically, perturbations in a free-streaming species are populating higher multipoles until $\ell \sim k\eta$, and thus in principle a safe scheme would be to cut for instance at $\ell \sim 2k\eta_0$, where η_0 is the conformal age of the Universe today. However, this is very time consuming and it is found that setting brutally Ψ_ℓ or Θ_ℓ to 0 above a too low $\ell_{\rm max}$ will generate errors at higher ℓ's that propagate to lower ones. It is thus common to use the improved truncation scheme from Ref. [412]. It is based on the solution of these equations in the absence of gravitational source term and cosmic shear (i.e. $\partial_\tau(\phi+\psi) = 0$). In this case, the time dependence of the analytical solution of the Boltzmann hierarchy is given by a bessel function $j_\ell(k\tau)$ for all ℓ's (only two being non-zero). From this, we assume that the solution still approximately holds even if the condition $\partial_\tau(\phi+\psi) = 0$ is not fulfilled anymore and make use of the recurrence relation for spherical Bessel functions to get

$$\Theta_{(\ell_{\rm max}+1)} \simeq \frac{(2\ell_{\rm max}+1)}{k\tau}\Theta_{\ell_{\rm max}} - \Theta_{(\ell_{\rm max}-1)}\,. \tag{2.1.82}$$

This improved truncation scheme has been generalized to include spatial curvature in Ref. [397].

2.1.2.4 *Massive neutrinos*

Before complexifying the Boltzmann equations, we finish by discussing the case of massive neutrinos. The difficulty for massive neutrinos is that it is no longer possible to do simplifications of eq. (2.1.63) into eq. (2.1.67). In general, it is possible to formally define the perturbed phase-space distribution :

$$f(\vec{x}, p, \vec{n}, t) = f^{(0)}(p,t)(1 + \Psi(\vec{x}, p, \vec{n}, t)) \quad , \tag{2.1.83}$$

To relate to the massless limit, it is possible to define the perturbations of the *integrated* phase-space distribution function as

$$F \equiv \frac{\int dpp^3 f^{(0)}\Psi}{\int dpp^3 f^{(0)}} \equiv \sum_\ell (-i)^\ell (2\ell+1) F_\ell(t,\vec{k})\mathcal{P}_\ell(\mu)\,, \tag{2.1.84}$$

and F can easily be related to Θ, introduced in eq. (2.1.66), when plugging eq. (B.2.17) into (2.1.83). It yields

$$\begin{aligned} F = \frac{\int dpp^3 f^{(0)}\Psi}{\int dpp^3 f^{(0)}} &= \frac{\int dpp^3\left(f - f^{(0)}\right)}{\int dpp^3 f^{(0)}} \\ &= \frac{\int dpp^3\left(f^{(0)} - p\frac{\partial f^{(0)}}{\partial p}\Theta - f^{(0)}\right)}{\int dpp^3 f^{(0)}} \\ &= -\frac{\int dpp^4 \frac{\partial f^{(0)}}{\partial p}\Theta}{\int dpp^3 f^{(0)}} \\ &= 4\frac{\int dpp^3 f^{(0)}\Theta}{\int dpp^3 f^{(0)}} \\ &= 4\Theta\,. \end{aligned} \tag{2.1.85}$$

However, given that such integration of the Boltzmann equation is not possible for massive neutrinos, it is more convenient to directly expand the angular dependence in a Legendre series:

$$\Psi(\vec{k},p,\mu,t) = \sum_\ell (-i)^\ell (2\ell+1)\Psi_\ell(t,\vec{k})\mathcal{P}_\ell(\mu)\,. \tag{2.1.86}$$

The perturbed energy density, pressure, energy flux and shear stress are related to Ψ through

$$\delta\rho = \int \frac{p^2 dpd\Omega}{(2\pi)^3} E f^{(0)}\Psi_0\,, \tag{2.1.87a}$$

$$\delta\mathcal{P} = \int \frac{p^2 dpd\Omega}{(2\pi)^3}\frac{p^2}{3\epsilon} f^{(0)}\Psi_0\,, \tag{2.1.87b}$$

$$-(\bar{\rho}+\bar{\mathcal{P}})\theta = \partial^i \int \frac{p^2 dpd\Omega}{(2\pi)^3} p f^{(0)}\Psi_1\,, \tag{2.1.87c}$$

$$-(\bar{\rho}+\bar{\mathcal{P}})\theta = \partial^i \int \frac{p^2 dpd\Omega}{(2\pi)^3}\frac{p^2}{3\epsilon} f^{(0)} f^{(0)}\Psi_2\,. \tag{2.1.87d}$$

Keeping only the first order terms, the general collisionless Boltzmann equation (2.1.63) can be written in terms of the perturbations of the phase-space distribution:

$$\frac{\partial\Psi}{\partial t} + \frac{\partial\Psi}{\partial x^i}\frac{p}{E}\frac{n^i}{a} - \frac{\partial \ln f^{(0)}}{\partial \ln p}\left[\frac{\phi}{x^i}\frac{E}{p}\frac{n^i}{a} - \frac{\partial\psi}{\partial t}\right] = 0\,. \tag{2.1.88}$$

By following the same steps as for the massless case, one can write the following hierarchy for massive neutrinos in Fourier space (where we safely trade ∂ for d in the derivative of the unperturbed phase space distribution):

$$\dot{\Psi}_0 = -k\frac{p}{E}\Psi_1 - \dot{\psi}\frac{d\ln f^{(0)}}{d\ln p} \tag{2.1.89a}$$

$$\dot{\Psi}_1 = \frac{k}{3}\left[\frac{p}{E}(\Psi_0 - 2\Psi_2) - \frac{E}{p}\phi\frac{d\ln f^{(0)}}{d\ln p}\right] \tag{2.1.89b}$$

$$\dot{\Psi}_\ell = \frac{p}{E}\frac{k}{(2\ell+1)}\left[\ell\Psi_{\ell-1} - (\ell+1)\Psi_{\ell+1}\right], \qquad \ell \geq 2. \tag{2.1.89c}$$

We then can conveniently rewrite this equation in terms of conformal quantity $y = ap$, $\epsilon = aE$ and $d\tau = dt/a$ to obtain:

- *Newtonian gauge:*

$$\boxed{\begin{aligned}
\Psi_0' &= -k\frac{y}{\epsilon}\Psi_1 - \dot{\psi}\frac{d\ln f^{(0)}}{d\ln y} && \text{(2.1.90a)}\\
\Psi_1' &= \frac{k}{3}\left[\frac{y}{\epsilon}(\Psi_0 - 2\Psi_2) - \frac{\epsilon}{y}\phi\frac{d\ln f^{(0)}}{d\ln y}\right] && \text{(2.1.90b)}\\
\Psi_\ell' &= \frac{y}{\epsilon}\frac{k}{(2\ell+1)}\left[\ell\Psi_{\ell-1} - (\ell+1)\Psi_{\ell+1}\right], \qquad \ell \geq 2. && \text{(2.1.90c)}
\end{aligned}}$$

- *Synchronous gauge*: The same set of equations is readily obtained in synchronous gauge thanks to the standard gauge transformations (2.1.56).

$$\boxed{\begin{aligned}
\Psi_0' &= -k\frac{y}{\epsilon}\Psi_1 - \frac{1}{6}h'\frac{d\ln f^{(0)}}{d\ln y} && \text{(2.1.91a)}\\
\Psi_1' &= \frac{k}{3}\frac{y}{\epsilon}(\Psi_0 - 2\Psi_2) && \text{(2.1.91b)}\\
\Psi_2' &= \frac{k}{5}\frac{y}{\epsilon}(2\Psi_1 - 3\Psi_3) - \left(\frac{1}{15}h' + \frac{2}{5}\eta'\right)\frac{d\ln f^{(0)}}{d\ln y} && \text{(2.1.91c)}\\
\Psi_\ell' &= \frac{y}{\epsilon}\frac{k}{(2\ell+1)}\left[\ell\Psi_{\ell-1} - (\ell+1)\Psi_{\ell+1}\right], \qquad \ell \geq 3. && \text{(2.1.91d)}
\end{aligned}}$$

Former truncation scheme can be readily adapted for massive neutrinos [412]

$$\Theta_{(\ell_{\max}+1)} \simeq \frac{(2\ell_{\max}+1)\epsilon}{yk\tau}\Theta_{\ell_{\max}} - \Theta_{(\ell_{\max}-1)}\ . \tag{2.1.92}$$

2.1.3 *Thomson scattering collision term and polarization anisotropies*

2.1.3.1 *A first word on CMB Polarization*

We now will explain the link between section 1.3.3 and the evolution of photons and baryons perturbations. Before recombination, photons and baryons are interacting through Compton scattering. We consider here times well after neutrino decoupling, i.e. $T \ll m_e$, such that the interactions happen in the low energy Thomson limit. We thus need to add a collision term for the process

$$e^-(\vec{q}) + \gamma(\vec{p}) \leftrightarrow e^-(\vec{q}') + \gamma(\vec{p}')\,.$$

The key point here is that Thomson scattering holds a strong dependence on the polarization of the photon: typically, for photons polarized in the scattering plane, the amplitude of the scattering is suppressed by a factor $\cos(\vec{p}\cdot\vec{p}')$, while it is unsuppressed for photons polarized normal to the scattering plane. This implies that the radiation in the CMB is expected to be (linearly) polarized because of Compton scattering. However, given that the CMB is globally isotropic the sum of all incoming photons will result in not net polarisation. In fact, only a *quadrupole* pattern can generate a net polarization. This fact is sketched in fig. 22, assuming radiations coming only from two perpendicular directions as a

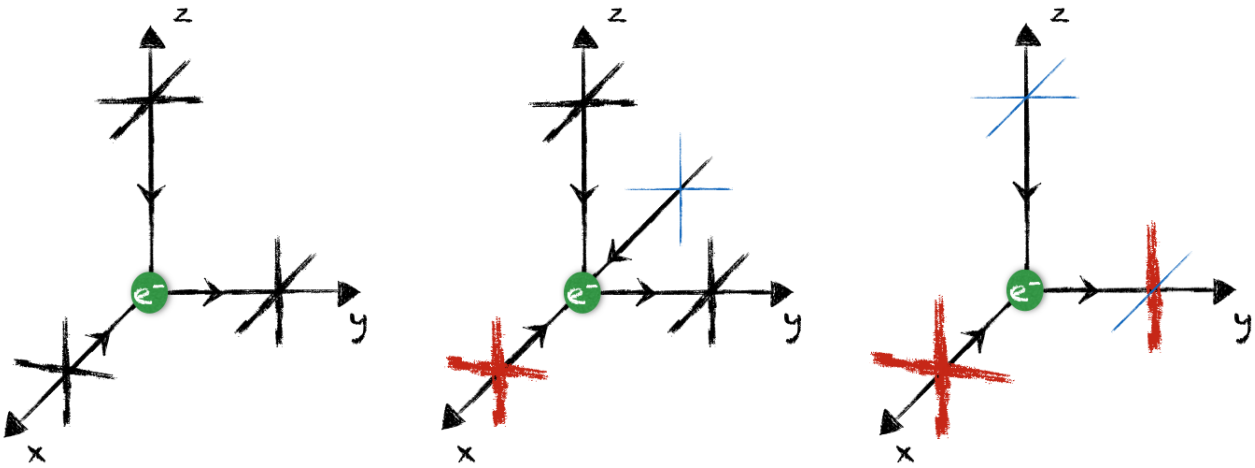

Figure 22: A schematic picture of the generation of linear polarization due to Thomson scattering. *Left panel* – An isotropic flux generates not net polarization. *Middle panel* – A dipole does not produce net polarization neither. *Right panel* – Only a quadripolar pattern can generate a net polarization. In this case, a positive Q component is generated since $E_z > E_x$. Adapted from Refs. [217], [330].

proof of principle. Because a quadrupole moment is generated only when photons start to free-stream, the polarization patterns seen today are created around the time of decoupling.

Just like temperature, one can derive evolution equations for polarization in the very same way as we just did. Polarization anisotropies can be generated by each type of perturbations, scalar vector or tensor, but we shall as well limit ourself to scalar perturbations, which are the most important ones for our study. The fundamental equations have been introduced by Refs. [111], [486] with large extension and all mathematical details of the statistics of these anisotropies by Refs. [331], [353], [378], [604]. We start with a monochromatic electromagnetic wave of frequency ν propagating in the z-direction. The components of the wave's electric field vector at a given point in space can be written as [347]

$$E_x = a_x(t)\cos[2\pi\nu t - \theta_x(t)] \qquad E_y = a_y(t)\cos[2\pi\nu t - \theta_y(t)]\,. \tag{2.1.93}$$

It is common to express the Stokes parameters, introduced to describe the shape of the ellipse in which the polarization vector evolves and more easily accessible experimentally. Their time averages are

$$I \equiv \langle a_x^2\rangle + \langle a_y^2\rangle\,, \tag{2.1.94a}$$
$$Q \equiv \langle a_x^2\rangle - \langle a_y^2\rangle\,, \tag{2.1.94b}$$
$$U \equiv \langle 2a_x a_y\cos(\theta_x - \theta_y)\rangle\,, \tag{2.1.94c}$$
$$V \equiv \langle 2a_x a_y\sin(\theta_x - \theta_y)\rangle\,. \tag{2.1.94d}$$

The I parameter is a physical observable that gives the intensity of the radiation, and is thus nothing but the temperature T we have already encountered. We shall make use of temperature perturbation units and measure intensity and polarization with respect to the mean CMB temperature. Q and U describe the linear polarization while V describes circular polarization. In general, it is trivial to show that they satisfy the relation

$$I^2 = Q^2 + U^2 + V^2\,, \tag{2.1.95}$$

thus there's only three degrees of freedom. In the early Universe, we do not expect any phase shift $\theta_x = \theta_y$, and equivalently there are no circularly polarized waves, thus we set V to 0. The sense and magnitude of the polarization is defined by the angle between the orientation of the quadrupole moment and the scattering direction. Setting the north pole at $\theta = 0$ (i.e. along z in Fig. 22), a polarisation component with $Q > 0$ (resp. $Q < 0$) is usually called a N-S (E-W), while a polarisation component $U > 0$ (resp. $U < 0$) is called a NE-SW (NW-SE).

Under a rotation α in the polarization plane, I and V remain invariant while Q and U transform as

$$Q' = \cos(2\alpha)Q + \sin(2\alpha)U \tag{2.1.96}$$
$$U' = -\sin(2\alpha)Q + \cos(2\alpha)U \tag{2.1.97}$$

This non-invariance of the Stoke parameter makes the study much more complicated when looking at photons coming at every direction in the sky. It is more convenient to build two quantities that transform as spin 2 objects under the action of rotation (here around a random direction $\hat{n}$)

$$(Q \pm iU)'(\hat{n}) = e^{\mp 2i\alpha}(Q \pm iU)(\hat{n}) \tag{2.1.98}$$

and then to use properties of the spherical harmonics of spin 2 to construct spin 0 (rotation invariant) quantitites. Such observation will be used when building the statistics of CMB, as we will construct the so-called CMB E and B modes as linear combination of the spherical harmonic expansion coefficients.

2.1.3.2 *Photon hierarchy*

We wish now to write the equations governing the evolution of temperature and polarization anisotropies for photons, i.e. for Θ_T, Q and U.

However, for scalar modes, which are plane wave perturbations only characterized by a given wave vector, it is always possible to choose our basis in the direction of the wave vector. The key point is that azimuthal symmetry around this axis ensures that only Q polarization can be generated. Its amplitude is thus $Q \equiv \Theta_P(\tau, k, \mu)$ where μ is the cosinus of the angle between the photon and the perturbation wave vector, $\mu \equiv \hat{n} \cdot \hat{k}$. In order to know how it evolves, we need to write down the linearized Boltzmann equation for both Θ_T and Θ_P with Thomson scattering collisions. Most of the work for Θ_T has already been done in previous section, and the collisionless part for Θ_P is even simpler as polarization is already a first order quantity and thus does not contain any metric contribution. In appendix B.2.2, we derive the Boltzmann equations for Θ_T including the angular dependence of the Thomson scattering. The evolution equation for Θ_P, and its contribution to the Θ_T equation, requires to follow a coupled system $\vec{T} = (\Theta_T, \Theta_P)$ with a more involved collision term. The full expression is given in Ref. [328] (eqs. (21) and (22) therein) while the detailed computation can be found in Ref. [378] and in textbooks [226], [479]. In the usual case of vanishing U and V terms, it simplifies to (in Newtonian gauge and Fourier space)

$$\dot{\Theta}_T + ik\mu\Theta_T = -\dot{\psi} - ik\mu\phi - n_e\sigma_T[\Theta_{T0} - \Theta_T + \hat{n}\cdot\vec{v}_b - \frac{1}{2}\mathcal{P}_2(\mu)\Pi]\,, \tag{2.1.99a}$$
$$\Pi = \Theta_{T2} + \Theta_{P2} + \Theta_{P0}\,, \tag{2.1.99b}$$
$$\dot{\Theta}_P + ik\mu\Theta_P = -n_e\sigma_T\left[-\Theta_P + \frac{1}{2}(1 - \mathcal{P}_2(\mu))\Pi\right]. \tag{2.1.99c}$$

These equations can be recast in the usual hierarchy, augmented by one equation for $\Theta_{P\ell}$, now in terms of conformal time.

- *Newtonian gauge:*

$$\delta' = -\frac{4}{3}\theta + 4\psi' \,, \tag{2.1.100a}$$
$$\theta' = k^2\left[\frac{\delta}{4} - \sigma + \phi\right] + an_e\sigma_T(\theta_b - \theta_\gamma) \,, \tag{2.1.100b}$$
$$\sigma' = \frac{16}{15}\theta_\gamma - \frac{6}{5}k\Theta_3 - \frac{18}{10}an_e\sigma_T\sigma + \frac{2}{10}an_e\sigma_T(\Theta_{P0} + \Theta_{P2}) \,, \tag{2.1.100c}$$
$$\Theta'_{Tl} = \frac{k}{(2\ell+1)}\left[l\Theta_{T(\ell-1)} - (\ell+1)\Theta_{T(\ell+1)}\right] - an_e\sigma_T\Theta_{T\ell} \qquad l \geq 3, \tag{2.1.100d}$$
$$\Theta'_{P\ell} = \frac{k}{(2\ell+1)}\left[l\Theta_{P(\ell-1)} - (\ell+1)\Theta_{P(\ell+1)}\right] + an_e\sigma_T\left[-\Theta_{P\ell} + \frac{1}{2}\Pi\left(\delta_{l0} + \frac{\delta_{l2}}{5}\right)\right] . \tag{2.1.100e}$$

- *Synchronous gauge:*

$$\delta' = -\frac{4}{3}\theta - \frac{2}{3}h' \tag{2.1.101a}$$
$$\theta' = k^2\left[\frac{\delta}{4} - \sigma\right] + an_e\sigma_T(\theta_b - \theta_\gamma) \tag{2.1.101b}$$
$$\sigma' = \frac{16}{15}\theta - \frac{6}{5}k\Theta_3 + \frac{8}{15}h' + \frac{16}{5}\eta' - \frac{18}{10}an_e\sigma_T\sigma + \frac{2}{10}an_e\sigma_T(\Theta_{P0} + \Theta_{P2}) \tag{2.1.101c}$$
$$\Theta'_{T\ell} = \frac{k}{(2\ell+1)}\left[l\Theta_{T(\ell-1)} - (\ell+1)\Theta_{T(\ell+1)}\right] - an_e\sigma_T\Theta_{T\ell} \qquad l \geq 3, \tag{2.1.101d}$$
$$\Theta'_{P\ell} = \frac{k}{(2\ell+1)}\left[l\Theta_{P(\ell-1)} - (\ell+1)\Theta_{P(\ell+1)}\right] + an_e\sigma_T\left[-\Theta_{P\ell} + \frac{1}{2}\Pi\left(\delta_{l0} + \frac{\delta_{l2}}{5}\right)\right] . \tag{2.1.101e}$$

The truncation scheme used is now modified to incorporate the effect of Thomson scattering. For $\ell = \ell_{\rm max}$, we use again the Ma&Bertschinger scheme [412], generalized to spatial curvature [397]

$$\dot{\Theta}_{T\ell} = k\Theta_{T(\ell-1)} - \frac{\ell+1}{\tau}\Theta_{T\ell} - an_e\sigma_T\Theta_{T\ell} \tag{2.1.102a}$$
$$\dot{\Theta}_{P\ell} = k\Theta_{P(\ell-1)} - \frac{(\ell+1)}{\tau}\Theta_{P\ell} - an_e\sigma_T\Theta_{P\ell} \,. \tag{2.1.102b}$$

2.1.3.3 *Baryon hierarchy*

For baryons, it is not necessary to make use of a full Boltzmann hierarchy. Indeed, as Baryons are non-relativistic, they have negligible pressure (or equation of state parameter $\omega = 0$) and develop no anisotropic stress σ. Thus it is enough to make use of the continuity and Euler equation, similarly to DM, however augmented to incorporate Thomson scattering. The Thomson scattering term can be simply obtained by considering momentum conservation between the photon and baryon fluid.
In practice, it is common to keep also the $\delta\mathcal{P}/\delta\rho$ term when it is multiplied by k^2, as it encodes effect of the baryons pressure below their Jeans length. In this work we shall work with isentropic primordial perturbations (this will be defined in 2.1.4.1). In that case, $\delta\mathcal{P}$ and $\delta\rho$ verifies

$$\delta\mathcal{P} = c_s^2\delta\rho \qquad \text{where} \qquad c_s^2 \equiv \frac{\dot{\mathcal{P}}}{\dot{\rho}} = \omega + \rho\frac{d\omega}{d\rho} \,. \tag{2.1.103}$$

In general, Thermodynamics teaches us that an ideal gas verifies $\mathcal{P} = nk_BT = \rho k_BT/\mu$ where $n = \rho/\mu$ has been used with μ the mean molecular weight in the gas (including e^- and H and He ions). We can thus readily compute c_s^2

$$\begin{aligned}\dot{\mathcal{P}} = \frac{dP}{dt} &= k_B\left\{\frac{dn}{dt}T + n\frac{dT}{dt}\right\} \\ &= \frac{k_B}{\mu}T\dot{\rho}\left\{1 + H\frac{\rho}{\dot{\rho}}\frac{d\ln T}{d\ln a}\right\} \\ &= \frac{k_B}{\mu}T\dot{\rho}\left\{1 - \frac{1}{3}\frac{d\ln T}{d\ln a}\right\} \\ \Rightarrow c_s^2 &= \frac{\dot{\mathcal{P}}}{\dot{\rho}} = \frac{k_B}{\mu}T\left\{1 - \frac{1}{3}\frac{d\ln T}{d\ln a}\right\}. \end{aligned} \tag{2.1.104}$$

Although the CLASS code incorporates such a term, we checked that it matters only for very high range of k (typically $k \geq 10^4$). Note that a similar test could be done for σ, but it would require to follow also higher moments of the distribution, and in any case it can be safely neglected in the range of k that matters for our observables. The set of equations for baryons thus takes the form

- *Newtonian gauge:*

$$\boxed{\begin{aligned}\delta_b' &= -\theta_{CDM} + 3\psi', \qquad (2.1.105a)\\ \theta_b' &= -\mathcal{H}\theta_{CDM} + k^2\phi + c_s^2k^2\delta_b + R^{-1}an_e\sigma_T(\theta_\gamma - \theta_b). \qquad (2.1.105b)\end{aligned}}$$

- *Synchronous gauge:*

$$\boxed{\begin{aligned}\delta_b' &= -\frac{1}{2}h' - \theta_b, \qquad (2.1.106a)\\ \theta_b' &= -\mathcal{H}\theta_b + c_s^2k^2\delta_b + R^{-1}an_e\sigma_T(\theta_\gamma - \theta_b). \qquad (2.1.106b)\end{aligned}}$$

We have introduced the baryon to photon ratio rescaled by $3/4$ R

$$R \equiv \frac{3}{4}\frac{\bar{\rho}_b}{\bar{\rho}_\gamma}. \tag{2.1.107}$$

2.1.4 *Initial conditions from Inflation*

We now want to describe how these perturbations can be produced in the first place. As we will see, this is related to the inflation mechanism, already introduced in sec. 1.2. The field $\phi(t)$ governs the energy density of the early universe $\rho(t)$, as well as the end of inflation. However, quantum mechanics teaches us that arbitrarily precise timing is not possible: hence the inflaton will have spatially varying fluctuations $\delta\phi(t,\vec{x}) \equiv \phi(t,\vec{x}) - \bar{\phi}(t)$ related to the local differences $\delta t(\vec{x})$ in the time when inflation ends. In other words, different regions of space inflate by slightly different amounts, which in turn leads to macroscopic $\delta\rho(t,\vec{x})$. The beauty of this mechanism is that inflation is not tuned to generate primordial fluctuations: it is a *prediction* in remarkable agreement with observations.

2.1.4.1 *Adiabatic and isocurvature fluctuations*

If the universe is composed initially of N uncoupled perfect fluids with N known sound speeds $c_s^2 = \delta\mathcal{P}_s/\delta\rho_s$, then there are $2N$ independent initial conditions corresponding to possible initial values of δ_s

and δ_s'. The simple picture that we just described leads to *adiabatic* initial fluctuations the local state of matter at some spacetime point $(t, \vec{x})$ is the same as in the *background* universe at some slightly different time $t + \delta t(\vec{x})$. $\delta t(\vec{x})$ is a common, local shift in time of all background quantities due to the slight time difference at the end of inflation. Densities and pressures are thus described as

$$\rho_i(t, \vec{x}) = \bar{\rho}_i(t + \delta t(\vec{x})) \simeq \bar{\rho}_i + \dot{\bar{\rho}}_i(t)\delta t(\vec{x}) \tag{2.1.108}$$

$$\mathcal{P}_i(t, \vec{x}) = \bar{\mathcal{P}}_i(t + \delta t(\vec{x})) \simeq \bar{\mathcal{P}}_i + \dot{\bar{\mathcal{P}}}_i(t)\delta t(\vec{x})\,, \tag{2.1.109}$$

where δt is the same for all species i. This implies

$$\delta t = \frac{\delta\rho_i}{\dot{\rho}_i} = \frac{\delta\rho_j}{\dot{\rho}_j}\,, \tag{2.1.110}$$

for all species i and j. Assuming no energy transfer between species at the background level, then the continuity equation is verified for all species separately $\dot{\bar{\rho}}_i = -3H(1 + w_i)\bar{\rho}_i$, which allows to write

$$\frac{\delta_i}{1 + w_i} = \frac{\delta_j}{1 + w_j}\,, \tag{2.1.111}$$

for all species i and j. Remarkable properties emerge: all matter/radiation components have the same fractional perturbations, and they are related by

$$\delta_r = \frac{4}{3}\delta_m\,. \tag{2.1.112}$$

For all species, we can define an adiabatic sound speed[3]

$$\frac{\delta\mathcal{P}_i(t, \vec{x})}{\delta\rho_i(t, \vec{x})} = \frac{\dot{\bar{\mathcal{P}}}_i(t)}{\dot{\bar{\rho}}_i(t)} \equiv c^2_{ad,i}(t)\,, \tag{2.1.113}$$

and the total perturbations can as well be described by an effective sound speed

$$\delta\mathcal{P} = c_s^2(t)\delta\rho(t, \vec{x}) \qquad \text{with} \quad c_s^2(t) \equiv \frac{\sum_i \dot{\bar{\rho}}_i(t)c^2_{ad,i}(t)}{\sum_i \dot{\bar{\rho}}_i(t)}\,. \tag{2.1.114}$$

In practice, adiabatic perturbations correspond to a change in the total energy density,

$$\delta\rho = \sum \bar{\rho}_i\delta_i\,. \tag{2.1.115}$$

$\delta\rho$ is dominated by the species that is dominant in the background since all δ_i are comparable.
The complement of adiabatic perturbations are *entropy* or *isocurvature* perturbations. They correspond to perturbations between the different components. The names come from the fact that, for each species, the total density (and therefore the spatial curvature) perturbation vanishes in the super-Hubble limit, except for two species having opposite density perturbations exactly compensating each other. Their definition is simply

$$\delta S_{ij} = \frac{\delta_i}{1 + w_i} - \frac{\delta_j}{1 + w_j}\,, \tag{2.1.116}$$

and it is common to use the photons as the reference species, thus defining isocurvatures modes with respect to them. In general the total pressure perturbations is

$$\begin{aligned}\delta\mathcal{P} &= c^2_{s,i}(t)\delta\rho(t, \vec{x}) \\ &= c_s^2(t)\delta\rho(t, \vec{x}) + \sum_{i\neq j}\frac{\partial\mathcal{P}}{\partial S_{ij}}S_{ij}\,.\end{aligned} \tag{2.1.117}$$

3 This feature gives the name to this type of initial conditions.

A good basis of independent initial conditions is thus composed of one growing adiabatic mode, $(N-1)$ non-decaying isocurvature modes, N decaying modes that are irrelevant since they cannot be observed. Single-field inflation predicts purely adiabatic perturbations, in perfect agreement with current observations, and thus we won't discuss isocurvature fluctuations further.
We can relate these density perturbations to metric perturbations thanks to Einstein equations and it takes a particularly trivial form under the assumption of adiabatic initial conditions. Indeed, since eq. (2.1.113) holds, we can combine Einstein equation (00) and (ii) to get

$$\psi'' + (2\mathcal{H}' + \mathcal{H}^2)\phi + \mathcal{H}\phi' + 2\mathcal{H}\phi' - \frac{1}{3}k^2(\phi - \psi) = -c_s^2[k^2\psi + 3\mathcal{H}(\mathcal{H}\phi + \psi')]\,. \tag{2.1.118}$$

This simplifies further under the assumption of negligible anisotropic shear, $\psi = \phi$ and constant equation of state $w \sim c_s^2$

$$\psi'' + 3(1+w)\mathcal{H}\psi' + wk^2\psi = 0\,. \tag{2.1.119}$$

On super-Hubble scales, the growing solution is $\psi = const.$ Through the Poisson equation in Newtonian gauge (or its generalized version, the (00) Einstein equation) we immediately get that for superhorizon scales

$$\delta \simeq -2\psi = -2\phi = const. \tag{2.1.120}$$

This means that for adiabatic initial conditions we have at the end of inflation for a radiation-dominated universe

$$\delta_m = \frac{3}{4}\delta_r \simeq -\frac{3}{2}\psi\,. \tag{2.1.121}$$

We will now make the link between these fluctuations and the inflaton ones.

2.1.4.2 *The conserved comoving curvature perturbation*

The first thing to discuss is a very important quantity which is conserved on super-Hubble scales for adiabatic fluctuations: the *comoving curvature perturbation* $\mathcal{R}$. The fact that it is conserved is essential as it allows to choose our "initial time" arbitrarily, provided that all modes of interest are outside of the Hubble radius, which is the case after inflation.
We start by computing the Ricci scalar R (or intrinsic curvature) associated to the spatial part of the general metric (2.1.7) restricted to scalar modes, which we call γ_{ij}

$$\gamma_{ij} = (1-2\psi)\delta_{ij} + 2\big(\partial_i\partial_j - \frac{1}{3}\delta_{ij}\nabla^2\big)\mu\,. \tag{2.1.122}$$

A lengthy but straight-forward computation yields

$$a^2 R_{(3)} = -4\nabla^2(-\psi - \frac{1}{3}\nabla^2\mu) \tag{2.1.123}$$

The quantity $-\psi - \frac{1}{3}\nabla^2\mu$ is called *curvature perturbation*. In the comoving gauge it is equal to $\mathcal{R}$ (hence the name). However, the usual expression of $\mathcal{R}$ is gauge-invariant, so one can easily express it in any gauge. Using eq. (2.1.56), one can construct the good gauge invariant expression for $\mathcal{R}$ given by

$$\mathcal{R} = -\psi - \frac{1}{3}\nabla^2\mu + \mathcal{H}(B+v)\,. \tag{2.1.124}$$

In the newtonian gauge, using Einstein equation (0i), it reduces to

$$\mathcal{R} = -\psi + \mathcal{H}v = -\psi - \frac{\mathcal{H}(\psi' + \mathcal{H}\psi)}{4\pi G a^2(\bar{\rho} + \bar{\mathcal{P}})}\,. \tag{2.1.125}$$

Taking the time derivative of eq. (2.1.125), using the homogeneous Friedmann and continuity equation and the Poisson equation leads to

$$-4\pi G a^2(\bar{\rho}+\bar{\mathcal{P}})\mathcal{R}' = 4\pi G a^2 \delta\mathcal{P}_{\rm en} + \mathcal{H}\frac{\bar{\mathcal{P}}'}{\bar{\rho}'}\nabla^2\psi\,. \tag{2.1.126}$$

where $\delta\mathcal{P}_{\rm en}$ was defined in eq. (2.1.40). Under the assumption of adiabatic fluctuations $\delta\mathcal{P}_{\rm en}=0$ and on super-Hubble scales $k \ll \mathcal{H}$, we find that $\mathcal{R}' \sim const.$ This means that the value of the comoving curvature perturbations at horizon crossing during inflation is conserved for those scales after inflation. It is possible to make use of the continuity equation to write

$$\mathcal{R} = -\psi + \mathcal{H}v = -\psi - \frac{2}{3(1+w)}\left(\frac{\phi'}{\mathcal{H}}+\phi\right), \tag{2.1.127}$$

and in the superhorizon limits $\psi'=0$ such that

$$\mathcal{R} = -\frac{5+3w}{3+3w}\psi\,. \tag{2.1.128}$$

So we can immediately relate superhorizon fluctuation in $\mathcal{R}$ to the metric potentials. In the radiation-dominated era $w=1/3$, while $w=0$ in the matter dominated era such that

$$\mathcal{R} = -\frac{3}{2}\psi_{\rm RD} = -\frac{5}{3}\psi_{\rm MD} \quad \rightarrow \quad \psi_{\rm MD} = \frac{9}{10}\psi_{\rm RD}\,. \tag{2.1.129}$$

Let's now relate $\mathcal{R}$ to the inflaton perturbations. In the *spatially flat gauge*, ψ and μ are taken to be 0. The gauge-invariant comoving curvature perturbation thus becomes

$$\mathcal{R} = \mathcal{H}(B+v)\,. \tag{2.1.130}$$

By computing the off diagonal part of the stress-energy tensor for a scalar field (1.2.21) we have

$$\partial T^0_j = g^{\mu 0}\partial_\mu\phi\partial_j\delta\phi = \bar{g}^{00}\partial_0\bar{\phi}\partial_j\delta\phi = \frac{\bar{\phi}'}{a^2}\partial_j\delta\phi\,, \tag{2.1.131}$$

which we can relate to the (scalar) perturbations of the stress-energy tensor

$$\begin{aligned}\delta T^0_j &= -(\bar{\rho}+\bar{\mathcal{P}})\partial_j(B+v)\\ &\Rightarrow B+v = -\frac{\delta\phi}{\bar{\phi}'}\,.\end{aligned} \tag{2.1.132}$$

This allows to link the comoving curvature perturbation to the fluctuations of the inflaton

$$\mathcal{R} = -\frac{\mathcal{H}}{\bar{\phi}'}\delta\phi\,. \tag{2.1.133}$$

This very important result will be used to deduce the initial conditions for all perturbations directly from the inflaton later on.

2.2 The CMB and matter power spectrum

Now that all necessary tools have been derived, we need to relate these theoretically useful equations to real observable quantities. It means that we need to calculate the evolution of inhomogeneities and anisotropies in the universe, and then build observable quantities that we want to measure. We will see that this is done thanks to the *power spectrum*, which quantifies the amplitude of the variance of each Fourier mode. In other words, power spectra are the "harmonic transforms" of the two-point correlation functions in real space. We will argue that knowledges of the power spectrum, within the minimal cosmological model, is enough to fully characterise the perturbations.
In linear perturbation theory, the power spectrum at a time t will be related to the initial power spectrum at t_0 times a transfer function which encodes all information about the evolution of each Fourier mode. In this chapter, we aim at a complete, self-contained, description of the CMB and matter power spectrum and its computation. After a brief introduction, we derive the initial conditions or so called *primordial power spectrum*. We then describe how to measure power spectra in practice thanks to CMB maps or galaxy surveys and show how to compute the power spectrum at an arbitrary time thanks to *transfer functions*, related to the equations we derived above. Finally, we discuss the physics behind the measured power spectra to understand the signatures that peculiar massive relics can create.

2.2.1 *Cosmology as a stochastic theory*

First of all, one needs to realize that, because of the stochastic nature of the initial conditions, the theory of cosmological perturbations is a *stochastic theory*, i.e. a theory for the evolution of random quantities. Cosmology cannot predict the value of perturbations of each fluid at each point in the universe, or what is the exact position of each galaxy around us, rather it can predict the *statistical properties* of the fluctuations at each time. Instead of describing the state of the universe at a given time by a definite spatial distribution of various functions, one describes it by the statistical properties of these distributions. Since we treat perturbations of a homogeneous and isotropic universe, these properties are invariant by translation and rotation: hence, it is convenient to go to Fourier space and to discuss the statistical properties of a Fourier mode k. Isotropy ensures that each Fourier mode with the same modulus k will have the same statistical properties, independently of the direction of the wave vector $\vec{k}$.
To describe the statistical properties of the distribution $\mathcal{P}_A(A, t, \vec{x})$ of a given perturbations $A(t, \vec{x})$ with no complete knowledge of it, one can evaluate its moments. Thus, cosmologists interest themselves in estimating these moments by computing the two-point correlation function, three-point correlation function and higher correlation functions, or conversely power spectrum, bi-spectrum and so on.
Standard inflation predicts that perturbations follow a Gaussian probability distribution. This simplifies a lot the job, since a Gaussian distribution is fully characterized by its first and second moment. Furthermore, since we deal with perturbations, we already know that the first moment is zero, hence only the variance of the distribution is important. It is encoded in the second moment of the distribution, which can be estimated via the 2-point correlation function.
To begin with, let's consider any given perturbations $A(\vec{x}, \tau)$ (e.g. ρ, θ, Θ ...). The 2-point correlation function is given by

$$\langle A(t, \vec{x}) A(t, \vec{x}') \rangle \equiv \xi(t, \vec{r}) \tag{2.2.1}$$

with $\vec{r} = \vec{x}' - \vec{x}$. Homogeneity and isotropy ensures that the 2-point correlation function depend only on $|\vec{r}|$. This real quantity can be expanded in complex comoving Fourier modes $\delta(\vec{k}, \tau)$, with the symmetry $\delta(\vec{k}, \tau)^* = \delta(-\vec{k}, \tau)$. Our FS definition is

$$A(t, \vec{k}) = \int \frac{d^3\vec{x}}{(2\pi)^{3/2}} A(t, \vec{x}) e^{-i\vec{k}\vec{x}} \tag{2.2.2a}$$

$$A(t, \vec{x}) = \int \frac{d^3\vec{k}}{(2\pi)^{3/2}} A(t, \vec{k}) e^{+i\vec{k}\vec{x}} \tag{2.2.2b}$$

and the 2-point correlation function in FS is

$$\langle A(t, \vec{k}) A^*(t, \vec{k}') \rangle = \int \frac{d^3\vec{x} d^3\vec{x}'}{(2\pi)^3} \langle A(t, \vec{x}) A(t, \vec{x}') \rangle e^{-i\vec{k}\vec{x} + i\vec{k}'\vec{x}'} \tag{2.2.3}$$

We perform the change of variable $\vec{x}' \to \vec{r} = \vec{x}' - \vec{x}$ and make use of the fact that

$$\int \frac{d^3\vec{x}}{(2\pi)^3} e^{i(\vec{k} - \vec{k}')\vec{x}} = \delta^{(3)}(\vec{k} - \vec{k}') \tag{2.2.4}$$

in order to get

$$\langle A(t, \vec{k}) A^*(t, \vec{k}') \rangle = \int d^3 r \xi(t, r) e^{i\vec{k}'\vec{r}} \delta^{(3)}(\vec{k} - \vec{k}') \,. \tag{2.2.5}$$

After performing integration over the angular part of $\vec{r}$ in a spherical coordinate system such that $\vec{k}' = (k, 0, 0)$, we simply get

$$\int d^3\vec{r} \zeta(t, r) e^{i\vec{k}'\vec{r}} = 2\pi \int dr r^2 \xi(t, r) \frac{\sin(kr)}{kr} \tag{2.2.6}$$

and it is common to define the *power spectrum* of A as

$$P_A(t, k) \equiv 4\pi \int r^2 dr \zeta_A(t, r) \frac{\sin(kr)}{kr} \tag{2.2.7}$$

to get the standard result

$$\langle A(t, \vec{k}) A^*(t, \vec{k}') \rangle = P_A(t, k) \delta^{(3)}(\vec{k} - \vec{k}') \,. \tag{2.2.8}$$

Hence, the properties of $A(t, k)$ at a given time t are entirely described by the variance $\sigma(t, k)$, encoded inside $P_A(t, k)$. Thanks to the linearity of the equations of motions, we are sure that the shape of the probability distribution of each mode will be preserved: only the variance can increase with time. Linearity allows the solution for A to be cast in the form

$$A(k, t) = A(k, t_i) T(k, t) \,, \tag{2.2.9}$$

where $A(k, t_i)$ is the initial perturbations for each k and $T(k, t)$, which encodes the evolution of each Fourier mode, is called the *transfer function*. At the power spectrum level, we have

$$P_A(k, t) = \left\langle |A(k, t_i)|^2 \right\rangle T^2(k, t) \,. \tag{2.2.10}$$

Therefore, to get the power spectrum of a variable at any given time, one only needs its initial condition, predicted from some starting assumptions or given by a theory such as inflation and the corresponding

transfer function.
Finally, it is common to introduce the "dimensionless power spectrum" as

$$\mathcal{P}(k) \equiv \frac{k^3}{2\pi^2} P(k)\,. \tag{2.2.11}$$

because observable quantities always derive from convolution of the power spectrum with a window function $f(k)$ in the following way

$$\begin{aligned}\int \frac{d^3\vec{k}}{(2\pi)^3} P_A(k) f(k) &= \frac{4\pi}{(2\pi)^3}\int dk k^2 P_A(k) f(k) \\ &= \int d\ln k\ \mathcal{P}(k) f(k)\,.\end{aligned} \tag{2.2.12}$$

$\mathcal{P}(k)$ stands for the weight of each logarithmic interval in the integral and is a dimensionless quantity. The term "scale-invariant power spectrum" refers to $\mathcal{P}(k)$ being independent of k, i.e. $P(k) \propto k^{-3}$.

2.2.2 *Primordial power spectrum from inflation*

We will not do the explicit derivation of the Primordial Power spectrum as it is a model dependent quantity. However, we know how to link fluctuations in ϕ (the inflaton field) to fluctuations in the comoving curvature perturbations $\mathcal{R}$, and thus we can compute the variance of a given mode

$$\langle|\mathcal{R}_k|^2\rangle = \left(\frac{\mathcal{H}}{\bar{\phi}'}\right)^2 \langle|\delta\phi_k|^2\rangle \tag{2.2.13}$$

where $\delta\phi$ are the inflation fluctuations in the spatially flat gauge. The reason $|\delta\phi_k|^2$ is non-zero in the first place is that quantum fluctuations induce a non-vanishing variance in the amplitudes of the oscillations

$$\langle|\delta\phi_k|^2\rangle \equiv \langle 0||\delta\phi_k|^2|0\rangle\,. \tag{2.2.14}$$

Outside the horizon, the quantum nature of the field becomes undistinguishable [371], and quantum expectation values are identified with the ensemble average of a classical stochastic field, i.e. actual macroscopic fluctuations.
For a single scalar-field, the (dimensionless) scalar power spectrum of $\delta\phi$ at horizon crossing is (see e.g. chapter 6 of Ref. [90] for a derivation)

$$\mathcal{P}_{\delta\phi}(k) \sim \left(\frac{H}{2\pi}\right)^2\Bigg|_{k=aH}\,. \tag{2.2.15}$$

This implies that

$$\mathcal{P}_{\mathcal{R}}(k) = \frac{1}{8\pi^2}\frac{1}{\varepsilon}\frac{H}{M_{\rm pl}^2}\Bigg|_{k=aH}\,, \qquad \text{where} \quad \varepsilon = \frac{\frac{1}{2}\dot{\phi}}{M_{\rm pl}^2 H^2}\,, \tag{2.2.16}$$

which is a pure function of k. If H and ε does not vary with time, one gets a pure scale-invariant power spectrum. However, (slow-roll) inflation does predict that both quantities slowly vary in time and thus should deviate from the scale invariant form. It is practical to parametrize the shape of the power spectrum as

$$\mathcal{P}_{\mathcal{R}}(k) \equiv A_s\left(\frac{k}{k_\star}\right)^{n_s-1}\,, \tag{2.2.17}$$

where A_s and n_s are respectively the amplitude and the tilt of the primordial scalar power spectrum, while $k_\star$ is a reference (or pivot) scale, often taken to be 0.05 Mpc^{-1}. n_s quantifies deviation from scale-invariance ($n_s = 1$), which has been detected by observations [19]. For small ε, we can relate n_s and the Hubble slow-roll parameters as

$$n_s - 1 = -2\epsilon - \eta \tag{2.2.18}$$

It is possible to quantify deviation from a power-law by introducing the running of the scalar index

$$\alpha_s \equiv \frac{dn_s}{d\ln k} \tag{2.2.19}$$

as well as the running of the running and so on.
The cleanest prediction of inflation is a spectrum of primordial gravitational waves, which are tensor perturbations to the spatial part of the metric (2.1.7). We refer again to textbooks such as ref. [89], [90], [438] for the full derivation. The most important model-independent prediction of inflation is the power spectrum of tensor perturbations

$$\mathcal{P}_t(k) = \frac{2}{\pi^2}\frac{H^2}{M_{\rm pl}^2}\bigg|_{k=aH}. \tag{2.2.20}$$

Contrary to the scalar power spectrum, its amplitude is a direct measurement of the expansion rate H during inflation. In analogy to the scalar counterpart, we define

$$\mathcal{P}_t(k) \equiv A_t\left(\frac{k}{k_\star}\right)^{n_t} \tag{2.2.21}$$

where A_t and n_t are respectively the tensor amplitude and spectral index. Note the different (historical) convention: scale-invariance now corresponds to $n_t = 0$. The amplitude of the tensors normalized to the scalar one is called *tensor-to-scalar ratio*

$$r \equiv \frac{A_t}{A_s}. \tag{2.2.22}$$

Current limit are at the level of $r \leq 0.11$ [19]. It is straightforwards to relate those parameters to ε. One gets

$$r = 16\varepsilon \tag{2.2.23}$$

$$n_t = -2\varepsilon \tag{2.2.24}$$

which implies a very important consistency relation allowing to test inflation, $n_t = -r/8$.

2.2.3 *The CMB power spectra*

2.2.3.1 *Generalities on the CMB power spectrum*

We wish now to explicitly relate temperature and polarization anisotropies computed in sec. 2.1.3.2 to the power spectrum. In order to perform the expansion on the sphere, it is better to work with quantities that have a definite value of spin, namely $(\Theta(\hat{n}), (Q+iU)(\hat{n}), (Q-iU)(\hat{n}))$, respectively of spin 0 and 2. The question we wish to develop here is how to measure it and how to compute it theoretically?

Experimental determination of the CMB power spectrum

An experiment like Planck measures temperature and polarization anisotropies of the CMB over the full sky, at a number of incoming directions or "spots on the sky". On the sphere, one can expend anisotropies in terms of spin-weighted spherical harmonics (equivalent of the Fourier space for flat space) [328], [353], [604]

$$\Theta(\hat{n}) = \sum_{\ell,m} a_{T,\ell m} Y_{\ell m}(\hat{n})\,, \tag{2.2.25a}$$

$$(Q+iU)(\hat{n}) = \sum_{\ell,m} a_{2,\ell m 2} Y_{\ell m}(\hat{n})\,, \tag{2.2.25b}$$

$$(Q+iU)(\hat{n}) = \sum_{\ell,m} a_{-2,\ell m -2} Y_{\ell m}(\hat{n})\,. \tag{2.2.25c}$$

More details on the basis of spherical harmonics of spin s, namely the ${}_sY_{\ell m}$, can be found in appendix of ref. [479]. As explained in sec 2.1.3, the main difficulty with the polarization power spectrum is that Q and U are not rotationally invariant, which leads to complicated calculation when considering not a single mode but a superposition coming from all directions in the sky. Thus, although $a_{\pm 2,\ell m}$ are actual observables whose power spectrum can be predicted, one usually performs two more transformations. First, we rather make use of the linear combination

$$a_{E,\ell m} = -(a_{2,\ell m} + a_{-2,\ell m})/2 \tag{2.2.26}$$

$$a_{B,\ell m} = -(a_{2,\ell m} - a_{-2,\ell m})/2i \tag{2.2.27}$$

which transforms differently under parity operation. $a_{E,\ell m}$ will remain the same while $a_{B,\ell m}$ changes sign, in analogy with the electric and magnetic field. Secondly, we can construct rotational invariant quantities using the relation between the spherical harmonics (e.g. [479])

$$(\partial^{\pm})^2 (Q \pm iU)(\hat{n}) = \sqrt{\frac{(\ell+2)!}{(\ell-2)!}} \sum_{\ell m} a_{\ell m}^{(\pm 2)} Y_{\ell m}(\hat{n})\,. \tag{2.2.28}$$

and we define the scalar quantites as

$$\tilde{E}(\hat{n}) = \sum_{\ell m} a_{\tilde{E},\ell m} Y_{\ell m}(\hat{n})\,, \tag{2.2.29}$$

$$\tilde{B}(\hat{n}) = \sum_{\ell m} a_{\tilde{B},\ell m} Y_{\ell m}(\hat{n})\,. \tag{2.2.30}$$

Thus, $\tilde{E}$ is parity even and measures gradient (curl-free) contribution while $\tilde{B}$ is parity odd and measures curl (divergence-free) contribution. Those properties are illustrated in fig. 23. We have seen in sec. 2.1.3.2 that the azimuthal symmetry of scalar anisotropies enforces that they can only generate Q types of polarization. Hence, a fundamental properties of scalar anisotropies is that they cannot generate B-modes! Actually, B-modes can only be generated by vector (which do not generate E-modes) and tensor perturbations (which can also generate E-modes) [330][4]. The coefficients can be

4 This is rigorously true only at first order in perturbation theory and neglecting *CMB lensing*, which we shall briefly describe later.

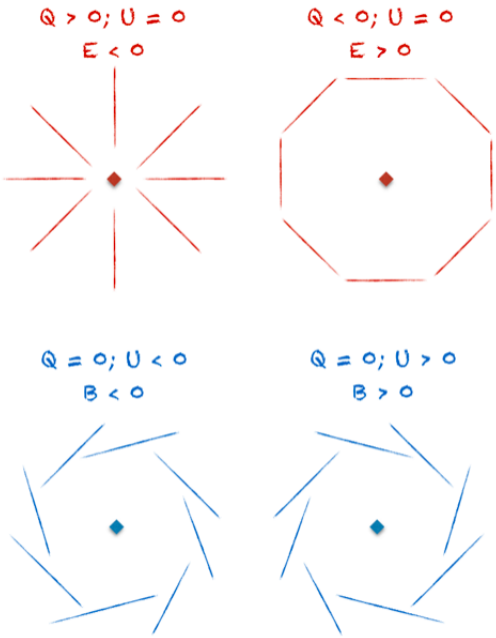

Figure 23: A schematic view of the E-polarization (top) and B-polarization (bottom) around the photon direction indicated as the center. A parity operation let the top two configurations unchanged while bottom ones are exchanged, in analogy with the electric and magnetic field.

extracted from the sky map through the relation

$$a_{\ell m} = \int d\hat{n} Y^*_{\ell m}(\hat{n})\Theta(\hat{n})\,, \tag{2.2.31}$$

$$a^{(\pm 2)}_{\ell m} = \int d\hat{n}\, {}_{\pm 2}Y^*_{\ell m}(\hat{n})(Q \pm iU)(\hat{n}) = \sqrt{\frac{(\ell+2)!}{(\ell-2)!}} \int d\hat{n} Y^*_{\ell m}(\hat{n})(\partial^{\mp})^2(Q \pm iU)(\hat{n})\,, \tag{2.2.32}$$

and eq. (2.2.28) implies that

$$a_{(\tilde{E},\tilde{B}),\ell m} = \sqrt{\frac{(\ell+2)!}{(\ell-2)!}} a_{(E,B),\ell m}\,. \tag{2.2.33}$$

The isotropy of the process generating the initial perturbations ensures that the distributions of the perturbations are the same in each direction of the sky. In analogy with the (Fourier) power spectrum, we have that the correlators of the expansion coefficients $a_{\ell m}$ are diagonal (we call them C_ℓ) and their mean value vanishes. For the special case of CMB observables, we have

$$\langle a_{T,\ell m}\rangle = 0 \quad ; \qquad \langle a_{T,\ell m} a^*_{T,\ell' m'}\rangle = \delta_{\ell\ell'}\delta_{mm'} C^{TT}_\ell\,, \tag{2.2.34}$$

$$\langle a_{\tilde{E},\ell m}\rangle = 0 \quad ; \qquad \langle a_{\tilde{E},\ell m} a^*_{\tilde{E},\ell' m'}\rangle = \delta_{\ell\ell'}\delta_{mm'} C^{EE}_\ell\,, \tag{2.2.35}$$

$$\langle a_{\tilde{B},\ell m}\rangle = 0 \quad ; \qquad \langle a_{\tilde{B},\ell m} a^*_{\tilde{B},\ell' m'}\rangle = \delta_{\ell\ell'}\delta_{mm'} C^{BB}_\ell\,, \tag{2.2.36}$$

while the parity properties ensures that the only non-vanishing cross-correlation is

$$\langle a_{T,\ell m} a^*_{E,\ell' m'}\rangle = \delta_{\ell\ell'}\delta_{mm'} C^{TE}_\ell\,. \tag{2.2.37}$$

It is important to note that, for a given ℓ, each $a_{\ell m}$ has the same variance, independently of m. Hence, to obtain an estimator of the C_ℓ, one computes the average of all $a_{\ell m}^{\rm obs}$'s with fixed ℓ over m

$$D_\ell \equiv C_\ell^{\rm obs} = \frac{1}{2\ell+1}\sum_{-\ell\leq m\leq \ell} |a_{\ell m}^{\rm obs}|^2 \,. \tag{2.2.38}$$

The estimator or "pseudo-C_ℓ" D_ℓ is obtained by averaging over $(2\ell+1)$ independent gaussian numbers centered at zero, each with variance C_ℓ. Hence, it obeys a χ^2 distribution with $(2\ell+1)$ degrees of freedom, a mean equal to C_ℓ and a variance $\sqrt{2/(2\ell+1)}C_\ell$. We see here the result of the cosmic variance. As already explained before, the theoretical errors on C_ℓ increases at large angular scales (low multipole ℓ), since we cannot average over a big number of independent realizations of the same stochastic process.

Theoretical determination of the CMB power spectrum

Since perturbation equations give us the evolution of Θ_ℓ, we need to relate these functions to the C_ℓ's. We start by expanding $\Theta(\tau_0,\vec{x}_0,\hat{n})$ in Fourier space and over Legendre polynomes as before thanks to eq. (2.1.76). Thus, we can express the two-point correlation function as

$$\langle\Theta_\ell(\tau_0,\vec{k})\Theta_\ell(\tau_0,\vec{k'})\rangle = \frac{2\pi^2}{k^3}\mathcal{P}_\mathcal{R}(k)[\Theta_\ell(\tau_0,k)]^2\delta^{(3)}(\vec{k}-\vec{k'}) \tag{2.2.39}$$

where $\mathcal{P}_\mathcal{R}(k)$ has been defined with respect to the conserved curvature perturbation $\mathcal{R}$, as introduced in previous section. In that case, we can insert the Legendre and Fourier expansion of $\Theta(\tau_0,\vec{x}_0,\hat{n})$ directly in eq. (2.2.34) to express the $a_{\ell m}$ as

$$a_{\ell m}(\tau_0,\vec{x}_0) = (-i)^\ell \int \frac{d^3k}{2\pi^2} Y_{\ell m}(\hat{k})\Theta_\ell(\tau_0,\vec{k}) \,. \tag{2.2.40}$$

where we have used the fact that the angular integral is non zero only if $\ell=\ell'$, in which case it is equal to $4\pi Y_{\ell m}(\hat{k})/(2\ell+1)$. We can also relate the two-point correlation function of $\Theta(\tau_0,\vec{x}_0,\hat{n})$ directly to the C_ℓ's by

$$\begin{aligned}
\langle\Theta(\tau_0,\vec{x}_0,\hat{n})\Theta(\tau_0,\vec{x}_0,\hat{n}')\rangle &= \sum_{\ell,\ell',m,m'} \langle a_{\ell m}a^*_{\ell' m'}\rangle Y_{\ell m}(\hat{n})Y^*_{\ell' m'}(\hat{n}') \\
&= \sum_\ell C_\ell \underbrace{\sum_{m=-\ell}^{\ell} Y_{\ell m}(\hat{n})Y^*_{\ell m'}(\hat{n}')}_{\frac{2\ell+1}{4\pi}P_\ell(\hat{n}\cdot\hat{n}'=\mu)} \\
&= \frac{1}{4\pi}\sum_\ell (2\ell+1)C_\ell P_\ell(\mu) \,.
\end{aligned} \tag{2.2.41}$$

We simply need to invert this equation to have our theoretical estimate of C_ℓ. Using eqs. (2.2.34), (2.2.39) and (2.2.40), we obtain

$$C_\ell = \int \frac{dk}{k}\mathcal{P}_\mathcal{R}(k)[\Theta_\ell(\tau_0,k)]^2 \tag{2.2.42}$$

A brute-force approach for computing the temperature anisotropy spectrum up to some multipole $\ell_{\rm max}$ consists in integrating all equations with at least $\ell_{\rm max}$ multipoles in the Boltzmann hierarchy

for the evolution of the photon distribution. This is very time consuming and does not really help in understanding the underlying physics. The alternative - standard - method is to use the so-called "line-of-sight" formalism introduced by Ref. [534], which helps to give an intuitive expression for the various expressions to each C_ℓ and speeds up Boltzmann codes in a spectacular way as it is usually enough to cut equations at $\ell_{\rm max} \sim 10$.

2.2.3.2 *The line-of-sight formalism*

Our goal is to integrate this Boltzmann equation (2.1.99) along the photon past light cone, or in other words along the line-of-sight. To get some insight on the results, we first will perform the integral *in real space*, ignoring the effect of polarization, along the line of ref. [392]. We shall then readily generalize to the full equations in Fourier space. In real space and in terms of conformal time, the generalized Boltzmann equation for photons (2.1.99), neglecting polarization contribution, reads

$$\Theta_T' + \hat{n}\cdot\vec{\nabla}\Theta_T + \psi' + \hat{n}\cdot\vec{\nabla}\phi = a n_e \sigma_T (\Theta_{T0} - \Theta_T + \hat{n}\cdot\vec{v}_B)\,. \tag{2.2.43}$$

To start with, we will compute the total derivative of the function $e^{-\kappa}(\Theta_T + \psi)$ along the trajectory between the last scattering surface and us. We add the exponential pre-factor to easily simplify terms in the Boltzmann equation. The total derivative of a function $\mathcal{F}(\tau, \vec{x}, \hat{n})$ along the past light cone of a photon coming from direction $\hat{n}$ reads

$$\frac{d}{d\tau}\mathcal{F}(\tau,\vec{x},\hat{n}) = \mathcal{F}' + \frac{dx_i}{d\tau}\frac{\partial\mathcal{F}}{\partial x_i} + \frac{dn_i}{d\tau}\frac{\partial\mathcal{F}}{\partial n_i}\,. \tag{2.2.44}$$

However, since in our case $\mathcal{F}$ is a first order quantity, only the first two terms will remain so. Indeed, in an unperturbed universe photons travel in straight line and $\frac{dn_i}{d\tau} = 0$. Hence, the last term is a second order quantity and can be neglected. Furthermore, at first order $\frac{dx_i}{d\tau} = \hat{n}$. Hence, we can write

$$\frac{d}{d\tau}\mathcal{F}(\tau,\vec{x},\hat{n}) = \mathcal{F}' + \hat{n}\cdot\vec{\nabla}\mathcal{F}\,. \tag{2.2.45}$$

Putting our function inside previous equation, we get

$$\frac{d}{d\tau}\left[e^{-\kappa}\left(\Theta_T + \phi\right)\right] = -\kappa e^{-\kappa}\left(\Theta_T + \phi\right) + e^{-\kappa}\left[\Theta_T' + \phi' + \hat{n}\cdot\vec{\nabla}\left(\Theta_T + \phi\right)\right]. \tag{2.2.46}$$

If we now multiply eq. (2.2.43) by $e^{-\kappa}$, we can equal it with previous equation to get

$$\frac{d}{d\tau}\left[e^{-\kappa}\left(\Theta_T + \phi\right)\right] = g\left(\Theta_{T0} + \phi + \hat{n}\cdot\vec{v}_B\right) + e^{-\kappa}\left(\phi' + \psi'\right), \tag{2.2.47}$$

where we have used the fact that $\kappa' = -a n_e \sigma_T$ and make use of already introduced visibility function $g(\tau) \equiv -\kappa(\tau)' e^{-\kappa(\tau)}$.
We now integrate this equation along the line-of-sight. This yields

$$\left(\Theta_T + \phi\right)|_{\rm obs} = \int_\tau^{\tau_0} d\tau \left[g\left(\Theta_{T0} + \phi + \hat{n}\cdot\vec{v}_B\right) + e^{-\kappa}\left(\phi' + \psi'\right)\right] \tag{2.2.48}$$

where the index "obs" means evaluated at the coordinate $(\tau_0, \vec{x}_0, \hat{n})$. The first term on the LHS is the temperature fluctuation for photons coming from a direction $\hat{n}$ observed today. The second term is the metric fluctuation today at the observer location, causing a local blueshifting of incoming photons as we live in a potential well. However, since this term is isotropic, a CMB experiment cannot distinguish

between this contribution and a shift in the average photon temperature. Furthermore, this effect is very tiny, of order $\mathcal{O}(10^{-5})$ and hence we will neglect it from now on.
It is physically instructive to make the "instantaneous decoupling approximation", which consists in replacing the visibility function by a Dirac delta $\delta_D(\tau - \tau_{\rm dec})$ and the $e^{-\kappa}$ term by a heavyside $H(\tau - \tau_{\rm dec})$. We can rearrange the term to obtain the very explicit expression

$$\Theta_T|_{\rm obs} = \underbrace{(\Theta_{T0} + \phi)|_{\rm dec}}_{\rm SW} + \underbrace{\hat{n}\cdot\vec{v}_B|_{\rm dec}}_{\rm Doppler} + \underbrace{\int_{\tau_{\rm dec}}^{\tau_0} d\tau\big(\phi' + \psi'\big)}_{\rm ISW} . \tag{2.2.49}$$

(i) The first term is called the Sachs-Wolfe (SW) term, in honor of the first persons who worked it out. It includes the intrinsic temperature term Θ_{T0} and the "gravitational Doppler shift" term ψ at one point on the last scattering surface. It is the dominant effect for describing large angular patterns on CMB maps, for which the microphysics is irrelevant. This expression would describe very well the map of the COBE satellite, which had limited angular resolution.
Now comes an important result. We have seen that adiabatic initial conditions ensures

$$\delta_\gamma = \frac{4}{3}\delta_B \,. \tag{2.2.50}$$

On super-hubble scales, the transfer functions are constant and using (00) component of Einstein equations, we get:

$$\begin{aligned} 4\Theta_{T0} = \delta_\gamma = \frac{4}{3}\delta_B = -2\phi = -2\psi \qquad & \text{radiation dominated universe}\,, \\ 4\Theta_{T0} = \delta_\gamma = \frac{4}{3}\delta_B = -\frac{8}{3}\phi = -\frac{8}{3}\psi \qquad & \text{matter dominated universe}\,. \end{aligned} \tag{2.2.51}$$

At decoupling, the universe is matter dominated. Then, assuming that the SW term dominates we have:

$$\Theta_T|_{\rm obs} = (\Theta_{T0} + \phi)|_{\rm dec} = \frac{1}{3}\phi|_{\rm dec} = -\frac{1}{8}\delta_\gamma|_{\rm dec} \tag{2.2.52}$$

This little calculation indicates that gravitation wins against pressure ! Indeed, an overdensity ($\delta_\gamma > 0$) on the last scattering surface, corresponding to a potential well ($\phi < 0$), leads to a cold spot in the observed map ($\Theta < 0$).

(ii) The second term is the standard Doppler term. Photons are emitted from a tightly coupled baryon-electron fluid with a different peculiar velocity at each point on the last scattering surface. The projection along the line of sight introduces a Doppler shift in the photon wavelength.

(iii) The last term is called the Integrated Sachs-Wolfe (ISW) term and contains all non-conservative gravitational effects occurring in a universe with non-static metric fluctuations. Photons going down a potential well (up a hill) gain (lose) energy and, if the value of the potentials don't change, lose (gain) it as they go up (down). On the other hand, a variation of the amplitude of the potentials will lead to a slight change in the photon energy.

This expression, although instructive, is not directly useful to compute the CMB power spectrum from eq. (2.2.42). One rather needs it in Fourier space and for each multipole moment ℓ. We will now perform the generalization to the full Boltzmann equation (2.1.99) along the line of ref. [534].
A very similar approach can be followed, expressing all terms involving Θ inside a total time derivative

and integrating along the line of sights. The exponential factor of the Fourier transform is replaced by $\exp\big(ik\mu(\tau-\tau_0)\big)$. Hence one gets

$$\Theta_T(\tau_0,k) = \int_\tau^{\tau_0} d\tau e^{ik\mu(\tau-\tau_0)}\big[g\big(\Theta_{T0}+\phi+\mu\vec{v}_B+\frac{1}{2}\mathcal{P}_2(\mu)\Pi\big)+e^{-\kappa}\big(\phi'+\psi'\big)\big]\,, \tag{2.2.53a}$$

$$\Theta_P(\tau_0,k) = -\frac{1}{2}\int_\tau^{\tau_0} d\tau e^{ik\mu(\tau-\tau_0)}e^{-\kappa}\dot{\kappa}[1-\mathcal{P}_2(\mu)\Pi]\,. \tag{2.2.53b}$$

From this, we want to go in multipole space and thus, we expand the exponential pre-factor in terms of Bessel functions and Legendre polynomials:

$$e^{-i\mu(\tau-\tau_0)} = \sum_{\ell=0}^{\infty}(2\ell+1)i^\ell j_\ell(k(\tau_0-\tau))P_\ell(\mu)\,. \tag{2.2.54}$$

To express the full hierarchy of moments, we plug this in previous equation and perform an integration by parts of μ, dropping all boundary terms since they either vanish when $\tau\to 0$ or are unobservable at $\tau=\tau_0$, affecting only the monopole. So in practice, when a term is multiplied by μ, it is simply changed by its time derivative. We end up with [534]:

$$\Theta_{\ell,(T,P)}(\tau_0,k) = \int_\tau^{\tau_0} d\tau S_{T,P}(\tau,k)j_\ell(k(\tau_0-\tau))\,, \tag{2.2.55a}$$

$$S_T(k,\tau) \equiv \underbrace{g(\Theta_{T0}+\phi)}_{\text{SW}}+\underbrace{(gk^{-2}\theta_B)'}_{\text{Doppler}}+\underbrace{e^{-\kappa}(\phi'+\psi')}_{\text{ISW}}+\underbrace{g\frac{\Pi}{4}-\left(g\frac{3\dot{\Pi}}{4k^2}\right)''}_{\text{Polarization}}, \tag{2.2.55b}$$

$$S_P(k,\tau) \equiv -g\frac{3\Pi}{4}-\left(g\frac{3\dot{\Pi}}{4k^2}\right)''. \tag{2.2.55c}$$

(2.2.55d)

This is the equation we wanted ! It allows to get the C_ℓ by plugging it into eq. (2.2.42). In the instanteneous decoupling approximation, $\Theta_{\ell,T}$ reduces to :

$$\begin{aligned}\Theta_{\ell,T}(\tau_0,k)\simeq\quad & [\Theta_{T0}(\tau_{\rm dec},k)+\phi(\tau_{\rm dec},k)]j_\ell(k(\tau_0-\tau_{\rm dec}))\\ +\quad & k^{-1}\theta_B(\tau_{\rm dec},k)j'_\ell(k(\tau_0-\tau_{\rm dec}))\\ +\quad & \int_{\tau_{\rm dec}}^{\tau_0} d\tau[\phi'(\tau,k)+\psi'(\tau,k)]j_\ell(k(\tau_0-\tau))\\ +\quad & \text{Polarization}\,.\end{aligned} \tag{2.2.56}$$

In the second line, the derivative of j_ℓ is taken with respect to its argument not conformal time. This result shows that the total C_ℓ can be decomposed into few contributions: the power spectrum of the SW term (first line), that of the Doppler term (second line), that of the ISW (third line), a subdominant polarization contribution and all cross terms (since it is the square of eq. (2.2.56) that enters in eq. (2.2.42)). Furthermore, for high ℓ's the bessel function and its derivative are very peaked near $x\simeq\ell$, hence the integral over k will pick up mainly modes with $k=\ell/(\tau_0-\tau_{\rm dec})$. This can also be geometrically justified from the definition of the multipole $\ell=\pi/\theta$, where θ is the angle that subtends the physical scale $\theta\times d_a(z_{\rm dec})$ on the last scattering surface, with $d_a(z_{\rm dec})$ the angular

diameter distance to objects of redshift z. For spherical harmonics, θ is the angle between a maximum and a minimum of the density wave. Hence, we have the following relation between k and ℓ:

$$\begin{aligned}\frac{\lambda}{2} &= a(\tau_{\rm dec})\frac{\pi}{k} = \theta d_a(z_{\rm dec}) \\ \Rightarrow \frac{a(\tau_{\rm dec})}{k} &= \frac{d_a(z_{\rm dec})}{\ell}\,.\end{aligned} \tag{2.2.57}$$

In a flat universe, the angular diameter distance at decoupling is given by $d_a(z_{\rm dec}) = a(\tau_{\rm dec})(\tau_0 - \tau_{\rm dec})$ and we find the result

$$k = \frac{\ell}{(\tau_0 - \tau_{\rm dec})}\,. \tag{2.2.58}$$

Hence, in the instantaneous decoupling limit and for large ℓ's (small angles), the SW contribution to the power spectrum can be approximated by

$$C_\ell^{\rm SW} \sim \langle|\Theta_{T0} + \phi|^2\rangle \qquad \text{at } (\tau, k) \simeq (\tau_{\rm dec}, l/(\tau_0 - \tau_{\rm dec})\,. \tag{2.2.59}$$

In the same limits, the Doppler term depends on the power spectrum of the baryon velocity divergence θ_B at the same time and scale

$$C_\ell^{\rm Doppler} \sim \langle|\theta_B|^2\rangle \qquad \text{at } (\tau, k) \simeq (\tau_{\rm dec}, l/(\tau_0 - \tau_{\rm dec})\,, \tag{2.2.60}$$

while the ISW term can be written approximately in terms of the integral

$$C_\ell^{\rm ISW} \sim \int_{\tau_{\rm dec}}^{\tau} d\tau(\tau_0 - \tau)\langle|\phi' + \psi'|^2\rangle \qquad \text{for all } (\tau, k) \simeq (\tau, l/(\tau_0 - \tau))\,. \tag{2.2.61}$$

Of course accurate computation require us to go beyond these approximations. We plot the power spectra computed with CLASS for the bestfit ΛCDM model of *Planck* 2016 high-ℓ TT,TE,EE + SIMlow [27] in fig. 63.

2.2.3.3 *Aspects of CMB physics: The tight-coupling approximation*

We wish here to describe the main features of the CMB power spectrum and some standard approximations, in order to get insight on the physics behind the acoustic peaks. This will allow us to better understand the modifications to the standard evolution that are introduced in models with decaying/annihilating relics and massive neutrinos.

At early times, when the Thomson opacity is large $an_e\sigma_T \equiv \Gamma_\gamma \gg H$, photons and baryons are tightly coupled, which means that Thomson interaction drives $v_b \to v_\gamma$, while $\sigma_\gamma \simeq 0$. It it thus straight-forward to combine equations (2.1.100) and (2.1.105) to eliminate the interaction term (or their equivalent in synchronous gauge) to get a simple equation for the photon temperature fluctuation

$$\Theta_{T0}'' + \frac{R'}{1+R}\Theta_{T0} + k^2c_s^2\Theta_{T0} = -\frac{k^2}{3}\phi + \frac{R'}{1+R}\psi' + \psi''\,. \tag{2.2.62}$$

We have used the fact that $R' = a\mathcal{H}R$ and introduced a fundamental quantity: the sound speed at which density waves propagate in the effective photons-baryons fluid

$$c_s^2 = \frac{\delta p_\gamma + \delta p_b}{\delta\rho_\gamma + \delta\rho_b} = \frac{1}{3(1+R)}\,. \tag{2.2.63}$$

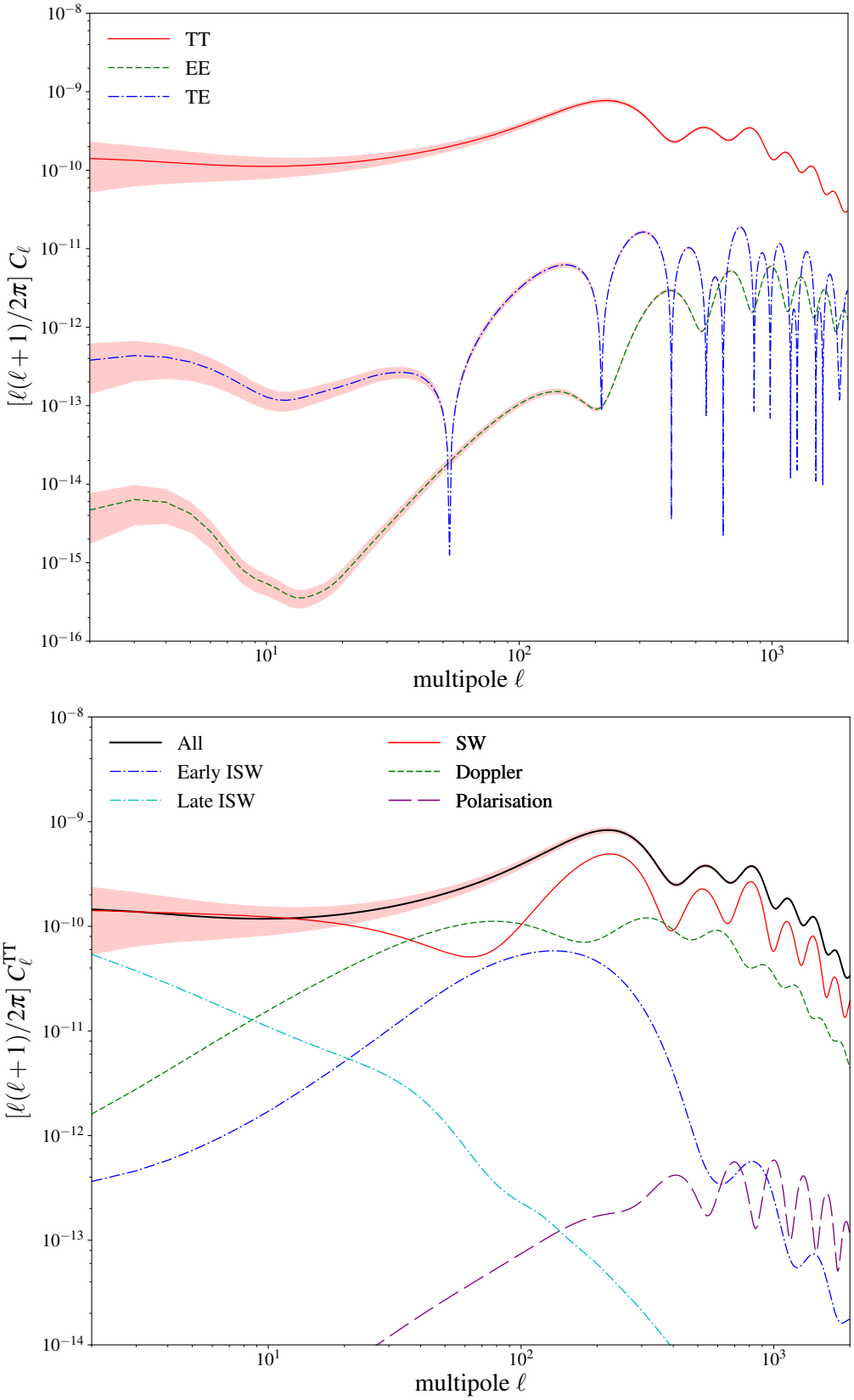

Figure 24: *Left panel:* Unlensed TT, TE, EE Power spectrum for the ΛCDM model bestfit of *Planck* 2016 high-ℓ TT,TE,EE + SIMlow [27] computed with the Boltzmann code CLASS. *Right panel:* Decomposition of the TT power spectrum per contribution.

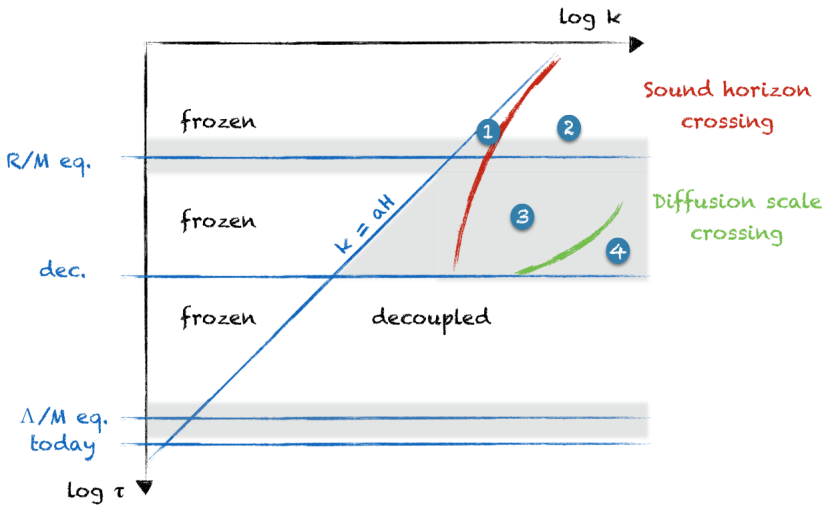

Figure 25: A sketch of the different evolution of k with time depending on the region in the (k, τ) plane. Adapted from Ref. [391].

This equation is the equation of a damped, driven harmonic oscillator. We can identify a pressure term with time-dependent characteristic frequency given by $\omega^2 = k^2 c_s^2$, the damping term is induced by $\frac{R'}{1+R}\Theta_{T0}$ and increases with increase baryonic density. The driving forces are due to gravitational effects, the first term is the standard gravitational force, while the others account for the so-called "dilation" effects.
In the $R \ll 1$ limit, i.e. when the universe is dominated by radiation, and in the absence of forces, eq. (2.2.62) reduces to

$$\Theta''_{T0} + k^2 c_s^2 \Theta_{T0} = 0 \quad \Rightarrow \quad \Theta_{T0} \propto \cos(k c_s \tau)\,. \tag{2.2.64}$$

We can introduce a fundamental quantity: the *comoving sound horizon*

$$r_s \equiv \int_{\tau_{\rm ini}}^{\tau} c_s d\tau \underset{\tau_{\rm ini} \ll \tau}{\simeq} c_s \tau\,. \tag{2.2.65}$$

It represents the comoving distance travelled by a wavefront since some arbitrary time deep inside the radiation-dominated regime. Because of the Universe's expansion, it is typically dominated by the upper limit of the integral. Its maximum value, attained at decoupling, is a correlation length between density fluctuations (or temperature in CMB maps), which can be calculated within our Cosmological model. Hence, it constitutes a *standard ruler*, as we defined them in sec. 1.1.3, and can be used to measure cosmological distances and deduce information on the background expansion of our Universe.

From the argument of the cosinusoidal function, we see that if the wavelength $\lambda = 2a\pi/k \gg a r_s$, then the solution is a constant, while $\lambda < a r_s$ corresponds to the oscillatory regime typical of the propagation of acoustic waves. Modes start oscillating when their wavelength becomes smaller than the sound horizon, and later on, the number of oscillations is given by the ratio between these two scales.
We sketch the evolution of wavelengths with time in fig. 25.

- Super-Hubble modes today, i.e. modes with $k \geq H_0$ are and remain frozen at all times in the past, their value is given by their initial value, up to some rescaling when the species that dominates the expansion rate of the universe changes.

- Modes in region ① experiences driven oscillations due to the gravitational terms. It typically enhances their amplitude and shifts the zero point of oscillations. Indeed, assuming equilibrium we have

$$\Theta_{T0}^{\text{eq.}} = \frac{1}{3c_s^2}\phi = -(1+R)\phi\,. \tag{2.2.66}$$

  However, metric potential quickly decays inside the sound horizon as illustrated in fig. 26 right panel, thus it reaches asymptotically zero on sub-sound-horizon scales. This shifting of the zero-point of oscillations towards negative values has important consequences phenomenologically. Indeed, we have seen in previous section that the power spectrum is obtained by summing the square of $\Theta_{T0} + \psi$. Thus, odd peaks will appear *higher* than even peaks and the relative height of the peaks allows a measurement of ω_b/ω_γ.

- Region ② represents modes deep inside sound-horizon during radiation domination. The metric terms are negligible and $R \ll 1$. Those are the modes experiencing acoustic oscillations we have already discussed, whose solutions are given by eq. (2.2.64).

- Modes in region ③ are inside sound horizon during the intermediate stage between matter-radiation equality and photon decoupling. Hence, R cannot be neglected anymore and the oscillator has a friction term and a decreasing time-varying frequency, as c_s decreases with time. The solution corresponds to damped acoustic oscillations.

- Finally, region ④ corresponds to modes with a diffusion length smaller than the (comoving) *diffusion length* r_d. Indeed, close to recombination, the tight-coupling approximation breaks down. Photon start to travel a non-negligible mean free path r_γ before interacting. If we treat the photon diffusion as a random walk, the mean free path is then given by $r_\gamma = \Gamma_\gamma^{-1}$ and thus

$$r_d \sim \int_{\tau_{\text{ini}}}^{\tau} d\tau \Gamma_\gamma r_\gamma^2 = \int_{\tau_{\text{ini}}}^{\tau} d\tau \Gamma_\gamma^{-1} = \int_{\tau_{\text{ini}}}^{\tau} \frac{d\tau}{a n_e \sigma_T}\,. \tag{2.2.67}$$

  Photon perturbations will erase perturbations with a wavelength smaller than $\lambda_d \equiv a r_d$. In Fourier space, scattering processes introduce an exponential cutoff in $\Theta_{T0}(\tau, k)$ shaped like $\exp[-(k/k_d)^2]$, with $k_d = 2\pi/r_d$ and in multipole space like $\exp[-(\ell/\ell_d)^2]$ with $\ell_d = \pi/\theta_d$ and $\theta_d = \lambda_d/d_s(\tau_{\text{dec}}) = a_{\text{dec}} r_d(\tau_{\text{dec}})/d_s(\tau_{\text{dec}})$. This effect is known as *diffusion damping* or *Silk damping*.

- Once baryons are decoupled from the photons, they start falling into the DM potential wells and perturbations start to grow, asymptotically reaching the DM ones.

In fig. 25 is also shown as shaded grey area the region in which gravitational (or metric) potential decays. Gravitational potential decays at early time, deep inside sound horizon, while they are static on all scales during matter domination. Moreover, they decay on all scales around the time at which the equation of state of the universe varies, i.e. z_{eq} and z_Λ. The decay of the potential at z_{eq} is a first source of early ISW (EISW) effect. One might expect that, since photon decouples in the matter-dominated era, this is the only one. However, because decoupling happens not too long after z_{eq}, metric

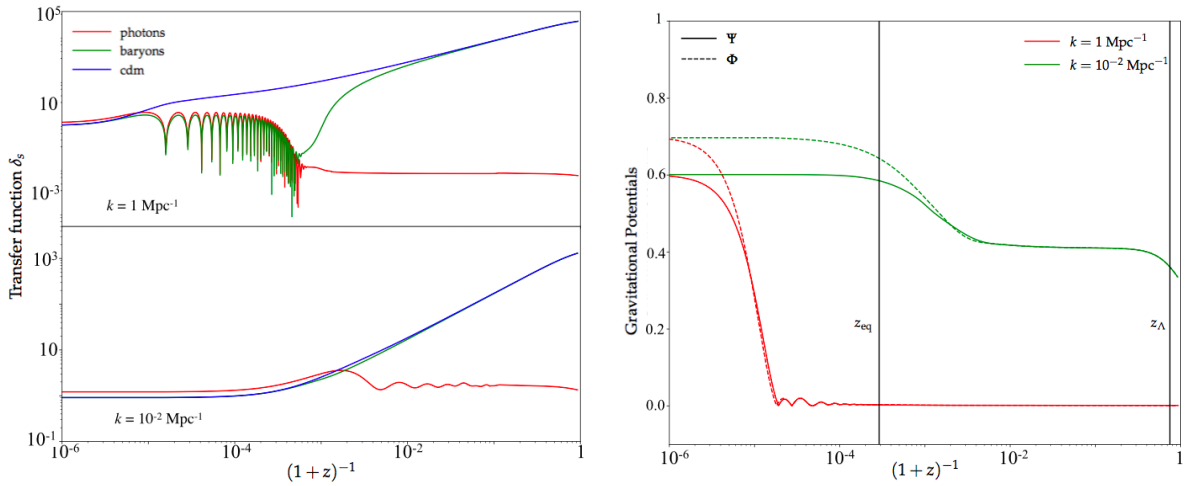

Figure 26: *Left panel* – Linear evolution of the density transfer functions for photons, baryons and cold dark matter. *Right panel* – Linear evolution of the gravitational potentials.

potentials have not yet had time to reach their freeze-out value when photon decouples, leading to a second source of EISW. The late ISW (LISW) on the other hand corresponds to variations due to the beginning of Λ domination. We will see in our study that non-standard relics (i.e. different from standard CDM) that interact only gravitationally (e.g. massive neutrinos, DM decaying into dark radiation) modify the evolution equation for the metric potential and tend to increase the ISW terms. We show in Fig. (26) a summary plot of the evolutions of the gauge-invariant metric potentials (AKA gravitational potentials) and transfer functions obtained thanks to the Boltzmann code CLASS for two modes: one much smaller than sound horizon during radiation domination which experiences a high number of acoustic oscillations and diffusion damping; another which enters sound horizon around the time equality and thus shows no acoustic oscillations in the baryon fluid, and no diffusion damping in the photon one. The difference between the two gravitational potentials on the right panel at early time is due to the anisotropic shear that develops in the presence of neutrinos (or more generally for any imperfect fluid).

2.2.3.4 *The ΛCDM model*

The shape of the CMB temperature power spectrum can be readily understood from previous discussions.

- For $\ell \ll 100$, modes are still outside sound horizon at decoupling. The spectrum is described by a SW plateau, that depends on the amplitude of the primordial power spectrum and the tilt, and is slightly affected by the effect of the LISW that tends to tilt the SW plateau.

- For $\ell \geq 100$, the spectrum exhibits a series of acoustic peaks, corrected by the Doppler peaks, which corresponds to the fundamental mode and harmonic decomposition of the sound horizon at decoupling. The modes are furthermore affected by various effects: their amplitude is globally suppressed due to the damping term that increases when R is non negligible, i.e. after matter-radiation equality; odd peaks are enhanced with respect to even peaks because of the shift of the zero-point of oscillation when R and ϕ are non-negligible; the first peak is further enhanced due to the EISW effect; diffusion damping exponentially suppresses anisotropies at high-ℓ.

- Reionization, which we had introduced in sec. 1.3.4, leads to a scale independent suppression of power for all scales inside the Hubble horizon at reionization, i.e. with $\ell \geq 40$, accounted for by a factor $\exp(-\tau_{\rm reio})$, where $\tau_{\rm reio}$ is the optical depth at reionization.

It is remarkable that the CMB power spectra can be extremely well fitted using only 6 free parameters

- The amplitude of the primordial power spectrum A_s and the primordial tilt n_s;
- The baryon density $\omega_b = \Omega_b h^2$;
- The total non relativistic matter density $\omega_M = (\Omega_B + \Omega_{cdm})h^2$;
- The Hubble rate today $H_0 = 100\ h\ \ {\rm km\ s^{-1}\ Mpc{-}1}$. In the minimal model, $\Omega_k = 0$, hence there is a one-to-one correspondence $h = \sqrt{\omega_m/(1-\Omega_\Lambda)}$ and one can also work with the cosmological constant density fraction Ω_Λ.
- The optical depth to reionization $\tau_{\rm reio}$.

An important caveat to emphasize is that $\omega_\gamma = \Omega_\gamma h^2$ is taken to be a fixed parameter because the CMB temperature today is accurately measured. However, in reality, CMB is (almost[5]) only sensitive to the *ratio* of densities ω_b/ω_γ, ω_m/ω_γ and Ω_m/Ω_Λ. Thus in practice the CMB temperature and polarisation unlensed spectra are determined by a number of effects which remains identical as long as one fixes quantities usually depending on distance and density ratios. The real degrees of freedom controlling the shape of the CMB temperature spectrum are often called (C1-C8). Those are

(C1) The sound horizon angular scale, given by the peak location, $\theta_s(z_{\rm dec}) = r_s(z_{\rm dec})/d_A(z_{\rm dec})$. The sound horizon depends on the pre-decoupling expansion history and sound speed, and it thus affect by changes in ω_b and ω_m. The angular diameter distance depends on the post-decoupling expansion era and is controlled by Ω_Λ or h.

(C2) The ratio odd/even peak depends on R because it enters the zero-point of oscillation and thus on ω_b/ω_γ.

(C3) The overall peak amplitude depends on the amount of expansion between equality and decoupling because of the damped oscillation during matter domination, and is thus controlled by ω_M/ω_γ. Smaller peaks means earlier equality and thus higher ω_m. In addition the EISW would be smaller because metric fluctuations have more time to stabilize.

(C4) The damping envelope at large ℓ is controlled by λ_d, which depends on the pre-decoupling expansion and recombination history. It is non-negligible only close to decoupling and thus depends mostly on ω_b (setting the number of free electrons) and ω_m (setting the expansion rate).

(C5) The global amplitude of the C_ℓ's is proportional to the amplitude of the primordial power spectrum A_s.

5 The absolute photon density controls the number of photons in the Wien tail of the distribution, thereby affecting the time of decoupling. Hence, an exquisite measurement of the peak location θ_s can potentially carry information about the photon temperature. However, this measurement is degraded by the Doppler contribution in the TT spectrum and the current sensitivity on the EE spectrum is too low to allow a determination of the photon temperature.

(C6) The global tilt of the C_ℓ's depends trivially on the tilt of the primordial power spectrum n_s.

(C7) The slope of the SW plateau is affected by the tilt of the primordial power spectrum n_s and the LISW, thus depends also on Ω_Λ/Ω_m. A larger Ω_Λ implies a longer Λ domination and thus an enhanced LISW effect.

(C8) Finally, the global amplitude of the spectrum at $\ell \geq 40$ is exponentially suppressed by the amount of photon rescattering after reionization, which is controlled by $\tau_{\rm reio}$.

The EE power spectrum is affected by similar (and even simpler!) effects as (C1-C7), but receives a much bigger correction around reionization known as the "reionization bump" (on top of the step-like suppression). It is typically out of phase with the TT spectrum because it contains mostly information on the quadrupole on the last scattering surface, which is correlated with the Doppler term.

2.2.3.5 *A quick word on vector and tensor perturbations*

We have not discussed vector and tensor perturbations. This is safe because different types of perturbations are decoupled at first order in perturbation theory. However they can potentially lead to additional temperature and polarization anisotropies. Vector modes can mostly produce B-modes polarization but we have already mentioned that they quickly decay in standard cosmology and are thus neglected. Tensor modes, which are related to gravitational waves, can be produced by several exotic mechanisms during the primordial universe. The most famous one being inflation. If tensor perturbations are sufficiently large at recombination or later, they can generate CMB temperature anisotropies, creating effects similar to the SW and ISW terms, and polarization anisotropies (both E and B-modes). At the current level of constraint on their amplitude, they are negligible for temperature anisotropies because they affect modes well below cosmic variance. However, tensor perturbations are still extensively studied nowadays because they can excite B-modes of polarization, which are absent in the presence of those perturbations, since scalar anisotropies cannot produce them (we have seen that they produce pure Q mode polarization) and vector modes decay[6]. The B-modes power spectrum is related to the primordial tensor power spectrum $\mathcal{P}_t(k)$ as follows

$$C_\ell^{BB} = \int \frac{dk}{k} \mathcal{P}_t(k) \Theta_{B\ell}^2(k)\,. \tag{2.2.68}$$

It has not yet been observed and despite current limits, it is still the best probe we have on inflation and many experiments are under construction to detect it.

2.2.3.6 *A quick word on secondary anisotropies and CMB lensing*

The distinction between *primary* and *secondary* anisotropies refers to phenomena *pre-* and *post-*decoupling respectively. However, this is purely artificial and any actual measurements is composed of both. We have already seen some sources of secondary anisotropies, those are the late ISW and stellar reionization. It would be meaningless to give here a list of all other secondary effects, which are however very important at the experimental level[7]. On the other hand, for our studies, the effect of *CMB*

6 Actually, they receive a contribution because E-modes can leak into B-modes due to lensing effects. This lensing contamination lead to a major foreground which limits the potential for detection of primordial gravitational waves.

7 More complete lists can for instance be found in Refs. [226], [323]

(weak) lensing caused by large-scale structure is of utmost importance and therefore deserves a short discussion. For an interested reader, a thorough review of CMB lensing can be found in Refs. [226], [401].

The basic idea is that the trajectories of CMB photons are slightly deflected by matter fluctuations localized at low redshifts, typically $z \leq 3$ in our ΛCDM universe. At leading order in perturbations, one can describe CMB lensing in terms of a two-dimensional deflection field $\hat{d}(\hat{n})$, representing the difference between the direction $\hat{n}$ in which photons have been emitted from the last scattering surface, and the direction $\hat{n} + \hat{d}(\hat{n})$ in which they are actually observed. It is therefore perpendicular to $\hat{n}$ and at lowest order induces a change $\delta T = \hat{d}(\hat{n}) \cdot \nabla_{\hat{n}} T(\hat{n})$, which is a second order quantity. Indeed, an important observation is that if the CMB were perfectly isotropic, the net effect of this deflection would vanish, since, by the conservation of photon number, as many photons would be deflected out of a small solid angle as into it. On the other hand, if there is no perturbation in the gravitational field, the latter is perfectly isotropic and the effect also vanishes. Hence, gravitational lensing of the CMB is a second-order effect and is not discussed within linear perturbation theory, to which we restricted our main calculation.

The deflection field is usually written in terms of a *lensing potential* φ to which it is simply related as the gradient (on the sphere perpendicular to $\hat{n}$) of the potential $\hat{d}(\hat{n}) \equiv \nabla_\perp \varphi$. One can relate φ to the Newtonian metric perturbations ψ and ϕ through a convolution along the line of sight [392]

$$\varphi(\hat{n}) = -\int_{\tau_{\rm LS}}^{\tau_0} d\tau \frac{\chi(\tau_{\rm LS}) - \chi(\tau)}{\chi(\tau)\chi(\tau_{\rm LS})} (\phi + \psi)|_{(\tau, \vec{x} = r(\tau)\hat{n})} \tag{2.2.69}$$

where $\chi(\tau)$ and $r(\tau)$ are defined in eqs. (1.1.41) and (1.1.44) respectively. During matter domination, one can relate ϕ and ψ (which are typically equal) to matter density fluctuations through the generalized Poisson equation. It is important to note that, because lensing is an effect happening at low redshift, it is completely uncorrelated with CMB anisotropies generated during the early Universe, i.e. on very small scales. On the other hand, the effect of lensing is usually negligible on large scales. We show the smoothing of small scale peaks and slight modification of the damping tail, typical impact of lensing on the CMB anisotropies and polarization power spectrum, in fig. 27. Moreover, lensing induces the leakage of E-modes into B-modes, an effect that has been discovered recently by the SPT collaboration [295], a major foreground for primordial gravitational wave searches.

Finally, it is also possible to construct the harmonic power spectrum $C_\ell^{\phi\phi}$ from the matter power spectrum $P(z, k)$ by convolving a given map $\varphi(\hat{n})$ in redshift space with an appropriate kernel. It can therefore be estimated from the 4-point correlation function of temperature maps [17]. The explicit computation of $C_\ell^{\phi\phi}$ is introduced in the context of forecast for neutrino masses detection in chapter 9, under the so-called "Limber approximation"[8], valid for small scales integrated over a (relatively) broad range of redshift.

2.2.4 *The matter power spectrum*

The power spectrum of the matter perturbation is also a very powerful probe of the models we study, either by itself because growth of structure is altered in those models, or because it helps to break degeneracies between cosmological parameters. In the following section, we describe in more details

8 It typically assumes that $P(k, z)$ is a slowly varying function of k and make use of orthogonal properties of spherical Bessel functions to simplify an integral over momentum.

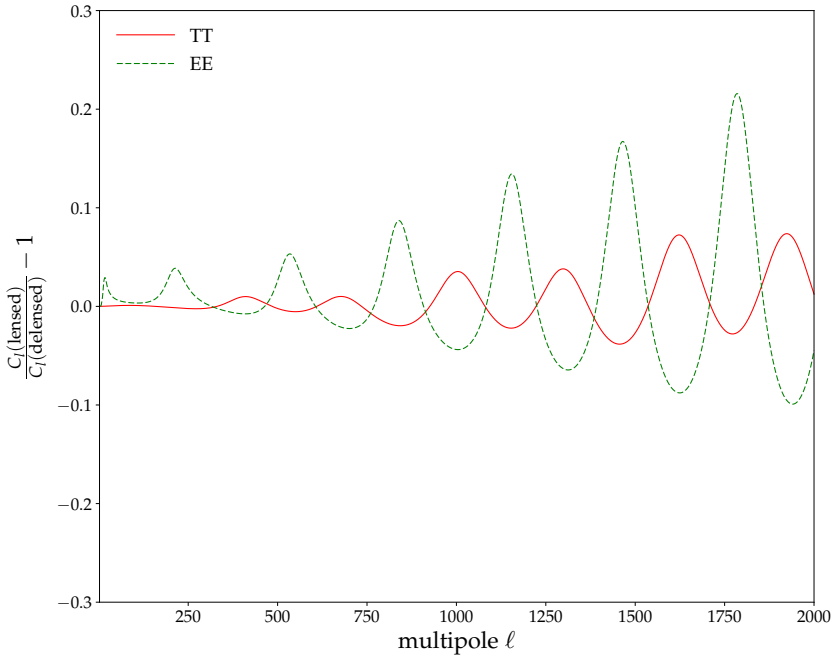

Figure 27: Comparaison of the lensed and delensed autocorrelation power spectrum (temperature and E-polarization) as predicted by the bestfit ΛCDM model of Planck high-l TT, EE, TE + SimLow [27].

its main properties to better understand the peculiar signatures of models under investigation. Our discussion is based on Refs. [391], [392], where the reader is referred for further details.

2.2.4.1 *Definition*

We have already introduced the total energy perturbation in the universe as

$$\delta\rho_{\rm tot} = \sum_i \delta\rho_i \,. \tag{2.2.70}$$

However, all the LSS observations probe the power spectrum when photons are subdominant and $\delta\rho_\gamma$ can be neglected, while $\delta\rho_\nu$ could matter for non-vanishing neutrino masses. Most of the Dark Energy (DE) models predict negligible amount of DE perturbations, for instance it vanishes in the cosmological constant scenario. Hence, in the context of LSS observations, one usually refers to the power spectrum $P(z,k)$ of the non-relativistic matter fluctuation δ_M defined as

$$\langle \delta_M(z,\vec{k})\delta_M^*(z,\vec{k}')\rangle = \delta(\vec{k}-\vec{k}')P(z,k)\,, \qquad \text{with} \quad \delta_M = \frac{\delta\rho_M}{\bar\rho_M} = \frac{\delta\rho_b + \delta\rho_{\rm cdm}}{\bar\rho_b + \bar\rho_{\rm cdm}}\,. \tag{2.2.71}$$

We have already seen that for Gaussian initial conditions, as long as perturbations are linear, the power spectrum at any given time can be written as

$$P(z,k) = \frac{2\pi^2}{k^3}\mathcal{P}_\mathcal{R}(k)\delta_M^2(z,k)\,, \tag{2.2.72}$$

where δ_M is the matter transfer function and $\mathcal{P}_\mathcal{R}(k)$ the primordial scalar power spectrum given by eq. (2.2.17).

2.2.4.2 *Transfer function evolution*

CDM evolution

We first start by neglecting baryons. In the newtonian gauge, we can combine the continuity and Euler equations (2.1.64) to get a master equation for $\delta_{\rm cdm}$

$$\delta''_{\rm cdm} + \mathcal{H}\delta_{\rm cdm} = -k^2\phi - 3\mathcal{H}\psi' - 3\psi'' \tag{2.2.73}$$

which resembles the one we had for photons density perturbations, without the pressure term, negligible for CDM. We know that on super-horizon scales, all perturbations are frozen and related by simple expressions (2.1.120) and (2.1.121). What we want is the sub-horizon evolution.
To go further, we need first to get some insight on the evolution of metric perturbations. Under the (wrong[9]) assumption that $\psi = \phi$, we have already obtained the master equation (2.1.118), and we plotted their (true) evolution thanks to numerical resolution in fig. (2.1.118) - right panel. During radiation domination, super-horizon scales are constant, while subhorizon ones oscillate with a quickly decaying amplitude. During matter domination, metric potentials are frozen on all scales. We can therefore safely neglect dilation effects. Quite surprisingly, it is possible to neglect radiation perturbations even if they are big, because below horizon they rapidly oscillate and therefore average to 0 over time (the so-called *fast modes* by Weinberg [589]). Using Poisson equation, we get the *Mészáros equation* (roughly) valid during all regime

$$\delta''_{\rm cdm} + \mathcal{H}\delta_{\rm cdm} - 4\pi G a^2 \bar{\rho}_{\rm cdm}\delta_{\rm cdm} = 0\,. \tag{2.2.74}$$

Analytical solutions to this equation can be obtained, but the numerical one is plotted in fig. (2.1.118) - left panel - for two modes. The important behaviour is that during radiation domination, $a \propto \tau$ and the growing mode scales like $\delta_{\rm cdm} \propto \log(k\tau)$, while during matter domination $a \propto \tau^2$ and $\delta_{\rm cdm} \propto \tau^2 \propto a$. Nowadays, during Λ domination, one should use the full Friedmann equation with both $\rho_{\rm cdm}$ and ρ_Λ, which would lead to a k-independent growth rate suppression. We can therefore readily understand the shape of the power spectrum plotted in fig. 28:

- The primordial power spectrum scales like $k^{-3}k^{n_s-1} = k^{n_s-4}$;
- All modes entering the horizon during the radiation domination era are enhanced by a factor $[\delta_{\rm cdm}(\tau_{\rm eq}, k)/\delta_{\rm cdm}(\tau_{\rm ini}, k)]^2 \simeq [\log(k\tau_{\rm eq})]^2$. The $k > k_{\rm eq}$ asymptote, with $k_{\rm eq} = a_{\rm eq}H_{\rm eq}$, is therefore $P(k) \propto k^{n_s-4}[\log(k)]^2$;
- Before Λ start to dominate at τ_Λ, modes inside the horizon grow like τ^2. Hence, the power spectrum for all modes that are inside the Hubble horizon at $\tau_{\rm eq}$ is enhanced by the same factor $(\tau_{\rm eq}/\tau_\Lambda)^4$. Since this is scale independent, the asymptotic shape for $k > k_{\rm eq}$ stays the same.
  Modes that enter the horizon during matter domination however receive more or less enhancement depending on their time of horizon crossing $\tau_* \sim 1/k$. Hence, the power spectrum receives a scale-dependent enhancement $(\tau_\Lambda/\tau_*)^4 \propto (k\tau_\Lambda)^4$ and the asymptotic behaviour of modes with $k < k_{\rm eq}$ is $P(k) \propto k^{n_s-4}k^4 = k^{n_s}$. Modes outside Horizon at τ_Λ are still shape like $P(k) \propto k^{n_s-4}$.

9 This is valid only if the anisotropic stress vanishes, which isn't the case in the radiation domination era due to free-streaming neutrinos. This is however a good approximation in the matter domination era.

- Finally the scale-independent reduced growth rate during Λ domination does not change the asymptotic shape of the power spectrum for modes already inside the horizon at τ_Λ. It only changes for the very small k's that enter horizon during Λ domination, which we do not detail here.

Baryonic corrections

Of course, the matter in the Universe is not only made of cdm. Hence, we must incorporate the effects of baryons on the power spectrum (at least) at the linear order. We know already that at early times, baryons are coupled to the photons and $\delta_b = \frac{3}{4}\delta_\gamma$. The question is, until when? The naive answer would be until photon decoupling. However, given the huge number of photons with respect to baryons, the laters keep track of the photon density until much later: the *baryon drag time*, where the drag depth $\tau_{\rm dr}$ defined as[10]

$$\tau_{\rm dr}(\tau) = \int_\tau^{\tau_0} d\tau' R^{-1} a n_e \sigma_T \,, \tag{2.2.75}$$

is roughly equal to 1. When baryons and photons are coupled this quantity tends to infinity, while it goes to 0 in the decoupled limit. Because $R \ll 1$, the release of baryons takes place *after* decoupling, typically at redshift of order $z_{\rm dr} \sim 200$. Before this redshift, CDM perturbations follow eq. (2.2.74) because δ_b are oscillating with the photons and are therefore negligible. After baryon drag, baryons collapse in the CDM potential gravitational wells and their perturbation start to grow, such that CDM will start to feel the gravity of baryons. On scales large enough to neglect the baryon pressure, one can write down coupled Mészáros equations

$$\delta_{\rm b}'' + \mathcal{H}\delta_{\rm b} = 4\pi G a^2(\bar\rho_b\delta_b + \bar\rho_{\rm cdm}\delta_{\rm cdm}) \tag{2.2.76}$$

$$\delta_{\rm cdm}'' + \mathcal{H}\delta_{\rm cdm} = 4\pi G a^2(\bar\rho_b\delta_b + \bar\rho_{\rm cdm}\delta_{\rm cdm})\,. \tag{2.2.77}$$

Introducing $D \equiv \delta_b - \delta_c$ and $\delta_M = \delta_b + \delta_{\rm cdm}$, we can decouple the equations, which take the following form during matter domination

$$D'' + \frac{2}{\tau}D' = 0 \tag{2.2.78}$$

$$\delta_M'' + \frac{2}{\tau}\delta_M' - \frac{6}{\tau^2}\delta_M = 0\,. \tag{2.2.79}$$

The growing solutions are thus $D = const$ and $\delta_M \propto \tau^2$, which means that

$$\frac{\delta_b}{\delta_c} = \frac{\bar\rho_M\delta_M + \bar\rho_{\rm cdm}D}{\bar\rho_M\delta_M - \bar\rho_b D} \to 1 \tag{2.2.80}$$

and δ_b approaches δ_c during matter domination. On scales smaller than the baryon Jeans length, baryon pressure prevents such collapse and baryonic perturbations are highly suppressed.

The important point is that baryons will have two effects on the total matter power spectrum: i) they slightly reduce the amplitude with respect to a pure cdm universe; ii) the oscillating behaviour of δ_b leaves a small imprint in the late time δ_M as an oscillation with scales called *baryonic acoustic oscillations* (BAO). Those are nothing but the counterpart of the photon oscillations observed in the CMB power spectra, and as such represent an important consistency check of the cosmological model. The BAO has been detected recently in LSS observations [229] and can be seen in fig. 28.

10 The name comes from the tendency for baryons to drag photons towards gravitational potential wells. However it is misleading as it corresponds to the end of baryon drag.

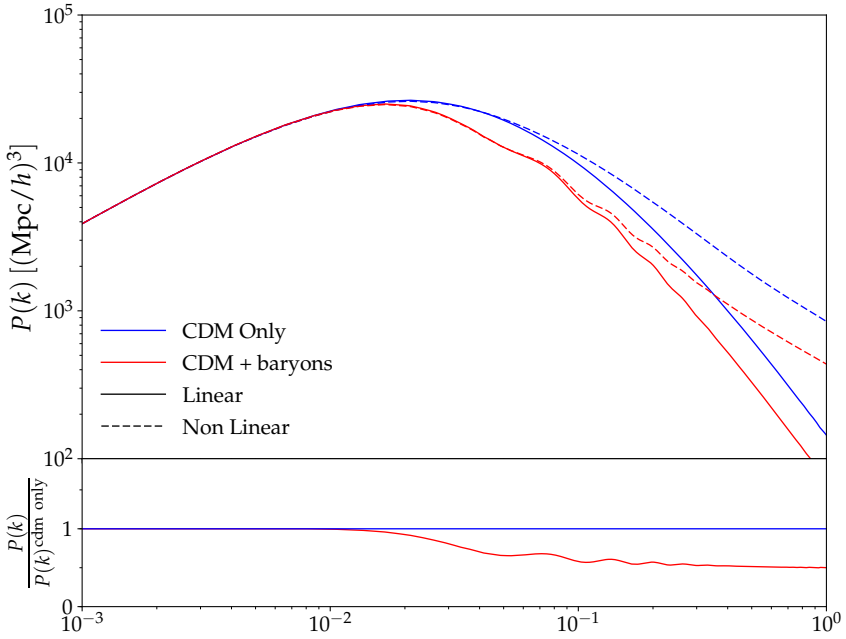

Figure 28: The matter power spectrum in a hypothetical CDM Universe compared to the one deduced from the best fit of *Planck* data [19]. The Non-Linear contribution is computed with HaloFit [558], [577].

2.2.4.3 *Parameter dependence*

Similarly to the CMB power spectrum, the Matter power spectrum can be accurately described within the ΛCDM models. In fact, it even depends on fewer parameters: the optical depth to reionization τ_{reio} does not play any role here. The parameters that matter are therefore

$$\{A_s, n_s, \omega_b, \omega_M, \Omega_\Lambda\}\,. \tag{2.2.81}$$

The important effects that determine the shape of the Matter power spectrum are often called (P1-P5).Those are

(P1) The time of matter-radiation equality, which determines the scale k_{eq} of the power spectrum peak. In the usual convention, the scale is expressed in units of $h\text{Mpc}^{-1}$, such that it depends on both z_{eq} and Ω_M, or in our parameter basis on ω_M and Ω_Λ.

(P2) The baryon-to-CDM fraction (ω_b/ω_c) alters the large-scale asymptote. When this fraction increases, the spectrum is suppressed for $k \geq k_{\text{eq}}$ and BAOs are more pronounced.

(P3) The phase of the BAO's depends on the sound horizon at baryon drag $r_s(\tau_{\text{dr}})$, while the exponential diffusion damping depends on the damping scale $r_d(\tau_{\text{dr}})$. Both parameters depend strongly on ω_b.

(P4) The overall amplitude depends on the primordial amplitude and on the scale independent suppression of the growth-rate during Λ domination. Hence it depends on A_s and Ω_Λ.

(P5) The overall tilt of the power spectrum depends trivially on the primordial tilt n_s.

In the future, experiments such as Euclid [386] and LSST [9] will perform accurate measurements of the power spectrum *at different redshifts*. This is crucial as one can deduce the low-redshift expansion history and thus tests model of dark energy versus a cosmological constant.

2.2.4.4 *A quick word on non linearities*

The linear theory used until now cannot describe small scale matter fluctuations at small redshift. Indeed, when perturbations δ_M on a given scale k become of the same order as $\bar{\rho}_M$, our formalism is not adapted as this scale becomes non-linear. Structure formation in the ΛCDM is said to be "bottom-top", i.e. that smaller scales enters earlier into the non-linear regime.

The midly non-linear power spectrum can be computed analytically (e.g. [100], [108]), but non-linear structure formation requires numerical simulation. It can be simulated with N-body codes based on newtonian gravity, such as gadget-2 [566], and including many subtle baryonic effects, or pure cdm simulation based on GR such as the recent gevolution [16].

In the Boltzmann code CLASS, we make use of an accurate fitting formula based on the result of the gadget-2 code called *halofit* [558], [577] and improved to incorporate the effect of neutrino masses [105]. It is based on the assumption that all the matter content in the Universe is bound in dark matter halos. Then, the power spectrum is decomposed into two terms, the so-called one- and two-halo terms:

$$\mathcal{P}(k) = \mathcal{P}_Q(k) + \mathcal{P}_H(k) \tag{2.2.82}$$

The one-halo term $\mathcal{P}_Q(k)$ describes matter correlations within the same dark matter halo, and is determined by the density profile of each halo. It typically dominates at small scales. On the other hand, the two-halo term $\mathcal{P}_H(k)$ arises from the correlation between two distinct halos and dominates at large scales. Their functional form can be found in the appendix of ref. [577]. We plot in fig. 28 the impact of non-linear structure formation on the matter power spectrum.

3

MASSIVE RELICS IN THE UNIVERSE

3.1 The Standard Model of Particle Physics in a nutshell

3.1.1 *The Standard Model and its main successes*

The Standard Model of Particle Physics (SMPP) is the model that describes the interactions among fundamental constituents of matter. It is a quantum field theory (QFT) obeying an action principle, i.e. its basic objects are quantum—operator valued—fields defined at spacetime points, with very specific symmetry properties: translational plus Lorentz-invariance (hence it is said to be a *relativistic* QFT), plus some local symmetries describing the dynamics. The latter are gauge symmetries, characterized by the non-abelian symmetry group $\mathsf{G}_{\rm SM} = \mathsf{SU}(3)_{\mathsf{c}} \otimes \mathsf{SU}(2)_{\mathsf{L}} \otimes \mathsf{U}(1)_{\mathsf{Y}}$. Matter is described by *fermionic* fields, transforming differently under (i.e. belonging to different representations of) $\mathsf{G}_{\rm SM}$: the six quark species (or *flavors*) are the only fermions interacting via strong interactions with the so-called QCD coupling constant, i.e. they transform non-trivially under $\mathsf{SU}(3)_{\mathsf{c}}$. The group $\mathsf{SU}(2)_{\mathsf{L}} \otimes \mathsf{U}(1)_{\mathsf{Y}}$ describes in a unified way electromagnetism and weak interactions via two additional coupling constants. The empirical observation that parity is violated in weak interactions has led to the insight that all known fermions are *chiral fields*, with the left-handed partners, arranged in doublets, also charged under $\mathsf{SU}(2)_{\mathsf{L}}$, while the right-handed partners are only charged under $\mathsf{U}(1)_{\mathsf{Y}}$. The symmetry $\mathsf{SU}(2)_{\mathsf{L}} \otimes \mathsf{U}(1)_{\mathsf{Y}}$ is *spontaneously* broken at low-energy, i.e. the vacuum does not obey the same symmetry properties of the full Lagrangian. Only the $\mathsf{U}(1)_{\rm e.m.}$ gauge symmetry describing electromagnetism survives at more familiar low energies. If classified in terms of electric charge, leptons, i.e. the other fermions not charged under $\mathsf{SU}(3)_{\mathsf{c}}$, can either be electrically charged (electron, muon and tau particle), or neutral (three types of neutrinos). Neutrinos thus only interact via weak interactions, arranged in a doublet with their charged lepton partner. As a result of general properties, each particle of the SMPP has an antiparticle of the same mass and opposite quantum numbers. Also note that the SMPP matter content appears arranged in three families (or *generations*), each containing a quark doublet, a lepton doublet, two quark singlets and one lepton singlet. Only particle masses distinguish a generation from another. The SMPP is a *local* theory (there is no instantaneous interaction at distance!) whose interactions are mediated by *bosonic*, vector fields, associated to the generators of the gauge group. Mathematically, the action of the SMPP is built via a Lagrangian density, under the further requirement that the theory is *renormalizable*, i.e. predictive up to *arbitrarily* high energies once a *finite* number of parameters are experimentally fixed. This condition essentially specifies most of the terms of the Lagrangian $\mathcal{L}_{\rm SM}$, given the particle and gauge content. However, the above-mentioned fact that the $\mathsf{SU}(2)_{\mathsf{L}} \otimes \mathsf{U}(1)_{\mathsf{Y}}$ symmetry is broken to $\mathsf{U}(1)_{\rm e.m.}$ (which is associated to the fact that the weak force carriers, $W^{\pm}$ and Z, are very massive, contrarily to the massless photon associated to $\mathsf{U}(1)_{\rm e.m.}$),

Fermions			$SU(3)_c$	$U(1)_Q$ (e)	T_3	Mass (MeV)		
Leptons								
$\begin{pmatrix} e^- \\ \nu_e \end{pmatrix}_L$	$\begin{pmatrix} \mu^- \\ \nu_\mu \end{pmatrix}_L$	$\begin{pmatrix} \tau^- \\ \nu_\tau \end{pmatrix}_L$	1	-1	$-1/2$	0.511	105	1777
				0	$1/2$	0(?)	0(?)	0(?)
e_R^-	μ_R^-	τ_R^-	1	-1	0	id. L-particles		
Quarks								
$\begin{pmatrix} u \\ d \end{pmatrix}_L$	$\begin{pmatrix} c \\ s \end{pmatrix}_L$	$\begin{pmatrix} t \\ b \end{pmatrix}_L$	3	$2/3$	$1/2$	3	1200	1.74×10^5
				$-1/3$	$-1/2$	7	120	4300
u_R	c_R	t_R	$\bar{3}$	$2/3$	0	id. L-particles		
d_R	s_R	t_R	$\bar{3}$	$-1/3$	0	id. L-particles		
I	II	III	Generation					

Table 1: The Standard Model fermion families after EW symmetry breaking and corresponding properties of the particles. Masses are given at a precision level enough for our studies but are known with much better accuracy. "id. L-particles" means âĂIJidentical to left-handed particlesâĂİ.

together with the fact that all fermions are *massive* (but for neutrinos, which have no right-handed field and no mass in the SMPP) requires additional ingredients for the mathematical consistency of the model. The SMPP is then fully specified by the requirement that this additional sector only contains a single $SU_L(2)$ *scalar* (or Higgs) doublet H, responsible at the same time for both mass-generating mechanisms. In particular, when spontaneous symmetry breaking occurs—associated to the fact that H acquires a non-zero vacuum expectation value—three out of the four degrees of freedom (dof) of the complex Higgs doublet are absorbed to create massive $W^\pm$, Z bosons, the last remaining dof being the Higgs boson. This is the so-called Brout-Englert-Higgs-Guralnik-Hagen-Kibble mechanism. A short summary of the standard model particles after EW symmetry breaking is given in tables 1 and 2.

The SMPP is beyond any doubt a huge experimental success. Nowadays, *all* its particles [1] have been observed at accelerators, including the Higgs boson, for a long time the missing piece of the puzzle. The Higgs was discovered in 2012 by the CMS and Atlas experiments [1], [154] and associated to the 2013 Nobel Prize awarded to Englert and Higgs. From a theoretical point of view, it is extremely satisfactory because it is renormalisable and automatically conserves baryon and lepton quantum numbers without invoking any discrete symmetry. However, the Standard Model fails to explain some observables, and gives rise to deep theoretical questions regarding some of its properties.

3.1.2 *Main issues with the Standard Model*

We give here a non-exhaustive list of the main issues of the SMPP, divided into empirical, observational and theoretical/aesthetic problems.

1 Technically, if you consider a particle distinct by its antiparticle, the $\bar{\nu}_\tau$ has not been observed, yet. It is one goal of the proposed SHiP experiment [34].

Bosons	$U(1)_Q$ (e)	$SU(3)_c$	Spin	Mass (GeV)	Role
γ	0	1	1	0	Electromagnetic Interaction
$W^{\pm}$	± 1	1	1	80	Weak Interaction
Z^0	0	1	1	91	
$g_1, \cdots, g_8$	0	8	1	0	Strong Interaction
H	0	1	0	125	Higgs Mechanism

Table 2: The Standard Model Bosons after EW symmetry breaking and corresponding properties of the particles. Masses are given at a precision level enough for our studies but are known with much better accuracy.

3.1.2.1 *Empirical Problems*

- *Neutrinos:* In the SMPP, neutrinos are massless and left-handed only. However, the observations of neutrino flavour oscillation *requires* neutrinos to be massive. This will be discussed in sec. 3.2.1. The existence of at least two sterile right-handed neutrinos could lead to a simple explanation of the neutrino masses. One sterile neutrino may also provide a viable DM candidate.

- *Muon anomalous magnetic moment:* There are a number of tensions between predicted and observed quantities in the SMPP. None of them has attained a high significance till now, and most past anomalies have disappeared with better data. However, it is not excluded that one or more of these will turn into a discovery, at some point. Currently, perhaps the most intriguing and long-standing tension is related to one of the greatest success of the SMPP: the agreement between theoretical predictions and experimental values for the magnetic moment of the electron g_e. At tree level $g_e = 2$, but 5 loop computations lead to $(g_e - 2)/2 = 0.001159652181643(764)$ [469] while the experimental determination is $(g_e - 2)/2 = 0.00115965218073(28)$ [291] in extremely good agreement. However, when one performs the same computation for the muon, the value is $(g_\mu - 2)/2 = 0.00116591803(69)$ [469] while the experimental determination is $(g_\mu - 2)/2 = 0.00116592091(9)$ [432] which represents a difference of order $4\,\sigma$. The theoretical prediction could be affected by new physics entering the loop corrections, but QCD corrections might be responsible for the discrepancy. This ambiguity between possible new physics interpretations and systematic effects in SMPP computations is quite typical of several anomalies currently under scrutiny.

3.1.2.2 *Observational (astrophysical and cosmological) Problems*

- *Dark Matter:* We have already discussed observations requiring the existence of a massive stable neutral particle. No particles within the SM fulfill this property, except neutrinos if they are massive. However, they do not have neither the good relic density, nor the good level of "coldness", i.e. before becoming non-relativistic they free-stream and suppress structure formation on scales below their free-streaming length. We will comment more extensively on this in chapter 9.

- *Matter-Antimatter asymmetry:* The non-zero value of the photon-to-baryon ratio η implies a tiny, but non-zero, asymmetry in the matter and antimatter production mechanism. The *Sakharov*

conditions [523] for such asymmetry to be produced are: i) Baryon number violation processes in order to produce an excess of barons over anti-baryons; ii) C- and CP-symmetry violation to avoid counterbalancing the previous asymmetry; iii) Interactions out of thermal equilibrium such that a relic abundance can be produced. The SMPP predicts some level of CP-asymmetry through weak interactions, but in too little amount to explain η. Also the expected departures from equilibrium and non-perturbative B violation present in the SMPP are quantitatively insufficient. Hence, this hints towards new sources of CP-symmetry breaking and/or new stronger departures from equilibrium (e.g. in decays, or during phase transitions), and/or possible new sources of B-violation at high energies. Here also, the existence of sterile neutrinos with specific interactions is often invoked to solve the problem. We shall comment on that later on.

- *Inflation*: If the paradigm is correct, new physics is required. Indeed, even if the Higgs, the only fundamental scalar field of the standard model, is the inflaton, a successful inflation demands non minimal coupling to Gravity [103]. Furthermore, the required value of the non-minimal coupling leads to a violation of Unitarity in the theory and therefore points to new physics below the Planck scale [134]. This model is known to be equivalent to the Starobinsky's inflation model [567], which as well requires extension of GR. Most of the models in the literature therefore make use of (at least) one new scalar field which has yet to be discovered.

3.1.2.3 *Theoretical/aesthetic problems*

- *Hierarchy Problem :* The large difference between the EW scale ($\mathcal{O}(100$ GeV)) and the Planck scale ($\mathcal{O}(10^{18}$ GeV)) is not very satisfactory. Even assuming that new degrees of freedom only appear at the Planck scale, in relation to quantum gravity, nothing prevents the Higgs mass to receive corrections from loops involving these new dof's, and acquire a mass of order of the Planck scale. Hence, the cancellation of the loop induced corrections to the propagator and the "bare" mass have to be exact at the incredible 10^{-32} precision level in order to get the right Higgs mass. Although this poses no phenomenological problem, this "coincidence" makes most theoretical physicists uncomfortable. However, if new physics exists at a scale Λ not too far above the electroweak one, it might prevent the running of the mass up to very high scale because of some symmetries. In SuperSymmetry (SUSY), this is naturally achieved thanks to the co-existence of fermionic and scalar loop corrections which exactly cancel each other, bringing the Higgs mass not far below the level Λ at which SUSY is broken, and which should also set the scale of some SUSY partner particles of the SMPP ones. This observation has motivated intense experimental efforts in searching for TeV-scale SUSY through the construction of the Large Electron-Positron Collider (LEP) first, the Tevatron next, and currently the Large Hadron Collider (LHC), hosted in the same tunnel of the former LEP. Unfortunately no SUSY particles have yet been observed and strong constraints nowadays apply to TeV-scale SUSY. We will return to SUSY later on as it naturally accommodates DM candidates. Another solution to this issue is achieved in the context of theory of extra-dimensions. Those extra dimensions allows to correct the apparent 4D value of the Planck mass and bring it back to the TeV scale. Those theories also naturally incorporate DM candidates and, as for the SUSY case, all searches for the new predicted states have come out empty handed till now.

- *Strong CP problem:* A CP-violating term is not prohibited in the Lagrangian of the strong sector. However, experimental measurements of the neutron electric dipole moment constrain

its amplitude to be smaller than 10^{-9}. Again, since this coefficient gets contributed to by a topological QCD term as well as by the argument of the determinant of the quark mass matrix, two apparently unrelated sectors of the SMPP, such a degree of cancellation is astonishing. A famous solution by Peccei and Quinn [470] to the problem is to invoke a new global U(1) symmetry, whose spontaneous breaking is associated to a pseudo-scalar (Nambu-Goldston) field called *the axion*. Non-perturbative effects at the QCD phase transition then ensure that the axion field dynamically relaxes to a vacuum expectation value that cancels the CP-violating term. Interestingly, the axion is another potential DM candidate. Also, some inflationary potentials have been inspired by the axion model.

- *Unification of Gauge Coupling:* Unification of forces is an old dream of theoretical physicists. Following the path of Maxwell unifying electric and magnetic forces and later on Glashow, Weinberg and Salam unifying electromagnetism and weak forces, people have tried to go further, aiming at the description of all interactions (or, at least, of all but gravity) within a single one. In the SMPP, the running of the three coupling constants under the action of the renormalisation group points towards a unification at very high energy scale, $\sim \mathcal{O}(10^{15}$ GeV). However, although they almost converge to a common value, there is still some difference. New physics could help in "focusing" the evolution of the gauge coupling towards the same point. This is for instance the case within SUSY, provided it is restored at sufficiently low scales. Evidently, this cannot be considered a problem, at best an "aesthetic" argument which is suggestive of new physics. These Grand Unified Theories (GUT) are extremely difficult to test at accessible energies, with the best hope clinging to the relatively generic prediction of proton decay. Unfortunately, no evidence in favor of this has been obtained, with current limits excluding the simplest and most predictive scenarios.

- *Parameters problem:* On a similar footing as the above-mentioned one, the SMPP contains about twenty free parameters. Unfortunately, nothing explain their values, nor their hierarchy. Hence, the huge difference ($\sim 10^4$) between the top mass and the electron mass is extremely unsatisfactory. (Actually, the mass difference becomes even 10^{13} if we wish explain tiny masses of neutrinos through the Higgs mechanism). Moreover, there is no explanations to the fact that the standard model particle content is made of three generations, which also gives rise to questions about the fundamental nature of the model. Note that most of the new physics models introduce above tend to even *increase* the number of free parameters.

3.2 Neutrino masses in Cosmology

In this section, we review the (recent) historical discovery of the neutrino oscillations, pointing to (at least) two non-zero neutrino masses, as well as the most common neutrino mass mechanisms. This section is based on the textbook [392] and review [22].

3.2.1 *Neutrino oscillations: evidence for neutrino masses*

Neutrinos are neutral spin 1/2 fermions whose existence has been postulated in 1930 by W. Pauli to explain the continuous spectrum observed in the beta decay of nuclei. They come in three flavours to accompany leptons within $\mathrm{SU}(2)_L$ doublet and are only charged under the weak interaction. Because

of that, they can travel a very long distance through matter without interacting and are therefore very hard to detect. Electron neutrinos were discovered by Reines and Cowan in 1956, muon neutrinos in 1962 at Brookhaven and tau neutrinos in 2000 at Fermilab, by the DONUT experiment. Until recently, no finite mass effect had been observed in processes involving neutrinos. Since in the SMPP mass arises from the Higgs mechanism, which couples left- and right-handed particles, neutrinos were thought to have no right-handed partner.
The situation has started to change with the observation of the solar neutrino flux. The Sun is a powerful source of MeV electron neutrinos, produced in the thermonuclear fusion reactions occurring in the core. As soon as technology able to detect the solar neutrino flux was developed in the 1970's, measurements showed a large discrepancy with the predicted flux, and in particular a deficit in ν_e. This was known as Solar Neutrino Problem. This issue was settled more recently thanks to the SuperKamiokande experiment, measuring the elastic scattering reaction $\nu_\alpha + e^- \to \nu_\alpha + e^-$ (which is enhanced for ν_e) and in particular the Sudbury Neutrino Observatory (SNO) measuring at the same time charged and neutral current, as well as the elastic scattering reaction. Those combined observations allow to compare the total flux, regardless of the flavor, to the electron neutrino flux: the first one was in agreement with models, while the second still show the same deficit, pointing at *neutrino flavour conversions* during their propagation. By far, the most plausible explanation invoked neutrino *oscillations*, and has hence been confirmed in numerous other experiments.

Neutrino oscillations have been postulated in the late 1950's by Pontecorvo [487], [488]. They are a quantum mechanical phenomenon due to neutrinos being produced via charged current interaction as flavour states, which are *not* mass eigenstates, and can be expressed as a linear combination of them. Introducing the Pontecorve-Maki-Nakagawa-Sakata (PMNS) matrix U, a 3×3 unitary mixing matrix, a particular *ket* state can be written as (generalizing to potential sterile degrees of freedom is trivial $3 \to 3 + N_s$)

$$|\nu_\alpha\rangle = \sum_{k=1}^{3} U^*_{\alpha k}|\nu_k\rangle \quad \text{with} \quad \alpha = e, \mu, \tau. \tag{3.2.1}$$

where greek indices label flavour states, latin indices mass states and we assume the normalisation $\langle\nu_\alpha|\nu_\beta\rangle = \delta_{\alpha\beta}$ and $\langle\nu_i|\nu_j\rangle = \delta_{ij}$. A useful quantity experimentally is the so-called *survival probability* $P_{\nu_\alpha\to\nu_\alpha}$, considering here oscillations in vacuum and expressed as a function of the distance of the detection point from the neutrino source [392]:

$$P_{\nu_\alpha\to\nu_\alpha}(L) = 1 - 4\sum_{k>j} |U^2_{\alpha k}||U^2_{\alpha j}| \sin^2\left(\frac{\Delta m^2_{kj}}{2|\vec{p}|}\frac{L}{c}\right). \tag{3.2.2}$$

while the *total transition probability* $1 - P_{\nu_\alpha\to\nu_\alpha}$ follows from unitarity. From the sinusoidal terms, we clearly see that experiment located at different L will be sensitive to a value of Δm^2 such that $\Delta m^2 L/(2E) \sim 1$. There are two typical regimes of oscillations: a slow one, governed by $\nu_1 \leftrightarrow \nu_2$ and a fast one corresponding to other oscillations. Solar oscillations are governed by the slow component $\nu_1 \leftrightarrow \nu_2$, and one can explain observations in a two neutrinos model ν_e, ν_x, with ν_x an undetermined mixture of ν_μ and ν_τ.
In fact, the Sun is not the only source of neutrinos available. Nuclear reactors typically produce electron neutrinos with energy in the MeV range, and are classifed between short ($\sim$ 10m) (SBL), long ($\sim$ 1km) (LBL) and very long ($\sim 10^2$ km) (VLBL) baseline experiments, sensitive to $\Delta m^2 \geq 0.1, 10^{-3}$ and 10^{-5} eV^2 respectively. A similar classification can be made for neutrino beams produced by accelerators in

the energy range 1-100 GeV due to the pion, kaon and muon decays and hence composed of both muon and electron neutrinos and antineutrinos. However, SBL are now characterized by $L \sim 1$ km, LBL by $L \sim 10^3$ km, while VLBL are still under study. Finally *atmospheric neutrinos* are produced when cosmic-rays, consisting mainly of protons or heavier nuclei, interact with atoms in our atmosphere. Those interactions create a lot of pions which decay into muons and neutrinos. The produced muons can subsequently decay into electrons and create additional neutrinos. For energy below GeV, the ratio of fluxes of muon neutrinos or antineutrinos over electron neutrinos should be almost equal to two.

The PMNS matrix is often parametrized in the following way to reflect the sensitivity of experiments to some of its terms:

$$U = \underbrace{\begin{pmatrix} 1 & 0 & 0 \\ 0 & c_{23} & s_{23} \\ 0 & -s_{23} & c_{23} \end{pmatrix}}_{\text{Atm. or LBL}} \underbrace{\begin{pmatrix} c_{13} & 0 & s_{13}e^{-i\delta} \\ 0 & 1 & 0 \\ -s_{13}e^{i\delta} & 0 & c_{13} \end{pmatrix}}_{\text{SBL Reactor}} \underbrace{\begin{pmatrix} c_{12} & s_{12} & 0 \\ -s_{12} & c_{12} & 0 \\ 0 & 0 & 1 \end{pmatrix}}_{\text{Solar and LBL Reactor}} \underbrace{\begin{pmatrix} e^{i\alpha_1} & 0 & 0 \\ 0 & e^{i\alpha_2} & 0 \\ 0 & 0 & 1 \end{pmatrix}}_{0\nu2\beta \text{ decay}} . \tag{3.2.3}$$

The parameters entering this matrix are $c_{ij} = \cos(\theta_{ij})$ and $s_{ij} = \sin(\theta_{ij})$ with θ_{ij} the mixing angle of mass states i and j, the Majorana $\alpha_{1,2}$ (probed by $0\nu2\beta$ decay experiments) and Dirac δ CP violating phases. The mass differences are taken to be

$$\delta m^2 = m_2^2 - m_1^2 > 0 \quad \text{and} \quad \Delta m^2 = m_3^2 - \frac{m_2^2 + m_1^2}{2} . \tag{3.2.4}$$

Solar and LBL reactor neutrino experiments (e.g. SNO, KamLAND) have measured the mass-mixing parameters $(\delta m^2, \theta_{12})$ in the $\nu_e \to \nu_e$ channel, while atmospheric and LBL experiments (e.g. SuperKamionkande, K2K and MINOS) have measured $(\Delta m^2, \theta_{23})$ in the $\nu_\mu \to \nu_\mu$ channel. Finally, SBL reactor experiments (e.g. Daya Bay, RENO and Double Chooz), which are mainly sensitive to $(\Delta m^2, \theta_{13})$, have provided information on the allowed range for the mixing angle θ_{13}. In matter, the presence of a high density of electrons can increase the effective mixing angle (see e.g. Ref. [392] for an introduction), an effect known at the Mikheyev-Smirnov-Wolfenstein (MSW) effect [427], [595][2]. Thanks to the correction to the above vacuum mixing picture due to the refraction in solar matter, solar neutrino studies have been able to deduce the sign of δm^2. On the other hand, the sign of Δm^2 is still unknown, which led to the introduction of a *normal hierarchy* (NH), if $m_1 < m_2 < m_3$ and *inverted hierarchy* (IH) if $m_3 < m_1 < m_2$. Recent determinations of these parameters are summarized in tab. 3.

The absolute scale of the neutrino mass is unknown as well. Cosmology is currently the best probe of it, through the effect of the sum of the neutrino masses $M_\nu = \sum_i m_i$. One can relate M_ν to the measured mass difference via

$$M_\nu = m_1 + \sqrt{m_1^2 + \delta m^2} + \sqrt{m_1^2 + \frac{\delta m^2}{2} + \Delta m^2}. \tag{3.2.5}$$

This number actually depends on the mass ordering. If NH is realised in nature, setting m_1 to 0 gives the minimal value it can take, $M_\nu|_{\min} \sim 60$ meV. On the other, if IH is realised, one can set m_3 to 0 to get $M_\nu|_{\min} \sim 110$ meV. Cosmological bounds are somewhat dependent on the choice of cosmological

2 In general, this effect is very important for the study of neutrino physics in the early Universe, when the electron density was very high. See e.g. Ref. [339] for more details in the context of BBN.

models and datasets. However, the most optimistic current bounds are very close to the minimum value of the IH [27], [199], [466].
Laboratory measurements of the absolute neutrino mass scale are also possible. Experiments typically look at the electron energy spectrum from tritium beta decay

$$^3\mathrm{H} \rightarrow {}^3\mathrm{He} + e^- + \bar{\nu}_e \,, \tag{3.2.6}$$

which has $Q_\beta = 18.591$ keV. By looking at the end point of the spectrum, one can hope to detect a small shift $Q_\beta - m_\beta$ where

$$m_\beta^2 = \sum_{k=1}^{3} |U_{ek}|^2 m_k^2 \,. \tag{3.2.7}$$

The present experimental bound is $m_\beta \leq 2.2$ eV at 95%C.L [115]. The future KArlsruhe TRItium Neutrino (KATRIN) β-experiment will be able to reduce such a limit by one order of magnitude [457]. Those experiments are not sensitive to the Majorana or Dirac nature of neutrinos—i.e. if neutrinos are their own antiparticles or not, see below—as information on the phases is lost when taking the square of the mixing matrix. To do so, $0\nu2\beta$ (neutrinoless double beta decay) experiments are studying processes of the type $(A, Z) \rightarrow (A, Z+2) + e^- + e^-$, only possible if neutrinos are Majorana particles since the process violate lepton number by 2 units. If the effect of finite neutrino mass dominates these nuclear transitions, those experiments are also sensitive to the absolute mass scale through the effective Majorana mass m_{ee}

$$m_{ee} = \left| \sum_i m_i U_{ei}^2 \right| \,. \tag{3.2.8}$$

Current bounds from GERDA, KamLAND and EXO-200 are at the level $m_{ee} \leq 0.2-0.4$ eV at 90%C.L. New experiments could reach the $m_e \sim 0.01$ eV level, but those bounds assume that neutrinos are Majorana particles and are therefore to be taken with caution.
Besides the mass scale, mass hierarchy and Majorana/Dirac nature of neutrinos, open questions in the neutrino sector include : i) the unitarity of the matrix U, as it could indicate that new (sterile[3]) neutrino(s) exist(s), or that new physics is at play; ii) possible CP violation in the leptonic sector: In particular, depending on the parameter δ and $\alpha_{1,2}$, neutrinos and antineutrinos may oscillate differently.
Neutrinos are definitely one of the hottest subjects nowadays, stimulating intense theoretical and experimental efforts. In the cosmological context, future LSS survey such as Euclid and LSST will aim at a cosmological neutrino mass detection. Chapter 9 is devoted to a forecast of the potential for detection in future cosmological data. The impact of neutrino mass on the CMB and matter power spectrum is reviewed in sec. 9.2, with a special emphasis on the phenomenology of very small neutrino masses, close to their minimal values allowed by oscillation data.

3 LEP data and Cosmology restrict the number of active neutrinos to three.

Parameters	best-fit ($\pm1\sigma$)	3σ range
$\delta m^2/10^{-5}$ eV^2	$7.54^{+0.26}_{-0.22}$	6.99-8.18
$\sin^2\theta_{21}$	0.308±0.017	0.259-0.369
$\Delta m^2/10^{-3}$ eV^2 (NH)	2.43±0.06	2.23-2.61
$\Delta m^2/10^{-3}$ eV^2 (IH)	2.38±0.06	2.19-2.56
$\sin^2\theta_{13}$ (NH)	$0.0234^{+0.0020}_{-0.0019}$	0.0176-0.0295
$\sin^2\theta_{13}$ (IH)	$0.0240^{+0.0019}_{-0.0022}$	0.0178-0.0298
$\sin^2\theta_{23}$ (NH)	$0.437^{+0.033}_{-0.023}$	0.374-0.628
$\sin^2\theta_{23}$ (IH)	$0.455^{+0.039}_{-0.031}$	0.380-0.641
δ/π (NH)	$1.39^{+0.38}_{-0.27}$	-
δ/π (IH)	$1.31^{+0.29}_{-0.33}$	-

Table 3: The best-fit values and 3σ allowed ranges of the 3-neutrino oscillation parameters, derived from a global fit analysis of oscillation data by Ref. [247]. At 3σ, no physical values of δ are disfavored. Table adapted from Ref. [469].

3.2.2 *Sterile neutrinos and neutrino mass mechanisms*

We have discussed observations that requires neutrinos to be massive, however we are still lacking a theoretical mechanism for such masses. First of all, it is possible to write down a *Dirac mass term* by simply introducing N_s sterile (i.e. a SM gauge singlet) right-handed neutrinos ν_{sR}, such that

$$\mathcal{L}_D = -(\bar{\nu}_{sR} M^D_{s\alpha} \nu_{\alpha L}) + \text{h.c.}\,, \tag{3.2.9}$$

where $\bar{\nu}_{sR} \equiv (\nu)^\dagger_{sR}\gamma^0$ is the Dirac adjoint and $M^D_{s\alpha}$ is a $N_s \times 3$ complex matrix. M^D cannot be a matrix of bare mass since this term violates weak isospin by $1/2$ unit . However, it can be generated for instance through the Higgs mechanism, in which case the diagonalised mass term is $m_\alpha = y_\alpha v$ with $v = 174$ GeV the Higgs vacuum expectation value and y_α the Yukawa couplings. It could be the only mass term provided that ν_{sR} has puzzling extremely weak Higgs-Yukawa coupling $y_\alpha \sim 3 \times 10^{-13} m_\alpha/(0.05\text{ eV})$. However, the introduction of RH sterile neutrinos has more interesting consequences in Cosmology, including in the context of our DM searches. Indeed, no gauge symmetries prevent the lepton number L from being explicitly violated. Since neutrinos are uncharged under unbroken gauge symmetries, one can write a Majorana mass term which connects a Weyl spinor with its own CP conjugate $(\nu)^c \equiv C\bar{\nu}^T$ where $C = i\gamma^2\gamma^0$ is the charge conjugation in the Weyl representation

$$\mathcal{L}_M = \frac{1}{2}\bar{\nu}^T_{sR} M^R_{ss'} \nu_{s'R} + \text{h.c.}\,. \tag{3.2.10}$$

where $M^R_{ss'}$ is a complex $N_s \times N_s$ matrix. Defining the row vector $\mathbf{N}^T_L \equiv (\nu_{\alpha L}, \nu^C_{s_i R})$ where α runs over the active neutrino flavours and i runs up to N_s, one can rewrite all mass terms in the single expression

$$\mathcal{L}^{D+M}_{\text{mass}} = \frac{1}{2}\mathbf{N}^T_L C^\dagger M^{D+M} \mathbf{N}_L + \text{h.c.}\,. \tag{3.2.11}$$

The mass matrix M^{D+M} is

$$M^{D+M} = \begin{pmatrix} 0 & M^{D^T} \\ M^D & M^R \end{pmatrix}, \tag{3.2.12}$$

which one can diagonalize as

$$M = \begin{pmatrix} M_\nu & 0 \\ 0 & M_{\nu_s} \end{pmatrix}, \tag{3.2.13}$$

by introducing the unitary transformations V_L^ν and V_R^ν acting on active and sterile degrees of freedom respectively, such that

$$M_\nu = -V_L^{\nu T} M^{D^T} \frac{1}{M^R} M^D V_L^\nu \qquad M_{\nu_s} = V_R^{\nu T} M^R V_R^\nu \,. \tag{3.2.14}$$

If responsible for the breaking of the (accidental) L symmetry, M^R is expected to be connected to a high mass scale. It is therefore common to consider the limit $M^R \gg M^D$, which corresponds to the so-called *type I seesaw mechanism*. In this case, the simplest realisation of such model corresponding to a single left- and right-handed neutrino state, and previous relations boil down to

$$m_\nu \sim \frac{{m_D}^2}{m_R}, \qquad m_{\nu_s} \sim m_R \,, \qquad \theta = \frac{m_D}{m_R} \,. \tag{3.2.15}$$

We emphasize that the number of new states is unconstrained and might have little to do with the neutrino mass mechanisms[4]. Without entering details, we just mention that depending on their mass, sterile neutrinos can play many different roles in Cosmology and Particle Physics. At the eV scale, their presence solve a mysterious disappearance of $\bar{\nu}_e$ in observation of $\bar{\nu}_e \to \bar{\nu}_e$ by the SBL experiments LSND and MiniBooNE. Given the corresponding mixing angle, those would be produced and thermalized in the very early Universe, and are therefore in strong tension with cosmological data through bounds on $N_{\rm eff}$ [19]. At the keV scale, they could provide a viable DM candidate, whose correct relic abundance can be achieved through resonant production of sterile neutrinos in matter [543]. They are often invoke to explain the 3.5 keV line observed in some clusters of galaxies [123], [132]. Moreover, at MeV-TeV scale, they can decay at early times and yield detectable signal in Cosmological data. Finally, neutrino oscillations can be linked to leptogenesis [22], [32]. We will extensively develop the search for sterile neutrinos in the keV-MeV scale in chapter 6.

3.3 Evidence for Dark Matter

3.3.1 *Galaxy rotation curves and density profiles*

We have already mentioned in the introduction that in the first half of the 20$^{\rm th}$ century many signs attesting to the existence of a dark component of matter were found. Those came first from i) the study of the rotation of stars within our Galaxy by J. Kapteyn [359], ii) the study of the thermodynamic properties of Galaxy cluster by F. Zwicky [610], [611], in particular their mass under the assumption that the virial theorem holds. However, the community really started to take this problem seriously

4 In fact, such a term might have nothing to do with sterile neutrinos. It could be generated in extended Higgs sector, e.g. from the expectation value of a scalar triplet (as known as *type II seesaw*), or by the exchange of triplet fermions (as known as *type III seesaw*). However, in the following we shall restrict the discussion to mechanisms involving sterile neutrino.

only later on, in the 1970's, when V. Rubin, K. Ford and N. Thonnard published their result on the observation of galaxy rotation curves within spiral galaxies [518], [519]. Of course at that time the non-baryonic nature of this DM was not yet established, since the BBN and CMB evidence arrived only later, but we will comment on these results with our recent knowledge and assume that the DM component is non-baryonic.

Applying standard Newtonian gravity to a test body at a distance r from the center of the galaxy, one can compute the orbital velocity v (assuming that the orbit is stable)

$$\frac{GmM(r)}{r^2} = m\frac{v^2}{r}\,. \tag{3.3.1}$$

The galaxy is described as a *bulge* of radius R_1 and (visible) density ρ_1, extended by a *disc* of radius R_2, thickness d and (visible) density ρ_2. Well inside the bulge, $r \ll R_1$ and the mass of the visible stars is

$$M(r) \simeq \frac{4}{3}r^3\rho_1 \quad \Rightarrow \quad v(r) = \sqrt{G\rho_1\frac{4}{3}\pi}r\,. \tag{3.3.2}$$

On the opposite limit, far outside the disc $r \gg R_2$ one typically gets

$$M(r) = M_{\rm tot} = \frac{4}{3}\pi R_1^3\rho_1 + \pi R_2^2 d\rho_2 \quad \Rightarrow \quad v(r) = \sqrt{\frac{GM_{\rm tot}}{r}}\,. \tag{3.3.3}$$

This famous result shows that the velocity of stars far away from the center should decay as $v \propto 1/\sqrt{r}$. However, thanks to the observation of redshifted Hydrogen Lyman-α line, they found that $v(r) \sim const$, which immediately implies that there should be a DM component $M(r) \propto r$ even far away from the center. This is illustrated with more recent observations by Ref. [95] in fig. 29.

Although these observations have been made in spiral galaxies, we generalize our discussion to other types (including e.g. Dwarf spheroidal galaxies). In terms of density, assuming spherical DM halos (typical of the isotropic and spherical collapse of a self-gravitating distribution of collisionless particles), one gets

$$M(r) = 4\pi\int_0^r \rho(r')r'^2dr' \propto r \quad \Rightarrow \quad \rho(r) \propto \frac{1}{r^2}\,. \tag{3.3.4}$$

A lot of efforts is devoted to the determination of the *halo density profile* $\rho(r)$. The most common models used are

- *The isothermal profile:* It is based on the solution of the Liouville equation for the DM distribution assuming a uniform velocity distribution (or "temperature" in microscopic terms), whose solution is the Maxwell-Boltzmann law

$$f(\vec{x},\vec{v}) = C\exp\left(-\frac{E}{m\sigma^2}\right), \tag{3.3.5}$$

  with C a normalization constant, $E = mv^2/2 + m\phi$ with ϕ the Newtonian gravitational potential and σ^2 the velocity dispersion, playing the role of a temperature identical (hence the name) in each point of the halo. This result can also be obtained from considering the hydrostatic pressure equilibrium of an ideal gas with gravity. From the Poisson equation for ϕ, this leads to a profile

$$\rho(r) = \frac{\sigma^2}{2\pi G}\frac{1}{r^2}\,, \tag{3.3.6}$$

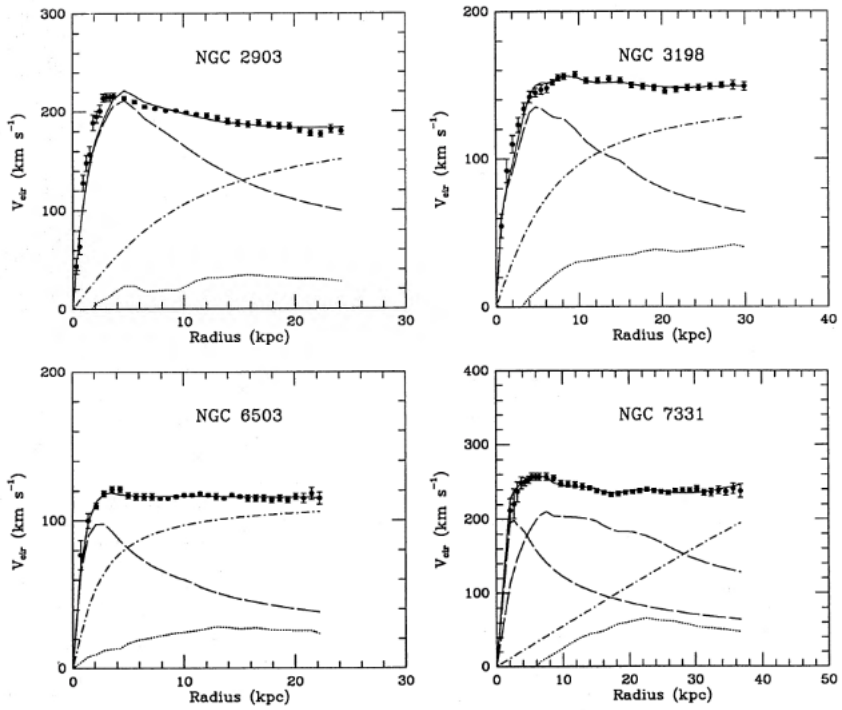

Figure 29: Rotation curves of spiral galaxies. Newtonian results from visible stars and gas give the long-dashed and dotted curves respectively. The dark matter halo corresponds to the dotted dashed curve and the solid line corresponds to the sum of the three components. Taken from Ref. [95]

which is in agreement with our guess (3.3.4). However, this profile diverges, therefore it is usual to introduce a constant density core ρ_s within a given radius r_s, such that

$$\rho(r) = \frac{\rho_s}{1 + \left(\frac{r}{r_s}\right)^2} \,. \tag{3.3.7}$$

- *The Burkert profile*: It is also a cored profile. It has been introduced to fit rotation curves better in ref. [135]. It is given by

$$\rho(r) = \frac{\rho_s}{\left[1 + \frac{r}{r_s}\right]\left[1 + \left(\frac{r}{r_s}\right)^2\right]} \,. \tag{3.3.8}$$

  The problem with the two former profiles is that M diverges when going at infinity from the center, they therefore cannot be the full solution.

- *N-body motivated profiles*: Numerical simulations allow us to estimate density profiles as well. The major finding of CDM only simulations is that profiles are *universal*. There are two types of profile, depending on the fitting function that has been used. The first one is

$$\rho(r) = \rho_s \left(\frac{r_s}{r}\right)^\gamma \left[1 + \left(\frac{r}{r_s}\right)^\alpha\right]^{(\gamma-\beta)/\alpha} \quad \text{where} \quad \rho_s = \rho_\odot \left(\frac{r_\odot}{r_s}\right)^\gamma \left[1 + \left(\frac{r_\odot}{r_s}\right)^\alpha\right]^{-(\gamma-\beta)/\alpha} , \tag{3.3.9}$$

  with $\alpha = 1$ and $\beta = 3$. The *NFW profile* [448] corresponds to $\gamma = 1$ and the *Moore profile* [215] to $\gamma = 1.16$. However, they both tend to diverge at low r and do not reproduce well the evolution of the slope of the profile when compared to simulations. To avoid that, an other class of profile has been introduced [449]

$$\rho(r) = \rho_s \exp\left\{-\frac{2}{\alpha}\left[\left(\frac{r}{r_s}\right)^\alpha - 1\right]\right\} \quad \text{where} \quad \rho_s = \rho_\odot \exp\left\{\frac{2}{\alpha}\left[\left(\frac{r_\odot}{r_s}\right)^\alpha - 1\right]\right\} . \tag{3.3.10}$$

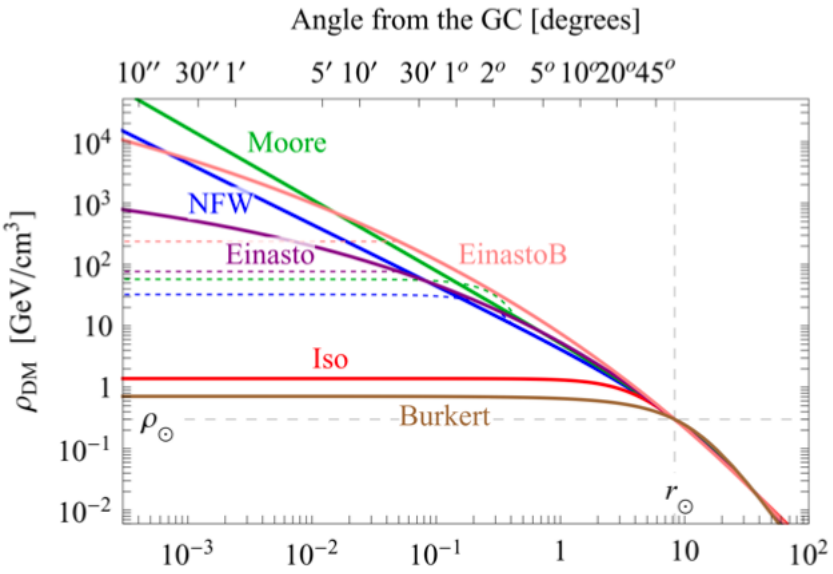

Figure 30: Radial DM density profile. The full lines represent the profiles *as is*, while the dashed lines correspond to modification of these profile to the remove Galactic center divergence. Taken from ref. [188].

where $\alpha = 0.17$ correspond to the *Einasto profile* and 0.11 to the *EinastoB profile*. When applied to our Galaxy, the parameters entering those profiles are the distance of the Sun from the Galactic center $r_\odot$, the local DM density $\rho_\odot$ and the normalisation, fixed by the total mass within a radius $r = 60$ kpc. Typical values are $r_\odot = 8.33$ kpc, $\rho_\odot = 0.3$ GeV/cm^3 and $M_{60} = 4.7 \times 10^{11} M_\odot$. More recently, simulations with baryons have shown that this universality can be spoiled by the presence of a significant baryonic fraction within the galaxy [581].

Those profiles are illustrated in fig. 30. Large uncertainties in the profile close to the Galactic center will lead to strong uncertainties on the signal coming from DM annihilations and decay in the context of indirect dark matter searches with cosmic-rays (especially for γ-rays) on which we comment further on. The satellite GAIA [478] launched in 2013 by ESA, which aims at a 3D mapping of more than a billion objects within our Galaxy, should be help in shedding light on the halo profile in our Galaxy a few kpc away from the solar system.

3.3.2 *Clusters of galaxy : X-rays and weak lensing*

Following the work of F. Zwicky, people have been interested in DM on the scale of galaxy clusters. There are several ways to learn more about their thermodynamics properties.
X-ray astronomy, developed in the 80's, allows one to measure the thermal emission of the ionized gas, which constitutes the dominant baryonic component of the cluster mass. From the spectral composition, one can get the temperature of the gas, while the intensity of the emission is linked to its density. Assuming that the gas is in thermodynamics equilibrium, i.e. that pressure forces equal gravitational ones, it is possible to deduce that the visible mass only represents about 10% of the total mass of the cluster. Experiments nowadays allow tracing the distribution of the gas within clusters. Another possibility is to use the Sunyaev-Zeldovich distortion of the CMB blackbody spectrum due to upscattering of photons by hot electrons. The satellite *Planck* has provided a map of the galaxy

Figure 31: The Bullet Cluster seen by Hubble. The ionised gas distribution observed by Chandra in X-rays is represented in pink. The mass distribution deduced from gravitational lensing is represented in blue. Taken from the website *http://apod.nasa.gov*.

cluster seen via this effect [18].
Finally, one can infer the total mass of the cluster thanks to the gravitational lensing effect. GR predicts that the trajectory of light emitted by a distant object should be bent due to intense gravitational potential along the way. From the deformation of the shape of objects, one can deduce the spatial distribution of the gravitational potential, and therefore of the mass. A "smoking gun" signal of DM has been claimed to be detected recently by Ref. [195] when observing the Bullet cluster. This object is actually a pair of colliding galaxy clusters. On one hand, it is possible to trace the gas distribution of the object thanks to X-ray emission. On the other hand, lensing provides a distribution of the total amount of matter. The result of this procedure is represented in fig. 31. It clearly shows that the two components do not coincide, giving a (new) strong hint of the existence of DM. Interestingly, the analysis of the Bullet cluster also allows us to derive an upper limit on the DM self-interaction cross-section [500]:

$$\frac{\sigma}{m_\chi} < 0.7 \text{ cm}^2/\text{g}\,. \tag{3.3.11}$$

3.3.3 *The Dark Matter relic abundance and the WIMP miracle*

We have already discussed the fact that BBN is sensitive to the photon-to-baryon ratio η. Measurements of the primordial elements abundances indicate that $\eta \sim 6 \times 10^{-10}$, which allows to determine ω_b once ω_γ is determined by an experiment such as COBE/Firas. We have also seen that the study of CMB anisotropies allows to determine at the same time ω_b and ω_M. The important point is that these numbers are very different, typically with the last *Planck* measurement we have

$$\omega_b = 0.02218 \pm 0.00015\,, \quad \omega_M = 0.14268 \pm 0.00155\,. \tag{3.3.12}$$

Those numbers being far off, they point to the existence of DM not only at the scales of galaxies and clusters of galaxies, but also at the cosmological scales. The very interesting point being that the amounts of DM needed are mutually consistent: For instance, the ratio of the two components in the

bullet cluster is compatible within errors to the above figures [195]. The *relic abundance* of DM is therefore

$$\omega_{\rm cdm} = 0.1205 \pm 0.0014\,. \tag{3.3.13}$$

However, what properties of the DM are necessary in order to produce such a relic density? We wish now to introduce the most common mechanism, inspired by the standard freeze-out of other particles that we have already discussed. We assume that a massive, stable or long-lived DM particle χ can annihilate with its antiparticle $\bar{\chi}$ into some particle f of the SMPP and that interactions between three or more particles are very unlikely. We thus consider the process

$$\chi + \bar{\chi} \leftrightarrow f + \bar{f}\,. \tag{3.3.14}$$

The density of a non-relativistic DM particle χ is governed by the following Boltzmann equation

$$\frac{dn_\chi}{dt} = \underbrace{-3Hn_\chi}_{\text{dilution}} + \underbrace{n_f^2\langle\sigma_{f\bar{f}\to\chi\bar{\chi}}v\rangle}_{\text{production}} - \underbrace{n_\chi^2\langle\sigma_{\chi\bar{\chi}\to f\bar{f}}v\rangle}_{\text{destruction}}\,, \tag{3.3.15}$$

where $\langle\sigma_{f\bar{f}\to\chi\bar{\chi}}v\rangle$ and $\langle\sigma_{\chi\bar{\chi}\to f\bar{f}}v\rangle$ are the *thermally averaged creation and destruction cross section times velocity* respectively. Since the collisions term has to vanish at chemical equilibrium, we find

$$\langle\sigma_{f\bar{f}\to\chi\bar{\chi}}v\rangle = \left(\frac{n_\chi^{(eq)}}{n_f^{(eq)}}\right)^2\langle\sigma_{\chi\bar{\chi}\to f\bar{f}}v\rangle\,. \tag{3.3.16}$$

and we usually write

$$\langle\sigma v\rangle \equiv \langle\sigma_{\chi\bar{\chi}\to f\bar{f}}v\rangle\,. \tag{3.3.17}$$

We assume that the species f is at equilibrium such that $n_f = n_f^{(eq)}$. Hence, eq. (3.3.15) reduces to

$$\frac{dn_\chi}{dt} = -3Hn - \langle\sigma v\rangle[n_\chi^2 - (n_\chi^{(eq)})^2]\,. \tag{3.3.18}$$

We introduce the time variable $x = m_\chi/T$ and the comoving density $Y_\chi = n_\chi/s$. If we assume that $T \propto a^{-1}$, i.e. that $h_{\rm eff} \sim const = h_{\rm eff}(M_\chi)$, we can write

$$\frac{dY_\chi}{dx} = -\frac{\lambda}{x^2}[\chi^2 - (Y_\chi^{(eq)})^2]\,, \qquad \lambda \equiv \frac{2\pi^2}{45}h_{\rm eff}(M_\chi)\frac{M_\chi^3\langle\sigma v\rangle}{H(M_\chi)}\,. \tag{3.3.19}$$

It is possible to solve eq. (3.3.19) numerically, and we plot a solution in fig. 32. We see that at high temperature $Y \to Y_{\rm eq}$, while at low temperature the equibrilibrium abundance becomes exponentially suppressed as the particles becomes non-relativistic, $Y \propto e^{-x}$. At some point, the χ particles become so rare that they are unable to find each other to annihilate and maintain the equilibrium abundance: this is the freeze-out. It is practical to perform the development of $\langle\sigma v\rangle$ as

$$\langle\sigma v\rangle = a + bv^2 + \mathcal{O}(v^4), \tag{3.3.20}$$

where a and b are independent of v and represent the so-called s- and p-wave annihilation channels. Assuming that the s-wave channel dominates the annihilations, we can deduce the comoving density today

$$Y_{\chi,0} \simeq \frac{x_f}{\lambda}\,, \tag{3.3.21}$$

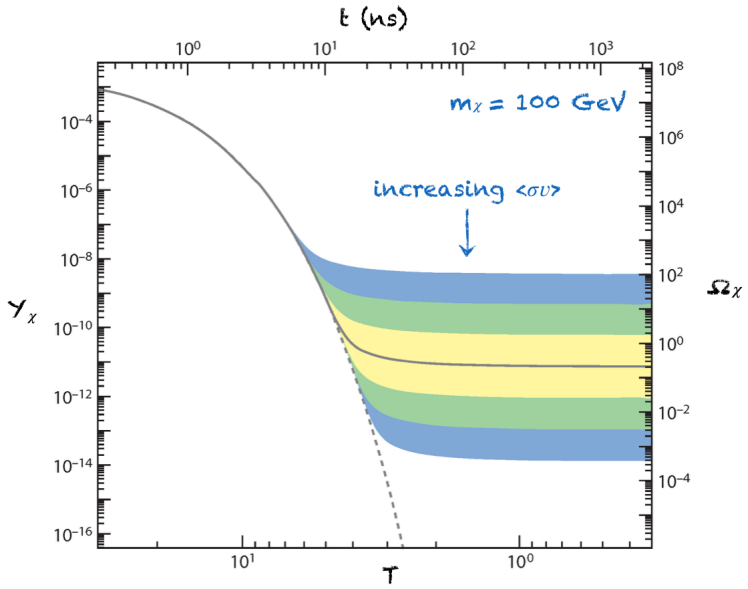

Figure 32: Evolution comoving abundance of DM particles as an illustration of the freeze-out mechanism. Adapted from J. Feng website *http://www.ps.uci.edu/˜jlf*.

where $x_f = m_\chi/T_f$ is the freeze-out time and T_f is the freeze-out temperature. By computing $H(x_f) = \Gamma(x_f)$, or thanks to numerical resolution, it is possible to get $x_f \sim \mathcal{O}(10)$ and typically $x_f \propto \ln(\langle\sigma v\rangle)$. Due to the dependence in λ, the higher $\langle\sigma v\rangle$, the later the freeze-out. Hence, the abundance today is smaller in models with more efficient annihilations: it is referred to as the *survival of the weakest*. Let's now relate the freeze-out abundance to the DM density today:

$$\Omega_{\rm cdm} \equiv \frac{\rho_{\rm cdm,0}}{\rho_{\rm crit,0}} = \frac{M_\chi n_{\chi,0}}{3M_{\rm pl}^2 H_0^2} = \frac{M_\chi Y_{\chi,0} s_0}{3M_{\rm pl}^2 H_0^2}\,. \tag{3.3.22}$$

If we now plug $Y_{\chi,0} = x_f/\lambda$ and $s_0 \equiv s(T_0)$ given by eq. (1.3.24), we can write $\omega_{\rm cdm} \equiv \Omega_{\rm cdm} h^2$ as

$$\omega_{\rm cdm} \simeq 0.12 \times \frac{3\times 10^{-26}{\rm cm}^3{\rm s}^{-1}}{\langle\sigma v\rangle}\,. \tag{3.3.23}$$

One can therefore get the good DM relic density for $\langle\sigma v\rangle \sim 3\times 10^{-26}{\rm cm}^3{\rm s}^{-1}$ which is typical for weakly interacting particles with masses of the order of the electroweak scale and has therefore become a benchmark value. The fact that a thermal relic with such a cross section gives the right DM abundance is called the *WIMP miracle*, where WIMP stands for *Weakly Interactive Massive Particle*.

3.4 Models predicting massive relics

Cosmology requires at least one new neutral stable particle, produced with the correct density and non-relativistic enough to initiate the formation of large scale structures. We have seen that the vanilla thermal production mechanism is associated with a WIMP particle. However, are there models predicting such particles? Indeed, there are many, and a large part of this thesis is devoted to finding some phenomenological consequences of them. However, in many extensions of the SMPP, there are other relics either unstable to processes injecting electromagnetic energy, or decaying into SM invisible

products. In fact, Cosmology has the potential to shed lights on those decaying relics as well, and we therefore shall not restrict ourself to the study of relics being DM candidates.
In the following, without entering mathematical details, we shall introduce broad lines of such models.

3.4.1 *WIMP Dark Matter candidates*

We first review some models proposed to solve issues of the SMPP, that gives a viable WIMP candidate whose main channel of detection is through potential annihilations into SM, as we have discussed in sec. 3.3.3.

3.4.1.1 *Supersymmetric candidates*

SUSY is a tentative to extend the Poincaré algebra, generating the group of the isometries of Minkowski's space-time, which includes translations and Lorentz transformations. The famous Coleman-Mandula theorem forbids any non-trivial extension of the Poincaré algebra. However, it is possible to extend it into a *superalgebra*, i.e. by adding new generators which *anticommute*. These operators change a boson into a fermion and vice-versa.
In the Minimal SuperSymmetric Model (MSSM), only one super partner is introduced and the minimal amount of extra symmetry is assumed. Each SM particle is grouped within *chiral or vector supermultiplets* with their supersymmetric partner, to which they differ by half a spin unit. To gauge bosons are associated new Majorana fermions called gauginos (the bino, the winos and the gluinos), and to SM fermions new scalar bosons called sfermions (selectron, smuon, stau, sneutrinos, squarks). Contrarily to the SM, a minimal Higgs sector consistent with SUSY requires two Higgs doublets, e.g. to avoid anomalies; their partners are called higgsinos. However, SUSY predicts that partners should have the same mass as the SM particles. Those have not been observed and thus SUSY must be broken at a scale higher than the EW scale. Therefore, mixing of particles can happen between neutral higgsinos and gauginos, those are called *neutralinos* χ^0 , as well as among charged ones, called *charginos* $\chi^{\pm}$. The precise phenomenology of SUSY depends on the symmetry breaking mechanism, hence it is difficult to draw general conclusions.
An important point is that SUSY implies fast decay of protons because lepton and baryon number are not conserved anymore. This issue is solved by means of the new R-parity conservation law, which states that the number $R = (-1)^{3B+3L-2s}$ is conserved, with B the baryon number, L the lepton number and s the spin. Each SM particle has $R = +1$ while their superpartners have $R = -1$, which in turn stabilizes the proton. For the same reason SUSY particles can only annihilate and be created in pairs, while the lightest SUSY particle (LSP) is automatically stable. The key point is that if the LSP is a neutralino, it is a suitable WIMP dark matter candidates as it is stable, neutral and ranges in the EW scale, while its annihilations into SM particles produce a signal that we can look for in the context of indirect detection with Cosmology. More details on SUSY can be found in Ref. [417].

3.4.1.2 *Extra-dimensions*

Models of extra-dimensions are based on the seminal idea of T. Kaluza [352] to unify electromagnetism and gravity, extended to include quantum aspects by O. Klein [372]. Kaluza postulates the existence of a fourth compactified space dimension. This idea has been generalized to a arbitrary number of

dimension n, each of them having an arbitrary size R_i. By Gauss theorem, we can relate the effective 4D Planck mass to the n dimensional Planck mass M_n as

$$M_p^2 = \left(\frac{c}{\hbar}\right)^n V_n M_n^{n+2} \tag{3.4.1}$$

with V_n the volume of the extra space. Depending on the value of V_n, one can get M_p^2 to be as low as the TeV scale and thus solve the hierarchy problem.
In the ADD models (Arkani-Hamed, Dimopoulos, Dvali) [61], the particles of the SM are bound to a 3-dimensional submanifold (the SM brane), while gravity can propagate in the whole higher dimensional spacetime (the bulk). The volume of the extra space is $V_n = (2\pi)^n \prod_{i=1}^n R_i$ with R_i sufficiently large to solve the Hierarchy problem. Since the gravitational potential falls off faster at small distances, short scale tests of gravity constrain n to be greater than 2. From the compactification of the extra dimension, the momentum of the graviton in the extra dimension is quantized, and appears in the brane as a mass term. These states are called *Kaluza-Klein excitations* and the exact mass hierarchy *KK-tower*. Often however, the SM couplings are so low that those models are difficult to observe in the context of indirect detection.
An alternative to ADD are Universal Extra Dimension models (UED) [50], which contains both large and small compactified dimensions. In that case, all particles can propagate in the whole higher dimensional spacetime, therefore generating KK-excitations for all SM particles. In both cases the phenomenology depends strongly on the assumed boundary conditions. However, because of these KK-towers for SM particles, EW precision tests might be spoiled. A Kaluza-Klein parity (which can appear naturally from geometrical effect in some theory) can be introduced to suppress the effect of some excitations onto the SM particles. The side effect is to make the lightest excited particle (LKP) stable, neutral, with mass in the EW range, making it a perfect DM candidate.

3.4.2 *Decaying massive relics*

We extend the previous discussion to the case of unstable massive relics, not necessarily being long-lived, in which case they can represent only a fraction of the total DM in our Universe.

3.4.2.1 *Sterile neutrinos*

As mentioned already in sec. 3.2.2, Majorana RH sterile neutrinos are decaying massive relics. Actually, below the MeV scale, they lifetime is typically long enough for them to be *a priori* viable DM candidates, while at higher masses they can decay during the history of the Universe, leaving potential traces of their existence in CMB and BBN datasets. Although the main decay channel is through neutrinos, a decay into a neutrino and a photon with a branching ratio at the % level is always possible, and above the MeV mass a decay into electrons with larger branching ratio opens up. We look for these signals in chapter 6.
However, e.m. channels are not necessarily always open. In chapter 4, we consider the case in which the decay products consist either of non-standard particles, or of standard model neutrinos produced with typical momenta much larger than their mass. A notable case of such a DM candidate is represented by the majoron J with mass m_J in the keV range, a pseudo-goldstone boson associated to the breaking of the global lepton number symmetry, acquiring a small mass plausibly due to quantum gravity effects, whose cosmological interest in a modern context has been revisited in Ref. [385] and

references therein. It is an example of DM models linked to sterile neutrino, whose leading decay channel is in two relativistic neutrinos. The majoron lifetime is then inversely proportional to the square of standard active neutrino masses m_ν and to the lepton number breaking scale v. Bounds on τ_J can be used to constrain the value of v as a function of the standard neutrino mass scale.

3.4.2.2 *Primordial Black Holes*

Black holes in a wide range of masses could have formed in the early universe due to the collapse of $\mathcal{O}(1)$ primordial inhomogeneities [146], [147], [296], usually associated to either extended inflationary models (such as hybrid inflation [131], [192], [263], [411], curvaton scenarios [363], [375], single-field and multi-field models in various frameworks [219], [236], [262], [264], [269], [355], [365], [436]), or to first and second-order phase transitions [348], [517]. PBH with masses $M \leq 10^{-17} M_\odot$ evaporate into standard model particles with a blackbody spectrum (the so-called Hawking radiation [298], [299]), leading to energetic particle injection which can be looked for in cosmic rays [82], γ rays [145] or CMB analysis (as we have develop). The intermediate mass range up to stellar masses is covered by a number of lensing constraints. From low to high masses, we mention femtolensing in gamma-ray bursts [80], microlensing in high-cadence observations of M31 [451] and of the Magellanic clouds [33], [463], [580]. The latter are however still controversial (e.g. Ref. [284], [300]), depending on the PBH clustering properties [192]; some results even point at a possible detection of anomalous microlensing events [33], [463]. Additional constraints from neutron stars and white dwarfs in globular clusters also exist in this range [140], [141], but depend on astrophysical assumptions. Stellar mass or heavier PBH are constrained by dynamical properties of ultra-faint dwarf galaxies [126], [283], [379], [404], by halo wide binaries [433], by X-ray or radio emission [257], [337], as well as by the cosmic microwave background (CMB) bounds discussed in the following[5]. Indeed, due to their gravitational attraction on the surrounding medium, such massive objects accrete matter, which heats up, gets eventually ionized and emits high-energy radiation. In turn, these energetic photons can alter the ionization and thermal history of the universe, affecting the statistical properties of CMB anisotropies.

However, in the case where such processes are negligible, our study in chapter 4 can be useful. Indeed, when PBH are experiencing a merging event, a non-negligible fraction of the PBH mass converts into gravitational waves, a form of dark radiation subject to the constraint discussed in this thesis. Hence, the time evolution of the initial mass function due to merging events can be strongly constrained by purely gravitational CMB bounds: in each merger with comparable BH masses, a few percent of their mass is converted into gravitational waves, i.e. “dark” radiation, a phenomenon that cannot involve more than a small fraction of the DM, due to alterations to the Sachs-Wolfe effect. Essentially no more than one merger per PBH on average is allowed between recombination and now, as we discuss in chapter 4.

3.4.2.3 *Other models*

Although we do not explicitly discuss them, the results of our studies apply to many more models. For instance, decaying massive particles can be the progenitors of the DM in ‘superWIMP’ models [240], or the DM itself can be unstable, provided its lifetime is much longer than the lifetime of the universe,

5 Further constraints exist, e.g. based on the emitted gravitational wave background [184], [193], [440], [529] or non-gaussianities in the primordial fluctuations [576], [602], which—while often quite stringent—are model dependent.

as in R-parity breaking SUSY models (see e.g. [120]). Our considerations also apply to an excited DM component [245], injecting energy when the metastable state de-excites. Other candidates also includes unstable supersymmetric particles such as gravitinos (e.g. [137], [524]). Many of these models typically lead to photons and leptons among their final states, with peculiar time evolution depending on the model considered.
However, in some scenarios, decay products might not always be electromagnetically charged. For instance, invisible daughters can be produced if the LSP and the next-to-lightest particle (NLSP) are respectively gravitinos and right-handed sneutrinos (see e.g. [41]), or in the presence of multiple sneutrino states (for a recent example see [77]). Moreover, in scenarios incorporating the Peccei-Quinn mechanism [470], [471] to solve the strong CP problem, the axion [588], [593] can play the role of an invisible radiation produced by the decay of its supersymmetric partner the axino or by gravitinos (see for instance [183] for an early proposal in this sense, or [75] for a modern review).

3.4.3 *A word on detection strategies*

Several strategies have been developed over the years to detect non-gravitational signatures of DM. In the context of WIMP particles, the thermal production mechanism requires a four-particle weak-like interaction between the DM and the SMPP. This gives rise to several avenues for DM searches, illustrated in fig. 33. This short recap is based on Refs. [187], [384].

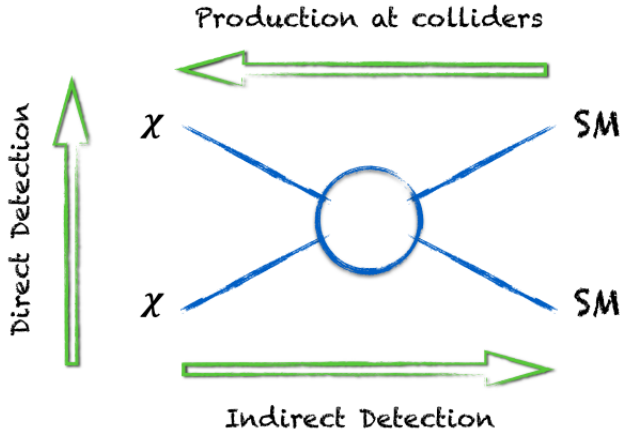

Figure 33: A schematic diagram of the four-point interaction between DM particles and the SMPP, and the link with the various search strategies.

3.4.3.1 *Indirect Detection*

The first strategy, which is of utmost interest in this work, is to look for the products of relic annihilations (or even possible decays) all along the history of the Universe. In the particle astrophysics context, DM annihilations within the halo which surrounds our Galaxy can contribute to the fluxes of *Cosmic Rays* measure on Earth. Cosmic Rays (CR), whose discovery dates from the beginning of the 20th century, are charged particles composed at 99% by nuclei (typically 90% of which are protons) and 1% of electrons. The origin of these CR is still debated, but it is commonly accepted that there

should be both a Galactic and an extra Galactic component. The first component, which corresponds to energy below roughly 10^{15} eV, could be produced by supernovae, while the main source of high-energy extra Galactic CR is attributed to active galactic nuclei. A very tiny fraction of Galactic CR is also made of antiparticles, whose origin is even more mysterious, part of which could be due to DM annihilations. It is believed that antiparticles are mainly of *secondary origin*, i.e. produced by the spallation onto hydrogen and helium nuclei of *primary particles* coming directly from the source. The key point is that, once primary fluxes and hydrogen/helium abundances in the galaxy are known, one can predict the (relatively small) background of secondary antiparticles.

The main difficulty with this strategy arises from the so-called *propagation* of CR within the galaxy: our Galaxy is embedded within a magnetic halo which imprints (what is believed to be) a random walk to charged particles. Many more processes can affect the initial distribution of CR (depending on the CR type and energy), including energy losses, diffusive re-acceleration (due to the motion of the magnetic diffusion centers), destruction and decay processes, and the interaction with the magnetic field of the Sun (an effect known as *solar modulation*) and the Earth. All this complicated physics, modelled with a semi-empirical diffusion equation which depends on a certain number of parameters, makes it in practice more complicated to have an accurate prediction. The usual strategy is to use the fluxes of pure secondary particles (historically the Boron flux of the Boron-to-Carbon ratio, its main progenitor, as well as ratios of unstable-over-stable nuclei) to fix the propagation parameters, predict the antiparticle fluxes (typically positrons, antiprotons and anti-deuterons) and look for deviation from these predictions within measurements.

Recently, it has been realized that particles that were thought to be pure secondaries in the historical paradigm might in fact receive primary contributions, whose normalisation is unknown. This is for instance the case of positrons. If positrons were pure secondaries, the so-called *positron fraction*, i.e. the quantity $e^+/(e^+ + e^-)$ is predicted to be a decreasing function of energy. Since the Pamela experiment [24] (which confirmed the first hints of the HEAT [83] and AMS-01 [29] experiments), it is clear that the positron fraction rises above a few GeV. The latest measurement by the AMS-02 experiment, which yielded the most precise measurement of the positron fraction [30], did not change the picture. This motivated a high activity of theoretical research, part of which attributes this excess to possible DM annihilations within our Galactic halo (e.g. [62] for a review of possible models). The main difficulty with such explication is that the best fit (restricting the data to the excess above 10 GeV) is for a TeV candidate annihilating preferably to leptons (to avoid antiprotons constraints) with a cross-section of order $\sim 10^{-23}\text{cm}^2/\text{s}$ (see e.g. [118], [119] for recent work). This is not only 3 orders of magnitude above the benchmark cross-section, thus requiring some peculiar boosting mechanism, but also excluded by the most recent CMB searches [19], [552]. Note that a decaying DM particle has also been suggested as a possible explanation to the excess, with lifetime of order $10^{26} - 10^{27}$ and main decay channel to leptons (e.g. [334]). Those are as well in tension with CMB data, as we shall see in chapter 6. Alternatives to the DM explanations are numerous, the most common one being probably the *Pulsar scenario* [313], in which high energy electrons and positrons are produced within the Pulsar Wind Nebula due to the presence of very high magnetic and electric fields. One or several pulsars could participate in giving the measured flux (e.g. [119]), and it will be very difficult to disentangle between this explanation and the DM one. It is however very likely that most of the rise comes from pulsars given current constraints on the DM scenario.

Other "golden" channels include antiprotons and anti-deuterons (with the GAPS experiment soon to

come[6]) but no clear detection has yet been made, allowing us to derive strong constraints on the DM annihilation cross-section and lifetime (e.g [271]). However, the recent literature is made of interesting positive signal [200] after the exquisite measurement of the antiproton flux and antiproton-to-proton ratio by AMS-02 [31].

Finally, we mention the possibility of looking within neutral particle fluxes as well ($\gamma-$rays, neutrinos), which have the advantage of propagating in straight lines (or rather geodesics). The $\gamma-$ray signal from DM is usually decomposed into a prompt component, produced directly by DM annihilations themselves, and a secondary component due to the ICS, bremsstrahlung and synchrotron radiation of the daughter particles. *Line searches*, which enter the first category, are motivated by the possibility of direct annihilations through a loop into two photons (or one photon plus a massive particle, like a Z or a Higgs), which would produce a line at the DM mass, or due to internal bremsstrahlung which produces a sharp feature. Depending on the energy range, a line feature is believed to be a smoking-gun signature of DM. The only known astrophysical mechanisms that could mimic such signals are atomic lines, expected to be emitted up to X-rays, and nuclear lines up to the MeV range. Numerous detections of such unexpected lines have been claimed in the literature, including the 130 GeV [127], [568], [591] and 511 keV line at the Galactic center (e.g. [549]) and more recently, the so-called 3.5 keV line [122], [350] in galaxy clusters. However, none of them could be attributed unambiguously to DM annihilations or decays. The secondary component and the decay of unstable daughter particles which composes the primary component lead to a continuous emission spectrum. The most investigated targets are (i) regions with high DM densities and/or (ii) regions where the signal from astrophysical origins is (believed to be) small and therefore the signal/noise ratio is enhanced. Example of such targets are: the Galactic center (i), which has already given a plethora of unexpected signals, including the recent GeV excess (e.g. [138]), and is known to be holding a potentially large number of unresolved sources like millisecond pulsars (e.g. [387]); satellite galaxies of the Milky Way (i)+(ii), mostly of the spheroidal dwarf galaxy type, expected to be DM-dominated (e.g. [13] for recent analysis); the Galactic halo (ii), where searches for prompt emission and secondary component of DM annihilations and decays are undertaken [11]. Of interest for us, we can also mention the isotropic $\gamma-$ray background (ii), which is the residual in the extragalactic $\gamma-$ray background after subtracting resolved extragalactic sources [14].

Neutrinos are also promising probes for looking at DM annihilations/decays. They are produced in the same cascade processes as the one producing other particles, have the advantage of propagating in straight line, but interact only very weakly with matter, which makes them difficult to detect. Nowadays, neutrinos are observed in very large underground (or under-ice/water) telescope thanks to the Cherenkov light that they emit when interacting with the material inside the detector or in its surrounding environment. The main background for these searches comes from atmospheric muons, such that experiments use the whole Earth width as a shield and focus on neutrinos that have traversed the Earth before interacting in the detector. Detectors have similar targets as for $\gamma-$ray searches, but also look at possible annihilations of DM within the center of the Sun (or even the Earth), where WIMP particles might have been gravitationally captured. Detection of high-energy neutrinos from the Sun, on top of the MeV scale neutrinos from nuclear reactions, would constitute a "smoking gun" for DM detection, as no known nuclear/astrophysical processes could produce them. No detection of such neutrinos has yet been reported, but the IceCube [3], SuperKamiokande [182] and Antares [23] collaborations produced stringent constraints on the DM annihilation cross-section and lifetime. Let

6 http://gamma0.astro.ucla.edu/gaps/

us also mention that the discovery of PeV-energy neutrinos by IceCube [2] opens the possibility of testing very heavy DM scenarios, as a decaying PeV DM could explain such events [439].

A summary plots of recent constraints, mostly for illustration and to get ideas on the relative power of each probe, is shown in fig. 34. Typically, for the channels and masses considered, antiproton and $\gamma-$ray searches yield the strongest constraints. This picture would change for annihilations into γ-rays and $e^{\pm}$ (depending on the mass, CMB bounds can be the strongest), or into neutrinos (IceCuce and Antares would be the most sensitive detectors).

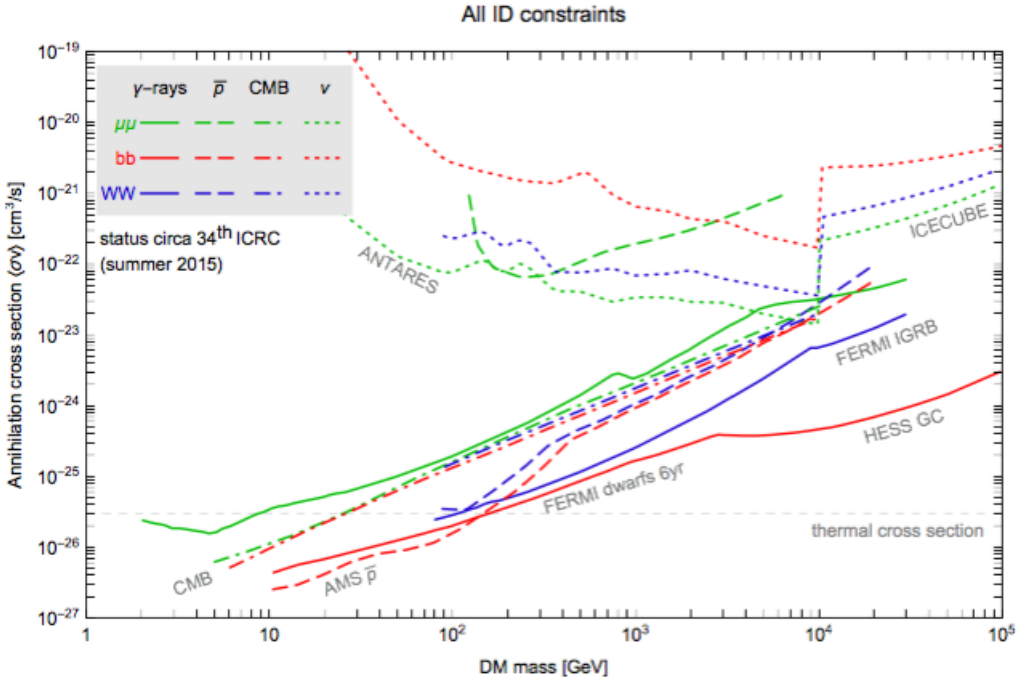

Figure 34: Illustrative summary plot of the current upper limits on the DM annihilation cross-section vs DM mass for different channels using the various probes discussed in the text. Although most of the bounds correspond to "official" ones (i.e. produced by the collaboration), some limits have been rescaled to account for the different assumptions (e.g. on the DM profile). Conservative limits have been chosen when several were available. Figure taken from [187], where the reader is referred for more details.

3.4.3.2 *Direct detection*

Another search strategy extensively followed by the community is the possibility of looking for the recoil of a nucleus (eventually an electron) hit by a DM particle within ultra-clean and ultra-sensitive *direct detection* experiments. Given the very low interaction cross-section of DM with standard matter, such events are extremely rare and the experiments have to be shielded as much as possible from cosmic rays, which correspond to the primary foreground for these searches. The strategy is therefore to locate these detectors in deep underground caverns, or deep under the Antarctic ice and to look for events *virtually above zero background*. However, instead of measuring the absolute number of events, it is also possible to look for the so-called *annual modulation* of the signal. Indeed, due to the rotation of the Galactic disk, itself embedded in an essentially non-rotating halo of DM particles, the solar system experiences an effective "wind" of WIMP particles. This in turn leads to an annual modulation

of the signal depending on the orientation of the Earth motion with respect to the WIMP wind. For standard assumptions, the maximum of the modulation happens at the beginning of June, while the minimum is predicted to be at the beginning of December. Numerous positive detections (both from the annual modulation and the absolute signal) have been reported over the years, none of them having been confirmed, and the current consensus is that there are stringent limits on a possible nucleus-DM interaction above 10 GeV masses. There is an irreducible background to these searches due to interaction of the detector with neutrinos coming from the Sun, the atmosphere, as well as the diffuse supernova neutrino background. A possibility advocated to go beyond this *neutrino floor* is to exploit the variation of the *direction* of the signal, which has a very peculiar signature because of the WIMP wind, but such experiments are still under development. We refer to Refs. [201], [253], [420] for more details on current and future direct detection experiments.

3.4.3.3 ***Searches at collider***

Finally, we mention the possibility to produce DM particles at colliders, if such interaction is allowed. However, because of their very low interaction with matter, DM particles are not seen in the standard detectors. Rather, they are expected to be detected in the form of *missing (transverse) energy or momentum*, when produced along with initial or final state radiation in the form of SM particles. The main difficulties lie in the correct reconstruction of the particles belonging to a given event (which can be a single photon, or a jet of particles) and on the presence of a standard "invisible" background in the form of neutrinos. Alternatively, within specific theoretical scenarios (e.g. neutralino DM candidates in constrained MSSM) model-dependent searches can be performed, where constraints on the lack of signatures of observable particles (e.g. gluino, squarks...) can be linked to DM-relevant quantities via theoretical relations among the parameters. No detection has yet been reported, and such searches produce the strongest constraints at energies below the reach of direct detection (for a review see Refs. [65], [277]). Both strategies are therefore extremely complementary.

3.5 **Electromagnetic cascade: an overview**

It is well known that electrons and photons injected by some sources in the cosmological plasma can modify key observables of the Cosmological model, such as BBN and the CMB. However, because of the huge number of photons per baryon, an injected photon or electron will not directly interact with baryons. Rather, it will initiate an *electromagnetic cascade* (e.m. cascade) by interacting with thermal photons, that will lead to the establishment of a non-thermal distributions of photons and electrons able to interact with baryons. The term e.m. cascade refers to the evolution of γ, $e^{\pm}$ particle numbers and energy distribution following the injection of a energetic γ or e in a medium filled with radiation, magnetic fields and matter. It is one of the physical processes most frequently encountered in particle astrophysics, in various domains from high-energy gamma-ray astrophysics to ultra-high-energy cosmic ray propagation, including the physics of the early universe which concerns us.
However, there are key differences between the e.m. cascade in the BBN context and the CMB ones, linked to the different epochs at which they take place. Indeed, e.m. reaction rates will always be much bigger than the Hubble rate when modifications to BBN yields are important (i.e. roughly before decoupling). This leads to a major simplification of the problem at hand, since one can neglect the Universe expansion and derive an accurate solution in the quasi-static approximation. On the other hand, this approximation is poor when computing modifications to CMB anisotropies as cooling

reaction rates can be smaller than the expansion rate. More involved numerical codes are then needed, often based on Monte Carlo resolution. This fact is illustrated in fig. 35 - right panel with a comparison of the total photon cooling time to the Hubble time, including all relevant processes (introduce hereafter).
We review now the broad line of the development of the cascade, describing the usual approximations that are made depending on the probe one is interested at, and present the main analytical and numerical results that we have used for our studies.

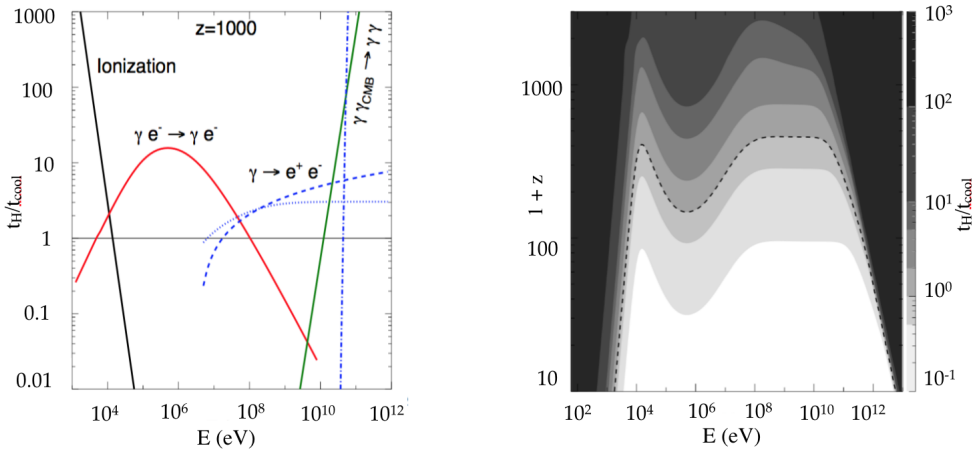

Figure 35: *Left panel:* A comparison of the photon cooling time to the Hubble time at $z = 1000$, for different photon energies. *Right panel:* A comparison of the photon cooling time (from all processes) to the Hubble time over the entire redshift range of interest. Both plots assume a He mass fraction of 1/4, with a density of 2.57×10^7 amu/cm^3 today and a standard reionization history. Taken from Ref. [554].

3.5.1 *Electromagnetic cascade at high redshift ($z \gg 1000$)*

We start by discussing a case in which the Universe expansion term is negligible compared to reaction rates. This regime is valid for instance well before decoupling, corresponding to the context of non-thermal BBN. Once a source has injected photons and electrons in a thermal bath, they can experience a bunch of reactions which will modify the shape of the non-thermal distributions f_γ and f_e. The most important processes entering the development of the e.m. cascade, ordered by their relative contributions, are

$$\begin{aligned}\frac{\partial f_\gamma(E_\gamma)}{\partial t} &= \left.\frac{\partial f_\gamma(E_\gamma)}{\partial t}\right|_{\rm S} + \left.\frac{\partial f_\gamma(E_\gamma)}{\partial t}\right|_{\gamma\gamma\to e^+e^-} + \left.\frac{\partial f_\gamma(E_\gamma)}{\partial t}\right|_{e^-\gamma\to e^-\gamma} \\ &+ \left.\frac{\partial f_\gamma(E_\gamma)}{\partial t}\right|_{\gamma e^-\to\gamma e^-} \left.\frac{\partial f_\gamma(E_\gamma)}{\partial t}\right|_{\gamma\gamma\to\gamma\gamma} + \left.\frac{\partial f_\gamma(E_\gamma)}{\partial t}\right|_{\gamma N\to e^+e^-N} + \left.\frac{\partial f_\gamma(E_\gamma)}{\partial t}\right|_{\rm exp.} \end{aligned} \tag{3.5.1}$$

$$\begin{aligned}\frac{\partial f_e(E_e)}{\partial t} &= \left.\frac{\partial f_e(E_e)}{\partial t}\right|_{\rm S} + \left.\frac{\partial f_e(E_e)}{\partial t}\right|_{\gamma\gamma\to e^+e^-} + \left.\frac{\partial f_e(E_e)}{\partial t}\right|_{e^-\gamma\to e^-\gamma} \\ &+ \left.\frac{\partial f_e(E_e)}{\partial t}\right|_{\gamma e^-\to\gamma e^-} + \left.\frac{\partial f_e(E_e)}{\partial t}\right|_{\gamma N\to e^+e^-N} + \left.\frac{\partial f_e(E_e)}{\partial t}\right|_{\rm exp.} . \end{aligned} \tag{3.5.2}$$

First of all, following the e.m. energy injection, a chain of pair production reactions takes place onto CMB photons followed by inverse Compton scattering (ICS) (if only electrons are injected, the cascade starts by an initial ICS event). Pair production has a threshold, and the spectrum will exhibit a sharp cutoff above

$$\epsilon_c = m_e^2/\epsilon_\gamma^{\max}\,, \tag{3.5.3}$$

where $\epsilon_\gamma^{\max}$ denotes the highest energy of the photon background onto which pairs can be effectively created. Indeed, all photons with energy higher than ϵ_c create a pair and therefore do not escape from the source.

The cascade starts at high-energy, where one of the particles (alternatively a photon and an electron) carries most of the incoming energy [437]. Once it reaches low energies, $e^\pm$ produced in pairs have the same energy $E_\gamma/2$, while the average energy loss fraction in an ICS event is [279]

$$f = \frac{\Delta E_e}{E_e} \simeq \frac{4}{3}\frac{E_e}{\epsilon_c} \tag{3.5.4}$$

where E_e is the incoming electron energy. Eventually, the energy of the outgoing γ-ray falls below the lowest possible energy for initiating a pair production. We thus expect the cascade to exhibit a transition at that energy ϵ_X. This transition corresponds to the energy of a outgoing photon experiencing a ICS event by a pair-produced $e^\pm$ at the lowest energy $\epsilon_c/2$:

$$\epsilon_X = fE_e = \frac{4}{3}\frac{E_e^2}{\epsilon_c} = \frac{\epsilon_c}{3}\,. \tag{3.5.5}$$

Above the transition energy the cascade is in a regime of "energy conservation" such that $EdN(E)/dE = const.$ On the other hand, below the threshold, the leading processes are $\gamma\gamma$-scattering and ICS which do not create new particles. It corresponds to a regime of "particle number conservation" $dN(E)/dE = const.$ Eventually, at very low energy $\gamma\gamma$-scattering scales as E_γ^6 and thus Compton scattering and pair-creation in nuclei start to play a role.

From previous considerations, one can readily show (e.g. Chapter VIII in [218]) that the cascade will lead to a *universal* "meta-stable" photon spectrum —attained on timescales much shorter than the thermodynamical equilibration scale— of the form:

$$\frac{dN_\gamma}{dE_\gamma} = \begin{cases} K_0\left(\frac{E_\gamma}{\epsilon_X}\right)^{-3/2} & \text{for } E_\gamma < \epsilon_X\,, \\ K_0\left(\frac{E_\gamma}{\epsilon_X}\right)^{-2} & \text{for } \epsilon_X \leq E_\gamma \leq \epsilon_c\,, \\ 0 & \text{for } E > \epsilon_c\,. \end{cases} \tag{3.5.6}$$

Refs. [231], [362], [498] are numerical studies leading to further justification of these parameters. The first two are based on Monte Carlo solutions while the last one works in the steady-state approximation allowing to find an integral solution to the Boltzmann equation. We shall adopt this approximation, well justified at high redshift, in chapter 5.

Once the non-thermal spectrum is computed, one can use it as an input for non-thermal BBN induced by nuclei photodissociation. Let us just emphasize again the main assumption behind the standard theory of e.m. cascade, namely that the injected energy is high enough for pair production. A key point that has been missed in the context of MeV to GeV energy injection is that this condition is *not* always fulfilled. Therefore, the standard result (3.5.6) is not always realised, in which case a new resolution of the set of Boltzmann equation is required with pair production switched off. Non-thermal BBN and this loophole to the standard theory of e.m. cascade are presented in chapter 5.

3.5.2 *Electromagnetic cascade close to and after recombination*

The second application that interests us concerns the generation of CMB anisotropies following any e.m. energy injection at redshift close to recombination and below. The problem at hand is now much more involved for a couple of reasons :

- One needs to follow the development of the cascade until atomic level energies, i.e. eV scale, while taking into account additional processes namely collisional heating, excitation and ionization for electrons/positrons and photoionizations for photons. At the lowest energies, $e^{\pm}$ annihilations must also be included.

- The Hubble rate is no longer much bigger than the total photon cooling rate (see fig. 35 - right panel) and the steady state approximation is no longer valid.

To accomodate for these complications, authors of Ref. [554] (refined in Refs. [261], [551]) have tackled the problem thanks to Monte Carlo simulations under a "factorization hypothesis" motivated by the observation of Fig. 35 - left panel: atomic processes (ionization, excitation, cooling) dominate over energy cooling processes at low energies, while they are irrelevant at high energies, where all the dynamics is dictated by the e.m. cascade development that we have discussed previously. Hence, the computation can be splitted in two parts.

- First, the high-energy cooling part, dealing with the redshifting due to Hubble expansion and the fact that the energy is not necessarly absorbed "on-the-spot", i.e. at the injection redshift. Note that now pair production is (almost) always off and the dominant cooling process is CS on electrons, whether free or bound. The outcome of the code is the fraction of the initial energy "deposited" to the medium, where the word "deposited" refers to low-energy particles below a given threshold (typically 3 keV, see Ref. [261] for a careful study of this threshold) which will subsequently lead to CMB spectral distortions and ionization, excitation and heating of the gas. The remaining energy corresponds to high-energy particles that can either free-stream until today, or be deposited at a lower redshift.

- Once the spectrum of low energy particles is known, another code takes care of the repartition between ionization, excitation and heating, which happens again at a rate much faster than the Hubble expansion. Eventually, particles with energy below the Lyman-α transition (10.2 eV) are considered lost and would contribute as spectral distortions of the CMB nowadays.

In practice, the high energy part is assumed to be independent of the ionization level x_e, but is highly redshift-dependent, while the low-energy part does not depend on the redshift but only on x_e. In fact, the low-energy code assumes that all initial particles are electrons *at* the threshold energy, the functions fitted on the output of the code are therefore independent of the injected high energy particles[7]. Anticipating a bit over our studies, we present the result of the low energy code from Ref. [261] compared to the older "SSCK" (Shull, Van Steenberg, Chen, Kamionkowski [155], [547]) prescription for the energy repartitions function χ in fig. 36. In Ref [261], this had been found to be rather accurate since the fraction of power deposited as ionization is relatively stable for $\sim$ 100 eV to 3 keV electrons. In this ref., it was shown that this approximation breaks down only for low

7 Photons between 10.2 eV and 3 keV do not behave like 3 keV electrons, but since $\mathcal{O}$(keV) photons mostly photoionize and then produce secondary electrons, this turns out not to be a too bad approximation [553].

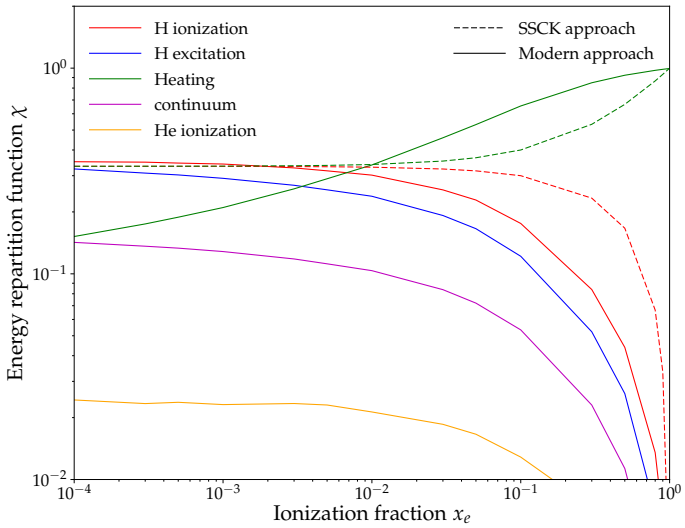

Figure 36: A comparison of the energy repartitions functions in the simple "SSCK" approximation and from the numerical resolution of Ref. [261]. The excitation fraction in the former case is equal to the ionization one and therefore it is not shown.

energy photons close to the Lyman-α transition, but such photons are produced in a relatively small quantity by high-energy particles. However, a more careful computation in Refs. [552], [553] showed that this factorization hypothesis could lead to wrong result for a specific energy range: at redshift below decoupling, photons upscattered by mildly relativistic electrons (i.e. below MeV kinetic energy) have too little energy to further interact with the gas. As a result, for such injected particles, the amount of energy going into ionization, excitation or heating of the gas is suppressed, relative to the case for 3 keV electrons, while lost photons are more numerous. In order to account for these complications, two strategies were adopted in Refs. [552], [553]: first going for the full resolution, dropping the factorization hypothesis, but assuming a fixed (standard) ionization history (ignoring reionization at low redshift); or relying on the 3 keV prescription, but correcting the deposited fraction to incorporate particles lost during the high energy cooling. This new scheme was dubbed "corrected 3 keV prescription" and those two approaches have been shown to yield similar results.

Another assumption that is still debated is whether neglecting the impact of the DM decay on the free electron fraction for the purpose of computing the efficiency of the energy deposition is reliable. Ref. [408], which extended the computation to include reionization, could test such hypothesis with an iterative approach. Obviously, increasing the ionization level tends to transfer energy devoted to ionization to heating. For CMB constraints, mostly dependent on the power going to ionization, the hypothesis is rather safe. However, for observables related to the IGM temperature (e.g. 21 cm), such an hypothesis could be poor, but this will require further (and harder) investigations. Note that, in the context of this approximation, one could argue that besides its limitations, the second approach (corrected 3 keV prescription) is more reliable in that it naturally incorporates the effect of a rising free electron fraction through the x_e-dependent low energy code (but not in the high-energy cooling code).

Alternatively, the authors of Ref. [233] have developed the MEDEA2 code which does not make the factorization hypothesis. Although very accurate in its low-energy part, the high-energy relies on the assumption of local energy deposition (or on-the-spot approximation), which leads to strong

overestimate of the deposited energy [554].
Analytical approach have also been introduced in Refs. [96], [189], [270], [445], which are unable to follow secondary cascade particles and assume either interaction only through ICS [270], [445] or take into account separately photoionization, ICS and Bethe-Heitler pair production [96], [189]. Those approaches typically lead to an overestimate of the impact of the e.m. energy injection, as in practice part of the energy is redshifted away or lost to sub-10.2 eV energy photons. More comments on these approaches are given in chapter 7.
In our studies we rely on the result of Ref. [553] under the "corrected 3 keV prescription", except when specified otherwise.

3.6 CMB spectral distortions

CMB spectral distortions, namely the fact that the actual CMB energy spectrum can have slight departure from a perfect blackbody, is a very important phenomenon that holds a wealth of information about cosmology and particle physics in the late and early universe. The main difficulty with their studies comes from the fact that the high accuracy measurement of the CMB blackbody spectrum by COBE/FIRAS in the 90's limits their amplitude to be smaller that one part in 10^5, i.e. those are smaller than temperature anisotropies [246]. This short review is based on Refs. [164], [168], [226].

3.6.1 *Basics of the thermalization problem*

The question one in practice wants to answer is "what processes led to the creation of the CMB spectrum that we observed today?" The first thing to say is that, if everything starts after reheating from a perfect blackbody, the uniform adiabatic expansion of the Universe alone (assuming no collisions and spatial perturbations) leaves the spectrum unchanged and simply shifts the temperature according to the famous law $T(z) = T_0(1+z)$. However, as soon as energy is injected into/taken from the thermal bath, a spectral distortion will momentarily be created, and the question is thus "was there enough time/were the processes efficient enough to restore the blackbody spectrum?" Typically following an energy injection (or removal) $\Delta\rho_\gamma/\rho_\gamma$, in order to thermalize the distortions, the photon field needs to rearrange its number density $\Delta N_\gamma/N_\gamma \sim (3/4)\Delta\rho_\gamma/\rho_\gamma$. Hence, photon changing number processes are needed, the most important ones being *double Compton scattering* $e^\pm + \gamma \leftrightarrow e^\pm + \gamma + \gamma$ (DC) and *bremsstrahlung* $e^\pm + X \leftrightarrow e^\pm + X + \gamma$ where X can be any nucleus or a free $e^\pm$. Those processes are efficient mainly at low photon energies. Hence, energy transport is required from the low to high energy part of the spectrum: this is achieved through *Compton scattering*, which we have already encountered in the context of CMB anisotropies. While those processes are efficient, any energy injection will simply result in changing the temperature of the blackbody, not creating any distortions. However those processes are not efficient at all epochs. Below $z_\mu \sim$ few $\times\, 10^6$, photon-number changing processes turn off, and energy injections typically lead to the creation of a chemical potential μ. On the other hand, Compton scattering becomes inefficient at redshift below $z < 50000$ and energy re-distribution is not achieved, leading to the creation of a non-zero comptonization-y parameter. Because no spectral distortion survives before $z \sim 10^7$, we restrict the discussion to $T < m_e$, i.e. after $e^\pm$ annihilations, when the thermal bath is simply composed of free e^-, p and γ. One might argue that if instead high energy photons are injected by some exotic processes, their energy will not fulfill this condition, however high-energy cooling mechanism (typically CS and ICS) are very efficient and on a very short

time scale bring those particles to energies to which our discussion applies.
We start by writing the Boltzmann equation for the *background* photons including the most important processes [164], [168], [226], [323], [329]

$$\frac{\partial f_\gamma(E_\gamma)}{\partial t} - \frac{\partial f_\gamma(E_\gamma)}{\partial t}\bigg|_{\rm exp.} = \frac{\partial f_\gamma(E_\gamma)}{\partial t}\bigg|_{\gamma e^-\to\gamma e^-} + \frac{\partial f_\gamma(E_\gamma)}{\partial t}\bigg|_{e^-\gamma\to e^-\gamma\gamma} + \frac{\partial f_\gamma(E_\gamma)}{\partial t}\bigg|_{e^- X\to e^- X\gamma} . \quad (3.6.1)$$

The collisional terms now include Compton scattering (in the non-relativistic limit $T \ll m_e$), double Compton scattering and bremsstrahlung. Trading E_γ for $x_e = E_\gamma/T_e$, they are given by (see e.g. Refs [164], [168], [226], [323], [329])

$$\begin{aligned}
\frac{\partial f_\gamma(x_e)}{\partial t}\bigg|_{\gamma e^-\to\gamma e^-} &= \frac{1}{\tau_K}\frac{1}{x_e^2}\frac{\partial}{\partial x_e}\left[x_e^4\left(\frac{\partial}{\partial x_e}f + f(1+f)\right)\right], &(3.6.2)\\
\tau_K &= \frac{m_e}{T_e}\frac{1}{n_e\sigma_T} .\\
\frac{\partial f_\gamma(x_e)}{\partial t}\bigg|_{e^- X\to e^- X\gamma} &= \frac{1}{\tau_{\rm ff}}\frac{e^{-x_e}\bar{g}_{\rm ff}(x_e)}{x_e^3}[1 - f(e^{x_e}-1)] , &(3.6.3)\\
\tau_{\rm ff}^{-1} &= 2\pi\sqrt{\frac{2\pi}{3}}n_e\sigma_T n_B\frac{\alpha}{T_e^3}\sqrt{\frac{m_e}{T_e}} .\\
\frac{\partial f_\gamma(x_e)}{\partial t}\bigg|_{e^-\gamma\to e^-\gamma\gamma} &= \frac{1}{\tau_{2\gamma}}\frac{1}{x_e^3}[1 - f(e^{x_e}-1)]I_{2\gamma} , &(3.6.4)
\end{aligned}$$

$$\tau_{2\gamma} = \frac{3\pi}{4\alpha\sigma_T n_e}\left(\frac{m_e}{T_e}\right)^2 , \qquad I_{2\gamma} = \int dx'_e (x'_e)^4 f(x'_e)[1+f(x'_e)] . \quad (3.6.5)$$

The first equation is the well known *Kompaneets equation*, and at equilibrium if other processes are irrelevant its solution is the Bose-Einstein distribution $f_{BE} = 1/(e^{x_e+\mu}-1)$. One can check that it verifies photon number conservation since

$$\frac{dn_\gamma}{dt} \propto \int dx_e x_e^2 \frac{\partial f}{\partial t} \propto \int dx_e \frac{\partial}{\partial x_e}\left[x_e^4\left(\frac{\partial}{\partial x_e}f + f(1+f)\right)\right] = 0 . \quad (3.6.6)$$

The second equation describing bremsstrahlung includes a Gaunt factor $\bar{g}_{ff}(x_e)$ related to the range of possible impact parameters in an event, whose value is typically [360]

$$\bar{g}_{ff}(x_e)\begin{cases} \frac{\sqrt{3}}{\pi}\ln\left(\frac{2.25}{x_e}\right) & \text{for} \quad x_e \le 0.37 , \\ 1 & \text{otherwise} . \end{cases} \quad (3.6.7)$$

The last equation represents double Compton scattering in the *soft photon limit* ($x_e < 1$ implies no recoil and a soft emitted photon). Actually, it is possible to go beyond the soft photon limit (i.e. for an arbitrary energy of the emitted photon) analytically by introducing the double Compton Gould factor $g_{\rm dc}$, which would modify the form of $I_{2\gamma}$ (e.g. Ref [164]).
The characteristic timescales for the processes are (almost) given by τ_K, $\tau_{\rm ff}$ and $\tau_{2\gamma}$. In fact, because of the additional frequency dependence in the equations, one expects that a process will freeze-out at different time for different frequencies, and typically the very low energy part of the spectrum tends to stay in full equilibrium longer. A comparison of these times with Hubble expansion shows that

DC is the dominant process above $z_\mu \sim 1.98\times 10^6(\Omega_b h^2/0.022)^{-2/5}[(1-Y_p/2)/0.88]^{-2/5}$, because it holds a high temperature dependence. Below this redshift both DC and bremsstrahlung are typically inefficient while comptonization still works. Because of the e^{-x_e} term in the DC equation, its efficiency is exponentially suppressed in the Wien tail of the distribution, and comptonization, i.e. doppler boosting of the photons due to scattering by electrons, is necessary to achieve thermalization. Below z_μ, in the so-called μ-era, DC and bremsstrahlung become inefficient and a μ distortion can be created as we work out in the next section.
However, before that, we should mention that comptonization can become inefficient as well. By computing the rate of change of the photon energy density due to Compton scattering $d\rho_\gamma/dt \propto \int x^2 df/dt|_{\rm CS} dx$ one finds,

$$\frac{d\rho_\gamma}{dt} = \frac{4}{t_K}\rho_\gamma\left[1-\frac{T_{\rm eq}}{T_e}\right] \qquad \text{with} \qquad T_{\rm eq} = \frac{h}{4k}\frac{\int d\nu f(1+f)\nu^4}{\int d\nu \nu^3 f} \tag{3.6.8}$$

which means that when $t_K/4$ becomes longer than the Hubble time, comptonization effectively turns off, further scattering will happen as a pure elastic event. This transition happens below $z_K \sim 5\times 10^4$, and the regime of spectral distortions therefore changes, entering in the so-called y-era.

3.6.2 *Usual analytical estimates: the μ and y parameters*

We now restrict the discussion to $z < z_\mu$, where only Compton scattering is relevant. As long as $z > z_K$, we know that a Bose-Einstein distribution is established rapidly at some temperature T_e and with chemical potential μ. The question we ask is, given an energy injection with $\delta\rho_\gamma$ and δn_γ, can we compute the temperature and the chemical potential of the distribution? For small $\mu \ll 1$, we may compute ρ and n and expand them around the Planck distribution in the following way

$$\rho_\gamma \approx \frac{T_e^4}{\pi^2}\int \frac{x_e^3 dx_e}{e^{x_e}-1} \stackrel{!}{=} \rho_\gamma^{\rm bb} + \delta\rho_\gamma = \frac{\pi^2}{15}T_\gamma^4(1+\epsilon)\,, \tag{3.6.9}$$

$$n_\gamma \approx \frac{T_e^3}{\pi^2}\int \frac{x_e^2 dx_e}{e^{x_e+\mu}-1} \stackrel{!}{=} n_\gamma^{\rm bb} + \delta n_\gamma = \frac{2\zeta(3)}{\pi^2}T_\gamma^3(1+\alpha)\,, \tag{3.6.10}$$

where the quantity $\epsilon \equiv \delta\rho_\gamma/\rho_\gamma^{\rm bb}$ and $\alpha \equiv \delta n_\gamma/n_\gamma^{\rm bb}$ have been introduced. On the other hand, one can expand the integrals as

$$\rho_\gamma = \frac{T_e^4}{\pi^2}\int \frac{x_e^3 dx_e}{e^{x_e+\mu}-1} = \frac{T_e^4}{\pi^2}\left[\int \frac{x_e^3 dx_e}{e^{x_e+\mu}-1} - 3\mu\int \frac{x_e^2 dx_e}{e^{x_e}-1}\right] = \frac{T_e^4}{\pi^2}\left[\frac{\pi^4}{15} - 6\zeta(3)\mu\right] \tag{3.6.11}$$

$$n_\gamma = \frac{T_e^3}{\pi^2}\int \frac{x_e^2 dx_e}{e^{x_e+\mu}-1} = \frac{T_e^3}{\pi^2}\left[\int \frac{x_e^2 dx_e}{e^{x_e}-1} - 2\mu\int \frac{x_e dx_e}{e^{x_e}-1}\right] = \frac{T_e^3}{\pi^2}\left[2\zeta(3) - \mu\frac{\pi^2}{3}\right]. \tag{3.6.12}$$

It is possible to invert the equations to isolate μ and $\delta = T_e/T_\gamma - 1$

$$\delta \simeq 0.64\frac{\delta\rho_\gamma}{\rho_\gamma^{\rm bb}} - 0.52\frac{\delta n_\gamma}{n_\gamma^{\rm bb}}\,, \quad \mu \simeq 1.4\left(\frac{\delta\rho_\gamma}{\rho_\gamma^{\rm bb}} - \frac{4}{3}\frac{\delta n_\gamma}{n_\gamma^{\rm bb}}\right). \tag{3.6.13}$$

In the absence of photon number changing processes, then $\delta n_\gamma = 0$, which leads to the standard estimate [571]

$$\mu \simeq 1.4\frac{\delta\rho_\gamma}{\rho_\gamma^{bb}}\,. \tag{3.6.14}$$

We can also compute what the distortions look like in frequency space at the level of the distribution itself, i.e. $\delta f \approx f^{\rm bb} - f^{\rm BE}$. A small complication comes from the fact $f^{\rm BE}$ depends both on T_e and μ. In order to isolate the spectral shape of the "pure" μ component $M(x)$, one needs to use the fact that Compton scattering conserves the photon number $\int x^2 M(x) dx = 0$ and to normalise the relative change of the photon energy density to unity ($\delta\rho_\mu/\rho^{\rm bb} = 1$). This yields

$$M(x) \approx 1.4 \frac{e^x}{(e^x-1)^2}\left[0.4561x - 1\right]. \tag{3.6.15}$$

We now focus on the opposite limit at $z < z_K$. We first write the Kompaneets equation as a function of $x \equiv E_\gamma/T_\gamma = (T_e/T_\gamma)x_e$ and switch for a new pseudo-time variable, the optical depth $\tau = c\sigma_T n_e dt$

$$\left.\frac{\partial f_\gamma(x_e)}{\partial \tau}\right|_{\gamma e^- \rightarrow \gamma e^-} = \frac{T_e}{x^2 m_e}\frac{\partial}{\partial x}\left[x^4\left(\frac{\partial}{\partial x}f + \frac{T_\gamma}{T_e}f(1+f)\right)\right]. \tag{3.6.16}$$

Let us start with a blackbody distribution at $\tau = 0$ and consider the distortion after a very short pseudo-time $\delta\tau \ll 1$

$$\delta f \approx \delta\tau \times \frac{T_e}{x^2 m_e}\frac{\partial}{\partial x}\left[x^4\left(\frac{\partial f^{\rm bb}}{\partial x} + \frac{T_\gamma}{T_e}f^{\rm bb}(1+f^{\rm bb})\right)\right] \tag{3.6.17}$$

Since $\partial_x f^{\rm bb} = -f^{\rm bb}(1+f^{\rm bb})$ we can rewrite

$$\begin{aligned}
\delta f &\approx \frac{\delta\tau(T_\gamma - T_e)}{x^2}\frac{\partial}{\partial x}x^4 f^{\rm bb}(1+f^{\rm bb}) \\
\Leftrightarrow \delta f &\approx \delta\tau\frac{(T_\gamma - T_e)}{m_e}\left[4x f^{\rm bb}(1+f^{\rm bb}) - x^2 f^{\rm bb}(1+f^{\rm bb})(1+2f^{\rm bb})\right] \\
&\equiv \delta\tau\frac{(T_e - T_\gamma)}{m_e}Y_{\rm SZ}(x)\,,
\end{aligned} \tag{3.6.18}$$

where we have introduced the *Compton-y* distortion $Y_{\rm SZ}(x)$ (originally discussed in Ref. [606]) which can be explicitly computed thanks to the useful relations $f^{\rm bb}(1+f^{\rm bb}) = e^x/(e^x-1)^2$ and $(1+2f^{\rm bb}) = \coth(x/2)$

$$Y_{\rm SZ}(x) = x\frac{e^x}{(e^x-1)^2}\left[x\coth(x/2) - 4\right]. \tag{3.6.19}$$

The important time scale of the problem is determined by the *Compton-y* parameter

$$y = \int_0^\tau \frac{(T_e - T_\gamma)}{m_e}d\tau' = \int_0^t \frac{(T_e - T_\gamma)}{m_e}\sigma_T n_e dt'\,. \tag{3.6.20}$$

Like the μ distortion, we can quickly relate the y parameter to any energy injection $\delta\rho_\gamma$ by

$$\delta\rho_\gamma = y\int x^3 Y_{\rm SZ}(x)dx = 4y\rho_\gamma^{\rm bb} \tag{3.6.21}$$

while of course we still have $\delta n_\gamma \propto \int x^2 Y_{\rm SZ}(x)dx = 0$. We plot in fig. 37 the spectral shape of the "pure" μ and y distortions compared to the blackbody spectrum. Of course in a real case, one would observe a superpositions of those. The simple approximations that we have introduced can be refined to take into account that i) the thermalization efficiency does not abruptly vanish at $z \simeq z_\mu$; ii) the transition between the μ and y era at z_K is not abrupt either. Fits calibrated to numerical solutions yield [170]:

$$\frac{\mu}{1.401} = \left[\frac{\Delta\rho_\gamma}{\rho_\gamma}\right]_\mu \simeq \int \mathcal{J}_{\rm bb}\mathcal{J}_\mu \frac{1}{\rho_\gamma}\left.\frac{dE}{dt}\right|_{e.m.} dt, \qquad \frac{y}{4} = \left[\frac{\Delta\rho_\gamma}{\rho_\gamma}\right]_y \simeq \int \mathcal{J}_{\rm bb}\mathcal{J}_y \frac{1}{\rho_\gamma}\left.\frac{dE}{dt}\right|_{e.m.} dt\,. \tag{3.6.22}$$

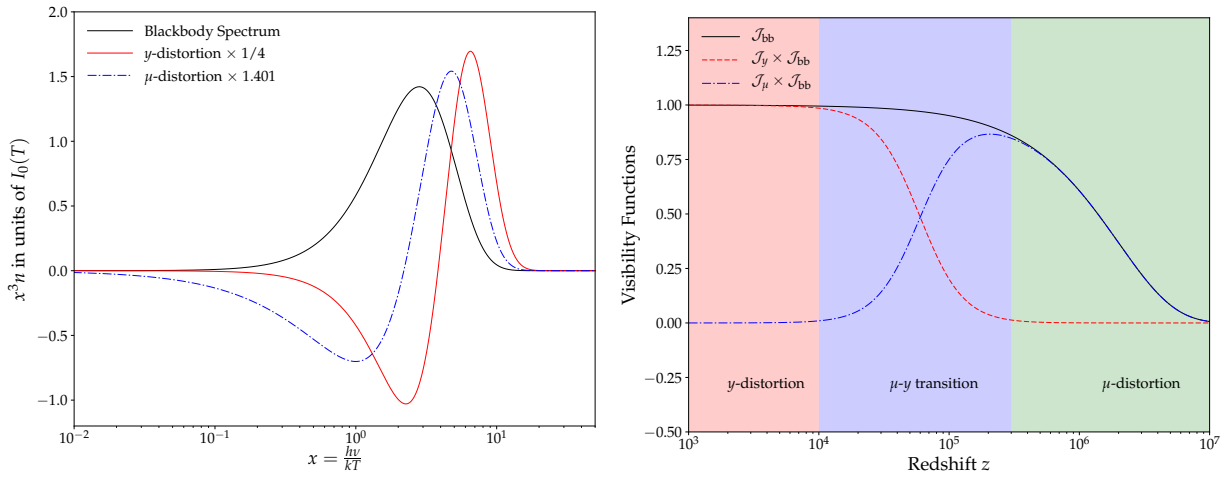

Figure 37: *Left panel:* Comparison of the y and μ spectral distortions to the blackbody spectrum. The spectra are normalized to the blackbody specific intensity $I_0(T) = (2h/c^2)(kT/h)^3 \approx 270$ MJy sr$^{-1}(T/2.725\text{K})^3$. Adapted from Ref. [168]. *Right panel:* The corresponding visibility functions.

where the visibility functions are given by

$$\mathcal{J}_{\rm bb}(z) \approx \exp[-(z/z_\mu)^{5/2}]\,, \quad \mathcal{J}_y(z) \approx \left[1 + \left(\frac{1+z}{6\times 10^4}\right)^{2.58}\right]^{-1}, \quad \mathcal{J}_\mu(z) \approx 1 - \mathcal{J}_y\,. \tag{3.6.23}$$

and $\mathcal{J}_\mu$ was chosen to ensure energy conservation. These equations can be trusted until the baryon drag time, for $z \geq 200$, but this is sufficient for our purpose. We show the visibility functions used in this analysis in fig. 37, right panel.

One can go beyond these simple analytical considerations thanks to numerical solutions. In our analysis, we neglect the fact that the exact transition era between y and μ is not simply a superposition of the two spectral distortions. From principal component analysis (PCA) one can define eigenvectors of the distortions, as done in Ref. [175]. The residual distortions created in μ-y transition era are usually dubbed r-distortions and enable to probe the history of the energy injection [169], [175]. Finally, let us mention the subtlety that the μ distortion as we defined it does not exactly correspond to an eigenvector: There is a slight deviation below $z \leq$ few$\times 10^5$, which will be neglected in the following. This is safe to derive constraints. However, if a signal is found, adopting the full Green's / PCA formulation would be needed [170], [175].

3.6.3 *Some sources of spectral distortions*

There are many potential sources of spectral distortions both from *standard* and *exotic* processes. We shall simply give a list of the ones expected *within* ΛCDM (or very basic extensions) based on Ref. [172], and discussed their potential discovery with the proposed next generation experiment for spectral distortion PIXIE, which improves sensitivity on the μ and y parameters by about three orders of magnitude [374].

- A major signal is expected from the reionization era. Once the Universe is reionized below $z_{\rm re} \sim 10$, a y-distortion is expected to be created by the up-scattering of photons by free-

electrons. A simple estimate assuming a sharp reionization at $z_{\rm re}$ and fixed electron temperature $T_{\rm re}$ (in a purely matter-dominated universe) gives

$$\begin{aligned} y &= \frac{\sigma_T}{T_{\rm re} n_e^0} m_e (1+z_{\rm re}+1)^2 \int_0^{z_{\rm re}} dz \frac{dt}{dz} (1+z)^5 \\ &\simeq 6.8\times 10^{-8} \left(\frac{\omega_b}{0.022}\right) \left(\frac{0.13}{\omega_M}\right)^{1/2} \left(\frac{1+z_{\rm re}}{11}\right)^{3/2} \left(\frac{T_{\rm re}}{10\,{\rm eV}}\right). \end{aligned} \tag{3.6.24}$$

The COBE/Firas limit $y < 10^{-5}$ translates into a bound on the reionization redshift

$$z_{\rm re} < 50 \left(\frac{T_{\rm re}}{10\,{\rm eV}}\right)^{2/3}. \tag{3.6.25}$$

- Moreover, in cluster of galaxies, one expects the temperature of the electron to be much higher, typically $T \sim$few keV, while densities are enhanced with respect to the background Universe. This leads to the so-called *thermal Sunyaev-Zeldovich effect* (tSZ), as originally studied in Ref. [572], which can be used to map the galaxy clusters by CMB experiments such as *Planck* [18]. Moreover, the motion of cluters induces in addition a *kinetic* contribution to the SZ effect (kSZ), which is often several times smaller than the tSZ.
  The signal actually depends on the cluster one looks at, but one can define an average over all sky (or y monopole), in which case the total signal expected depends on the cluster distribution or *halo function* dn/dM. Typically one expects to see a total distortion at the order of $\langle y\rangle_{\rm clust} \sim 2\times 10^{-6}$, a *guaranteed* discovery with a PIXIE-like experiment [172], [303], but also constitutes a major foreground for more exotic searches[8]. In our studies, we assume that this signal can be disentangled, and we therefore neglect this contribution.

- As originally introduced by authors of Ref. [570], another exotic signal corresponds to the damping of small-scale density fluctuations set up by inflation. The approximate heating rate is given by [176]

$$\frac{1}{\rho_\gamma}\frac{dE}{dt} \approx 4A^2 \partial_z k_D^{-2} \int_{k_{\rm min}}^{\infty} \frac{k^4 dk}{2\pi^2} P_\zeta(k) e^{-2\frac{k^2}{k_D^2}}, \tag{3.6.26}$$

  where P_ζ defines the usual curvature power spectrum of scalar perturbations and k_D is the photon damping scales, both quantities beeing described in chapter 2. A is a heating efficiency, which is equal to $A^2 \approx 0.813$ for adiabatic modes. The minimal scale k that contributes to the integral is usually set at $k \approx 0.1{\rm Mpc}^{-1}$ [169]. Within ΛCDM at its actual best-fit values this signal lies between a μ and a y distortion (smaller scales damp earlier), and is right at the edge of PIXIE's sensitivity, $\mu \sim 2\times 10^{-8}$ [172]. A null detection of μ could teach us about a significant negative running of the spectral index [136].

- Because the temperature of baryonic matter decreases at a faster pace than radiation ($(1+z)^2$ instead of $(1+z)$), one expects that the coupling of baryons to photons until the baryon drag time leads to a *negative* μ and y distortion, since photons need to transfer their energy to heat the baryons. The effective energy extraction term is given by [164]

$$\frac{1}{\rho_\gamma}\frac{dE}{dt} \approx -\frac{3}{2}\frac{n_H(1+f_{\rm He}+x_e)kT_\gamma}{\rho_\gamma(1+z)}. \tag{3.6.27}$$

8 At these high temperatures small relativistic corrections become noticeable. These corrections as well are well detectable by PIXIE [303] and allow to break the degeneracy between the electron density and temperature in the intracluster medium.

The difficulty is that it is a very weak signal, one order of magnitude below the damping one, and unfortunately it partially compensates it [172].

- We have already mentioned in section 1.3.3.6 the *cosmological recombination lines*, which are fingerprint of the recombination era, encoding very distinct spectral features of the recombination processes. We refer to that section and ref. [173] for more details.

- Exotic decays and annihilations of course provide an important source of spectral distortions. We compare current and future sensitivity on those models, together with other cosmological probes, in chapter 5 and 6.

Part II

SIGNATURES OF DECAY AND ANNIHILATIONS OF MASSIVE RELICS IN COSMOLOGICAL OBSERVABLES

It has been known for a long time that Big Bang Nucleosynthesis and the Cosmic Microwave Background are very sensitive probes of physics beyond the Standard Model, being sensitive even to purely gravitational effects. In the case of BBN, we have identified a loophole in the standard theory of electromagnetic cascades onto a photon background, with consequences of utmost importance for new physics searches. First of all, it can increase current non-thermal BBN bounds by up to more than one order of magnitude. But perhaps the most spectacular consequence of this loophole is the possibility of purely electromagnetic solutions to the so-called "cosmological lithium problem", which were thought to be excluded by other cosmological constraints. We present our studies of non-thermal BBN and a solution to the lithium problem in chapter 5, including a comparison with contraints coming from spectral distortions of the CMB blackbody spectrum. Those constraints are the dominant ones when the electromagnetic energy injection occurs below $\tau \sim 10^{12}$ s.

On the other hand, CMB anisotropies constitute by far the most sensitive probe available of massive relics after that time. First of all, as we have seen in sec. 2.2.3 it yields the most precise measurements of $\omega_{\rm cdm}$ to date. But more information can potentially be extracted from their study, especially about hypothetic decays or annihilations of those relics in the Universe.

For instance, one can see from the result of the line of sight formalism, eq. (2.2.55a), that any modifications of the gravitational potential wells at the last scattering surface, or their time evolution, can in turn lead to a modification of the SW and ISW terms. These effects are studied in chapter 4 in order to characterize the impact of a massive relic decaying into invisible radiation.

However, the CMB power spectra also depend on the visibility function g and optical depth $\tau_{\rm depth}$. This means that modifications of the background ionization history can as well have a strong impact on the observed C_ℓ's. The effects of a electromagnetically decaying particles are studied in chapter 6, while annihilations of DM particles, with a special emphasize on the impact of halo formations at late time and its synergy with star reionization, is the topic of chapter 7. Chapter 5 is adapted from publications in Physical Review Letters [491] and Physical Review D [495], while chapters 4, 6 and 7 are adapted from papers published in JCAP, namely Refs. [490], [493], [494] and PRD [492].

4

DARK MATTER INVISIBLE DECAY

This chapter is adapted from a publication in JCAP [494].

4.1 Introduction and models

The current concordance model of cosmology (ΛCDM, supplemented by the inflationary paradigm) discussed in previous chapters has been established very robustly over the past couple of decades, surviving a large number of tests and cross-checks. Nonetheless, it remains a *parametric* model, with most of the energy content of the universe in a "dark" sector whose nature remains puzzling. In particular, although there are plenty of proposed candidates for what makes the dark matter (DM) of the Universe, none of them have been detected through smoking gun probes independent from the gravitational ones, and thus DM lacks identification.

In the quest for the nature of DM, cosmology itself provides useful diagnostics, being sensitive to a large range of spatial and time scales. We have argued in sec. 3.4.2 that, at the very least, a finite DM lifetime would leave (mostly) linear cosmological signatures, purely via gravitational effects. Often, cosmological constraints are not as constraining as observables targeted to specific DM models (such as gamma-ray fluxes for vanilla WIMP DM models). Yet, they are valuable as essentially based on linear theory, thus setting the robust and model-independent yardstick against which we can gauge the strength of other constraints—in general depending on non-linear physics, non-gravitational interactions, and a number of astrophysical assumptions.

In this work, we provide several improvements as well as an important generalisation over the treatment in Ref [70]. First and foremost, we allow for a fraction $f_{\rm dcdm}$ of decaying DM smaller than unity. One immediate consequence is that a much larger parameter space for the decay width (or inverse lifetime) $\Gamma_{\rm dcdm}$ is now open, with a richer set of consequences on the CMB anisotropy pattern and power spectrum modifications which we shall duly describe. One (perhaps phenomenologically compelling) motivation for such a refined study is the recurring recent claim that some tensions in global fits of cosmological observables, like CMB ones vs. the low-redshift determination of σ_8 and the Hubble parameter [18], [302], [508], [509], may be resolved due to a non-trivial time evolution of the DM content of the universe, such as the one associated with a (partial) decay of the DM constituents [99], [186], [232]. From a theoretical point of view, the case $f_{\rm dcdm} < 1$ is also interesting, with several possible physical interpretations: 1) DM may be multi-component, with one unstable component disintegrating into (dark) radiation; 2) DM may decay into several particles, including a fraction $(1 - f_{\rm dcdm})$ of cold daughter particles and a fraction $f_{\rm dcdm}$ of (dark) relativistic daughter particles, such as neutrinos, gravitons, or some BSM (beyond the standard model) species.

Throughout the study, we shall assume that the stable fraction of the DM (or byproduct of the DM disintegration) is exactly cold. This can be certainly achieved in scenario 1), while being an approximation in scenario 2): the recoil received by the daughter non-relativistic particle(s) is responsible for some velocity dispersion in the daughter DM phase-space distribution. A number of specific implications of these so-called superWIMP candidates have been known since more than a decade [152]. Dealing with this scenario would require making specific assumption on the final state kinematics. Qualitatively, we expect our bounds to be still valid for scenarios of type 2) as well, since the sizable DM free streaming would impose further and typically more stringent constraints. The analysis presented in [49], which focuses on a scenario of type 2) (i.e. with a specific choice of DM two-body decay into radiation plus one massive relic) obtains indeed tighter constraints than the present work.

The generality of purely gravitational constraints does not imply, however, that such bounds are always "weak": for several particle physics candidates without sizable signals in non-gravitational channels, they are the strongest available ones. For instance, this is the case for a number of models, including the Majoron scenario and merging PBH, we introduced in sec. 3.4.2. This work is structured as follows: in Sec. 4.2, for the sake of completeness and in order to correct an error present in past literature, we explicitly report the key equations solved. In Sec. 4.3 we describe the effects of the decaying DM models on CMB and power spectrum observables. We also discuss some potential degeneracies with other physical effects, notably the one of massive neutrinos. In Sec. 4.4 we present our results, while in section 4.5, after a discussion, we report our conclusions.

4.2 Boltzmann equations for the decaying Dark Matter

We wish here to recall the main equations describing the gravitational impact of the DM decay, assuming that the decay products are ultrarelativistic and invisible—hence dubbed "dark radiation", denoted with the subscript "dr". Following the standard procedure, we consider small perturbations over a homogeneous background and hence, we split up the evolution equations for the energy density and momenta of the decaying cold DM (denoted with the subscript "dcdm") and its daughter radiation between zeroth and first order contributions. Higher orders terms are neglected. The overall DM abundance is denoted with the subscript "dm"; $f_{\rm dcdm}$ is the ratio of the decaying DM fraction to the total one. Its complement to one is also dubbed stable DM fraction, denoted with subscript "sdm". A full derivation can be found in appendix C.

4.2.1 *Background equations*

To take dark matter decay into account, one can for instance modify the stress energy tensor of cold DM and dark radiation by respectively subtracting and adding a decay term. By considering the covariant conservation of $T_{\mu\nu}$ that follows from Bianchi identities, one would arrive at [354] (see also [70])

$$\rho'_{\rm dcdm} = -3\frac{a'}{a}\rho_{\rm dcdm} - a\Gamma_{\rm dcdm}\rho_{\rm dcdm} \ , \tag{4.2.1}$$

$$\rho'_{\rm dr} = -4\frac{a'}{a}\rho_{\rm dr} + a\Gamma_{\rm dcdm}\rho_{\rm dcdm} \ . \tag{4.2.2}$$

Above and henceforth, prime quantities denote a derivative with respect to conformal time; $\Gamma_{\rm dcdm}$ is the decay rate defined with respect to proper time, which in a specific model can be computed

as customary by integrating over the phase space (the modulus square of) the transition matrix element. Using the public version of the CLASS[1] [109], [390] Einstein-Boltzmann solver, it is possible to specify the total fractional energy density in both dcdm and dr, either *today* ($\Omega_{\rm dcdm}+\Omega_{\rm dr}$) or *initially* ($(\Omega_{\rm dcdm}+\Omega_{\rm dr})^{\rm ini}$). The latter parameter is defined precisely in [70], but can be loosely understood as "the value of the initial densities $\rho_{\rm dcdm}(t_{\rm ini})$ and $\rho_{\rm dr}(t_{\rm ini})$ such that if we were to take $\Gamma_{\rm dcdm}=0$, we would get a fractional density $\Omega_{\rm dcdm}+\Omega_{\rm dr}=(\Omega_{\rm dcdm}+\Omega_{\rm dr})^{\rm ini}$ today"; the splitting between $\rho_{\rm dcdm}(t_{\rm ini})$ and $\rho_{\rm dr}(t_{\rm ini})$ is computed automatically in order to take consistently into account the tiny amount of transfer of energy from dcdm to dr between $t\longrightarrow 0$ and $t_{\rm ini}$, assuming that there is no dark radiation for $t\longrightarrow 0$. This parametrisation has the advantage of preserving the early cosmological evolution until DM starts to decay.

4.2.2 *Perturbation equations in gauge invariant variables*

In ref. [70], the scalar perturbations equations at zeroth and first order had been obtained starting from the continuity and Euler equations, which describes the exchange of energy and momenta between the decaying DM and the dark radiation. Here, we report the result starting from the Boltzmann equation describing the evolution of the two species, which is also needed to derive the Boltzmann hierarchy of the dark radiation. The full Boltzmann equation, with decay term, written in terms of conformal time and momentum is

$$\frac{df}{d\tau}=\frac{\partial f}{\partial\tau}+\frac{\partial f}{\partial x^i}\frac{dx^i}{d\tau}+\frac{\partial f}{\partial q}\frac{dq}{d\tau}+\frac{\partial f}{\partial n^i}\frac{dn^i}{dt}=\pm a\Gamma_{\rm dcdm}f_{\rm dcdm}\equiv\pm D\,, \tag{4.2.3}$$

where the $-$ $(+)$ sign refers to the decaying DM (dark radiation). Let us stress an important point, that has been overlooked in a previous study deriving bounds on the model we are dealing with [335]. As long as one does not consider perturbations in the distribution, the previous form of the decay term still holds. However, the decay term D is *not* a gauge invariant quantity. At the level of perturbations, such a simple form of the decay rate is only valid in the gauge *comoving* with the decaying DM, which is a restriction of the synchronous gauge to a system in which the velocity divergence of the decaying DM vanishes. Note that, as pointed out in Ref. [70], the comoving gauge of the DM and decaying DM are the same for adiabatic initial conditions. Hence we can work with the synchronous gauge comoving with all DM, in which metric perturbations read

$$ds^2=a^2(\tau)\Big\{-d\tau^2+(\delta_{ij}+H_{ij})dx^idx^j\Big\} \tag{4.2.4}$$

(with in Fourier space $H_{ij}=\hat{k}_i\hat{k}_jh+(\hat{k}_i\hat{k}_j-\frac{1}{3}\delta_{ij})6\eta$), and with the newtonian gauge with metric perturbations

$$ds^2=a^2(\tau)\Big\{-(1+2\psi)d\tau^2+(1-2\phi)dx^idx^j\Big\}\,. \tag{4.2.5}$$

One can relate both gauges via the following identities

$$\psi = \mathcal{H}\alpha+\alpha' \tag{4.2.6}$$

$$\phi = \eta-\mathcal{H}\alpha \tag{4.2.7}$$

$$\delta(new) = \delta(syn)+\frac{\bar{\rho}'}{\bar{\rho}}\alpha \tag{4.2.8}$$

$$\theta(new) = \theta(syn)+k^2\alpha \tag{4.2.9}$$

1 class-code.net

where $\alpha \equiv \frac{(6\eta+h)'}{2k^2}$. All definitions of the potentials and perturbations variables can be found in Ref. [412]. We will use these relations later in order to get the evolution equations in the newtonian gauge. Starting with the decaying DM, in the comoving synchronous gauge one can re-express eq. (4.2.3) in the following form:

$$\frac{\partial f_{\rm dcdm}}{\partial \tau} + \frac{\partial f_{\rm dcdm}}{\partial x^i}\frac{p^i}{E} + p\frac{\partial f_{\rm dcdm}}{\partial p}\left[\eta' - \frac{1}{2}\left(h' + 6\eta'\right)\left(\hat{k}\cdot n\right)^2 - \mathcal{H}\right] = -D \tag{4.2.10}$$

where we have now traded q for p (the physical momentum) to let the expansion term appear explicitly. Integrating the distribution over the phase-space and using the fact that decaying DM is pressureless, it is straightforward to get

$$\rho'_{\rm dcdm} + \frac{\partial(\rho_{\rm dcdm} v^i_{\rm dcdm})}{\partial x^i} + \frac{1}{2}h'\rho_{\rm dcdm} + 3\mathcal{H}\rho_{\rm dcdm} \;=\; -a\Gamma\rho_{\rm dcdm}\,. \tag{4.2.11}$$

We introduce the usual notation $\rho_{\rm dcdm} = \bar{\rho}_{\rm dcdm}[1+\delta_{\rm dcdm}]$ and set in our gauge $\theta_{\rm dcdm} = \partial_i v^i_{\rm dcdm} = 0$. At this level, if we were to collect all zeroth order terms, we would arrive at Eq. (4.2.1). Collecting instead all first order terms and dividing by $\bar{\rho}_{\rm dcdm}$, one gets

$$\delta'_{\rm dcdm} = -\frac{h'}{2}\,. \tag{4.2.12}$$

In a similar way, taking the divergence of the first moment of eq. (4.2.11) leads to

$$\theta'_{\rm dcdm} \;=\; -\mathcal{H}\theta_{\rm dcdm}, \tag{4.2.13}$$

which is consistent with keeping $\theta_{\rm dcdm} = 0$ in the comoving synchronous gauge. We can make use of relations (4.2.6-4.2.9) to express previous equations in the newtonian gauge:

$$\delta^{(n)'}_{\rm dcdm} \;=\; -a\Gamma\phi + 3\psi - \theta^{(n)}_{\rm dcdm}\,, \tag{4.2.14}$$

$$\theta^{(n)'}_{\rm dcdm} \;=\; -\mathcal{H}\theta^{(n)}_{\rm dcdm} + k^2\phi\,. \tag{4.2.15}$$

Following the development of Ref. [70], we introduce the gauge invariant variables $\mathfrak{m}_{\rm cont}$ and $\mathfrak{m}_\psi$ to write these equations as

$$\delta'_{\rm dcdm} \;=\; -\theta_{\rm dcdm} - \mathfrak{m}_{\rm cont} - a\Gamma\mathfrak{m}_\psi\,, \tag{4.2.16}$$

$$\theta'_{\rm dcdm} \;=\; -\mathcal{H}\theta_{\rm dcdm} + k^2\mathfrak{m}_\psi \tag{4.2.17}$$

where the expression of the metric source terms in the synchronous and newtonian gauges are given in table 10.

	Synchronous	Newtonian
$\mathfrak{m}_{\rm cont}$	$h'/2$	$-3\phi'$
$\mathfrak{m}_\psi$	0	ψ
$\mathfrak{m}_{\rm shear}$	$(h'+6\eta')/2$	0

Table 4: Continuity and euler type of metric source terms for scalar perturbations in synchronous and Newtonian gauge.

Although these equations are sufficient to describe the dynamics of the decaying DM, one needs to write the full Boltzmann hierarchy to follow the perturbations in the dark radiation. For that purpose, several strategies can be adopted; we follow again the formalism of Ref. [70]. We introduce the perturbations of the integrated phase-space distribution function and expand it over Legendre polynomials $\mathcal{P}_\ell$ in the following way

$$F_{\rm dr} \equiv \frac{\int dqq^3 f_{\rm dr}^{(0)} \Psi_{\rm dr}}{\int dqq^3 f_{dr}^{(0)}} r_{\rm dr} \equiv \sum_\ell (-i)^\ell (2\ell+1) F_{{\rm dr},\ell}(t,\vec{k}) \mathcal{P}_\ell(\mu) \tag{4.2.18}$$

where $\Psi_{\rm dr}$ is defined at the level of the perturbed phase-space distribution:

$$f_{\rm dr}(\vec{x},p,\vec{n},\tau) = f_{\rm dr}^{(0)}(p,\tau)(1+\Psi_{\rm dr}(\vec{x},p,\vec{n},\tau)) \,, \tag{4.2.19}$$

and $r_{\rm dr}$ is defined as

$$r_{\rm dr} \equiv \frac{\bar{\rho}_{\rm dr} a^4}{\rho_{cr,0}} \,. \tag{4.2.20}$$

$\rho_{cr,0}$ is the critical energy density today (where $a_0 = 1$), introduced to make $r_{\rm dr}$ dimensionless. The use of $r_{\rm dr}$ will help us to cancel the time-dependence of $F_{\rm dr}$ due to the background distribution function f_{dr}^0. The derivative of $r_{\rm dr}$ is simply

$$r'_{\rm dr} = a\Gamma_{\rm dcdm} \frac{\bar{\rho}_{\rm dcdm}}{\bar{\rho}_{\rm dr}} r_{\rm dr} \,, \tag{4.2.21}$$

(here we corrected a typo with respect to eq. (2.16) Ref. [70]). Splitting between $m = 0, 1, 2$ and $m > 2$ leads to the following gauge-independent hierarchy

$$F'_{\rm dr,0} = -kF_{\rm dr,1} - \frac{4}{3} r_{\rm dr} \mathfrak{m}_{\rm cont} + r'_{\rm dr}(\delta_{\rm dcdm} + \mathfrak{m}_\psi) \,, \tag{4.2.22}$$

$$F'_{\rm dr,1} = \frac{k}{3} F_{\rm dr,0} - \frac{2k}{3} F_{\rm dr,2} + \frac{4k}{3} r_{\rm dr} \mathfrak{m}_\psi + \frac{r'_{\rm dr}}{k} \theta_{\rm dcdm} \,, \tag{4.2.23}$$

$$F'_{\rm dr,2} = \frac{2k}{5} F_{\rm dr,1} - \frac{3k}{5} F_{\rm dr,3} + \frac{8}{15} r_{\rm dr} \mathfrak{m}_{\rm shear} \,, \tag{4.2.24}$$

$$F'_{{\rm dr},\ell} = \frac{k}{2\ell+1} \left(\ell F_{{\rm dr},\ell-1} - (\ell+1) F_{{\rm dr},\ell+1} \right) \qquad \ell > 2. \tag{4.2.25}$$

The expression for $\mathfrak{m}_{\rm shear}$ in newtonian and synchronous gauge is given in table 10. This set of equations must be truncated at some maximum multipole order $\ell_{\rm max}$. To do so, we use the improved truncation scheme of Ref. [412] which has been generalised to spatial curvature in Ref. [397].
To check how the multipole moments transform, one can use their relations to the standard variables δ and θ, as well as the gauge-invariant variable σ, which describes the anisotropic stress developing in the fluid:

$$F_{\rm dr,0} = r_{\rm dr}\delta_{\rm dr} \,, \qquad F_{\rm dr,1} = \frac{4r_{\rm dr}}{3k}\theta_{\rm dr} \,, \qquad F_{\rm dr,2} = 2\sigma r_{\rm dr} \,. \tag{4.2.26}$$

Eqs. (4.2.6-4.2.9) then immediately tell us how these moments change under a transformation from the synchronous to newtonian gauge:

$$F^{(s)}_{\rm dr,0} = F^{(n)}_{\rm dr,0} - r_{\rm dr} \frac{\bar{\rho}'_{\rm dr}}{\bar{\rho}_{\rm dr}} \alpha \,, \qquad F^{(s)}_{dr,1} = F^{(n)}_{\rm dr,1} - \frac{4r_{\rm dr}k}{3}\alpha \,, \tag{4.2.27}$$

whereas $F_{\rm dr,2}$ is gauge invariant. Using eq. (4.2.26), one can easily check that we get the same equations as the ones coming from considering energy and momentum conservation:

$$\delta'_{\rm dr} = -\frac{4}{3}(\theta_{\rm dr}+\mathfrak{m}_{\rm cont}) + a\Gamma_{\rm dcdm}\frac{\rho_{\rm dcdm}}{\rho_{\rm dr}}(\delta_{\rm dcdm}-\delta_{\rm dr}+\mathfrak{m}_\psi)\ , \tag{4.2.28}$$

$$\theta'_{\rm dr} = \frac{k^2}{4}\delta_{\rm dr} - k^2\sigma_{\rm dr} + k^2\mathfrak{m}_\psi - a\Gamma_{\rm dcdm}\frac{3\rho_{\rm dcdm}}{4\rho_{\rm dr}}\left(\frac{4}{3}\theta_{\rm dr}-\theta_{\rm dcdm}\right)\ . \tag{4.2.29}$$

$$\tag{4.2.30}$$

Finally, one can compare our final set of equations in the newtonian gauge with the one of Ref. [335]. It turns out that this reference omitted the $\mathfrak{m}_\psi$ term in the evolution equations of $\delta_{\rm dcdm}$ and $\delta_{\rm dr}$. Hence, even besides the fact that we are using more recent data, we do not expect our results to match the ones reported in [335].

4.3 Cosmological effects of a decaying Dark Matter fraction

In this section we show the impact of the decaying DM on the CMB and matter power spectra from purely gravitational effects, as a function of the DM lifetime. This was already described in Ref. [70] in the case of long-lived fully-decaying DM, but we aim at generalizing this study to the case of multi-component DM splitted as $\Omega_{\rm dm} = \Omega_{\rm sdm} + \Omega_{\rm dcdm}$. In such models, the important parameters are the fraction of decaying DM, $f_{\rm dcdm} = \Omega_{\rm dcdm}/\Omega_{\rm dm}$, and its decay rate $\Gamma_{\rm dcdm}$, which we report in units[2] of Gyr^{-1}. When $f_{\rm dcdm}$ is small enough, the decay rate can in principle be very large, leading to different comsological effects than in the fully-decaying DM model.

4.3.1 *Impact of Dark Matter decay on the CMB*

In order to show the effect of varying $\Gamma_{\rm dcdm}$ on the CMB angular power spectra, some choice must be made about what to keep constant. Here we choose to set all the parameters so that the early cosmological history stays the same as in the standard ΛCDM (until the decay starts). To do so, as in ref. [70], we compare decaying models with a given value of $\omega^{\rm ini}_{\rm dm} = \omega_{\rm sdm} + \omega^{\rm ini}_{\rm dcdm}$ with ΛCDM models having the same $\omega_{\rm cdm}$. We also keep fixed the baryon abundance $\omega_{\rm b} \equiv \Omega_b h^2$, the amplitude of primordial perturbation accounting for the late-time absorption $\exp(-2\tau_{\rm reio})A_s$, the index of the primordial perturbation spectrum n_s, the redshift of reionisation $z_{\rm reio}$[3] and the angular size of the sound horizon θ_s. This choice implies that if the decay happens at late times, the small-scale / high-ℓ part of the CMB spectra, influenced mainly by the early evolution, should be preserved up to lensing effects. We fix all parameters to their best-fit value for Planck 2015 TT,TE, EE+low-P [19]: $\{\theta_s$=1.04077, $\omega^{\rm ini}_{\rm dm}$ or $\omega_{\rm cdm} = 0.1198$, $\omega_{\rm b} = 0.02225$, $\ln(10^{10}A_s\exp(-2\tau_{\rm reio}))$=1.882, n_s=0.9645, $z_{\rm reio}$=9.9$\}$. Note that by fixing these parameters and varying $\Gamma_{\rm dcdm}$ and $f_{\rm dcdm}$, we expect to obtain different values for the actual $\omega_{\rm dm}$ today, for H_0 and for $\tau_{\rm reio}$. Hence $\Gamma_{\rm dcdm}$ and $f_{\rm dcdm}$ can in principle be constrained by the data and lead to different predictions for H_0, σ_8 and $\Omega_{\rm m}$, that may either increase or reduce the tension with astronomical data, see our comments in section 4.4.2.2.

2 For translation with other works making use of km s^{-1}Mpc^{-1}, we recall that 1 km s^{-1}Mpc^{-1} = 1.02×10^{-3} Gyr^{-1}.

3 We follow the standard parameterisation of reionisation with a sharp hyperbolic tangent step in the ionisation fraction, centered at $z_{\rm reio}$ and of width $\Delta z_{\rm reio} = 0.5$.

For illustration purposes, let us set the fraction of decaying DM to 20% and compute the TT and EE CMB power spectra for three typical decay rates $\Gamma_{\rm dcdm} = 0.1, 10^3, 10^6$ Gyr^{-1}. The spectra and their residuals are plotted in Fig. 38, together with the (binned) cosmic variance uncertainty. These rates were chosen to highlight three qualitatively different regimes:

- The first regime (Fig. (38), blue curve, $\Gamma_{\rm dcdm} = 0.1$ Gyr^{-1}) corresponds to a DM decaying well *after* recombination. At the background level, the decrease of $a^3\rho_{\rm m}$ with time would tend to increase the angular diameter distance to the last scattering surface. Since we are fixing θ_s, this effect gets compensated by an increase in ρ_Λ and Ω_Λ, which in turn shifts the matter-Λ equality redshift z_Λ to higher values, and enhances the Late Integrated Sachs-Wolfe (LISW) effect, as can be seen in the low-ℓ part of the curve. On top of this, at the perturbation level, the modification of the DM density at late times generates a damping of the metric fluctuations through the Poisson equation, which further contributes to the LISW enhancement. Finally, the amount of lensing is significantly reduced. The consequences at high-ℓ (contrast between minima and maxima and damping tail) are hardly visible by eye on the figure, but the data is sensitive to this effect.
  In the EE spectrum, the different late-time evolution of $\rho_{\rm m} + \rho_\Lambda$ induces a peculiar pattern around $l \sim 10$. Indeed, the reionisation optical depth $\tau_{\rm reio}$ [4] is an integrated quantity along z, and therefore also feels modification in the background expansion. Hence, for a fixed parameter $z_{\rm reio}$, the value of the optical depth $\tau_{\rm reio}$ and the details of the reionisation history slightly depend on $\Gamma_{\rm dcdm}$. For a fixed product $\exp(-2\tau_{\rm reio})A_s$, this has consequences in the low-ℓ part of the EE (and also TT) spectra. However, this effect is unimportant because for a given (small) $\Gamma_{\rm dcdm}$ the LISW effect is stronger. For the maximal allowed values of $\Gamma_{\rm dcdm}$, reionisation effects remain below cosmic variance.
  On the other hand, lensing impacts the C_ℓ^{EE} more strongly than C_ℓ^{TT} [258]. Hence, the high-ℓ part of the polarisation spectrum is expected to help for better constraining the lifetime and fraction of the dcdm component. This statement will be explicitly checked in section 4.4.
  In summary, in this regime, the DM lifetime is probed through the LISW and lensing effect. We can further distinguish two sub-cases depending on the value of $\Gamma_{\rm dcdm}$:
  (i) for $\Gamma_{\rm dcdm} > H_0 \sim 0.7$ Gyr^{-1}, most of the decaying DM has disappeared nowadays, and even before the redhsifts range $0 < z < 3$ which is important for the LISW and lensing effects. So in this regime we expect to get bounds on $f_{\rm dcdm}$ nearly independent of $\Gamma_{\rm dcdm}$.
  (ii) for very small $\Gamma_{\rm dcdm} < H_0$, only a fraction of dcdm had time to disappear. Factorizing out the expansion term, it is possible to write the evolution of the background DM density as

$$\begin{aligned}\Omega_{\rm dm} &= \Omega_{\rm sdm} + \Omega_{\rm dcdm} \\ &= (1 - f_{\rm dcdm})\Omega_{\rm dm}^{\rm ini} + f_{\rm dcdm}\exp(-\Gamma_{\rm dcdm}t)\Omega_{\rm dm}^{\rm ini} \\ &= (1 - f_{\rm dcdm})\Omega_{\rm dm}^{\rm ini} + f_{\rm dcdm}[1 - \Gamma_{\rm dcdm}t + \mathcal{O}((\Gamma_{\rm dcdm}t)^2)]\Omega_{\rm dm}^{\rm ini} \\ &= [1 - f_{\rm dcdm}\Gamma_{\rm dcdm}t + \mathcal{O}((\Gamma_{\rm dcdm}t)^2)]\Omega_{\rm dm}^{\rm ini}\ . \end{aligned} \tag{4.3.1}$$

  In the limit $\Gamma_{\rm dcdm} \ll H_0$, terms of order two or higher can be neglected, and the remaining relevant parameter is simply $\xi_{\rm dcdm} \equiv f_{\rm dcdm}\Gamma_{\rm dcdm}$: multiplied by the age of the universe, it fully encodes the fraction of DM density which decayed into dark radiation until today. Hence this should be the quantity constrained by the data.

4 defined using $\tau(z) = \int_0^z \sigma_T x_e(z') n_H(z') \frac{dt}{dz'} dz'$, with $\frac{dt}{dz'} = -((1+z')H(z'))^{-1}$.

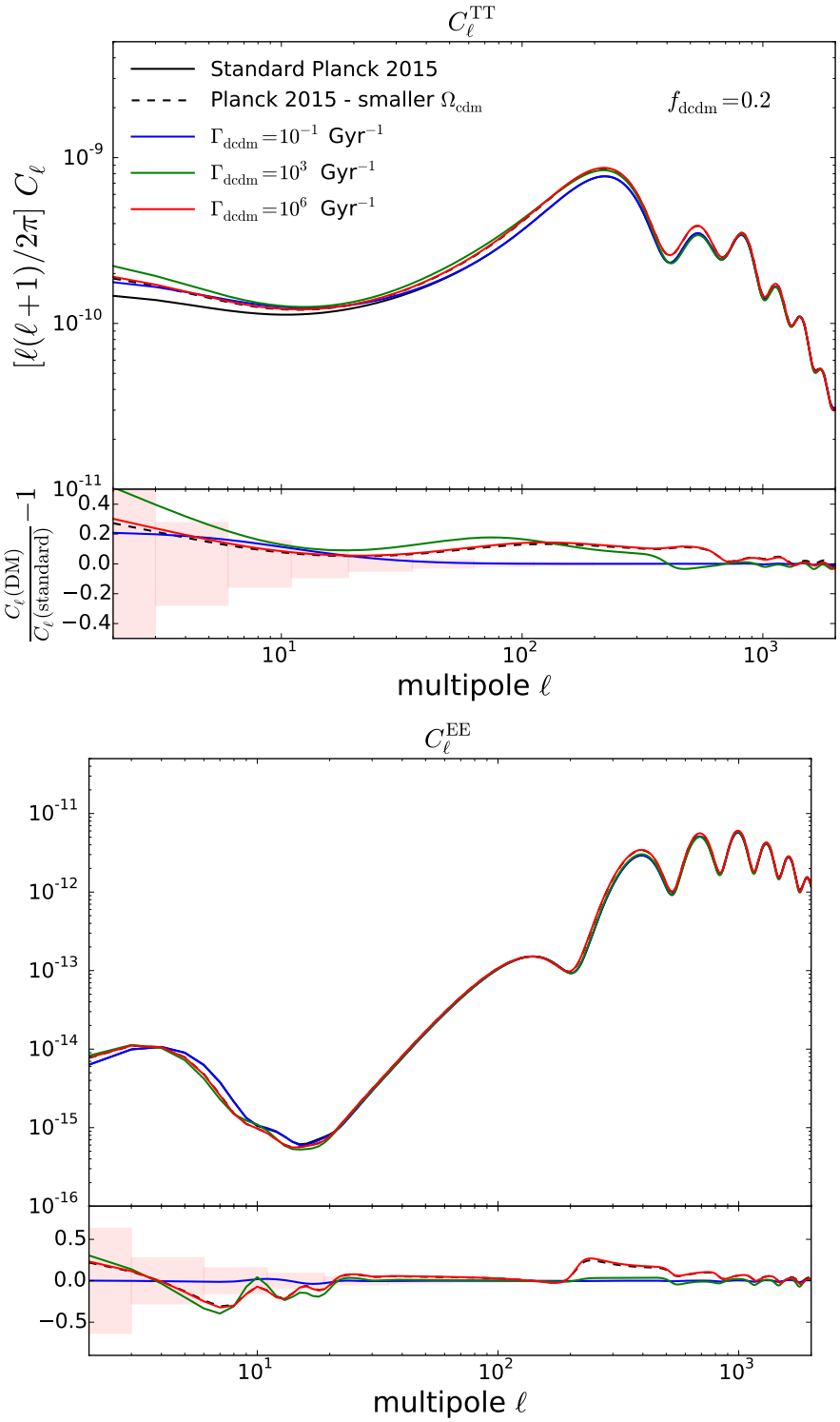

Figure 38: Comparison of the lensed TT (top) and EE (bottom) power spectra for several decaying DM lifetimes and a fixed abundance $f_{\rm dcdm} = 0.2$. Boxes show the (binned) cosmic variance uncertainty.

- The second regime (Fig. (38), green curve, $\Gamma_{\rm dcdm} = 10^3$ Gyr^{-1}) is an intermediate regime for which the unstable DM component would start to decay *around* the recombination epoch and has fully disappeared by now. In the CMB power spectra, one can see, on top of previously described effects, the impact of a bigger Early Integrated Sachs Wolfe (EISW) effect, since the metric terms are further damped due to the DM decay. The affected multipole ℓ depends on the DM lifetime whereas the amplitude of the variation depends on the fraction allowed to decay. The angular power spectra are sensitive to the two independent parameters $f_{\rm dcdm}$ and $\Gamma_{\rm dcdm}$.

- In the third case, for very large $\Gamma_{\rm dcdm}$ (Fig. (38), red curve, $\Gamma_{\rm dcdm} = 10^6$ Gyr^{-1}), the unstable component of DM has decayed well *before* recombination, and eventually even before matter-radiation equality. One can see the admixture of previous effects together with a bigger Sachs Wolfe term, because in models with smaller $\Omega_{\rm dm}$, the growth of potential wells is reduced and therefore their amplitudes at the time of last scattering is smaller. Eventually, there is also a modification of the gravitationally driven oscillations that affect modes well inside the sound horizon during radiation domination, leading to small wiggles at high-ℓ's (visible even in the unlensed spectrum ratios). Finally, although not very pronounced in our case, if the matter radiation equality is shifted, the different expansion evolution would result in a different sound horizon at decoupling. Since we have fixed the peak scale, the code has to adapt the angular diameter distance at recoupling $d_A(z_{\rm rec})$ by adjusting Ω_Λ. However, $d_A(z_{\rm rec})$ also enters the diffusion damping angular scale, resulting in a small decrease in the slope at high-ℓ's.
  Let us note an important point in this regime. The spectra of a model with early decaying DM are very close to those of a stable ΛCDM model, with a different value of $\Omega_{\rm dm}$ corresponding to the density after the decay (compare the red and black-dashed curves in figure 38). Hence models of this type must be allowed, provided that the final DM density is close to the best-fit value for ΛCDM. Therefore we expect that the constraints on $f_{\rm dcdm}$ start to relax as one moves to shorter and shorter lifetimes, accompanied however by an increase in the value of $\Omega^{\rm ini}_{\rm dcdm}$. Different regimes are also expected, depending if the DM decays before or after matter radiation equality. Indeed a shift of $z_{\rm eq}$ induces very peculiar effects, see section 4.4.

4.3.2 *Impact of the decaying Dark Matter on the matter power spectrum*

Let us now discuss the effects on the matter power spectrum, an essential step in view of including data on Large Scale Structure (LSS). We adopt the same strategy as for the description of the CMB power spectra, i.e. we fix $\{\theta_s,\ \omega^{\rm ini}_{\rm dm},\ \omega_{\rm b},\ A_s\exp(-2\tau_{\rm reio}),\ n_s,\ z_{\rm reio}\}$ to the Planck 2015 TT, EE, TE+low-P best fit parameters (which means that we consider a fixed early cosmological history).

As for the CMB power spectra, we show in Fig. 39 (top panel) the impact of DM decay for three different regimes:

- For lifetimes comparable or longer than the age of the Universe (blue curve), the impact on the matter power spectrum is relatively small. Mostly, one finds a small shift of the matter power spectrum towards larger scales/smaller wavenumbers. Indeed, the DM decay shortens slightly the matter dominated era[5]. Hence the ratio $k_{\rm eq}/(a_0H_0)$ governing the location of the

5 the DM decay at late time implies a smaller conformal age of the universe τ_0, while the time of radiation–matter equality $\tau_{\rm eq}$ is fixed. This implies smaller ratios $\tau_0/\tau_{\rm eq}$ and $k_{\rm eq}/(a_0H_0)$.

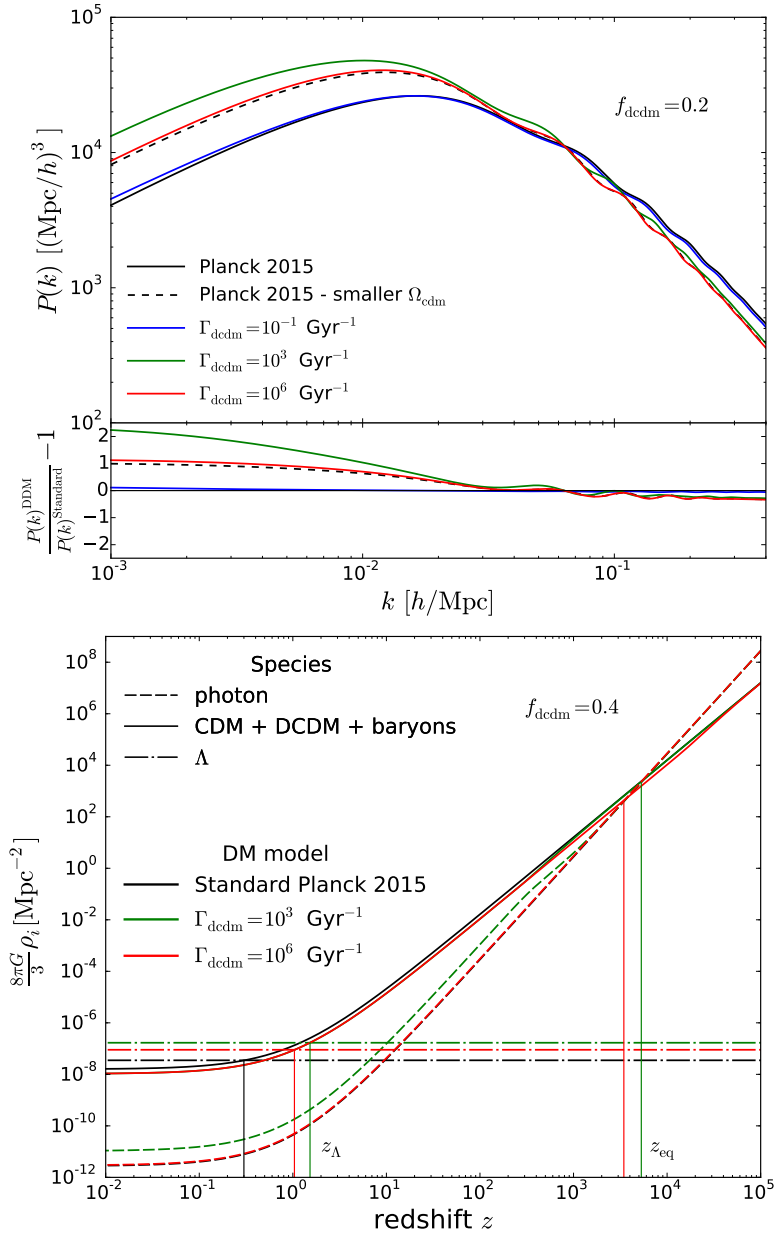

Figure 39: Top panel − Comparison of the matter power spectrum for several decaying DM lifetimes and a fixed abundance $f_{\rm dcdm} = 0.2$. Bottom panel − Evolution of the background densities for two different models of DM with $f_{\rm dcdm} = 0.4$, compared to the standard ΛCDM model. The vertical lines indicates the value of the matter-radiation and matter-Λ equalities in each model. Note that matter-radiation equality happens at the same redshift in the standard ΛCDM and the DCDM model with $\Gamma_{\rm dcdm} = 10^3$ Gyr^{-1}, therefore lines are superimposed.

maximum in the matter power spectrum[6] is smaller. Apart from this small shift, the shape of the matter power spectrum is unchanged, because all the cosmological evolution until the time of recombination and of baryon drag is fixed.

- For a decay starting around the time of baryon drag (green curve in Fig. 39), the impact is much stronger and can be decomposed in three effects:
  (i) we observe the same shift to larger scales/smaller wavenumbers as in the previous case, occurring for the same reason, but much more pronounced.
  (ii) the amplitude on large scales is bigger. Indeed, the amplitude of the matter power spectrum $P(k)$ (expressed in units of $h^{-3}\mathrm{Mpc}^3$ versus k in $h\mathrm{Mpc}^{-1}$) on scales $k \ll k_{\rm eq}$ depends on the primordial spectrum multiplied by $(g(a_0, \Omega_{\rm m})/\Omega_{\rm m})^2$ [392]. Here $g(a, \Omega)$ is the function expressing how much the growth rate of structures $D(a)$ is suppressed during Λ domination: it is the ratio $D(a)/a$ normalised to one before Λ domination, and in a flat FLRW universe, it depends only on a and $\Omega_m = 1 - \Omega_\Lambda$. So $g(a_0, \Omega_{\rm m})$ is a simple function of $\Omega_{\rm m}$, growing with $\Omega_{\rm m}$ and reaching one for $\Omega_{\rm m} = 1$. However $g(a_0, \Omega_{\rm m})$ does not increase as much as $\Omega_{\rm m}^2$, so the ratio $(g(a_0, \Omega_{\rm m})/\Omega_{\rm m})^2$ decreases with $\Omega_{\rm m}$. In the dcdm model that we are considering now, the decay leads to a smaller matter density at late times, and to maintain a constant angular diameter distance to recombination and a constant θ_s, one needs to increase Λ. Hence $\Omega_{\rm m}$ is smaller and the large–scale power spectrum is enhanced.
  (iii) the small-scale power spectrum is suppressed and has a different shape. Indeed we are considering a fixed value of $\Omega_{\rm b}$, while $\Omega_{\rm dm}$ is smaller in the dcdm model. This means that the ratio $\Omega_{\rm b}/\Omega_{\rm dm}$ is bigger. Since baryons are coupled to photons until the baryon drag epoch, a larger $\Omega_{\rm b}/\Omega_{\rm dm}$ implies a strong small-scale suppression and larger Baryon Acoustic Oscillations (BAOs). There is also a slight shift of the BAO phase, due to the change in the value of the sound horizon at baryon drag.

- The effects described in the previous regime do not keep increasing monotonically when the lifetime decreases. On the contrary, for a decay happening well before baryon drag, the impact of the decay becomes smaller (red curve in Fig. 39). This is related to the variation of $\Omega_{\rm m}$ with the dcdm lifetime, when θ_s and all other cosmological parameters are kept fixed. As long as the DM lifetime is longer than the recombination time, it impacts $\theta_s = d_s/d_A$ only through the angular diameter distance to the last scattering surface d_A, because the expansion history is different after decoupling. Once the DM lifetime becomes smaller than the recombination time, the time of radiation–matter equality changes, and θ_s is also impacted through the value of the sound horizon at decoupling d_s. In all cases Ω_Λ is automatically adjusted in order to get the same θ_s, but in a non-monotonic way. This is true also for $\Omega_{\rm m} = 1 - \Omega_\Lambda$, which first decreases with $\Gamma_{\rm dcdm}$ and then increases. This explains why in the left panel of Fig. 39, the amplitude of the small-scale matter power spectrum first goes up with $\Gamma_{\rm dcdm}$, and then goes down. The bottom panel helps to understand what is going on with the background evolution in the different models. On top of this effect, the different value of the sound horizon at decoupling leads to further shift in the BAO phase.

6 We recall that $k_{\rm eq}$ is defined through the relation $k_{\rm eq} \equiv a_{\rm eq} H_{\rm eq}$ where the subscript "eq" stands for matter-radiation equality. The horizontal axis in Figure 39 displays k in units of $[h/\mathrm{Mpc}]$, with the implicit assumption that $a_0 = 1$. In fact, this axis represents the ratio $k/(a_0 H_0)$, and the peak position is given by $k_{\rm eq}/(a_0 H_0)$ [394].

Finally and as expected, in the limit of a very small DM lifetime, the matter power spectrum asymptotes to the limit of a stable CDM model with a smaller $\Omega_{\rm dm}$ (dashed black curve), corresponding to the DM density of the dcdm model after full decay.

4.3.3 *Potential degeneracy with the neutrino mass*

In the past literature, the DM lifetime has been found to be partially degenerate with several other parameters. For instance, ref. [70] studied extensively the degeneracy between $\Gamma_{\rm dcdm}$, the curvature of the universe and the tensor mode amplitude. They found some degeneracy at the level of primary CMB anisotropies, fortunately broken by CMB lensing and matter power spectrum data. Other authors, for instance ref. [99], [232], have found some correlation between $\Gamma_{\rm dcdm}$ and (H_0, σ_8), as expected from the previous discussion. They pointed out that this could be helpful in resolving tensions with low redshift astronomical data. In the next section, we scrutinize this claim.

Moreover, in principle, one could expect a degeneracy between the DM decay and neutrino mass effects. This has been paid virtually no attention till now, hence we discuss it in the following. Neutrinos are relativistic at early time, and then experience a non-relativistic transition. Schematically, one could say that decaying DM goes the opposite, since the model features a non-relativistic species which, through its decay into dark radiation, undergoes a sort of "relativistic transition". For a fixed value of neutrino mass, one can play with the fraction of dark matter that decays in order to cancel exactly the increase in $\Omega_{\rm m}$ coming from the neutrino sector. At the same time, one can adjust the time of the decay to match the neutrino non-relativistic transition time.

We wish to check this simple statement by looking at the power spectra. As it is well known, the effects of the neutrino mass on the CMB power spectra highly depends on the epoch at which the non-relativistic transition occurs, and therefore on the value of the neutrino mass (see e.g. Ref. [392], [394] reviews). The larger it is, the earlier the transition happens, eventually even before matter radiation equality for $m_\nu > 1.5$ eV. Such high masses are completely ruled out by observations[7] and our discussion will be restricted to masses for which the non-relativistic transition happens after recombination, $m_\nu < 0.6$ eV.

For such masses, neutrinos simply affect the CMB through post-recombination effects: EISW and LISW, lensing, and a modification of the angular diameter distance to the last scattering surface. We want to check whether we can cancel these effects with some appropriate amount of DM decay. Hence we compare different models with common parameters $\{\theta_s, \omega_{\rm dm}^{\rm ini}$ or $\omega_{\rm dm}, \omega_{\rm b}, A_s, n_s, \tau_{\rm reio}\}$, three degenerate massive neutrino species, and different values of $M_\nu = 3m_\nu$, $\Gamma_{\rm dcdm}$ and $f_{\rm dcdm}$. Note that all these models share the same cosmological evolution until the time at which either DM decays, or neutrinos become non-relativistic (in particular, for $m \ll 1.5$ eV and a lifetime much bigger than the time of radiation–matter equality, $\tau_{\rm eq}$ is the constant). Moreover, by fixing θ_s, we remove one of the potential effects of neutrino masses listed above. Fixed values of θ_s are obtained by adjusting Ω_Λ in each model, which only leaves a signature at the level of the late ISW effect.

- *CMB temperature spectrum.* In Fig. 40, top panel, one can check that while varying the neutrino mass with only stable CDM, the lensed TT spectrum is only affected in the late ISW region (depletion for $\ell \leq 20$), early ISW region (depletion for $20 \leq \ell \leq 200$) and lensing region (small

7 We anticipate that there is no need to put this conclusion to renewed scrutiny, since the potential degeneracy between DM decay and neutrino mass effects is in fact lifted given current data.

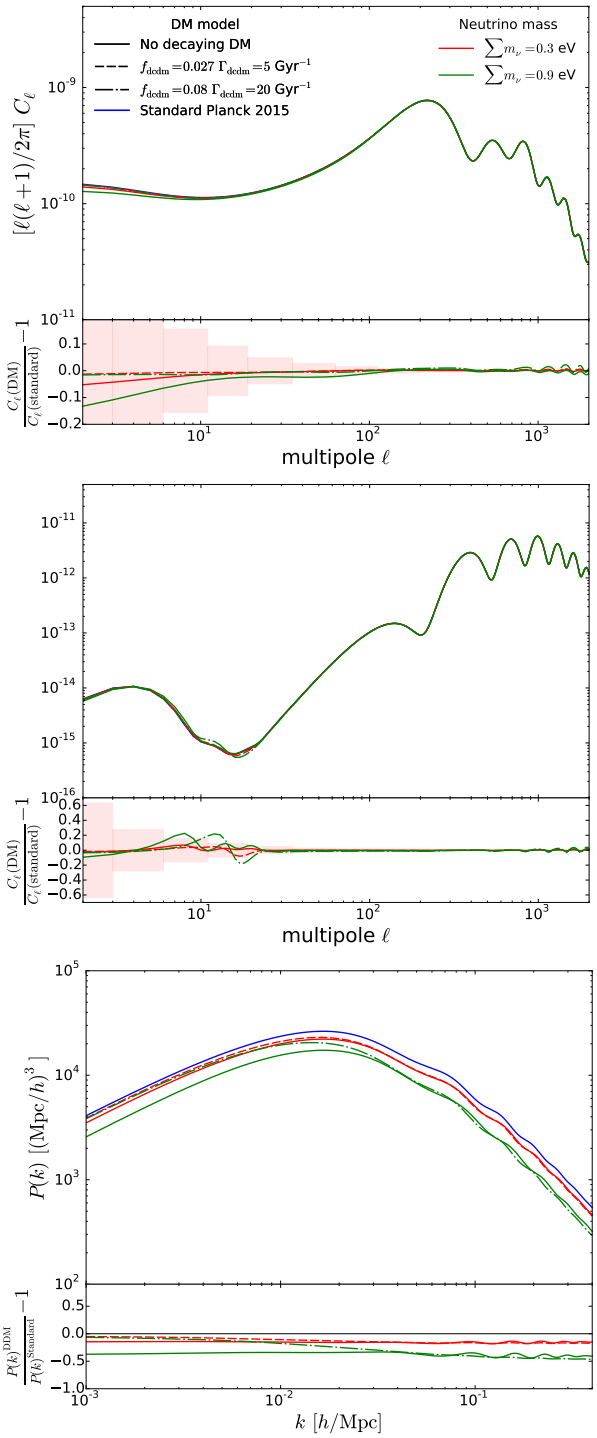

Figure 40: Comparison of the lensed TT (top), EE (middle) and matter (bottom) power spectra for several decaying DM lifetimes and several neutrino masses. The value $f_{\rm dcdm} = 0.027$ (resp. 0.08) has been chosen in order to compensate the effect of $M_\nu = 0.3$ eV (resp. 0.9 eV) and obtain the same total dark matter density today, $\omega_{\rm m}$. The inverse of $\Gamma_{\rm dcdm}$ has been adjusted to the time of the neutrino non-relativistic transition. Boxes show the (binned) cosmic variance uncertainty.

wiggles for $\ell \geq 1000$). Then, for a given neutrino mass, we increased $f_{\rm dcdm}$ in order to obtain roughly the same total $\omega_{\rm m} = \omega_{\rm b} + \omega_{\rm sdm} + \omega_{\rm dcdm} + \omega_\nu$ today, and choose a value of $\Gamma_{\rm dcdm}$ cancelling

as much as possible the neutrino effects. This allows to counter–act neutrino masses at the level of the unlensed spectrum: the ISW effects nearly disappear. However, the lensing effects remain at large ℓ.

- *CMB polarisation spectrum.* In the EE spectrum (Fig. 40, middle panel), the degeneracy is not as effective as one could expect. This is mainly because the EE spectrum is very sensitive to modifications in the reionisation history at late time. As already argued in section 4.3, even for a fixed thermal history and ionisation function versus redhsift $x_e(z)$, changes in the background densities affect the redshift–to–time relation $z(t)$. The effect of neutrinos becoming non–relativistic and of decaying DM can never exactly cancel each other in the expansion history $a(t)$, hence $x_e(t)$ is always slightly different, and this can be seen in the EE spectrum, for $\ell \leq 30$ (i.e., for modes entering the Hubble radius around the reionisation time). Features are present on those scales even if we try to fix $\tau_{\rm reio}$ instead of $z_{\rm reio}$. So, despite the magnitude of cosmic variance on those scales and our ignorance on the cosmic reionisation history, we expect the EE spectrum to contribute somewhat to the breaking of the degeneracy. Besides, like for temperature, the degeneracy is broken at large ℓ by lensing effects.

- *Matter power spectrum.* Since CMB lensing effects depend on the matter power spectrum, we now look at $P(k)$ for the same models (bottom panel of fig. 40). It is well-known that the direct effect of neutrino masses is a step–like suppression of the small-scale matter power spectrum, coming mainly from a reduction of the growth rate of CDM fluctuations in presence of a free-streaming component. This effect in the matter power spectrum is best seen by fixing both $\Omega_{\rm m}$ and $\omega_{\rm m}$, in order to get the same behaviour of fluctuations on scales bigger than the neutrino free-streaming scale, in the regime where neutrino and cdm perturbations are equivalent. With fixed ($\Omega_{\rm m}$, $\omega_{\rm m}$), or equivalently, fixed ($\Omega_{\rm m}$, h), one clearly sees that neutrino masses suppress $P(k)$ only on small scales. However, in the matter power spectrum comparison presented in this section, we wish to keep the same choice as in our previous CMB spectrum comparison: namely, we fix θ_s, since this quantity is very accurately measured by the CMB, and we also fix $\omega_{\rm dm}$ and $\omega_{\rm b}$, in order to keep the same early cosmological evolution. In that case, models with different neutrino masses will also have different values of $\Omega_{\rm m}$ and of $h = \sqrt{(\omega_{\rm dm} + \omega_{\rm b} + \omega_\nu)/\Omega_{\rm m}}$, in order to achieve the same θ_s. Since the value of $\Omega_{\rm m}$ affects the amplitude of the matter power spectrum on small scales $k \ll k_{\rm eq}$, we do not expect to see the usual step-like suppression on small scales.

  To explain the variation of the matter power spectrum with respect to the neutrino mass when θ_s, $\omega_{\rm b}$, $\omega_{\rm dm}$ and the primordial spectrum are fixed, we need to remember that in the ΛCDM model, the regime $k \ll k_{\rm eq}$ of $P(k)$ depends only on $\Omega_{\rm m}$, while that of the small-scale power spectrum depends only on $z_{\rm eq}$ and on the baryon fraction (this can be checked e.g. in [392], from equation (6.39); to obtain the dependence on $z_{\rm eq}$, on needs to eliminate $\tilde{k}_{\rm eq}$ in favour of $z_{\rm eq}$ using equations (6.32, 6.35, 6.36)). Suppose that we first increase $\Omega_{\rm m}$ while keeping $\omega_{\rm b}$, $\omega_{\rm dm}$ and ω_ν fixed. This will suppress the power spectrum at large scales, while keeping the same amplitude on small scales, since $z_{\rm eq}$ is not changing. Now let us increase neutrino masses. We add another step-like suppression, this times acting on small scales. After these two transformations, it is not obvious if the power spectrum gets more suppressed on small or large scales.

  It turns out that when the neutrino mass is varied for fixed θ_s, $\omega_{\rm b}$, $\omega_{\rm dm}$, the amplitude of the suppression on small and large scales is nearly the same. In that case, the neutrino mass does

not manifest itself as a step–like suppression, but as a decrease in the global amplitude. In other words, in this basis, neutrino masses are responsible for a shift in the amplitude of the matter power spectrum, while the amplitude of the CMB spectra remains constant. This effect comes together with a shift in BAO phases, because the angular diameter distance to small redshifts is changing (unlike the angular diameter distance to recombination).

We can now turn on DM decay with the same motivation as before: by adjusting the dcdm fraction, we can get the same total matter density $\omega_{\rm m}$ today. The quantity of DM decaying into radiation gets exactly compensated by the amount of neutrinos becoming non-relativistic. In that case, the background history becomes much closer to that of the initial model, and we have seen that ISW effects in the CMB are also compensated. For the matter power spectrum, the story is different. We now have the same $\omega_{\rm m}$ and nearly the same (H_0, Ω) in the original ΛCDM model and in the mixed DM decay + massive neutrino model. Hence the amplitude of the matter power spectrum is preserved on large scales, the BAO scale readjusted, and the usual step-like suppression caused by neutrino masses appears clearly, not masked by other large–scale effects. This is why the difference between these two models in Fig. 40, lower panel, looks like in a canonical comparison between models with massive or massless neutrinos for fixed ($\Omega_{\rm m}$, $\omega_{\rm m}$).

In summary, the degeneracy which is superficially present in CMB angular spectra is clearly broken at the level of the matter power spectrum, and hence also at the level of the lensed CMB spectra, even neglecting the small distinctive features in the polarisation spectra on large angular scales. To cross–check this conclusion, we performed some fits to the data with free M_ν, $f_{\rm dcdm}$ and $\Gamma_{\rm dcdm}$ simultaneously. We found no significant correlations between these parameters, and got neutrino mass bounds extremely close to those obtained with stable DM. We can conclude that the bounds of the next sections, obtained with massless neutrinos, are very robust against the addition of neutrino masses.

4.4 Application of the decaying Dark Matter model

4.4.1 *Constraints from the CMB power spectra only*

It is well known that ΛCDM provides a good fit to Planck results, suggesting that bounds on decaying DM (rather than evidence in favour of it) should be achievable by an appropriate analysis of the data. We compare the constraining power of the TT, TE and EE spectra, since the Planck collaboration made available several likelihoods, corresponding to differents data sets [26]. For ℓ's >30, we can use data from the TT spectrum only, or use data coming from TT, TE and EE spectra at the same time. For the small ℓ's however, it would not make sense to consider such decomposition since the TT spectrum alone is very weakly sensitive to $\tau_{\rm reio}$: more precisely, its effect is highly degenerate with A_s. We thus simply consider the combination of all data sets {TT, TE, EE} which allows one to break the $A_s/\tau_{\rm reio}$ degeneracy. Further cosmological information is encoded in the likelihood of the *lensing* reconstruction, which we also use in the following. We refer to the combination of high-ℓ's TT + low-ℓ's + lensing reconstruction as Planck$^{\rm TT}$, and to high-ℓ's TT,TE,EE + low-ℓ's + lensing reconstruction as Planck$^{\rm TTTEEE}$. Ref. [258] has found that despite their rather poor signal-to-noise ratio, the constraining power of the EE and TE spectra alone is as good as or even better than the TT alone. In fact, they found that C_ℓ^{TE} improves the determination of $\omega_{\rm dm}$ by 15%. One therefore expects similar improvements when using Planck$^{\rm TTTEEE}$ with respect to Planck$^{\rm TT}$.

We run Monte Carlo Markov chains using the public code MONTE PYTHON [68]. The basics of Bayesian statistics and other mandatory details on parameter extraction and convergence technicalities are described in appendix B.3. We perform the analysis with a Metropolis Hasting algorithm and assumed flat priors on the following parameters:

$$\{\omega_b, \theta_s, A_s, n_s, \tau_{\rm reio}, \omega^{\rm ini}_{\rm cdm}, f_{\rm dcdm}, \Gamma_{\rm dcdm}\}\,.$$

Although not specified here for brevity, there are many nuisance parameters that we analyse together with the cosmological ones. To this end, we make use of a Choleski decomposition which helps in handling the large number of nuisance parameters [399]. We consider chains to be converged using the Gelman-Rubin [265] criterium $R-1<0.01$, except if specified otherwise.
As extensively discussed in section 4.3, the effects of the decay are very different depending on the lifetime of the decaying DM. Therefore, the parameter space should have a non-trivial shape: we therefore split our analysis in three different parts, corresponding to different decay epochs. In Fig. 41 and Fig. 42, with blue curves and contours, we show the constraints in the $\{f_{\rm dcdm}, \Gamma_{\rm dcdm}\}$ plane for each regime from the Planck$^{\rm TT}$ dataset only.

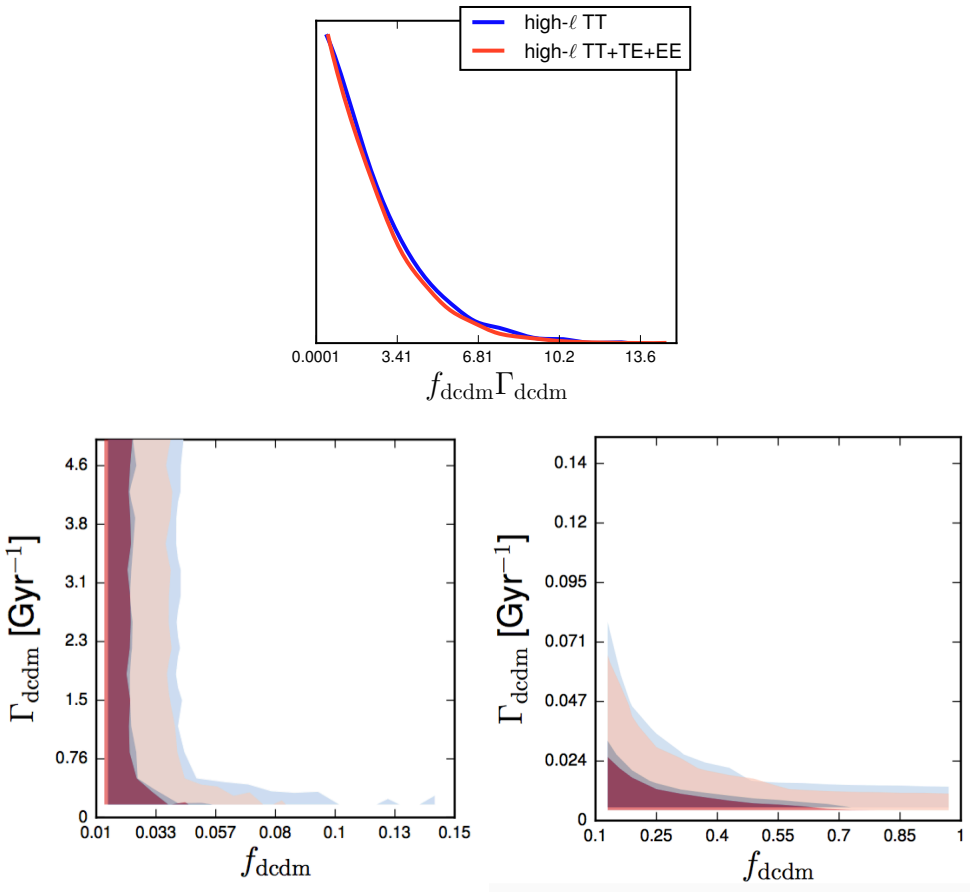

Figure 41: Constraints on the decaying dark matter fraction $f_{\rm dcdm}$ as a function of the lifetime $\Gamma_{\rm dcdm}$ in the long-lived and intermediate regime. All datasets also include CMB low-ℓ data from each spectrum and the lensing reconstruction. Blue (red) lines and contours refer to the case without (with) high-ℓ polarization data. Inner and outer coloured regions denote $1\,\sigma$ and $2\,\sigma$ contours, respectively.

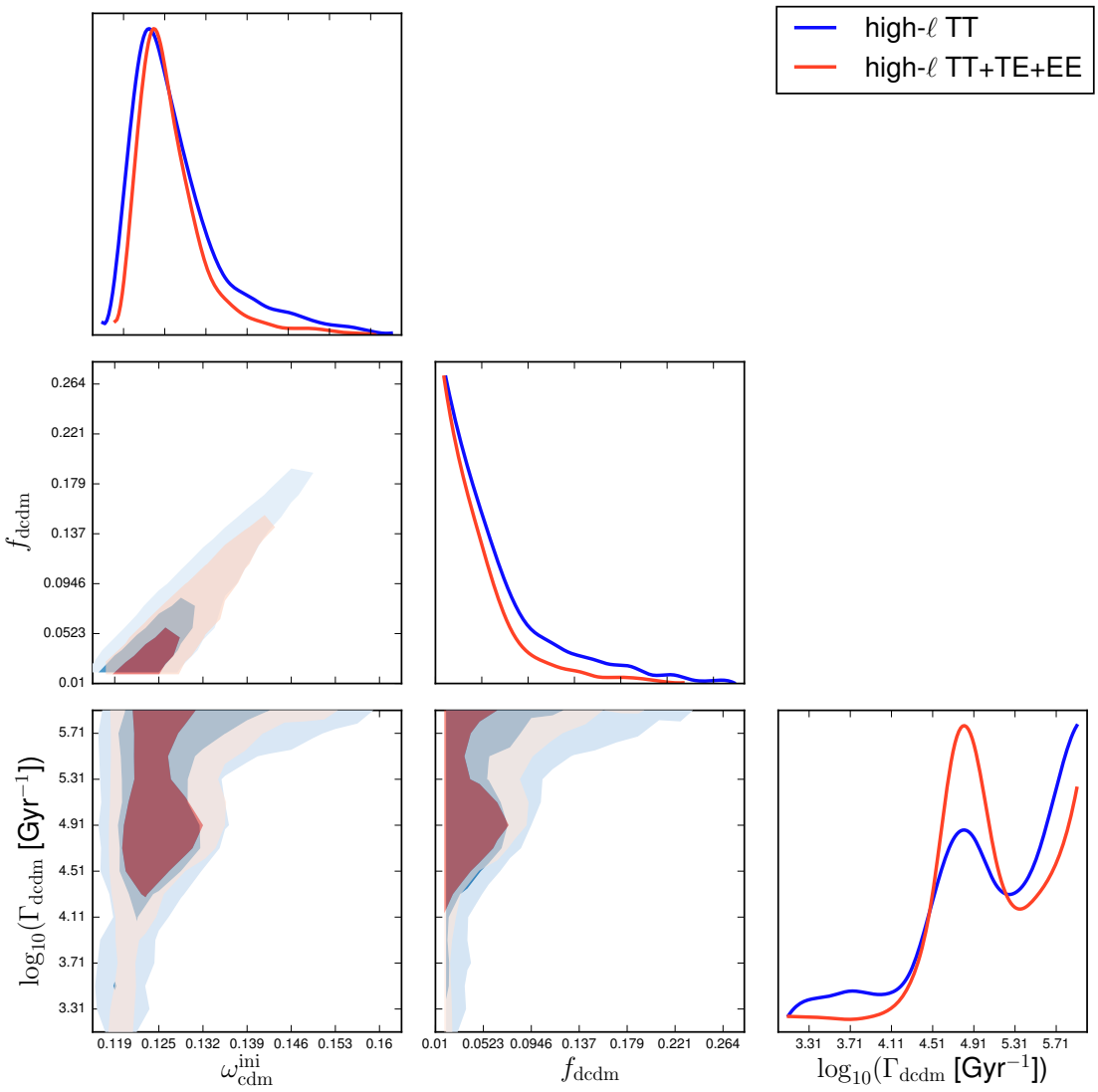

Figure 42: Constraints as in Fig. 41, but for the short-lived dcdm regime. We also show how the distribution of the initial cdm density evolves when the decay rate and dcdm fraction increase.

- The constraints in the long-lived dark matter regime ($\Gamma_{\rm dcdm} < H_0$) is represented on the upper and bottom-left panels of Fig. 41. In that regime, a sizable fraction of the decaying DM component is still present today. As anticipated in section 4.3.1, first bullet, the key parameter in that case is the product $f_{\rm dcdm}\Gamma_{\rm dcdm}$, with an exact two parameters description leading to less than 10% differences in the bounds. The constraints on this parameter is $f_{\rm dcdm}\Gamma_{\rm dcdm} < 6.7 \times 10^{-3}$ Gyr^{-1} at 95% CL with Planck$^{\rm TT}$ dataset.

- We argued in section 4.3.1, second bullet, that there is an intermediate regime given roughly by $\Gamma_{\rm dcdm} \in [10^{-1}, 10^{3}]$ Gyr^{-1}, for which the DM decay starts after recombination and decaying DM has totally disappeared by now. Results for this case are shown in the bottom-right panel of Fig. 41. In that case, the CMB is mostly insensitive to the time of the decay. Our runs show that in this regime, the CMB can tolerate up to 4.2% of dcdm at 95% CL. This is an important number, standing for the fraction of dark matter that can be converted entirely into a dark

radiation after recombination, without causing tensions with the data. Although we do not show the full parameter space up to $\Gamma_{\rm dcdm} \simeq 10^3$ Gyr^{-1}, we have checked that the behaviour stays the same (this can also be inferred from the smallest values of $\Gamma_{\rm dcdm}$ plotted in Fig. 42.)

- Finally, we show in Fig. 42 the constraints applicable to the short-lived regime, $\Gamma_{\rm dcdm} > 10^3$ Gyr^{-1}, for which the decay happens before recombination. To accelerate the exploration of the parameter space, we scan over $\log_{10}(\Gamma_{\rm dcdm})$ with a flat prior. We however cut at 10^6 Gyr^{-1} for obvious convergence issues, and consider chains as converged when $R-1<0.1$. Changing the upper bound would not change at all our conclusions. Note that with such a bound, we are also covering the region of parameter space for which the decay happens before the onset of matter domination. One can see a very interesting behaviour in that regime: the bound on $f_{\rm dcdm}$ starts to relax, accompanied by an increase in the initial total dark matter density. In principle, cosmologies with a large initial cold DM abundance are acceptable, provided that the decaying DM, in excess with respect to Planck ΛCDM best fit value for $\omega_{\rm dm}$, had time to decay before recombination. In practice, we see two different regimes, responsible for non-monotonic features in the contours of Fig. 42 in the $\{f_{\rm dcdm}, \log_{10}(\Gamma_{\rm dcdm})\}$ plane. The first regime, for which the constraints relax more slowly, corresponds to decay happening mostly in between matter-radiation equality and recombination. The second regime corresponds to decay happening mostly before matter-radiation equality. The difference in the slope of the relaxation of the constraints is therefore mostly due to the fact that, in the first regime, the matter-radiation equality redshift $z_{\rm eq}$ is shifted towards earlier time. This in turn modifies the background evolution—therefore the sound horizon and the diffusion damping scale—but also directly affects the growth of both metric and density perturbations. Indeed during matter domination, the growth of matter perturbations deep inside the sound horizon is linear, whereas it is only logarithmic in the radiation domination era. Hence, a longer matter domination results in a bigger amplitude of the matter density perturbations. On the other hand, as already explained, if matter-radiation equality happens earlier, metric perturbations have more time to stabilize resulting in a suppression of the EISW term.

Going from Planck$^{\rm TT}$ to Planck$^{\rm TTTEEE}$ datasets (i.e. switching between Fig. 41 and Fig. 42 from blue curves and contours to orange/red ones) does not alter the picture very much, but helps tighten further the allowed decaying DM fraction. In the long-lived regime, the product $f_{\rm dcdm}\Gamma_{\rm dcdm}$ is now constrained to $f_{\rm dcdm}\Gamma_{\rm dcdm} < 6.3\times10^{-3}$ Gyr^{-1}, which is an improvement of 7%. In the intermediate lifetime case, one can see a $\mathcal{O}(10\%)$ improvement: the fraction of dcdm has to be as small as 3.8% for $\Gamma_{\rm dcdm} > 0.3$ Gyr^{-1}. This results is also in agreement with Ref. [186], which found a bound of 4% on $f_{\rm dcdm}$ in this regime for Planck TT,TE,EE + low-P but no lensing likelihood. Finally, in the short-lived regime the constraint tightens more, by about $\mathcal{O}(20-30\%)$, or even up to a factor 2 below $\Gamma \simeq 10^4$ Gyr^{-1}. This was expected from the previous discussion, since the impact of a varying $\Omega_{\rm dm}$ is strong on both EE and TE spectra, either through lensing or reionisation effects.

4.4.2 *Adding low redshift astronomical data*

Let us now add data from BAO, H_0 and matter power spectrum measurements to our dataset, in order to tighten the diagnostic power on decaying DM models. This turns out not to be very straightforward, for at least a couple of reasons: i) a technical one is that some of these "low redshift" data, notably

the CFHT ones [302], provide weak lensing measurements of the matter power spectrum up to $k \simeq 5$ h/Mpc. Unfortunately the calculation of the decaying DM model matter power spectrum in the non-linear regime raises some concerns, which will be described in Sec. 4.4.2.1 below. ii) At face value, the measurements of H_0, σ_8, Ω_m from low-redshift probes seem to be in tension with CMB-inferred determinations. For instance, the reduced Hubble parameter today derived by Planck is $h = 0.6727 \pm 0.0066$ (Planck 2015 TT,TE,EE+lowP [19]). This is about $3.0\,\sigma$ lower than the most recent value of Ref. [509], $h = 0.7302 \pm 0.0179$, obtained from the Hubble Space Telescope (HST) data. The CMB-inferred values of σ_8 and $\Omega_{\rm m}$ also at more than $2\,\sigma$ than the ones coming from cluster counts [18] or weak lensing CFHT tomographic analysis [302]. There are two ways out to this tension: a) Since the comparison can only be done within a given cosmological model, it may be that ΛCDM is incomplete, and the tension would be eventually resolved if data were analyzed within "the true" cosmological model. Perhaps the decaying DM hypothesis works exactly in the sense wanted. Further considerations on this important issue will be the topic of sec. 4.4.2.2. b) Alternatively, there are perhaps underestimated systematics in one or several of the datasets used. Without entering the difficult question of what those errors may be, in Sec. 4.4.2.3 we explore the implications for decaying DM constraints of combining only data which are mutually consistent.

4.4.2.1 *Linear vs Non-linear matter power spectrum*

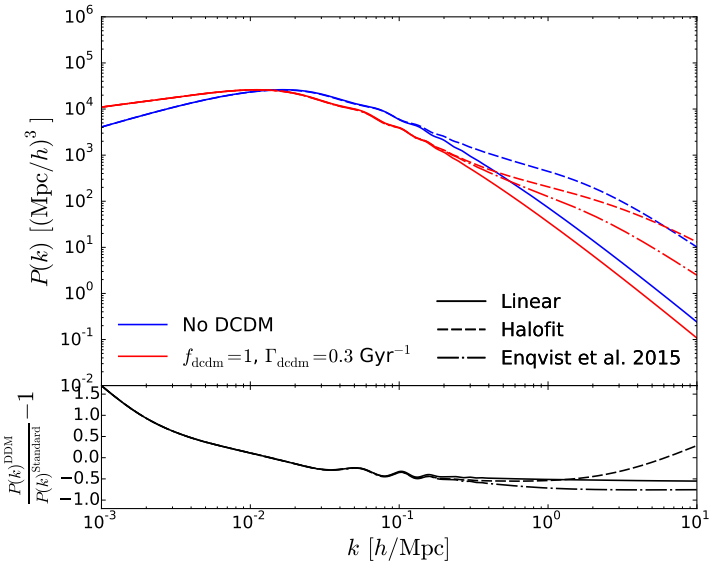

Figure 43: The non-linear matter power spectrum computed using halofit for a universe with dcdm compared to the standard ΛCDM cosmology. We fix all parameters to their best-fit value for Planck 2015 TT,TE, EE+low-P [19]: {θ_s=1.04077, $\omega_{\rm dm}^{\rm ini}$ or $\omega_{\rm cdm}$ = 0.1198, $\omega_{\rm b}$ = 0.02225, ln($10^{10}A_s$)=3.094, n_s=0.9645, $z_{\rm reio}$=9.9}.

The most straightforward way to deduce the non-linear matter power spectrum in presence of decaying DM is obviously via N-body simulations. This approach has been considered in Ref. [232], in which the N-body code Gadget2 [566] has been modified by considering an evolving "N-body particles" mass. Unfortunately we cannot rely fully on their results for a couple of reasons: first, they only consider a model in which the whole DM is decaying (i.e. $f_{\rm dcdm} = 1$); hence, by definition their results only apply to long-lived decaying DM, leaving out most of the parameter space of interest for us. The

second one is perhaps more subtle: for the specific case at hand, it is unclear to which extent one can fully rely on simulations of relatively small cosmological "boxes". To understand why, let us remind the reader that linear theory essentially predicts that decaying DM yields a power-spectrum suppression, almost constant in fraction, at sufficiently large k (see solid curve in the bottom panel of Fig. 43). Numerical simulations of Ref. [232] match this behaviour, eventually showing a stronger suppression at larger k (see dot-dashed curve in Fig. 43, based on the fitting formula reported in [232].) However we also know that: i) A strong impact of the decaying DM is to enhance the amplitude of the matter power spectrum on very large scales (very small k's), as discussed in section 4.3.2. This is again visible in the solid curve in the bottom panel of Fig. 43, reporting the linear result. ii) Deeply in non-linear regime, IR and UV mode-mode coupling is potentially important. Unfortunately, the size of boxes adopted in [232] is insufficiently large to capture this behaviour at small k, hence may be also missing its consequence at large k. A further caveat may be added if one compares the results of the simulations with a simple-minded use of the halofit function [558], see dashed curves in Fig. 43. Although this fitting function has been derived in the context of standard ΛCDM cosmology (extended to non-zero neutrino mass [577]), the main impact of the decaying DM on the DM properties should be to slightly modify the $(1+z)^3$ dilution term, without a priori changing any of its clustering properties. One could argue that halofit is still reliable for such models, but unfortunately the result departs from the one of the simulations of ref. [232]: On small scales, the non-linear power spectrum in the decaying DM universe increases and even exceeds the one in a ΛCDM cosmology. The bottom line is that it is unclear up to which values of k one can rely either on the simulations of [232] or halofit results. A safe bet is to limit the analysis to modes $k < 0.4 - 0.5\,h/\mathrm{Mpc}$, where all results agree and the departure from linear theory is minor. One implication of this cautionary approach is that we cannot rely on the full $P(k)$ from CFHT, extending to $k \simeq 5$ h/Mpc. For our considerations in the next section, we will simply make use of the inferred values of $\sigma_8\Omega_{\rm m}^{\alpha}$, which are at the hearth of the claimed discrepancies. Of course, in models departing from ΛCDM the whole procedure used by CFHT to extract $\sigma_8\Omega_{\rm m}^{\alpha}$ should also be affected, and a different value of $\sigma_8\Omega_{\rm m}^{\alpha}$ might result. Unfortunately, we cannot check this point explicitly, and we will limit ourselves to perform analyses similar to the existing literature on this subject.

4.4.2.2 *The low-redshift data discrepancies*

In this section, let us assume that the discrepancies are physical, and thus hint to departures from the ΛCDM model. Numerous alternative explanations are available in the literature: we can mention a possible interaction between dark matter and dark radiation [393] or in the dark energy sector [496], or adding sterile neutrinos with pseudoscalar self-interactions [60]. Actually, it has been pointed out that even decaying DM could help in solving these discrepancies [99], [186], [232]. Here we wish to revisit these claims. Qualitatively, it is easy to understand why decaying DM may provide the needed ingredient. Since $\Omega_{\rm dcdm}$ and $\Omega_{\rm m}$ decrease with time and CMB data pins down very precisely the value of $\omega_{\rm cdm} \equiv \Omega_{\rm cdm}h^2$, the value of h has to be bigger than in ΛCDM to compensate for the decay. Similarly, cluster count and weak lensing data[8] measure the combination $\sigma_8\Omega_{\rm m}^{\alpha}$. Hence, a smaller $\Omega_{\rm m}$ has to be accompanied by a bigger σ_8. Thus, one could in principle hope to find a model which satisfies both CMB and low redshift astronomical data. In fact, this seems to be the

8 In reality, CFHT is a measure of the $P(k)$ up to scales deep in the non-linear regime. As explained in section 4.4.2.1, we cannot reliably modelize the non-linear growth of structure in the dcdm universe and therefore only make use of the $\sigma_8\Omega_{\rm m}^{\alpha}$ measurement.

case according to Ref. [99], where best-fit models were found for $\{f_{\rm dcdm}, \Gamma_{\rm dcdm}\} \simeq \{10\%, 1\,{\rm Gyr}^{-1}\}$. In practice, however, we have seen that CMB is still very sensitive to modification of cosmology below the redshift of recombination, so that our analysis based on all CMB datasets disfavours a fraction of DM decaying between recombination and today larger than about 3.8%; it is then reasonable to anticipate that in a global analysis no fully satisfactory solution to the tension can be found, at best marginal improvements. Yet, in the recent article [186] a fit of a decaying DM model to Planck TT, TE, EE, lensing and cluster counts, as well as to an earlier H_0 determination [508], has been claimed to improve over ΛCDM by almost $2.5\,\sigma$[9]. On the other hand, Ref. [232] fitted a model with $f_{\rm dcdm} = 1$ to Planck TT spectrum, WMAP09 polarisations, CFHT and BAO data, and did not find more than $\sim 1\,\sigma$ improvement over ΛCDM. As a contribution to clarify the situation, we repeat the analysis, combining Planck CMB data with CFHT [302] and Planck cluster [18] constraints on $\sigma_8\Omega_{\rm m}^{\alpha}$, BAO measurements from [47] and the H_0 determination from [509], which is an update of the former 2011 result of ref. [508]. Results are summarized in Table 5 and shown in Figs. 44, 45, 46. These figures just illustrate how we can reproduce, at least qualitatively, results of the past literature: Fig. 44 shows the tension in ΛCDM vs. low-redshift data, Fig. 45 the improvement in a short-lived dcdm cosmology and Fig. 46 in a long-lived dcdm cosmology. To gauge how important the discrepancy and the improvement are, however, let us inspect more in detail the numerical entries in Table 5. Within ΛCDM, one can see that the addition of the data in tension, namely HST, CFHT and Planck clusters (only 3 datapoints, dubbed dataset Ext$_A$), degrades the $\chi^2_{\rm min,eff}$, defined as $-2\log$(Likelihood), by 31.2 (cf. Planck$^{\rm TTTEEE}$+Ext$_B$ vs Planck$^{\rm TTTEEE}$+Ext$_A$+Ext$_B$ in Table 5; the dataset Ext$_B$ is composed of BAO data and the WiggleZ galaxy power spectrum, in agreement with Planck CMB data). When turning to the dcdm model, we qualitatively confirm the previous claims in that an improvement is present, corresponding to a shift in the best–fit value of h, and a small preference for lower Ω_m and bigger σ_8 values. However, $\chi^2_{\rm min,eff}$ improves at most by 6.7 (slightly above $2\,\sigma$) at the price of adding two new parameters to the model; had we dealt with a satisfactory physical model, we should have expected an improvement in $\chi^2_{\rm min,eff}$ of about 30. We therefore conclude that global fits to current data are only marginally improved when switching to a decaying DM cosmology, at the price of complexifying the model by the addition of two new parameters. However, since there is a weak preference for a non-vanishing decaying DM fraction, in this framework the bound on $f_{\rm dcdm}\Gamma_{\rm dcdm}$ (not surprisingly) weakens to $f_{\rm dcdm}\Gamma_{\rm dcdm} < 15.9 \times 10^{-3}$ Gyr^{-1} at 95% CL.

4.4.2.3 *Bounds on the decaying DM fraction and lifetime from mutually consistent data*

Finally, if assuming that the tension between CMB and low redshift astronomical measurements are due to unknown systematics in the latter ones, one may ask what is the improvement on decaying DM constraints in a global analysis of *mutually consistent* datasets. We thus add to the Planck$^{\rm TTTEEE}$ dataset defined previously the BAO measurements at $z = 0.32$ and 0.57 of the BOSS collaboration [47] and the $P(k)$ data from WiggleZ [468][10], collectively dubbed Ext$_B$. The result for the different regimes are shown in Fig. (47).

9 These authors also underline that improvements are very sensitive to small tensions between Planck's best estimation of the lensing amplitude from the TT, TE, EE spectra and from the full lensing reconstruction using 4-point correlation functions. We do not wish to enter here into these details and refer interested readers to that study. We simply quote their best fit result to all datasets.

10 It is safe for us to use this dataset since it only probes $k \leq 0.5$ h/Mpc, which is only a weakly non-linear regime, as discussed in Sec. 4.4.2.1.

dataset	ΛCDM	DCDM ($\Gamma_{\rm dcdm} > H_0$)		DCDM ($\Gamma_{\rm dcdm} < H_0$)	
	$\chi^2_{\rm min,eff}$	$\chi^2_{\rm min,eff}$	$f_{\rm dcdm}$	$\chi^2_{\rm min,eff}$	$f_{\rm dcdm}\Gamma_{\rm dcdm}$ (Gyr^{-1})
Planck$^{\rm TT}$	11272.3	11272.3	$< 4.2\%$	11272.3	$< 6.7\times10^{-3}$
Planck$^{\rm TTTEEE}$	12952.4	12952.4	$< 3.8\%$	12952.2	$< 6.3\times10^{-3}$
Ext$_A$	4.665	4.19	–	3.691	< 0.14
Planck$^{\rm TTTEEE}$+Ext$_B$	13775.5	13775.5	< 3-3.6%	13775.5	$< 5.9\times10^{-3}$
Planck$^{\rm TTTEEE}$+Ext$_A$+Ext$_B$	13806.7	13804.1	< 3.5-4.2%	13800.0	$< 15.9\times10^{-3}$

Table 5: Comparaison of the $\chi^2_{\rm min,eff}$ and constraints on $f_{\rm dcdm}$ or $f_{\rm dcdm}\Gamma_{\rm dcdm}$ as a function of the dataset, in the ΛCDM and the DCDM models. The dataset Ext$_A$ is composed of CFHT, BAO, HST and Planck Clusters, which we refer as the discrepant dataset in the text. The dataset Ext$_B$ is instead composed of BAO data and the WiggleZ galaxy power spectrum, all in agreement with Planck CMB data.

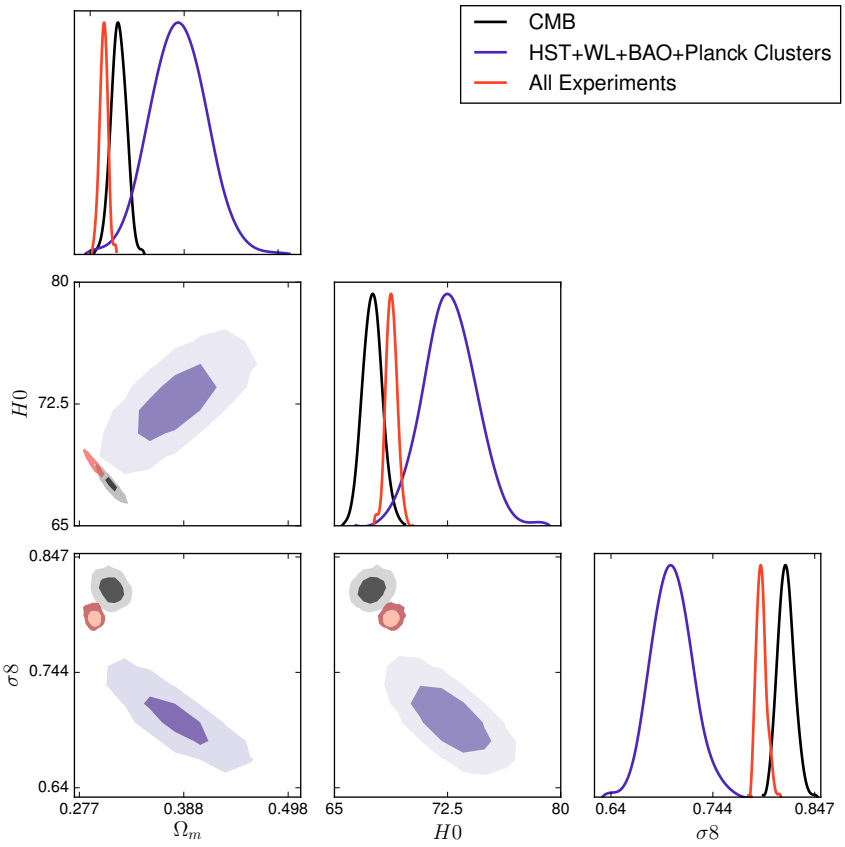

Figure 44: Illustration of the discrepancies between measurements of σ_8, Ω_m and H_0 coming from the CMB and low-redshift experiments in the ΛCDM model. Inner and outer coloured regions denote $1\,\sigma$ and $2\,\sigma$ contours, respectively.

The bounds on $f_{\rm dcdm}\Gamma_{\rm dcdm}$ now tightens to $f_{\rm dcdm}\Gamma_{\rm dcdm} < 5.8 \times 10^{-3}$ Gyr^{-1}, or equivalently $\tau_{\rm dcdm}/f_{\rm dcdm} > 170$ Gyr. If we compare to previous result [70], the use of Planck 2015 data improves only by about 6% previous bounds derived with Planck 2013 and polarisation data from WMAP9 [304]. In the intermediate regime, the additional data improve the bound, but now in a way slightly

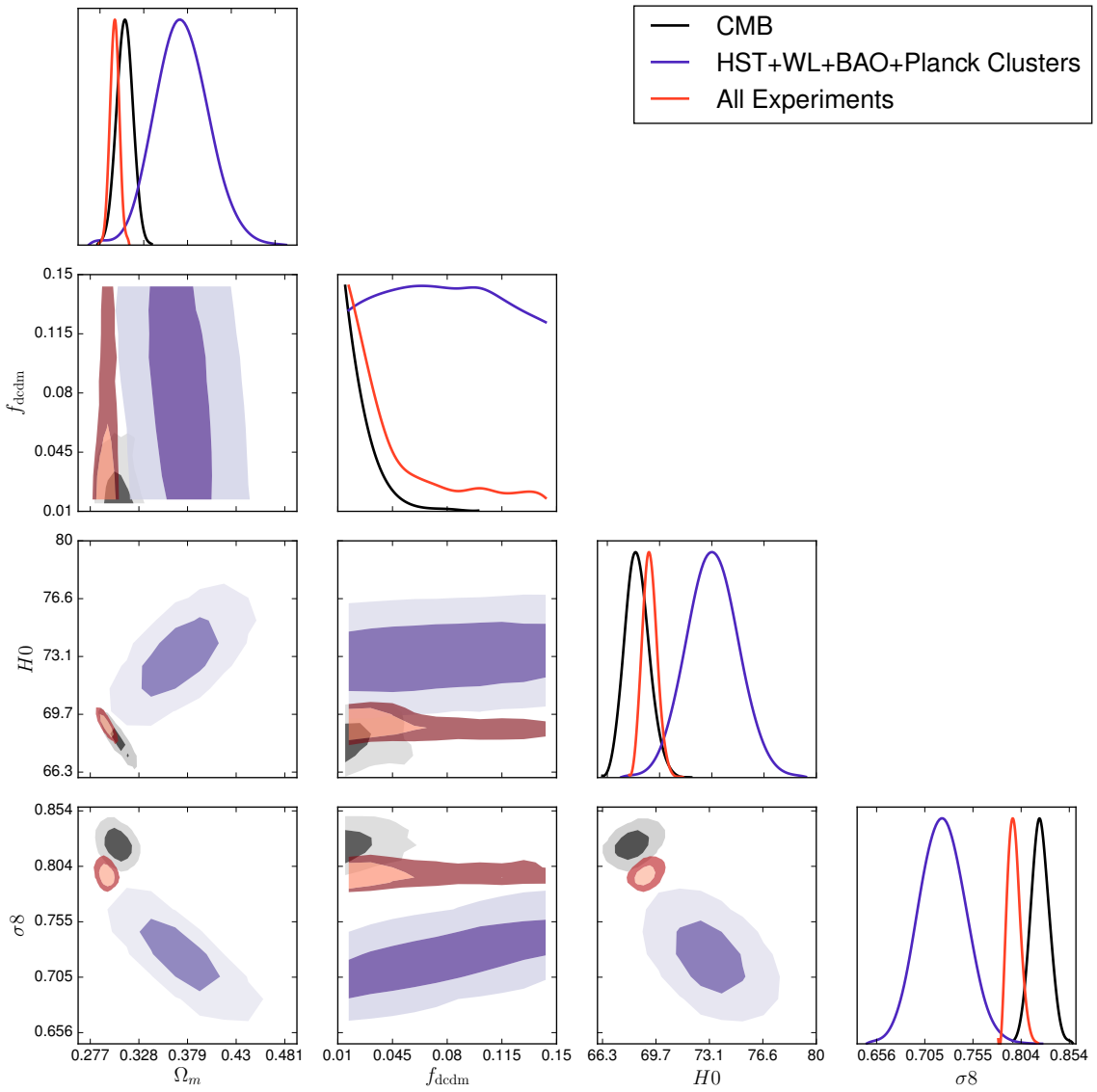

Figure 45: As in Fig. 44, but in the dcdm model with $\Gamma_{\rm dcdm} > H_0$.

dependent on the lifetime: Roughly, the 95% CL bound on $f_{\rm dcdm}$ evolves from 3% for $\Gamma_{\rm dcdm} \simeq 10$ Gyr^{-1} up to 3.6% at $\Gamma_{\rm dcdm} \simeq 0.5$ Gyr^{-1}, and then relaxes as CMB-only bounds for longer lifetimes. Finally, in the short-lived regime constraints are improved for particles decaying around matter-radiation equality by up to a factor 2. For other lifetimes, LSS data do not tighten CMB bounds.

4.5 Conclusions

In this work, we have revisited the issue of cosmological bounds on decay of a *fraction* of dark matter into some form of inert, or "dark" radiation, i.e. relativistic degrees of freedom not interacting electromagnetically. Within the standard model, neutrinos or gravitational waves are the only candidates with the right properties, but beyond the standard model, additional particles may play this role.

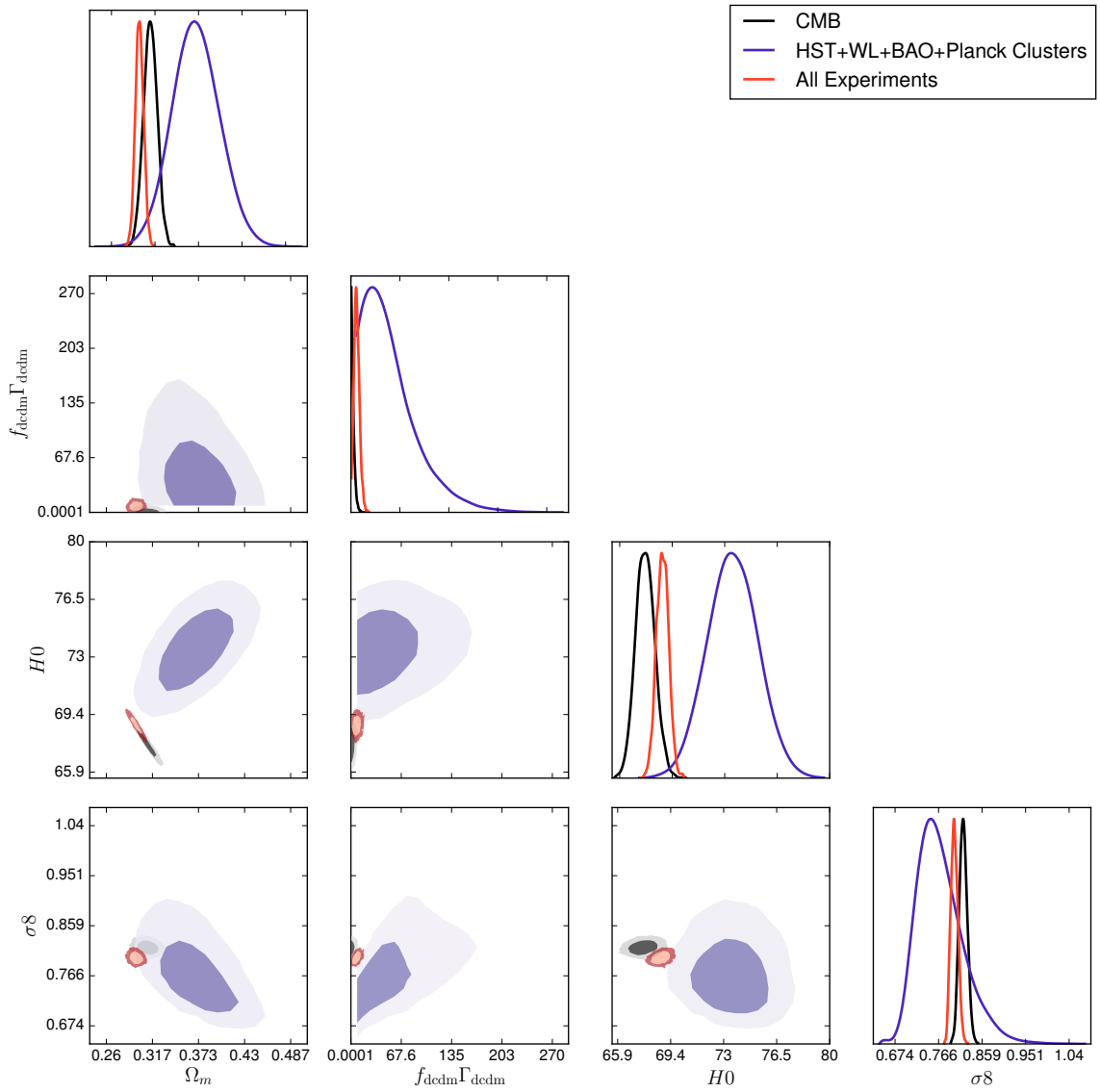

Figure 46: As in Fig. 44, but in the dcdm model with $\Gamma_{\rm dcdm} < H_0$.

With respect to the past literature, we have improved in several respects: The most obvious one is that we have been using the most recent datasets available, which should ideally lead to tighter constraints. Note also that we have corrected a mistake in the older work of [335] with a similar aim, which implies that we do not expect our constraints to match those of this reference, and does not justify a direct comparison. We have described in detail the impact of the DM decay on the TT and EE CMB power spectra, and on the matter power spectrum. This impact depends a lot on the order of magnitude of the DM lifetime. We have extended the parameter space to much smaller lifetimes, which provides a very rich phenomenology. For the first time, we also checked that degeneracies with massive neutrinos are broken when information from the large scale structure is used. Even secondary effects like CMB lensing suffice to this purpose. All constraints were derived using the most recent data of Planck [19], BAO [47] and WiggleZ [468]. Our results suggest that the bounds derived from 2015/16 CMB data are slightly stronger than 2013 ones derived in [70]: basically CMB alone is now

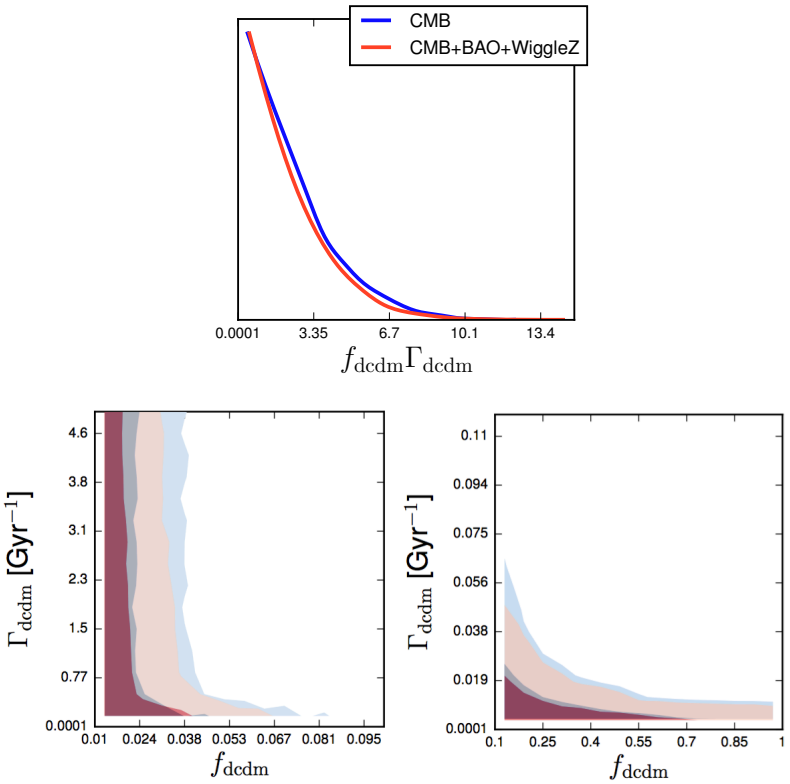

Figure 47: Strongest constraints on the decaying dark matter fraction $f_{\rm dcdm}$ as a function of the lifetime $\Gamma_{\rm dcdm}$ in the long-lived and intermediate regime.

as constraining as the global combination used in [70]. A global analysis of mutually consistent data improves the bounds further, albeit not by much: roughly by 6% at large lifetime, reaching as much as a 25% improvement at intermediate ones, before slowly degrading to the CMB-only ones for very early decays. While this points to a substantial robustness of the cosmological bound, when adding low-redshift measurements of σ_8 [18], [302] and H_0 [509], the situation is more puzzling: A tension emerges, as noted in the recent past. Although some amount of decaying DM goes in the right direction to reconcile the discrepancy, quantitatively the situation improves only marginally: no evidence in favour of decaying DM can be thus inferred, but at the same time the existing tension (not surprisingly) degrades the derived bounds by a factor of ~ 3. It appears more likely that the discrepancy requires either a different (and possibly major) alteration of the ΛCDM model, or derives from some yet unknown systematic effect.

Compared to the bounds applying to the case where the totality of the DM is assumed to be unstable, the implications of our bounds on a decaying *fraction* of DM are much broader and possibly far reaching. Although we do not aim at an exhaustive review of the model-dependent consequences of our results, let us just mention one interesting implication: Recently the possibility that a sizable if not dominant fraction of the DM is in fact in the form of stellar mass primordial black holes (BH) has been reconsidered, see for instance [104], [192], [194]. Naively, this possibility is in contradiction with existing bounds (see e.g. [506]), which however could be evaded for instance if the current BH population is much more massive than the initial one, due to a rich merger history [194]. In BH mergers, however, a sizable fraction of their mass is converted into gravitational waves. In the only merger detected to date by the LIGO detectors [7], about 5% of the mass was converted into gravitational radiation!

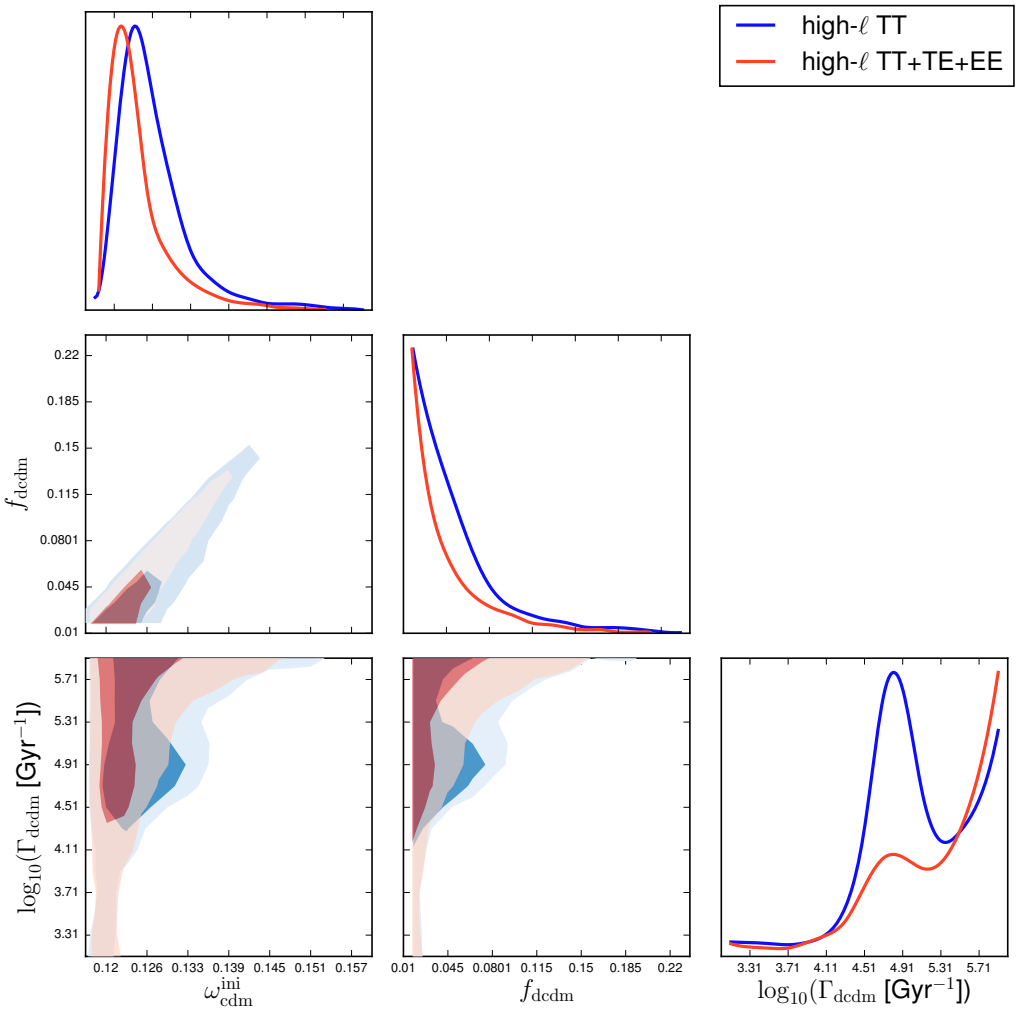

Figure 48: Strongest constraints on the decaying dark matter fraction $f_{\rm dcdm}$ as a function of the lifetime $\Gamma_{\rm dcdm}$ in the short-lived dcdm regime.

Remarkably, our CMB bound for the DM fraction converting into dark radiation has two features: i) for a large range of decay timescales, it is largely independent of the decay rate, suggesting that the bound may apply also to more complicated evolution histories than those described by a simple decay, at least to the DM fraction converted in radiation between recombination time to recent epoch. ii) numerically, if all of the DM is made of primordial BH, it excludes that in average they could have undergone even a *single* merger event with a fractional gravitational wave energy release comparable to the one detected by LIGO [7]. While a specific study for a given merger history would be needed to draw strong conclusions, qualitatively this is a new powerful argument to disfavor that a sizable fraction of DM is in the form of primordial black holes, if they undergo substantial reprocessing of the initial mass function. Actually, this is perhaps the only generic constraint that applies to primordial black hole DM candidates of *any mass*.

Let us conclude with a comment: In this work, we have ignored effects associated to the recoil velocity of daughter particles in what we dubbed "scenario 2" in Sec. 7.1. While our CMB bounds also apply to this case, typically (but this is a model-dependent statement!) more stringent cosmological

and astrophysical constraints apply. This is suggested by a number of publications, such as [49], [156]—-which incidentally also conclude that in those decaying DM models it is challenging to reconcile CMB tension with $\{\sigma_8, \Omega_m\}$ determinations from clusters—or [106]—where an effective equation of state for the semi-relativistic daughter particle is derived and constrained with the SN Ia Hubble expansion diagram. It is also expected that these models have a rich phenomenology at non-linear scales, possibly associated to the resolution of long-standing issues in the comparison of observed properties of small-scale structures with ΛCDM expectations. These studies require however dedicated simulations, which have recently started to be performed, see e.g. [587]. Definitely, the study of decaying DM scenarios, notably in the non-linear clustering regime, may still reserve some surprises.

5

NON-THERMAL BBN FROM ELECTROMAGNETICALLY DECAYING PARTICLES

This chapter is adapted from publications in Physical Review Letters [491] and Physical Review D [495].

5.1 Introduction

Electromagnetic cascade, namely the evolution of γ, $e^{\pm}$ particle numbers and energy distributions following the injection of energetic γ or e into a medium filled with radiation, magnetic fields and matter, are one of the physical processes most frequently encountered in astroparticle physics, in domains as disparate as high-energy gamma-ray astrophysics, ultra-high-energy cosmic ray propagation, or the physics of the early universe. As discussed in sec. 3.5, the elementary theory of such a cascade onto a photon background has been well known since decades, and can be shown via a textbook derivation (see Chapter VIII in [218], for instance) to lead to a universal "meta-stable" spectrum—attained on timescales much shorter than the thermodynamical equilibration scale—of the form:

$$\frac{dN_\gamma}{dE_\gamma} = \begin{cases} K_0 \left(\frac{E_\gamma}{\epsilon_X}\right)^{-3/2} & \text{for } E_\gamma < \epsilon_X \,, \\ K_0 \left(\frac{E_\gamma}{\epsilon_X}\right)^{-2} & \text{for } \epsilon_X \leq E_\gamma \leq \epsilon_c \,, \\ 0 & \text{for } E > \epsilon_c \,. \end{cases} \tag{5.1.1}$$

In the above expression, $K_0 = E_0 \epsilon_X^{-2} [2 + \ln(\epsilon_c/\epsilon_X)]^{-1}$ is a normalization constant enforcing that the total energy is equal to the injected electromagnetic energy, E_0; the characteristic energy $\epsilon_c = m_e^2/\epsilon_\gamma^{\max}$ denotes the effective threshold for pair-production ($\epsilon_\gamma^{\max}$ being the highest energy of the photon background onto which pairs can be effectively created); $\epsilon_X \leq \epsilon_c/3$ is the maximum energy of up-scattered inverse Compton (IC) photons.

A notable application of this formalism concerns the possibility of a non-thermal nucleosynthesis phase in the early universe (for recent review on this and other aspects of primordial nucleosynthesis, or BBN, see [339], [489]). The determination of the baryon energy density of the universe Ω_b inferred from the CMB acoustic peaks measurements can be used in fact to turn the standard BBN into a parameter-free theory. The resulting predictions for the deuterium abundance (or ^{2}H, the most sensitive nuclide to Ω_b) are in remarkable agreement with observations, providing a tight consistency check for the standard cosmological scenario. As discussed in sec. 1.3.2.3, The ^{4}He and ^{3}He yields too are, broadly speaking, consistent with this value, although affected by larger uncertainties. The ^{7}Li prediction, however, is a factor ~ 3 above its determination in the atmosphere of metal-poor halo stars. If this is interpreted as reflecting a cosmological value—as opposed to a post-primordial

astrophysical reprocessing, a question which is far from settled [338], [565]—it requires a non-standard BBN mechanism, for which a number of possibilities have been explored [339], [489].

In particular, cosmological solutions of the lithium problem based on electromagnetic cascades have been proposed in the last decade, see for instance [202]. However, typically they do not appear to be viable [489], as confirmed also in recent investigations (see for instance Fig. 4 in [251], dealing with massive "paraphotons") due to the fact that whenever the cascade is efficient in destroying enough ^{7}Li, the destruction of ^{2}H is too extreme, and spoils the agreement with the CMB observations mentioned above. Actually, this tension also affects some non-e.m. non-thermal BBN models, see for instance [383].

This difficulty can be evaded if one exploits the property that ^{7}Be (from which most of ^{7}Li come from for the currently preferred value of Ω_b, via late electron capture decays) has the lowest photodissociation threshold among light nuclei, of about 1.59 MeV vs. 2.22 MeV for next to most fragile, ^{2}H. Hence, to avoid any constraint from ^{2}H while being still able to photo-disintegrate some ^{7}Be, it is sufficient to inject photons with energy $1.6 < E_\gamma/\mathrm{MeV} < 2.2$, with a "fine-tuned" solution (see e.g. the remark in [489] or the discussion in [382]). Nonetheless, it turns out to be hard or impossible to produce a sizable reduction of the final ^{7}Li yield, while respecting other cosmological bounds, such as those coming from extra relativistic degrees of freedom ($N_{\rm eff}$) or spectral distortions of the CMB. A recent concrete example of these difficulties has been illustrated in [341], which tried such a fine-tuned solution by studying the effects of O(10) MeV sterile neutrino decays.

In this work, we point out that, depending on the epoch, *at sufficiently low energies of injection the cascade develops differently and the final spectrum is significantly altered with respect to Eq. (5.1.1)*, which has been incorrectly used till recently, see e.g. [341], [382]. This corresponds to the situation when the photons injected at energy E_γ are not sufficiently energetic to induce pairs onto the background photons at temperature T, and can be translated in the condition $E_\gamma \leq 10\, T_{\rm keV}^{-1}$ MeV (we use natural units with $c = k_B = 1$). For T of order $\mathcal{O}$(keV) down to $\mathcal{O}$(eV) characteristic of the period between the end of BBN to the formation of the cosmic microwave background (CMB), these energies are typically higher than the photodisintegration thresholds of light nuclei, denoted by $E_{\rm th}$.

As a concrete application, we show first the impact on the constraints in the abundance vs lifetime plane for unstable early Universe relics, decaying electromagnetically, and derived from the deuterium, ^{4}He and ^{3}He measurements. Our main conclusion is that the bounds are non universal and that they may be significantly more stringent than commonly thought. In the following, we will compare the constraints obtained from different elements in the hypothesis of the universal spectrum with the actual constraints obtained for monochromatic photon injections at different energies, below the pair production threshold ϵ_c. This parametrization is used solely for the sake of clarity; the differences would persist for any spectrum (either primary photons or secondary due e.g. to upscattering of background photons via the IC by energetic $e^\pm$) injected below the critical energy.
Secondly, we show that this re-opens a window to a cosmological solution to the ^{7}Li problem via e.m. decays. Additionally, one expects peculiar signatures associated to such scenarios, which can be probed with cosmological observations. We will discuss this both in a proof-of-principle example and in the context of a particle physics model, involving one sterile neutrino. This was chosen for its simplicity and to allow for a direct comparison with the results of [341], which studied a similar model.

This work is structured as follows. In Sec. 5.2, we describe the features of the electromagnetic (e.m.) cascades and the breakdown of the universal nonthermal spectrum, as well as our method to solve the relevant Boltzmann equations. In Sec. 5.3, we describe the nonthermal nucleosynthesis formalism and

the observational constraints being used in the following. In Sec. 5.4 we review the constraints coming from the CMB, notably from its spectral distortions, to which we will compare the BBN ones. We present our non-universal constraint in Sec. 5.5, while the solution to the Lithium problem is described in Sec. 5.6. Finally, Sec. 5.7 contains a discussion with our conclusions.

5.2 E.m. cascades and breakdown of universal nonthermal spectrum

In general, in order to compute the nonthermal photon spectrum which can photodisintegrate nuclei, one has to follow the coupled equations of both photon and electron-positron populations presented in sec. 3.5. For the problem at hand, however, where we limit ourselves to inject photons *incapable* of pair production, it is a good first approximation to ignore the nonthermal electrons; while the injected photons will in general Compton scatter and produce them, a further process, typically IC onto the photon background, is needed to channel back part of their energy in the photon channel. The energy of these photons is significantly lower than the injected photon one: whenever they are reinjected below nuclear photodissociation thresholds they are actually lost for nonthermal nucleosynthesis; otherwise they would contribute to *strengthening* the bounds, although only by a few percent, for the cases discussed below. For simplicity, let us also start by assuming that all photon interactions are *destructive*; i.e. photons are not downscattered to a lower energy. Within this approximation, the Boltzmann equation describing the nonthermal photon distribution function f_γ reads

$$\frac{\partial f_\gamma(E_\gamma)}{\partial t} = -\Gamma_\gamma(E_\gamma, T(t)) f_\gamma(E_\gamma, T(t)) + \mathcal{S}(E_\gamma, t)\,, \tag{5.2.1}$$

where $\mathcal{S}(E_\gamma, t)$ is the source injection term, Γ_γ is the total interaction rate, and we neglected the Hubble expansion rate since interaction rates are much faster and rapidly drive f_γ to a quasistatic equilibrium, $\frac{\partial f_\gamma(\epsilon_\gamma)}{\partial t} \approx 0$. Thus, we simply have

$$f_\gamma^{\rm S}(E_\gamma, t) = \frac{\mathcal{S}(E_\gamma, t)}{\Gamma_\gamma(E_\gamma, t)}\,, \tag{5.2.2}$$

where the term $\mathcal{S}$ for an exponentially decaying species with lifetime τ_X and density $n_X(t)$, of which the total e.m. energy injected per particle is E_0, can be written as

$$\mathcal{S}(E_\gamma, t) = \frac{n_\gamma^0 \zeta_X (1+z(t))^3\, e^{-t/\tau_X}}{E_0 \tau_X}\, p_\gamma(E_\gamma, t)\,, \tag{5.2.3}$$

with $z(t)$ being the redshift at time t and the energy parameter ζ_X (conventionally used in the literature) is simply defined in terms of the initial comoving density of the X particle n_X^0 and the actual one of the CMB, n_γ^0, via $n_X^0 = n_\gamma^0 \zeta_X / E_0$. We shall use as a reference spectrum the one for a two body decay $X \to \gamma U$ leading to a single monochromatic line of energy E_0, corresponding to $p_\gamma(E_\gamma) = \delta(E_\gamma - E_0)$. If the unspecified particle U is (quasi)massless, like a neutrino, one has $E_0 = m_X/2$, where m_X is the mass of the decaying particle. Note that here, we will be interested in masses m_X between a few and $\mathcal{O}(100)$ MeV, and at temperatures of order few keV or lower, hence the thermal broadening is negligible, and a Dirac delta spectrum as the one above is appropriate.

We calculate Γ_γ by summing the rates of processes that degrade the injection spectrum, namely:

- Scattering off thermal background photons, γ_{th}: $\gamma + \gamma_{th} \to \gamma + \gamma$.
  This has been studied in Ref. [573], and the scattering rate of a γ-ray with energy E_γ over a blackbody with temperature T is given by

$$\Gamma_{\gamma\gamma} = -0.1513\alpha^4 m_e \left(\frac{E_\gamma}{m_e}\right)^3 \left(\frac{T}{m_e}\right)^6 . \tag{5.2.4}$$

- Bethe-Heitler pair creation : $\gamma + N \to e^\pm + N$.
  The cross section for this process is given by [349]

$$\sigma_{\rm BH} \simeq \frac{3}{8}\frac{\alpha}{\pi}\sigma_{\rm Th}\left(\frac{28}{9}\ln\left(\frac{2E_\gamma}{m_e}\right) - \frac{218}{27}\right) Z^2 . \tag{5.2.5}$$

- Compton scattering over a thermal electron : $\gamma + e^\pm_{th} \to \gamma + e^\pm$. For the temperature of interest of $\mathcal{O}$(keV), one can consider electrons to be at rest. In this case, we have [362]

$$\Gamma_{\rm CS} = \bar{n}_e \frac{3\sigma_{\rm Th}}{4x}\left[\left(1 - \frac{4}{x} - \frac{8}{x^2}\right)\ln(1+x) + \frac{1}{2} + \frac{8}{x} - \frac{1}{2(1+x)^2}\right] ,$$

  where $x = \frac{2E_\gamma}{m_e}$ and $\bar{n}_e$ is the number density of background electrons and positrons.

In reality, not all scattered photons will be "lost": even ignoring the energy transferred to e^- and e^+, Compton scattering and $\gamma\gamma$ scattering still leave lower-energy photons in the final state. This effect can be accounted for by replacing the rhs of Eq. (5.2.1) by the following term:

$$\mathcal{S}(E_\gamma, t) \to \mathcal{S}(E_\gamma, t) + \int_{E_\gamma}^{\infty} dx K_\gamma(E_\gamma, x, t) f_\gamma(x\,, t) . \tag{5.2.6}$$

The additional term of which the kernel is K accounts for scattered photons and is obtained by summing the differential rates for the $\gamma\gamma$ scattering off background photons and the Compton scattering over thermal electrons, respectively given by [573]

$$\frac{d\Gamma_{\gamma\gamma}(E_\gamma, E'_\gamma)}{dE'_\gamma} = \frac{1112}{10125\pi}\alpha^2 r_\epsilon^2 m_e^{-6} \times \frac{8\pi^4 T^6}{63} E'^2_\gamma \left[1 - \frac{E_\gamma}{E'_\gamma} + \left(\frac{E_\gamma}{E'_\gamma}\right)^2\right]^2 , \tag{5.2.7}$$

$$\frac{d\Gamma_{\rm CS}(E_\gamma, E'_\gamma)}{dE'_\gamma} = \pi r_e^2 \bar{n}_e \frac{m_e}{E'^2_\gamma}\left[\frac{E'_\gamma}{E_\gamma} + \frac{E_\gamma}{E'_\gamma} + \left(\frac{m_e}{E_{\gamma'}} - \frac{m_e}{E_\gamma} - 1\right)^2 - 1\right] . \tag{5.2.8}$$

The integral in Eq. (5.2.6) now depends on f_γ. We numerically solve this Boltzmann equation using an iterative method: we start from the Dirac distribution and the algebraic solution of Eqs. (5.2.2) and (5.2.3), plug in the result thus obtained in Eq. (5.2.6) to estimate the new "effective" source term, and proceed. Note that the zeroth-order solution of Eqs. (5.2.2) and (5.2.3) is exact at the end point $E_\gamma = E_0$, with further iterations essentially improving the description at lower and lower energies. We stop iterating when the resulting improvement on the constraints is smaller than 3%. Figure 49-left panel shows the resulting spectrum proportional to f_γ according to the prefactor of Eq. (5.2.3)] for an injected monochromatic photon of 70 MeV at the temperature $T = 100\,$eV in the commonly used universal spectrum approximation (long-dashed red line) and for the actual solution of the Boltzmann equation, as a function of the iteration (short-dashed blue lines). For this example, one can estimate $\epsilon_c \simeq 100\,$MeV and $\epsilon_X \simeq 30\,$MeV. Two features are clearly visible: i) the universal spectrum grossly

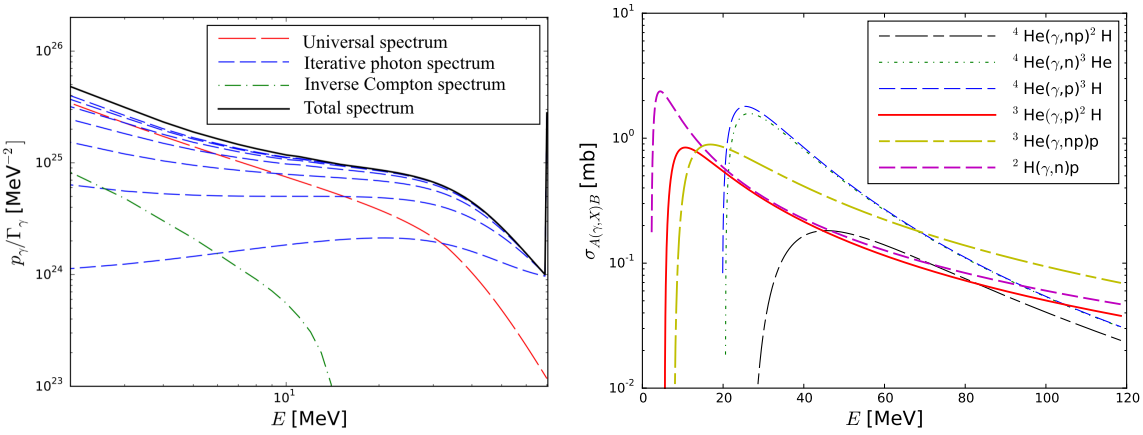

Figure 49: *Left panel:* Spectrum computed in this work (solid black line) compared with approximated one used in the literature (long-dashed red line), for the case $E_0 = 70\,\mathrm{MeV}$ at $T = 100\,\mathrm{eV}$. The short-dashed, blue lines show the contribution from the photon population as computed in our iterative treatment, with the number of iterations increasing from 1 to 7 from bottom to top. The dot-dashed curve is the estimated contribution to the photon spectrum from the nonthermal population of electrons excited by the energy loss channels of the photons. *Right panel:* Cross sections for the relevant photodisintegration processes.

fails for $E_\gamma \geq \epsilon_X$, as expected, since it imposes an artificial suppression; ii) the exact solution is significantly harder at intermediate energies, but attains the same slope as the universal spectrum at low energies. However, the low-energy normalization is altered, since the universal spectrum is unphysical in pushing too many photons to low energies (below nuclear thresholds).

Although neglected so far, an analogous treatment can be applied to the nonthermal electron distribution f_e: the source term will be given by the Compton scattering and Bethe-Heitler processes of nonthermal photons, and the "loss term" into the photon channel essentially by IC scattering. The latter will in turn correspond to a new source term in Eq. (5.2.6), the impact on the photon spectrum is reported in Figure 49-left panel with a dot-dashed green line. It is clear that, unless the injected photon energies are too high, this only brings a modest correction to the *low-energy* tail of the spectrum, with the expected improvement in the constraints being even less prominent. The iterative solution technique adopted above would still perform correctly, although a detailed evaluation would render the calculation unnecessarily lengthy, and will not be pursued further here. We checked in fact that, for the cases discussed in the following, four iterations for the photon spectrum are enough to obtain bounds accurate at the 10% level (and often better) and always on the conservative side.

Since the critical energy for pair production is a dynamical quantity that increases at later times due to the cooling of the Universe, it may happen that the primary photons energy E_0 is above threshold for pair production at early times and below it at late times (we do take into account that the decay is not instantaneous). In general, at each time we will compare E_0 with ϵ_c and use the universal spectrum when $E_0 > \epsilon_c$ or the monochromatic spectrum with the complete expression for $\mathcal{S}$ when $E_0 < \epsilon_c$. This gives always a qualitatively correct solution, albeit it is somewhat approximate when $E_0 \sim \epsilon_c$. Since this is realized only in a very narrow interval of time, however, the final results are also quantitatively robust, barring artificial "fine-tuned" results in a specific region of the parameter space.

5.3 Nonthermal nucleosynthesis

5.3.1 *Review of the formalism*

At temperatures of few keV or lower, the standard BBN is over, and the additional nucleosynthesis can be simply dealt with as a postprocessing of the abundances computed in the standard scenario, for which we use the input values from Parthenope [481], with the updated value of Ω_b coming from Ref. [19].

As long as the amount of injected energy is small compared to the density of background CMB photons, one can neglect its impact on the expansion history. Thus, the nonthermal nucleosynthesis due to electromagnetic cascades can be described by a system of coupled differential equations of the type

$$\frac{dY_A}{dt} = \sum_T Y_T \int_0^\infty dE_\gamma f_\gamma(E_\gamma, t)\sigma_{\gamma+T\to A}(E_\gamma) - Y_A \sum_P \int_0^\infty dE_\gamma f_\gamma(E_\gamma, t)\sigma_{\gamma+A\to P}(E_\gamma) \,, \quad (5.3.1)$$

where: $Y_A \equiv n_A/n_b$ is the ratio of the number density of the nucleus A to the total baryon number density n_b (this factors out the trivial evolution due to the expansion of the Universe); and $\sigma_{\gamma+T\to A}$ is the photodissociation cross section of the nucleus T into the nucleus A, i.e. the production channel for A; $\sigma_{\gamma+A\to P}$ is the analogous destruction channel. Both cross sections are actually vanishing below the corresponding thresholds. In general one also needs to follow secondary reactions of the nuclear byproducts of the photodissociation, which can spallate on or fuse with background thermalized target nuclei, but none of that is relevant for the problem at hand. According to Ref. [202], the only signification secondary production is that of ^{6}Li. Despite extensive work in the past, the current observational status of ^{6}Li as a reliable nuclide for cosmological constraints is doubtful, given than most claimed detections have not been robustly confirmed, and a handful of cases are insufficient to start talking of a "cosmological" detection, see [338]. We shall thus conservatively ignore these nuclide and the secondary reactions in the following.

With standard manipulations, namely by transforming Eq. (5.3.1) into redshift space, defining $H(z) = H_r^0(1+z)^2$ as appropriate for a Universe dominated by radiation (with $H_r^0 \equiv H_0\sqrt{\Omega_r^0}$, H_0 and Ω_r^0 being the present Hubble expansion rate and fractional radiation energy density, respectively), one arrives at

$$\frac{dY_A}{dz} = \frac{-1}{H_r^0(z+1)^3} \times \left[\sum_T Y_T \int_0^\infty dE_\gamma f_\gamma(E_\gamma, z)\sigma_{\gamma+T\to A}(E_\gamma) - Y_A \sum_P \int_0^\infty dE_\gamma f_\gamma(E_\gamma, z)\sigma_{\gamma+A\to P}(E_\gamma)\right] \quad (5.3.2)$$

which is solved numerically for the cases of interest.

5.3.2 *Light element abundances*

Among light elements, as discussed in section 1.3.2.3, we can broadly speak of an agreement of standard BBN predictions with observations for the case of ^{4}He, ^{3}He, and ^{2}H, while at face value the ^{7}Li yield is overpredicted by a factor ~ 3 with respect to observations. Since the interpretation of ^{7}Li observations in terms of a primordial yield is still a subject of debate, see Refs. [338], [339], [489], one can consider

two possibilities: either the observed values are not representative of the cosmological production mechanism, in which case it would be meaningless to derive constraints based on those observations, or alternatively, modifications to the standard BBN scenario, including electromagnetic cascades, *could* reconcile the envelope of ^{7}Li observed values with a primordial origin. In the following, we will adopt the former, more conservative option, and hence we will not use ^{7}Li for constraints on e.m. cascades. We discuss the latter possibility in sec. 5.6.

For the observationally imposed limits, we use the following (already introduced in section 1.3.2.3): for ^{4}He, which can only be destroyed by nonthermal BBN, we just impose the 2-σ lower limit on the mass fraction $Y_p > 0.2368$ from Ref.[74]. For ^{2}H we adopt the 2-σ limit $2.56 \times 10^{-5} < {}^2\mathrm{H/H} < 3.48 \times 10^{-5}$ from Ref. [455]; similar results would follow by adopting the combination value compiled in Ref. [339], namely $2.45 \times 10^{-5} < {}^2\mathrm{H/H} < 3.31 \times 10^{-5}$, which is also closer to the results of Ref. [480]; our interval also overlaps with the recent determination in Ref. [507]. For ^{3}He we impose no observational lower limit, but the 2-σ upper limit from [78] $^3\mathrm{He/H} < 1.5 \times 10^{-5}$. It is worth noting that, had we used some alternative recent determinations such as [345] for ^{4}He or [197] for ^{2}H, some mild tension with the standard BBN predictions for the value of η recently reported, e.g., by Planck would have appeared. These discrepancies are much smaller than the one affecting ^{7}Li, and could be easily accommodated with a more conservative error attribution: for ^{4}He this is the conclusion supported, e.g., in Ref. [455] or the recent Ref. [203], essentially consistent with the value we quoted above; for ^{2}H it is also a possibility suggested by the slightly anomalous dispersion of several measurements around the mean (see e.g. the discussion in Ref. [339]). Alternative possibilities to reduce the tension with one or several of these determinations include a slightly different value of η between the BBN epoch and the CMB one, the addition of exotic phenomena such as cascades, and possibly others. In the following we shall adopt a similar attitude to the one adopted before for ^{7}Li and consider conservatively the more generous observational ranges reported above. This is also justified to ease the comparison with earlier analyses of cascade nucleosynthesis bounds, which used similar ranges. Our main emphasis here is in fact to gauge the impact of a more correct treatment of electromagnetic cascades, rather than deriving the most aggressive bounds achievable. Needless to say, should more precise observational values be confirmed in future studies, if in agreement with standard BBN expectations, it would be worth it to derive updated stringent bounds; if not, it would be interesting to rediscuss possible explanations in the context for instance of cascade nucleosynthesis, as we do for ^{7}Li in sec. 5.6.

For the current application, the network of reactions used is reported in Fig. 49-right panel, and follows the parametrization in the appendix of [202]. (Actually, the reaction $^4\mathrm{He}(\gamma, {}^2\mathrm{H})^2\mathrm{H}$ is significantly suppressed with respect to the others and thus not shown in the figure but is included in our numerical treatment.) Note that all cross section share the same qualitative features: they rise fast just above threshold, go through a peak (the so-called giant dipole resonance), eventually showing a decreasing tail at higher energies. We shall compare the bounds thus obtained with the ones coming from CMB spectral distortions and entropy production, briefly recalled in the following section.

5.4 Constraints from the CMB

It is well known that a late injection of photons in the thermal bath can lead to additional measurable cosmological alterations.

For instance, the injection of a significant amount of energy can lead to modification of the photon-baryon ratio η or equivalently to the increase of the comoving entropy. Since the inferred values of Ω_b

at the BBN and CMB epoch are compatible, no major entropy release could have taken place between nucleosynthesis and decoupling. It can be shown that, in a Universe dominated by radiation and by considering that the decays have happened at $t \sim \tau$, we have for a small fractional change in entropy (see e.g. Ref. [341])

$$\frac{\Delta S}{S} \simeq \ln \frac{S_f}{S_i} = 2.14 \times 10^{-4} \left(\frac{\zeta_{X\to\gamma}}{10^{-9}\ \mathrm{GeV}} \right) \left(\frac{\tau_{\mathrm{x}}}{10^6\ \mathrm{s}} \right)^{1/2}, \tag{5.4.1}$$

with a slight abuse of notation since $\zeta_{X\to\gamma}$ now has to be intended to include any electromagnetically interacting decay products, all of which contribute to modify the photon-baryon ratio. To derive a statistically sound constraint, one should combine BBN and CMB data, allowing for an entropy increase between the two epochs. Since, as we shall see, this constraint is typically much weaker than others, such an exercise would bring us far beyond the scope of this study adding a lengthy and unnecessary complication. We shall thus limit ourselves to illustrate the constraint that would follow by allowing a maximal 2% increase in the entropy between the two periods. This is an educated guess of the order of the bounds that one can expect, roughly corresponding to the 2-σ error bars on Ω_b from Planck 2015 [19].

Furthermore, as discussed in sec. 3.6, the spectrum of the CMB itself can also be affected through two types of deformation: a modification of the chemical potential μ and a modification of the Compton-y parameter, which are related to the energy gained by a photon after a Compton scattering. For the relatively early time we focus on, the constraints come essentially from μ-type distortions. We follow here the results of Ref. [164], which contains improvements with respect to the ones given in Ref. [322], notably for $z \leq 2 \times 10^6$, while Ref. [322] is accurate enough at late times (see Fig. 16 in Ref. [164]). Hence, we adopt

$$\mu \simeq 8.01 \times 10^2 \left(\frac{\tau_X}{1\ \mathrm{s}} \right)^{1/2} \times \mathcal{J} \times \left(\frac{\zeta_{X\to\gamma}}{1\ \mathrm{GeV}} \right), \tag{5.4.2}$$

with

$$\mathcal{J} = \begin{cases} \exp\left[-\left(\frac{\tau_{\mathrm{dC}}}{\tau_X} \right)^{\frac{5}{4}} \right] & \text{for } z < 2 \times 10^6 \\ 2.082 \left(\frac{\tau_{\mathrm{dC}}}{\tau_X} \right)^{\frac{10}{18}} \exp\left[-1.988 \left(\frac{\tau_{\mathrm{dC}}}{\tau_X} \right)^{\frac{10}{18}} \right], & \text{otherwise,} \end{cases} \tag{5.4.3}$$

where $\tau_{\mathrm{dC}} = 1.46 \times 10^8\, (T_0/2.7\ \mathrm{K})^{-12/5} (\Omega_b h^2)^{4/5} (1 - Y_p/2)^{4/5}$ is the "double Compton" interaction time in terms of the current CMB temperature T_0, with $Y_p \simeq 0.25$ the primordial mass fraction of ^{4}He. We use the limit given by COBE on the chemical potential: $|\mu| \leq 9 \times 10^{-5}$ [246], but we will also show the sensitivity that should characterize the future experiment PIXIE, of the order of $\mu \geq 5 \times 10^{-8}$, at 1-$\sigma$ [374].

5.5 Non Universal constraints from BBN

One of the most peculiar features of the spectral nonuniversality of photons injected below the pair production threshold is that the final outcome reflects the energy distribution of the injected photons *with respect to* the shape of the relevant photodisintegration cross sections, shown in Fig. 49- right panel. This motivated us to choose in the following for each nuclide, the results for two representative examples of monochromatic injection: one close to the resonant peak and another one well after it. The markedly different outcomes obtained in the two cases should thus convincingly argue that constraints of actual models are going to be determined not only by the decay time and the overall energy injected but also by the energy range at which the bulk of the photons lies.

5.5.1 *Constraints from ^{4}He*

The simplest situation is certainly the one concerning ^{4}He: being the only abundant nucleus subject to photodisintegration, its nonthermal e.m. production is irrelevant, and one only has to care about its destruction; i.e. only the term proportional to Y_A at the rhs of Eq. (5.3.2) is important. The results obtained by using a monochromatic injection at 70 MeV (hatched/light shaded red), at 30 MeV (dark shaded red), and the universal spectrum are shown in Fig. 50. The vertical lines indicate the time at which the threshold energy for pair production ϵ_c starts exceeding the corresponding injected energy. One might naively expect that this is the time at which the constraints obtained from the incorrect use of the universal spectrum start to deviate from the actual ones. However, when taking into account the fact that the decay is not instantaneous, it turns out that constraints already start to deviate at $\sim \tau_X/5$, and the closer to the post-threshold cross section resonance we inject energy, the earlier deviations appear.

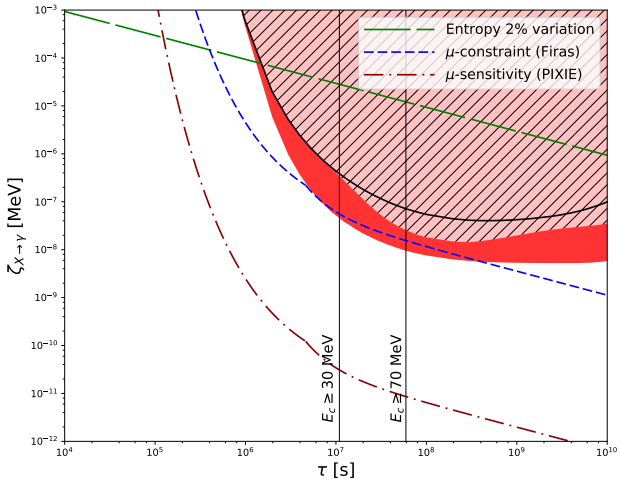

Figure 50: Constraints from ^{4}He depletion in the standard case (black line) and for a non-universal spectrum with $E_0 = 30$ MeV (dark shaded red) and E_0=70 MeV (hatched/light shaded red). We also show the sensitivity to the entropy variation constraint (green dashed line), current constraints from CMB spectral distortions (excluded above the short-dashed blue line), and the sensitivity reach of the future mission PIXIE [374] (above the red dot-dashed line).

Although the BBN bounds coming from excessive depletion are typically (but not always!) weaker than CMB distortion bounds, also reported in the figure, note that in both cases bounds can differ from the ones derived with the universal spectrum by a large factor, up to an order of magnitude if the energy of the photons is around the peak of the photodissociation cross section. For higher-injected energies, they tend to become closer to the universal spectrum constraints, as it should. In fact one can envisage fine-tuned situations in which they become slightly weaker, albeit this conclusion does depend on the extrapolation of the photodisintegration cross sections, of which the reliability at high energy has never been quantitatively assessed in the context of BBN applications.

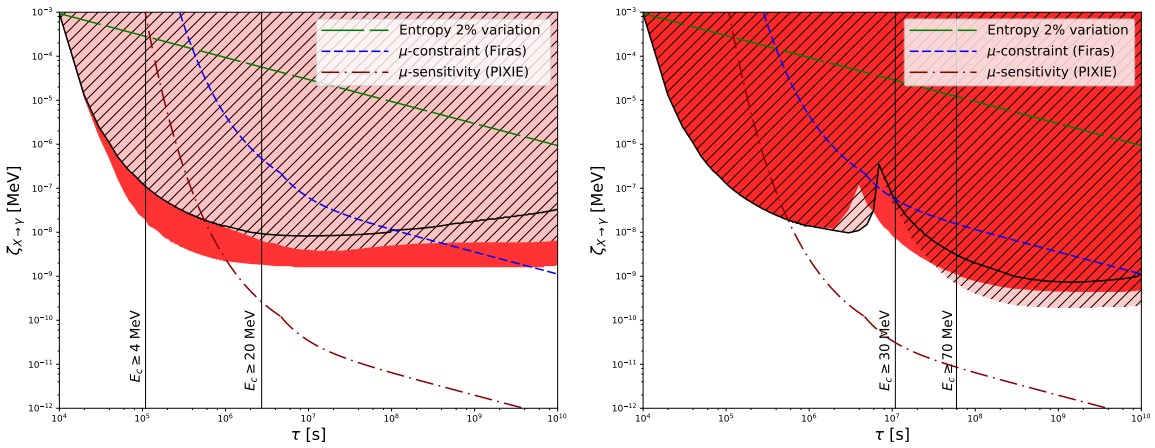

Figure 51: *Left panel:* Constraints from deuterium depletion in the standard case, with $E_0 \leq 20$ MeV (black solid line) and for a nonuniversal spectrum with $E_0 = 4$ MeV (dark shaded red) and E_0=20 MeV (hatched/light shaded red). All other constraints/sensitivities shown as in Fig. 50. *Right panel:* Constraints from Deuterium depletion and production in the standard case, with $E_0 \geq 20$ MeV (black solid line) and for a nonuniversal spectrum with $E_0 = 30$ MeV (dark shaded red) and E_0=70 MeV (hatched/light shaded red). All other constraints/sensitivities shown as in Fig. 50.

5.5.2 *Constraints from ^2H*

For deuterium, the situation is more complicated because several regimes are present. At low τ_X, ϵ_c is below ^{4}He photodissociation threshold (and in some cases also below $A = 3$ nuclei photodissociation thresholds, which are, however, less relevant). Hence, only constraints from overdestructions are present. At high τ_X, however, what dominates is the overproduction from ^{4}He destruction.

Figure 51-left panel, shows the illustrative case where production channels are turned off: this is exact for $E_0 \leq 8\,\mathrm{MeV}$, but a good approximation till $E_0 \leq 20\,\mathrm{MeV}$. Note the qualitative similarity to the ^{4}He case, apart for the modifications due to the different features of the respective cross sections.

Whenever production channels from ^{4}He are open, which requires $E_0 \geq 20\,\mathrm{MeV}$, the constraints are significantly stronger at large τ_X, as shown in Fig. 51-right panel. Once again, a violation of universality (and a sensitivity to the energy dependence of the cross section) is clearly manifest by the two cases shown, $E_0 = 30\,\mathrm{MeV}$ and $E_0 = 70\,\mathrm{MeV}$.

It is also worth noting that for deuterium the constraints are significantly stronger than the ones coming from CMB spectral distortions. By improving the sensitivity to μ down to $\mu \geq 5 \times 10^{-8}$, the sensitivity expected by the future mission PIXIE [374] (shown by the red, dot-dashed curve) would greatly strengthen these constraints, with the exception of very small lifetimes where deuterium overdestruction would still provide the dominant bounds.

5.5.3 *Constraints from ^3He*

First of all, a premise is necessary: there are in fact two nuclei with $A = 3$, ^{3}He, and ^{3}H, the latter being unstable to beta decay into ^{3}He with a half-time of over 12 years, or about 4×10^8 s. Practically, however, for the purposes of the constraints discussed here, one can sum the equations for ^{3}He and ^{3}H and treat them as a single effective nucleus with $A = 3$. The reason is twofold: first, we only

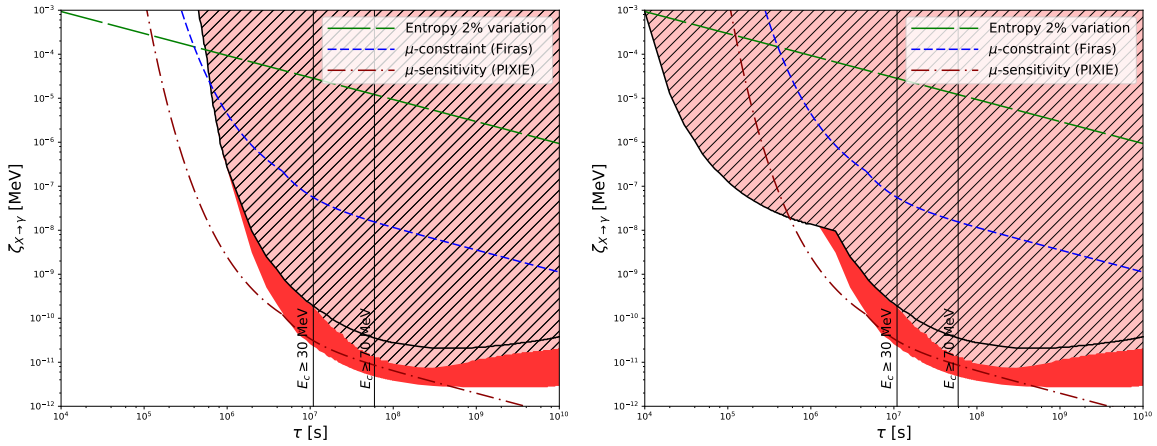

Figure 52: *Left panel:* Constraints from the ^{3}He production in the standard case (black line) and for a nonuniversal spectrum with $E_0 = 30$ MeV (dark shaded red) and E_0=70 MeV (hatched/light shaded red). All other constraints/sensitivities shown as in Fig. 50. *Right panel:* Global BBN best constraints in the standard case (black line) and for a nonuniversal spectrum with $E_0 = 30$ MeV (dark shaded red) and E_0=70 MeV (hatched/light shaded red). All other constraints/sensitivities shown as in Fig. 50.

require ^{3}He not to be overproduced with respect to the observational upper limit. Hence, the key reactions are the *production* channels by single nucleon photodisintegration from ^{4}He, which are only open above 20 MeV, rather than the destruction ones. Second, ^{3}He and ^{3}H are "mirror nuclei" under the isospin symmetry $n \leftrightarrow p$, and their nuclear properties are in fact very similar: the corresponding thresholds in nuclear cross sections, for instance, only differ by some 0.8 MeV (compare the two curves in Fig. 49-right panel.) From Fig. 52-left panel, where we report our results, it is clear that the photodisintegration cross section for single nucleon emission from ^{4}He, when open, is so important that very stringent nucleosynthesis constraints follow. In fact, they are much stronger than the current ones coming from CMB spectral distortions, although future PIXIE sensitivity might improve over them over most of the parameter space.

Notice the importance of the nonuniversality: the two cases with 30 or 70 MeV monochromatic injections lead to significantly different constraints, and in both cases depart from the "universal spectrum" ones.

5.6 A solution to the cosmological lithium problem

5.6.1 *Proof of principle*

If the injected energy is $1.59 < E_0/\text{MeV} < 2.22$, the only open non-thermal BBN channel is $\gamma + {}^7\text{Be} \to {}^3\text{He} + {}^4\text{He}$, whose cross-section [1] we denote with $\sigma_\star$. Furthermore, the problem at hand is much simpler for a couple of reasons: i) The resulting secondary or tertiary photon are typically at too low-energies to contribute to photo-dissociations and can be neglected. We thus rely on eq. 5.2.3. The results that we obtain are in this respect slightly conservative, by an amount which we estimated to be of the order of a few %. ii) There are no relevant nuclei that can act as a source term and only one evolving

1 It is worth reporting that the cross-section for this process reported in the appendix of [202] is erroneous. This has already been pointed out in [341], which we agree with. The correct formula is used in the following.

species (since $Y_7 \ll Y_{3,4}$). From eq. 5.3.2, we have for the final (at z_f) to initial (at z_i) abundance ratio

$$\ln\left(\frac{Y_{^7\mathrm{Be}}(z_i)}{Y_{^7\mathrm{Be}}(z_f)}\right) = \int_{z_f}^{z_i} \frac{n_\gamma^0 \zeta_X\, \sigma_\star(E_0)\, c\, e^{-1/(2H_r^0 \tau_X (z'+1)^2)}}{E_0 H_r^0 \tau_X \Gamma(E_0, z)} dz' \,. \tag{5.6.1}$$

By construction, equating the suppression factor given by the RHS of the Eq. (5.6.1) to $\sim 1/3$ provides a solution to the ^{7}Li problem which is in agreement with all other constraints from BBN. In Fig. 53-left panel, the lower band shows for each τ_X the range of ζ_X corresponding to a depletion from 40% to 70%, for the case $E_0 = 2\,\mathrm{MeV}$. Similar results would follow by varying E_0 by 10% about this value, i.e. provided one is not too close to the reaction threshold. The upper band represents the analogous region if we had distributed the same injected energy according to the spectrum of Eq. (5.1.1), up to $\min[\epsilon_c\,, E_0]$. It is clear that in the correct treatment a large portion of this region survives other cosmological constraints, described below, while none survives in the incorrect treatment.

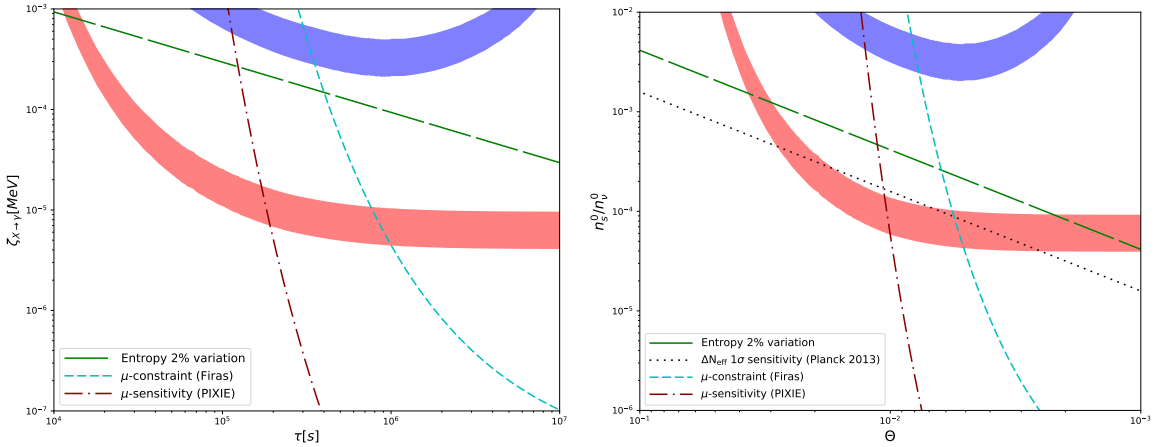

Figure 53: *Left panel:* The lower band is the range of abundance parameter $\zeta_{X\to\gamma}$ vs. lifetime τ_X, for which the primordial lithium is depleted to 40% to 70% of its standard value, for a monochromatic photon injection with energy $E_0 = 2\,\mathrm{MeV}$. The upper band represents the analogous region if we had distributed the same injected energy, up to $E_0 = 2\,\mathrm{MeV}$, according to the erroneous spectrum of Eq. (5.1.1). Above the solid green curve, a change in entropy (and Ω_b) between BBN and CMB time larger than the 2σ error inferred from CMB would be obtained. The region to the right of the short-dashed cyan curve is excluded by current constraints from μ-distortions in the CMB spectrum [246] according to the computation of [164]. The dot-dashed red curve is the forecasted sensitivity of the future experiment PIXIE, corresponding to $|\mu| \sim 5 \times 10^{-8}$[374]. *Right panel:* Constraints for the sterile neutrino model discussed in the text. The legend is the same as for case 1.

For illustration, in Fig. 53 the solid blue line represent the level of entropy release associated to a variation of 2σ around the best-fit measured value of Ω_b by Planck, $\Delta S/S \simeq 0.022$ [17]. Since the level of injected energy needed to solve the lithium problem via a monochromatic line is up to two orders of magnitude below the bounds, it is clear that this constraint is very weak, but for very short lifetimes of the order of $10^4\,\mathrm{s}$.

The μ-type spectral distortion bound excludes the region to the right of the dot-dashed, green curve in Fig. 53. For comparison, the dashed cyan curve reports the much weaker bound that would follow from the approximations in [322]. We also checked that the extra constraint due to extra "dark radiation" parameterized by $N_{\rm eff}$ is irrelevant as long as the branching ratio in extra relativistic species is not

larger than *a couple of orders of magnitudes* with respect to the photon one. We thus conclude that there is a significant interval of lifetimes ($10^4 \leq \tau_X/\mathrm{s} < 10^6$) and corresponding energy injection parameter $10^{-3} > \zeta_{X\to\gamma}/\mathrm{MeV} > 1.3\times10^{-6}$ for which a perfectly viable solution is possible. We remind once again that this possibility appeared to be closed due to the use of Eq. (5.1.1) beyond its regime of applicability.

5.6.2 *A concrete realisation with a sterile neutrino*

One may wonder how realistic such a situation is in a concrete particle physics model. Although we refrain here from detailed model-building considerations, it is worth showing as a proof-of-principle that models realizing the mechanism described here while fulfilling the other cosmological constraints (as well as laboratory ones) can be actually constructed. Let us take the simplest case of a sterile Majorana neutrino, as introduced in sec. 3.2.2, with mass in the range $3.2 < M_s/\mathrm{MeV} < 4.4$, mixing *mainly* with flavour α neutrinos via an angle θ_α. We also define $\Theta^2 \equiv \sum_\alpha \theta_\alpha^2$. The three main decay channels of this neutrino are (see e.g. [102] and refs. therein):

- $\nu_s \to 3\nu$, with rate $\Gamma_{\nu_s\to3\nu} \simeq \frac{G_F^2 M_s^5 \Theta^2}{192\pi^3}$;
- $\nu_s \to \nu_\alpha e^+e^-$, with a rate depending on single θ_α's;
- $\nu_s \to \nu\gamma$, with a rate $\Gamma_{\nu_s\to\nu\gamma} \simeq \frac{9G_F^2\alpha M_s^5}{256\pi^4}\Theta^2$.

The resulting branching ratios for the masses of interest and $\theta_e \ll \Theta$ are of the level of $0.9 : 0.1 : 0.01$, respectively. It is physically more instructive to normalize the abundance of the ν_s, n_s^0, in terms of one thermalized neutrino (plus antineutrino) flavour species, n_ν^0. In Fig. 53 - right panel, we show the corresponding range of parameters in the $\Theta - n_s^0/n_\nu^0$ plane, for $M_s = 4.4\,\mathrm{MeV}$, for which the ^{7}Li problem is solved, fulfills cosmological constraints and, provided that $\theta_e \ll \Theta$, also laboratory ones [266]. It is worth noting that: i) the entropy release bound is now close to the region of interest, since the decay mode $\nu_s \to \nu_\alpha e^+e^-$, which is useless as far as the ^{7}Be dissociation is concerned, dominates the e.m. energy injection. ii) A non-negligible fraction of relativistic "dark energy" is now injected, mostly via the dominant decay mode $\nu_s \to 3\nu$; hence we added the current $1\,\sigma$ sensitivity of Planck to N_{eff} [17], with ΔN_{eff} computed similarly to what done in [341]. The needed abundance could be obtained in scenarios with low reheating temperature [266].

5.7 Conclusions

We have argued that the universality of the photon spectral shape in electromagnetic cascades has often been used in cosmology even beyond its regime of applicability. When the energy of the injected photons falls below the pair production threshold, i.e. approximately when $E_\gamma \leq m_e^2/(22\,T) \sim 10\,T_{\mathrm{keV}}^{-1}\,\mathrm{MeV}$, the universal form breaks down.
In sec. 5.5, we showed how important the modifications to the photon spectrum in this regime are for the constraints from nonthermal BBN. This required the numerical solution of the relevant Boltzmann equations, which we attacked by an iterative scheme. The constraints we obtained, for illustrative cases of monochromatic energy injection at different epochs, are often much stronger than the ones presented in the literature (up to an order of magnitude), notably when the injected photon energy falls close to the peak of the photodisintegration cross section of the relevant nucleus. In fact, the breaking of the

nonuniversality is nontrivial and is essentially controlled by the energy behavior of the cross sections: in the universal limit, most of the photons lie at relatively low-energies, so that the cross-section behaviour at the resonance just above threshold is what matters the most. In the actual treatment, the photons may be also sensitive to the high-energy tail of the process. Future studies aiming at assessing the nuclear physics uncertainties affecting these types of bounds would benefit from this insight. It cannot be excluded that in some cases constraints *weaken* a bit with respect to what is considered in the literature.

We also compared BBN bounds with constraints coming from CMB spectral distortions. A summary plot of the "best constraints" is reported in Fig. 52-right panel, for two choices of the monochromatic photon energy. We concluded that BBN limits are improving over *current* constraints from COBE via the requirement not to underproduce ^{2}H (at low injection lifetime τ_X), or not to overproduce ^{3}He (at high τ_X), while ^{4}He is never competitive. The bounds from a future CMB spectral probe such as PIXIE would not only greatly improve current CMB constraints but would also reach the level of current constraints from ^{3}He (often improving over them) allowing for an independent consistency check. This is reassuring, since the cosmological reliability of ^{3}He constraints does stand on some astrophysical assumptions. Below $\tau_X \sim 5 \times 10^5$ s, however, ^{2}H constraints would probably remain the most stringent ones for a long time to come. Fortunately they are i) quite robust, relying on the single, well-known cross section $^2\mathrm{H}(\gamma, n)p$, and ii) easy to compute, since no coupled network of equations needs to be solved, the problem reducing to the numerical evaluation of a single integral. This is also the region where constraints coming from hadronic decay modes (not revisited here) are quite stringent. A synergy between BBN and CMB is thus going to be necessary for this kind of physics even in the decades to come.

However, the most striking consequences of our better treatment of the E.M. cascade problem in the early universe is perhaps that it can potentially re-open the possibility of electromagnetic cacade solutions to the so-called "lithium problem", which were thought to be excluded by other cosmological constraints. In sec. 5.6, we substantiated this point with a proof-of-principle example of a photon line injection at ~ 2 MeV from a particle decay, satisfying by construction all other BBN constraints but, not trivially, also all other cosmological bounds plaguing previous attempts. Although we did not indulge into particle model building, we proved that the right conditions can be actually satisfied in a simple scenario involving a ~ 4 MeV sterile neutrino mostly mixed with ν_τ and/or ν_μ with effective mixing angle $\Theta \sim 10^{-2}$.

The possibility to find new mechanisms to deplete the standard BBN prediction of lithium abundance in a consistent way is probably the most spectacular consequence of our investigation. In turn, this could stimulate more specific model-building activities. For instance, decays of relatively light new neutral fermionic particles X for which the $\nu+\gamma$ channel is the only two body SM channel opened—as it is the case for the light gravitinos in supergravity models—constitute a natural class of candidates. Alternatively, one may think of decaying scenarios involving a pair of quasi degenerate mass states X and Y, which are potentially much heavier than the MeV scale. Some of these scenarios may be motivated by other astroparticle or particle physics reasons and certainly deserve further investigation. We also showed how improvements in the determination of $\mu-$type spectral distortions bounds of the CMB might be crucial to test these scenarios: testing frameworks for the particle physics solutions to the lithium problem may thus provide additional scientific motivations for future instruments like PIXIE [374]. Computations of distortions corresponding to specific injection histories may also be re-

fined: for instance, for short lifetimes relativistic corrections to the double Compton and Compton scattering may be important to improve the theoretical accuracy [171].

In conclusion, our work suggests that models in the literature that fulfilled the BBN constraints with less than an order of magnitude margin should perhaps be reconsidered. In particular, those characterized by soft gamma-ray emissions and/or at relatively late times should have been more prone to incorrect conclusions about their viability. Our study also suggests that actual bounds should be derived via a case-by-case analysis. Finally, we provided further arguments supporting the usefulness of an improved constraint from CMB spectral distortion of the μ type, since it would not manifest the unexpected sensitivity to the shape of the energy injection that we have uncovered.

6

COSMOLOGICAL CONSTRAINTS ON EXOTIC INJECTION OF ELECTROMAGNETIC ENERGY

This chapter is adapter from publications in JCAP [490] and PRD [492].

6.1 Introduction

We have presented in chapters 2 and 3 the astrophysical and cosmological evidences for a sizable dark matter component, whose nature is however still largely unknown. It is even possible for instance that light and "dark" relativistic particles are present in the cosmic soup, whose cosmological properties are partially degenerate with neutrino ones, or that DM is made of different components with wildly different nature and properties such as coupling with ordinary matter or lifetime. We have presented in chapter 4, the purely gravitational constraints from CMB anisotropies and LSS, i.e. the minimum requirement to fulfill for any model. However, a large number of relics from the early universe have been proposed in many extensions of the standard model of particle physics, in some cases unstable to processes injecting electromagnetic (e.m.) forms of energy. We introduced some of them in sec. 3.4.2. We have seen in chapter 5 that BBN and/or CMB spectral distortions provide constraints to the amount of energy injected at early epochs. We will now show that CMB anisotropy considerations become more relevant for longer lifetimes. It is important to assess the relative constraining power of these different tools, which is the main task we address in the following. Also, forthcoming 21 cm surveys promise to open a window on the yet unconstrained "Dark Ages". It is interesting to estimate whether this probe has the potential to improve over current CMB constraints. For DM annihilation, it has been shown recently [409] that, as long as astrophysical uncertainties on star formation dominate, CMB anisotropies would have a better sensitivity than 21 cm. However, the situation may be different for exotic physics entering the game at specific ages, as we will discuss in the following.

In section 6.2, we focus on CMB power spectra constraints, describing for the first time the effects of the e.m. energy injection onto the CMB power spectra *as a function of the lifetime* of the decaying particles. In section 6.3, we briefly review how to compute spectral distortions and BBN constraints, introduced in section 3.6 and chapter 5 respectively. Those typically dominate when the lifetime is below 10^{12} s, whereas CMB anisotropies are very powerful at constraining energy injection after this time. The lifetime dependence of the CMB anisotropy bounds that we derived also inspired us in proposing an *on-the-spot* approximation to the more accurate treatment, whose accuracy we tested. In section 6.4, we apply our treatment to a few candidates of interest introduced in section 3.4.2: first, we deal with PBHs of relatively low mass, $10^{13.5}\,\mathrm{g} \leq M \leq 10^{16.8}\,\mathrm{g}$, that can affect CMB power spectra due to their evaporation. To our knowledge, realistic constraints on this scenario have never been computed so far, yet our results show that the bounds are competitive with existing ones. We

also develop the large mass PBH scenario ($M \geq M_{\odot}$), which, due to matter accretion, lead to e.m. energy injection in the surrounding plasma/gas. Then, we show the application of our results to sterile neutrinos with keV-MeV mass scale. Finally, we provide a first estimate of the room for improvement left for forthcoming 21 cm experiment SKA [1], comparing it with the reach of a proposed satellite targeting CMB spectral distortions (PiXiE [374]) and the CMB angular power spectrum accuracy achievable with a next-generation satellite (CORE-like [117]). We show that the best and most realistic opportunity to look for this signal (or to improve over current constraints) in the 21 cm probe is to focus on the Cosmic Dawn epoch, $15 \leq z \leq 30$, where the qualitatively unambiguous signature of a spectrum *in emission* can be present, with negligible effects expected from astrophysical sources. We finally report our conclusions in section 6.5.

6.2 CMB power spectra constraints

In this section, we describe our treatment of the injection of electromagnetic energy in the cosmological medium and its effects on the CMB power-spectra. Although the injection history is model dependent, a useful proxy is to assume the decay of an exotic 'particle'. Since this also describes the scenario most commonly found in the literature, henceforth we will thus refer to a decaying particle. Our considerations are however more generic than that, as we will show later on with a specific example. Also, we neglect gravitational effects, i.e. we assume that only a small fraction of the total dark matter density is decaying (or that its lifetime is much longer than the age of the universe, if its abundance is not small). In general, whenever an e.m. decay channel is non-negligible, the bounds obtained are many orders of magnitude stronger than the purely gravitational ones (see refs [70], [494] for recent treatments). The main effect of the decay byproducts is then their impact on the free electron fraction, which in turn affects CMB anisotropy angular spectra. The separation of scales between purely gravitational effects and e.m. ones also allow us to isolate the latter, described in details in what follows.

6.2.1 *Standard equations*

Both *stable* and *unstable* standard model (anti)particles are found among the final states of the exotic particle decay. The latter decay into standard model stable (anti)particles very quickly compared to other relevant timescales, hence one can limit oneself to treat only the energy deposition problem of stable standard model particles and antiparticles. These particle are either "inert", simply losing energy adiabatically via redshift, or interact with the gas (primordial plasma) after (before) recombination, transferring their energy to the photons and light element atoms (electrons and nuclei). It is usual to neglect the energy deposited by protons/antiprotons and neutrinos: The latter are basically invisible to the medium and simply carry away part of the energy, hence neglecting them is an excellent approximation. Ignoring the energy deposition by protons and antiprotons has also been checked to loosen the bounds at the 10% level [592]. Neglecting those processes thus leads only to modestly conservative bounds, while permitting a significant reduction of the computing time. As a result, the deposition process essentially concerns energetic photons and electrons/positrons [155]. Their injection in the medium initiates the development of a high energy electromagnetic (e.m.) cascade, reviewed in

1 https://www.skatelescope.org/

sec. 3.5, which proceeds in the following schematic way: i) the number of non-thermal particles grows, while their average energy decreases, mostly due to interactions with relic photons; ii) when the non-thermal particles energy reach the keV range, they start interacting with atoms, mostly hydrogen. Some interaction also involves helium atoms (but this has been shown to be a sub-leading, often negligible effect [261]) and free electrons. An accurate description of the evolution of the daughter particle spectra over many energy and time scales is necessary in order to correctly capture the energy deposition process. Indeed, it has been shown that at redshift around and below recombination the injected energy is often not absorbed *on-the-spot*, rather can redshift away before being deposited [554]. As discussed in sec 3.5.2, dedicated numerical tools have been developed to deal with the relevant physical processes, and we shall make use of the results from Ref. [554] recently updated in Ref. [552]. The main e.m. impact of exotic particle decay is to modify the fraction of free electrons x_e, either through direct ionization or collisional excitation followed by photoionization by a CMB photon. An indirect effect is via the heating of the intergalactic medium (IGM), whose temperature we denote with $T_{\rm M}$, and which has a feedback on the evolution of x_e. This in turn modifies the optical depth and visibility function and thus affects CMB anisotropy power spectra.

In order to follow the evolution equations for x_e and $T_{\rm M}$ we use the numerical code Recfast [531] v1.5, which we extensively discussed in sec. 1.3.3, as implemented in the Boltzmann code CLASS v2.5. We recall that in this code, the evolution of the free electron fraction is ruled by a system of coupled differential equations of the type[2]

$$\begin{aligned}\frac{dx_e(z)}{dz} &= \frac{1}{(1+z)H(z)}\left(R(z)-I(z)-I_X(z)\right)\,,\\ \frac{dT_{\rm M}}{dz} &= \frac{1}{1+z}\left[2T_{\rm M}+\gamma(T_{\rm M}-T_{\rm CMB})\right]+K_h\,.\end{aligned} \tag{6.2.1}$$

where the R and I terms are the standard recombination and ionization rates given by

$$R(z)=C\left[\alpha_H x_e^2 n_H\right],\qquad I(z)=C\left[\beta_H(1-x_e)e^{-\frac{h\nu_\alpha}{k_b T_{\rm M}}}\right]. \tag{6.2.2}$$

$I_X(z)=I_{Xi}(z)+I_{X\alpha}(z)$ is an effective ionization rate where the rate of direct ionization I_{Xi} and excitation+ionization $I_{X\alpha}$ are given by:

$$I_{Xi}=-\frac{1}{n_H(z)E_i}\frac{dE}{dVdt}\bigg|_{{\rm dep},i}\,,\quad I_{X\alpha}=-\frac{(1-C)}{n_H(z)E_\alpha}\frac{dE}{dVdt}\bigg|_{{\rm dep},\alpha}\,, \tag{6.2.3}$$

where E_i and E_α are respectively the average ionization energy per baryon, and the Lyman-α energy. Finally, the rate K_h at which DM decays or annihilations heat the plasma is defined as:

$$K_h=-\frac{2}{H(z)(1+z)3k_b n_H(z)(1+f_{He}+x_e)}\frac{dE}{dVdt}\bigg|_{{\rm dep},h}\,. \tag{6.2.4}$$

We refer to sec. 1.3.3 for further definitions and more details on each coefficient.

We recall that the energy *deposited* in the plasma at redshift z, $\frac{dE}{dVdt}\big|_{\rm dep}$ is split between ionization,

2 In reality Recfast contains equations that are modified with fudge factors calibrated on more accurate code such as CosmoRec [165], [180] and HyRec [38]. It is not necessary to go beyond the use of Recfast as long as the ionization history around recombination, for which high precision calculation is mandatory, is not too far away from ΛCDM. Since large energy injections around recombination are ruled out, it is safe for us to work with Recfast only. We have checked this explicitly by comparing results with the last public version of HyRec.

excitation of the Lyman-α transition, heating and very low energy photons ($\leq$10.2 eV) unable to interact. In case of a decaying particle with lifetime τ, the rate of energy injection per unit volume is given by

$$\left.\frac{dE}{dV\,dt}\right|_{\rm inj} = (1+z)^3 \Xi\, \Omega_{\rm DM} \rho_c c^2 \Gamma\, e^{-\Gamma\, t} \quad , \tag{6.2.5}$$

where ρ_c is the current critical density, Γ is the width (inverse lifetime), Ξ is the relative amount of energy released into e.m. for a single decay, arbitrarily normalized to the current total cold DM abundance, $\Omega_{\rm DM}$. For instance, a species constituting 1% of the total DM abundance decaying into $\nu\gamma$ corresponds to $\Xi = 1/200$. We follow the by now standard method of Refs. [244], [551] to take into account e.m. energy injection in the periods concerned. In that case, the deposited energy is related to the injected one by:

$$\left.\frac{dE}{dV\,dt}\right|_{{\rm dep},c} = f_c(z, x_e) \left.\frac{dE}{dV\,dt}\right|_{\text{inj, long-lived}} \quad . \tag{6.2.6}$$

where the subscript c denotes the "channel" (ionization, excitation,...). Here, $\frac{dE}{dV\,dt}|_{\text{inj, long-lived}}$ corresponds to the injection rate in case of a long-lived particle and the exponential factor $e^{-\Gamma\, t}$ is absorbed in the definition of the $f_c(z, x_e)$ functions. These functions encode all the physics of the energy deposition, introduced in sec. 3.5.2 and we will describe them in the following. In principle, transport equations accounting for all standard model electromagnetic processes (from high-energy QED ones to atomic processes) allow one to compute the functions $f_c(z, x_e)$ "case by case". In practice, at very least for computing time limitations, some simplifications are needed if one wants to study a large range of models. For instance, it is standard to perform the factorization approximation

$$f_c(z, x_e) \simeq f(z)\, \chi_c(x_e) \tag{6.2.7}$$

which has been shown to work very well for injection energies $\geq$10 MeV [553] and that corresponds to a factorization between high-energy processes (determining $f(z)$) and low-energy processes, approximately universal, responsible for the absorption repartition fractions $\chi_c(x_e)$. We have already introduced and plotted the $\chi_c(x_e)$ functions in sec. 3.5.2. Those have been computed in several references, the most recent one being Ref. [261], which we adopt.

The $f(z)$ functions are usually obtained in terms of the transfer functions $T_i(E, z, z')$, describing what fraction of the initial energy E of a particle i (in practice either $e^{\pm}$ or γ's) injected at z' is deposited at z. The transfer functions are then simply convoluted with the energy spectrum of each particle i, dN_i/dE, integrated in time for $z' > z$, hence accounting for the time evolution of the density of the decaying particles, and finally summed over the species, i.e. according to the formula:

$$f(z) = H(z) \frac{\sum_\ell \int \frac{d\ln(1+z')}{H(z')} e^{(-\Gamma\, t(z'))} \int T^{(\ell)}(z', z, E) E \frac{dN^{(\ell)}}{dE}\big|_{\rm inj} dE}{\sum_\ell \int E \frac{dN^{(\ell)}}{dE}\big|_{\rm inj} dE} \,. \tag{6.2.8}$$

The transfer functions have been computed in Refs. [551], [554] and updated recently in Refs. [552], [553]. As explained in section 3.5.2, the main update of latter references over the former is to take into account low energy photons (below 10.2 eV and therefore unable to interact) produced *during* the cooling of the high energy particles. Technically, Refs. [552], [553] give the transfer functions *per channel* for a given ionization history (Recfast-like, without reionization). We cannot make use of the transfer function per channel directly since a large part of the parameter space we are dealing with consists in modification of the reionization history, for which $x_e \simeq 0.1 - 1$. However, we can

use what the authors of the above mentioned references call *simplified scheme with (corrected) 3 keV prescription*, i.e. we rely on the factorization introduced in Eq. (6.2.7) and that gives very good result for energy injected above $\sim$ 10 MeV. Our treatment corresponds thus to state-of-the art methods of recent literature, although for specific applications *ad hoc* calculations might still be needed. In the following, we will limit ourselves to the injection of $e^{\pm}$ and γ with a monochromatic energy spectrum. This is not necessarily unphysical, since there are many models with a dominant e.m. two body final state. The $\gamma\,\nu$ mode is for instance relevant to unstable gravitinos with mass below the W gauge boson one; it is also the only "visible" decay of a sterile neutrino lighter than 1 MeV. The $\gamma\,\gamma$ final state is the paradigmatic decay channel of the well-known axions/axionlike particles, but it also applies to other cases: One example is a light scalar linearly coupled to matter through the trace of the standard energy-momentum tensor, proposed e.g. as a dark matter candidate from R^2 gravity in [151]. In the same model, if the scalar is heavier than 1 MeV, the $e^{\pm}$ mode we consider below is the phenomenologically dominant one. Our choice is however mostly dictated by simplicity, since in most decay models a continuous spectrum of e.m. particles is emitted: while our formalism can be applied to any final state with a generic $e^{\pm}$ and γ energy distribution (see Eq. (6.2.8)), it would necessarily be more model-dependent and time-consuming to compute the actual bounds in those cases. Nonetheless, the results obtained in the following are indicative also of cases with a more complicated energy distribution for the final state particles: Since the energy deposition efficiency is typically a smooth function of the particle energy, the energy distributions of the daughter particles can be fairly approximated by replacing them with the deterministic average value, and just correcting for the average energy fractions in e.m. particles. This approximation can be suitably encoded in the parameter Ξ previously introduced. For instance, consider the decay mode $X \to \nu e^+ e^-$: if we denote with x the average energy fraction carried away by the neutrino, often a fair proxy of the bound can be obtained from the constraint on the decay of a particle Y into a monochromatic final state, $Y \to e^+ e^-$, provided one adopts $m_Y = (1-x) m_X$, and downscales the parameter Ξ by a factor $(1-x)$. In sec. 6.4.3, we will apply this approximate treatment to the specific case of a $\sim$ 130 MeV sterile neutrinos whose dominant e.m. decay mode is $\nu_s \to \nu\, e^+ e^-$. In Fig. 54 we plot the functions $f(z)$ for decays into electrons and photons, for several injected (kinetic) energies (chosen to bracket the energy deposition efficiency) and for three lifetimes (10^{13} s, 10^{15} s, and 10^{20} s). For comparison, in the two cases for which the lifetime is shorter than the age of the universe, we also plot the decay law $\exp(-t(z)/\tau)$ (green curve, with rapid drop at low z) to illustrate its difference with $f(z)$, due to peculiar effects of energy deposition. Obviously, unless the lifetime is very long, $f(z)$ drops dramatically with decreasing z due to the exponential decay factor (top panels). However, even for very long lifetimes such that $\exp(-t(z)/\tau) \sim 1$, $f(z)$ can have a substantial evolution caused by significant changes in the efficiency of energy transfer for particles in a given energy range (bottom panel for the 100 GeV case).

In order to speed up the evaluation of constraints involving different particle physics parameters, such as different masses or final state channels, further approximations are often introduced. A very popular one is the effective *on-the-spot* approximation. In the context of decaying particles, this approach relies on two assumptions: first, that energy deposition happens at the same redshift as energy injection ($T^{(\ell)}(z', z, E) \propto \delta(z' - z)$ in Eq. (6.2.8)); second, that the energy deposition efficiency is constant over time up to a factor $e^{-\Gamma t}$, which amounts in assuming that the function $f(z)$ is simply of the form

$$f(z) = f_{\rm eff}\, e^{-\Gamma\, t(z)}, \tag{6.2.9}$$

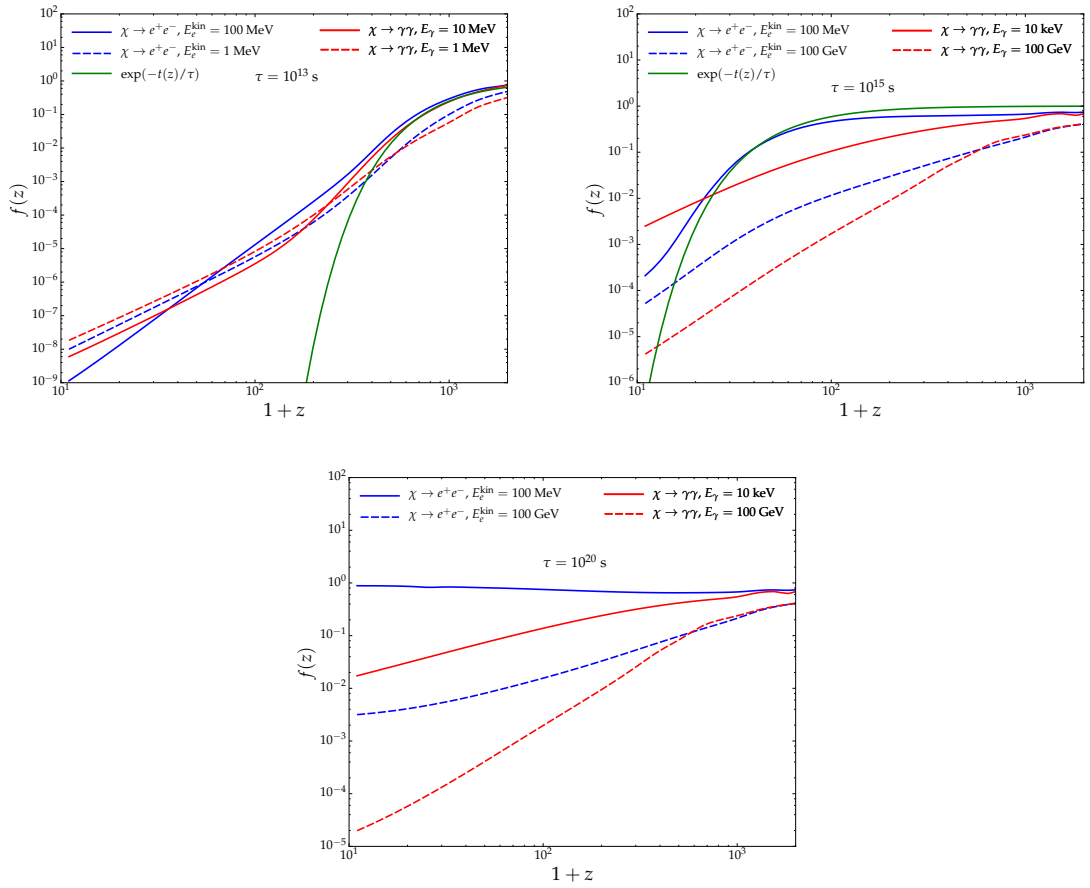

Figure 54: $f(z)$ functions for particles decaying into electrons and photons, for several injected (kinetic) energies and for three different lifetimes. In the top panels, the simple exponential decay law for the same lifetime is also reported, for comparison.

where the factor $f_{\rm eff}$ only depends on the mass m_χ and on the e.m. branching ratios (i.e. decay channel(s)). One can think of different Ansätze for relating this effective coefficient to the particle properties.

In section 6.3.2, we will compute bounds on the e.m. decay model without such an approximation. Then we will use the beyond-on-the-spot results to physically motivate one particular ansatz for $f_{\rm eff}$. Finally we will discuss the accuracy of the effective on-the-spot approximation with this ansatz. We can already anticipate here that we will define $f_{\rm eff}$ as the value of the beyond-on-the-spot function $f(z)e^{\Gamma t(z)}$ evaluated at $z \simeq 300$. We will see that this gives approximate bounds correct at the 20% level for lifetimes $> 10^{14}$ s, despite the fact that the exact impact of the decay on x_e, for instance, might be poorly described. For shorter lifetimes, no easy criterion emerges.

Let us conclude this section by a technical note. We have modified the Recfast [531] v1.5 routine of the Boltzmann code CLASS [109], [390] v2.5 following recommendations of Refs. [177], [453], namely we consistently evaluate the photon ionization coefficient using the photon temperature instead of the electron one. However, we neglect collisional heating, since this will never be relevant for the level of energy injection not excluded by the CMB constraints: for all the allowed cases of interest, $T_{\rm M}$ never increases above 10^4 K.

6.2.2 *Effects of electromagnetic decays on the ionization history and the CMB power spectra*

In this section, we describe the impact of the exotic particle decay on the ionization history and on the CMB TT and EE angular power spectra as a function of the lifetime Γ^{-1}. We show some TT and EE spectra for models whose basic cosmological parameters $\{\theta_s, \omega_b, \omega_{DM}, A_s, n_s, z_{\rm reio}\}$ have been fixed to Planck 2016 TTTEEE+SIMlow best fit [27]. We illustrate the impact of energy injection for the specific case of a decay into $e^{\pm}$, but very similar conclusions can be reached for photons and therefore for any e.m. decay product. For each lifetime, we take two different injected energies, that were chosen to roughly bracket the possible energy deposition efficiencies. A general comment is that, for a given lifetime, different energy deposition histories might lead to slightly different effects on the C_ℓ's, giving thereby a potential handle to identify the decay channel and the mass of the decaying particle. Hence, in case of detection, there would be a possibility to pin down the particle physics scenario causing the signal, rather than just measuring the lifetime and abundance of the mother particle. A more careful "case-by-case" analysis for interesting scenarios would be needed to further support this statement.

We wish to test already in this section the accuracy of the on-the-spot approximation, used in most of past literature, but with our updated ansatz for $f_{\rm eff}$ that will be motivated in section 6.3.2. As already hinted above, this consists in replacing $f(z)$ by $f(z=300)e^{-\Gamma[t(z)-t(300)]}$.

Let us consider separately different possible orders of magnitude for the particle lifetime:

- as found in previous literature (see e.g. Refs. [155], [214], [453]), for a lifetime bigger than the age of the universe, $\tau_u \simeq 10^{18}$ s, the main effect of the particle decay is to initiate slowly the reionization of the IGM at high redshift $z > 100$ (Fig. 55, top-left panel). Looking at the CMB power spectra plotted on Fig. 56–upper panels, the decay of long-lived particles imply a step-like suppression of the TT and EE power spectra, plus a much stronger and wider reionization bump in the case of the EE spectrum.
  In the case of long-lived particles, most of the effect of the decay on the CMB spectra is well captured by our on-the-spot approximation, as can be seen on the same figure, red curve. The exponential factor is very close to unity even at $z = 0$, and the effect of the decay can be fully described by the unique combination of parameters

$$\xi \equiv f_{\rm eff}\,\Xi\,\Gamma \tag{6.2.10}$$

  which has the dimension of a rate.
  The CMB temperature spectrum probes the reionization history after recombination mostly through the integrated quantity $\tau_{\rm reio}$. Hence, the scenarios presented in the figure (all sharing the same $z_{\rm reio}$) give identical temperature spectra up to corrections below the percent level, despite of differences in the ionization history in the range $z_{\rm reio} \leq z \leq 10^3$. However, the EE spectra is more sensitive to the ionization history and we can see variations of the order of 50% at $\ell < 10$ for the 100 GeV case. Note that the quality of the on-the-spot approximation decreases when the injected energy increases and the energy deposition efficiency goes down.

- For $\Gamma^{-1} \geq 10^{14}$ s (Fig. 55, top-right panel), a bump in the free electron fraction appears, localized around the time of the decay. However, the recombination history is not impacted. The enhancement of the optical depth integrated up to the surface of last scattering leads to a larger step-like suppression of the TT and EE spectrum on small angular scales (Fig. 56, bottom panels). The slightly increased probability of photons to re-scatter at intermediate redshifts (between

recombination and reionization) generates extra polarization, and leads to a characteristic bump in the EE spectrum, peaking on smaller angular scales than the usual reionization bump (around $\ell \simeq 20$ in the examples displayed in Fig. 56–bottom-right panel, instead of $\ell = 3$ for reionization). This could be a rather unique signature of the peculiar reionization history in these models, and the measurement of the bump location in multipole space would give a direct indication on the DM lifetime.

Comparing now the results of the accurate treatment with the on-the-spot approximate version, we find that the latter works well for particles decaying with substantial energy deposition efficiency (here for 100 MeV), but not for high injected energies (100 GeV in the example of Fig. 56, bottom panel, green curve). At 100 GeV, the error is as large as 10% around $\ell \simeq 50$ in the TT spectrum, and 100% around $\ell \simeq 20$ in the EE spectrum.

- Finally, for very short lifetimes $\Gamma^{-1} \leq 10^{13}$ s (Fig. 55–bottom-left panel), the decay starts to modify also the recombination era, eventually delaying it. The most visible consequence in the CMB temperature spectra is a stronger damping tail (Fig. 57, top panels). This comes from the enhanced Silk damping effect caused by a larger width of the last scattering surface. The bump coming from extra re-scattering and polarization is also visible, but is less sharp than in the previous case. For a lifetime of $\Gamma^{-1} \simeq 10^{12}$ s, some more peculiar patterns appear even on large angular scales (Fig. 57–bottom panels). The reason is that we are running CLASS with a fixed angular sound horizon scale θ_s. In these models, recombination is delayed significantly, and the sound horizon at recombination is larger. The code automatically adapts the angular diameter distance to the last scattering surface by *decreasing* H_0, to maintain the same θ_s. Hence the late-time expansion history is modified and this results in a smaller "late integrated Sachs-Wolfe" effect on large scales.

  Fig. 55 shows again the results obtained using the on-the-spot approximation with our Ansatz $f_{\rm eff} = f(300)e^{\Gamma t(300)}$. In the short lifetime limit, we see that this approach does not capture the effects of the decay, and would not lead to reliable constraints, which is not surprising because most particles decay *before* $z = 300$. Hence one would need to adapt the ansatz for each lifetime. In the specific case of $\Gamma^{-1} = 10^{13}$ s, we have been able to find by trial and error that the ansatz $f_{\rm eff} = f(z_{\rm decay})e^{\Gamma t(z_{\rm decay})}$ (with $t(z_{\rm decay}) = \Gamma^{-1}$ by definition) leads to effects similar to the beyond-on-the-spot result. In that case, the curves are still in reasonable agreement, especially in the TT spectrum where the agreement reaches the percent level, while differences in the EE spectrum are kept below 30%. On the other hand, in the case of $\Gamma^{-1} \sim 10^{12}$ s, the on-the-spot spectra fails even to predict the correct shape for the effect of the decay on the CMB spectra. For such small lifetimes, the lack of a meaningful physical criterion to even define an on-the-spot approximation makes any simplification attempt hazardous. A more refined search for a phenomenological criterion, e.g. via a principal component analysis as done in the DM annihilation case [551], would probably be useless. In that case, in order to get reliable constraints, one has to do MCMC scans for each lifetime, as we shall perform in the following.

In summary, we have illustrated the discrepancy between the on-the-spot approximation and the more accurate beyond-on-the-spot treatment, for different lifetimes, injected energies and decay products. These discrepancies are more obvious in $x_e(z)$ than in the C_ℓ's. We found that *for lifetimes* $\geq 10^{13}$ *s the approximation can reach the % level agreement if an appropriate criterion is chosen*, like our ansatz $f_{\rm eff} = f(300)e^{\Gamma t(300)}$ that we will further justify in the next section. However, the error increases when the energy deposition efficiency is very different from an exponentially decaying

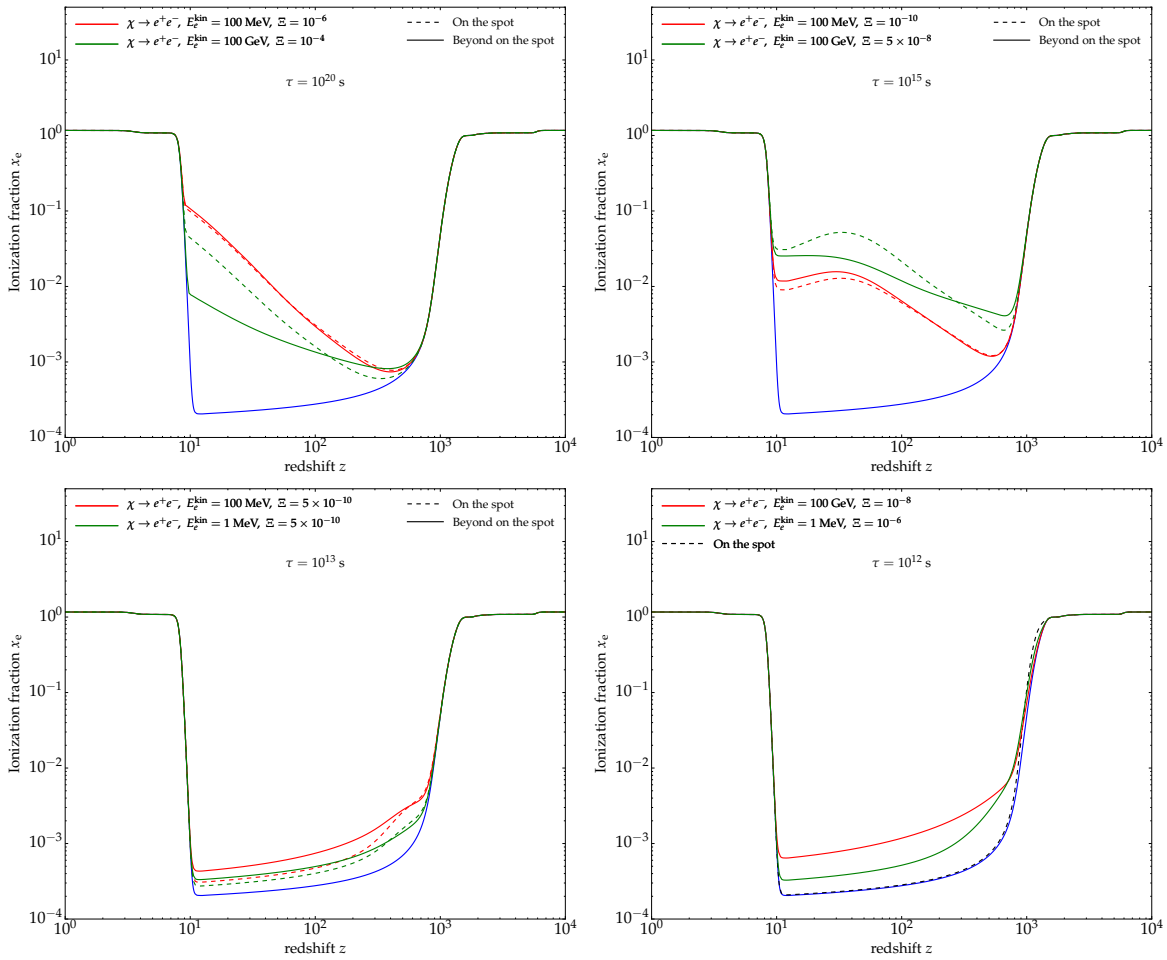

Figure 55: Comparison of the on-the-spot and beyond on-the-spot treatment on the ionization history. We assume a decaying DM model $\chi \to e^+e^-$, with $E_e^{\rm kin} = 100$ MeV, 100 GeV with lifetimes $\Gamma^{-1} = 10^{20}$ s and 10^{15} s (top-left and top-right panels respectively), $E_e^{\rm kin} = 1$ MeV, 100 GeV with lifetime $\tau = 10^{13}$ s bottom-left panel) and $E_e^{\rm kin} = 1$ MeV, 100 MeV with lifetime $\Gamma^{-1} = 10^{12}$ s (bottom-right panel). The blue curves on each plot represent result in the Planck 2016 ΛCDM model.

function: this is the case for large injected energies and thus high DM masses. The error can largely exceed the 10-20% accuracy expected from a state-of-the-art treatment in terms of tabulated transfer functions. Furthermore, for shorter lifetimes —although we did not investigate deeper in this issue—no simple criterion emerges which is at the same time accurate and universal enough to be of practical use. Hence, the on-the-spot approximation should only be used for estimating the order of magnitude of the CMB bounds in a restricted window in parameter space. In the next section we will work with the beyond-on-the-spot approach, in order to get results accurate at the 10-20% level.

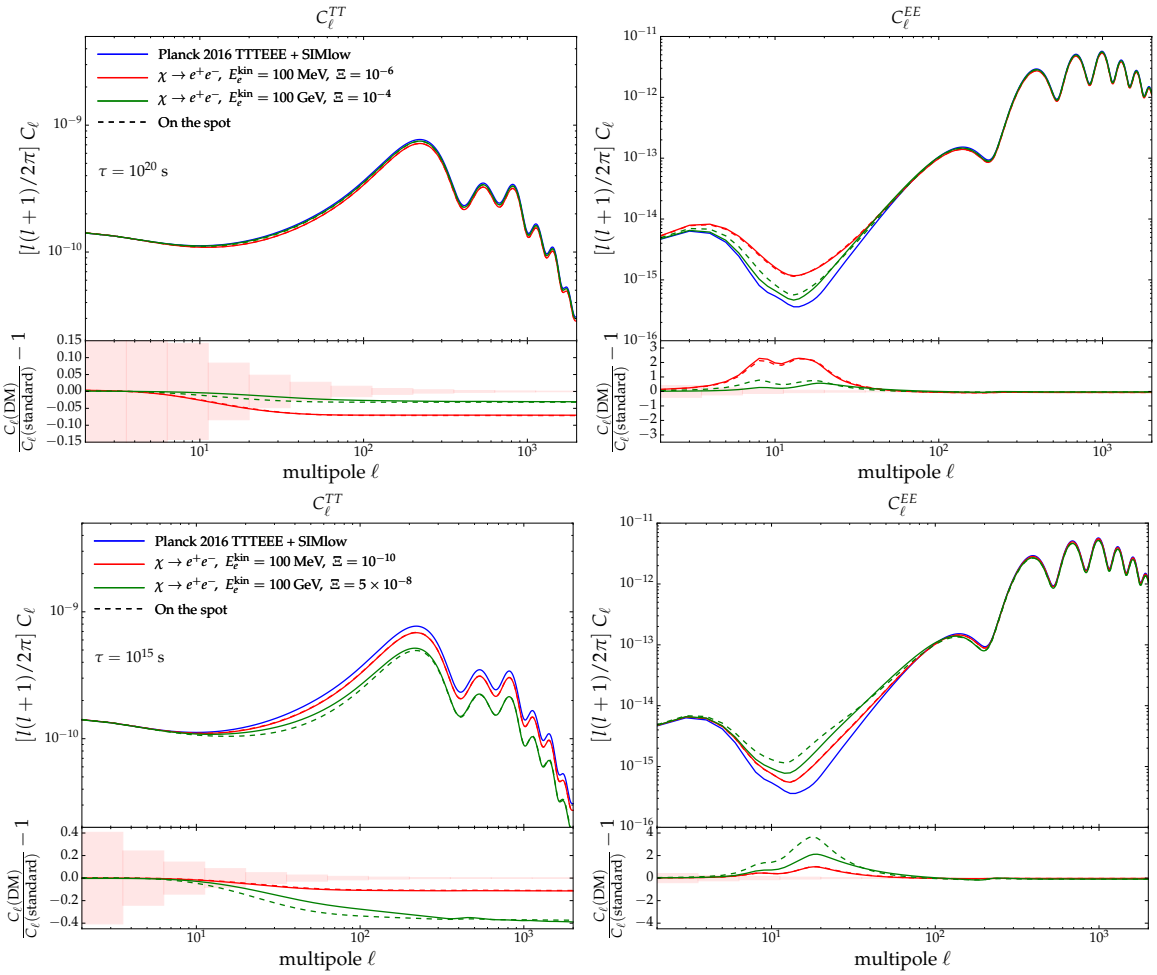

Figure 56: Comparison of the on-the-spot and beyond on-the-spot treatment on the lensed temperature and E-mode polarization power spectra, as well as their residuals. We assume a decaying DM model $\chi \to e^+e^-$, with $E_e^{\rm kin} = 100$ MeV, 100 GeV with lifetimes $\Gamma^{-1} = 10^{20}$ s (top panels) and 10^{15} s (bottom panels).

6.3 Results: Summary of constraints and comparison with other probes

6.3.1 *Methodology*

We perform our study of CMB anisotropy constraints with Monte Carlo Markov chains, using the public code MONTE PYTHON [68] and the Metropolis Hasting algorithm, as explained in appendix B.3. Beyond the on-the-spot approximation and for each decay channel, the sector of e.m. decaying particles can be described by three independent parameters, e.g. the particle mass, lifetime and effective energy density parameter Ξ defined in section 6.2.1. For a better efficiency of MCMC runs, our strategy consists in scanning a grid of values for the lifetime $\tau \equiv \Gamma^{-1}$ in the range $[10^{12}\text{s}; 10^{26}\text{s}]$, and for values of the mass m leading to byproducts with (kinetic) energies in the range [10 MeV; 1 TeV]. For each set of (τ, m) values, we perform a fit to the data with flat priors on the following set of parameters:

$$\Lambda\text{CDM} \equiv \{\omega_b, \theta_s, A_s, n_s, \tau_{\rm reio}, \omega_{\rm DM}\} + \Xi\,.$$

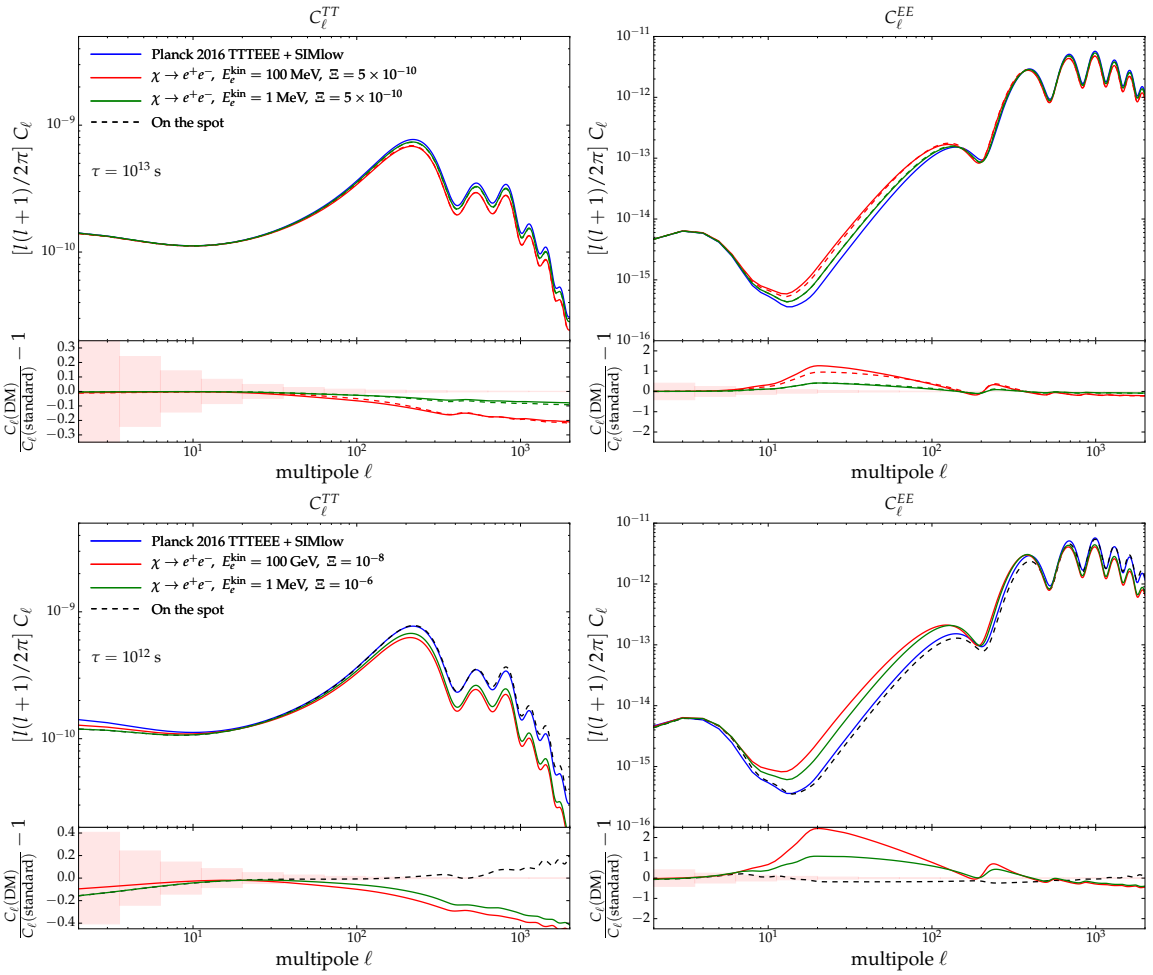

Figure 57: As in Fig. 56 for decaying DM $\chi \to e^+e^-$ with lifetime $\Gamma^{-1} = 10^{13}$ s and injected energies $E_e = 1$ MeV and 100 MeV (top panels), as well as lifetime $\Gamma^{-1} = 10^{12}$ s and injected energies $E_e = 1$ MeV and 100 GeV (bottom panels).

We use a Choleski decomposition to handle the large number of nuisance parameters in the Planck likelihood [399]. We consider chains to be converged when the Gelman-Rubin [265] criterium gives $R - 1 < 0.05$. We use the Planck 2015 high-ℓ TT,TE,EE likelihood, a prior on $\tau_{\rm reio}$ taken from the Planck 2016 results based on the new SimLow likelihood [27], and the Planck 2015 lensing likelihood. Since the effect of a long-lived decay is similar to modifications of the reionization history, one might expect constraints to depend on the way in which reionization itself is modelled. Thus we first perform a couple of runs in order to assess the impact of assuming either instantaneous ("camb-like") reionization, or the redshift-asymmetric parametrization of [220], discussed in sec. 1.3.4. For these test runs, we use for simplicity the on-the-spot approximation, and we are only interested in long-lived particles. Hence the only relevant parameter describing the e.m. decay sector is the combination ξ defined in Eq. (6.2.10). With camb-like reionization, we obtain $\xi < 5.28 \times 10^{-26}\,{\rm s}^{-1}$ (95% CL), whereas the use of the redshift-asymmetric parameterization yields $\xi < 6.03 \times 10^{-26}\,{\rm s}^{-1}$ (95% CL), which is comparable to the results of Ref. [453]. The difference is only at the level of 15%, which is anyway the accuracy level expected for the theoretical calculation of transfer functions in the beyond-on-the-spot

approximation, and hence the precision with which we expect to estimate the decay lifetime in general using CMB data. We conclude that assumptions on the reionization history have a marginal impact on lifetime bounds, and from now on we will always rely on the instantaneous camb-like parametrization.

6.3.2 *Results and comparison of various constraints*

We summarise the constraints on massive particles decaying into photons and $e^{\pm}$ with kinetic energies in [10 MeV; 1 TeV] in Fig. 58. In fact, due to the behaviour of injection efficiency with energy, see [553], the range of CMB constraints thus obtained also covers the case of smaller injected energies, down to about 10 keV. Hence, we can safely assume that the band displayed gives a very good estimate of constraints for energies in the range [10 keV; 1 TeV]. For each lifetime, we report lower bounds on the effective energy density parameter Ξ, defined in section 6.2.1. Given this definition, if the decaying particle accounts for 100% of cold dark matter, Ξ is expected to be equal to one or at least of order one, unless no sizable amount of $e^{\pm}$ and photons are produced by the decay (e.g. the particle may decay entirely into neutrinos or dark radiation, a case considered separately in Ref. [494]). If at least a small fraction of the injected energy goes into photons, electrons and positrons, a bound $\Xi \ll 1$ implies that the particle contributes to the total dark matter density by a negligible amount.

For each assumed lifetime, injected energy and decay channel (γ or $e^{\pm}$), our MontePython run gives a CMB upper bound on Ξ that we report on the figure. We obtain two bands, one for each decay channel, with a width corresponding to extreme assumptions on the injected energy. We also repeat the analysis with the on-the-spot approximation and show the results with dashed lines.

The bounds from CMB angular power spectra are not the only cosmological bounds available. In order to assess their relevance, we compare them with: i) the constraints from CMB *spectral* distortions, based on the experimental FIRAS bounds, and obtained by integrating equations (3.6.22) as discussed in sec. 3.6; ii) the constraints from light nuclei overproduction/destruction with respect to standard BBN prediction computed in chapter 5.

The complementarity of the CMB anisotropy constraints with those from CMB spectral distortions and BBN is obvious. The constraints from the angular power spectra dominate for long lifetimes, $\Gamma^{-1} \geq 10^{12}\,\mathrm{s}$. They reach a remarkable sensitivity around $\Gamma^{-1} \sim t_c \equiv \Gamma_c^{-1} \equiv 10^{14}\,\mathrm{s}$, excluding values of Ξ as low as $\sim 10^{-11} - 10^{-10}$. For smaller lifetimes, they degrades roughly by a factor Γ_c/Γ. Hence the CMB is maximally sensitive to particles decaying during the dark ages following photon decoupling, around a redshift $z_c \simeq 300$ corresponding to the time-redshift conversion of t_c.

This suggests that the impact of e.m. decay on CMB anisotropies depends in first approximation on the amount of energy deposited around the time $t \sim t_c$, i.e. around the redshift z_c. A posteriori, we can thus propose $f(z) \longrightarrow f(z_c)e^{-\Gamma(t(z)-t_c)}$ as a physically motivated ansatz for the on-the-spot scheme: this approximation captures the quasi-exponential shape of $f(z)$, and goes through the true value of $f(z)$ near the most relevant epoch $t \simeq t_c$. Following the definition of $f_{\rm eff}$ in Eq. (6.2.9), this corresponds to $f_{\rm eff} = f(300)e^{\Gamma t(300)}$.

Figure 58 summarises the accuracy of this fast approximation scheme (dashed lines). The on-the-spot bounds are found to be biased at the $10-50\%$ level for the channels, energies and lifetimes ($\geq 10^{14}$s) considered here. For shorter lifetimes, one would need to change Ansatz, which we did empirically in sec. 6.2 by adjusting $f_{\rm eff}$ to $f(z_{\rm decay})e^{\Gamma t(z_{\rm decay})} = f(z_{\rm decay})e$ for $\tau \simeq 10^{13}\,\mathrm{s}$. With this new Ansatz, we checked that the on-the-spot bound (not shown explicitly on the plot) is correct at the $20-50\%$ level.

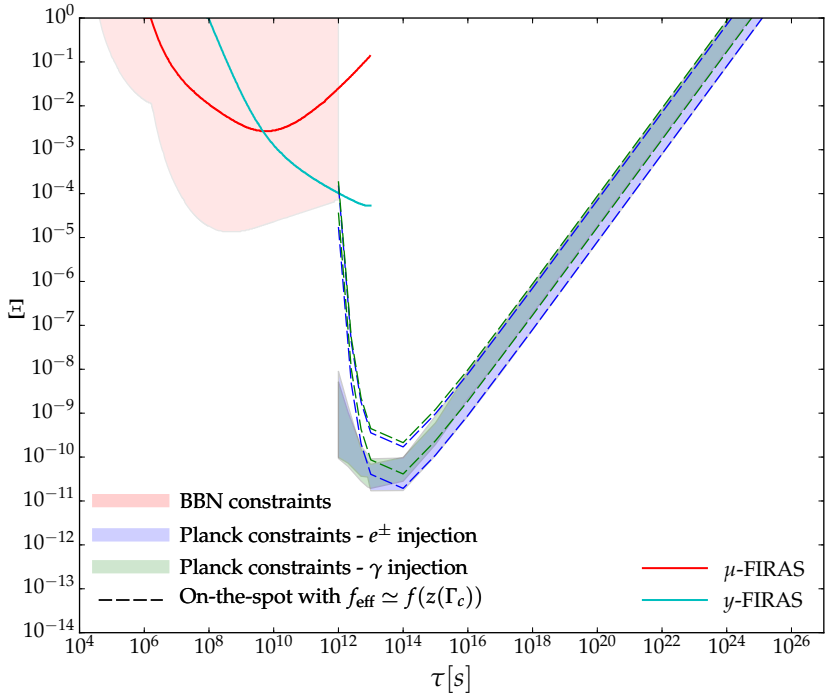

Figure 58: Cosmological constraints on the effective energy density parameter Ξ of exotic particles with e.m. decay channels. The effective energy density Ξ is normalised to the CDM energy density, and incorporates an efficiency factor (thus $\Xi = 1$ means that the particle makes up 100% of CDM, and that 100% of the decay energy goes into stable photons and $e^{\pm}$). We report bounds coming from Big Bang Nucleosynthesis (shaded red area), CMB spectral distortions (full lines) and CMB anisotropies measured by Planck (shaded blue area for $e^{\pm}$ and shaded green area for γ; the width of the band is obtained by scanning over the kinetic energy of the injected particles in the range [10 keV; 1 TeV]). In the case of CMB anisotropies, we compare the use of the full treatment for the energy deposition with the on-the-spot approximation (dashed lines).

For lifetimes below 10^{13} s, as illustrated in sec. 6.2, the on-the-spot approximation fails at describing correctly the physical effects of the decay. We conclude that the on-the-spot approximation is barely sufficient for deriving order-of-magnitude estimates of the bounds in the range $\tau \geq 10^{13}$ s.

Not surprisingly, earlier universe probes are more sensitive to shorter lifetimes, although the bounds are never as strong as from the CMB angular power spectra for $\Gamma^{-1} \sim 10^{14}$ s. It is remarkable that cosmological probes, combined, achieve a sensitivity over more than 20 orders of magnitude in lifetime! A few comments are in order:

- There exist other bounds of astrophysical nature (e.g. from gamma-ray flux measurements, see for instance [190]), which we do not discuss here in details. For energy injection happening mostly in the late universe ($z \ll 1$) and involving sufficiently high energy particles ($E \gg$ MeV), these bounds can be more constraining than the cosmological ones. This is why we do not indulge here in the otherwise interesting parameter space in the upper-right part of Fig. 58.

- Although we kept the point implicit until now, different probes are sensitive to different energies ranges. BBN is the most limited in this sense, since only photons or $e^{\pm}$ more energetic than the disintegration thresholds of light nuclei (from few to few tens of MeV) may have an effect. The CMB angular spectra constraints apply in principle to a much broader range of energies,

virtually as low as $\sim 10.2\,\mathrm{eV}$, below which no ionization can be induced. However, the range of validity of the transfer functions can be questioned below the keV scale, and the factorization approximation of Eq. (6.2.7) might not be reliable below the ∼10 MeV scale [408]. In practice, unless one wants to run a "case by case" simulation, one is limited by the regime of validity of the approximations used. Finally, the CMB spectral distortions, although yielding the least restrictive of the constrains reported here, are in principle sensitive to a wide range of injected energies, even very low ones (although, to the best of our knowledge, bounds have always been derived under the restrictive assumption of injected particles being more energetic than the ones of the medium). Thus, even if we summarized the bounds in a larger parameter space with one extra dimension for the injected energy, the different cosmological probes would remain very complementary.

Let us finish this section by a comparison with previous works. In Ref. [551], CMB anisotropies constraints have been derived for DM decaying into $e^{\pm}$ and photons, for several masses and lifetimes. We can compare our results to their Fig. 7, in which a forecast for Planck was presented. This forecast turns out to be in fairly good agreements with our results for lifetimes $\geq 10^{13}\,\mathrm{s}$, with a factor ∼2 difference in the long lifetime limit. However, differences are larger for very short lifetimes. We attribute them to i) the new energy deposition functions; ii) the known fact that Planck slightly underperformed with respect to earlier expectations regarding polarization errors. Nonetheless, Planck has improved by nearly one order of magnitude over the pre-existing WMAP 7 constraints. Another estimate of these constraints in the on-the-spot approximation has been made in Ref. [608]. If we take into account the limitations of their treatment, our results are in agreement with their Planck forecast (c.f. their Fig. 2).

6.4 Applications and forecasts

6.4.1 *Low mass primordial black holes*

We have argued in sec. 3.4.2 that a notable application of our results concerns the possibility of constraining the abundances of PBH at high ($\geq M_\odot$) and low ($\leq 10^{-15} M_\odot$) masses. We focus first on the "low mass" PBH case, for which energy injection is due to the evaporation of the PBH (the so-called Hawking radiation), a regime which is rather well understood and straightforward to implement. Quite interestingly, with the exceptions of Refs. [97], [144] on which we will comment below, CMB constraints to this scenario have been overlooked in the past. A proper computation, to the best of our knowledge, was never performed so far, which is rather surprising since the bounds we derive (see below) turn to be competitive with the best ones in the mass range $10^{15}\,\mathrm{g}$ to $10^{16.6}\,\mathrm{g}$, which are given by the extragalactic gamma-ray background (EGB) [144], [148] [3], and to be the dominant ones in the range $10^{13.3}\,\mathrm{g}$ to $10^{14.4}\,\mathrm{g}$.

We summarize here the basic results of PBH evaporation, following ref. [144]. In a seminal couple of papers [298], [299], Hawking showed that a Schwarzschild black hole of mass M should emit black body spectra of particles at a temperature

$$T_{\mathrm{BH}} = \frac{1}{8\pi G M} \simeq 1.06 \left(\frac{10^{13}\,\mathrm{g}}{M}\right) \mathrm{GeV}\,. \tag{6.4.1}$$

3 Note that other gamma-ray bounds exist, like the Galactic ones considered in [145]. While potentially stronger, they are more model-dependent, as also argued in [148], and we will not consider them in the following.

The mass-loss rate of an evaporating black holes can be expressed as

$$\frac{dM}{dt} = -5.34 \times 10^{-11} \mathcal{F}(M) \left(\frac{M}{10^{13}\,\mathrm{g}}\right)^{-2} \mathrm{s}^{-1}\,, \tag{6.4.2}$$

where the function $\mathcal{F}(M)$, normalized to 1 if $M > 10^{17}\,\mathrm{g}$, counts the number of (relativistic) particles species emitted by the PBH, and increases with decreasing mass. For instance, at $10^{15}\,\mathrm{g}$ also electrons and positrons (besides photons, neutrinos and gravitons) can be emitted, and $\mathcal{F}(M) \simeq 1.568$ [413], which further rises (due to muon production) to about 2.1 for $M \simeq 10^{14}\,\mathrm{g}$. The number of degrees of freedom quickly rises for lower masses (when temperatures above the QCD phase transition one are attained) with $\mathcal{F}$ saturating at 15.35 when $M \leq \text{few} \times 10^{10}\,\mathrm{g}$, assuming the standard model to be the correct theory. By integration of Eq. (6.4.2) over time, one obtains the lifetime

$$\Gamma_{\rm PBH}^{-1} \simeq 4.07 \times 10^{11} \left(\frac{\mathcal{F}(M)}{15.35}\right)^{-1} \left(\frac{M}{10^{13}\mathrm{g}}\right)^{3} \mathrm{s}\,. \tag{6.4.3}$$

and the energy injection rate for low mass PBH is given in full generality by

$$\left.\frac{dE}{dV dt}\right|_{\rm inj,\ PBH} = \frac{\Omega_{\rm DM}\rho_c c^2 (1+z)^3 f_{\rm PBH} c^2}{M_{\rm PBH}^{\rm ini}} \left.\frac{dM}{dt}\right|_{\rm e.m.}\,, \tag{6.4.4}$$

where $dM/dt\big|_{\rm e.m.} = f_{\rm e.m.} dM/dt$ with $f_{\rm e.m.}$ the e.m. branching ratio of an evaporating PBH, which depends on its mass. If $M \geq 10^{15}\,\mathrm{g}$, the PBH lifetime is longer than the age of the universe, and its mass and lifetime are roughly time-independent parameters: for instance, a PBH of initial mass 10^{15} g would weight 9.6×10^{14} g today. Since we do not aim anyway at better than $\mathcal{O}(10\%)$ level accuracy, in this mass range we assume that both M and the lifetime Γ^{-1} are time independent, which leads to a simple exponential decay law, similar to the case of decaying particles with lifetime given by Eq. (6.4.3). On the other hand, in this range, we do calculate the ionization and heating efficiency on the basis of a reasonable approximation for the spectrum of emitted particles. The spectra of particles emitted by the BH per unit of time with energy between E and $E + dE$ are given by:

$$\frac{d\dot{N}_s}{dE} \propto \frac{\Gamma_s}{e^{E/T_{\rm BH}} - 1(-1)^{2s}}\,, \tag{6.4.5}$$

where s is the spin of the particle, and the dimensionless absorption coefficient Γ_s can be written in the high-energy limit $E \gg T_{\rm BH}$ as [461]:

$$\Gamma_s(M, E) = 27 E^2 G^2 M^2\,. \tag{6.4.6}$$

It is also known that the spectra fall rapidly at low energy. To avoid unnecessary complication, in what follows we thus approximate the spectra as vanishing below $E = 3\,T_{\rm BH}$, while sticking to the high energy limit formula above this energy. Note that a slightly different choice would not have changed our conclusions significantly, since in most cases the energy deposition functions are not strongly dependent on the energy. Also note that we do not need to worry about the normalization in Eq. (6.4.5), since we use it to compute the deposition functions, which only depend on the energy shape (See Eq. (2.8)). Put otherwise, the correct normalization is assured by using the appropriate M, Γ, and the correct branching ratio in e.m. channels. On the other hand, the above-mentioned approximations for the spectra assume relativistic particles. For $e^{\pm}$, this becomes too crude for masses above $\sim 10^{16.8}\,\mathrm{g}$, hence we limit our considerations to lighter PBHs. Also note that EGB constraints

tend to dominate anyway at these masses, and beyond that GRB femtolensing constraints at the level of $\Omega_{\rm PBH} \leq 0.1\,\Omega_{\rm DM}$ take over [81], [148], making a detailed computation of CMB bounds less appealing for such high masses. For a few cases in the mass interval $10^{15}\,{\rm g} \leq M \leq 10^{16.8}\,{\rm g}$ we recompute the energy deposition functions $f_c(z, x_e)$ without relying on the factorization hypothesis, since it breaks down for some of the injection energies of interest. We conservatively assume the standard reionization scenario to compute the $f_c(z, x_e)$'s [4]. Our results for $M = 10^{15}$g and $10^{16.7}$g are shown in Fig. 59, together with the resulting free electron fractions.

For masses $M \leq 10^{13}\,{\rm g}$, the evaporation takes place before $10^{12}\,{\rm s}$, hence we expect CMB anisotropies to be insensitive in that range (see Fig. 58). In the range $10^{13}\,{\rm g} \ll M \ll 10^{15}\,{\rm g}$, the actual time dependence of the evaporation is important. The emitted spectrum is rapidly changing with the mass, which complicates substantially the treatment, in particular in terms of computational time. While leaving a complete computation of the constraints to a future work, it is however interesting to show how the non-trivial time dependence of the mass affects the bounds. To make this effect apparent, we simplify the treatment of the energy deposition function and resort to the on-the-spot approximation. Indeed, for PBHs with masses $\geq 10^{14.5}\,{\rm g}$, most of the evaporation happens at times $\geq 10^{14}\,{\rm s}$. Hence, we expect the effective criterion derived in sec. 6.3 to apply relatively well. We can estimate the efficiency of this approximation by comparing with the full treatment for masses $> 10^{15}\,{\rm g}$, finding a reasonably good agreement.

In order to compute a value of the effective energy deposition efficiency in the on-the-spot limit, we perform further approximations: a) we only consider the branching ratio into $e^{\pm}$ and γ, neglecting the energy eventually deposited by the decay products of heavier particles like muons and pions (if kinematically allowed). b) We fix this branching ratio to the *initial* one (i.e. given the initial mass of the PBH). c) We neglect the evolution in energy of the injected spectra, fixing it to the initial value. Eventually, in the very last stages of the life of the PBH all standard model particles are produced, and the energy spectra of the emitted particles change, so all these approximations break down. However, most of the PBH mass has been radiated away at an earlier epoch, hence on a purely "calorimetric" ground our choices are reasonable and should capture the bulk of the effect. Note that approximation a) should slightly underestimate the bounds. Approximation b) should push towards overestimating a bit the bound, while approximation c) can play in either sense, but is expected to be rather mild: For most of the time the typical particle energies range from ~ 10 MeV to few hundreds of MeV, hence the time evolution in deposition functions should not be extreme. By performing such simplifications, one can readily integrate Eq. (6.4.2) and find an analytical solution (different from previous constant decay rate) for the time evolution of the PBH mass. We plot the free-electron fraction for the illustrating case $M_{\rm PBH} = 10^{13.7}\,{\rm g}$ in Fig. 59–left panel. It shows a very singular behavior with a peak coming from the peculiar energy injection history, making it in principle distinguishable from an exotic particle decay.

Using CLASS and MontePython, we run ΛCDM + $f_{\rm PBH} \equiv \Omega_{\rm PBH}/\Omega_{\rm DM}$ for 10 different PBH masses distributed between $10^{13.5}$ g and $10^{16.8}\,{\rm g}$, using Planck high-ℓ TT,TE,EE + simlow (prior on $\tau_{\rm reio}$) and lensing likelihood. The results of the MCMC scan in the plane $\{f_{\rm PBH}, M_{\rm PBH}\}$ are shown in Fig. 60, together with constraints coming from the EGB from Ref. [144], as well as CMB constraints from Ref. [608] applied to the case of low-mass PBH in Ref. [144] via a simple prescription. Our constraints

4 This is not strictly correct, but only approximately true as long as x_e stays very small. Also, an iterative treatment, starting from a recfast-like ionization history and recomputing the transfer functions once the effects of the decay on the ionization fraction have been included, showed not only a quick convergence but that the approximate results are, if anything, conservative [408].

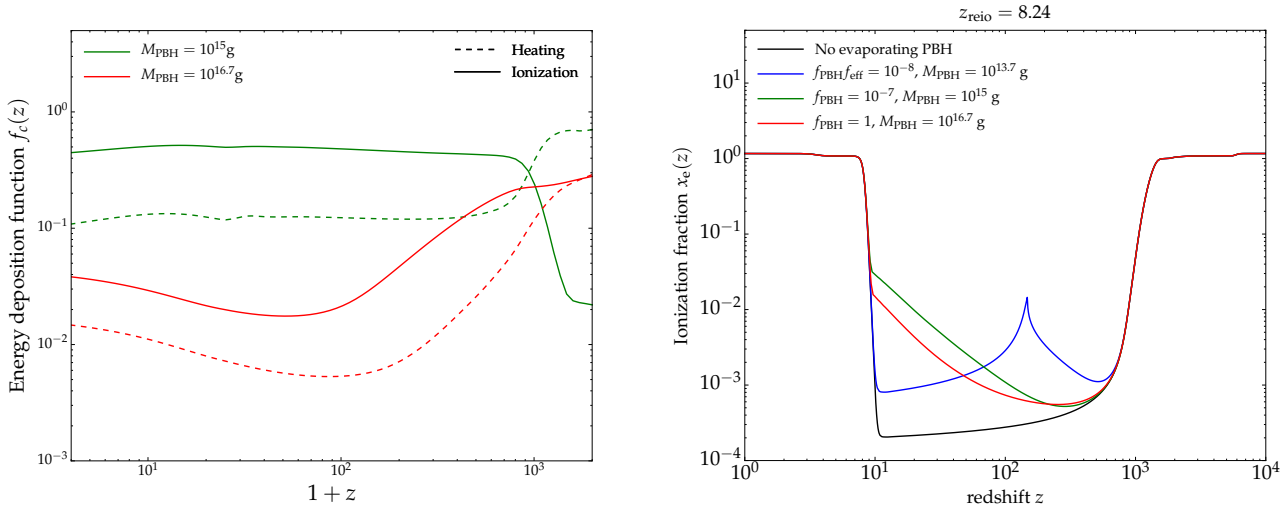

Figure 59: *Left panel* – Energy deposition functions computed following ref. [553] in the case of evaporating PBH of masses 1×10^{15}g and $10^{16.7}$g. *Right panel* – Corresponding free electron fractions.

turn out to be very competitive with γ-ray background one in the range 10^{15} g to $10^{16.6}$ g and to dominate in the range $10^{13.5}$ g to $10^{14.4}$ g. We do not extend the study to lower masses since the on-the-spot approximation is known to fail. We expect however the constraints to rapidly degrade at lower masses. Note that the constraint in the low mass range, while very strong, is not simply the prolongation of the high-mass one: the "shoulder" below 10^{15} g is due to the combined effect of new channels like muon pairs opening up (which, being less effective in releasing energy, lower the "useful" e.m. branching ratio), and on the slightly less efficient energy deposition at the correspondingly higher injection energies. Also note that the similarity of the constraints with those derived in Ref. [144] is accidental: the data available almost a decade ago where significantly less constraining, but the treatment in [144] overestimated the constraining power due to a number of approximations: for instance they did not follow the proper time-evolution of the mass; they did not estimate the efficiency of the energy deposition (they implicitly worked with $f_{\rm eff} = 1$) which overestimates the energy deposition by a factor 2 to 3 depending on the PBH mass. Finally, our constraints are not nearly as good as γ-ray background one in the range $10^{14.4}$ g – 10^{15} g. That said, there is still room for improvement with respect to our current treatment, notably for masses below 10^{15} g.

Let us finish this section with a quick comparison with Ref. [97]. In this work, an estimate of the impact of PBH within the mass range 10^{16} g–10^{17} g was made. They assumed an effective "on-the-spot" approximation, working out the value of the absorption efficiency (which would roughly correspond to our $f_{\rm eff}$) under some simplified assumptions for the energy losses and spectra of evaporated particles. However, what might lead to the biggest difference with our work is that they compute $x_e(z)$ using Saha formula. Hence, the energy injected to the medium affect the ionization history only through reheating, which in turns lead to very different evolution for x_e as can be seen from our Fig. 59– right panel, compared to their Fig. 6. Our more accurate computation, that takes into account both the impact of energy injection through heating and the ionization (as well as excitation) of the atoms, shows that the free electron fraction evolution departs significantly from Saha equation, with a reionization starting already at redshift of few hundreds. Thus, the constraints of Ref. [97] should not be considered quantitatively reliable.

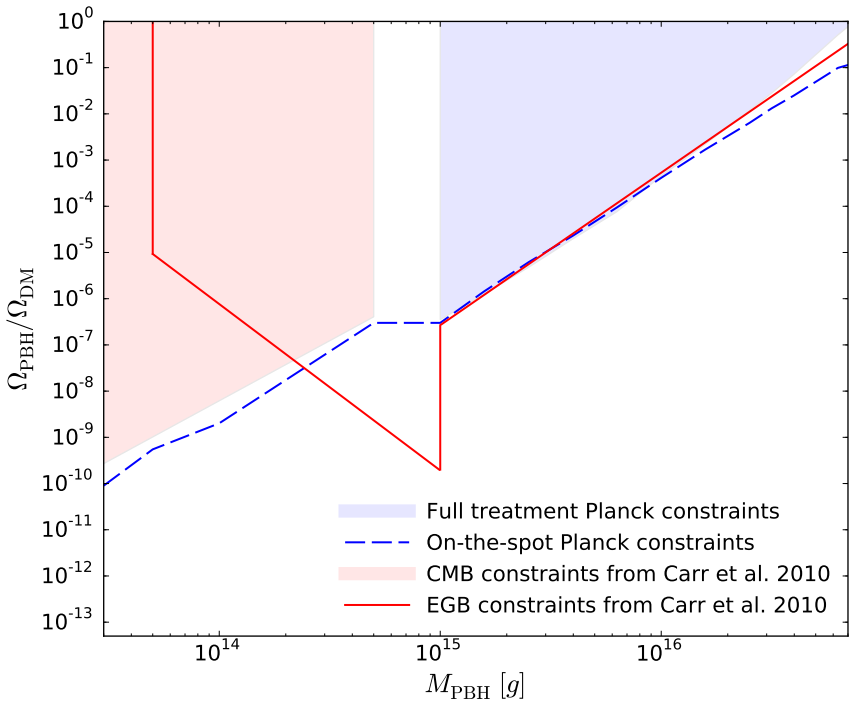

Figure 60: Constraints on the abundance of PBH normalized to the DM one as a function of the PBH mass with the full treatment (shaded blue area) and its approximate version (blue, dashed). Limits from extragalactic γ-ray background (solid, red) and CMB anisotropies (pink shaded area) from Ref. [144] are also shown.

6.4.2 *High mass primordial black holes*

6.4.2.1 *Introduction*

The scenario of high masses primordial black holes beeing DM has received a lot of attention after the aLIGO discovery of three or four binary black hole (BH) mergers of tens of solar masses [6]–[8], including one with a progenitor spin misaligned with the orbital momentum. Intriguingly, their merging rate is compatible with the expectation from binaries formed in present-day halos by a BH population whose density is comparable to the DM one [104], [194], although Refs. [499], [526] argue that this is significantly lower than the merger rate of binaries formed in the early universe, which would thus overshoot the aLIGO observed rate. Very stringent constraints (excluding PBH as DM with $M \geq 0.1\ M_\odot$) have been thus derived on this scenario by studying the impact of PBH accretion onto the CMB statistics already a decade ago [506]. These bounds (as well as their update in Ref. [314]) have been recently revisited and corrected in Ref. [39] (see also Ref. [43]), yielding significantly weaker constraints $M \leq 10-100\ M_\odot$ if PBH constitute the totality of the DM, depending on the assumption on radiation feedback. In this section, we revisit the CMB anisotropy constraints on the PBH abundance, which have been derived until now assuming *spherical* accretion of matter onto BH. We revisit this hypothesis and find plausible arguments suggesting that an *an accretion disk* generically forms in the dark ages, between recombination and reionization possibly already at $z \sim \mathcal{O}(1000)$. A firm proof in that sense would require deeper studies of the non-linear growth of structures at small scales, accounting for the peculiarities of PBH clustering and for the time-

dependent building-up of the baryonic component of halos. A first step to motivate such studies, however, is to prove that they have a potentially large impact: in presence of disks, CMB constraints on PBH improve by (at least) two orders of magnitude, excluding the possibility that PBH with masses $M \geq 2\ M_\odot$ account for the totality of the DM. As we will argue, we expect the bounds to be greatly improved if the baryon velocity at small scales is not coherent and comparable with (or smaller than) their cosmological thermal velocity, and/or if a sizable baryon filling of the PBH halos is present already at $z \geq \mathcal{O}(100)$.

This section is structured as follows: In Sec. 6.4.2.2, we provide a short—and necessarily incomplete—review of the current understanding of accretion, and discuss its applicability in the cosmological context. The crucial arguments on why we think plausible that the accretion (at least the one relevant for CMB bounds) should proceed via disks is discussed in Sec. 6.4.2.3. In Sec. 6.4.2.4 we review the expected high-energy luminosity associated to these accretion phenomena and describe benchmark prescriptions used afterwards. Section 6.4.2.5 described our procedure on obtaining CMB bounds. In section 6.5, we summarize our results and draw our conclusions.

6.4.2.2 *Essentials on accretion in cosmology*

The problem of accretion of a point mass M moving at a constant speed $v_{\rm rel}$ in a homogeneous gas of number density n_∞ (and mass density ρ_∞, where the subscript ∞ means far away from the point mass) was first studied by Hoyle and Lyttleton [319]–[321] in a purely ballistic limit, i.e. accounting only for gravitational effects but no hydrodynamical or thermodynamical considerations. They found the accretion rate (natural units $c = \hbar = k_{\rm B} = 1$ are used throughout, unless stated otherwise)

$$\dot{M}_{\rm HL} \equiv \pi r_{\rm HL}^2 \rho_\infty v_{\rm rel} \equiv 4\pi \rho_\infty \frac{(GM)^2}{v_{\rm rel}^3}\,, \tag{6.4.7}$$

where we introduced the Hoyle-Lyttleton radius $r_{\rm HL}$, the radius of the *cylinder* effectively sweeping the medium. This model does not describe the motion of the particles once they reach the (infinitely thin and dense) accretion line in the wake of the point mass, when pressure and dissipation effects prevail. Also, it is clearly meaningless in the limit of very small velocity $v_{\rm rel}$. A first attempt to address the former problem and account for the accretion column was done by Bondi and Hoyle [114], suggesting a reduced accretion by up to a factor two. The second problem is linked to neglecting pressure. It has only been solved exactly for an accreting body at rest in a homogeneous gas, when the accretion is spherical by symmetry. Its rate has been computed by Bondi [112], yielding the so-called *Bondi accretion rate*:

$$\dot{M}_{\rm B} \equiv 4\pi\lambda\, \rho_\infty c_{{\rm s},\infty} r_{\rm B}^2 \equiv 4\pi\lambda\, \rho_\infty \frac{(GM)^2}{c_{{\rm s},\infty}^3}\,, \tag{6.4.8}$$

where $r_{\rm B}$ is the Bondi radius, i.e. the radius of the equivalent accreting *sphere* (as opposed to a cylinder, hence the 4π geometric factor), $c_{s,\infty}$ is the sound speed far away from the point mass, depending on the pressure P_∞ and density ρ_∞ and λ is a parameter that describes the deviation of the accretion from the Bondi idealised regime. In the cosmological plasma, one typically has:

$$c_{{\rm s},\infty} = \sqrt{\frac{\gamma \mathrm{P}_\infty}{\rho_\infty}} = \sqrt{\frac{\gamma(1+x_{\rm e})T}{m_{\rm p}}} \simeq 6\frac{\rm km}{\rm s}\sqrt{\frac{1+z}{1000}}\,, \tag{6.4.9}$$

$$\Rightarrow r_{\rm B} \equiv \frac{GM}{c_{{\rm s},\infty}^2} \simeq 1.2\times 10^{-4}{\rm pc}\frac{M}{M_\odot}\frac{10^3}{1+z}\,, \tag{6.4.10}$$

$m_{\rm p}$ being the proton mass, and γ is the polytropic equation of state coefficient for monoatomic ideal gas. The approximation at the RHS of Eq. (6.4.9) typically holds for $100 \leq z \leq 1000$. The mean cosmic gas density in the early universe is given by:

$$n_\infty \simeq \frac{\rho_\infty}{m_{\rm p}} \simeq 200\,{\rm cm}^{-3}\left(\frac{1+z}{1000}\right)^3 . \tag{6.4.11}$$

Finally, λ is a numerical parameter which quantifies non-gravitational forces (pressure, viscosity, radiation feedbacks, etc.) partially counteracting the gravitational attraction of the object. Historically, Bondi computed the maximal value of λ as a function of the equation of state of the gas, finding $\lambda \sim \mathcal{O}(1)$, ranging from 0.25 ($\gamma = 5/3$, adiabatic case) to 1.12 ($\gamma = 1$, isothermal case).

There is no exact computation of the accretion rate accounting for the finite sound speed and a displacement of the accreting object. However, as argued by Bondi in Ref. [112], a reasonable proxy can be obtained by the quadratic sum of the relative velocity and the sound speed at infinity, which leads to an effective velocity $v_{\rm eff}^2 = c_{s,\infty}^2 + v_{\rm rel}^2$. We thus define the Hoyle-Bondi radius and rate[5]

$$\dot{M}_{\rm HB} \equiv 4\pi\lambda\,\rho_\infty v_{\rm eff} r_{\rm HB}^2 \equiv 4\pi\lambda\,\rho_\infty \frac{(GM)^2}{v_{\rm eff}^3} . \tag{6.4.12}$$

Despite the fact that the Bondi analysis was originally limited to spherical accretion, this formalism is commonly used to treat non-spherical cases, with e.g. formation of an accretion disk, by choosing an appropriate value for λ. Although it has been shown for instance that the simple analytical formulae can overestimate accretion in presence of vorticity [380] or underestimates it in presence of turbulence [381], typically Eq. (6.4.12) provides a reasonable order-of-magnitude description of the simulations (see for instance [230] for a recent simulation and interpolation formulae).

6.4.2.3 *Relative baryon-PBH velocity and disk accretion in the early universe*

In the cosmological context, one might naively estimate the relative velocity between DM and baryons to be of the order of the thermal baryon velocity or of the speed of sound, Eq. (6.4.9). In that case, the appropriate accretion rate would be the Bondi one, Eq. (6.4.8). The situation is however more complicated, since at the time of recombination the sound velocity drops abruptly and the baryons, which were initially tightly coupled to the photons in a standing acoustic wave, acquire what is an eventually supersonic relative stream with respect to DM, coherent over tens of Mpc scales. In linear theory, one finds that the square root of the variance of the relative baryon-DM velocity is basically constant before recombination and then drops linearly with z [227], [583]:

$$\sqrt{\langle v_{\rm L}^2 \rangle} \simeq \min\left[1, \frac{1+z}{1000}\right] \times 30\,{\rm km/s} . \tag{6.4.13}$$

Yet, this is a linear theory result, and it is unclear if it can shed any light on the accretion, which depends on very small, sub-pc scales (Bondi radius, see Eq. (6.4.10)). In Ref. [583], the authors first studied the problem of small-scale perturbation growth into such a configuration, by a perturbative expansion of the fluid equations for DM, baryons, and the Poisson equation around the exact solution with uniform bulk motion given by Eq. (6.4.13), *further assuming zero density contrast, and zero Poisson potential.* Their results suggest that small-scale structure formation and the baryon settling

5 Actually, our rate definition is a factor 2 larger than the original proposal, but has been confirmed as more appropriate even with numerical simulations, see Ref. [544].

into DM potential wells is significantly delayed with respect to simple expectations. Equation (6.4.13) has also entered recent treatments of the Hoyle-Bondi PBH accretion rate, see Ref. [39], yielding a correspondingly suppressed accretion. In particular, by taking the appropriate moment of the function of velocity entering the luminosity of accreting BH over the velocity distribution, Ref. [39] found

$$v_{\rm eff} \equiv \left\langle \frac{1}{(c_{s,\infty}^2 + v_{\rm L}^2)^3} \right\rangle^{-1/6} \simeq \sqrt{c_{s,\infty} \sqrt{\langle v_{\rm L}^2 \rangle}}\,, \tag{6.4.14}$$

with the last approximation only valid if $c_{s,\infty} \ll \sqrt{\langle v_{\rm L}^2 \rangle}$, which is acceptable at early epochs after recombination, of major interest in the following.

The application of the above perturbative (but non-linear) theory to the relative motion between PBH and the baryon fluid down to sub-pc scales appears problematic. A first consideration is that the behavior of an ensemble of PBH of stellar masses is very different from the "fluid-like" behavior adopted for microscopic DM candidates like WIMPs. The discreteness of PBHs is associated to a "Poissonian noise", enhancing the DM power spectrum at small scale, down to the horizon formation one [25], [157], [274], [609]. Our own computation suggests that a density contrast of $\mathcal{O}(1)$ is attained at $z \simeq 1000$ at a comoving scale as large as $k_{\rm NL} \sim 10^3$ Mpc^{-1} for a population of $1\,M_\odot$ PBH whose number density is comparable to the DM one. Even allowing for fudge factors (e.g. $f_{\rm PBH} \sim 0.1$, different mass) the non-linearity scale is unavoidably pertinent to the scales of interest. In fact, the PBH formation mechanism itself *is* a non-linear phenomenon, and peaks theory suggests that PBH are likely *already born* in clusters, on the verge of forming bound systems [157], [158]. Our first conclusion is that the application of the scenario considered in Refs. [227], [583] to the PBH case is not at all straightforward. In particular, a more meaningful background solution around which to perturb would be the one of vanishing initial baryon perturbations in the presence of an already formed halo (and corresponding gravitational potential) at a scale $k_{\rm NL} \geq 10^3$ Mpc^{-1}. A second caveat is that the treatment in Refs. [227], [583] uses a fluid approximation, i.e. it does not account for "kinetic" effects such as the random (thermal) velocity distribution around the bulk motion velocity given by Eq. (6.4.13). One expects that "cold" baryons (statistically colder than the average) would already settle in the existing PBH halo at early time, forming a virialized system—albeit still under-dense in baryons, with respect to the cosmological baryon to DM ratio. One may also worry about other effects, such as shocks and instabilities, which may hamper the applicability of the approach of Ref. [583] to too small scales and too long times.

Assuming that the overall picture remains nevertheless correct in a more realistic treatment, we expect that the PBH can generically accrete from two components: the high-velocity, free-streaming fraction at cosmological density and diminished rate of Eqs. (6.4.12) and (6.4.14), as considered in Ref. [39], and a virialized component, of initial negligible density but growing with time and eventually dominating, with typical relative velocity of the order of the virial ones. If we normalize to the Milky Way halo ($10^{12}\,M_\odot$) value $v_{\rm vir} \sim 10^{-3}\,c$, and adopt the simple scaling of the velocity with the halo mass over size, $v_{\rm vir}(M_{\rm halo}) \propto (M_{\rm halo}/d_{\rm halo})^{1/2} \propto M_{\rm halo}^{1/3}$, we estimate $v_{\rm vir} \sim 0.3\,$km/s to $3\,$km/s for a halo mass of $10^3\,M_\odot$ to $10^6\,M_\odot$. The latter roughly corresponds to the smallest dwarf galaxies one is aware of, see e.g. [116] [6]. At $z \simeq \mathcal{O}(1000)$, it is likely that the fast, unbound baryons constitute the dominating source of accretion. But at latest when the density of the virialized baryon component attains values comparable to the *cosmological average* density—which given the z-dependences

6 The PBH distribution can hardly be dominated by heavier clumps, or the lack of predicted structures at the dwarf scales would automatically exclude them as dominant DM component.

Eq. (6.4.9) and Eq. (6.4.13) appears unavoidable for $z \leq \mathcal{O}(100)$—the accretion is dominated by this halo-bound component.

After these preliminary considerations, we are ready to discuss disk formation. The basic criterion used to assess if a disk forms is to estimate the angular momentum of the material at the accretion distance: if this is sufficient to keep the matter in Keplerian rotation at a distance $r_{\rm D} \gg 3\, r_{\rm S}$ (i.e. well beyond the innermost stable orbit, where we introduced the Schwarzschild radius $r_{\rm S} \equiv 2\, G\, M$) at least for BH luminosity purposes, dominated by the region close to the BH, a disk will form [28], [340], [521], [540]. To build up angular momentum, the material accreted at the Hoyle-Bondi distance along different directions must have appreciable velocity or density differences. The angular momentum per unit mass of the accreted gas scales like

$$l \simeq \left(\frac{\delta\rho}{\rho} + \frac{\delta v}{v_{\rm eff}} \right) v_{\rm eff} r_{\rm HB}\,, \tag{6.4.15}$$

where $\delta\rho/\rho$ represent typical inhomogeneities at the scale $r_{\rm HB}$ in the direction *orthogonal* to the relative motion PBH-baryons, and $\delta v/v_{\rm eff}$ the analogous typical velocity gradient at the same scale (see e.g. [28]). The above quantity can be compared to the specific angular momentum of a Keplerian orbit,

$$l_{\rm D} \simeq r_{\rm D} v_{\rm Kep}(r_{\rm D}) \simeq \sqrt{G M r_{\rm D}}\,, \tag{6.4.16}$$

to extract r_D. For instance, in the case of inhomogeneities, if we adopt the effective velocity at the RHS of Eq. (6.4.14) as a benchmark, as in Ref. [39], we obtain:

$$\frac{r_D}{r_S} \simeq \left(\frac{\delta\rho}{\rho}\right)^2 \frac{c^2}{2\, v_{\rm eff}^2} \simeq 2.5 \times 10^8 \left(\frac{\delta\rho}{\rho}\right)^2 \left(\frac{1000}{1+z}\right)^{3/2}\,, \tag{6.4.17}$$

so that, already soon after recombination, gradients $\delta\rho/\rho \gg 10^{-4}$ in the baryon flow on the scale of the Bondi radius are sufficient for a disk to form. We find this to be largely satisfied already at $z \sim 1000$ because of the "granular" potential due to neighboring PBHs.

Equivalently, given the similar way the fractional fluctuation of velocity and density enter Eq. (6.4.15), the condition for a disk to form can be written as a lower limit on the absolute value of the velocity perturbation amounting to

$$\delta v \gg 1.5 \left(\frac{1+z}{1000}\right)^{3/2} \text{m/s}\,. \tag{6.4.18}$$

At least the component of virialized baryons, whose velocity dispersion is ≥ 0.1 km/s as argued above, should easily match this criterion.

But even for a "ideal", free-streaming homogeneous gas moving at a bulk motion comparable to Eq. (6.4.13) without any velocity dispersion, the disk formation criterion is likely satisfied, if the non-linear PBH motions at small scales are taken into account. Since this is in general a complicated problem, we cannot provide a cogent proof, but the following argument makes us confident that this is a likely circumstance. In general, the BH motion within its halo at very small scale is influenced by its nearest neighbors. The simplest scenario (see for instance [526]) amenable to analytical estimates is that a sizable fraction of PBH forms binary systems with their nearest partner, under the tidal effect of the next-to-nearest. According to [526], for PBH constituting a sizable fraction of the DM, it is enough for their distance to be only slightly below the average distance at matter-radiation equality

for a binary to form. Under the assumption of an isotropic PBH distribution and monochromatic PBH mass function of mass M, this distance can be estimated as

$$d \sim \left(\frac{3M}{4\pi\rho_{\rm PBH}}\right)^{1/3} = \frac{1}{1+z_{\rm eq}}\left(\frac{2GM}{H_0^2 f_{\rm PBH}\Omega_{\rm DM}}\right)^{1/3}, \tag{6.4.19}$$

i.e.

$$d \sim 0.05\,{\rm pc}\left(\frac{M}{f_{\rm PBH}\,M_\odot}\right)^{1/3}\frac{3400}{1+z_{\rm eq}}\,. \tag{6.4.20}$$

If bound, the two PBH (each of mass M) orbit around the common center of mass on an elliptical orbit whose major semi-axis is a with the Keplerian angular velocity

$$\omega = \sqrt{\frac{2\,G\,M}{a^3}}\,. \tag{6.4.21}$$

We conservatively assume $a = d/2$ for a quasi-circular orbit, although for the very elongated orbits usually predicted for PBH a value $a = d/4$ is closer to reality. Note that the orbital size of the order of Eq. (6.4.20) is typically larger than (or at most comparable to) the Bondi-Hoyle radius, so that to a good approximation the gas—assumed to have a bulk motion with respect to the PBH pair center of mass—accretes around a single PBH, which is however rotating with respect to it.

In the PBH rest-frame, Eq. (6.4.15) is simply replaced by

$$l \simeq \omega\, r_{\rm HB}^2\,, \tag{6.4.22}$$

or, equivalently, one can apply Eq. (6.4.18) with $\delta v = \omega\, r_{\rm HB}$.

If we adopt the effective velocity at the RHS of Eq. (6.4.14), this leads to the disk formation condition ($z \leq 1000$):

$$f_{\rm PBH}^{1/2}\frac{M}{M_\odot} \gg \left(\frac{1+z}{730}\right)^3\,. \tag{6.4.23}$$

Whenever $M \geq M_\odot$ and PBH constitute a sizable fraction of the DM, this is satisfied at the epoch of interest for CMB bounds.

In fact, we have shown in previous section that most of the constraining power of CMB anisotropies on exotic energy injection *does not* come from redshift 1000 and above, rather around a typical redshift of ~ 300 for an energy injection rate scaling like $\propto (1+z)^3$. In the problem at hand, the constraining power should be further skewed towards lower redshifts, given the growth of the signal at smaller z due to the virializing component.

We believe that these examples show that disk formation at relatively early times after recombination is a rather plausible scenario, with spherical accretion which would rather require physical justification. Note that we have improved upon the earlier discussion of this point in Ref. [506] by taking into account the essential ingredient that stellar mass PBH are clustered in non-linear structures at small scales and early times, greatly differing from WIMPs in that respect. In the following, we shall assume that the disk forms at all relevant epochs for setting CMB bounds, and deduce the consequences of this Ansatz. In the conclusions, we will comment on the margins for improvements over the current treatment.

6.4.2.4 *Luminosity*

In addition to $\dot{M}$, the second crucial quantity for accretion luminosity is the radiative efficiency factor ϵ, which simply relates the *accretion luminosity* $L_{\rm acc}$ to the accretion rate in the following way:

$$L_{\rm acc} = \epsilon \dot{M}. \tag{6.4.24}$$

The radiative efficiency is itself tightly correlated with the accretion geometry and thus the accretion rate, since it directly depends on the temperature, density and optical thickness of the accretion region. Hence, a coherent analysis determines both parameters λ and ϵ jointly. In practice, no complete, first-principle theory exists, although a number of models have been developed to compute $L_{\rm acc}$ (which is the main observable in BH physics) under different assumptions and approximations. A typical fiducial value is $\epsilon = 0.1$, to be justified below. A useful benchmark upper limit to $L_{\rm acc}$ is the so-called Eddington luminosity, $L_E = 4\pi G M m_p/\sigma_T = 1.26 \times 10^{38}\,(M/M_\odot)\,{\rm erg/s}$, which is the luminosity at which electromagnetic radiation pressure (entering via the Thomson cross section σ_T) balances the inward gravitational force in a hydrogen gas, preventing larger accretion, unless special conditions are realized. In practice, for the parameters of cosmological interest, it turns out that we will always be below L_E.

The simplest and most complete theoretical treatment applies to spherical accretion, going back to Shapiro in Refs. [537], [538] in the case of non-rotating BHs and Ref. [539] for rotating (Kerr) BHs, accounting for relativistic effects. Since we have argued that this case is unlikely to apply to the cosmological context of interest, we will not review it here, but address for instance to Ref. [39] for a recent and detailed treatment. We will only refer to this case for comparison purposes, and for these cases we follow the equations in Ref. [39].

For *moderate or low disk* accretion rate, which is the case of interest here, there are two main models:

If the radiative cooling of the gas is *efficient*, a geometrically thin disk forms, which radiates very efficiently. This is the "classical" disk solution obtained almost half a century ago by Shakura and Sunyaev [536]. In this case, the maximal energy per unit mass available is uniquely determined by the binding energy at the innermost stable orbit. This can be computed accurately in General Relativity, yielding ϵ from 0.06 to 0.4 when going from a Schwarzschild to a maximally rotating Kerr BH. This range, which justifies the benchmark value $\epsilon = 0.1$ mentioned above, is often an upper limit to the radiative efficiency actually inferred from BH observations. Also note that, since the disk can efficiently emit radiation, the temperatures characterizing the disk emission are relatively low, below a few hundreds of keV.

If the radiative cooling of the gas is *inefficient*, then hot and thick/inflated disks (or torii) form, with advection and/or convective motions dominating the gas dynamics and inefficient equilibration of ion and electron temperature, with the former that is much higher and can easily reach tens of MeV. This regime is widely (albeit with a little abuse of notation) known under the acronym ADAF, "advection-dominated accretion flow" (see [603] for a review). It has been discovered in the pioneering articles [336] and later [503], but has been extensively studied only after its "rediscovery" and 1D self-similar analytical treatment in Ref. [443]. It is worth noting that in the ADAF solution, the viscosity α plays a fundamental role in accretion: Indeed the viscously liberated energy is not radiated and dissipated away, but instead is conveyed into the optically thick gas towards the center. As a consequence, the accretion rate is typically diminished by an order of magnitude with respect to the Bondi rate with $\lambda = 1$ (see [442] for a short pedagogical overview). In practice, α is degenerate with the previously introduced parameter λ, so that one might roughly capture this effect by assuming

as benchmark $\lambda = 0.1$. In "classical" ADAF models, the efficiency scales roughly linearly with $\dot{M}$, attaining (and stabilizing at) a value of the order of 0.1 only for a critical accretion which is about $0.1\,L_E$. Overall, this class of models provides a moderately satisfactory description (at least for $\alpha \leq 0.1$) of "median" X-ray observations of nuclear regions of supermassive black holes, see e.g. [475] (in particular the lower dashed curve in Fig. 3).

A further refinement takes into account that gas outflows and jets typically accompany this regime, so that the accretion rate becomes in general a function of radius [107]. We will still normalize the (diminished) accretion rate responsible for the bulk of the luminosity to the one at the Bondi radius. For a specific example, we rely on some recent numerical solutions [599] which suggest: i) On the one hand, a more significant role of outflows, so that only $\sim 1\%$ of the accretion rate at the Bondi radius is ultimately accreted in the inner region most relevant for the luminosity of the disk. We shall model that by benchmarking $\lambda = 0.01$. ii) On the other hand, an increase of the fraction, δ, of the ion energy shared by electrons. Typically, in classical ADAF models, such a fraction is considered to be very small, $\delta \ll 1$. A greater efficiency δ implies a corresponding higher efficiency ϵ, somewhat intermediate between the thin disk and the classical ADAF solution, also scaling with a milder power of the mass accretion ($\epsilon \propto \dot{M}^{0.7}$) at low accretion rates. In Ref. [599], suitable fitting formulae have been provided, which we rely upon in the following. In particular, we adopt the parameterization in Eq. (11), with parameters taken from Tab. 1 for the ADAF accretion rate regime. In Fig. 61, we compare the spherical case with $v_{\rm eff} = \sqrt{c_{s,\infty}\langle v_L\rangle^{1/2}}$ to our benchmark $\delta = 0.1$, as well as a more optimistic $\delta = 0.5$ and a more pessimistic[7] $\delta = 10^{-3}$: the accretion rate (top panel) reduces when a disk forms (independently of δ), but the luminosity (bottom panel) is enhanced. Since in the redshift range of interest (blue band in bottom panel of Fig. 61, as we show in previous section) the latter is enhanced despite the fact that the former is reduced (whatever the value of δ), we expect the CMB bound to improve appreciably in our more realistic disk accretion scenario.

6.4.2.5 *Computing the CMB bound*

The total energy injection rate per unit volume is:

$$\frac{{\rm d}E}{{\rm d}V\,{\rm d}t} = L_{\rm acc} n_{\rm pbh} = L_{\rm acc} f_{\rm pbh} \frac{\rho_{\rm DM}}{M}\,. \tag{6.4.25}$$

which can be related to the deposited rate thanks to the usual treatment 6.2.8. The only ingredient left is thus the spectrum of the radiation emitted via BH accretion. Note that it is only the shape that enters Eq. (6.2.8), which is indeed an efficiency function, while the overall normalization was discussed in Sec. 6.4.2.4. In the spherical accretion scenario (see [39], [537], [538]) the spectrum is dominated by Bremsstrahlung emission, with a mildly decreasing frequency dependence over several decades and a cutoff given by the temperature of the medium near the Schwarzschild radius T_s

$$L_\omega \propto \omega^{-a} \exp(-\omega/T_s)\,, \tag{6.4.26}$$

where $T_s \sim \mathcal{O}(m_{\rm e})$ (we used 200 keV in the following for definiteness) and $|a| \leq 0.5$ ($a = 0$ was used in [39]).

7 It is worth noting that such a low value is reported in Ref. [599] rather for historical reasons, being associated to the early analytical solutions of Ref. [443] and thus being an old benchmark, than because of theoretical or observational arguments related e.g. to Sgr A^*: The authors of Ref. [599] make clear that all evidence points to a higher range for δ, with $\delta = 0.1$ being on the *conservative* side, and any $\delta \leq 0.3$ is in agreement with data from Sgr A^* [442].

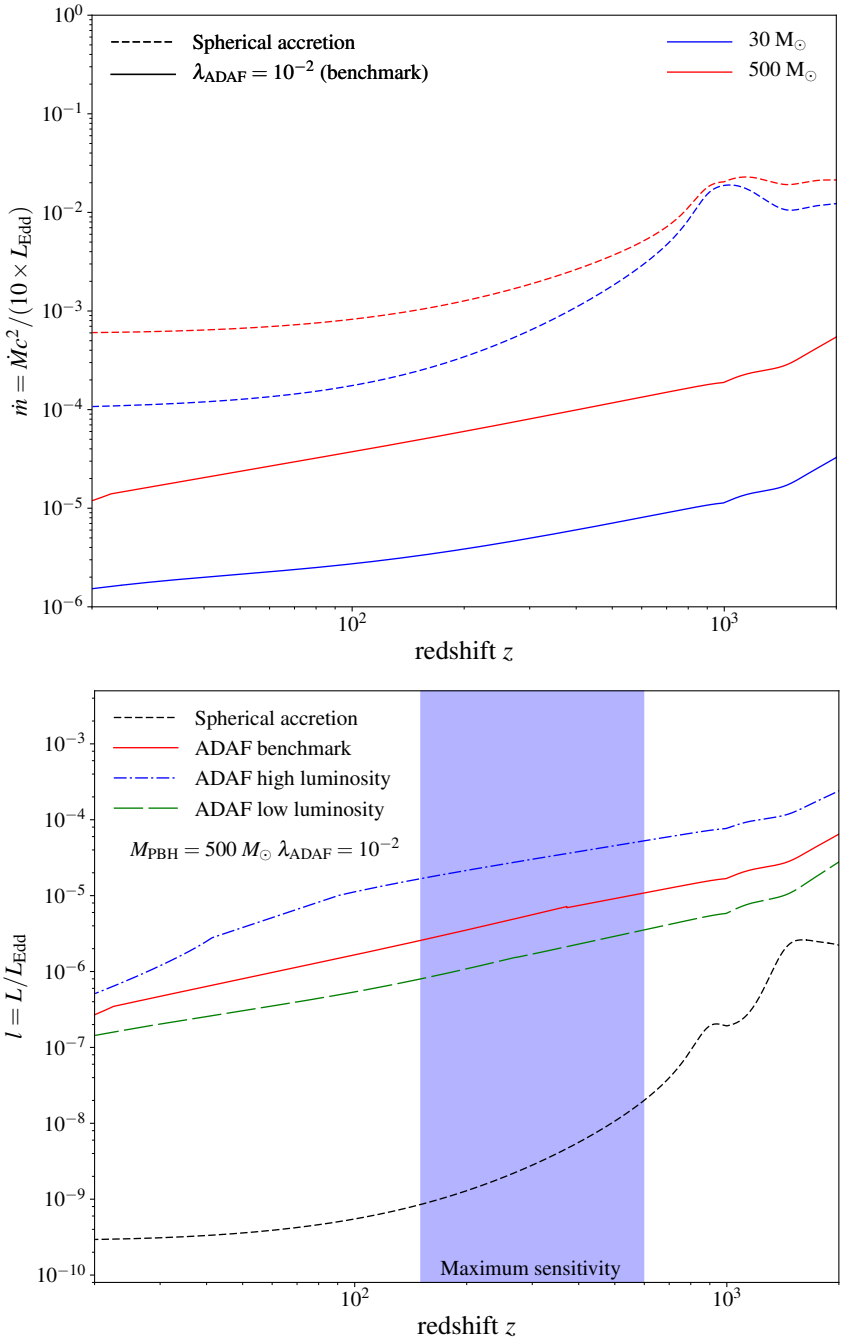

Figure 61: *Top panel:* The dimensionless accretion rate $\dot{m}$ as a function of redshift for different accretion modeling and PBH mass. Our benchmark model corresponds to the result of simulations attested by observations. *Bottom panel:* The dimensionless luminosity l as a function of redshift for different accretion modeling. The benchmark model stands for $\delta = 0.1$, while the low-luminosity and high-luminosity scenarii corresponds to $\delta = 10^{-3}$ and 0.5 respectively.

For consistency with our discussion in Sec. 6.4.2.4, we base our disk accretion spectra on the numerical results for ADAF models reported in Ref. [603], Fig. 1. In particular, we adopt

$$L_\omega \propto \Theta(\omega - \omega_{\rm min})\omega^{-a}\exp(-\omega/T_s)\,, \tag{6.4.27}$$

with a choice for T_s as above. We ignore the dependence of T_s upon accretion rate and PBH mass, which is very mild in the range of concern for us. We consider $a \in [-1.3; -0.7]$, with a hardening linear in the log of $\dot{M}$ (as from the caption in that figure) with -0.7 corresponding almost to the limiting case of the thick disk. We take $\omega_{\rm min} = (10\,M_\odot/M)^{1/2}\,$eV. Note that such cutoff at low energy only affects the normalization at the denominator of Eq. (6.2.8), i.e. the "useful" photon fraction of the bolometric luminosity, normalized as described in Sec. 6.4.2.4. On the other hand, the cutoff at the numerator in Eq. (6.2.8) is in principle given by the ionization or excitation threshold (depending on the channel), since photons of lower energy do not contribute to the efficiency. In practice, the transfer functions are only directly available for energy injection above 5 keV. However, we can safely extrapolate the transfer function down to $\sim$ 100 eV: It has been shown in Ref. [261] that the energy repartition fractions are to an extremely good approximation independent of the initial particle energy in the range between $\sim$ 100 eV and a few keV. In fact, this behaviour is at the heart of the "low energy code" used by authors of Ref. [553] to compute their transfer functions. Below $\sim$ 100 eV, the power devoted to ionization starts to drop, and we conservatively cut the integral at the numerator at this energy. We show the $f_c(z, x_{\rm e})$-functions for the spherical accretion scenario and the disk accretion scenario in Fig. 62 - top panel (we chose a mass which we estimate to be among the least efficient at depositing energy). We incorporated the effects of accretion into a modified version of the Recfast module [531] of the Boltzmann solver CLASS [109]. It is enough for our purpose to work with a modified Recfast that has been fudged to reproduce the more accurate calculation from CosmoRec [166] and HyRec [35]. The impact of the accretion on the free-electron fraction for a PBH mass of $500M_\odot$ is shown in the bottom panel of Fig. 62: It is much more pronounced in the disk accretion scenario (we chose a PBH fraction $\sim$ 300 times smaller!), even if the energy deposition efficiency is lower. In Fig. 63, the corresponding impact on the CMB power spectra is illustrated. The effects are typical of an electromagnetic energy injection: The delayed recombination slightly shifts acoustic peaks and thus generates small wiggles at high multipoles ℓ in the residuals with respect to a standard ΛCDM scenario. Meanwhile, the increased freeze-out fraction leads to additional Thomson scattering of photons off free electrons along the line-of-sight, which manifests itself as a damping of temperature anisotropies and an enhanced power in the polarization spectrum. Note that in principle the different accretion recipes could be distinguished via a CMB anisotropy analysis. Indeed, each accretion scenario has a peculiar energy injection history which does not lead to a simple difference in the normalization: the actual shape of the power spectra slightly changes. This behavior is also present when changing the PBH mass, but is much less pronounced, albeit still above cosmic variance in the EE spectrum (not shown here to avoid cluttering). Hence, if a signal were found, it is conceivable that some constraints could be put on the PBH mass and (especially) accretion mechanism, but a strong statement would require better characterization of the signal, which goes beyond our present goals.

We compute the 95% CL bounds using data from *Planck* high-ℓ TT TE EE+lensing [19] and a prior on $\tau_{\rm reio}$ [27], by running an MCMC using the MontePython package [68] associated to CLASS. For ten PBH masses log-spaced in the range $[M_{\rm min}, 1000M_\odot]$ we perform a fit to the data with flat priors on the following set of parameters:

$$\Lambda{\rm CDM} \equiv \{\omega_b, \theta_s, A_s, n_s, \tau_{\rm reio}, \omega_{\rm DM}\} + f_{\rm PBH}\,,$$

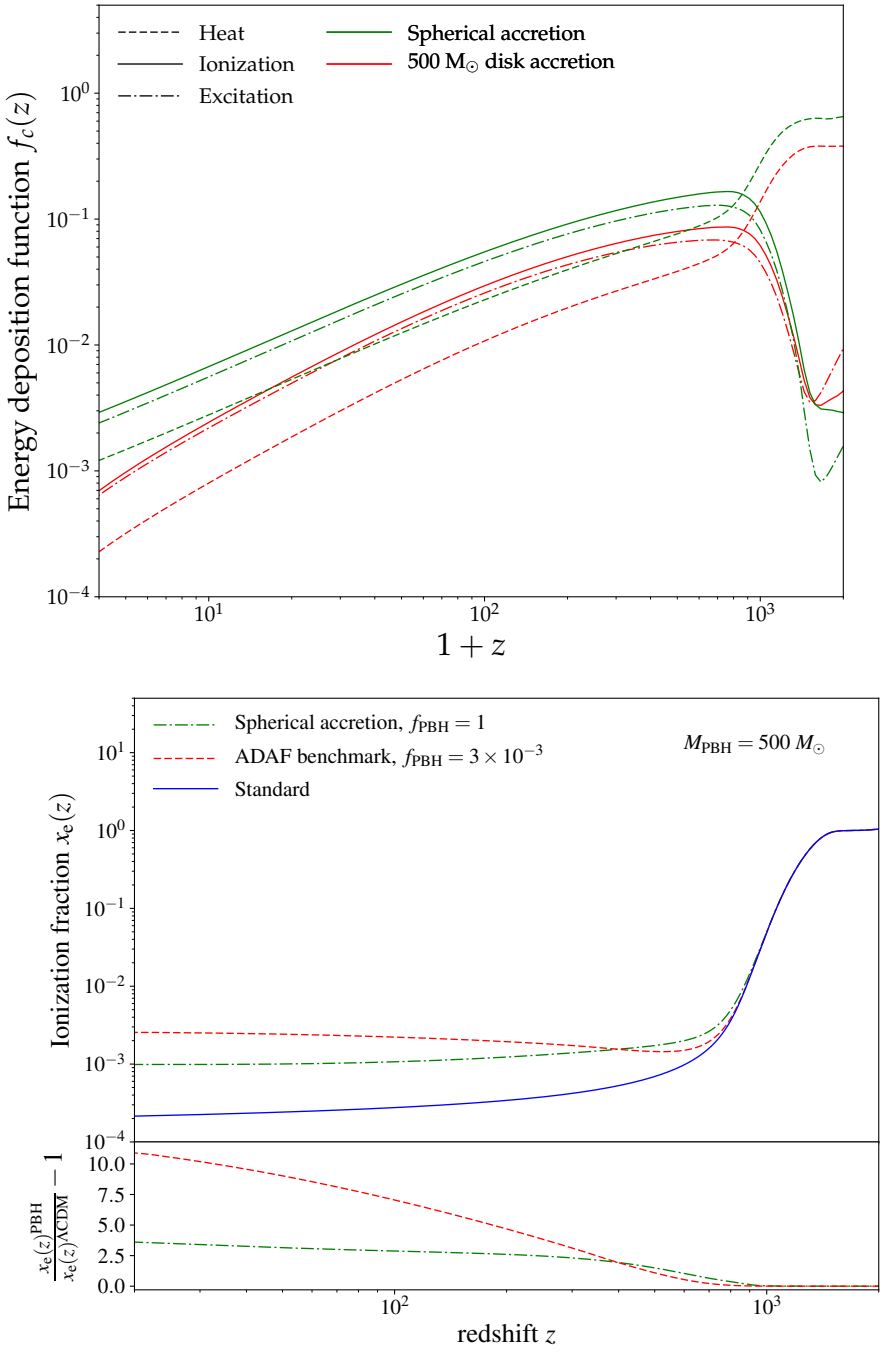

Figure 62: *Top panel:* Energy deposition functions computed following ref. [553] in the case of accreting PBH. *Bottom panel:* Comparison of the free electron fractions obtained for a monochromatic population of PBH with masses 500 $M_\odot$ depending on the accretion recipe used. The curve labelled "standard" refers to the prediction in a ΛCDM model whose parameters have been set to the best fit of Planck 2016 likelihoods high-ℓ TT,TE,EE + LOWSim [27].

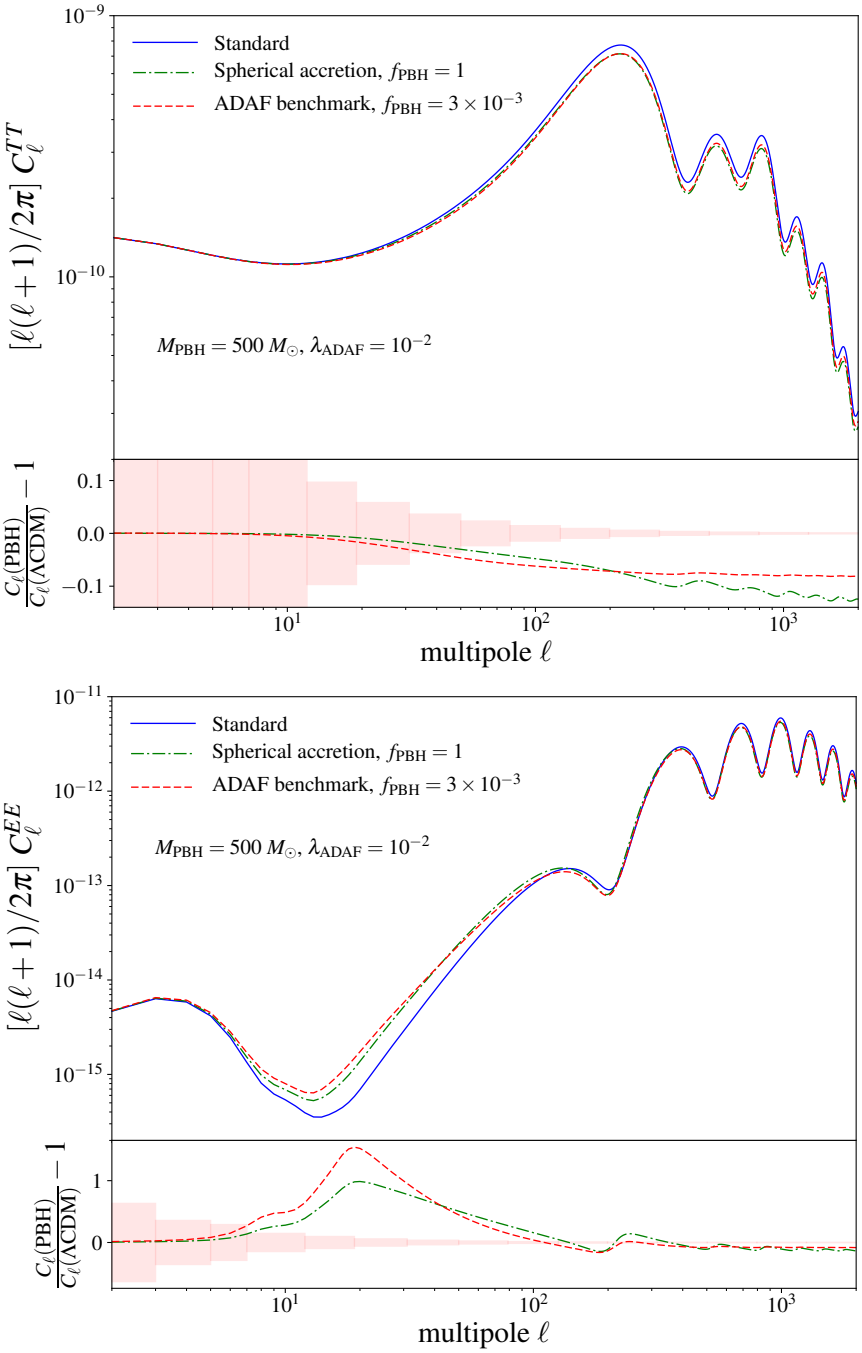

Figure 63: CMB TT (top panel) and EE (bottom panel) power spectrum obtained for a monochromatic population of PBH with masses 500 $M_\odot$ depending on the accretion recipe used.

with $M_{\rm min}$ fixed by a preliminary run where $f_{\rm PBH}$ has been set to one, and the PBH mass $M_{\rm PBH}$ has been let free to vary (with a flat prior as well)[8]. We use a Choleski decomposition to handle the large number of nuisance parameters in the Planck likelihood [399]. We consider chains to have converged when the Gelman-Rubin [265] criterium gives $R-1<0.01$. First, to check our code, we run it *under the same hypotheses as* [39] (the conservative, collisional ionization case), finding the constraint $M_{\rm PBH}<150\,M_\odot$ for $f_{\rm PBH}=1$, as opposed to their $M_{\rm PBH}\leq 100\,M_\odot$. We attribute the 50% degradation of our bound compared to Ref. [39] to our more refined energy deposition treatment. We checked that an agreement at a similar level with Refs. [314], [505] is obtained if we implement their prescriptions, but since some equations in Ref. [505] (re-used in Ref. [314]) have been shown to be erroneous [39], we do not discuss them further.

Our fiducial conservative constraints (at 95% C.L.) are represented in Fig. 64 with the blue-shaded region in the plane $(M_{\rm PBH}, f_{\rm PBH})$: We exclude PBH with masses above $\sim 2\,M_\odot$ as the dominant form of DM. The constraints can be roughly cast in the form:

$$f_{\rm PBH}<\left(\frac{2\,M_\odot}{M}\right)^{1.6}\left(\frac{0.01}{\lambda}\right)^{1.6}. \tag{6.4.28}$$

This is two orders of magnitudes better than the spherical accretion scenario, and it improves significantly over the radio and X-ray constraints from Ref. [257], without dependence on the DM halo profile as those ones. Lensing constraints are nominally better only at $M\leq 6\,M_\odot$. Note also the importance of the relative velocity between PBH and accreting baryons: If instead of Eq. (6.4.14) we were to adopt $v_{\rm eff}\simeq c_{s,\infty}$—representative of a case where a density of baryons comparable to the cosmological one is captured by halos at high redshift—the bound would improve by a further order of magnitude, to $M\leq 0.2\,M_\odot$ (light-red shaded region in Fig. 64). This is also true, by the way, for the spherical accretion scenario, where—all other conditions being the same—adopting $v_{\rm eff}\simeq c_{s,\infty}$ would imply $M\leq 15\,M_\odot$, to be compared to $M\leq 150 M_\odot$ previously quoted. The "known" uncertainties in disk accretion physics are probably smaller: When varying—at fixed accretion eigenvalue λ—the electrons heating parameter δ within the range described in section 6.4.2.3, for the 30 $M_\odot$ benchmark case reported in the bottom panel of Fig. 61, the radiative efficiency ϵ varies by a factor ~ 3, reflecting correspondingly on the constraints. To help the readers grasp the dependence of the bound upon different parameters, we also derive a parametric bound, obtained from a run where we assumed that $v_{\rm eff}$ is constant over time (and the accretion rate is always small, i.e. $\dot{M}_{\rm B}<10^{-3}L_{\rm Ed}$), scaling as

$$f_{\rm PBH}<\left(\frac{4\,M_\odot}{M}\right)^{1.6}\left(\frac{v_{\rm eff}}{10\ {\rm km/s}}\right)^{4.8}\left(\frac{0.01}{\lambda}\right)^{1.6}. \tag{6.4.29}$$

We have also extended the constraints to a broad log-normal mass distribution of the type

$$M\frac{{\rm d}n}{{\rm d}M}=\frac{1}{\sqrt{2\pi}\sigma M}\exp\left(\frac{-\log_{10}(M/\mu_{\rm PBH})^2}{2\sigma_{\rm pbh}^2}\right). \tag{6.4.30}$$

i.e. with mean mass $\mu_{\rm PBH}$ and width $\sigma_{\rm pbh}$. Our constraints in the plane $(\sigma_{\rm pbh},\mu_{\rm PBH})$ assuming that PBH represent 100% of the DM are shown in Fig. 65. It is clear that the bound on the median PBH mass is robust and can only get more stringent if a broad, log-normal mass function is considered,

8 We have checked that making use of a logarithmic prior *improves* the bound by roughly 50%. We thus conservatively stick to the linear prior, which also eases comparison to previous works.

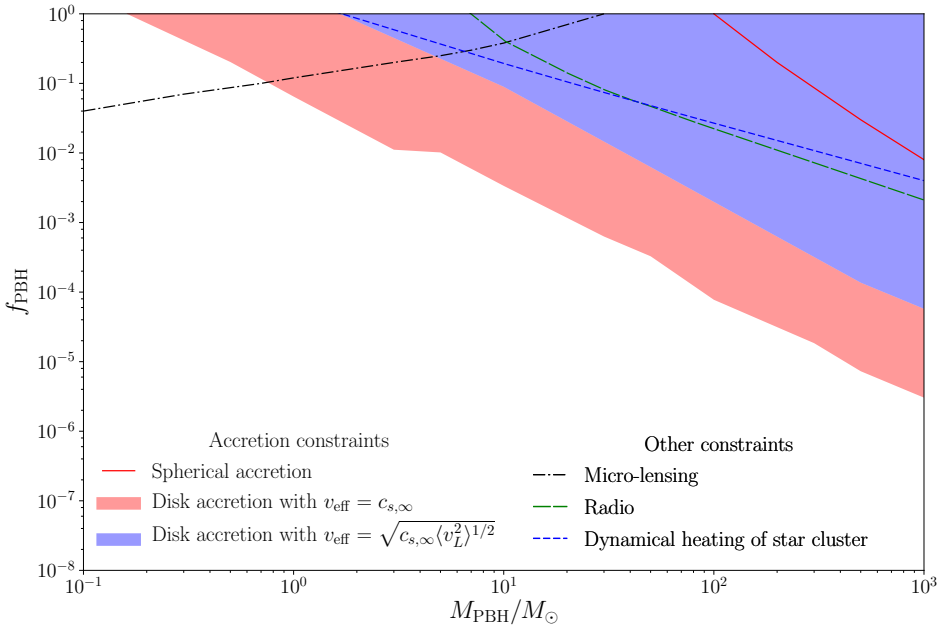

Figure 64: Constraints on accreting PBH as DM. Our constraints, derived from a disk accretion history (blue region: Eq. (6.4.14); light-red region: $v_{\rm eff} \simeq c_{s,\infty}$), are compared to: i) the CMB constraints obtained assuming that spherical accretion holds as in Ref. [39] (red full line); ii) the non observation of micro-lensing events in the Large Magellanic Cloud as derived by the EROS-2 collaboration [580] (black dot-dashed line); iii) the non observation of disk-accreting PBH at the Galactic Center in the radio band, extrapolated from Ref. [257] (green long-dashed line); iv) constraints from the disruption of the star cluster in Eridanus II [283] (blue short-dashed line, see text for details).

confirming the overall trend discussed in Ref. [149]. However, we estimate that the tightening of the constraints for a broad mass function is more modest than the corresponding one from some dynamical probes. This is illustrated by the blue dashed line in Fig. 65, which is the result of our calculation of the constraints from the disruption of the star cluster in Eridanus II, following the method and parameters of Ref. [283] (cluster mass of 3000 $M_\odot$, timescale of 12 Gyr, initial and final radius of 2 pc and 13 pc respectively and a cored DM density of $\rho_{\rm DM} = 1 M_\odot {\rm pc}^{-3}$).

6.4.3 *Sterile neutrinos*

As discussed in sec. 3.2, the discovery that neutrinos oscillate, hence that at least two of them are massive, is one of the few hints (and the only laboratory one) for physics beyond the standard model. The most minimal extension of the SM is probably the one presented in sec. 3.2.2, requiring right-handed neutrinos, which are SM gauge singlets (hence 'sterile') and so weakly interacting that usually astrophysical and cosmological observables are better suited to probe them than laboratory ones. If these neutrinos are of Majorana type, they can have an extra mass term whose parametric size is a

priori unconstrained by theoretical considerations. Obviously, the weaker their coupling, the harder they are to constrain. These neutrinos are however unstable: provided that they are light enough, cosmology can help, since it can probe very long timescales. As long as the sterile neutrino (ν_s) mass is below $\sim 1\,\mathrm{MeV}$, the only channels open are [278], [351], [462], [546]

- $\nu_s \to 3\nu$, with $\Gamma_{3\nu} \simeq \frac{G_F^2 M_s^5 \Theta^2}{192\pi^3} \simeq \left[3\times 10^4\,\mathrm{s}\left(\frac{\mathrm{MeV}}{M_s}\right)^5 \Theta^{-2}\right]^{-1}$;
- $\nu_s \to \nu_\alpha + \gamma$, with $\Gamma_{\nu\gamma} \simeq \frac{9 G_F^2 \alpha M_s^5 \Theta^2}{256\pi^4} \simeq 0.016\,\Gamma_{3\nu}$.

In the above formulae, we introduced $\Theta^2 \equiv \sum_\alpha \theta_\alpha^2$, where θ_α is the mixing angle with active neutrino of flavour α. When the ν_s mass exceeds $2\,m_e$ a third channel, $\nu_s \to \nu_\alpha e^+ e^-$, is also open, with a rate depending on single θ_α's, but in general with a b.r. of $\sim 30\%$ as long as its mass does not exceed $m_{\pi^0} \simeq 135$ MeV above which pionic channels are also open. These relations imply that, as long as $(M_s/\mathrm{MeV})^5\,\Theta^2 \ll 1$, these particles decay at "cosmologically interesting times", with an associated b.r. into e.m. channels ranging from 1.6% at masses below the MeV to O(30%) at masses up to ~ 130 MeV. The CMB is capable of constraining such particles even if they only constitute a negligible fraction of the DM. It is straightforward to translate the Ξ-lifetime constraints derived in Fig. 58 in more meaningful parameters for sterile neutrinos, such as their mixing angle and relative abundance with respect to the total active neutrino species (including antineutrinos), which we do in Fig. 66 for two values of the masses. Note that we have assumed monochromatic spectra for the daughter particles. This is basically exact in the 10 keV case, for which the only visible decay mode is $\nu_s \to \nu_\alpha + \gamma$ and the doppler broadening is negligible. In the 130 MeV case, the dominant e.m. decay mode is $\nu_s \to \nu_\alpha e^+ e^-$, which was treated as described in Sec. 6.2.1. For the typical 10 keV mass scale required for sterile neutrino to be the DM, we obtain bounds comparable to [453], which are typically weaker

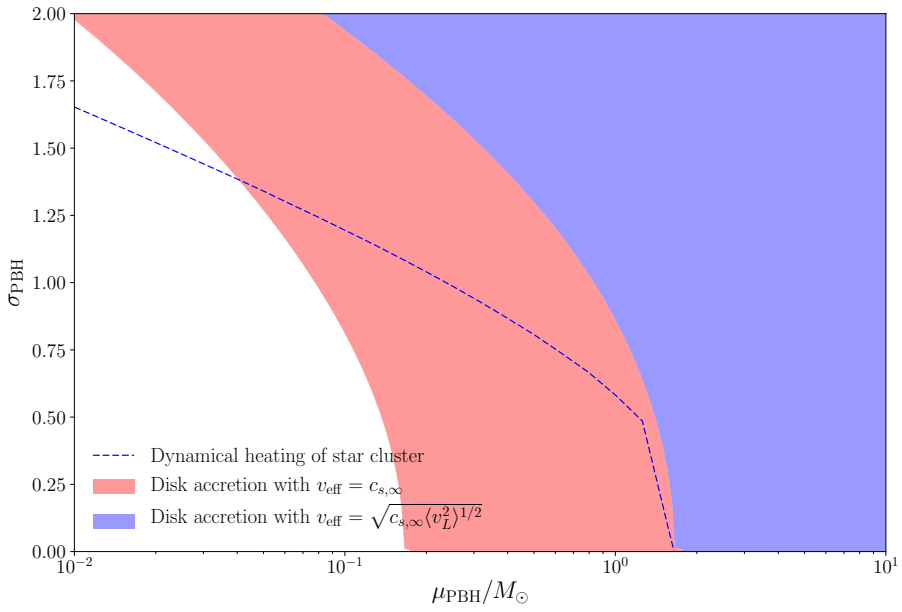

Figure 65: Constraints on the width $\sigma_{\rm pbh}$ of a broad mass spectrum of accreting PBH as from Eq. (6.4.30) as a function of the mean mass $\mu_{\rm PBH}$, assuming that they represent 100% of the DM. For comparison the dashed blue line represents our calculation of the best constraint from the dynamical heating of the star cluster in the faint dwarf Eridanus II, following the method and parameters of Ref. [283].

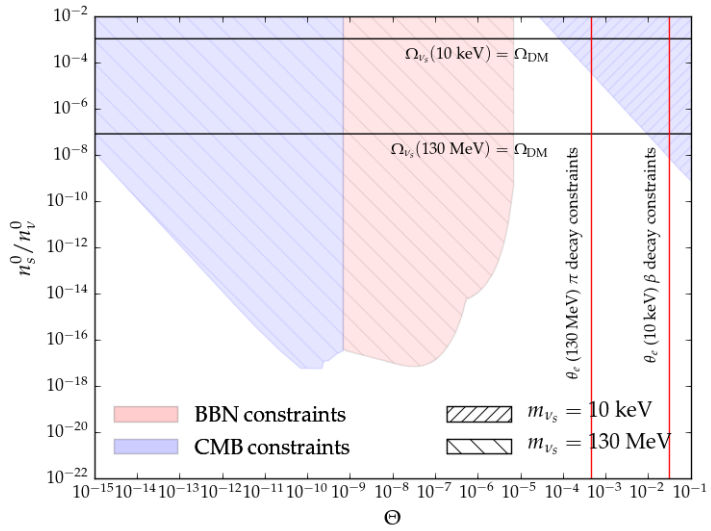

Figure 66: Cosmological constraints on the abundance of sterile neutrinos (including antineutrinos) normalized to the total active neutrino density, with no prior on their production mechanism. We consider a sterile neutrino mass of 10 keV, the typical scale for sterile neutrinos being DM candidates, as well as the heavier scale of 130 MeV for much weaker couplings, a parameter space usually ignored.The solid horizontal lines indicate the condition $\Omega_{\nu_s} = \Omega_{\mathrm{DM}}$, which is only a function of the mass: The bounds above those lines, for the corresponding shaded areas, are only nominal, since the parameter space is most excluded by the overclosure condition $\Omega_{\nu_s} > \Omega_{\mathrm{DM}}$. Red vertical lines correspond to direct laboratory constraints from nuclear β decay [280] and π decay [128], assuming mixing with electron neutrino species.

than bounds from astrophysical probes, notably X-ray lines. In general, however, even higher masses and lower abundances can be constrained. For instance, a 130 MeV sterile neutrino would represent a sizable amount of DM only if its population is larger than a fraction $\geq 10^{-8}$ of the active neutrino one [9], yet the CMB can constrain a fraction up to a billion times smaller than that, for incredibly tiny mixing angles smaller than 10^{-10}! To put the latter constraints into a context, one may compare them with the ones reported in Fig. 7 of Ref. [5]. In particular, our new constraints are relevant in the upper-left corner of the parameter space (labelled as $\tau < t_{\mathrm{today}}$) i.e. the region where sterile neutrino relics from the early universe were indicated as decaying "without constrainable effects and make no contribution to the present matter density". Note that the laboratory constraints from β decay nuclei [280] and π decay [128], are far from being competitive with our cosmological ones. For reference, in Fig. 66 we have indicated with vertical red lines the best laboratory upper bounds available for the two masses assuming mixing with electron neutrino species, since direct bounds on other mixings are much weaker: For the heavier mass case, see [456], [600]; for the 10 keV neutrino mass case, it is argued in [280] that no model-independent laboratory bounds exist on those mixings.

Are these parameter values of any interest, given the masses and mixing knowledge on active neutrinos? In fact, some relations between mass-scale and mixing angles exist, once the phenomenological

9 Note that in the upper part of the parameter space of Fig. 66, above the solid horizontal lines indicating the condition $\Omega_{\nu_s} = \Omega_{\mathrm{DM}}$ (which is only a function of the mass), our constraints are only nominal, since we are assuming no major departure from the standard history of ΛCDM. That parameter range is likely excluded by an unacceptably large modification of the expansion history of the universe due to the "overclosure" condition $\Omega_{\nu_s} > \Omega_{\mathrm{DM}}$, although we do not compute these constraints in detail here.

knowledge on the smallness of (active) neutrino mass is factored in. This is nicely reviewed in [34], notably in its chapter 4. The Yukawa couplings, or equivalently a combination the mixing angle elements U and masses M_I of the right-handed neutrinos should obey the relation

$$\sum_{\alpha,I} U_{\alpha \mathrm{I}}^2 \, M_I^2 \geq M_{\min} \sum m_\nu = 10^{-5} \mathrm{MeV}^2 \frac{m_\nu}{0.1\,\mathrm{eV}} \frac{M_{\min}}{1\,\mathrm{MeV}} \,, \tag{6.4.31}$$

where $M_{\min}$ is the lightest sterile neutrino contributing to the mass of the standard model neutrinos. Ignoring for the moment any cosmological or particle physics constraints, this relation together with the empirically constrained mass scale of neutrinos suggests that the lightest extra neutrino mass eigenstate involved in the active neutrino mass mechanism should have an effective mixing element $U_{\alpha \mathrm{I}}^2 \simeq \Theta^2 \geq 10^{-5} M_{\mathrm{MeV}}^{-1}$. We conclude that cosmology is typically sensitive to neutrinos more weakly coupled than those implied in the mechanism giving mass to the active neutrinos. This is a qualitatively important point: while the existence of *two* right handed neutrinos is needed to account for the observed oscillation phenomenology, and is remarkably sufficient to account for leptogenesis via the oscillation mechanism first described in [32], the number, masses and mixing of additional right-handed neutrinos are not otherwise constrained by particle physics constraints or fundamental physics conditions, rather must be suggested by observational arguments. For instance, in the so-called νMSM [63], [64], a three right handed neutrino scenario is invoked, with the lightest one being responsible for the DM of the universe, not certainly for the particle physics consistency; the third state must then essentially be decoupled from the active ones, contributing negligibly to their mass generation mechanism. This example shows that additional decoupled states might be only be relevant for cosmological consequences. Our calculations above shows that the potentially interesting parameter range to alter recombination or reionization history is much wider than the one invoked to account for sterile neutrino DM, extending to MeV or GeV masses. Needless to say, from the conceptual point of view, having as many handles as possible on the existence of extra sterile neutrino states is important, since they could give us hints or constraints on the underlying symmetries of these extensions of the standard model.

6.4.4 *The 21 cm signal from the Dark Ages*

We have considered scenarios where e.m. energy injection takes place at some time in the history of the Universe. We saw that the CMB is particularly sensitive to energy injected around or just after recombination, while BBN and CMB spectral distortions probe earlier times. What about cosmological probes of the more recent universe? Just after recombination, the universe is dark, cold and almost structureless, hence the name of "Dark Ages" for this period. When z drops below $\sim$300, however, the baryons thermally decouple from the CMB photons, and start cooling more rapidly. The gas eventually warms up significantly above the CMB temperature around the epoch of reionization ($z \sim 10$), where a significant contribution of stellar and astrophysical sources is expected to take over the dynamical evolution of the gas. Thus, at redshift $z \leq$300 the conditions of temperature and ionization of the (mostly neutral) cosmic gas can be in principle probed via the hyperfine transition in neutral hydrogen atoms: it is natural to ask oneself whether significant exotic traces can be found in this highly redshifted 21 cm signal. Although the detection of the 21 cm signal from very high redshifts will probably stay beyond reach for a long time to come, prospects for the SKA experiment should allow detection capability up to $z \simeq 27$ [377]. Such a sensitivity would be sufficient to open a yet unexplored window

in the history of the universe. But is it useful to probe non-standard processes as well? For the most widely studied signals of DM annihilation, earlier results were rather encouraging about the discovery perspectives [234], [255], [584]. The authors of the recent paper [409] have reinvestigated these forecasts with the most up-to-date tools, unfortunately finding them to be very challenging. In particular, due to the large uncertainties in the reionization modeling, it appears hard to unambiguously isolate an exotic DM annihilation signal.

However, the situation may be significantly better for energy injection processes concentrated at an earlier epoch, as for instance associated to a fraction of DM decaying in the so-called "Cosmic Dawn" period $15 \leq z \leq 30$. The astrophysical processes are expected to be relatively mild at that epoch. In fact, observationally we know that they should not perturb too much the medium, e.g. triggering a too early ionization epoch, in order to be in agreement with the optical depth measurement by Planck. In addition, all modern parametric studies of astrophysical effects at this epoch indicate that they should be unable to reheat the gas above the CMB temperature, i.e. the 21 cm should be seen "in absorption" with respect to the CMB (see for instance [431], Fig. 1). This is also the case for exotic signals such as annihilating DM in halos [409] above redshift $z \simeq 20$. Here, we wish to briefly assess the possibility that models where a fraction of DM decays via e.m. channels, *not yet excluded by CMB* or other probes, can be uniquely tested via 21 cm observations at the Cosmic Dawn. While we certainly expect peculiar signatures in the power-spectrum (and possibly higher order statistics) of the 21 cm signal, for this preliminary study we will content ourselves with showing that a smoking gun signal is potentially present already at the level of the average differential brightness temperature $\delta T_b(\nu)$. This quantity is obtained by comparing lines of sight through a neutral hydrogen cloud to patches of the sky with clear view of the CMB. Following a textbook calculation (see e.g. Ref. [256]), one can easily compute the theoretical average signal (neglecting perturbations):

$$\delta T_b(\nu) = \frac{T_S - T_{\rm CMB}}{1+z}\left(1 - e^{-\tau_{\nu 21}}\right) \simeq 27 x_{\rm HI}\left(1 - \frac{T_{\rm CMB}}{T_S}\right)\sqrt{\left(\frac{1+z}{10}\right)\left(\frac{0.15}{\Omega_m h^2}\right)}\left(\frac{\Omega_b h^2}{0.023}\right), \qquad (6.4.32)$$

where $x_{\rm HI}$ is the neutral hydrogen fraction and T_S the spin temperature, the excitation temperature of the 21 cm transition. It is defined via $n_1/n_0 = 3\exp(-T_{21}/T_S)$ with $T_{21} = 0.068\,\mathrm{K}$. Assuming equilibrium between excitation processes (typically CMB photons absorption, collisions within atoms and scattering of UV photons from stars) and de-excitations ones, one can write a solution to the radiative transfer equation and get the evolution of the spin temperature:

$$T_S^{-1} = \frac{T_{\rm CMB}^{-1} + x_c T_{\rm M}^{-1} + x_\alpha T_c^{-1}}{1 + x_c + x_\alpha} \qquad (6.4.33)$$

where x_c and x_α are coupling coefficients for collisions and UV scattering respectively and T_c is the effective color temperature of the UV radiation field. Radiative transfer typically drives T_c to $T_{\rm M}$ [256], but in our case ($z > 20$) we expect a negligible stellar contribution and simply set x_α to zero (this is a conservative assumption given the point we want to make).The collisional coupling x_c can be computed as:

$$x_c = A_{10}^{-1}\frac{T_{21}}{T_{\rm CMB}}(n_H \kappa_{10}^{HH} + n_e \kappa_{10}^{eH})\,. \qquad (6.4.34)$$

In Eq. (6.4.34), $A_{10} = 2.85 \times 10^{-15}\mathrm{s}^{-1}$ is the Einstein spontaneous emission coefficient of the 21 cm transition and the κ_{10}^{iH} are the de-excitiation rates in hydrogen atom collisions [10] with species i. They

10 The role of Helium is not expected to change qualitatively this picture and is neglected here.

are tabulated in Ref. [256]. We have computed the temperature history and the mean differential brightness temperature for decays of exotic particles with different lifetimes. The typical result is shown in Fig. 67 for the two cases $\Gamma^{-1} = 10^{15}\,\mathrm{s}$ and $\Gamma^{-1} = 10^{18}\,\mathrm{s}$. For definitiveness, we consider a 2-body decay into electrons with the fraction of decaying DM fixed to its upper limit from previous analysis. With respect to the conventional evolution in the Cosmic Dawn, characterized by a negative δT_b (see solid black curve in the bottom panel), the models considered here show a *positive* δT_b, i.e. would be associated to a 21 cm signal seen *in emission* already at $z \simeq 20 - 25$ (for the case of PBH, this peculiar feature was already noted in [414]). The effect is particularly noticeable for the shorter lifetime case, $\Gamma^{-1} = 10^{15}\,\mathrm{s}$, but remains appreciable also for timescales comparable with the universe lifetime, $\Gamma^{-1} = 10^{18}\,\mathrm{s}$, due to the small fraction of decays happening early on. The appearance of a signal in emission should constitute a smoking gun: if SKA were to observe an absorption signal from Cosmic Dawn, as expected, it would put constraints on these exotic scenarios. At the same time, it also means that 21 cm studies have significant room for discovery. To gauge the level of the effect, it is worth bearing in mind that the SKA should have a sensitivity to δT_b at $\mathcal{O}$(1-10) mK level at $z \simeq 25$, see Fig. 4 in [377]. The orange band of Fig. 68 shows the parameter range creating a 5 to 10 mK increase in δT_b with respect to standard model expectation, which as argued would also lead to a change of sign in the signal. Here we limit ourselves to the specific case of the 2-body decay into electrons with decaying particle mass $m = 200$ MeV, but it is clear that even these crude considerations show great potential to go beyond the parameter space currently constrained. Also note that we have not included informations on the power spectrum of the 21 cm signal, so that the true reach should be actually deeper.

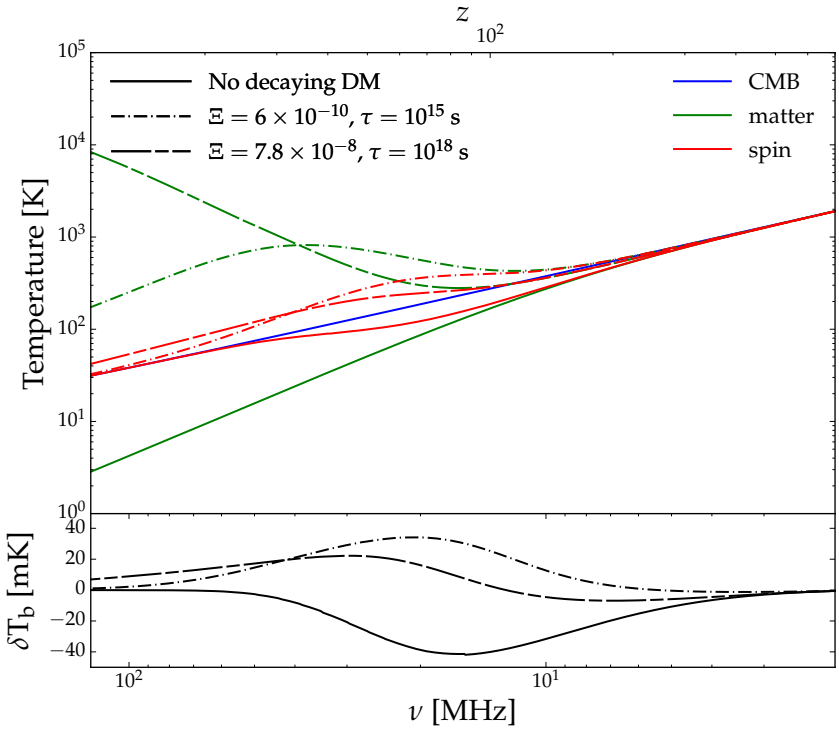

Figure 67: Temperature history and mean differential brightness temperature during the Dark Ages for $\chi \to e^+e^-$ with decaying particle mass $m = 200$ MeV, compared to the standard ΛCDM model. The decaying particle abundance is just within the currently allowed range.

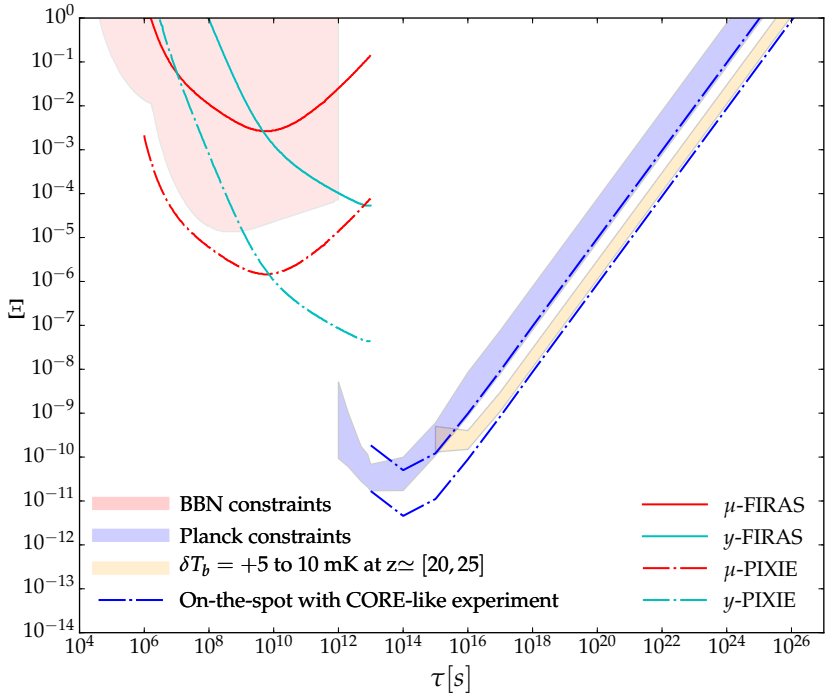

Figure 68: A comparison between current constraints on e.m. decaying exotic particles and a forecast using the sensitivity of SKA on the global differential brightness temperature δT_b in the redshift range $[20, 25]$, PiXiE sensitivity on μ and y distortions, as well as a CORE-like experiment. The blue shaded area, labeled as Planck constraints, now regroups $e^{\pm}$ and γ results. The orange band is obtained for $\chi \to e^+e^-$ with decaying particle mass $m = 200$ MeV.

To put this result into some context, we also compare it with a forecast for the sensitivity reach in CMB spectral distortions with PiXiE [374] and CMB temperature and polarization anisotropies measurements by a CORE-like experiment [117] with sky coverage $f_{\rm sky} = 0.70$. We find that PiXiE would give constraints up to one order of magnitude better than BBN ones, whereas minimal information from an *approved* 21 cm experiment would already have comparable sensitivity to the *proposed next* generation CMB experiment, making it indeed a very powerful probe. Note that CMB experiment would however still dominate in the energy injection regime corresponding to modifications at the recombination era or shortly thereafter, so the complementarity of different techniques will still be holding in the future.

6.5 Conclusion

Cosmological probes (BBN, CMB spectral distortions and CMB angular power spectra) lead to stringent bounds on the e.m. decay of exotic particles, spanning about 12 orders of magnitude in abundance and more than 20 orders of magnitude in lifetime. We have re-evaluated these constraints with state-of-the-art tools: Our main results are summarized in Fig. 58. The main focus of our work has been the computation of CMB anisotropy constraints. For that purpose we have used the most up-to-date available tools, and we expect our bounds to be realistic within the parameter space covered by this analysis. Instead, the BBN and spectral distortions have been reported mostly for comparative purposes. They were derived under conservative assumptions, and in specific cases the actual bounds

may be stronger: for instance one could go beyond the simplistic μ and y type of CMB distortions, or take into account the actual photon spectrum leading to photo-hadronic dissociation of light elements, rather than the approximate "universal spectrum" limit.

One of the major novelties of our work is the throughout description of the physical effects leading to the CMB bounds, notably for the case of particles whose lifetime is much shorter than the age of the universe. In particular, CMB is sensitive to particles decaying around the time of recombination, a phenomenon that can lead to peculiar modifications of the power spectra. Based on our results, we also proposed a physical criterion for an approximate "on-the-spot" treatment of the problem. This approximation can be used to derive order-of-magnitude estimates of upper bounds, but should be considered with caution if an actual signal was discovered, since it may lead to significant errors with respect to a full calculation of the free electron fraction and CMB power spectra.

The results we obtained can be applied to numerous models, of which we provided a few examples: We computed the constraints on evaporating low-mass PBHs, whose strength happens to be comparable or stronger than the ones following from extragalactic gamma-ray background limits for masses a couple of orders of magnitude around 10^{15} g. Our results provide for instance an independent cosmological argument excluding that the totality of DM can be made of PBHs lighter than $\sim 10^{16.8}$ g. A second application concerns PBH with masses above $\sim M_\odot$. Pure cosmological constraints on high mass PBH as DM are essential are they do not rely on any "local" measurements and are thus very hard to evade. However, they are affected by a large uncertainty associated to the accretion recipe. Until now, studies have focused on the case of spherical accretion. In this work, we argued that, based on a standard criterion for disk formation, all plausible estimates suggest that a disk forms *soon after recombination*. This is essentially due to the fact that stellar-mass PBH are in a non-linear regime (i.e. clustered in halos of bound objects, from binaries to clumps of thousands of PBH) at scales encompassing the Bondi radius already *before recombination*. This feature was ignored in the pioneering article [506], which assumed that massive PBH cluster like WIMPs and deduced the adequacy of the spherical accretion approximation, eventually adopted by all subsequent studies. Our 95% CL fiducial bounds preclude PBH from accounting for the totality of DM if having a monochromatic distribution of masses above $\sim 2\,M_\odot$, the bound on $f_{\rm PBH}$ improving roughly like $M^{1.6}$ with the mass. All in all, the formation of disks improves over the spherical approximation of Ref. [39] by two orders of magnitude. We also checked that the constraints derived on the monochromatic mass function apply to the average mass value of a broad, log-normal mass distribution too, actually becoming more stringent if the distribution is broader than a decade.

A realistic assessment of "known" astrophysical uncertainties, like for instance the electron share of the energy in ADAF models, suggests that our quantitative results can only vary within a factor of a few, not enough to change qualitatively our conclusions. Nonetheless, we believe that our constraints are conservative rather than optimistic. In particular, we assumed accretion from an environment at the *average cosmological density*: This is less and less true when PBH halos gradually capture baryonic gas in their potential wells. Alone, capturing from a pool of baryons of density comparable to the cosmological one, but bound to PBH halos, would reduce the relative PBH-baryon velocity and improve the bounds to $\sim 0.2 M_\odot$. Once baryons accumulate well above the cosmological average, the accretion rate $\dot{M}$ from this bound component grows correspondingly, and the constraining power more than linearly with it. It would be interesting to reconsider the CMB bounds on stellar-mass PBH once a better understanding of the halo assembly history in these scenario is achieved, a task probably requiring dedicated hydrodynamical simulations.

Together with other constraints discussed recently (see for instance [126], [257], [283], [337], [379], [433]) our bounds suggest that the possibility that PBH of stellar masses could account for an appreciable fraction of the DM is excluded. It remains to be seen if the small $f_{\rm PBH}$ allowed by present constraints may still be sufficient to explain LIGO observations in terms of PBH and, in that case, to find signatures of their primordial nature, possibly peculiar of some specific production mechanism: Such signatures become all the more crucial since both PBH mass (of stellar size) and their small DM fraction (for instance, in a halo of the Milky Way size about 0.1% of the DM should be made of astrophysical BH) cannot be easily used as diagnostic tools to discriminate PBH from astrophysical ones. It is worth noting that we expect forthcoming CMB polarization experiments (very sensitive to energy injection) and 21 cm experiments [274], [578] (the golden channel for searches looking at energy-injection during the Dark Ages) will be able to give more insights on PBH scenarios, including stellar mass ones, even if the possibility that they may contribute to a high fraction of the DM has faded away.

We have also applied our results to sterile neutrinos: while the past literature has been focusing on masses of a few keV typically invoked for sterile neutrino DM, we have shown that cosmological bounds are also relevant for heavier and more weakly coupled relics, which are usually overlooked. Finally, we have studied some perspectives for future improvements over the current cosmological constraints. In particular, we sketched why we expect forthcoming 21 cm surveys to have some discovery potential, or to improve somewhat over existing bounds. The most promising window to overcome astrophysical uncertainties and aiming at a smoking gun feature is to look for an *emission* signal in the "Cosmic Dawn" epoch $15 \leq z \leq 30$. The perspectives to discover this kind of exotic physics are certainly cleaner than those for DM annihilation, see [409]. We also briefly discussed the good chances for improvements over the current status achievable with future missions proposed to study CMB spectral distortions (PiXiE) and CMB angular power spectrum (CORE), as well as their complementarity.

The above examples do not obviously exhaust the list of applications. Even limiting oneself to the above topics, however, it is clear that each of them would deserve dedicated and deeper studies. For instance, given the limitations of the existing study [506], a revisitation of the cosmological bounds to PBHs of stellar mass (or heavier) is of high priority. A proper exploration of the cosmologically interesting sterile neutrino parameter space (well beyond the DM-inspired mass-coupling usually considered) remains to be tackled. The actual reach of the 21 cm window should be reassessed with a calculation of the modified power spectrum, a task which we expect will lead to an improved sensitivity to these models.

Let us finally comment on very recent work, appeared during or after the final completion of this study. Firstly, we find that our results are comparable with the one from article [555] (see in particular their Fig. 11 and compare with our Fig. 58), whenever referring to similar models. Also note that our physical prescription for the effective $f(z)$ function, inspired by inspection of the results in Fig. 58, finds a technical justification in the principal component analysis developed in [555]. For the rest, the two articles are rather complementary in the applications: for instance ref. [555] develops a detailed study for very long lived DM, which we chose here to barely treat for the reasons recalled in Sec. 6.3. On the other hand, we also describe applications to non-decaying DM relics, such as PBH, and also cover in better details the constraints on short lifetimes, coming either from CMB or other channels, as well as some perspectives for future cosmological probes. We also present a throughout description of the physics involved in the CMB effects (Sec. 6.2).

Secondly, after our work has appeared in preprint form, ref. [191] was finalized. Its content largely overlaps with the one of our Sec. 6.4.1. Apart for minor technical differences and their focus only on the higher range of the PBH masses considered by us, we agree qualitatively with their results. Yet, an appreciable quantitative difference exists, with their bounds being systematically stronger than ours. We believe that the main reason for the difference is that we run our chains by leaving all the cosmological parameters of the extended ΛCDM model free, while they explicitly state (Sec. IV.C) that they fix the ΛCDM parameters to their fiducial values. For a specific mass, they estimate this effect to be a factor 3; we checked that in some cases it can easily reach a factor ~ 5. Accounting for this difference, the results are mutually consistent.

7

DARK MATTER ANNIHILATIONS IN HALOS AND HIGH-REDSHIFT SOURCES OF REIONIZATION

This chapter is adapted from a publication in JCAP [493].

7.1 Introduction

We have presented in section 3.3.3 the so-called "WIMP miracle", in which the thermal freeze-out of a massive relics with electroweak type of interaction allows to achieve the right relic density. We then introduced in section 3.4.1 some of the (many) extensions of the standard models of particle physics (including electroweak scale supersymmetry) which naturally accommodate a (quasi-)stable weakly interacting massive particle, that can act as excellent dark matter candidate. Additionally, WIMP residual annihilations (or, in some models, decays) can inject sufficient "visible" energy that can be searched for. Notably, we discussed in sec. 3.4.3 that high energy cosmic ray and gamma rays fluxes are routinely analysed to reveal excesses that could be attributed to a DM origin, or conservatively to constrain particle physics parameters such as the annihilation cross-section times velocity $\langle \sigma v \rangle$ (averaged over the velocity distribution, hereafter called "the cross-section").

We have already argued that CMB observations can in fact tell us more about the nature of DM. We have shown in chapter 4 that purely gravitational arguments can lead to robust constraints on its lifetime, independently of the particle physics models (see e.g. [70], [205], [335], [357]). On the other hand, we studied in chapter 6, how constraints on the DM lifetime evolve as soon as one switch on e.m. branching ratio, showing that they improve dramatically. Similarly, annihilations of relics inject non-thermal photons and electrons in the intergalactic medium (IGM) that can delay recombination and change the relic abundance of free electrons after decoupling. Hence, WIMP annihilations can jeopardize the observed CMB temperature and polarization anisotropy angular power spectra and therefore can be constrained by an experiment like Planck.

DM annihilations in the homogenous smooth background have been well studied and documented in the last decade [96], [155], [189], [235], [244], [259], [261], [270], [332], [333], [361], [410], [447], [460], [551], [552], [554], [601], [608]. The most realistic calculations for WIMPs have been done by Refs. [235], [554] and updated recently in Ref. [553], where authors carefully computed how much of the initial DM particle energy is deposited into the medium, as well as how this energy is separated between ionization of hydrogen atoms, excitation of these atoms and heating of the plasma. They also found that the impact of DM annihilations depend sizably on the mass and the produced particles (electrons, quarks, etc.). The Planck collaboration in a very recent paper [19] has reported very strong bounds on the cross-section, excluding thermal WIMPs for any standard model annihilation channel for masses

up to 10 GeV, also ruling out WIMP explanations of cosmic ray lepton spectral features discussed in recent years.

Previous CMB studies mostly focused on the impact of annihilations in the averaged cosmological density field of DM. However, at relatively low redshift, the DM fluid clusters under the action of gravity into virialised structures, so-called "DM halos". This process increases the averaged density square $\langle\rho^2\rangle$ with respect to the square of the smooth background density, $\langle\rho\rangle^2$, while the two are nearly equal at high redshift. One could naively expect that this results in a large enhancement of the annihilation rate and therefore in a significantly bigger impact of DM annihilation on the CMB power spectra. But the effects of halos are more subtle since, as we will see, the way in which energy is deposited into the medium changes as well. Thus, the modification of the bounds on DM annihilation cross-section cannot be trivially obtained.

Another interesting feature of DM halos is their possible impact on the ionization history. In the standard picture, it is assumed that stars are the only reionization sources. Unfortunately, our knowledge of first stars formation in the universe is very rudimentary, and hence also is our knowledge of the ionization history. The formation of halos, if it increases significantly the DM annihilation rate, could introduce a new source of reionization in the universe and leave a very peculiar imprint on the history of the ionization fraction $x_e(z)$ and temperature of the IGM $T_{\rm M}$, also referred to as the matter temperature. In the past, this has been invoked as a way to solve a tension on the measurement of the reionization optical depth $\tau_{\rm reio}$ coming from WMAP data [304] (preferring a high value of $\tau_{\rm reio}$ and therefore a relatively high ionization fraction at redshift $z > 10$) and the so-called Gunn-Peterson effect as it is measured in astrophysics [238], [422], [528] (requiring a relatively high neutral hydrogen fraction above $z \simeq 6.5$ and hence pointing towards smaller values of $\tau_{\rm reio}$) [96], [189]. The new Planck data in the most conservative case yield $\tau_{\rm reio} = 0.079 \pm 0.017$ (Planck TT,TE,EE+lowP, 95%CL [19]) and therefore have reduced this tension to a $\sim 2\,\sigma$ level, since now a single-step reionization ending at $z = 6.5$ is marginally compatible with Gunn-Peterson bounds [19]. Yet, it remains interesting to quantify the potential contribution of DM halos to this observable.

Only a handful of articles have investigated the impact of DM annihilation in halos, notably [96], [189], [270], [332], [410], [445]–[447]. Unfortunately, previous authors follow different formalisms and are difficult to compare with each other. More importantly, they arrived at different conclusions. For instance, the impact of annihilation on reionization is substantial even for baseline parameters according to Ref. [270], relevant for light particles models according to [445], [447]; while Refs. [96], [189], [332], and [410] find it to be negligible. One of the few points on which all agree is that DM annihilation in halos cannot be the *only* source of reionization in the universe: even in ref. [270], an astrophysical contribution is needed at least to account for the Gunn-Peterson observations. What is less well understood is the role that DM annihilation in halos can play in mixed reionization scenarios, perhaps easing tensions between Gunn-Peterson observations and CMB ones. In order to clarify this situation, we first evaluate the impact of DM annihilation in halos on the ionization history and compute the optical depth to reionization $\tau_{\rm reio}$ in models with *conventional* reionization from stars: We find that halos can play only a minor role, confirming the conclusions found in most previous literature. We check that Planck data do not alter the sensitivity to the halo contribution. To clearly explain why it is so, we also characterize the impact of the annihilation in halos onto the CMB temperature and polarization power spectra, thus updating the study [447]. In doing that, we identify and correct a few mistakes and oversimplifying assumptions used in the previous literature [270], [447]. We also provide two major improvements over previous works: first, by adopting a phenomenological

model for the star formation rate and corresponding injection of high-energy photons, we study the dependence of the signals of interest from the astrophysical model adopted. In fact, till now all works have studied the problem within a single type of parameterization for the astrophysical reionization history. Second, we amend an unjustified simplification in the treatment of the IGM temperature evolution, by adding an astrophysical source term reflecting the corresponding one in the reionization history. Finally, we discuss how and why both the ionization history and IGM temperature evolution provide more promising perpectives as DM probes via the halo term.

This chapter is structured as follow. In section 7.2, we present our formalism, emphasizing the differences between the DM annihilation and decay scenarios, and describing how to compute DM annihilations in presence of halo formation. In section 7.3, we compare the impact of annihilations in halos on the reionization history to the more realistic star reionization modelling introduced in sec. 1.3.4. We also revisit the question about the possible contribution of halos to solve the slight tension between CMB and Gunn-Peterson concerning the reionization optical depth $\tau_{\rm reio}$. In section 7.4, we present our results concerning the impact of DM annihilation in halos on the CMB power spectra. Section 7.5 contains a summary of our results, as well as a discussion of possible observables where DM halos can play a non-negligible role, that would be worth studying in the future. Some remarks on the energy deposition functions and a complete comparison between the formalisms followed by different authors is developped in appendix D.1. Appendix D.2 summarizes our treatment of halo formation. Finally, appendix D.3 contains a discussion of the reionization optical depth $\tau_{\rm reio}$ measured by Planck, compared to the *real* optical depth to reionization, which aims at justifying (to the best of our knowledge, for the first time) within which errors one can assume them to coincide.

7.2 Ionization and thermal evolution equations

We have already introduced in sec. 1.3.3 and 6.2.1 the standard recombination equations and we refer to those sections for necessary details. In the absence of stars and annihilating/decaying DM, the high-z evolution of x_e and $T_{\rm M}$ is the result of solving Eqs. (6.2.1), without additional source terms. However, the resulting evolution would be clearly unphysical in the range $z \leq \mathcal{O}(10)$. At very least, we know that the low-z universe is ionized and relatively hot. This is due to the reionization of our Universe, as described in sec. 1.3.4. In cosmological applications, (the bulk of) this is implicitly attributed to unspecified astrophysical sources, either unaccounted for or described by some prescription by hand. Apart from using such a modified $x_e(z)$, no modification at all is included in the evolution of $T_{\rm M}$, i.e. no astrophysical sources of heating are considered. Basically all previous treatments have followed a similar approach. As explained in sec. 1.3.4, we attempt for the first time to quantify the effect of these approximations, comparing them with a more realistic treatment of the astrophysical source terms, inspired by recent literature. All the formalism is described in section 1.3.4 and we refer to this section for the technical details. Once star reionization is modelled, we can add to this picture DM annihilations. We now described in more details the difference with the decaying DM scenario developed in chapter 6.

7.2.1 *Dark Matter annihilation in the smooth background*

The only difference actually lies in the energy density injection rate $\frac{dE}{dVdt}|_{\rm inj}$. It can be readily computed as the product among the number density of pairs of DM particles $n_{\rm pairs}$, the annihilation probability per time unit $P_{\rm ann}$, and the released energy per annihiliation $E_{\rm ann}$:

$$\left.\frac{dE}{dVdt}\right|_{\rm inj}(z) = \left(n_{\rm pairs} = \kappa\frac{n_{\rm DM}}{2}\right)\cdot\left(P_{\rm ann} = \langle\sigma_{\rm ann}v\rangle n_{\rm DM}\right)\cdot\left(E_{\rm ann} = 2m_{\rm DM}c^2\right)\,. \tag{7.2.1}$$

Taking only into account the smooth cosmological DM distribution, we can write this rate as

$$\left.\frac{dE}{dVdt}\right|_{\rm inj,smooth}(z) = \kappa\rho_c^2c^2\Omega_{\rm DM}^2(1+z)^6\frac{\langle\sigma_{\rm ann}v\rangle}{m_{\rm DM}}\quad. \tag{7.2.2}$$

In the equations above, $\langle\sigma_{\rm ann}v\rangle$ is the cross-section, $n_{\rm DM} = \rho_c\Omega_{\rm DM}(1+z)^3$ the number density of DM particles, $\rho_c = 3H_0^2/8\pi G$ the critical density of the Universe today, $\Omega_{\rm DM}$ the current DM abundance relative to the critical density and $m_{\rm DM}$ the DM mass. If DM is made of self-conjugated particles, such as Majorana fermions, one has $\kappa = 1$, which is what we shall assume in the following; if DM particles and antiparticles differ (as in the case of Dirac fermions) and are equally populated, $\kappa = 1/2$ since only half of the pairs that one can form (the ones made by one particle and one antiparticle) are suitable for annihilation.

As in previous study, the response of the medium to the energy injection is conveniently parametrized by a dimensionless *efficiency function* $f(z)$ [554] such that:

$$\left.\frac{dE}{dVdt}\right|_{\rm dep}(z) = f(z)\left.\frac{dE}{dVdt}\right|_{\rm inj,\ smooth}(z)\quad. \tag{7.2.3}$$

Note that in this study, we again make use of the factorization approximation (6.2.7) and compute the $f(z)$ function following eq. (6.2.8). Several authors have shown that the redshift-dependence of $f(z)$ is of very little relevance for CMB constraints [244], [259], [270], [333]. This is because the main impact of smooth DM annihilation on the CMB is to inhibit recombination, enforcing x_e to freeze out near redshift $z\sim 600$ at larger values than in standard ΛCDM. Thus, the effects of DM annihilation is usually parameterized by a single quantity $p_{\rm ann}$ defined as:

$$p_{\rm ann} \equiv f_{\rm eff}\frac{\langle\sigma_{\rm ann}v\rangle}{m_{\rm DM}}\quad,\quad \text{where } f_{\rm eff}\equiv f(z=600)\,. \tag{7.2.4}$$

However, it is important to keep in mind that because they have an influence at low redshift, the influence of DM halos on the ionization and thermal history of the Universe cannot be captured with only one model-independent parameter. Furthermore, in order to be able to use the same parametrization, it is necessary to recompute these $f(z)$ functions in the presence of halo formation, and this will be the main focus of the next section.

7.2.2 *Dark Matter annihilation in halos*

The spatial average of the annihilation rate is proportional to the average square dark matter density. The main impact of structure formation is to increase this average with respect to the smooth background case, by an amount usually parametrized through a boost factor $\mathcal{B}(z)$:

$$\langle\rho^2\rangle(z) = (1+\mathcal{B}(z))\ \langle\rho\rangle^2(z). \tag{7.2.5}$$

One now has:

$$\left.\frac{dE}{dVdt}\right|_{\text{inj, smooth+halos}} = \rho_c^2 c^2 \Omega_{\text{DM}}^2 (1+z)^6 \frac{\langle \sigma_{\text{ann}} v \rangle}{m_{\text{DM}}} (1 + \mathcal{B}(z)) \ . \tag{7.2.6}$$

Several ways to compute $\mathcal{B}(z)$ have been proposed. We summarize our approach in Appendix D.2. The two key (unknown) physical quantities are the maximal overall boost factor due to halos and the epoch for the onset of formation of virialised objects. The simplest choice adopted in our model was to choose as free parameters the characteristic redshift z_h, related to the time of halo formation (occurring near $z = 2z_h$), and a parameter f_h related to the amplitude of the boost factor today (since $\mathcal{B}(z=0) = f_h \,\text{erfc}(1/(1+z_h))$, see equation (D.2.5)). The range of values explored relies on results found in the literature, see Appendix D.2 for quantitative details. The evolution of $\langle \rho^2 \rangle(z)$ for different values of these parameters is shown in figure 69.

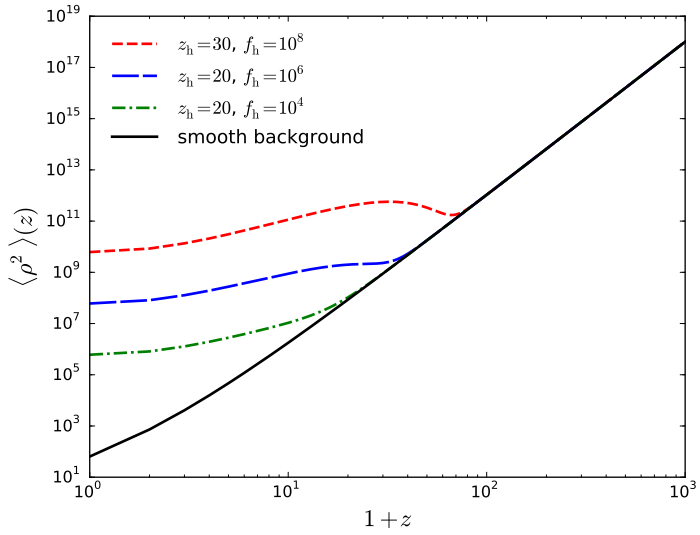

Figure 69: DM squared density vs. redshift z for several models of halo evolution.

Some treatments of the effect of DM (including halos) has been presented in the past: for instance, Giesen et al. [270] performed this calculation on the basis of a simplified formalism developped by Natarayan [445]–[447], accounting only for energy deposition through the Inverse Compton Scattering (ICS) effect, and taking as a source for the ICS the energy injection function of the smooth case. Here however we adopt a treatment based on a more straightforward generalization of the equation (7.2.3) which is equivalent to the one reported in [410]. We define $f(z)$ as

$$\left.\frac{dE}{dVdt}\right|_{\text{dep, smooth+halos}} = f(z) \left.\frac{dE}{dVdt}\right|_{\text{inj, smooth+halos}} \ , \tag{7.2.7}$$

where now equation (6.2.8) generalizes as

$$f(z) = \frac{\int d\ln(1+z') \frac{(1+z')^3}{H(z')} (1+\mathcal{B}(z')) \sum_\ell \int T^{(\ell)}(z', z, E) E \frac{dN}{dE}\big|_{\text{inj}}^{(\ell)} dE}{\frac{(1+z)^3}{H(z)} (1+\mathcal{B}(z)) \sum_\ell \int E \frac{dN}{dE}\big|_{\text{inj}}^{(\ell)}} \ . \tag{7.2.8}$$

It is clear that when setting $\mathcal{B} = 0$ one recovers the standard expressions for the smooth contribution. In app. D.1, to highlight where differences in the result could arise from, we perform an explicit

comparison of our formalism with the semi-analytical treatment of the energy deposition discussed in Refs. [96], [189], [270], [447].

In order to assess the impact of the improved calculation of the boost factor and of the new Planck data, we computed the energy deposition function for two baseline models with annihilation channel $\chi\chi \to e^+e^-$ and $\chi\chi \to \mu^+\mu^-$, as well as for the two masses $m_{\rm DM} = 1$ GeV and 1 TeV, following the generalization of the method of [551] described above and making use of the numerical tools provided by the authors[1].

The generalization of the calculation for more DM models would only require to adapt the injected spectra. Since we aim at being model-independent, we selected (and limit ourselves to) these two final state examples for two reasons: first, CMB bounds are particularly interesting for them, since light leptonic final states are the most difficult models to constrain through other methods; second, they represent two extreme cases for the corresponding values of $f(z)$ (high for e, low for μ), and hence they are sufficient to bracket typical constraints, if re-expressed in terms of $\langle\sigma_{\rm ann}\rangle$.

Figure 70 shows our result for the total $f(z)$ for each baseline models, with $m_{\rm DM} = 1$ GeV or 1 TeV, and with halo parameters $[z_{\rm h} = 30, \mathcal{B} = 10^6]$ or $[z_{\rm h} = 20, \mathcal{B} = 10^{12}]$, compared to the functions computed from annihilation in the smooth background only. Note that at high redshift, when $\mathcal{B} \ll 1$, our result is asymptotically equal to that obtained in [551], [554] in the absence of DM halos. Note also that we only performed the calculation down to redshift $z = 10$, since Ref. [261] does not provide transfer functions below this redshift. Physically, with our definition, we do not expect big changes of the deposition function at low redshift. Hence we assume that $f(z)$ remains constant below $z = 10$, as shown in Figure 70. If this assumption turned out to be inaccurate, our final results would not be much affected, because observable effects at low redshift are given by the product of $f(z)$ by the factor $(1 + \mathcal{B}(z))$ on which there is a huge uncertainty, and that we treat as a free parameter (see eqs . 7.2.6 and 7.2.7).

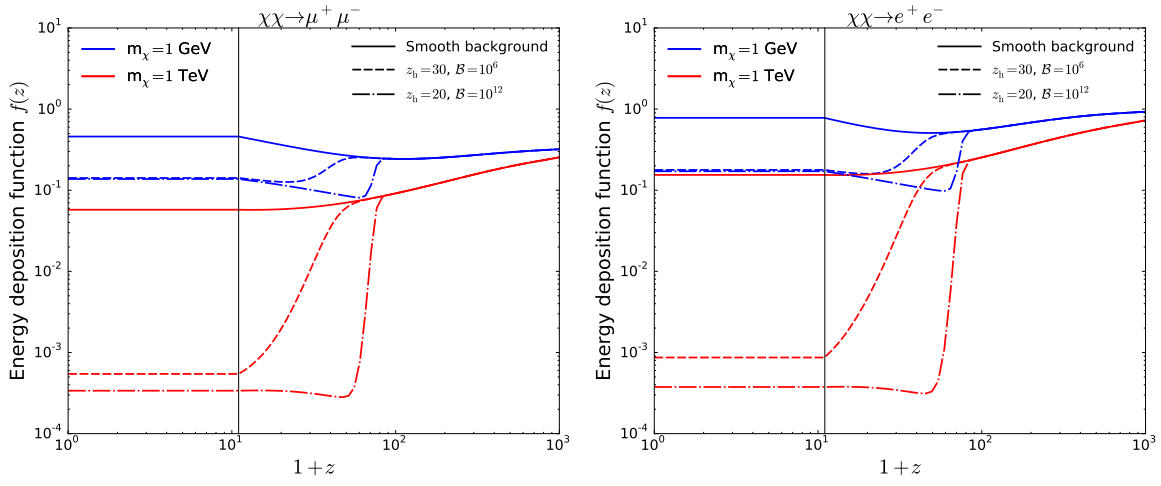

Figure 70: Energy deposition functions in the two baseline models, for two values of the dark matter mass and several halo parameters, compared to the case with annihilation in the smooth background only. Below $z = 10$, we assume that these functions remain constant.

1 http://nebel.rc.fas.harvard.edu/epsilon/

7.3 Impact of high redshift sources on the reionization history

There is no compelling reason to invoke an extra ingredient such as DM annihilation to explain the reionization history of the universe. Actually, our knowledge of pristine star formation and its impact on the ionization history $x_e(z)$ is so rudimentary that currently, we can treat the ionization history $x_e(z)$ caused by star formation almost as a free function, and some room for an exotic source of reionization is definitely possible. To illustrate this point, in the left panel of Fig. 71 we show two possible reionization histories of astrophysical origin: the green curve represents the standard step-like model "put by hand", while the red curve represents a model inspired by actual astrophysical data and normalized (via the parameter $A_* \simeq 3$) so that the optical depths for the two models are the same. As far as cosmological observations are concerned, they are essentially indistinguishable, as we will stress again in the following. The points report constraints from [238], [422], [528]. In the right panel of Fig. 71 we report the corresponding gas temperature evolution, compared with the CMB temperature evolution (purple curve): the blue curve represents the typical approximation in which this quantity has been evolved in past literature, with only the feedback for the x_e evolution accounted for (no heating source term). The green and red curves represent the evolution of the temperature if a source term similar to the corresponding one adopted for x_e is included (green: "sudden" heating, put by hand; red: redshift evolution inspired by an actual astrophysical model). The yellow band represents some indicative constraints from ref. [91]. Our aim here is not to determine a viable heating history, rather to show the rudimentary status of these treatments (with large uncertainties in the astrophysical term) and the large room for exotic sources of heating.

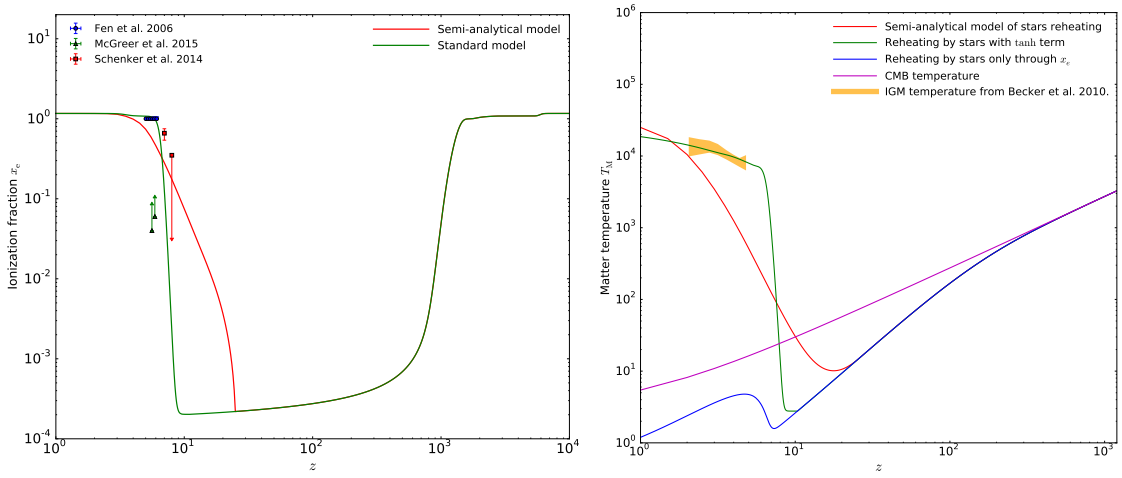

Figure 71: Evolution of $x_e(z)$ (left panel) and $T_{\rm M}(z)$ (right panel) in the different approximations described in the text, for two prescriptions for describing the effect of astrophysical sources.

Despite the somewhat unsatisfactory situation, some consensus has been reached on important points concerning the reionization history. For instance, in the past the question has been raised if the totality of the reionization related phenomenology could be accounted for by DM only, but it is now acknowledged to have a negative answer. Even in Ref. [270], which finds potentially large effects at high redshift due to DM in halos, an astrophysical contribution is needed to account for the Gunn-Peterson effect, requiring the presence of a non-negligible neutral hydrogen fraction at redshift $z \sim 6.5$. On the other hand, CMB observations need the Universe to be significantly ionised at higher redshift, in order to get a correct integrated optical depth to reionization $\tau_{\rm reio}$, compatible with measurements

of the temperature and polarization spectra [2]. Although early measurements (notably by WMAP 1 [563]) hinted to the necessity for non-trivial reionisation history (e.g. multiple stellar populations or exotic DM contribution) because of a tension between these two observables, this is by now mostly gone: latest Planck data [19] prefer a lower value of $\tau_{\rm reio}$ and even a single-step reionization ending at $z \sim 6.5$ is marginally compatible with Gunn-Peterson bounds, reducing the tension to a 2-σ effect. In a single step model, the measurement $\tau_{\rm reio} = 0.079 \pm 0.017$ (Planck TT,TE,EE+lowP, 95%CL [19]) translates for instance into $z_{\rm reio} = 10.0^{+1.7}_{-1.5}$.

However, mixed reionisation scenarios involving a relevant DM role are still of interest: for instance, one may wonder to what extent CMB upper bounds on $\tau_{\rm reio}$ may lead to stronger constraints on DM annihilation than those coming from the smooth background. This was for instance the conclusion found in Ref. [270]; even in Ref. [447], it was argued that at least light (few GeV's) thermal relics may have measurable effects. Articles such as [96], [189], [332], [410] find it to be instead negligible, for comparable choices of parameters. We want to reconsider this with a state-of-the-art approach, correcting some errors and going beyond the approximations that we have identified in Refs. [96], [189], [270], [447] as mentioned in Sec. 7.2.1 and developped at the end of Appendix D.1. We also want to compute the full CMB power spectrum, while Refs. [96], [189] only estimated $\tau_{\rm reio}$. This extra step may be instructive in establishing to what extent future data may improve over current constraints, a possibility raised for instance in Ref. [447]. In the following, we fix the key parameter $p_{\rm ann}$ close to the current 95%CL upper bound inferred from Planck TT,TE,EE+lowP data[3] [19] with annihilation in the smooth background only, namely, $p_{\rm ann} = 2.3 \times 10^{-7}{\rm m}^3/{\rm s}/{\rm kg} = 4.1 \times 10^{-28}{\rm cm}^3/{\rm s}/[{\rm GeV}/c^2]$. If for this maximal value, we find the role of DM annihilation in halos to be negligible, then it will be *a fortiori* true for any viable $p_{\rm ann}$ value.

As a first sanity check that DM annihilation cannot have a dominant role in a consistent reionization history, having fixed $p_{\rm ann}$ to its maximum value, we vary the halo formation redshift z_F and find the value of the boost factor $\mathcal{B}(z=0)$ giving a reionization optical depth of $\tau_{\rm reio} \in [0.045, 0.0113]$ (the 95%CL interval inferred from Planck TT,TE,EE+lowP data). Even if the values of the parameters depends on the DM mass and annihilation channels, we find that reaching the minimal allowed $\tau_{\rm reio} \simeq 0.079$ while assuming the maximal $p_{\rm ann}$ requires halos to form very early and to be very concentrated, e.g., $[z_h = 50, \mathcal{B}(z=0)) = 10^{11}]$ for a 1000 GeV DM annihilating into muons or $[z_h = 40, \mathcal{B}(z=0)) = 10^{10}]$ for a 1 GeV DM annihilating into electrons. Cosmic ray data [12] and N-body simulations [533], [535] are hardly compatible with $\mathcal{B}(z=0) \geq 10^8$. Hence, reionization from DM annihilation would require even greater halo formation redshifts than the maximal value we consider: $z_F \geq 50$. Even if very little is known about the first halos in the universe from the observational point of view, such early halo formation times do not appear realistic and are in general not considered in the literature. We can conclude in agreement with previous studies that for conventional assumptions on annihilating DM models and on halo formation, DM annihilation cannot play a dominant role in reionizing the Universe and can at most coexist with stellar reionization.

A posteriori, this justifies our choice to fix the value of $p_{\rm ann}$: If plausible reionization models involving DM annihilation could produce an exceedingly high $\tau_{\rm reio}$, we could use the measurement of the optical depth by the Planck satellite to derive new upper bounds on this parameter. Since this is not the case,

2 Strictly speaking, the parameter called reionization optical depth by the Planck collaboration is the physical optical depth to reionization only within some assumptions (see appendix D.3 for details).

3 We checked that the result is exactly the same with the analysis pipeline used in the Planck paper [19], based on camb [402] and cosmoMC [400], or using the class version used as a baseline in this work (version 2.4.3) [390] and MontePython [68].

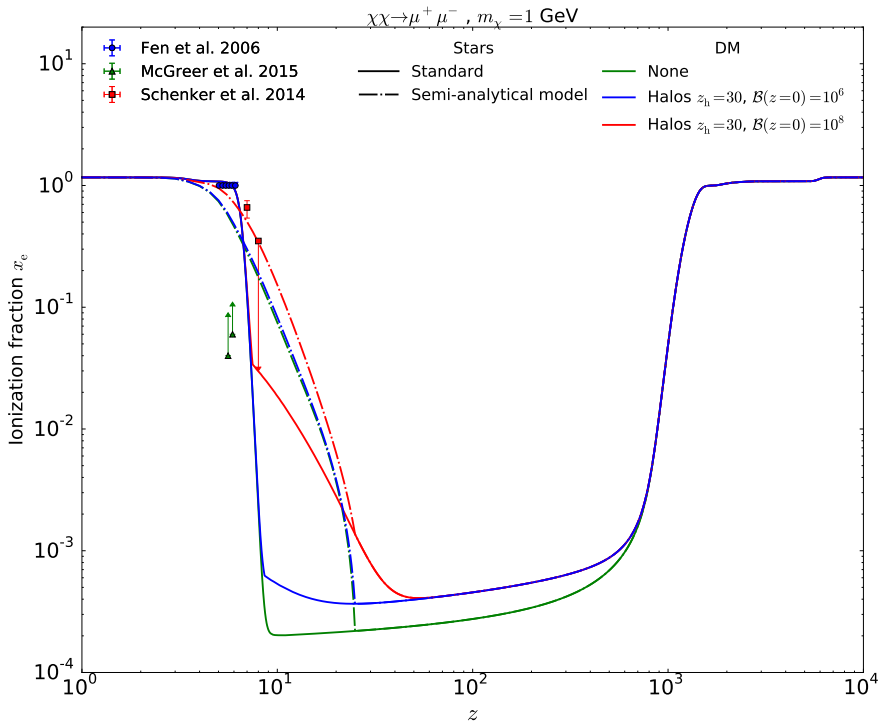

Figure 72: Ionization fraction $x_e(z)$ as a function of redshift for several mixed reionization models. Green lines are benchmark, purely astrophysical reionization scenarios (solid: single step; dot-dashed, phenomenological). The blue and red versions of the corresponding lines show the case where both smooth DM injection and halo one have been added as well, with growing role of halos, respectively. We assume $p_{\rm ann}$ fixed to its most optimistic value.

and since we have no precise information on star formation, we can always obtain the correct $\tau_{\rm reio}$ by assuming the maximal realistic effect from DM annihilation and a complementary effect from stars. The only hope to obtain new bounds on DM annihilation from CMB observations is to analyse the full shape of the CMB temperature and polarization spectra: this will be the topic of section 7.4.

It is interesting to explore a bit further mixed reionization scenarios. In Fig. 72, we show in green the benchmark, purely astrophysical reionization scenarios (solid: single step with $z_{\rm reio} = 6.5$, as suggested by the Gunn-Peterson bound; dot-dashed, phenomenological). The blue and red versions of the corresponding lines show the case where both smooth DM injection and halo one have been added as well, with growing role of halos, respectively. We have fixed there $p_{\rm ann}$ to the maximum value allowed by Planck [19]. The free parameters are the halo ones, $z_{\rm h}$ and $\mathcal{B}(0)$, besides the DM model (annihilation channel and mass), here fixed to the muon final state and 1 GeV mass.

In Figure 73, we vary these two categories of parameters, and find $\tau_{\rm reio}$ as a function of them (in the step-like reionization scenario), together with 68% and 95% confidence limits from Planck TT,TE,EE+lowP data, and bounds on $\mathcal{B}(z = 0)$ inferred from N-body simulations by Ref. [535]. Figure 73 shows that in absence of DM annihilation in halos, there is a marginal ($\sim 2\sigma$) tension between the model without DM annihilation in halos and the Planck bounds on $\tau_{\rm reio}$. At the same time, we can also see that DM annihilations in e^+e^- and $\mu^+\mu^-$ for realistic values of the boost factor (blue band) do not significantly enhance $\tau_{\rm reio}$. The conclusions would be similar for other annihilation channels (all being bracketed by these two) or masses. Note that in all these models, we decided to

saturate the CMB bound coming from annihilation in the smooth background. This means that we fixed the observable quantity $p_{\rm ann}$, but not the fundamental parameter $\langle\sigma v\rangle$. This explains why in Figure 73, the effect seems to be stronger in the muon case than in the electron case; if the cross-section were fixed, the conclusion would be opposite. In this observable, the result is also independent of the reionization model adopted, provided that they are responsible for the same optical depth. In all cases, our main conclusion is that one needs to push the halo contribution to the same unrealistic values as before to remove the marginal tension between CMB and the Gunn-Peterson bound.

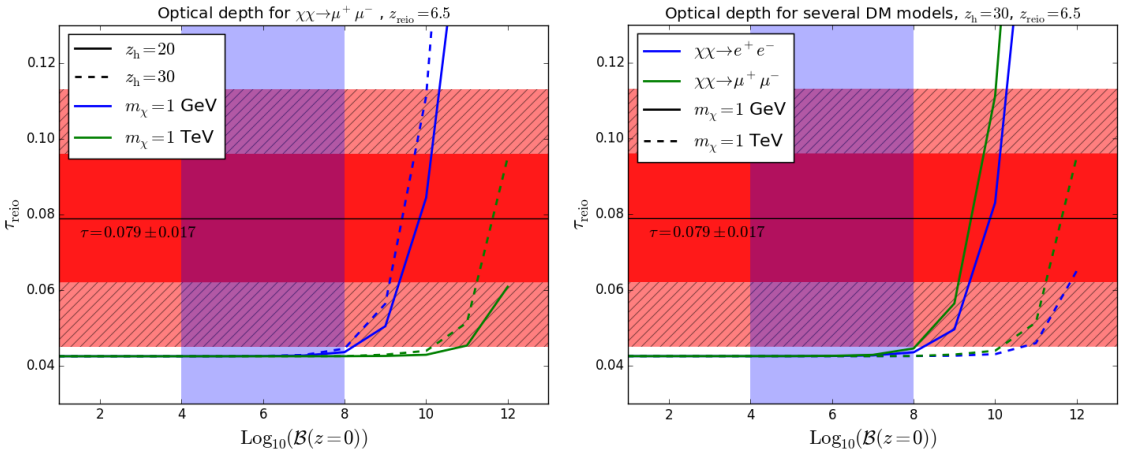

Figure 73: Reionization optical depth $\tau_{\rm reio}$ in mixed reionization models, for different DM masses, annihilation channels and halo parameters. $p_{\rm ann}$ has been fixed to its most optimistic value and the redshift od reionization from stars to $z_{\rm reio}^{\rm star}=6.5$. The red stripe shows the most conservative bound from Planck on $\tau_{\rm reio}$ [19] and the blue one the most conservative interval for the values of the halo amplitudes at $z=0$ according to Refs. [533], [535].

In summary, our main conclusion is that *considering DM annihilation in halos formation seems neither to yield better constraints on the DM properties, nor to solve the slight tension between CMB and Gunn-Peterson data*. We thus essentially confirm similar results obtained in the past, see e.g. [410]. Planck data are not changing these conclusions in any significant way. On one hand, this reassures us about the robustness of the reionization constraints to DM obtained by considering only the smooth contribution. On the other hand, this suggests that it is very hard to improve over them by including the relatively low-z contribution from halos. Barring very different particle physics or halo assembly histories (for some example see e.g. [214]), it appears that the only hope to revisit this conclusion in the future and to reveal some contribution of DM halos would be to measure x_e or $T_{\rm M}$ as a function of z, especially at high redshift ($z\geq10$), and at the same time, to improve our knowledge (both theoretically and observationally) on reionisation by the first stars.

7.4 Impact of reionization histories on the CMB spectra

In this section we go one step further in the discussion of CMB sensitivity to different reionization models, beyond the simple integral constraint on $\tau_{\rm reio}$ discussed in the previous section. While unnecessary to settle the issue of current sensitivity to DM halo signals, this is useful to assess the capabilities to improve over current constraints with future CMB data.

A first important point to make is that the CMB spectrum is in principle sensitive to the entire ionization history $x_e(z)$. The main effect of DM annihilation is to delay recombination, to increase the width of the last scattering surface, and to enhance the number of residual free electrons after decoupling. A larger ionization fraction x_e results in more Thomson scattering of photons along the line-of-sight. As long as x_e remains close to its asymptotic freeze-out value, rescattering impacts CMB observables at a very small level (although not totally negligible). When stars and/or DM halo formation start, x_e increases with time, and the fraction of rescattered CMB photons becomes significant. Temperature and polarization anisotropies are damped on sub-Hubble scales, and regenerated on scales comparable to the Hubble radius.

Typically, for usual models assuming single-step reionization in the range $6 \leq z \leq 12$, high l's probe only the integrated parameter $\tau_{\rm reio}$, since the temperature and polarization anisotropy spectra are mainly suppressed by a factor $e^{-2\tau_{\rm reio}}$ (this behavior can be spoiled to some extent by a more complicated reionization history, see appendix D.3 for details). However, small ℓ's are sensitive to the full reionization history – especially as far as polarization is concerned. Even in single-step models with a fixed $\tau_{\rm reio}$, the shape of the CMB spectra in the range $\ell \sim 20 - 40$ keeps an imprint of the details of the reionization history. In presence of DM annihilation in halos, x_e tends to increase slowly at higher redshift, and a wider multipole range $\ell \sim 20 - 200$ can in principle be impacted.

In Fig. 74 we show the temperature (left) and EE polarization (right) multipole spectra computed for the two models of astrophysical reionization, with the bottom panels showing the relative difference between the two models, compared with the cosmic variance (shaded areas). They have been produced with CLASS version 2.4.3 for a few DM models with fixed $\theta_s = 1.04077 \times 10^{-2}$ and $\tau_{\rm reio} = 0.079$, in agreement with Planck measurement (TT,TE,EE+lowP [19]). The same θ_s is obtained by adjusting H_0 (with fixed ω_b, $\omega_{\rm cdm}$). The fact that the variations shown in these plots are well within the limits

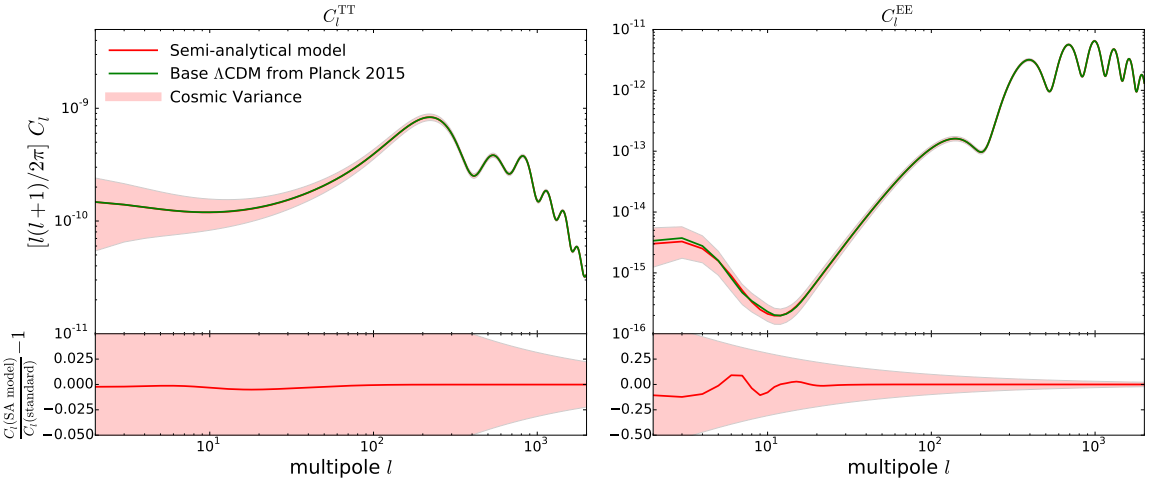

Figure 74: Upper pannels – C_l^{TT}, C_l^{EE} for the two models of astrophysical reionization. The shaded area represents cosmic variance. The baseline ΛCDM model is assumed, with $\tau_{\rm reio} = 0.079$ and $\theta_s = 1.04077 \times 10^{-2}$ fixed in agreement with Planck measurement (TT,TE,EE+lowP [19]). Lower pannels – Relative difference between the two models.

of cosmic variance exemplifies why, despite the fact that a sensitivity to $x_e(z)$ is present in principle, it is considered to be hopeless to infer information on different astrophysical reionization scenarios via CMB observations, and why to a large extent in this framework it is an excellent approximation to

assume that CMB is only sensitive to $\tau_{\rm reio}$. Nonetheless, note that a greater sensitivity to $x_e(z)$ of the EE polarization with respect to TT spectrum is still manifest.

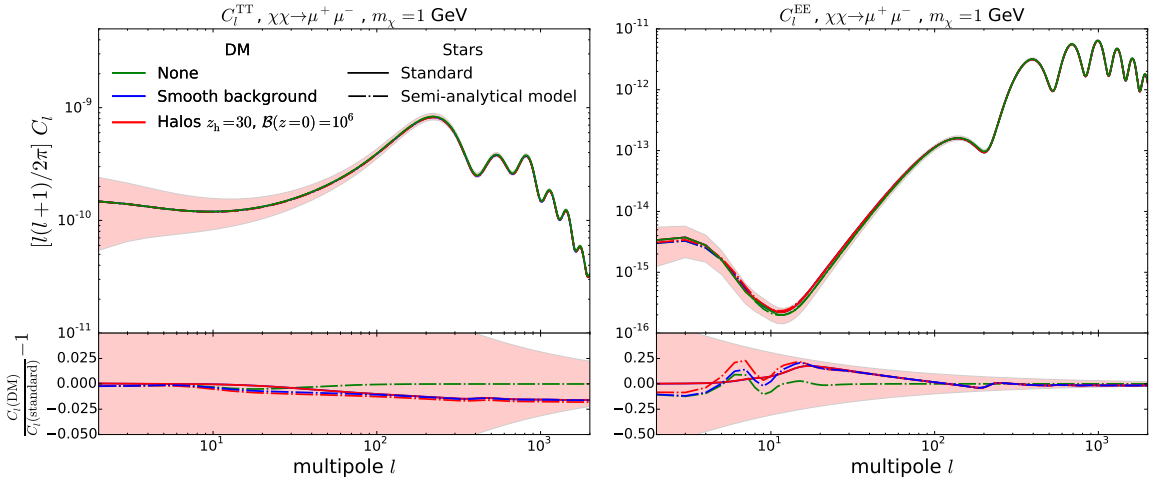

Figure 75: As in Fig. 74, but with the DM effects (both smooth and in halos) now added, for a single reference case of halo boost factor.

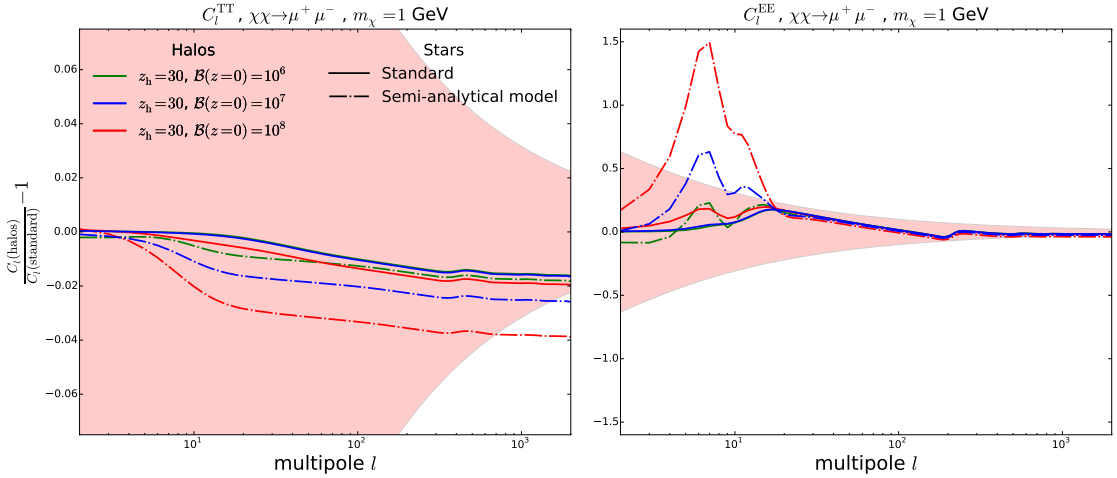

Figure 76: Zoom on the residuals with respect to the baseline models reported in Fig. 74, with several assumptions for the halo contribution reported and for two choices of the astrophysical reionization.

The situation is partially altered if DM annihilation in halos is added. In Fig. 75, we show plots similar to Fig. 74, with the DM effects (both smooth and in halos) now added; we fix the DM channel to the muon one, the DM mass to 1 GeV, and $p_{\rm ann} = 2.3 \times 10^{-7}$, saturating current bounds. While in Fig. 75 only a single, realistic value 10^6 for the boost factor is shown, in Fig. 76, we present the residuals with respect to the reference ΛCDM models, with growing effect of the halo term (besides the 10^6 one, also a factor 10 and 100 larger). It is clear that, at least for the phenomenological model for the astrophysical reionization, potentially detectable effects emerge. Since we fixed θ_s and $\tau_{\rm reio}$, we nearly eliminated any oscillatory patterns and step-like discrepancy between the set of curves describing the TT spectrum. This is not entirely true in models with a significant effect of annihilation in halos, for which a residual step-like effect can be clearly observed in Figure 76. This has to do with the ambiguity

in defining $\tau_{\rm reio}$ in presence of partial reionisation at high-redshift, as explained in Appendix D.3. By just fixing $\tau_{\rm reio}$, we do not eliminate completely the dependance of the high-ℓ temperature spectrum on the reionisation history. Apart from this effect, which could be compensated by a shift in the reionisation time or in the overall normalisation of the primordial spectrum, changes remain very modest and limited to small scales (where degeneracies with other parametrical extensions of ΛCDM are likely present). On the other hand, they can become sizable and characterized by a peculiar pattern at low-l on the polarization power spectrum, coming from the enhanced rescattering of photons at intermediate redshifts $z_{\rm reio} \leq z \leq 600$. While for realistic values of the halo parameters and DM mass it is still likely that this falls within the cosmic variance, it cannot be excluded that more extreme values of the parameters could be independently ruled out by CMB polarization observables, provided that forthcoming final release of Planck data manages to keep under control the systematics at low$-\ell$.

7.5 Discussion and prospects

The CMB temperature and polarization anisotropy pattern is sensitive to the energy injection by DM annihilation, essentially only via its constraints on the reionization optical depth $\tau_{\rm reio}$ (we clarified in appendix D.3 in which limit this is actually true). In turn, the optical depth $\tau_{\rm reio}$ probed by the CMB depends on the reionization history, i.e. the function $x_e(z)$, which itself couples to the thermal history of the gas, controlled by the function $T_{\rm M}(z)$. One major element of novelty of this work has been to study for the first time the dependence of the cosmological observables $x_e(z)$ and $T_{\rm M}(z)$ from the underlying astrophysical reionization/heating source model, both in presence and absence of DM sources. We modified the dynamical equations for x_e and $T_{\rm M}$ arguing that virtually all previous treatments have been incomplete and inconsistent in that respect.

We have then revisited the problem of current CMB constraints on dark matter annihilation in halos, with a state-of-the-art treatment. We have followed the by now standard formalism of Ref. [554] and made use of the numerical tools provided in [551], to compute precisely how the energy is deposited in the medium. We have clarified and corrected a few mistakes in previous work and improved over them. In appendix D.1, we provide a detailed comparison of the many formalisms used in the literature to study DM annihilation in halos and carefully explain where are the few mistakes or approximations over which we have improved. Appendix D.2 describes in details the parametric model of DM halo formation adopted in our calculations, although a generalization to different parameterizations is straightforward and would not alter our conclusions.

In agreement with most previous literature, we have confirmed that with conventional assumptions on DM models and halo formation, DM annihilation fails to play a dominant role in reionizing the universe, and can at most coexist with reionization from stars. Only very unrealistic halos could give a significant contribution to the reionization optical depth, and even then, such models are hardly compatible with astrophysical measurements of the ionization fraction at low redshift. No plausible DM model can produce a too high reionization optical depth, hence CMB measurements of $\tau_{\rm reio}$ do not provide additional constraints on the annihilation cross section. At face value, this means that previous constrains derived assuming DM annihilation in the smooth background only are robust and independent of uncertainties on structure formation. Note that the recent update of the tools to compute the energy deposition in the medium provided by [553], following the results of Ref. [261] would not alter our conclusions: since the account for the new channel of energy loss through very low energy photons (with energy < 13.6 eV) produced during the development of the

electromagnetic cascade, such a refinement would only make the impact of dark matter annihilations in halos even slightly weaker. We have checked this conclusion following the so-called "approximate" method described in Refs. [261], [553] which consists in withdrawing some power to the transfer functions of [551], using a specific new table supplied in Ref. [553]. This method is, according to the authors, as precise as the new transfers functions and is better suited for our treatment.

To assess if these rather pessimistic conclusions are linked to the intrinsic insensitivity of the CMB to these effects or merely to the current lack of precision, in section 7.4 we have computed the CMB angular power spectra, and compared the results with or without annihilation in halos. We have shown that, *within standard assumptions for the astrophysical reionization* and for plausible halo models, both the effects on the TT and EE multipole spectra are unobservable, falling below the level of cosmic variance. One would conclude that fits of CMB spectra in presence of DM annihilation in halos cannot provide (even in principle) better constraints on DM models. However, we have also shown that to some extent this conclusion can be altered if a different scenario for the astrophysical source of reionization is adopted. At present, it cannot be excluded that some extreme but viable DM halo parameter space might be eventually probed by CMB polarization data, provided errors can be kept at the level of the cosmic variance. To the best of our knowledge, it is the first time that this effect is highlighted.

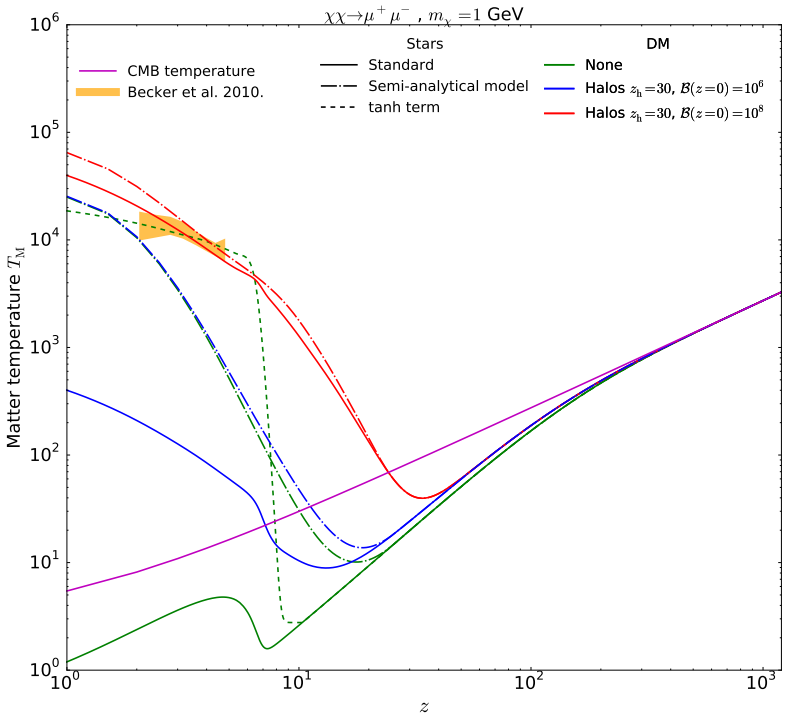

Figure 77: As in Fig. 72 (see also the right panel in Fig. 71) but for the IGM temperature.

Looking beyond the CMB probe, our results also leave the door open to some encouraging perspectives to further constrain DM annihilation in halos via other obserbables, more directly linked to $x_e(z)$ or $T_M(z)$. To illustrate this point, one can look for instance at Fig. 77, where we report the evolution of T_M for several mixed reionization models, analogous to what shown in Fig 72 for the evolution of $x_e(z)$. In particular, green lines are benchmark evolutions for purely astrophysical scenarios (dashed: single step reionization/reheating; dot-dashed, phenomenological one; solid line: standard case where

only the feedback from $x_e(z)$ is included in the dynamics of $T_{\rm M}$). The blue and red versions of the corresponding lines show the case where both smooth DM injection and halo one have been added as well, with growing role of halos: DM annihilation in halos with $z_{\rm h} = 20$, $\mathcal{B}(z = 0) = 10^6$ are reported in blue, and $z_{\rm h} = 30$, $\mathcal{B}(z = 0) = 10^8$ in red, respectively.

The dot-dashed red line shows that already with current rudimentary constraints, if one could trust the phenomenologically motivated model for the astrophysical heating, extreme halo parameters could be excluded. At the same time, as shown by the solid green curve, it is immediately obvious that current treatments of the $T_{\rm M}(z)$ evolution are strongly inadequate, and a significant effort should be put in achieving a realistic modeling of the sources of heating. The qualitatively most interesting effect of DM annihilation in halos is the possibility of a sign shift in the difference between T_γ and $T_{\rm M}$ at much higher redshift than expected for astrophysical models. This could be detectable for instance with 21cm surveys, since the signal would appear either in absorption or in emission (e.g. [51] and reference therein). Tomographic surveys of the cosmological 21cm observable, sensitive both to $x_e(z)$ and $T_{\rm M}(z)$, are certainly the most promising avenue to progress in the knowledge of these redshift epochs. Numerous experiments such as PAPER 64 [4], 21CMA [5], MWA [6], LOFAR [7], HERA [8] or SKA [9], are now (or will be) attempting at measuring the 21 cm signal. Hopefully, it could be possible to see the impact of halos through such a sign shift at relatively high redshift, when the stars are not yet "polluting" the signal. If not, a good description of the influence of stars on $T_{\rm M}$ and x_e would be of first importance, as we have illustrated using semi-empirical models taken from [121], [485], [510], [511]. Some authors are also trying to improve on the modelling of these effects using numerical simulation (such as 21cmFAST [234], [426], [584]). Achieving a sufficiently accurate treatment of the interplay of stellar and exotic sources is definitely a complicated task and a long term goal, but certainly it deserves further investigations.

4 http://eor.berkeley.edu
5 http://21cma.bao.ac.cn
6 http://www.mwatelescope.org
7 http://www.lofar.org
8 http://reionization.org
9 http://www.skatelescope.org

Part III

NEUTRINO PROPERTIES FROM CURRENT AND FUTURE COSMOLOGICAL DATA

As we have seen in sec. 3.2, the existence of three flavors of neutrinos in the Universe is by now well established thanks to a series of experiments, starting from Reines and Cowan in the 1950's. On the theory side, although neutrinos are part of the Standard Model of particle physics, we know that their description *cannot* be complete as this model does not incorporate a satisfactory mechanism for neutrino masses.

On the other hand, CMB anisotropies and structure formation are extremely sensitive to the gravitational impact of neutrinos, and therefore to mass eigenstates, providing us with a very powerful probe of the absolute mass scale of neutrinos. However, because they do not directly probe neutrinos through the weak current, one might wonder whether cosmological neutrinos behave as we expect from standard model ones.

Because of this peculiarity of cosmological data, we study in chapter 8 the typical signatures of the fluctuations of free-streaming neutrinos, extending over previous studies to the case of non-zero masses. We also relax various assumptions, in order to assess whether it is possible to make robust statements about the detection of the cosmic neutrino background by CMB experiments.

In chapter 9, we perform a forecast on the potential for neutrino mass detection in future cosmological surveys. However, in order to exploit the complementarity of the different redshift probes, a deep understanding of the physical effects driving the impact of massive neutrinos on CMB and large scale structures is required. We therefore start by carefully studying the effects on cosmological data of the sum of neutrino masses close to its minimum allowed value, showing that parameter degeneracies can be removed by appropriate combinations of datasets, leading to robust and model independent constraints. A joint forecast of the sensitivity of Euclid and DESI surveys together with a CORE-like CMB experiment (the proposed next generation satellite) leads to a 1σ uncertainty of 14 meV on the summed neutrino mass, while an independent measurement of the optical depth with accuracy $\sigma(\tau_{\rm reio}) = 0.001$ (potentially achievable with future 21-cm experiment) would decrease the uncertainty down to $\sigma(M_\nu) = 12$ meV. Those chapters are adapted from papers published in JCAP, namely Refs. [53], [71].

8

ROBUSTNESS OF COSMIC NEUTRINO BACKGROUND DETECTION IN THE CMB

This chapter is adapted from a publication in JCAP [71].

8.1 Introduction

As discussed in chapter 3, neutrinos are the only dark matter component that has been directly detected. Despite neutrinos not being cold and not being the bulk of the dark matter in the Universe, they are a particularly interesting component to study. Not only because of the synergy between astrophysical observations and particle physics experiments, but also because they contribute a significant fraction of the energy density in the Universe during the radiation dominated stage. The first indirect confirmation of the existence of a cosmological neutrino background has been obtained by assuming standard neutrino properties, and adding only one extra parameter to the standard ΛCDM model: the effective number of neutrino species, $N_{\rm eff}$, equal to 3.046[1] [416] in the standard model. By using Cosmic Microwave Background (CMB) observations, the WMAP collaboration showed to high statistical significance that $N_{\rm eff} > 0$ [224], [376], yielding therefore a confirmation, albeit indirect, of the existence of the cosmic neutrino background. With recent data from Planck, $N_{\rm eff} = 0$ is disfavoured at the level of about 10σ [21].

But $N_{\rm eff}$ does not only count the number of neutrino species. Even assuming standard neutrino physics, departures from $N_{\rm eff}$ could be caused by any ingredient contributing to the expansion rate of the Universe in the same way as a radiation background. The possibilities for this extra ingredient are many: extra relativistic particles (either decoupled, self-interacting, or interacting with a dark sector), a background of gravitational waves, an oscillating scalar field with quartic potential, departures from Einstein gravity, large extra dimensions or something else. Such a component is usually dubbed "dark radiation" [e.g., 4], [10], [46], [55], [110], [210], [276], [297], [366], [418], [561], [590]. In principle, we could even assume that the cosmic neutrino background does not exist, while another dark radiation component explains the measured value of $N_{\rm eff}$[2].

It is well known that free streaming particles like decoupled neutrinos leave specific signatures on the CMB, not only through their contribution to the background evolution, but also because their density/pressure perturbations, bulk velocity and anisotropic stress are additional sources for the gravitational potential via the Einstein equations (see for example [84], [316], [392] and references

1 The number of (active) neutrinos species is 3. As the neutrino decoupling epoch was immediately followed by e^+e^- annihilation, the value of $N_{\rm eff}$ for 3 neutrino species is slightly larger than 3.

2 This of course would be possible only in very exotic particle physics scenarios, and we shall not enter into details of such models.

therein for a detailed discussion). On that basis, several analyses have shown that the CMB can make a more precise statement on the existence of a cosmic neutrino background in the Universe than by just measuring $N_{\rm eff} > 0$ and showing that it is compatible with the standard value. The CMB seems to prove that the perturbation of neutrinos – or more precisely, the perturbation of free-streaming particles with the required abundance – are needed to explain the data.

The strategy of several recent works [54], [56], [57], [213], [267] was to introduce[3] two phenomenological parameters, $c_{\rm eff}$ and $c_{\rm vis}$. The effect of the parameter $c^2_{\rm eff}$ is to generalize the linear relation between isotropic pressure perturbations and density perturbations, while $c^2_{\rm vis}$ directly modifies the anisotropic stress equation for neutrinos. These parameters allow to distinguish the perturbations of relativistic free-streaming species, corresponding to $(c^2_{\rm eff},\, c^2_{\rm vis}) = (1/3,\, 1/3)$, from those of a perfect relativistic fluid with $(c^2_{\rm eff},\, c^2_{\rm vis}) = (1/3,\, 0)$, or a scalar field scaling like radiation with $(c^2_{\rm eff},\, c^2_{\rm vis}) = (1,\, 0)$, or a more general case with arbitrary $(c^2_{\rm eff},\, c^2_{\rm vis})$. Self-interacting neutrinos or other types of dark radiation candidates might not be exactly equivalent to these models with definite and constant value of $(c^2_{\rm eff}, c^2_{\rm vis})$ (see for instance [204], [454]), but this parametrisation is considered flexible enough for providing a good approximation to several alternatives to the standard case of free-streaming particles. We will come back to the motivations for this parametrisation in section 8.2.

Previous works found that the allowed window for $c^2_{\rm eff}$ is shrinking close to 1/3, and that the data starts to be very sensitive also to $c^2_{\rm vis}$, although this parameter has a smaller effect. For instance, using Planck 2013 data, ref. [267] obtained $(c^2_{\rm eff}, c^2_{\rm vis}) = (0.304 \pm 0.026, 0.60 \pm 0.36)$ at the 95% CL. The next Planck data release is expected to bring even better sensitivity, thanks to better temperature and new polarisation data.

However, recent results on $(c^2_{\rm eff},\, c^2_{\rm vis})$ were derived in the context of the minimal ΛCDM model, with negligible neutrino masses. The point of the present study is to answer the two important questions: Are these bounds stable when considering massive neutrinos, instead of the purely massless limit? And could $(c^2_{\rm eff},\, c^2_{\rm vis})$ be degenerate with other cosmological parameters, like e.g., $N_{\rm eff}$, a running of the primordial spectrum index, or the equation of state of dynamical dark energy? These issues are important to better assess the meaning of current bounds, and also to prepare the interpretation of future results. Indeed, if future data bring stronger evidence for standard neutrino perturbations, we will need to understand whether such conclusions are robust or model-dependent. On the other hand, if a deviation from the standard behaviour is found in the context of the minimal ΛCDM model, we will need to know whether extended cosmological models have the potential to reconcile observations with standard values of $(c^2_{\rm eff},\, c^2_{\rm vis})$. The rest of this work is organised as follows: In section 8.2 we present the set of equations describing a massless relativistic component with arbitrary $(c^2_{\rm eff}, c^2_{\rm vis})$, and its generalisation to the case of species becoming non-relativistic at late times. In section 8.3 we analyse the physical effect of the phenomenological parameters on the observables. In section 8.4 we describe our methodology and introduce the data sets used. We present our results in section 8.5 and we discuss and conclude in section 8.6.

8.2 Modelling the properties of the (dark) radiation component

While the parameter $N_{\rm eff}$ affects the expansion rate of the early universe, we want to introduce some parameters describing the behaviour of perturbations. If we were comparing ordinary neutrinos

3 Indeed we are referring here to the definition of $(c^2_{\rm eff},\, c^2_{\rm vis})$ first introduced by these authors. This parametrisation is however strongly inspired from earlier works, e.g., [84], [324], [325], [559], [582].

with a concrete physical model (e.g., neutrinos with a given collision or self-interaction term [59], [594], oscillating scalar field with quartic potential, etc.), there would be no ambiguity in the set of equations and parameters to compare with data. We are not in this situation: we want to define some effective parameters, chosen to provide an exact or approximate description of a wide variety of non-standard models for the radiation component in the universe. From now on, we follow the notations of Ma & Bertschinger [412].

The logic followed by previous authors and leading to the definition of $(c^2_{\rm eff},\, c^2_{\rm vis})$ is to postulate a linear relation between isotropic pressure perturbations and density perturbations given by a squared sound speed $c^2_{\rm eff}$, assumed for simplicity to be independent of time. The approach is then extended to anisotropic pressure by introducing another constant, the viscosity coefficient $c^2_{\rm vis}$.

Technically, this amounts in writing the usual continuity and Euler equations, valid for any decoupled species, and replacing the pressure perturbation $\hat{\delta p}$ by $c^2_{\rm eff}\hat{\delta\rho}$. The hats mean that we are referring to the pressure and density defined in the frame (or in the gauge) comoving with the fluid we are studying, i.e., in which the energy flux divergence θ vanishes. From the gauge transformations (2.1.56) one can show that in an arbitrary gauge, the density perturbations $\delta\rho$, the pressure perturbation δp and the energy flux divergence θ are related to the comoving density/pressure perturbations by

$$\hat{\delta\rho} = \delta\rho + 3\frac{\dot a}{a}(1+w_{\rm dr})\bar\rho\frac{\theta}{k^2}\,, \tag{8.2.1}$$

$$\hat{\delta p} = \delta p + 3\frac{\dot a}{a}(1+w_{\rm dr})c_a^2\bar\rho\frac{\theta}{k^2}\,, \tag{8.2.2}$$

where a is the usual scale factor, the dot indicates derivative with respect to conformal time, $w_{\rm dr}\equiv\bar p/\bar\rho$ and $c_a^2\equiv\dot{\bar p}/\dot{\bar\rho}$. The pressure perturbation appears as a source term in the continuity equation and the Euler equation (see eqs. (2.1.54) and (2.1.58)). If we assume $\hat{\delta p} = c^2_{\rm eff}\hat{\delta\rho}$, we should replace δp in these two places by

$$\delta p = c^2_{\rm eff}\left(\delta\rho + 3\frac{\dot a}{a}(1+w_{\rm dr})\bar\rho\frac{\theta}{k^2}\right) - 3\frac{\dot a}{a}(1+w_{\rm dr})c_a^2\bar\rho\frac{\theta}{k^2}\,. \tag{8.2.3}$$

8.2.1 *Massless neutrinos*

In the relativistic limit, eq. (8.2.3) becomes

$$\frac{\delta p}{\bar\rho} = c^2_{\rm eff}\left(\delta + 4\frac{\dot a}{a}\frac{\theta}{k^2}\right) - \frac{4}{3}\frac{\dot a}{a}\frac{\theta}{k^2}\,. \tag{8.2.4}$$

For decoupled massless neutrinos, the Boltzmann equation can be integrated over momentum, leading to a Boltzmann hierarchy in which the first two equations are equivalent to the continuity and Euler equation. Replacing the two occurrences of δp in these equations by the above expression gives:

$$\dot\delta_\nu = \left(1-3c^2_{\rm eff}\right)\frac{\dot a}{a}\left(\delta_\nu + \frac{4}{k^2}\frac{\dot a}{a}\theta_\nu\right) - \frac{4}{3}(\theta_\nu + M_{\rm continuity})\,, \tag{8.2.5}$$

$$\dot\theta_\nu = \frac{k^2}{4}(3c^2_{\rm eff})\left(\delta_\nu + \frac{4}{k^2}\frac{\dot a}{a}\theta_\nu\right) - \frac{\dot a}{a}\theta_\nu - k^2\sigma_\nu + M_{\rm Euler}\,, \tag{8.2.6}$$

where the subscript ν refers to the neutrino (or dark radiation) component. The above equations are valid in any gauge provided that the two quantities $(M_{\rm continuity},\, M_{\rm Euler})$ refer to the right combination of metric perturbations, e.g. $(\dot h/2, 0)$ in the synchronous gauge and $(-3\dot\phi, k^2\psi)$ in the Newtonian gauge

(see sec. 2.1.1 for the definition of h, ϕ and ψ). When $c^2_{\rm eff}$ is set to 1/3, the standard equations are recovered, since for relativistic free-streaming species the sound speed squared is exactly 1/3.

While δp appears as a source term for δ and θ, the anisotropic pressure σ is sourced in the next equation of the Boltzmann hierarchy by $\theta + M_{\rm shear}$. Extending the previous logic to the level of anisotropic pressure can be done by multiplying this source term by $(3c^2_{\rm vis})$. Then, for $c^2_{\rm vis} = 1/3$, standard equations will be recovered by construction. This prescription leads to:

$$\dot{F}_{\nu 2} = 2\dot{\sigma}_\nu = (3c^2_{\rm vis})\frac{8}{15}(\theta_\nu + M_{\rm shear}) - \frac{3}{5}kF_{\nu 3}\,, \tag{8.2.7}$$

where $F_{\nu\ell}$ are the Legendre multipoles of the momentum integrated neutrino distribution function as defined in sec. 2.1.2. $M_{\rm shear}$ is 0 in the Newtonian gauge and given by $(\dot{h} + 6\dot{\eta})/2$ in the synchronous gauge.

The next equations in the hierarchy are left unmodified. A coefficient $c^2_{\rm vis}$ was first introduced by Hu [324], as an approximate way to close the Boltzmann hierarchy at order $l = 2$. For that purpose, the term $F_{\nu 3}$ was eliminated from equation (8.2.7). The above parametrisation was introduced later in ref. [54], keeping that term, in order to recover the standard equations in the limit $c^2_{\rm vis} = 1/3$. The limit $c^2_{\rm vis} = 0$ describes a species with isotropic pressure (like, for instance, a perfect fluid), since in that limit, σ_ν and all multipoles $F_{\nu\ell}$ with $\ell \geq 3$ remain zero at all times.

8.2.2 *Massive neutrinos*

We will now present original results, showing how the previous parametrisation can be extended to the case of light relics experiencing a non-relativistic transition such as massive neutrinos. In the massive neutrino case, the Boltzmann equation cannot be integrated over momentum, and one must solve one hierarchy per momentum bin. We wish to introduce the $(c^2_{\rm eff},\, c^2_{\rm vis})$ factors in the same way as for massless neutrinos, assuming for simplicity that they affect each momentum equally. The strategy is again to identify the source terms corresponding to $\hat{\delta p}$ in the continuity/Euler equation and multiply them by $(3c^2_{\rm eff})$, and similarly to identify the source term for σ in the quadrupole equation and multiply it by $(3c^2_{\rm vis})$.

One can define several statistical momenta of the background phase-space distribution $f_0(q)$, including the usual background density $\bar{\rho}$ and pressure $\bar{p}$, and also a quantity called the pseudo-pressure in [545]:

$$\tilde{p} = \frac{4\pi}{3}a^{-4}\int_0^\infty dq \frac{q^6}{\epsilon^3} f_0(q)\,, \tag{8.2.8}$$

where ϵ is the comoving energy of the particle. Throughout this work, we use the Boltzmann code CLASS to compute observable spectra. It happens that the pseudo-pressure is always computed by CLASS, because it enters into the expression of the fluid approximation switched on deep inside the Hubble radius [396]. Pseudo-pressure is also useful in the present context, since the comoving pressure perturbation $\hat{\delta p}$ of eq. (8.2.2) can also be expressed as

$$\hat{\delta p} = \delta p + \frac{\dot{a}}{a}(5\bar{p} - \tilde{p})\frac{\theta}{k^2}\,. \tag{8.2.9}$$

One can write down the continuity and Euler equation, decomposing each perturbation as an integral over momentum, involving the Legendre momenta of the perturbed phase-space distribution $\Psi_l(k,\tau,q)$. Then, like for massless neutrinos, we identify the two terms involving $\hat{\delta p}$ and replace them by

$$\delta p = c^2_{\rm eff}\left(\delta\rho + 3\frac{\dot a}{a}(\bar\rho+\bar p)\frac{\theta}{k^2}\right) - \frac{\dot a}{a}(5\bar p - \tilde p)\frac{\theta}{k^2}\ . \tag{8.2.10}$$

Finally, assuming that $c^2_{\rm eff}$ is a momentum-independent coefficient[4], we can remove the integral over q and obtain a modified Boltzmann hierarchy for each momentum q:

$$\dot\Psi_0 = \frac{\dot a}{a}\left(1-3c^2_{\rm eff}\right)\frac{q^2}{\epsilon^2}\left[\Psi_0 + 3\frac{\dot a}{a}\frac{5p-\tilde p}{\rho+p}\frac{\epsilon}{kq}\Psi_1\right] - \frac{qk}{\epsilon}\Psi_1 + \frac{1}{3}M_{\rm continuity}\frac{d\ln f_0}{d\ln q}\ , \tag{8.2.11}$$

$$\dot\Psi_1 = c^2_{\rm eff}\frac{qk}{\epsilon}\left[\Psi_0 + 3\frac{\dot a}{a}\frac{5p-\tilde p}{\rho+p}\frac{\epsilon}{qk}\Psi_1\right] - \frac{\dot a}{a}\frac{5p-\tilde p}{\rho+p}\Psi_1 - \frac{2}{3}\frac{qk}{\epsilon}\Psi_2 - \frac{\epsilon}{3qk}M_{\rm euler}\frac{d\ln f_0}{d\ln q}\ . \tag{8.2.12}$$

Finally, in the $l=2$ equation, we multiply again the source term of the shear by $(3c^2_{\rm vis})$ and obtain:

$$\dot\Psi_2 = \frac{qk}{5\epsilon}\left(6c^2_{\rm vis}\Psi_1 - 3\Psi_3\right) - 3c^2_{\rm vis}\frac{2}{15}M_{\rm shear}\frac{d\ln f_0}{d\ln q}\ . \tag{8.2.13}$$

Higher momenta in the Boltzmann hierarchy are left unchanged. Again, when $(c^2_{\rm eff}, c^2_{\rm vis}) = (1/3, 1/3)$, we recover exactly standard equations.

8.3 Impact of $(c^2_{\rm eff}, c^2_{\rm vis})$ on observables

We implemented the previous equations of motion into CLASS in order to study the impact of $(c^2_{\rm eff}, c^2_{\rm vis})$ on observable quantities. There is no need to modify initial conditions, because on super-Hubble scales perturbations are insensitive to pressure gradients, and hence to $c^2_{\rm eff}$. The perturbations also have negligible anisotropic pressure in the super-Hubble limit, so $c^2_{\rm vis}$ is not playing a role either. Unless otherwise stated, for all parameters that take fixed values, we adopt the same settings as in the "base model" of the Planck 2013 parameter work [21].

8.3.1 *Effect on neutrino perturbations*

In figure 78 we plot the time evolution of the neutrino density perturbations (δ_ν) and the ratio of the metric fluctuations[5] ($\eta \equiv \Phi/\Psi$) at a fixed scale $k = 0.03$ Mpc^{-1}. We show the case of (three) massless neutrinos (top panels) and the case of (three degenerate) massive neutrinos with $m = 0.02$ eV per species (middle panels) and 0.1 eV per species (bottom panels). We have chosen five models in these plots, one reference model in which $c^2_{\rm eff} = c^2_{\rm vis} = 1/3$, two models in which we set $c^2_{\rm eff}$ to 0.30 and 0.36, and two models that correspond to $c^2_{\rm vis}$ set to 0.30 and 0.36. Note that on these plots δ_ν is always negative: this is because we choose a mode normalised arbitrarily to positive curvature perturbation (i.e., positive gravitational potential) at initial time.

4 We shall discuss this assumption *a posteriori* in the Conclusions

5 Φ and Ψ are two gauge-independent combinations of scalar metric fluctuations, equivalent to the Bardeen potentials up to minus signs, and coinciding in the Newtonian gauge with the metric fluctuations ϕ and ψ such that $ds^2 = -(1+2\psi)dt^2 + a^2(1-2\phi)d\vec{x}^2$.

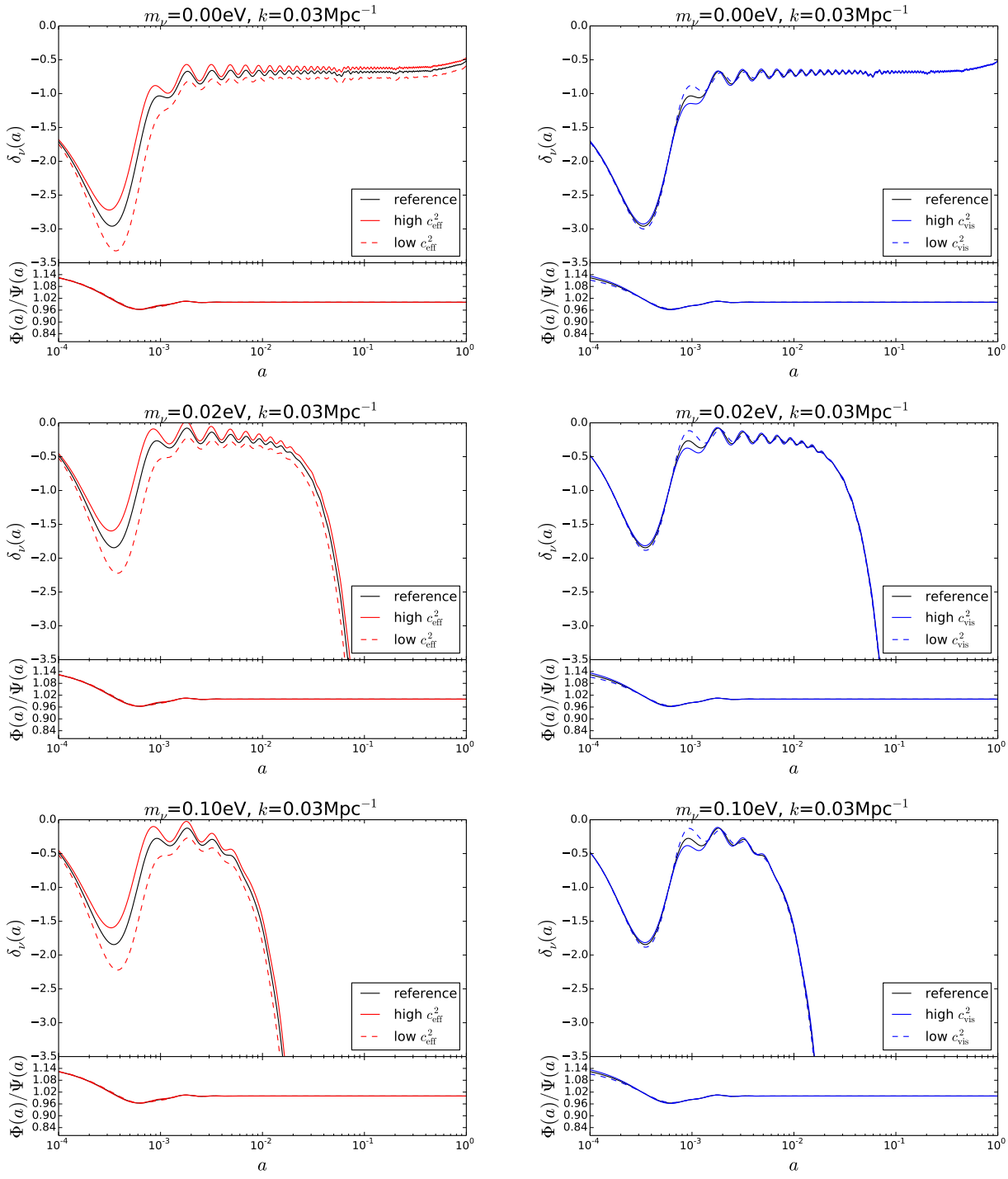

Figure 78: Neutrino density perturbations as a function of scale factor for a ΛCDM model with massless neutrinos (top panels), three degenerate neutrinos with $m_\nu = 0.02$ eV each (middle panels), and $m_\nu = 0.10$ eV (bottom panels). All panels show the evolution of the perturbations for a fixed scale of 0.03 Mpc^{-1}. Solid black lines show a reference model with $c^2_{\rm eff} = c^2_{\rm vis} = 1/3$. In the left panels, solid red lines and dashed red lines correspond to $c^2_{\rm eff} = 0.36$ and 0.30 respectively, whereas in the right panels solid blue lines and dashed blue lines correspond to $c^2_{\rm vis} = 0.36$ and 0.30 respectively. For reference, the evolution of the ratios of the gravitational potentials are shown for every case.

In general, after entering the Hubble radius, the perturbations of a given component grow as a power law of the scale factor ($\delta \propto a^{1+3w}$) above the sound-horizon (hereafter SH), and start oscillating with a decaying amplitude below the SH. The effective SH of a particular species is defined as

$$s_{\rm eff} = \int c_{\rm eff} d\tau = c_{\rm eff}\tau \,,$$

where τ is conformal time, and the last equality holds for constant sound speeds. Therefore, it is clear that increasing the squared sound speed $c^2_{\rm eff}$, the time at which perturbations stop growing by entering the SH decreases. We expect then a bigger amplitude of the density perturbations $|\delta_\nu|$ for models with lower values of $c^2_{\rm eff}$. Inside the SH, fluctuations are damped, with an oscillatory pattern $\sim \cos(kc_{\rm eff}\tau)$ depending on the SH and hence on the effective sound speed. But they are not completely erased: they reach an equilibrium value depending precisely on the pressure to density perturbation ratio. Models with a smaller $c^2_{\rm eff}$ have less pressure perturbations, and hence keep a higher residual density contrast $|\delta_\nu|$ at equilibrium. The decrease of the density contrast observed at late times for massless neutrinos (upper panels) is due to cosmological constant domination (Λ suppresses density perturbations by diluting them with the accelerated expansion). Finally, when neutrinos become non-relativistic, their pressure perturbation becomes negligible and they start to collapse gravitationally. A smaller value of $c^2_{\rm eff}$ implies that the pressure perturbation becomes negligible a bit earlier, so the density contrast $|\delta_\nu|$ grows earlier, and moreover starting from a larger equilibrium value. In summary, a smaller $c^2_{\rm eff}$ implies a larger density contrast $|\delta_\nu|$ at all times between the approach of SH crossing and today, and this is what we observe on the left panels of figure 78.

The viscosity parameter $c_{\rm vis}$ mimics the effect of increasing or decreasing the mean free path of particles in an imperfect fluid with interactions. The limit $c_{\rm vis} = 0$ corresponds to a negligible mean free path, i.e., to the strongly interacting regime where the pressure remains isotropic. A small decrease of $c^2_{\rm vis}$ below $1/3$ implies that it takes more time for neutrinos to transfer power from a monopole and dipole pattern (i.e., density and velocity perturbations) to a quadrupole pattern (i.e., anisotropic pressure/stress σ_ν), like in a weakly interacting fluid with less viscosity. Once the quadrupole is excited, power is transferred to even higher multiples and density fluctuations are damped. Hence the main effect of $c_{\rm vis}$ is to change slightly the evolution of δ_ν near the SH crossing time, which is precisely the time at which the anisotropic stress is excited. Models with a smaller $c^2_{\rm vis}$ keep a larger density contrast for a slightly longer time. Then the density reaches the damped oscillation regime in slightly longer or shorter time, so the phase of the oscillations is slightly affected by $c^2_{\rm vis}$.

In the lower part of each plot, we can see that at early times the evolution of the ratio of the two gravitational potentials Φ and Ψ is weakly model dependent. In particular, by varying the viscosity parameter, we change the offset between the two metric fluctuations, controlled by the traceless transverse Einstein equation

$$k^2(\Phi - \Psi) = 12\pi G a^2(\rho + p)\sigma \,. \tag{8.3.1}$$

The total anisotropic stress on the right-hand side receives contribution from photon perturbations after photon decoupling, and also from neutrino perturbations until their power is transferred to higher multipoles after SH crossing. In models with a lower $c^2_{\rm vis}$, the neutrino anisotropic stress grows more slowly before SH crossing, leading to a reduced difference between the two potentials.

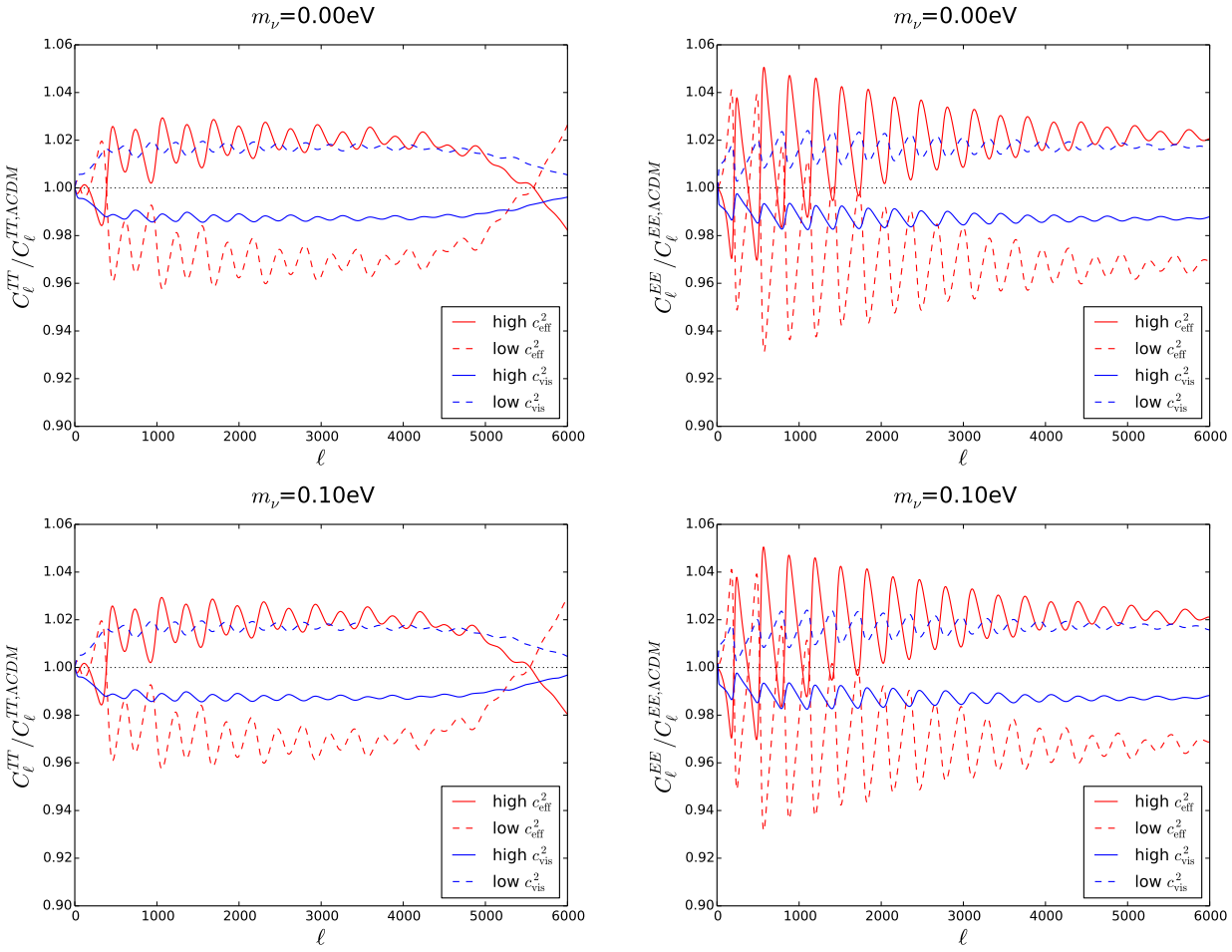

Figure 79: CMB power spectrum multipoles for the temperature (left column) and E-mode polarisation (right column) for a ΛCDM model with massless neutrinos (top panels), and three degenerate neutrinos with $m_\nu = 0.10$ eV (bottom panels). All models are normalised to a reference model with $c^2_{\rm eff} = c^2_{\rm vis} = 1/3$. Solid red lines and dashed red lines correspond to a $c^2_{\rm eff}$ of 0.36 and 0.30 respectively, whereas solid blue lines and dashed blue lines correspond to a $c^2_{\rm vis}$ of 0.36 and 0.30 respectively. Top and bottom panels are almost identical, showing that the relative effect of ($c^2_{\rm eff}$, $c^2_{\rm vis}$) is independent of neutrino masses.

8.3.2 *CMB temperature and polarisation*

In figure 79 we show the CMB power spectra of our four models with non-standard values of $c^2_{\rm eff}$ and $c^2_{\rm vis}$, normalised to the reference model with standard neutrino properties. The left column shows the ratio of the temperature power spectra, whereas the right column shows the ratio of the E-mode power spectra.

The CMB is sensitive to neutrino perturbations through gravitational interactions [84], [316], [392]. The amplitude of photon oscillations (i.e., acoustic waves) is usually boosted near the time of SH crossing by the decay of metric fluctuations. In the presence of a smooth free-streaming component like standard neutrinos, metric fluctuations get extra damping and the boosting is enhanced. After that time, photon perturbations oscillate with a higher amplitude on sub-SH scales. The enhanced boosting also implies that the phase of oscillations in the photon-baryon fluid is slightly shifted towards earlier times in presence of neutrinos. In the observable temperature and polarisation spectra, this induces a small displacement of CMB peaks towards larger angular scales. This "neutrino drag" effect is very characteristic of the presence of relativistic particles in the universe before photon decoupling [84].[6]

In the temperature power spectrum, the most prominent effect of $c^2_{\rm eff}$ and $c^2_{\rm vis}$ is a change in the amplitude of the spectrum, caused by different amounts of gravitational boosting. A lower $c^2_{\rm eff}$ leads to more density contrast in the neutrino species, so the metric fluctuations decay more slowly near SH crossing. The boosting of photon perturbations is reduced and the amplitude of the CMB fluctuations is lower. The effect of $c^2_{\rm vis}$ is less straightforward, since it impacts the evolution of Ψ and Φ in a different way around the time of SH crossing for neutrino perturbations, i.e., near the time at which the neutrino anisotropic stress grows slightly faster / slower, then reaches a maximum and decays. For a smaller $c^2_{\rm vis}$, the neutrino anisotropic stress is smaller at the time when the gravitational boosting of photon fluctuations is relevant, and this results in larger fluctuations. The change of amplitude observed in figure 79 is qualitatively different in the case of $c^2_{\rm eff}$ and $c^2_{\rm vis}$, and is also different from a change in the primordial amplitude A_s, since it does not affect scales that are above the SH at decoupling: it reaches a constant amplitude only for multipoles with roughly $\ell > 300$, thus affecting the first and the second peak of the CMB in different ways and thereby changing the shape of the spectrum.

Besides the oscillation amplitude, the parameters $(c^2_{\rm eff}, c^2_{\rm vis})$ also change the phase of the acoustic oscillations, as one can see from the oscillatory patterns in figure 79. Indeed we have seen in the previous section that the oscillation period of δ_ν depends slightly on $(c^2_{\rm eff}, c^2_{\rm vis})$. This shift is propagated to the photon-baryon fluid through the neutrino drag effect. In the polarisation power spectrum we find effects similar to those present in the temperature power spectrum. However, although the change in amplitude is similar to the one in the temperature power spectrum, the shift in the position of the peaks is even more clear, because for polarisation there is no contribution from Doppler effects.This explains the strong oscillations in the ratios shown in the right column of figure 79.

By comparing the top and bottom panel of figure 79, we see that the relative effect of $(c^2_{\rm eff}, c^2_{\rm vis})$ does not seem to depend on mass, even though the underlying power spectra do depend on mass. This is not unexpected. When neutrinos have a small mass and become non-relativistic after photon decoupling, they affect the CMB through small effects: shift in the diameter angular distance, early

6 Instead of probing the existence of the cosmic neutrino background by varying the effective parameters $c^2_{\rm eff}$ and $c^2_{\rm vis}$, one could directly introduce a parametrization of the CMB phase and investigate observational constraints on this phase, see Ref. [248].

integrated Sachs-Wolfe effect, and weak lensing. The first effect is totally independent of perturbations, and hence of $(c^2_{\rm eff},\, c^2_{\rm vis})$. The second and third effects can in principle be affected by $(c^2_{\rm eff},\, c^2_{\rm vis})$, but since this is a modulation of a small effect by another small effect, the impact of the effective speeds and of neutrino masses are independent of each other to a very good approximation. Hence the effect of neutrino masses cancels out in the C_l ratios shown in figure 79, at least in the neutrino mass range explored here.

8.3.3 *Matter power spectrum*

We complete the previous analysis of the effects on the CMB power spectra of the effective parameters $(c^2_{\rm eff},\, c^2_{\rm vis})$ with an analysis of potential signatures on the large scale structure of the universe, focusing on the shape of the matter power spectrum at redshift $z = 0$.

In figure 80, as in the previous subsection, we plot the ratios of our four non-standard models with respect to the reference model with standard neutrinos. On large scales ($k \leq 10^{-2}{\rm Mpc}^{-1}$) the effects of these non-standard values of $c^2_{\rm eff}$ and $c^2_{\rm vis}$ are below 1%. However, on smaller scales the effects become more important, especially for $c^2_{\rm eff}$.

The effect of $c^2_{\rm eff}$ on the matter power spectrum is easy to understand. Once the neutrino or dark radiation particles are non-relativistic, they fall into the gravitational potential wells of Cold Dark Matter. The growth rate of δ_ν is larger than the one of $\delta_{\rm cdm}$ until the neutrino overdensities matches the CDM overdensities. We have seen in section 3.1. that for a smaller $c^2_{\rm eff}$, the density contrast $|\delta_\nu|$ starts growing a bit earlier and from a slightly larger equilibrium value. Hence, the ratio $\delta_\nu/\delta_{\rm CDM}$ at a given scale and given time is larger for smaller $c^2_{\rm eff}$.

The growth rate of CDM and baryon fluctuations is slightly reduced when neutrino perturbations are negligible. With a smaller $c^2_{\rm eff}$, there is a larger density contrast $|\delta_\nu|$ in the neutrinos, hence CDM and baryon collapse at a slightly faster rate and the small-scale matter power spectrum is enhanced.

At scales between 0.01 and 0.2 Mpc^{-1} increasing (decreasing) any of the two sound speed parameters cause a decrease (increase) in the power spectrum. This amplitude modulation is still below 1% when we change $c^2_{\rm vis}$ within the limits explored here, but $c^2_{\rm eff}$ can introduce modulations of up to 5% within the range 0.30-0.36. Interestingly, at $k = 0.2$ Mpc^{-1} the modulation due to $c^2_{\rm vis}$ changes its sign and an increase in its value produces a decrease of the power spectrum, however the effect remains below 1% even at $k = 1$ Mpc^{-1} for the range considered here. As in the CMB power spectrum, we also detect no relative effects of the neutrino mass on these ratios. These considerations indicate that the effect of a modest change in $c^2_{\rm eff}$ is relatively large in the shape of the matter power spectrum: large volume, forthcoming large-scale structure surveys should have the statistical power to measure sub-percent effects on these scales. For these reasons, it would be interesting to compare our results with those of [464], [465], where the authors use Lyman-α forest data to get constraints on massive neutrinos. Moreover the different behaviour of the two parameters on scales $k \geq 0.1$ Mpc^{-1} means that any degeneracy between the two parameters can be lifted.

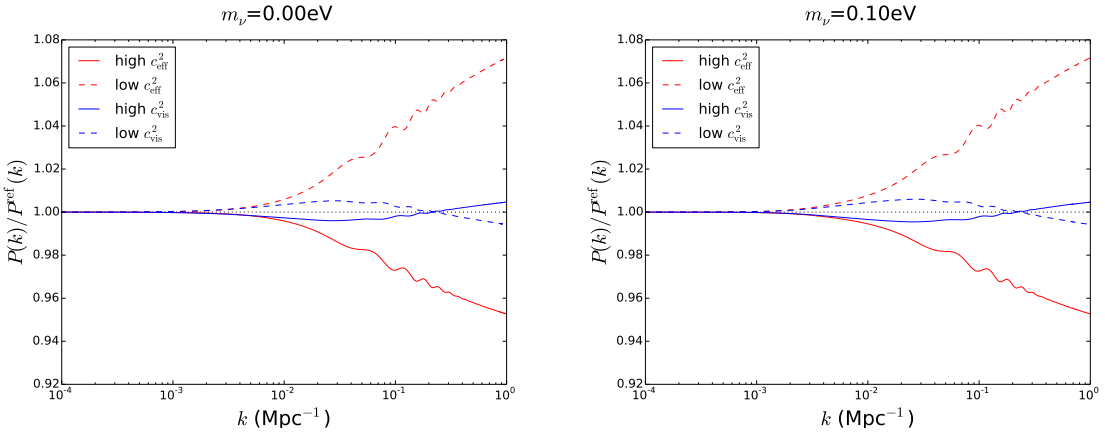

Figure 80: Matter power spectrum for a ΛCDM model with massless neutrinos (left panel) and three degenerate neutrinos with $m_\nu = 0.10$ eV each (right panel). All models are normalised to a reference model with $c^2_{\rm eff} = c^2_{\rm vis} = 1/3$. Solid red lines and dashed red lines correspond to $c^2_{\rm eff} = 0.36$ and 0.30 respectively, whereas solid blue lines and dashed blue lines correspond to $c^2_{\rm vis} = 0.36$ and 0.30 respectively. These two plots are almost identical, showing that the relative effect of $(c^2_{\rm eff}, c^2_{\rm vis})$ is independent of neutrino masses.

8.4 Models and data set

We consider six different models. All models share the six parameters of the flat ΛCDM model, with the additional $c^2_{\rm vis}$ and $c^2_{\rm eff}$:

$$\{\omega_b, \omega_{\rm cdm}, h, A_s, n_s, \tau_{\rm reio}, c^2_{\rm vis}, c^2_{\rm eff}\}.$$

We recall that the first six cosmological parameters denote the baryon and cold dark matter physical densities, the reduced Hubble parameter, the amplitude and tilt of the initial curvature power spectrum at the pivot scale $k_* = 0.05$/Mpc, and the optical depth to reionisation. Those parameters have been described in sec. 2.2.3.4, while the effective parameters $c^2_{\rm vis}$ and $c^2_{\rm eff}$ have been described in section 8.2.

8.4.1 *Model descriptions*

Since this 8-parameter model is our "minimal" model, we refer to it as "M". We further explore possible degeneracies between $(c^2_{\rm vis}, c^2_{\rm eff})$ and the total neutrino mass $M_\nu \equiv \sum m_\nu$ and/or the effective number of relativistic species $N_{\rm eff}$. These 3 additional models are referred to as M+m_ν, M+$N_{\rm eff}$ and M+m_ν+$N_{\rm eff}$ and have 9, 9 and 10 parameters respectively.

We also check for degeneracies with the dark energy equation of state parameter w (and this model is referred to as M+w), and the running of the primordial spectrum tilt $\alpha_s \equiv dn_s/d\log k$ (model called M+α).

Unless otherwise stated, when parameters take a fixed value we adopt the same settings as in the "base model" of the Planck 2013 parameter work [21]. In particular, when the neutrino mass is not a free parameter, we assume two massless neutrino species, and one species with a small mass $m_\nu = 0.06$ eV, motivated by the minimal values in the normal hierarchy scenario. In that case, we assign the same $(c^2_{\rm vis}, c^2_{\rm eff})$ to the massless and massive species. We checked explicitly that the bounds

on $(c^2_{\rm vis}, c^2_{\rm eff})$ obtained in that way are indistinguishable from what we would get by assuming three massless families. Indeed, a neutrino mass $m_\nu = 0.06$ eV is too small to change the evolution of perturbations at CMB times, independently of the value of $(c^2_{\rm vis}, c^2_{\rm eff})$. Such a small mass affects the CMB only through a modification of the angular diameter distance to decoupling. Hence, like in the standard case with $(c^2_{\rm vis}, c^2_{\rm eff})$=$(1/3, 1/3)$, the only impact of this fixed mass is a small shifting of the best-fit value of H_0 by roughly -0.6 km s^{-1} Mpc^{-1} [21].

When the neutrino mass is considered as a free parameter, we consider for simplicity three degenerate neutrinos with equal mass and $(c^2_{\rm vis}, c^2_{\rm eff})$ parameters, and the bounds we report are always on the total neutrino mass M_ν. It is well-known that for a fixed total mass, current observations are not sensitive to the mass splitting between the three families of active neutrinos.

When $N_{\rm eff}$ is left free, we assume one massive species with $m_\nu = 0.06$ eV and $N_{\rm ur} = N_{\rm eff} - 1$ massless species, all with the same $(c^2_{\rm vis}, c^2_{\rm eff})$ (here 'ur' stands for ultra-relativistic). Finally, when varying $N_{\rm eff}$ and m_ν at the same time, we take one massive species with mass m_ν, and $N_{\rm ur} = N_{\rm eff} - 1$ massless ones, all with the same $(c^2_{\rm vis}, c^2_{\rm eff})$. Of course, the decision to assign the same $(c^2_{\rm vis}, c^2_{\rm eff})$ to all species in all cases is somewhat arbitrary. For instance, it could be the case that only one species of neutrinos has significant interactions with a dark sector. This choice is dictated by simplicity. Also, as long as everything keeps being consistent with standard neutrino perturbations, this choice will probably be sufficient in order to establish whether more complicated models are worth investigating.

8.4.2 *Data sets and parameter extraction*

The parameter extraction is done with the public code Monte Python [68], using the Metropolis Hastings algorithm, and a Cholesky decomposition in order to better handle the large number of nuisance parameters [399]. We adopt flat priors on all cosmological parameters. We also use importance sampling for exploring small deviations to the posterior coming from additional datasets. We compare our six different models to 3 sets of experiments.

The CMB set includes the Planck [482] temperature power spectrum [483], the low-ℓ information from WMAP polarisation [98], as well as high-ℓ ACT [550] and SPT [504] data [21]. The adopted Planck likelihood functions are the low-ℓ Commander likelihood and the high-ℓ CAMspec [483]. The CMB+lensing set contains in addition the Planck lensing reconstruction [484]. The recent expansion history of the Universe as measured via the Baryon Acoustic Oscillations (BAO) technique is also considered as an additional data set and we use the determinations of refs. [47], [101], [249], [514].

8.5 **Results**

ΛCDM+$c^2_{\rm eff}$+$c^2_{\rm vis}$ $\equiv$ M: Results for the minimal model ΛCDM+$c^2_{\rm eff}$+$c^2_{\rm vis}$ (M) are reported in tables 6, 7, 8 for the three different datasets, and illustrated by the left panel of figure 82. The standard values ($c^2_{\rm eff}$, $c^2_{\rm vis}$) are always well within the 95% confidence intervals, so the data gives no indication of exotic physics in the dark radiation sector. These findings can be seen as further evidence in favour of the detection of the cosmic neutrino background. Our results in this case reproduce those of ref. [267] and confirm that current data are sensitive to $c^2_{\rm vis}$ and especially to $c^2_{\rm eff}$. The effect of the neutrino anisotropic stress is detected albeit at small statistical significance: $c^2_{\rm vis} = 0$ is disfavoured at the 2.5σ level for CMB and CMB +lensing but (slightly) above 3σ when BAO data are included. For all dataset combinations, we observe (figure 82) a small anti-correlation between the two effective

parameters. Indeed we have seen in section 3 that they affect the amplitude of CMB oscillations in different directions. Apart from the overall amplitude, their effects are clearly distinct as shown by figure 2 which explains the weakness of the correlation.

The bounds on the parameters of the ΛCDM model are significantly broader than in the base ΛCDM case. In fact, the effect of $c^2_{\rm eff}$+$c^2_{\rm vis}$ discussed in section 3 turn out to be degenerate with subtle combinations of ω_b, ω_{cdm}, n_s and A_s (see figure 81). In particular, a high $c^2_{\rm vis}$ requires low ω_b, ω_{cdm}, and high n_s and A_s. Better CMB data could help break these degeneracies, and bring stronger constraints on ($c^2_{\rm eff}$, $c^2_{\rm vis}$).

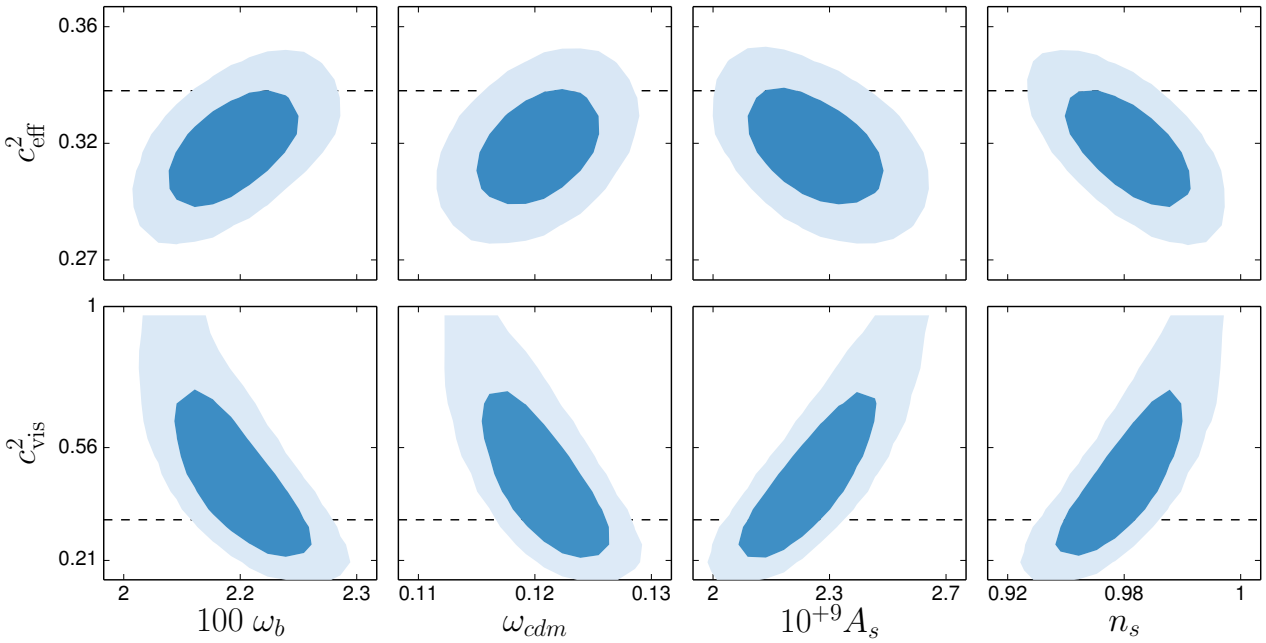

Figure 81: Degeneracies between the parameters ($c^2_{\rm vis}, c^2_{\rm eff}$) and the parameters ω_b, ω_{cdm}, A_s and n_s. A combination of CMB+lensing data is used for this plot, in which a ΛCDM+$c^2_{\rm vis}$+$c^2_{\rm eff}$ model is assumed. Dashed lines correspond to the standard values ($c^2_{\rm eff}, c^2_{\rm vis}$) = (1/3, 1/3).

This also indicates that the significance of the deviation from a scale invariant power spectrum relies on assuming standard neutrino properties. If this assumption is relaxed our knowledge of the shape of the primordial power spectrum is also degraded.

M+m_ν: The effect of adding m_ν can be seen in tables 6, 7, and in the right panel of figure 82. There is no degeneracy between $c^2_{\rm eff}$+$c^2_{\rm vis}$ and the neutrino mass. This is an important new result, helping to establish the robustness of constraints on neutrino/dark radiation perturbations. Adding m_ν slightly decreases the mean value for $c^2_{\rm eff}$ and increases the mean value for $c^2_{\rm vis}$, but not by a statistically significant amount.

Extended cosmologies: We considered extended cosmologies for the CMB+lensing dataset. Parameter constraints are reported in table 7. Selected two-dimensional posterior distributions involving ($c^2_{\rm eff}$, $c^2_{\rm vis}$) and the extra cosmological parameters are shown in figures 83 and 84. The ($c^2_{\rm eff}$, $c^2_{\rm vis}$) constraints are robust to the addition of extra cosmological parameters. There is no significant degeneracy between ($c^2_{\rm eff}$, $c^2_{\rm vis}$ and $N_{\rm eff}$) or w. There is a small anti-correlation between $c^2_{\rm eff}$ and α_s which however does not change the conclusion that $c^2_{\rm eff}$ is compatible with the standard value of 1/3 and α_s is consistent with 0.

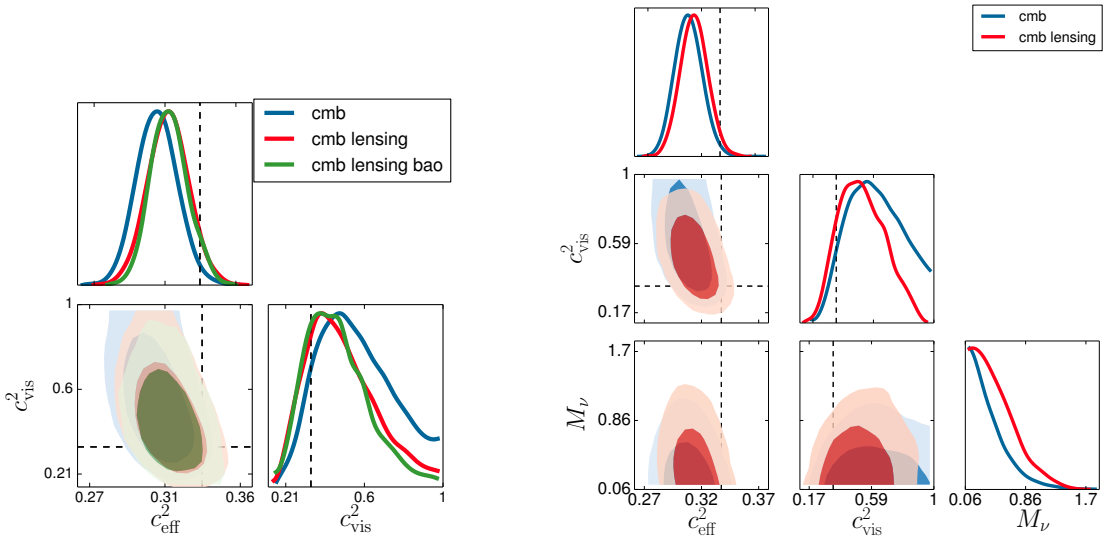

Figure 82: *Left.* Constraints in the $(c^2_{\rm vis}, c^2_{\rm eff})$ plane for combination of CMB, CMB+lensing and CMB+lensing+BAO data, in the ΛCDM+ $c^2_{\rm vis} + c^2_{\rm eff}$ model. Marginalised posterior distributions for both parameters are also shown. *Right.* Constraints on $(c^2_{\rm vis}, c^2_{\rm eff})$ and the total neutrino mass M_ν for CMB and CMB+lensing datasets in the ΛCDM+$c^2_{\rm vis}$+$c^2_{\rm eff}$+m_ν model. Dashed lines correspond to the standard values $(c^2_{\rm eff}, c^2_{\rm vis}) = (1/3, 1/3)$.

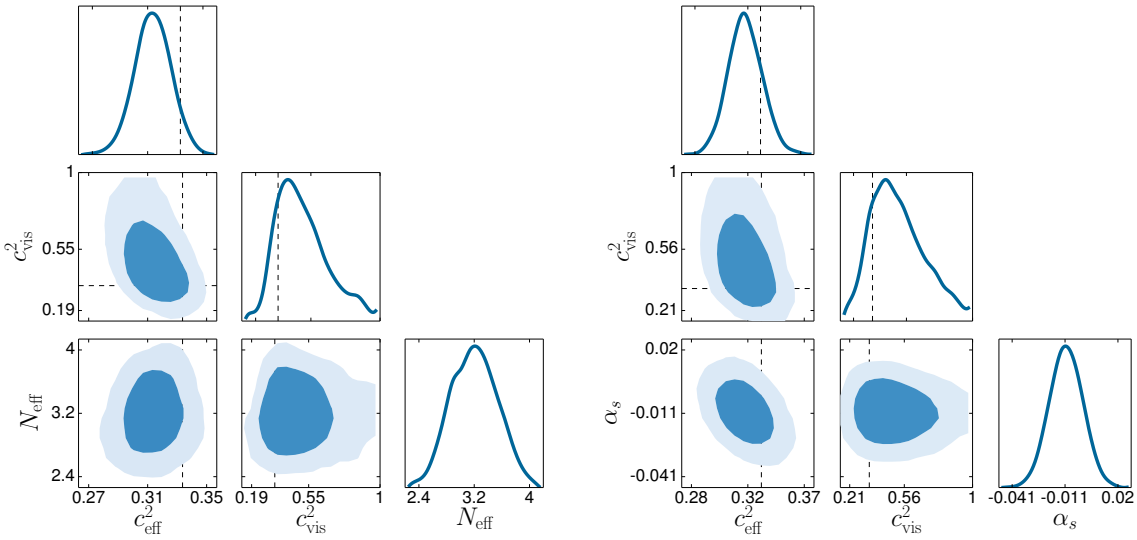

Figure 83: *Left.* Two-dimensional posterior distributions for $(c^2_{\rm vis}, c^2_{\rm eff})$ and $N_{\rm eff}$ for CMB+lensing data set in the ΛCDM+$c^2_{\rm eff}$+$c^2_{\rm vis}$+$N_{\rm eff}$ model, where we considered one massive (m_ν=0.06 eV) and two massless neutrinos. *Right.* Constraints on $(c^2_{\rm vis}, c^2_{\rm eff})$ and the running spectral index α_s for CMB+lensing data in the ΛCDM+$c^2_{\rm eff}$+$c^2_{\rm vis}$+α_s model. Dashed lines correspond to the standard values $(c^2_{\rm eff}, c^2_{\rm vis}) = (1/3, 1/3)$.

M+$N_{\rm rel}$+m_ν: Finally even in the 10 parameters model where all parameters describing neutrino and dark radiation properties are left to vary we find no significant degeneracies with the $c^2_{\rm eff}$, $c^2_{\rm vis}$ parameters. The effective number of species is still compatible with the standard value and its error-bar (±0.34) has not degraded compared to the ΛCDM+$N_{\rm eff}$ case (±0.33) in [21]. The 95% limit on the

CMB		
Parameter	ΛCDM+$c^2_{\rm eff}$+$c^2_{\rm vis}$	+ m_ν
$100\ \omega_b$	$2.132^{+0.044}_{-0.054}$	$2.107^{+0.046}_{-0.056}$
ω_{cdm}	0.1164 ± 0.0040	$0.1166^{+0.0039}_{-0.0041}$
H_0	68.0 ± 1.3	$65.0^{+3.4}_{-1.8}$
$10^{+9}A_s$	2.37 ± 0.14	$2.40^{+0.14}_{-0.13}$
n_s	$0.991^{+0.021}_{-0.019}$	$0.992^{+0.022}_{-0.017}$
τ_{reio}	$0.090^{+0.013}_{-0.014}$	$0.090^{+0.013}_{-0.014}$
$c^2_{\rm eff}$	$0.307^{+0.013}_{-0.014}$	$0.304^{+0.013}_{-0.014}$
$c^2_{\rm vis}$	$0.56^{+0.15}_{-0.25}$	$0.61^{+0.17}_{-0.24}$
M_ν [eV]	–	< 0.88

Table 6: Constraints from CMB data on the values of the cosmological parameters for the ΛCDM+$c^2_{\rm eff}$+$c^2_{\rm vis}$ and the ΛCDM+$c^2_{\rm eff}$+$c^2_{\rm vis}$ + m_ν models. We report the 95% C.L. upper limit for the total neutrino mass M_ν, the mean values and 1σ ranges for all the other parameters.

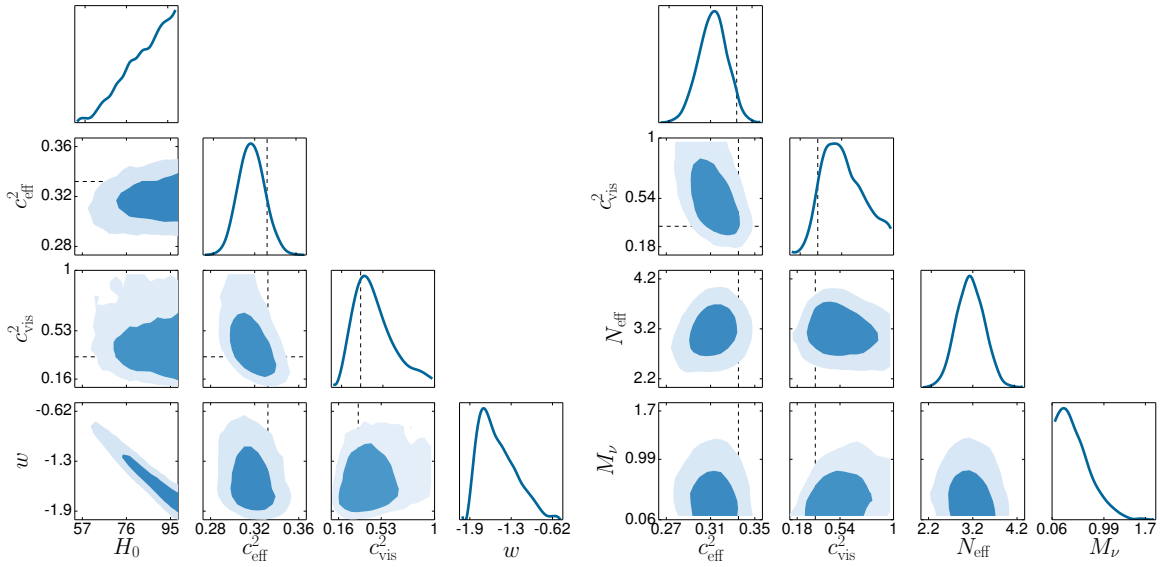

Figure 84: *Left.* Constraints on the interesting parameters for CMB+lensing data in the ΛCDM $c^2_{\rm eff}$+$c^2_{\rm vis}$+w model, where also the dark energy equation of state w is let free to vary. We also include the contour in H_0 due to the strong degeneracy of this parameter with w. Remarkably, a prior on H_0 from direct measurements of the Hubble constant would break this degeneracy without changing our constraints on ($c^2_{\rm vis}$, $c^2_{\rm eff}$). *Right.* Constraints on the interesting parameters for CMB+lensing data in the ΛCDM+$c^2_{\rm eff}$+$c^2_{\rm vis}$+$N_{\rm eff}$+m_ν model. We report the constraints on the total neutrino mass M_ν in eV. Dashed lines correspond to the standard values $(c^2_{\rm eff}, c^2_{\rm vis}) = (1/3, 1/3)$.

total neutrino mass is $M_\nu < 1.05$ eV, which is only slightly degraded compared with the ΛCDM+m_ν case $M_\nu < 0.85$ eV.

CMB + lensing						
Parameter	ΛCDM+$c^2_{\rm eff}$+$c^2_{\rm vis}$	+$N_{\rm eff}$	+m_ν	+w	+ α_s	+ $N_{\rm eff}$ + m_ν
$100\ \omega_b$	$2.162^{+0.047}_{-0.052}$	$2.174^{+0.057}_{-0.055}$	$2.124^{+0.048}_{-0.056}$	$2.179^{+0.052}_{-0.056}$	$2.180^{+0.050}_{-0.056}$	$2.136^{+0.060}_{-0.068}$
ω_{cdm}	$0.1163^{+0.0037}_{-0.0034}$	$0.1181^{+0.0054}_{-0.0051}$	$0.1186^{+0.0037}_{-0.0036}$	$0.1164^{+0.0037}_{-0.0035}$	0.1163 ± 0.0035	0.1184 ± 0.0055
H_0	68.3 ± 1.1	69.6 ± 2.9	$63.7^{+4.1}_{-2.6}$	$85.5^{+14.0}_{-4.5}$	$68.3^{+1.1}_{-1.2}$	$65.4^{+4.0}_{-4.2}$
$10^{+9}A_s$	$2.31^{+0.12}_{-0.15}$	$2.34^{+0.12}_{-0.16}$	2.36 ± 0.13	$2.27^{+0.12}_{-0.15}$	$2.35^{+0.13}_{-0.15}$	2.39 ± 0.14
n_s	$0.984^{+0.021}_{-0.020}$	$0.991^{+0.024}_{-0.025}$	$0.981^{+0.020}_{-0.018}$	$0.979^{+0.022}_{-0.021}$	$0.980^{+0.022}_{-0.019}$	$0.987^{+0.025}_{-0.022}$
τ_{reio}	$0.090^{+0.012}_{-0.014}$	$0.093^{+0.013}_{-0.015}$	$0.093^{+0.013}_{-0.014}$	$0.088^{+0.012}_{-0.014}$	$0.095^{+0.013}_{-0.016}$	$0.094^{+0.013}_{-0.016}$
$c^2_{\rm eff}$	0.314 ± 0.013	0.314 ± 0.013	$0.309^{+0.013}_{-0.014}$	$0.318^{+0.013}_{-0.014}$	$0.320^{+0.014}_{-0.016}$	$0.312^{+0.014}_{-0.013}$
$c^2_{\rm vis}$	$0.49^{+0.12}_{-0.22}$	$0.49^{+0.11}_{-0.21}$	$0.51^{+0.14}_{-0.19}$	$0.46^{+0.11}_{-0.23}$	$0.50^{+0.13}_{-0.22}$	$0.56^{+0.14}_{-0.24}$
$N_{\rm eff}$	–	$3.22^{+0.32}_{-0.37}$	–	–	–	$3.17^{+0.34}_{-0.37}$
M_ν [eV]	–	–	< 1.03	–	–	< 1.05
w	–	–	–	$-1.49^{+0.18}_{-0.38}$	–	–
α_s	–	–	–	–	-0.010 ± 0.010	–

Table 7: Constraints from CMB+lensing data on the values of the cosmological parameters for the ΛCDM+$c^2_{\rm eff}$+$c^2_{\rm vis}$, ΛCDM+$c^2_{\rm eff}$+$c^2_{\rm vis}$ + $N_{\rm eff}$, ΛCDM+$c^2_{\rm eff}$+$c^2_{\rm vis}$ + m_ν, ΛCDM+$c^2_{\rm eff}$+$c^2_{\rm vis}$ + w, ΛCDM+$c^2_{\rm eff}$+$c^2_{\rm vis}$ + α_s and ΛCDM+$c^2_{\rm eff}$+$c^2_{\rm vis}$+$N_{\rm eff}$+m_ν models. We report the 95% C.L. upper limit for the total neutrino mass M_ν, the mean values and 1σ ranges for all the other parameters.

8.6 Conclusions

In this work we have elucidated the physical effects of the $c^2_{\rm eff}$ and $c^2_{\rm vis}$ parameters on the CMB temperature and polarisation power spectra and the matter power spectrum. We find that the main signatures in the temperature and polarisation spectra are a shift of acoustic peaks, and a scale-dependent amplitude modulation for multipoles $\ell < 300$ i.e., including the first peak, whereas the amplitude change is roughly constant beyond that scale and up to multipole $\ell = 5000$. Interestingly, an increase in the $c^2_{\rm eff}$ parameter causes an increase in the amplitude, whereas an increase in the $c^2_{\rm vis}$ parameter causes the opposite effect. A similar amplitude change is found in the polarisation power spectrum. The matter power spectrum on the other hand, is mainly unaffected by these parameters at large scales, but it shows some dependence on these parameters at scales below matter-radiation equality. While $c^2_{\rm vis}$ effects are within 1%, we find that $c^2_{\rm eff}$ can cause changes of several percent already at $k = 0.2$ Mpc^{-1} for the values we have studied. Forthcoming large-scale structure surveys covering volumes of several Gpc^3 have in principle the statistical power to measure sub-percent effects on these scales. In practice, however, the accurate determination of the shape of the matter power spectrum and its interpretation in terms of the linear power spectrum on these scales is affected by other astrophysical processes and it remains to be seen whether a sub-percent accuracy can be achieved realistically.

We have also investigated the existence of degeneracies between these dark energy perturbation effective parameters and cosmological parameters, such as the total neutrino mass M_ν, effective number of relativistic species $N_{\rm eff}$, equation of state of dark energy w, and running of the spectral index α_s.

CMB + lensing + BAO		
Parameter	ΛCDM+$c^2_{\rm eff}$+$c^2_{\rm vis}$	$+m_\nu$
$100\ \omega_b$	$2.167^{+0.048}_{-0.054}$	$2.145^{+0.042}_{-0.058}$
ω_{cdm}	$0.1167^{+0.0020}_{-0.0023}$	$0.1150^{+0.0023}_{-0.0025}$
H_0	$68.25^{+0.63}_{-0.65}$	$67.60^{+0.98}_{-0.93}$
$10^{+9}A_s$	$2.30^{+0.10}_{-0.12}$	2.37 ± 0.13
n_s	$0.982^{+0.017}_{-0.014}$	$0.992^{+0.018}_{-0.014}$
τ_{reio}	0.090 ± 0.012	$0.094^{+0.013}_{-0.014}$
$c^2_{\rm eff}$	$0.314^{+0.011}_{-0.013}$	0.309 ± 0.013
$c^2_{\rm vis}$	$0.47^{+0.12}_{-0.19}$	$0.54^{+0.17}_{-0.18}$
M_ν [eV]	–	< 0.33

Table 8: Constraints from CMB+lensing+BAO data on the values of the cosmological parameters for the ΛCDM+$c^2_{\rm eff}$+$c^2_{\rm vis}$ and ΛCDM+$c^2_{\rm eff}$+$c^2_{\rm vis}$ + m_ν models. We report the 95% C.L. upper limit for the total neutrino mass M_ν, the mean values and 1σ ranges for all the other parameters.

We note that our constraints on (ω_b, $\omega_{\rm cdm}$, A_s, n_s) are significantly broader than in the standard case, but in this work we concentrate on results for $c^2_{\rm eff}$ and $c^2_{\rm vis}$ and on their degeneracies with extended cosmology parameters. We find that the $c^2_{\rm eff}$ and $c^2_{\rm vis}$ parameters are anti-correlated, that α_s is slightly anti-correlated with $c^2_{\rm eff}$, but also that there are no major correlations between ($c^2_{\rm eff}$, $c^2_{\rm vis}$) and $N_{\rm eff}$, and for the first time, we show that there is no significant correlation with the total neutrino mass M_ν either.

One can argue that our choice of constant $c^2_{\rm eff}$ and $c^2_{\rm vis}$ is arbitrary and may not be sufficient to describe massive neutrinos from low momenta to high momenta. We have to bear in mind that these are effective parameters: in the absence of any significant deviations from their standard, constant, values they should be interpreted in the light of a null test hypothesis. We can however go beyond this interpretation by assuming that $c^2_{\rm eff}$ depends on the momentum q and expand this dependence to linear order: $c^2_{\rm eff}(q) = c^2_{\rm eff(0)} + c^2_{\rm eff(1)}\,(q - q_{\rm avg}) + \ldots$, where $q_{\rm avg}$ ($\simeq 3.15$) is the average momentum for neutrinos. From this expansion, it follows that being sensitive to $c^2_{\rm eff(1)}$ is equivalent to being sensitive to some $c^2_{\rm eff}$ for a relativistic momentum bin versus a non-relativistic momentum bin. On the other hand, a modification of the neutrino mass produces a similar effect, since it regulates the time scale at which massive neutrinos become non-relativistic. In our analysis we found that, by fixing the values of ($c^2_{\rm eff}, c^2_{\rm vis}$), the dependence on the mass is negligible. This finding indicates therefore that our choice of constant ($c^2_{\rm eff}, c^2_{\rm vis}$) is a good approximation even for a q-dependent $c^2_{\rm eff}$.

Already with state-of the art CMB data available[7] (i.e., Planck 2013 data release and WMAP low ℓ polarisation data) alone or in combination with other data sets (e.g., BAO), we can conclude that these parameters are not significantly degenerate with any other, and hence that the detection of the anisotropies of the cosmic neutrino background is robust. We find no evidence for deviations from the standard neutrino model, i.e., 3 neutrino families with effective parameters ($c^2_{\rm eff}$, $c^2_{\rm vis}$)=(1/3, 1/3) when we consider CMB data only (including CMB lensing).

7 This study was completed before the 2015 data release by *Planck*. In Ref. [19], bounds on ($c^2_{\rm vis}$, $c^2_{\rm eff}$) have now shrunk down to (0.331 ± 0.037,0.3242 ± 0.0059), and hence corroborate our conclusions.

However the inclusion of ($c^2_{\rm eff}$, $c^2_{\rm vis}$) parameters degrades the constraints on some of the ΛCDM model parameters, such as the physical matter density and the slope of the primordial power spectrum. In particular, high values of n_s, including a scale invariant power spectrum ($n_s = 1$), become allowed. This indicates that the significance of the deviation from a scale invariant power spectrum, with all its consequences for inflationary models, relies on assuming standard neutrino properties. It also means that future data sets providing independent measurements of these parameters, such as the matter power spectrum from galaxy surveys or smaller scale CMB polarization, could help to remove degeneracies and greatly improve the sensitivity to ($c^2_{\rm eff}$, $c^2_{\rm vis}$). This is expected to be the case for the full Planck data on temperature and polarisation anisotropies. Measurements of the shape of the matter power spectrum, even on linear scales, should also greatly help to lift the $\{n_s, c^2_{\rm eff}, c^2_{\rm vis}\}$ degeneracies.

9

PHYSICAL EFFECTS OF NEUTRINO MASSES IN FUTURE COSMOLOGICAL DATA

This chapter is adapted from a publication in JCAP [53].

9.1 Introduction

A wide program of future cosmological experiments is planned or proposed, in order not only to pin down cosmological parameters, but also to shed light on fundamental physics related to cosmology. These cosmological experiments include high precision galaxy redshift surveys, such as Euclid, DESI, WFIRST (see [250] and references therein), high precision cosmic shear surveys, such as Euclid and LSST, and finally Cosmic Microwave Background experiments aimed at more accurate polarization measurements, such as CORE [117], [207], [208] and CMB-Stage IV [42], [311].

However, besides experimental sensitivity, parameter constraints are limited by degeneracies: a degeneracy indicates the ability of one parameter to mimic the effect of another parameter on a particular observable, making it impossible to disentangle them and to determine the value of each parameter separately. The key approach to tackle this problem consists in a joint analysis of complementary probes with different degeneracy directions in parameter space. For that reason, the next step in the era of precision cosmology will be based on the synergy of high- and low- redshift probes.

One of the parameters that will benefit from such an approach is the neutrino mass sum (hereafter M_ν) introduced in section 3.2.1. Indeed the impact of massive neutrinos on cosmological observables comes from a very special effect: light massive neutrinos behave as radiation before their non-relativistic transition, while afterwards they gradually become a matter component; therefore their impact on cosmological probes at different redshifts is closely related to their mass.

The neutrino mass effects have been widely studied in the literature [84], [293], [392], [395] and their impact on CMB and large scale structures on linear scales is well known. Even on non-linear scale, the neutrino mass effect is better understood thanks to recent progress in N-body simulations [36], [105], [124], [125]. However, neutrino cosmology is about to face a revolution for two reasons.

First of all, current upper bounds on the neutrino mass sum are getting closer and closer to the minimum value allowed by the inverted hierarchy $M_\nu \sim 0.11$ eV [27], [199], [466]. Thus, future experiments will look at ultra-light neutrinos that became non-relativistic in a relatively recent cosmological epoch. Very small neutrino masses will have a different effect on the cosmological evolution and, thus, a different impact on cosmological observables. For instance, even if the majority of neutrinos with $m_\nu \leq 600$ meV go non-relativistic after photon decoupling, a small number of them (contributing to the low momentum tail of the phase space distribution) are already partially non-relativistic at decoupling. For $m_\nu \sim 300$ meV this could still have small effects, but not for $m_\nu \sim 60$ meV. Similarly,

neutrinos becoming relativistic soon after photon decoupling can produce a distortion of the CMB temperature spectrum through the early Integrated Sachs-Wolfe effect, but again this can only be significant for masses of a few hundreds of meV. Instead, the neutrinos studied in this work could have individual masses of at most 100 meV.

Secondly, future galaxy surveys will reach a very high sensitivity on very small scales. As for now, the use of small scale data is limited by the uncertainty on non-linear structure formation, which is difficult to model, especially in presence of massive neutrinos [58], [142], [150], [225], [254]. A major theoretical goal in the next few years will be to provide a better understanding of the processes governing clustering on small scales. Having the non-linear effects under control, we will be able to exploit small scale data in order to break degeneracies. The neutrino mass effects are already important on linear scales, but by including smaller and smaller scales one would have a better lever arm and improve the constraints on M_ν.

The aim of this work is to investigate the physical effects induced by massive neutrinos as they will be unveiled by future cosmological data.

We will pay particular attention to the correlation between M_ν and other cosmological parameters, and show that directions of degeneracy are very sensitive to probes of the cosmic history at different epochs. For some combinations of CMB and Large Scale Structure data sets, a correlation between M_ν and $\tau_{\rm reio}$ has already been observed in references [42], [407], but its interpretation is far from obvious and requires a detailed investigation. This correlation is very important, for the reason that independent measurements of the optical depth by 21cm surveys will lead to a remarkable improvement on the sensitivity to the neutrino mass [407]. We will confirm this expectation with a dedicated forecast showing that even the minimum allowed value of the summed neutrino mass could be detected at the 5σ level in a time scale of about ten years.

The study is organized as follows: In section 9.2, 9.3 and 9.4 we study in detail the effect of a variation of the summed neutrino mass in CMB, Baryonic Acoustic Oscillation (BAO) and Large Scale Structure (LSS) observables, respectively. In particular we will carefully describe and explain the degeneracies with other relevant cosmological parameters. In section 9.5 we will present the results of our Markov Chain Monte Carlo forecast of the sensitivity of future CMB, BAO, LSS and 21cm experiments. Finally in section 9.6 we will draw our conclusions.

9.2 Effect of a small neutrino mass on the CMB

9.2.1 *General parameter degeneracies for CMB data*

In the minimal, flat, 6-parameter ΛCDM model, it is well-known that the CMB temperature and polarisation unlensed spectra are determined by a number of effects[1], which remain identical as long as one fixes quantities usually depending on distance and density ratios, such as:

- the sound horizon angular scale $\theta_s(z_{\rm dec}) = \frac{d_s(z_{\rm dec})}{d_A(z_{\rm dec})}$ at decoupling,
- the diffusion angular scale $\theta_d(z_{\rm dec}) = \frac{d_d(z_{\rm dec})}{d_A(z_{\rm dec})}$ at decoupling,
- the baryon-to-photon ratio $R_{\rm dec} = \frac{3\rho_b}{4\rho_\gamma}\Big|_{\rm dec}$ at decoupling,

1 For a review of these effects, see e.g. [323], section 5.1 of [392], and [317].

- the redshift of radiation-to-matter equality $z_{\rm eq} = \frac{\rho_m^0}{\rho_r^0} - 1$,
- the redshift of matter-to-cosmological-constant equality $z_\Lambda = \left(\frac{\rho_\Lambda^0}{\rho_r^0}\right)^{1/3} - 1$.

The CMB spectra also depend on a few extra parameters, like the scalar amplitude and tilt (A_s, n_s) and the optical depth at reionization $\tau_{\rm reio}$. However, bearing in mind that the small-ℓ (large angular) part of the spectra is loosely constrained due to cosmic variance, the parameters z_Λ, A_s and $\tau_{\rm reio}$ are always less constrained by CMB data than $(\theta_s, \theta_d, R, z_{\rm eq}, n_s)$, and also than the combination $A_s e^{-2\tau_{\rm reio}}$ giving the overall spectrum normalisation on small angular scales. The fact that we actually measure lensed CMB spectra gives extra information on the amplitude and slope of the matter power spectrum $P(k, z)$ at low redshift: in practice, this increases the sensitivity to the parameters (A_s, z_Λ), which enter into the normalisation of $P(k, z)$.

Adding neutrino masses to the model leads to several new effects studied extensively in the literature [315], [317], [392]:

(A) Neutrino masses affects the background expansion history. If we rely on standard assumptions for the photon and background densities ($T_{\rm cmb} = 2.726$ K, $N_{\rm eff} = 3.046$) and further fix ω_b and $\omega_{\rm cdm}$, the changes in the background evolution caused by neutrino masses are confined to late times. Then, the values of $d_s(z_{\rm dec})$, $d_d(z_{\rm dec})$, $R_{\rm dec}$ and $z_{\rm eq}$ are preserved, and the neutrino masses only impacts the angular diameter distance (and therefore, θ_s and θ_d in an equal way) and z_Λ (and hence, the loosely constrained late ISW effect). It is even possible to choose an appropriate value of the cosmological constant for each set of neutrino masses, in order to keep a fixed $d_A(z_{\rm dec})$: in that case, the impact of neutrino masses on the background is confined to variations of z_Λ and of the late ISW effect, and cannot be probed accurately due to cosmic variance, unless external non-CMB datasets come into play.

(B) At the perturbation level, massive neutrinos interact gravitationally with other species and produce small distortions in the CMB peaks. For individual neutrino masses m_ν smaller than ~ 600 meV, the neutrinos become non-relativistic after recombination: in that case the distortions can only be caused by the early ISW effect, and affect the CMB temperature spectrum in the multipole range $50 < \ell < 200$ [315], [392], [395]. Note that this neutrino-mass-induced early ISW effect takes place even if the redshift of equality is kept fixed: it is different from the redshift-of-equality-induced early ISW effect, which affects the height of the first CMB peak in the range $100 < \ell < 300$.

(C) Finally, at the lensing level, massive neutrinos slow down the growth of small-scale structure (leading to the well-known suppression factor $1 - 8\omega_\nu/\omega_m$ in the small-scale matter power spectrum at redshift zero) and globally decrease the impact of CMB lensing: the peaks are less smoothed and the damping tail less suppressed [401].

All these effects have played a role in previous constraints on neutrino masses from CMB data alone, or combined with other probes. Interestingly, while the sensitivity of CMB instruments increases with time, different effects come to dominate the neutrino mass constraints: early ISW effects **(b)** with WMAP alone [305], lensing effects **(c)** with Planck alone [19], and background effects **(a)** when combining CMB data with direct measurements of H_0 [509]. There are now several combinations of cosmological probes giving a 95%CL upper bound on the summed mass $M_\nu \equiv \sum m_\nu$ of the order of

120 meV to 150 meV [27], [199], [272], [466], while neutrino oscillation data enforces $M_\nu \geq 60$ meV at 95%CL [275]. The remaining conservatively allowed window is so narrow, $\Delta M_\nu \sim 90$ meV, that the impact of a realistic variation of the neutrino masses on the CMB is getting really small. Our purpose in section 9.2.3 is to study precisely this impact, and to understand the degeneracy between M_ν and other parameters when using future CMB data only, specifically for the very low mass range 60 meV$< M_\nu <$ 150 meV. This requires some preliminary remarks in section 9.2.2.

9.2.2 *CMB data definition*

The discussion of degeneracies is meaningless unless we specify which data set, and which experimental sensitivities, we are referring to. In this work, we take as a typical example of future CMB data a next-generation CMB satellite similar to the project COrE+, submitted to ESA for the call M4. A new version of CORE was recently submitted again for the call M5 [207], [208], with a small reduction of the instrumental performances, mainly in angular resolution. However, COrE+ and CORE-M5 are very similar, and the conclusions of this work would not change significantly by adopting the CORE-M5 settings.

When displaying binned errors in C_l plots, and when doing MCMC forecasts with mock data and synthetic likelihoods, we assume that this CORE-like experiment is based on 9 frequency channels with sensitivity and beam angles given in footnote[2]. We mimic the effect of sky masking by adopting a Gaussian likelihood with an overall rescaling by a sky fraction $f_{\rm sky} = 0.70$.

Our dataset consists primarily of temperature and E-mode polarisation auto-correlation and cross-correlation spectra $C_\ell^{TT}, C_\ell^{EE}, C_\ell^{TE}$. To get more information on CMB lensing, one can either analyse B-mode maps (in absence of significant primordial gravitational waves, the B-mode only comes from CMB lensing and foregrounds) and add the C_ℓ^{BB} spectrum to the list of observables; or perform lensing extraction with a quadratic or optimal estimator [419], and add the CMB lensing potential spectrum $C_\ell^{\phi\phi}$ to the list of observables (equivalently one could use the deflection spectrum $C_\ell^{dd} = \ell(\ell+1)C_\ell^{\phi\phi}$). We cannot use both C_ℓ^{BB} and $C_\ell^{\phi\phi}$ in the likelihood: the same information would be counted twice. Here we choose to use the lensing potential spectrum, which better separates the contribution of different scales to lensing, that would be mixed in the C_ℓ^{BB} spectrum by some integration kernel. To give an example, we will see in Figure 85 (bottom plots) that the neutrino mass effect on $C_\ell^{\phi\phi}$ is more pronounced on small angular scales, while in the lensed C_ℓ^{BB} this effect would be nearly independent of ℓ[3].

So the CMB data set that we have in mind consists in measurements for $C_\ell^{TT}, C_\ell^{EE}, C_\ell^{TE}, C_\ell^{\phi\phi}$, with a synthetic Gaussian likelihood similar to that in [477], and a lensing extraction error spectrum $N_\ell^{\phi\phi}$ based on the quadratic estimator method [452] for the EB estimator. In the likelihood, we keep the lensed $C_\ell^{TT}, C_\ell^{EE}, C_\ell^{TE}$. Indeed, unlike C_ℓ^{BB}, these spectra are only weakly affected by lensing, and the lensing information redundancy between lensed temperature/polarisation spectra and the $C_\ell^{\phi\phi}$ spectrum is small enough for being negligible at the instrumental sensitivity level of a CORE-like experiment [206].

2 Assumed specifications for a COrE+ - like experiment: frequencies in GHz: [100, 115, 130, 145, 160, 175, 195, 220, 255]; $\theta_{\rm fwhm}$ in arcmin: [8.4, 7.3, 6.46, 5.79, 5.25, 4.8, 4.31, 3.82, 3.29]; temperature sensitivity in [μK arcmin] : [6.0, 5.0, 4.2, 3.6, 3.8, 3.8, 3.8, 5.8, 8.9]; polarisation sensitivity in [μK arcmin] : [8.5, 7.0, 5.9, 5.0, 5.4, 5.3, 5.3, 8.1, 12.6].

3 However, we will also see that *within the range in which error bars are small*, the neutrino mass effect on $C_\ell^{\phi\phi}$ is also *nearly* ℓ-independent, so we may expect that trading $C_\ell^{\phi\phi}$ against C_ℓ^{BB} in the likelihood would have a minor impact on our conclusions.

9.2.3 *Degeneracies between very small M_ν's and other parameters with CMB data only*

We will discuss the impact of increasing the neutrino mass, while keeping various parameters or combination of parameters fixed. We illustrate this discussion with the plots of Figure 85, showing the spectrum ratio between different models sharing a summed mass $M_\nu = 150$ meV and a baseline model[4] with $M_\nu = 60$ meV. The plots shows the residuals of the lensed TT (top), lensed EE (middle) and lensing potential (bottom) power spectrum, as a function of multipoles ℓ with a linear (left) or logarithmic (right) scale. The light/pink and darker/green shaded rectangles refer respectively to the binned noise spectrum of a cosmic-variance-limited or CORE-like experiment, with linear bins of width $\Delta\ell = 25$. All spectra are computed with the Boltzmann solver CLASS[5] [109], [390], [396], version 2.5.0, with the high precision settings cl_permille.pre.

Our discussion will also be illustrated by the results of Monte Carlo Markov Chains (MCMC) forecasts for our CORE-like experiment: Figure 86 gives the 2D probability contours for the pairs of parameters most relevant to our discussion. The MCMC forecasts are done with the MONTEPYTHON package[6] [68].

The main conclusions can be reached in four steps:

1. We first assume that we increase neutrino masses with respect to the baseline model, while keeping the parameters $\{\omega_b, \omega_{\rm cdm}, h, n_s, A_s, \tau_{\rm reio}\}$ fixed (green solid curve in Figure 85). Given the discussion in point **(a)**, we expect that this is not a very clever choice, because the angular diameter distance is not preserved. So if the baseline model is a good fit to the data, the new model will be discrepant. Indeed, by looking especially at the top left and middle left plots in Figure 85, we see even-spaced oscillations signaling a change in the angular diameter distance, and the residuals are far above the instrumental noise.

2. We then perform the same increase in M_ν, but now with a fixed angular diameter distance to recombination, which means that $\{\omega_b, \omega_{\rm cdm}\}$ are still fixed, but h varies. With CLASS, this is easily achieved by keeping the input parameter $100\theta_s$ constant. Since the early cosmology and the sound horizon at decoupling are fixed, fixing θ_s means adjusting H_0 and the angular diameter distance for each M_ν. Then, the angular diffusion scale θ_d is also automatically fixed. In Figure 85, this transformation corresponds to the dashed red residuals. As expected, the previous oscillations disappear in the residuals. The only visible effects are much smaller oscillations, some tilt at large ℓ due to a different level of CMB lensing, and a tilt at small ℓ due to a different late ISW effect. However, both effects are below cosmic variance. We conclude that, the measurement of the temperature and E-mode spectra alone does not allow us to distinguish between $M_\nu = 60$ meV

4 Our discussion is general and the value of cosmological parameters for the baseline model is unimportant. We choose Planck-inspired values, $\{\omega_b, \omega_{\rm cdm}, h, n_s, A_s, \tau_{\rm reio}, M_\nu\} = \{0.02214, 0.12070, 0.6663, 0.9624, 2.12 \times 10^{-9}, 0.0581, 0.06\,{\rm eV}\}$, giving an angular sound horizon at recombination θ_s (which defines the angular scale of the CMB acoustic peaks) roughly equal to $100\,\theta_s = 1.04075$. In this work, our total neutrino mass M_ν is assumed to be shared equally among the three species, like in the degenerate (DEG) model. This choice is not random: it is motivated by the fact that the cosmological impact of different mass splittings is negligible, at least as long as one compares some DEG, NH (Normal Hierarchy) and IH (Inverted Hierarchy) models all sharing the same total mass M_ν. This is not necessarily true when comparing them with a model with "one massive, two massless neutrinos", which departs by a much larger amount at the level of the matter power spectrum [392], [395]. Hence, by varying the mass M_ν of the DEG model, we obtain results which apply at the same time, in very good approximation, to the two realistic cases NH and IH.

5 http://class-code.net

6 http://baudren.github.io/montepython.html

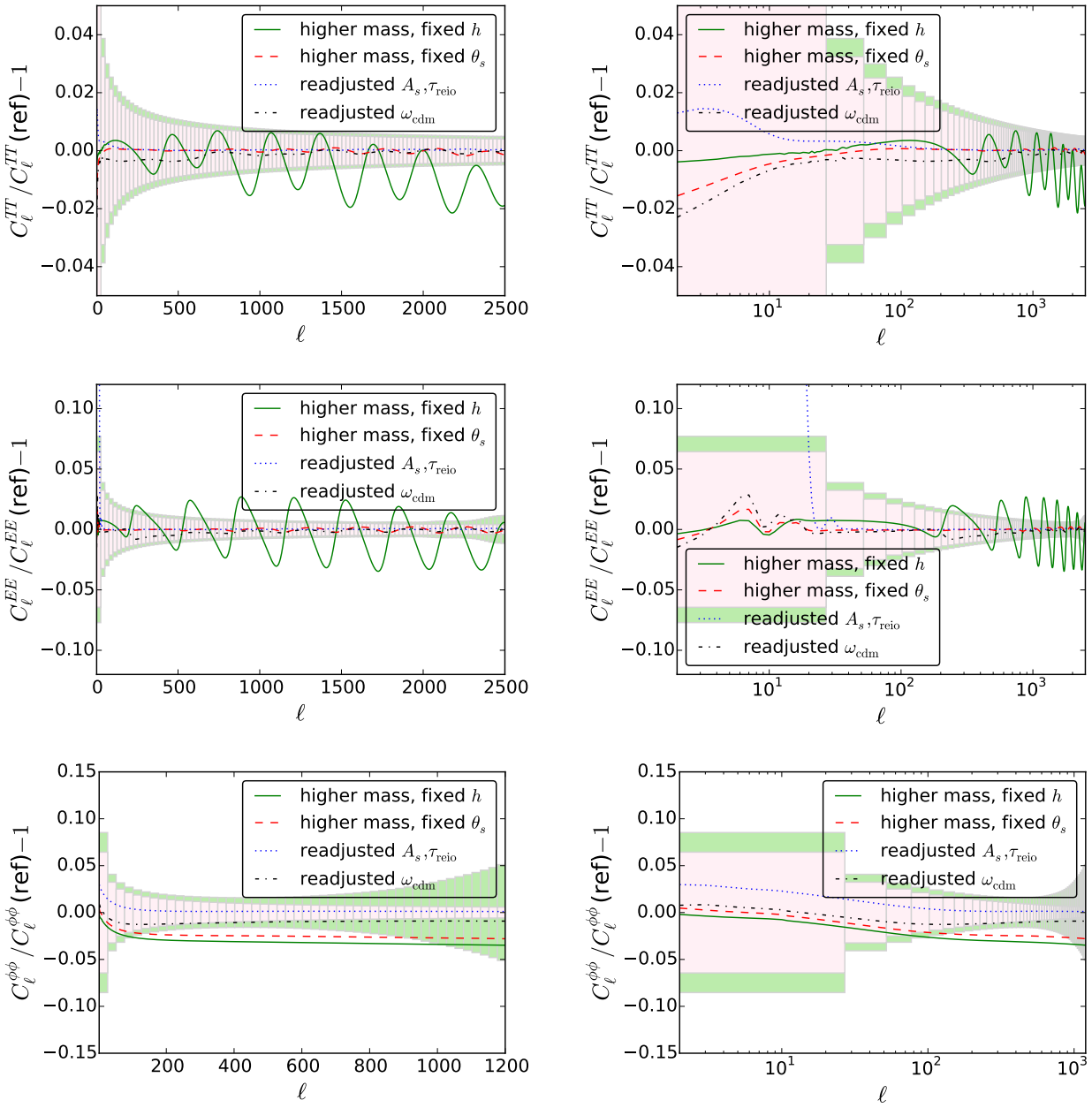

Figure 85: Relative change in the CMB spectra induced by increasing the summed neutrino mass from $M_\nu = 60$ meV to $M_\nu = 150$ meV. The plots show the residuals of the lensed TT (top), lensed EE (middle) and lensing potential (bottom) power spectrum, as a function of multipoles ℓ with a linear (left) or logarithmic (right) scale. The light/pink and darker/green shaded rectangles refer, respectively, to the binned noise spectrum of a cosmic-variance-limited or CORE-like experiment, with linear bins of width $\Delta\ell = 25$. The physical baryon density ω_b and the scalar spectral index n_s are kept fixed. In the first case (green solid line) the value of the Hubble constant is fixed at the reference value, while in all the other cases (labeled as fixed θ_s) h decreases in order to keep θ_s consistent with the reference model. Moreover, in the third case (dotted blue line), we tried to compensate for the changes in the lensing spectrum by increasing A_s, and in the fourth case (dotted-dashed black) we aim at the same result by increasing $\omega_{\rm cdm}$.

and 150 meV, and that in a CMB analysis the parameters (M_ν, H_0) are inevitably correlated, as it is well known, and illustrated by the upper left plot in Figure 86.

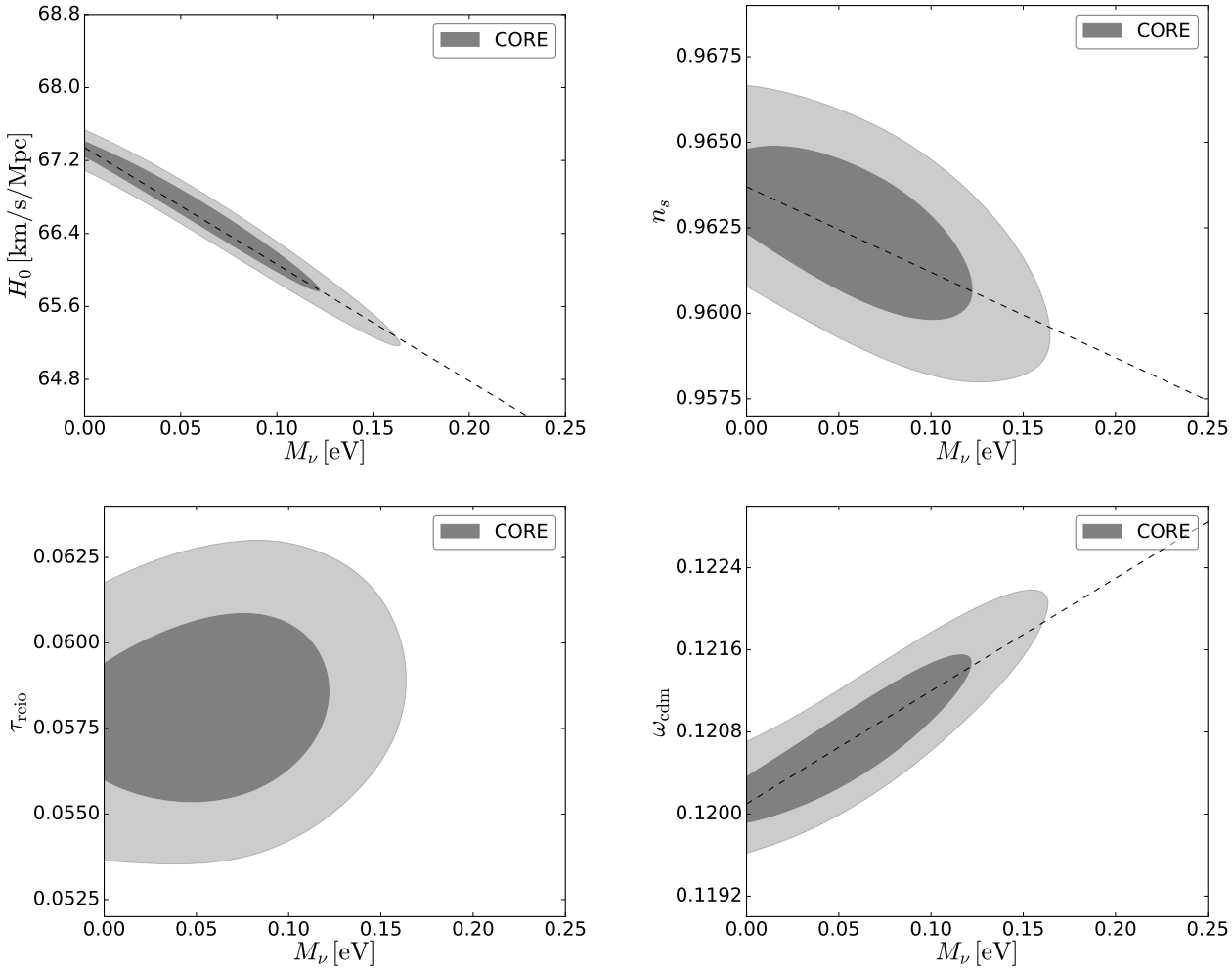

Figure 86: 68% and 95% CL posterior probability contour levels for different pairs of parameters, for an MCMC forecast of the sensitivity of a CORE-like experiment to the parameters of a 7-parameter model (ΛCDM plus total neutrino mass M_ν). The CMB data is assumed to consist of measurements of the TT, EE, TE and lensing potential spectra.

We can try to quantify this correlation. A simple numerical exercise shows that in order to keep the same value of θ_s while fixing $\{\omega_b, \omega_{\rm cdm}\}$ and varying M_ν, one finds a correlation

$$\Delta h \simeq -0.09 \left(\frac{\Delta M_\nu}{1\ {\rm eV}}\right) \ . \tag{9.2.1}$$

We will come back to this relation later, and show that the correlation angle changes slightly when other effects are taken into account.

We now look at the bottom plots in Figure 85, showing variations in the lensing potential spectrum. The dashed red line is consistent with the fact that a higher neutrino mass implies more suppression in the small-scale matter power spectrum $P(k, z)$, and hence in the large-ℓ lensing potential spectrum $C_l^{\phi\phi}$. A comparison with the instrumental errors show that this

effect is potentially relevant: the dashed red residual is outside the 68% error bars in about 30 consecutive bins, leading to a χ^2 increase by many units. It is also visible that the neutrino mass effect would be detectable only in a range given roughly by $50 \leq \ell \leq 800$, in which the effect is nearly equivalent to a suppression by some ℓ-independent factor (by about 3% in our example).

Hence, we see that a CORE-like CMB experiment could in principle discriminate between $M_\nu = 60$ meV and 150 meV, and that the effect of the neutrino mass with fixed $\{\omega_b, \omega_{\rm cdm}, \theta_s, n_s, A_s, \tau_{\rm reio}\}$ can be simply summarised as an apparent mismatch between the normalisation of the TT,TE,EE spectra and that of the CMB lensing spectrum. To check whether the distinction can be made in reality, and not just in principle, we must consider whether the variation of other cosmological parameters could cancel this effect, and lead to new parameter correlations with M_ν.

As explained in references [20], [467], in a pure ΛCDM model with no massive neutrinos, the dependence of the global amplitude of $C_\ell^{\phi\phi}$ on the cosmological parameters is given approximately by:

$$\ell^4 C_\ell^{\phi\phi} \propto A_s \left(\Omega_m^{0.6} h\right)^{2.5} \quad (\ell > 200),$$

and in terms of ω_m

$$\ell^4 C_\ell^{\phi\phi} \propto A_s \omega_m^{3/2} h^{-1/2} \quad (\ell > 200),$$

plus an additional minor dependence on Ω_m. If we include massive neutrinos, the linear growth of structure becomes scale dependent, thus the exact impact of M_ν on $C_\ell^{\phi\phi}$ is ℓ-dependent, but only by a small amount in the range constrained by observations. Anyway, given that the neutrino mass slows down the growth of cold dark matter perturbations, we can generally assume:

$$\ell^4 C_\ell^{\phi\phi} \propto A_s \omega_m^{3/2} h^{-1/2} M_\nu^{-\alpha}, \tag{9.2.2}$$

with $\alpha > 0$. This qualitative result shows that in order to compensate an increase of M_ν, we have a priori two possibilities: increasing A_s, or increasing ω_m. We will explore them one after each other in the next points, and arrive at interesting conclusions.

3. We have the possibility to increase A_s in order to compensate for the neutrino mass effect in $C_\ell^{\phi\phi}$, while keeping $A_s e^{-2\tau_{\rm reio}}$ fixed, in order to have the same overall normalisation of the large-ℓ temperature and polarisation spectra. Hence, this transformation implies a higher reionisation optical depth $\tau_{\rm reio}$. We could expect that, this change in the optical depth is unobservable due to cosmic variance, which would mean that there is a parameter degeneracy at the level of CMB data, and that the three parameters $(M_\nu, A_s, \tau_{\rm reio})$ are correlated.

   This turns out not to be the case. In our example, the higher neutrino mass shifts the lensing potential down by 3%. This could be compensated by increasing A_s by 3% as well, and shifting $\tau_{\rm reio}$ by $\Delta\tau_{\rm reio} = \frac{1}{2}\log 1.03 \simeq 0.015$. This is a very big shift compared to the expected sensitivity of a CORE-like experiment, $\sigma(\tau_{\rm reio}) \simeq 0.002$. Hence this degeneracy should not be present.

   This is illustrated by the third set of curves (dotted blue) in Figure 85. We estimated numerically the reduction factor for $C_{400}^{\phi\phi}$ in the second model (red dashed). We increased A_s by exactly this factor, keeping $A_s e^{-2\tau_{\rm reio}}$ fixed. The new model has a much larger reionisation bump in C_ℓ^{EE}, with a residual largely exceeding the error bars.

   The lower left plot in Figure 86 brings the final confirmation that in a global fit of CMB data, with lensing extraction included, there is no significant correlation between M_ν and $\tau_{\rm reio}$.

At this point, we still expect that very small neutrino masses could be accurately measured by CMB data alone, unless the other way to compensate for the neutrino mass effect in the lensing potential (by increasing ω_m) works better than increasing A_s, and does lead to some parameter degeneracy. This is what we will explore in the final step of this discussion.

4. Considering that ω_b is accurately determined by the first peak ratios, we can increase $\omega_{\rm m} = \omega_{\rm b} + \omega_{\rm cdm}$ by enhancing $\omega_{\rm cdm}$ only. It is difficult to infer analytically from equation (9.2.2) the amount by which $\omega_{\rm cdm}$ should be enhanced in order to cancel the effect of M_ν in the lensing potential, because during the transformation, we must keep θ_s fixed; since θ_s depends on both h and $\omega_{\rm m}$, the Hubble parameter will also change. In the example displayed in figure 85, we found numerically the factor by which we should increase $\omega_{\rm cdm}$ (with fixed $\omega_{\rm b}$ and θ_s), in order to nearly cancel the neutrino mass effect in the lensing power spectrum. This leads to the dotted-dashed black curve. In the lensing potential plots (bottom), the new residual is back inside the cosmic variance band.

   The problem with the previous attempt was that changing $\tau_{\rm reio}$ had "side effects" (namely, on the reionisation bump) potentially excluded by the data. Increasing $\omega_{\rm cdm}$ also has "side effects": it affects the redshift of radiation/matter equality $z_{\rm eq}$, and hence the amplitude of the first two peaks (through gravity boost effects and through the early ISW effect); it also affects the redshift of matter/Λ equality z_Λ and the late ISW effect; and finally, it has a small impact on the angular diameter distance. All these effects can be identified by looking at the details of the dotted-dashed black residuals in figure 85. The key point is that a tiny enhancement of $\omega_{\rm cdm}$ is enough to compensate for the neutrino mass effect in $C_\ell^{\phi\phi}$, in such way that the "side effects" all remain well below cosmic variance. Hence, we expect a parameter degeneracy between M_ν and $\omega_{\rm cdm}$ when using CMB data alone, that will compromise the accuracy with which the neutrino mass can be pinned down, and lead to a correlation between these parameters. We notice that this correlation between M_ν and $\omega_{\rm cdm}$ is completely driven by CMB lensing. Removing lensing extraction would diminish the correlation factor. The residual correlation would be due to the lensing of the C_ℓ^{TT} spectrum (related to the tiny deviation of the black dot dashed line from the red dashed line on small scales in the top left panel of figure 85), and it would disappear with delensing.

   This is confirmed by the lower right plot in Figure 86: in a global fit of CMB data, we obtain a degeneracy direction approximately parametrised by the slope of the dashed curve in that plot,

$$\Delta\omega_{\rm cdm} = 0.01\,\Delta M_\nu \sim \Delta\omega_\nu \ . \tag{9.2.3}$$

   Which is exactly the relation we used in figure 85, when transforming to the fourth model (dotted-dashed black curves).

We can reach the main conclusion of this section: for CMB data alone (including lensing extraction), there is no significant parameter degeneracy between $(M_\nu, A_s, \tau_{\rm reio})$, but there is one between M_ν and $\omega_{\rm cdm}$. This is the most pronounced parameter degeneracy involving the neutrino mass when the cosmological model is parametrised by $\{\omega_b, \omega_{\rm cdm}, \theta_s, n_s, A_s, \tau_{\rm reio}\}$, and the correlation is given approximately by equation (9.2.3).

If instead the model is parametrised by $\{\omega_b, \omega_{\rm cdm}, h, n_s, A_s, \tau_{\rm reio}\}$, for the obvious reasons discussed previously, there is an additional clear correlation between M_ν and h. We return to the correlation

factor, that we estimated before to be given by equation (9.2.1). This equation is actually not a very good fit of the contours in the upper left plot of Figure 86: the dashed line in that plot corresponds to

$$\Delta h \simeq -0.13 \left(\frac{\Delta M_\nu}{1\ \mathrm{eV}}\right) \ . \tag{9.2.4}$$

The explanation for this mismatch is simple. Equation (9.2.1) assumed fixed θ_s *and* $\omega_{\rm cdm}$ values. If instead we try to keep θ_s fixed while varying $\omega_{\rm cdm}$ according to equation (9.2.3), we see increased correlation between M_ν and h, as shown by equation (9.2.4)[7].

Hence, with CMB data only, the clearest and most important degeneracies involving the summed neutrino mass are between M_ν and $\omega_{\rm cdm}$ (due to lensing) and M_ν and h (due to the angular diameter distance). There are other correlations, but they are much less pronounced. The third one would be between M_ν and n_s [268]. This can be understood by looking closely at the dotted-dashed line in figure 85 (lower right plot). The variation of $\omega_{\rm cdm}$ did not only rescale the amplitude of the CMB lensing potential, it also generated a small positive tilt. The reason is that we have decreased the ratio $\omega_{\rm b}/\omega_{\rm cdm}$, thus changing the shape parameter controlling the effective spectral index of the matter power spectrum $P(k)$ for $k > k_{\rm eq}$: a smaller baryon amount relative to CDM implies a bluer spectrum. Hence, the (M_ν, $\omega_{\rm cdm}$) degeneracy is more pronounced when it goes together with a tiny decrease of the tilt n_s, by such a small amount that it would not conflict with temperature and polarisation data. This negative correlation is visible in Figure 86, upper right plot.

9.3 Effect of neutrino mass on the BAO scale

The acoustic oscillations of the baryon-photon fluid that we observe in the CMB power spectrum produce a characteristic feature in the two point correlation function. In Fourier space the feature is located at a peculiar scale, the BAO scale, $k_{\rm BAO} = 2\pi/r_s(z_{\rm drag})$, where $r_s(z_{\rm drag})$ is the comoving sound horizon at baryon drag

$$r_s(z_{\rm drag}) = \int_0^{\tau_{\rm drag}} c_s d\tau = \int_{z_{\rm drag}}^{\infty} \frac{c_s}{H(z)} dz.$$

The observed scale, assuming an isotropic fit of a galaxy sample[8], provides the ratio $r_s(z_{\rm drag})/D_V(z_{\rm BAO})$, where D_V is the volume distance, defined as

$$D_V(z) = \left[z/H(z)(1+z)^2 d_A(z)^2\right]^{1/3},$$

and $D_A = (1+z)d_A(z)$ is the comoving angular diameter distance. In the ΛCDM model with massive neutrinos, the ratio $r_s(z_{\rm drag})/D_V(z_{\rm BAO})$ can only depend on the four parameters $\{\omega_{\rm b}, \omega_{\rm cdm}, \omega_\nu, h\}$. More precisely, $r_s(z_{\rm drag})$ depends on the three parameters $\{\omega_{\rm b}, \omega_{\rm cdm}, h^2\}$, while for redshifts below the non-relativistic transition, $z \ll z_{\rm nr} \sim 2\times 10^3 (m_\nu/1\,\mathrm{eV})$, $D_A(z)$ depends only on $\omega_{\rm tot} = \omega_{\rm b} + \omega_{\rm cdm} + \omega_\nu$ and on h, because it can be approximated as

$$D_A(z) = \int_0^z \frac{c dz'}{H(z')} \simeq 3000 \int_0^z \frac{dz'}{\sqrt{\omega_{\rm tot}(1+z')^3 + (h^2 - \omega_{\rm tot})}}\ \mathrm{Mpc}. \tag{9.3.1}$$

7 Note that we estimated the correlation factor in equation (9.2.3) with one significant digit, and in equation (9.2.4) with two significant digits: this is consistent with the fact that the correlation is much more clear and pronounced in the second case (the ratio of the minor over major axis is much smaller).

8 Anisotropic fit allow to disentangle the longitudinal information (i.e. the radial scale Hr_s) from the transverse one (i.e. the tangential scale D_A/r_s).

Note that the term inside the square root is a polynomial in z' in which the constant term is precisely h^2 (so as expected, for small redshifts $z \ll 1$, $D_A(z)$ depends *only* on the h parameter, like in a Hubble diagram).

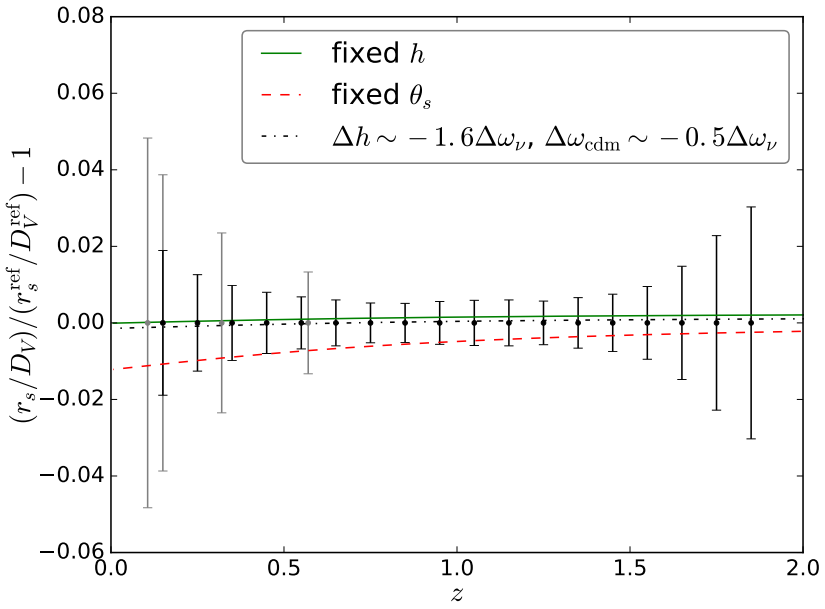

Figure 87: Relative error on r_s/D_V. Gray error bars refer to the current BAO measurements: from left to right 6dFGRS [101], SDSS MGS [514], LOW-Z, C-MASS [47]. Black error bars mark the expected sensitivity of the future DESI experiment [42], [250]. Green solid line and red dashed lines are the same as in figure 85, i.e. higher M_ν with fixed h (green solid line) and higher M_ν with fixed θ_s and varying h (red dashed line). However, here the black dot dashed line is obtained by increasing M_ν and varying h and $\omega_{\rm cdm}$ as in equations (9.3.2).

In figure 87 we show the residuals of current and future BAO measurements, taking as a reference the same model as before with $M_\nu = 60$ meV, as well as the relative difference on $r_s(z_{\rm drag})/D_V(z_{\rm BAO})$ between several models with a higher mass $M_\nu = 150$ meV (already introduced in section 9.2.3) and the reference model. For future measurement we take the example of DESI, assuming the same sensitivity as in Refs. [42], [250].

We first vary only M_ν with fixed $\{\omega_b, \omega_{\rm cdm}, h, n_s, A_s, \tau_{\rm reio}\}$ (green solid line). This means that the early cosmological evolution is identical, while the matter density is slightly enhanced at late times (after the neutrino non-relativistic transition), by about one percent. Thus $d_s(z_{\rm dec})$ and $r_s(z_{\rm drag})$ are fixed, but $d_A(z_{\rm dec})$, $d_A(z_{\rm BAO})$ and $D_V(z_{\rm BAO})$ are subject to change. We have seen that this transformation shifted the CMB peaks by a detectable amount. However, the accuracy with which CORE will measure θ_s ($< 0.01\%$) is much greater than that with which DESI will measure the BAO angular scales ($\sim 1\%$). From equation 9.3.1 we can see analytically that the typical variation of $D_A(z)$ between the two models is negligible for $z \ll 1$ and of the order of $\frac{1}{2}\frac{\Delta\omega_\nu}{\omega_{\rm tot}} \simeq 0.25\%$ for $1 < z < z_{\rm nr}$. This explains why the green curve in figure 87 remains within the BAO error bars.

This preliminary discussion brings us to the key points of this section:

- *the BAO data alone can bound the neutrino mass, but not with great accuracy.* We showed previously that increasing M_ν with fixed $\{\omega_b, \omega_{\rm cdm}, h\}$ had no detectable effects, but this was

because the mass variation was too small. If one keeps increasing ω_ν with the other parameters fixed, the function inside the square root in equation 9.3.1 keeps increasing for the same value z', and $D_A(z)$ decreases. To avoid a BAO bound on M_ν, one could try to exactly compensate the variation $\Delta\omega_\nu$ by an opposite variation in either $\omega_{\rm b}$ or $\omega_{\rm cdm}$, to keep $D_A(z)$ exactly constant. But in that case, the early cosmological evolution would change (sound speed, redshift of equality, redshift of baryon drag) and the ratio $r_s(z_{\rm drag})/D_V(z_{\rm BAO})$ would be shifted anyway. Hence there is no parameter degeneracy cancelling exactly the effect of M_ν in BAO observables, at least in the ΛCDM+M_ν model. This explains why in figures 88 and 89, the contours involving M_ν are closed for DESI data alone, setting an upper bound on the summed mass of a few hundreds of meV.

- *the strong degeneracy between M_ν and h observed in the CMB case cannot exist with BAO data.* This denegeracy came from the possibility to keep constant angular scales ($\theta_s(z_{\rm dec})$, $\theta_d(z_{\rm dec})$) by varying h with fixed $\{\omega_b, \omega_{\rm cdm}\}$. Indeed, when fitting CMB data with different neutrino masses, one can keep the same value of $d_A(z_{\rm dec})$ by altering the late time cosmological evolution: while M_ν tends to enhance the density at late times, one can decrease h and the cosmological constant in order to compensate for this effect. This cannot be done with BAO data, because they probe $d_A(z)$ at several small values of z, comparable to the redshift of the transition z_Λ. The proof is particularly obvious if we look at equation 9.3.1 again. Whatever change in h modifies the constant term inside the square root, and thus the value of $D_A(z)$ for $z \leq 1$. Thus the (M_ν, h) degeneracy discussed in the CMB section must be broken by BAO data. We get a first confirmation of this by looking at the red dashed curve in figure 87, obtained by increasing M_ν with a constant $\theta_s(z_{\rm dec})$: the new model departs from the other one by a detectable amount, at least given BAO-DESI errors (especially at $z \ll 1$, as expected from this discussion). The second confirmation comes from the right plot in figure 88, showing very different correlations between M_ν and h for CMB-CORE alone and BAO-DESI alone.

- *there exists, however, a correlation between M_ν, h and $\omega_{\rm cdm}$ with BAO data, but along different angles than with CMB data.* This comes from the possibility to modify parameters in such a way that both $r_s(z_{\rm drag})$ and $D_V(z_{\rm BAO})$ get shifted, but almost by the same relative amount. To compensate for the effect of an increasing ω_ν, one has three parameters to play with: $\{\omega_b, \omega_{\rm cdm}, h\}$. However, ω_b is precisely fixed by CMB data alone, and for that reason we keep it to its Planck best-fit value. We then find that variations of the other two parameters by approximately

$$\Delta\omega_{\rm cdm} \sim -0.5\Delta\omega_\nu \ , \qquad \Delta h \simeq -0.017 \left(\frac{\Delta M_\nu}{1\ {\rm eV}}\right) \simeq -1.6\,\Delta\omega_\nu \tag{9.3.2}$$

  achieve a nearly constant ratio $r_s(z_{\rm drag})/D_V(z_{\rm BAO})$ in the redshift range best probed by the BAO-DESI experiment. As argued before, this ratio is more sensitive to h than $\omega_{\rm cdm}$ in that range, so the correlation between $\omega_{\rm cdm}$ and ω_ν is weak, while that between h and ω_ν is strong (see Figure 88).

The parameter correlations found in eq. (9.3.2) for BAO data are very different from those found in the previous section for CMB data:

$$\Delta\omega_{\rm cdm} \sim \Delta\omega_\nu \ , \qquad \Delta h \simeq -0.13 \left(\frac{\Delta M_\nu}{1\ {\rm eV}}\right) \simeq -12\,\Delta\omega_\nu \ . \tag{9.3.3}$$

The combination of CMB and BAO data can thus break these degeneracies, as it is often the case when combining high and low redshift probes of the expansion history. The breaking does not arise from the joint measurement of $\omega_{\rm cdm}$ and ω_ν (because BAO data are much less sensitive to $\omega_{\rm cdm}$ alone than CMB data), but from that of h and ω_ν, for which the different directions of degeneracy appear very clearly on figure 88. Thus, the future BAO-DESI data will contribute to tighter constraints on M_ν.

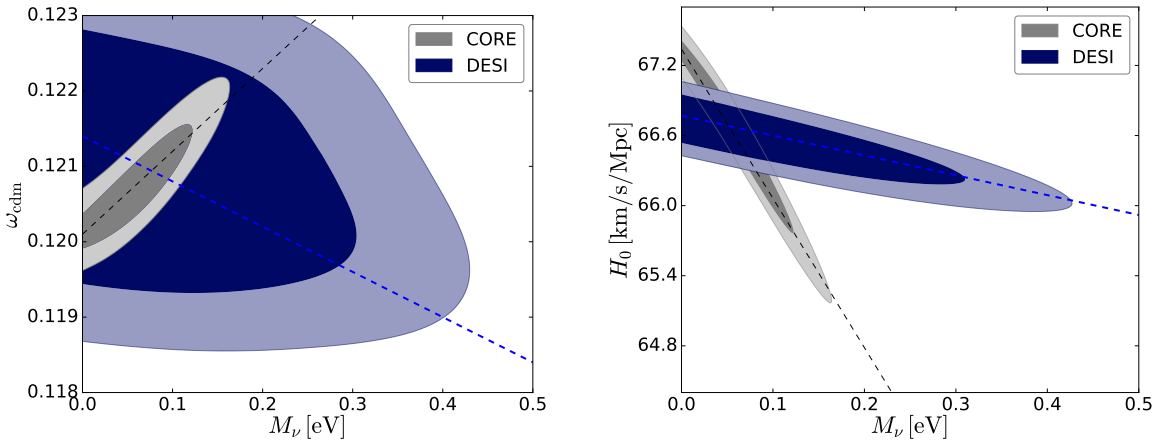

Figure 88: Marginalized one- and two- σ contours in the plane $(\omega_{\rm cdm}, M_\nu)$ (left panel) and (H_0, M_ν) (right panel), for CMB-CORE or BAO-DESI mock data. The black dashed lines show the directions of degeneracy given in equations (9.3.3), and the blue ones in equations (9.3.2).

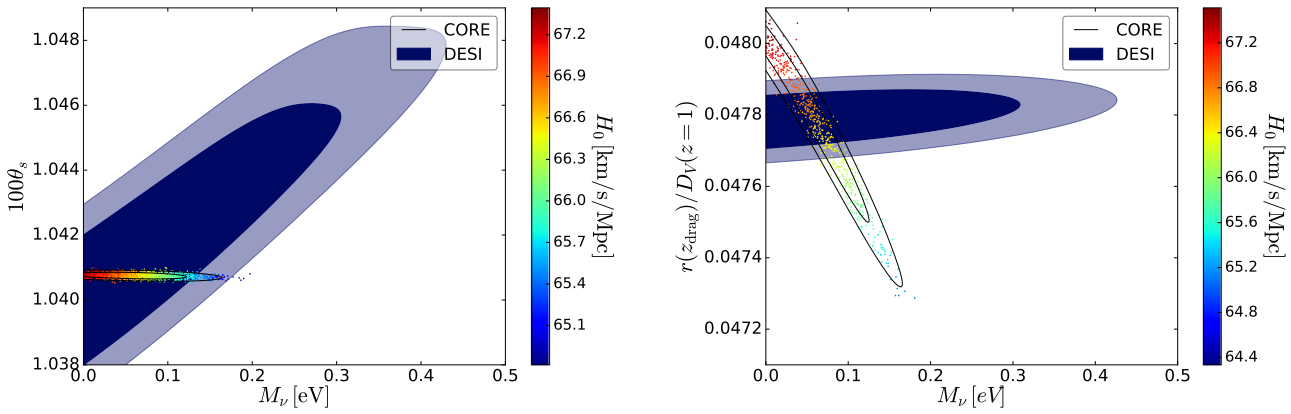

Figure 89: Marginalized one- and two- σ contours in the plane $(\theta_s(z_{\rm dec}), M_\nu)$ (left) and $(r(z_{\rm drag})/D_V(z=1), M_\nu)$ (right), for CMB-CORE or BAO-DESI mock data. In the CORE contours, samples are coloured according to the value of H_0.

Another way to illustrate the degeneracies discussed here is to fit CMB data or BAO data alone with a ΛCDM+M_ν model, and to plot the results in the space of parameters $(M_\nu, \theta_s(z_{\rm dec}))$ and $(M_\nu, r_s(z_{\rm drag})/D_V(z_{\rm BAO}))$ for a median redshift $z_{\rm BAO} = 1$. This is shown in figure 89. When fitting CMB alone, thanks to the degeneracy of equations (9.3.3), we can increase M_ν while keeping $d_A(z_{\rm dec})$ and $\theta_s(z_{\rm dec})$ fixed (left plot), but this is at the expense of decreasing the BAO angular scale by more than allowed by observational errors (right plot). Conversely, when fitting BAO data alone, we can

play with the degeneracy of equations (9.3.2) to keep the BAO angular scale fixed, but this requires $\theta_s(z_{\rm dec})$ to vary. The right plot in figure 89 illustrates, in an alternative way to the right plot of figure 88, how the combination of the two data sets can improve neutrino mass bounds.

Finally, we expect, as a secondary indirect effect, that the correlation between M_ν and $(A_s, \tau_{\rm reio})$ will be more noticeable in a combined analysis of CMB and BAO than for CMB alone. In section 9.2.3, we mentioned in points 3 and 4 that the impact of M_ν on CMB lensing could be compensated in two ways: by increasing either $(A_s, \tau_{\rm reio})$ (point 3) or $\omega_{\rm cdm}$ (point 4). We explained why the former option is favoured with CMB data alone. Since we just argued that BAO data can reduce the degeneracy between neutrino masses and $\omega_{\rm cdm}$, the latter option is more relevant when the data are combined with each other. Indeed, we will see a small correlation between $(M_\nu, \tau_{\rm reio})$ in the combined results presented in section 9.5, one that was hardly noticeable with CMB alone. Of course, this degeneracy is not perfect, and extends only up to the point at which $\tau_{\rm reio}$ becomes too large to be compatible with CMB polarisation data.

9.4 Effect of neutrino mass on Large Scale Structure observables

9.4.1 *Cosmic shear and galaxy clustering spectrum*

The Euclid satellite, whose launch is scheduled for 2020, will provide the most accurate ever galaxy redshift survey, measuring cosmological observables, such as cosmic shear and galaxy clustering, with 1% accuracy. Euclid data will certainly lead to a major breakthrough in precision cosmology thanks to very precise low redshift measurement which will break the CMB degeneracies among cosmological parameters (see references [52], [69], [85], [86], [143], [211], [212], [288], [441]). Here we use the information extracted from the cosmic shear power spectrum projected in angular harmonics (2D) and the galaxy clustering power spectrum (3D). Both observables are related to the non-linear matter power spectrum depending on wavenumber and redshift, $P_{\rm m}(k, z)$. In our forecasts, we estimate this quantity using the HALOFIT algorithm, updated by [577] and also by [105] for the effect of neutrino masses, as implemented in CLASS v2.5.0.

Cosmic shear. The cosmic shear auto and cross correlation angular power spectrum in the i and j redshift bins is given in the Limber approximation by:

$$C_\ell^{ij} = H_0^4 \int_0^\infty \frac{dz}{H(z)} W_i(z) W_j(z) P_{\rm m}\left(k = \frac{l}{r(z)}, z\right), \tag{9.4.1}$$

where the window functions are given by

$$W_i(z) = \frac{3}{2}\Omega_m(1+z) \int_0^\infty dz_s \frac{n_i(z_s)(r(z_s) - r(z))}{r(z_s)}, \tag{9.4.2}$$

and the number of galaxies per steradian in the i bin is given by

$$n_i(z) = \frac{\int_{z_i^{\rm min}}^{z_i^{\rm MAX}} dn/dz \mathcal{P}(z, z_{\rm ph}) dz_{\rm ph}}{\int_0^\infty dn/dz \mathcal{P}(z, z_{\rm ph}) dz_{\rm ph}}$$

with $\mathcal{P}(z, z_{\rm ph})$ being the error function

$$\mathcal{P}(z, z_{\rm ph}) = \frac{1}{\sqrt{2\pi\sigma_{\rm ph}^2}} \exp\left[-\frac{1}{2}\left(\frac{z - z_{\rm ph}}{\sigma_{\rm ph}}\right)\right].$$

We use the Euclid prescription for the galaxy surface density

$$dn/dz = z^2 \exp\left[-(z/z_0)^{1.5}\right]$$

with $z_{\rm mean} = 1.412 z_0$. Finally we consider a photometric redshift error $\sigma_{\rm ph} = 0.05(1+z)$, sky fraction $f_{\rm sky} = 0.3636$, mean internal ellipticity 0.22 and total number of observed galaxies 30 per arcmin^2.

Galaxy clustering. For galaxy clustering the observed power spectrum reads:

$$P(k_{\rm ref}, \mu, z) = \frac{D_A(z)^2_{\rm ref} H(z)}{D_A(z)^2 H(z)_{\rm ref}} b(z)^2 \left[1 + \beta(z, k(k_{\rm ref}, \mu, z))\mu^2\right]^2 \times P_{\rm m}(k(k_{\rm ref}, \mu, z)) e^{-k(k_{\rm ref},\mu,z)^2, z)\mu^2\sigma_r^2},$$

where μ is the cosine of the angle between the line of sight and the wavenumber in the reference cosmology (ref) $k_{\rm ref}$, k is the wavenumber in the true cosmology and it is defined as a function of $k_{\rm ref}$

$$k^2 = \left(\frac{(1-\mu^2) D_A(z)^2_{\rm ref}}{D_A(z)^2} + \frac{\mu^2 H(z)^2}{H(z)^2_{\rm ref}} \right) k^2_{\rm ref}.$$

The factor $\left[D_A(z)^2_{\rm ref} H(z)\right] / \left[D_A(z)^2 H(z)_{\rm ref}\right]$ encodes the geometrical distortions related to the Alcock-Paczynski effect. The bias can be written as $b = \sqrt{(1+z)}$, β encodes the redshift space distortions

$$\beta(k, z) = \frac{1}{2b(z)} \frac{d \ln P_{\rm m}(k, z)}{d \ln a},$$

and finally the spectroscopic redshift error is $\sigma_r = dr(z)/dz \sigma_z$.

Both the C_ℓ^{ij} and the $P(k)$ provide information on a broad range of scales; therefore, given the same survey sensitivity, they are more efficient than BAO in constraining cosmological parameters; however, for the very same reason, they are more prone to systematic effects such as residual errors in the estimate of non-linear corrections, non-linear light-to-mass bias or redshift space distortions (see e.g. [287], [502]). For that reason, we include in our forecast a theoretical error on the observable power spectrum, increasing above a given redshift-dependent scale of non-linearity (see [69], or [76] for a more refined treatment).

The assumed theoretical error amplitude has a direct impact on the galaxy clustering sensitivity to cosmological parameters. Here we stick to the approach of [69], and we refer to this work for details and equations. As emphasised in [76], this approach is extremely (and maybe overly) conservative, because the error is assumed to be uncorrelated between different k-bins. The error grows as a function of the ratio $k/k_{\rm nl}(z)$, where $k_{\rm nl}(z)$ is the redshift-dependent scale of non linearity, with a shape and amplitude inspired from the typical residuals between different N-body codes[9]. Choosing a value for the error amplitude parameter ϵ amounts to estimating the accuracy of grids of N-body simulations and of models for various non-linear and systematic effects in a few years from now. The baseline choice in [69] was $\epsilon = 0.05$. In this work, given the progress in the field observed since 2012, we choose to reduce it to $\epsilon = 0.025$, meaning that the uncorrelated theoretical error saturates at the 2.5% level in the deep non-linear regime. This error is explicitly shown in figure 91 for $z = 0.5$ and $z = 2$, and its impact on the lensing harmonic spectrum appears in figure 90 for the lowest and highest redshift bins of the Euclid lensing survey. In presence of a theoretical error, the issue of where to cut the integrals in the galaxy clustering likelihood becomes hardly relevant, provided that the cut-off is chosen in the

9 The error function is explicitly given by $\alpha(k,z) \equiv \frac{\Delta P_{\rm m}(k,z)}{P_{\rm m}(k,z)} = \frac{\ln[1+k/k_{\rm nl}(z)]}{1+\ln[1+k/k_{\rm nl}(z)]}\epsilon$, where $k_{\rm nl}(z)$ is identical to the quantity $k_\sigma(z)$ computed at each redshift by HALOFIT, and the error amplitude parameter ϵ is the unique free parameter in this model. The asymptotic error in the deep non-linear regime is then given by 100ϵ % .

region where the theoretical error dominates. In what follows, we will cut the observable $P(k_{\rm ref}, \mu, z)$ at $k_{\rm max} = 0.6\,h/{\rm Mpc}$ for all redshifts. For cosmic shear, the inclusion of the theoretical error is also important, although the observational error bar does not decreases indefinitely with ℓ due to the finite angular resolution of the shear maps. In our forecasts, we perform a cut at $\ell_{\rm max} = 2000$.

9.4.2 *Degeneracies between M_ν and other parameters*

In figure 90 and 91 we show the relative shift in the shear power spectrum and in the galaxy power spectrum that is obtained when increasing the summed neutrino mass while keeping various quantities fixed. We also show for comparison the observational and theoretical errors computed in the same way as in Ref. [69], using the survey specifications listed above. We will study the impact of increasing the summed neutrino mass on these observables: (1) when keeping the usual cosmological parameters fixed, (2) when tuning h at the same time in order to keep the same angular peak scale in the CMB, and (3) when playing with other parameters in order to minimize the impact of neutrino mass on LSS observables. The discussion in (2) (respectively, (3)) is relevant for understanding the degeneracy between M_ν and other parameters when fitting CMB+LSS data (respectively, LSS data alone).

As in the previous sections, we will then check our theoretical conclusions through an MCMC forecast of the sensitivity of future experiments that will measure the spectra discussed above. In figure 93 we plot the marginalized one- and two- σ contours showing the degeneracies at study: $(\omega_{\rm cdm}, M_\nu)$ (upper left panel), (H_0, M_ν) (upper right panel), (n_s, M_ν) (bottom left panel), (A_s, M_ν) (bottom right panel). The CORE only contours (in gray) are the same as in figure 88. The Euclid related contours have been obtained through an MCMC forecast including either galaxy clustering (in green) or cosmic shear (in red), following the specifications listed in section 9.4.1. Fitting Euclid mock data alone would return wide contours in parameter space. Given that the two quantities best measured by CMB experiments are the angular scale of the acoustic horizon and the baryon density, the question in which we are most interested is: assuming that information on ω_b and θ_s is provided by a CORE-like CMB experiment, what is the pull on other parameters coming from Euclid alone? To address this, when fitting Euclid data, we impose two uncorrelated gaussian priors on respectively ω_b and θ_s, with standard deviations taken from our previous CORE-CMB forecast, while keeping $\tau_{\rm reio}$ fixed, since the latter does not affect galaxy clustering and shear observables in any way.

1. *Neutrino mass effects with all standard cosmological parameters fixed: the usual neutrino–induced step–like suppression.*

   Like in the previous sections, we start by increasing the summed neutrino mass from $M_\nu = 0.06$ eV to $M_\nu = 0.15$ eV, keeping all the other cosmological parameters $\{\omega_b, \omega_{\rm cdm}, h, n_s, A_s, \}$ fixed (green solid line). Note that in most of the literature, the effect of neutrino masses on the matter power spectrum is discussed precisely in that way. One reason is that fixing $\{\omega_b, \omega_{\rm cdm}, n_s, A_s, \}$ amounts in keeping the same "early cosmological evolution" until the time of the neutrino non-relativistic transition. The choice to fix also h is mainly a matter of simplicity.

   As expected, the larger M_ν induces a relative suppression of power on small scales compared to large scales, visible both in the shear and in the galaxy power spectrum. To be precise, in the redshift range surveyed by Euclid, $0 < z < 2.5$, neutrinos with a mass $M_\nu > 0.05$ eV are already well inside the non-relativistic regime, thus, the spectrum is suppressed on scales smaller than the free-streaming scale $k > k_{\rm fs}(z)$. In the redshift range of interest, $0 < z < 2.5$, the free streaming

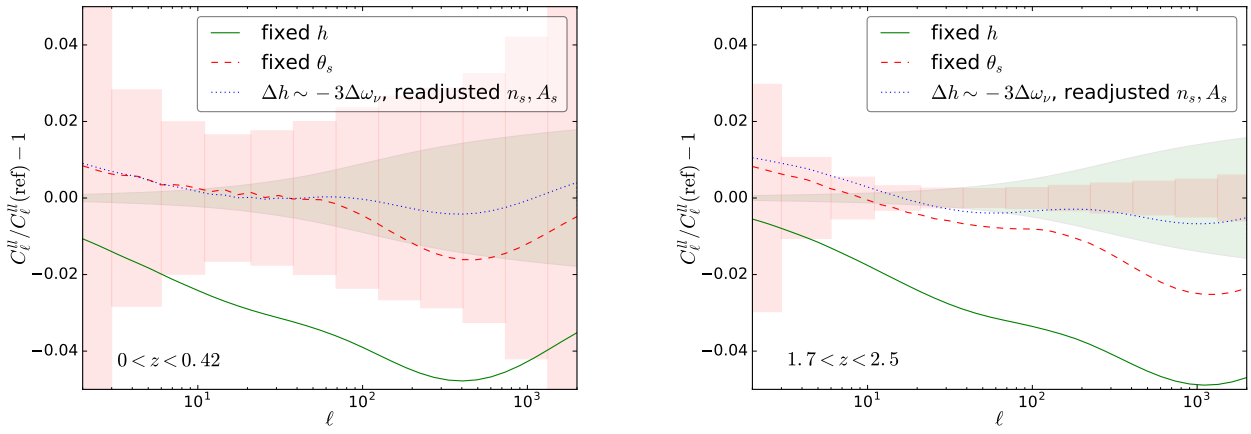

Figure 90: Relative error on the galaxy lensing C_ℓ^{ll} in the first redshift bin ($0 < z < 0.42$, left panel) and in the tenth redshift bin ($1.7 < z < 2.5$, right panel). Here the redshift range is $0 < z < 2.5$ and is divided in ten equi-populated redshift bins. The light pink rectangles refers to the observational error. The light green shaded area shows the relative error associated to our model for the theoretical uncertainty on $P_m(k, z)$. Green solid and red dashed lines are the same as in figure 85, i.e. higher M_ν with fixed h (green solid line) and higher M_ν with fixed θ_s and varying h (red dashed line). The blue dotted line, besides the higher M_ν, implies a smaller value of h ($\Delta h \sim -3\Delta\omega_\nu$), an increase of n_s by 0.4% and of A_s by 2%.

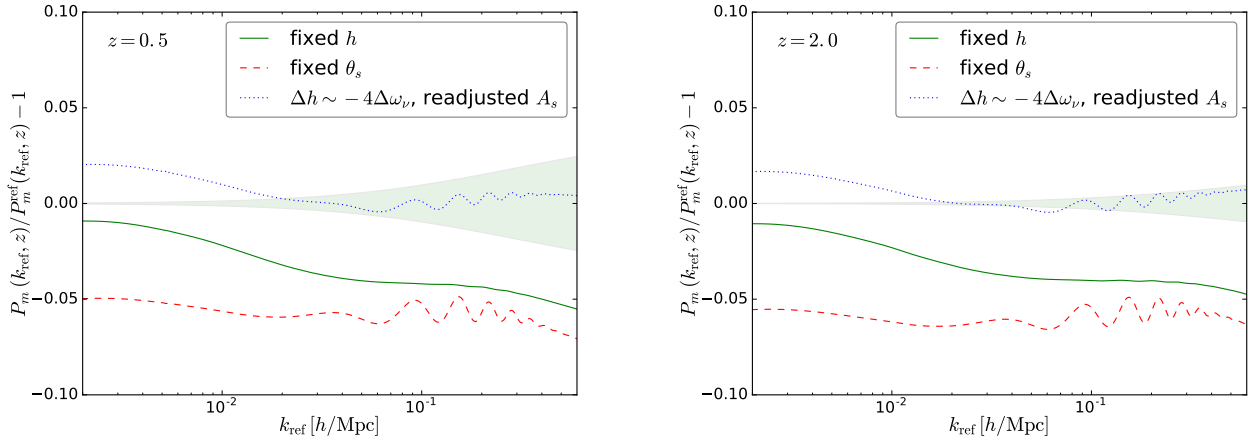

Figure 91: Relative error on the non linear matter power spectrum $P_{\mathrm{m}}(k_{\mathrm{ref}}, z)$ perpendicular to the line of sight ($\mu = 0$) at redshift $z = 0.5$ (left panel) and $z = 2$ (right panel). The light pink shaded area refers to the observational error, including cosmic variance. The light green shaded area shows our model for the theoretical uncertainty. Here the redshift range is $0.5 < z < 2$ and is divided in 16 redshift bins. Green solid and red dashed lines are the same as in figure 85, i.e. higher M_ν with fixed h (green solid line) and higher M_ν with fixed θ_s and varying h (red dashed line). The blue dotted line, besides the higher M_ν, implies a smaller value of h ($\Delta h \sim -4\Delta\omega_\nu$) and an increase of A_s by 5%.

wavenumber spans the range $[0.0077 - 0.0041]h\mathrm{Mpc}^{-1}$ (respectively, $[0.0192 - 0.0103]h\mathrm{Mpc}^{-1}$)

for $M_\nu = 0.06$ eV (respectively, $M_\nu = 0.15$ eV)[10]. The suppression in power makes both the C_ℓ^{ij} and the $P(k)$ directly sensitive to the neutrino mass sum, while this was not the case for the purely geometrical information encoded in BAO measurements.

This sensitivity is reinforced by non-linear effects which are well visible on figures 90 and 91. In the shear spectrum of figure 90, in absence of non-linear corrections, the green curve would be almost constant for $\ell > 100$. Non-linear gravitational clustering produces a characteristic "spoon shape" or dip [105]. The minimum of the dip is seen at $\ell \sim 40$ in the first redshift bin and $\ell \sim 1000$ in the last one. In figure 91, non-linear effects are responsible for the further decrease of the green curve for $k \geq 0.1\,h/\mathrm{Mpc}$.

2. *Neutrino mass effects with h varied to keep the CMB angular scales fixed: why does LSS data lift the (M_ν, h) degeneracy?*

   The second part of the discussion consists in increasing M_ν by the same amount, while varying h like in section 9.2.3, in such way as to keep a constant angular diameter distance to recombination, constant sound horizon angular scale, and constant damping angular scale (red dashed line). As we have seen in Section 9.2.3 this procedure leads to the well known (M_ν, h) CMB degeneracy.

   We showed that this degeneracy is broken by BAO data, because the lower value of h increases the angular diameter distance at low redshift (see Section 9.3). This conclusion is valid also for galaxy $P(k)$ and shear C_ℓ^{ij}, since the red dashed residuals in figures 90, 91 are well outside the observational and theoretical error bars. For clarity, we should explain the shape of these red dashed lines, which is slightly counter-intuitive.

   In the case of galaxy clustering, the higher value of M_ν and lower value of h lead to an almost constant suppression of power on every scale, plus some wiggles on small scales (see figure 91). This may sound surprising since we are used to seeing more suppression on small scales when increasing the neutrino mass. This is true for fixed h, but here we are decreasing the Hubble rate at the same time. Since $\omega_\mathrm{m} = \Omega_\mathrm{m} h^2$ is kept fixed, this means that we are increasing Ω_m. For subtle reasons which can be understood analytically, the large-scale branch of the matter power spectrum is suppressed by the increase of Ω_m[11], while the small-scale branch is suppressed by massive neutrino free-streaming, coincidentally by roughly the same amount. This explains the almost constant suppression of power in the galaxy clustering spectrum (red dashed line, figure 91). The wiggles located around $k \sim 0.1\,h\mathrm{Mpc}^{-1}$ are related to the shift of the BAO scale due to the different angular diameter distance at low redshift, as we have explained in section 9.3 (see also reference [494]).

10 The free streaming length depends on the mass of each neutrino rather than on the sum. Here we have assumed three massive degenerate neutrinos.

11 In order to understand the observed behaviour, we have to elaborate on the matter power spectrum P_m entering equation 9.4.1. An analytic study of the linear power spectrum expressed in units of $(\mathrm{Mpc}/h)^3$ as a function of k in units of h/Mpc shows that at any given redshift, the large-scale branch ($k \ll k_\mathrm{eq}$) depends only on a factor $(g(\Omega_\mathrm{m}, z)/\Omega_\mathrm{m})^2$ coming from the Poisson equation and from the behaviour of matter perturbations during Λ domination (see e.g. [392], equation (6.39)). The function $g(\Omega_\mathrm{m}, z) \leq 1$ is related to the decrease of matter perturbations during Λ domination. When increasing Ω_m, we decrease this factor $(g(\Omega_\mathrm{m}, z)/\Omega_\mathrm{m})^2$ and we suppress the large-scale power spectrum, but not the small-scale one. Indeed, looking again at equation (6.39) in [392], the small-scale branch receives an extra factor $\tilde{k}_\mathrm{eq}^4$ (i.e. k_eq^4 with k_eq in h/Mpc). This new factor is actually proportional to $z_\mathrm{eq}^2 \Omega_\mathrm{m}^2$ (eq. (6.32) in the same reference), and the latter cancels the former Ω_m^{-2} factor.

The situation is a bit different for the galaxy lensing spectrum C_ℓ^{ij} (red dashed line, figure 90) which probes metric fluctuations instead of matter fluctuations. As a result[12], the large-scale branch of the C_l^{ij}'s slightly increases when we decrease h and increase $\Omega_{\rm m}$. Instead, the small-scale branch remains nearly constant due to the antagonist effects of neutrino free-streaming and of the increase in $\Omega_{\rm m}$, but the neutrino effect wins on non-linear scales. As can be seen on the right panel of figure 90, for the highest redshift bins, the lensing data is able to discriminate this effect and to lift the (M_ν, h) degeneracy, although with less significance than the galaxy clustering data.

These conclusions are confirmed by the (M_ν, h) joint probability contours presented in the upper right panel of figure 93, for CORE, Euclid-lensing and Euclid-pk. Indeed, the slope of the (M_ν, h) degeneracy is different from the one observed in CMB data, and it is mainly driven by the CMB prior on θ_s.

3. *Degeneracy between M_ν and other parameters from Large Scale Structure data alone.*

Finally we increase M_ν, decrease h by a smaller amount than the one required for fixing θ_s, and, at the same time, we vary the primordial power spectrum parameters, the amplitude A_s and also the index n_s in the case of cosmic shear (blue dotted lines). It is clear from figures 90 and 91 that this procedure can almost cancel the effect induced by a larger M_ν both in the shear C_ℓ^{ij} and in the galaxy $P(k)$, leading to a new degeneracy. We shall now explain the reasons for this degeneracy.

Considering that the primordial power spectrum of scalar perturbations is given by

$$\frac{k^3\mathcal{P}_\mathcal{R}(k)}{2\pi^2} = A_s\left(\frac{k}{k_0}\right)^{n_s-1}, \tag{9.4.3}$$

the matter power spectrum $P_{\rm m}$ can be written as

$$P_{\rm m}(k,z) \propto A_s\left(\frac{k}{k_0}\right)^{n_s} T(k,z)^2 \tag{9.4.4}$$

where $T(k,z)$ is the time and scale dependent linear transfer function of matter density fluctuations (not separable in the case of massive neutrinos). As we have already explained, neutrinos induce a relative suppression of power on scales $k > k_{\rm fs}$; this suppression is encoded in the transfer function $T(k,z)$ of equation 9.4.4. In figure 92 we show how $T(k,z)$ is suppressed by a larger neutrino mass sum on $k > k_{\rm fs}$ at redshift $z = 0$ and $z = 2$. Changing (n_s, A_s) affects only the primordial power spectrum, while leaving $T(k,z)$ unchanged, therefore, since we keep ω_b and $\omega_{\rm cdm}$ fixed, any deviation from the green solid line is due only to the variation of h and Ω_m. If, besides increasing M_ν, we decrease h to keep θ_s fixed (red dashed line), then the suppression of $T(k,z)$ extends to $k < k_{\rm fs}$ (because of the $(g(\Omega_{\rm m},z)/\Omega_{\rm m})^2$ factor) and the wiggles, due to the shift of the BAO scale, appear at smaller scales. This graphically explains what we have already discussed in point 2. Reducing the tweaking on h (blue dotted line) implies less reduction of power on the large scale branch and a smoothing of the wiggles; anyhow, the massive neutrino suppression of

12 Since the lensing spectrum directly depends on metric fluctuations, it does not share with the matter power spectrum the factor $\Omega_{\rm m}^{-2}$ coming from the Poisson equation. Indeed, the factor $\Omega_{\rm m}^{-2}$ discussed in the previous footnote is exactly cancelled by a factor $\Omega_{\rm m}^2$ that appears in equation 9.4.1 when replacing the window functions with equation 9.4.2. As a result, the large-scale branch of the C_l^{ij}'s depend on $g(\Omega_{\rm m},z)^2$ only, while the small-scale branch is proportional to $\Omega_{\rm m}^2$.

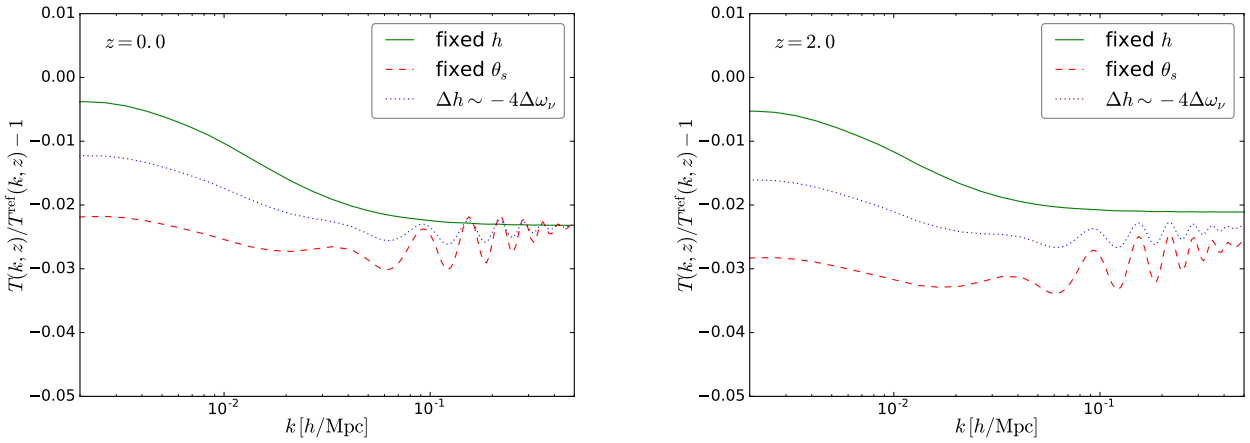

Figure 92: Relative error on the linear transfer function $T(k)$ at redshift $z = 0$ (left panel) and $z = 2$ (right panel). The line color/style - model correspondence is the same as in figure 91.

the transfer function is not fully compensated. However, if we look at equation 9.4.4 it is clear that a red tilt of the primordial power spectrum, combined with a smaller normalization, can mimic the same effect of a larger neutrino mass, reducing power on small scales respect to large scales.

The left and right bottom panels of figure 93 show the degeneracies between M_ν and (n_s, A_s). We can see that the degeneracy between M_ν and n_s is mildly positive in galaxy lensing, as expected from the discussion above, while it is negative in CMB, as explained at the end of section 9.2.3, and mildly negative in galaxy clustering. The reason why this positive (M_ν, n_s) correlation emerges with cosmic shear, but not with galaxy correlation data, is related to the window function. Indeed, since the window function (equation 9.4.2) for each redshift bin is given by the integral over the line of sight, the C_ℓ^{ij}'s of equation 9.4.1 receive contributions from a larger range of scales. Therefore, being sensitive to a wider lever arm in k space, cosmic shear will be particularly sensitive to scale dependent variations of the power spectrum.

Notice that here the tweaking of A_s is larger than the one we performed at point 3 of section 9.2.3. Thus, the corresponding $\Delta\tau_{\rm reio} \sim 0.5\ln(1.05) \sim 0.027$ would lead to an enhancement of the reionization bump even bigger than the one we observed in the blue dotted line of the C_ℓ^{EE} plot (figure 85, second row, right panel). This already shows that the degeneracy discussed here can be lifted by combining LSS data with CMB data. Nevertheless this discussion was important to understand the pulls in parameter space appearing when all data sets are combined with each other.

Figure 93 confirms the points discussed previously, and provides a comprehensive graphical summary of the complementarity between future CMB and LSS data in the context of neutrino mass measurement.

First, we see that even when adopting CMB-derived priors on ω_b and θ_s, the LSS data cannot efficiently constrain the neutrino mass, due to the degeneracy discussed in the previous paragraphs (point 3), involving mainly (M_ν, A_s, H_0), and to a lesser extent, n_s. We have seen that this degeneracy requires a milder correlation between M_ν and H_0 than the CMB data: $\Delta h \sim -3\Delta\omega_\nu$ for LSS alone,

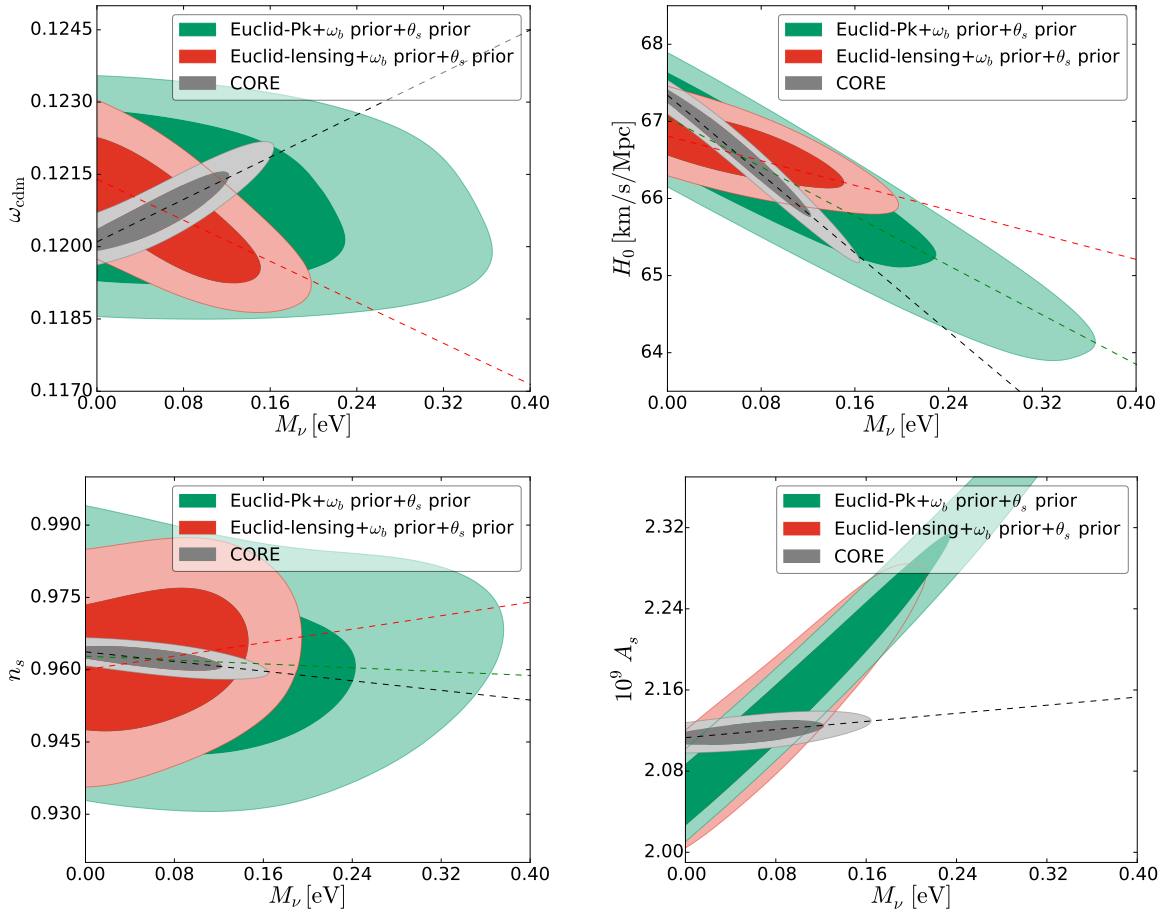

Figure 93: Marginalized one- and two- σ contours in the plane $(\omega_{\rm cdm}, M_\nu)$ (upper left panel), (H_0, M_ν) (upper right panel), (n_s, M_ν) (bottom left panel), (A_s, M_ν) (bottom right panel). The black dashed lines show the degeneracies encoded in CMB data, the red and green dashed lines account for some of the most prominent correlations arising from cosmic shear and galaxy clustering, respectively.

instead of $\Delta h \sim -12\Delta\omega_\nu$ for CMB alone. Since in Figure 93 the Euclid mock data was fitted together with a prior on θ_s, the final correlation angles represent compromises between these values. The lensing data also exhibits a negative correlation between M_ν and $\omega_{\rm cdm}$.

The CMB and LSS contours of Figure 93 clearly intersect each other for several pairs of parameters:

- The CMB and LSS data prefer different directions of degeneracy in (M_ν, H_0) space, hence the combination between them can strongly reduce the uncertainty on both M_ν and H_0.
- The CMB data lifts the (M_ν, A_s) degeneracy present in the LSS data, for the reason mentioned above: the shift in A_s would need to be compensated by a shift in $\tau_{\rm reio}$ producing a reionisation bump incompatible with the data. However, in the combined data set, the LSS data would keep pulling towards more positive correlation between M_ν and A_s.
- the very different correlations in (M_ν, $\omega_{\rm cdm}$) space reduces uncertainties on $\omega_{\rm cdm}$, with a side effect on the CMB side. We have seen that the effect of neutrino masses on the CMB lensing spectrum can be compensated either by playing with $\omega_{\rm cdm}$, or with $(A_s, \tau_{\rm reio})$. The CMB alone

would favour the first option. Like BAO data, weak lensing data breaks the $(M_\nu, \omega_{\rm cdm})$ degeneracy and leaves only the second option. This goes in the same direction as the previous point: pulling towards more positive correlation between M_ν and A_s.

Hence we can already anticipate that the combination of CMB plus LSS data leads to an enhanced degeneracy between (M_ν, A_s) compared to CMB data alone. As a consequence, in order to maintain a fixed combination $A_s e^{-2\tau_{\rm reio}}$, the combined data may generate a significant correlation in $(M_\nu, \tau_{\rm reio})$ space.

The goal of the next section is to check these partial conclusions with a global fit of all data sets at the same time.

9.5 Joint analysis results

9.5.1 *Combination of CMB, BAO and galaxy shear/correlation data*

In this section we will present the results of our Markov Chain Monte Carlo forecast of the combined sensitivity of future CMB, BAO and LSS experiments to the cosmological parameters described in Section 9.2, in particular to the neutrino mass sum. As already mentioned in Section 9.2.3, our MCMC forecast will be performed using the MONTEPYTHON code[13] [68], interfaced with the Boltzmann solver CLASS[14] [109], [390], [396]. We already commented at the end of section 9.4.1 our conservative choices for the precision parameters: theoretical error parameter $\epsilon = 0.025$, cut-off at $k_{\rm max} = 0.6\,h/{\rm Mpc}$ for galaxy correlation, and at $\ell_{\rm max} = 2000$ for cosmic shear. Still this choice comes from a subjective estimate of the accuracy with which non linear corrections and systematic effects will be modelled in the future, and different assumptions would lead to different parameter sensitivities.

	$\sigma(M_\nu)/[{\rm meV}]$	$\sigma(\tau_{\rm reio})$	$\sigma(10^9 A_s)$	$\sigma(n_s)$	$\sigma(\omega_{\rm cdm})$	$\sigma(h)$
CORE	42	0.0020	0.0084	0.0018	0.00052	0.0052
CORE+DESI	19	0.0020	0.0080	0.0014	0.00026	0.0022
CORE+DESI+Euclid-lensing	16	0.0020	0.0078	0.0014	0.00023	0.0019
CORE+Euclid (lensing+pk)	14	0.0020	0.0079	0.0015	0.00025	0.0017
CORE+Euclid (lensing+pk)+21cm	12	$--$	0.0042	0.0014	0.00021	0.0017

Table 9: Expected $1\,\sigma$ sensitivity of CORE, CORE + DESI, CORE + DESI + Euclid (lensing), CORE + Euclid (lensing+pk), CORE + Euclid (lensing+pk) + "21cm-motivated $\tau_{\rm reio}$ prior" to the parameters $\{M_\nu, \tau_{\rm reio}, 10^9 A_s, n_s, \omega_{\rm cdm}, h\}$. We did not combine DESI and Euclid-pk in order to avoid double counting the information coming from the wiggly part of the spectrum.

In the first four lines of table 9 we report the expected sensitivity of CORE, CORE+DESI, CORE+DESI+Euclid-lensing and CORE+Euclid (lensing+pk)[15] to M_ν and other cosmological parameters playing a crucial role in our analysis of parameter degeneracies: $\tau_{\rm reio}$, $10^9 A_s$, n_s, $\omega_{\rm cdm}$ and h (the last independent parameter, $\omega_{\rm b}$, is always very well constrained by CMB data alone). In figure 94 we plot the one dimensional posteriors and the one- and two-σ marginalized contours for the same parameters.

13 http://baudren.github.io/montepython.html
14 http://class-code.net
15 Contrarily to an earlier version of this work, to avoid any possible "double counting" of the BAO information, we will not combine DESI and Euclid-pk data.

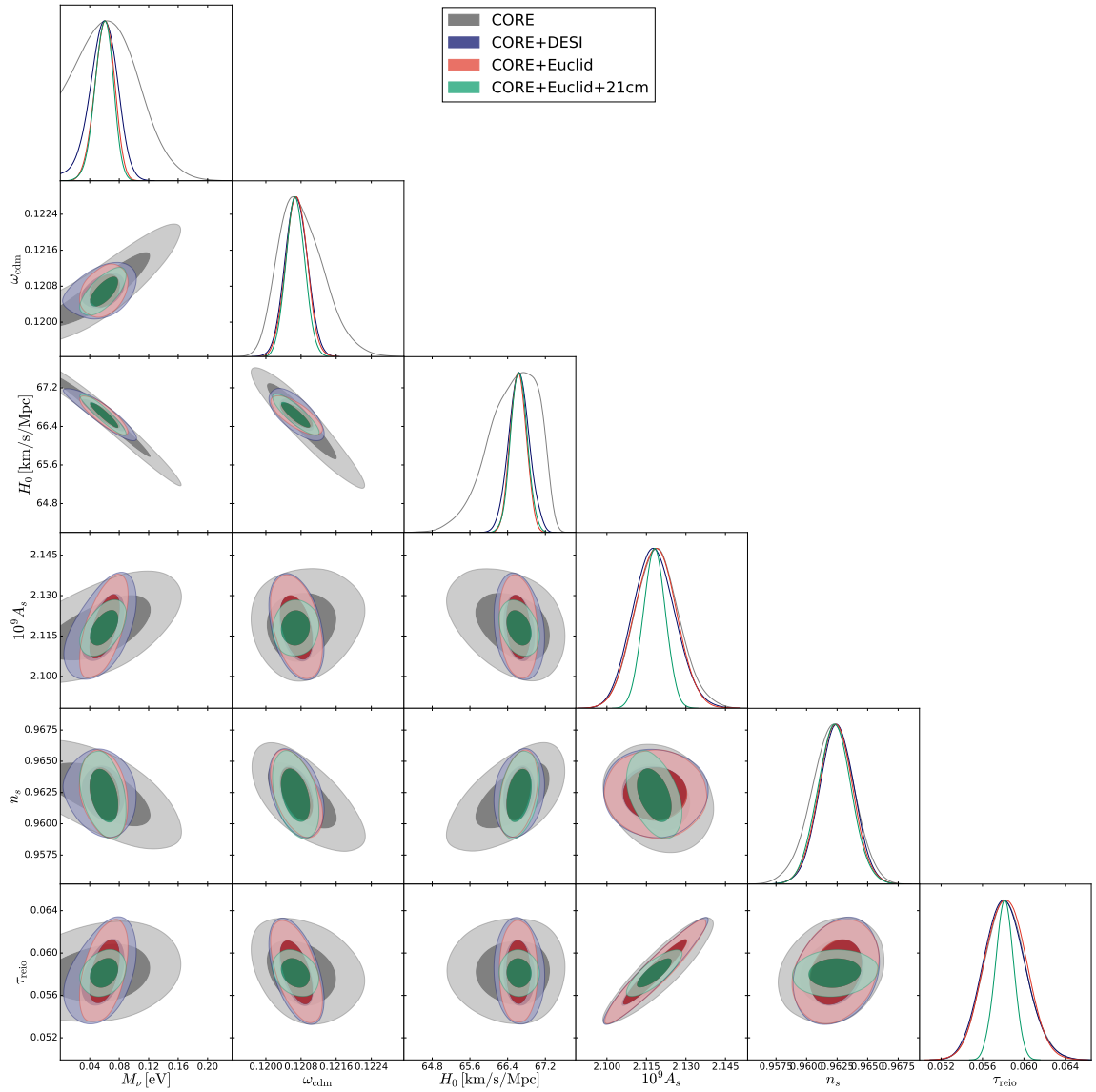

Figure 94: Marginalized one− or two−σ contours and one dimensional posteriors in the $(M_\nu, \omega_{\rm cdm}, H_0, A_s, n_s, \tau_{\rm reio})$ parameter space, showing the expected sensitivity of various future experiments: CORE only (gray contours), CORE+DESI (blue contours), CORE+Euclid (red contours) and CORE+Euclid+21cm (green contours). The last independent parameter, $\omega_{\rm b}$, is always very well constrained by CMB data alone.

First of all we notice that the projected $1\,\sigma$ errors in table 9 and 1D distributions in figure 94 reflect the theoretical points we have discussed in the previous sections: both DESI and Euclid greatly improve the sensitivity to M_ν, $\omega_{\rm cdm}$ and h. The uncertainty on M_ν tightens by more than a factor two for CORE+DESI and a factor three for CORE+Euclid, compare to the CORE only sensitivity. The error on H_0 shrinks by a factor larger than two for CORE+DESI and a factor three for CORE+Euclid. However once more we want to stress that in the case of DESI the improved sensitivity arises from reducing the degeneracy between H_0 and M_ν, while in the case of Euclid the longer lever arm of the shear data is specifically sensitive to the suppression of power at small scales induced by M_ν.

The first column of figure 94 shows all the degeneracies with respect to M_ν. Let us describe the evolution of those correlations with the addition of the different datasets:

1. *CORE data only.* When only CMB data are considered, correlations follow the directions expected from our extensive discussion of section 9.2.3. Let us just note that contrarily to ΛCDM runs *without* neutrino mass as a free parameter, the mild correlation between A_s and n_s is negative, which is a result of the mild negative (resp. positive) correlation between M_ν and n_s (resp. A_s).

2. *Adding DESI data.* In general, the size of the 2D-distributions shrink by a factor ∼2. The extended regions defining the positive correlations between (M_ν, A_s) and $(M_\nu, \tau_{\rm reio})$ become steeper, since it is not possible anymore to play with H_0 or $\omega_{\rm cdm}$ to compensate the effect of the summed neutrino mass on the CMB lensing spectrum. Indeed, as described in section 9.3, moving along this degeneracy direction would lead to very different BAO angular scales. Thus, the effect of the summed neutrino mass on CMB lensing is rather compensated by playing with parameters to which BAO data are insensitive[16], namely A_s and $\tau_{\rm reio}$.

3. *Adding Euclid (lensing + $P(k)$) data.* Most of the discussion on the inclusion of DESI data still applies here, since Euclid data contains information on the BAO scale at different redshift. However the matter / shear power spectra contain extra information on cosmological perturbations, and lift or reinforce some parameter degeneracies, consistently with our previous discussion in section 4.2, point 3. The (M_ν, H_0) degeneracies are considerably reduced because the LSS data would prefer a different correlation angle between these two parameters. As expected, the Euclid data considerably tightens the positive correlation between M_ν and A_s, and as a side effect the combined data leads to a clear positive correlation between M_ν and $\tau_{\rm reio}$. The degeneracy between M_ν and $\omega_{\rm cdm}$ is lifted by the weak lensing data. All these degeneracy reductions lead to an overall shrinking of all contours involving M_ν, H_0 and $\omega_{\rm cdm}$ by a factor of order 3 between CMB and CMB+LSS data. The neutrino mass value is accurately determined independently of the value of n_s, and the mild correlation between M_ν and n_s in CMB data disappears with additional LSS data.

Compared to figure 94, table 9 presents the results of one more MCMC run featuring CORE, DESI and Euclid weak lensing, but not the Euclid galaxy clustering information. The comparison of these results with those for CORE and Euclid weak lensing+galaxy clustering show the importance of geometrical information (BAO angular scales) versus shape information (full matter power spectrum), although both runs do contain some shape information coming from the weak lensing data. We clearly see that adding more shape information on the matter power spectrum benefits only to the determination of M_ν and H_0, and actually by a modest amount (10 to 15% per cent). At face value, this means that even if the analysis of future galaxy clustering data was plagued by unexpected systematics (besides the level that we conservatively took into account with our theoretical error bar), the prospects to accurately determine the summed neutrino mass with future surveys would not collapse.

In order to further improve the measurement of the neutrino mass with cosmological data, one should try to add independent constraints on the parameters that remain most strongly correlated

16 As side remarks, note that such compensation cannot be done by playing with n_s: as a consequence, both the (M_ν, n_s) degeneracy and the (A_s, n_s) degeneracy are lifted when BAO data are added; finally, because of the different neutrino mass compensation driven by the inclusion of BAO data, the correlations of $\omega_{\rm cdm}$ and H_0 with respect to $A_s, n_s, \tau_{\rm reio}$ are lifted, as well.

with M_ν in the CMB+LSS contours: these are H_0, A_s and $\tau_{\rm reio}$. The role of a very precise determination of H_0, free of astrophysical systematics, for the measurement of the neutrino mass, has already been stressed e.g. in [434]. It was also previously noticed in Ref. [407] that 21cm surveys could improve the determination of the optical depth to reionization, and thus of the summed neutrino mass. Having understood the physical explanation for the $(M_\nu, \tau_{\rm reio})$ degeneracy, we wish to further investigate this possibility, while keeping our conservative assumption on the matter power spectrum theoretical error.

9.5.2 *Adding 21cm surveys*

In the near future, many experimental efforts will be devoted to measuring precisely the epoch of recombination (EoR), mostly through the 21 cm line created by the hyperfine transition of the Hydrogen atom[17], including the value of $\tau_{\rm reio}$. In general, details of the EoR are strongly connected to fundamental questions in cosmology and astrophysics. They could shed light on many properties of the first galaxies and quasars, measure the time at which they form, explain how the formation of very metal-poor stars proceeded, and reveal whether the first galaxies were indeed the only re-ionizing source.

However, these experiments can also have great implications for neutrino physics in cosmology. Indeed, the independent measurement of the epoch of reionization by 21cm surveys may break the degeneracy between A_s and $\tau_{\rm reio}$ [407], [586] which appears in combined analyses of future CMB+LSS data.

To assess the impact of 21cm surveys on $\sigma(M_\nu)$, we performed a final MCMC run combining CORE+Euclid mock data with a gaussian prior on the value of $\tau_{\rm reio}$. In agreement with forecasts on the sensitivity of HERA or SKA, we fixed the prior variance to $\sigma(\tau_{\rm reio}) = 0.001$ [407], [525]. Note that by doing so, we are being conservative, since 21cm surveys will not only measure the evolution of the mean free electron fraction $x_e(z)$ (and thus the optical depth $\tau_{\rm reio}$), but also the power spectrum of the 21cm signal at different redshifts, $P_{21cm}(k, z)$, related to variations along the line of sight of the free electron fraction $x_e(\hat{n}, z)$ [423]. We are therefore using the minimal amount of information that one can extract from these experiments, and one could go beyond following e.g. the procedure of Refs. [407], [458], [459], [586].

The results of our MCMC forecast are summarized by the last line of table 9, and the green contours in figure 94.

The main impact of the $\tau_{\rm reio}-$prior is to reduce the possibility of varying of A_s, necessary to adjust the CMB parameter $A_s \exp(-2\tau_{\rm reio})$, by almost a factor two. Since M_ν was correlated directly with A_s and indirectly with $\tau_{\rm reio}$, the sensitivity to the summed neutrino mass also improves thanks to 21cm data, going from $\sigma(M_\nu) = 14$ meV for CORE+Euclid to 12 meV. As a side effect, the positive correlation between M_ν and $\omega_{\rm cdm}$ and the negative correlation between M_ν and h get steeper.

Thus, even if nature has chosen the summed neutrino mass to be close to the lower limit of the normal hierarchy, $M_\nu = 60$ meV, we expect that the joint analysis of CORE + Euclid + 21cm data will detect it at more than 5 σ.

17 e.g. PAPER 64: http://eor.berkeley.edu, 21CMA: http://21cma.bao.ac.cn, MWA: http://www.mwatelescope.org, LOFAR: http://www.lofar.org, HERA: http://reionization.org or SKA: http://www.skatelescope.org.

9.6 Conclusions

The foundations of a new era in precision cosmology are based on two cornerstones: the high sensitivity of future CMB and galaxy survey experiments, and a deep understanding of the physics governing the processes of recombination and structure formation. The extreme accuracy of future data will offer the opportunity to constrain particle physics with cosmology, exceeding in many cases the precision of laboratory experiments. However, in order to exploit the new data, cosmologists will need a sufficiently accurate theoretical model taking into account the underlying physics.

Neutrinos provide an excellent example of how the sensitivity of future cosmological surveys may lead to such an important result as the summed neutrino mass detection, even when uncertainties on the details of the cosmological model are marginalised over.

In this work we have provided a careful discussion of the physical effects induced by massive neutrinos and their impact on cosmological observables, as they will appear in the data analysis of the next generation of cosmological experiments. We have shown how the unique nature of light neutrinos, being relativistic until very late times and behaving as a matter component after the non relativistic transition, makes it possible to identify different signatures at different epochs of the cosmic history. Therefore the correlation between the summed neutrino mass and the other cosmological parameters changes, depending on the redshift range probed by the various data sets.

Our results on the sensitivity of future CMB-CORE and BAO-DESI experiments to the summed neutrino mass are consistent with the literature (see Refs. [42], [407]). Moreover, the results of our forecasts including a Euclid-like survey prove the importance of cosmic shear and galaxy clustering as complementary probes. We pointed out that the results of our Euclid cosmic shear + galaxy correlation forecasts depend very much on the choice of the theoretical error introduced to account for the systematics coming from the deep non-linear regime. Nevertheless, they are again compatible with previously published results. For instance, Ref. [288] found $\sigma(M_\nu) = 11$ meV for Planck + Euclid cosmic shear / galaxy correlation, but with a different treatment of the uncertainty on non linear corrections. Ref. [68] found a larger error, close to 20 meV, but for Planck + Euclid cosmic shear or Planck + Euclid galaxy correlation, not trying to combine the two LSS probes together and without CORE data. Ref. [407] found $\sigma(M_\nu) = 12$ meV for Planck + CMB-Stage-IV + BAO-DESI + 21cm-HERA, identical to our estimate for CORE + Euclid + 21cm-$\tau_{\rm reio}$-prior.

Anyhow, the main goal of this study was not to present a new set of forecasts, but to discuss the details of physical effects and parameter degeneracies involving neutrino masses. In particular, we clarified the reason for which an unexpected degeneracy between the neutrino mass sum and the optical depth at reionization will appear in the analysis of future high precision galaxy surveys, as already pointed out e.g. in [42], [407]. We showed that this degeneracy is not present in a CMB-only analysis, because the neutrino mass effects on CMB lensing can be compensated by playing with h and $\omega_{\rm cdm}$ in a better way than by adjusting $(A_s, \tau_{\rm reio})$. However, the former degeneracy is alleviated once BAO and LSS low redshift measurements are taken into account. Moreover, we demonstrated that the LSS data introduce a strong correlation between M_ν and A_s, which finally leads to a clear $(M_\nu, \tau_{\rm reio})$ degeneracy in the combined CMB+LSS analysis.

These conclusions clarify why further independent measurements of the optical depth will be beneficial for the neutrino mass determination, as previously noticed by the authors of [407]. For instance, the results from the HERA or SKA 21cm surveys will provide an independent constraint on $\tau_{\rm reio}$, thus breaking this degeneracy. Our results indicate that this could reduce the error on M_ν with respect to

the CMB+LSS case, leading to a robust detection of the summed neutrino mass at more than 5 σ for CORE+Euclid+HERA or SKA. In principle, it would be possible to do even better if H_0 could be measured in an independent and robust way with an error below $\sigma(H_0) \sim 0.17$km/s/Mpc.

In conclusion, the remarkable complementarity of future different cosmological data will lead to extremely accurate constraints on the neutrino mass sum and, possibly, on other neutrino properties, answering some of the still open questions of modern physics.

GENERAL CONCLUSIONS

This work aimed at a better characterization of dark matter and neutrino properties in cosmology, by looking for their peculiar electromagnetic and gravitational signatures. Special attention has been given to CMB anisotropies, which are known to hold a wealth of information on many aspects of physics, from General Relativity to the Standard Model of Particle Physics. We emphasized the synergy of CMB anisotropies with spectral distortions of the CMB energy distribution and BBN, much more sensitive to e.m. processes happening before decoupling.

We started by a thorough review in chapters 1 to 3 of the standard tools needed to compute those observables. We derived in chapter 4 the strongest constraints to date on a decaying massive relics from the pure gravitational effects of the decay, extending the phenomenology to multicomponent models with very high decay rate. The most important point is that those constraints basically always apply, independently of the particle physics model. Remarkably, despite their generality, we showed how they bring significant elements for discussion to currently hot topics in cosmology, such as models for discrepancies between local and cosmological determinations of the Hubble expansion rate, H_0, or models where primordial black holes contribute to a sizable fraction of the DM.

In chapter 5 we reviewed the computation of standard BBN constraints on e.m. energy injection and showed how a loophole to the standard theory of e.m. cascade allowed us to: i) improve the bounds by up to one order of magnitude in the [MeV-GeV] mass range; ii) reopen the window to a purely e.m. solution to the cosmological Lithium problem, with an explicit toy model proof given with a ~ 4 MeV sterile neutrino decay.

Chapter 6 focused on CMB anisotropy constraints on e.m. decaying particles, illustrating the fundamental complementarity of CMB spectral distortions and BBN studies, while future 21cm surveys could gain at least one order of magnitude more sensitivity on some models. We applied our bounds explicitly to both low and high masses Primordial Black Holes, as well as sterile neutrinos, deriving the strongest cosmological bounds to date on these models. We then studied in chapter 7 the impact of annihilating relics, with a special attention on annihilations in halos and its interplay with stars in reionizing our Universe. Our major finding is that, barring unrealistic halo models, DM halo formation do not enhance the annihilation rate sufficiently to make DM contribute in a significant way to the Universe reionization. However, measurements of the IGM temperature and 21 cm signal could be significantly affected, but this deserves further investigation and more data.

The last part of this work was devoted to the cosmological determination of neutrino properties with current and future data. Using peculiar clustering properties of neutrinos, we started by assessing in chapter 8 that it is possible to make a robust statement about the detection of the cosmic neutrino background by CMB experiments. We then carefully studied the effects on cosmological data of a summed neutrino mass close to its minimum, showing that parameter degeneracies can be removed by appropriate combinations of datasets. A joint forecast of the sensitivity of Euclid and DESI surveys together with a CORE-like CMB experiment and a prior on the optical depth based on future 21 cm experiment, leads to a 1σ uncertainty $\sigma(M_\nu) = 12$ meV. This would allow for the first $5\,\sigma$ cosmological detection of neutrino masses.

Cosmology, since the birth of General Relativity, has been the realm of many theoretical and experi-

mental successes. However, as it is often the case in physics, with those successes came deep mysteries. Obviously, here we have not reached any final word on the longstanding dark matter and neutrino mass puzzles, but contributed to answer a number of questions. Many current experimental efforts are devoted to improve LSS surveys, with the Euclid and LSST experiments, and our understanding of the cosmic reionization and cosmic dawn era with 21 cm experiments. Those observables can have great implications for the models investigated in this work, and therefore represent one of the main research direction deserving further exploration. We also hope that this work contributes in showing the great potential of further CMB studies, for which several ground based and space experiments have been recently proposed and/or accepted. Both anisotropies and the spectral shape of the CMB still hold a wealth of information that should be fully exploited. Finally, in the era of gravitational wave astronomy, let us mention the possibility of linking source of gravitational waves to DM candidates, such as in the PBH scenarios. For sure, the synergy of e.m. probes with purely gravitational ones has not exhausted its potential.

More generally, this work illustrates the great potential of cosmological observables, a message of hope especially in the light of null results in searches for new physics at accelerators. We are confident that a multifaceted and multimessenger approach, combining information from many experiments, will shed light on some of the remaining mysteries of our Universe.

Part IV

APPENDIX

A

APPENDIX TO CHAPTER 1

A.1 Basics of the Boltzmann equation in an expanding Universe

We wish to describe the evolution of the distribution under the influence of the Universe expansion and potential interactions creating and destructing particles. This is encoded inside a *Boltzmann equation*, which has the schematic form

$$\frac{df}{dt} = \mathcal{C}[f]\,. \tag{A.1.1}$$

The RHS is called the collision operator and contains all possible interactions terms, it can be pretty complicated. In the absence of collisions, one gets the Liouville equation $df/dt = 0$, meaning that the number of particles in a given element of the phase space does not change with time, even if the phase space elements are moving in time in a complicated way due to nontrivial metric. For a given species i, the distribution f_i is a function of energy (or modulus) and time only, and the total derivative can be expanded as

$$\frac{df}{dt} = \frac{\partial f}{\partial t} + \frac{\partial f}{\partial E}\frac{dE}{dt}\,. \tag{A.1.2}$$

We know that $E \propto a^{-1}$, which immediately yields $dE/dt = -aHE$ and thus

$$\frac{df}{dt} = \frac{\partial f}{\partial t} - aHE\frac{\partial f}{\partial E}\,. \tag{A.1.3}$$

Integrating over momentum and assuming first no collision terms, from eq. (1.3.12) we get

$$\frac{dn_i}{dt} - 3Hn_i = 0 \Leftrightarrow \frac{1}{a^3}\frac{d(a^3 n_i)}{dt} = 0\,. \tag{A.1.4}$$

This simply encodes the evolution of the number density with the Universe expansion. We however need to take into account particle creation and destruction processes. Considering only 2-body interactions between species i, j and k, l of the type

$$i + j \leftrightarrow k + l\,,$$

we can write

$$\frac{dn_i}{dt} = -3\frac{\dot{a}}{a}n_i - c(ij \to kl) + c(kl \to ij). \tag{A.1.5}$$

The c-terms quantify the number of reactions per unit volume and time, the sign - (+) attest that the process destroy (create) particles. Those terms can be computed according to :

$$c(ij \to kl) = \int \tilde{dp_i} f_i \int \tilde{dp_j} f_j \int \tilde{dp_k} \int \tilde{dp_l} (2\pi)^4 \delta^3(p_i + p_j - p_k - p_l)\delta(E_i + E_j - E_k - E_l) \times |M_{ij\to kl}|^2 (1 \pm f_k)(1 \pm f_l)\,, \tag{A.1.6}$$

where $\tilde{dp} = \frac{d^3\vec{p}}{(2\pi)^3 2E}$ is the Lorentz invariant phase-space element . The $(1 \pm f)$ terms encode the Pauli principle for fermions, with a minus sign (i.e. that if $f = 1$ the cross-section is zero) and stimulated emission for bosons with a plus sign. The δ functions ensure energy-momentum conservation while the matrix elements $|M|^2$ are obtained from Feynman diagrams and the computation of scattering processes.

This expression is highly symmetric. Inverting ij and kl while using the CPT theorem:

$$|M_{ij\to kl}|^2 = |M_{kl\to ij}|^2,$$

we find that at equilibrium (i.e. when the expansion rate is much smaller than the reaction rates), a stationary solution ($dn/dt = 0$) can be obtained if distributions verify

$$f_k f_l (1 \mp f_i)(1 \mp f_j) = f_i f_j (1 \mp f_k)(1 \mp f_l),$$

which is only possible if

$$\frac{f_i}{1 \mp f_i} = \exp[(E_p - \mu_i)/T] \quad \text{with} \quad \mu_i + \mu_j = \mu_k + \mu_l.$$

By inverting this equation, we find the well-known result that at equilibrium particles follow Fermi-Dirac or Bose-Einstein distribution (1.3.9).

It is possible to introduce the cross-section $\sigma_{ij\to kl}$ for the process $ij \to kl$

$$c(ij \to kl) = \int \tilde{dp_i} f_i \int \tilde{dp_j} f_j \sigma_{ij\to kl} v_{ij}\,, \tag{A.1.7}$$

where v_{ij} is the relative velocity between the species i and j. We can rewrite the reaction rates per unit volume as

$$\begin{aligned} c(ij \to kl) &= \int \tilde{dp_i} f_i \int \tilde{dp_j} f_j \times \frac{\int \tilde{dp_i} f_i \int \tilde{dp_j} f_j \sigma_{ij\to kl} v_{ij}}{\int \tilde{dp_i} f_i \int \tilde{dp_j} f_j} \\ &= \int \tilde{dp_i} f_i \int \tilde{dp_j} f_j \langle \sigma_{ij\to kl} v_{ij} \rangle \\ &= n_i n_j \langle \sigma_{ij\to kl} v_{ij} \rangle\,. \end{aligned} \tag{A.1.8}$$

Given that, at thermal equilibrium, the collision term has to vanish, the "detailed balance principle" ensures the equality between reaction rates

$$n_i^{\rm eq} n_j^{\rm eq} \langle \sigma_{ij\to kl} v_{ij} \rangle_{\rm eq} = n_k^{\rm eq} n_l^{\rm eq} \langle \sigma_{kl\to ij} v_{kl} \rangle_{\rm eq}\,. \tag{A.1.9}$$

We approximate the velocity averaged cross-section by their value at equilibrium,

$$\langle \sigma_{ij\to kl} v_{ij} \rangle \sim \langle \sigma_{ij\to kl} v_{ij} \rangle_{\rm eq} \equiv \langle \sigma v \rangle\,,$$

thus we can rewrite

$$\frac{dn_i}{dt} = -3\frac{\dot{a}}{a} n_i + \left[\left(\frac{n_i n_j}{n_k n_l} \right)^{\rm eq} n_k n_l - n_i n_j \right] \langle \sigma v \rangle\,, \tag{A.1.10}$$

where the subscript "eq" means that each number density is evaluated at equilibrium. This form of the Boltzmann equation will be the starting point of our discussion in sec. 1.3 and we will extend it to incorporate perturbations to the metric and the exact form of the Thomson scattering in chapter 2.

B

APPENDIX TO CHAPTER 2

B.1 Technical details regarding the perturbed Einstein equations

B.1.1 *Proofs of the general gauge transformation*

In sec. 2.1.1 we gave the relations encoding how metric transforms when performing a gauge transformation, define as

$$X^\mu \to \tilde{X}^\mu \equiv X^\mu + \xi^\mu(\tau, \vec{x}), \quad \text{where} \quad \xi^0 \equiv T,\ \xi^i \equiv S^i = \partial^i S + \hat{S}^i \ . \tag{B.1.1}$$

We now will compute explicitelty the transformation.
Using the invariance of ds^2 under a coordinate transformation, we can write :

$$ds^2 = g_{\mu\nu}(X) dX^\mu dX^\nu = \tilde{g}_{\alpha\beta}(\tilde{X}) d\tilde{X}^\alpha d\tilde{X}^\beta \quad . \tag{B.1.2}$$

Using $dX^\alpha = \left(\frac{\partial \tilde{X}^\alpha}{\partial X^\mu}\right) dX^\mu$ one gets

$$g_{\mu\nu}(X) = \frac{\partial \tilde{X}^\alpha}{\partial X^\mu} \frac{\partial \tilde{X}^\beta}{\partial X^\nu} \tilde{g}_{\alpha\beta}(\tilde{X}) \, . \tag{B.1.3}$$

For this calculation, it is necessary to remember that, since we deal with small perturbations, we can restrict ourself to zeroth and first order terms.
The (00) component is therefore

$$g_{00}(X) = \frac{\partial \tilde{X}^\alpha}{\partial \tau} \frac{\partial \tilde{X}^\beta}{\partial \tau} \tilde{g}_{\alpha\beta}(\tilde{X}) \quad , \tag{B.1.4}$$

which has for only non-negligible terms $\alpha = \beta = 0$, thus yielding

$$g_{00}(X) = \left(\frac{\partial \tilde{\tau}}{\partial \tau}\right)^2 \tilde{g}_{00}(\tilde{X}) \, . \tag{B.1.5}$$

Using the coordinate transforms B.1.1 gives $\tilde{\tau} = \tau + T \Rightarrow \frac{\partial \tilde{\tau}}{\partial \tau} = 1 + T'$ and therefore

$$\begin{aligned} a^2(\tau)(1+2\phi) &= (1+T')^2 a^2(\tau+T)(1+2\tilde{\phi}) \\ &= (1+2T'+\cdots)(a(\tau)+a'T+\cdots)^2(1+2\tilde{\phi}) \\ &= (a^2(\tau)+2a(\tau)^2T'+2a(\tau)a'T+\cdots)(1+2\tilde{\phi}) \\ &= a^2(\tau)(1+\underbrace{2\mathcal{H}T+2T'+2\tilde{\phi}}_{2\phi}+\cdots) \quad , \end{aligned} \tag{B.1.6}$$

where $\mathcal{H} \equiv a'/a$ is the Hubble parameter in conformal time. This immediately implies

$$\boxed{\phi \to \tilde{\phi} = \phi - T' - \mathcal{H}T} \quad . \tag{B.1.7}$$

The $(0i)$ component yields

$$\begin{aligned}
g_{0i}(X) &= \frac{\partial \tilde{X}^\alpha}{\partial \tau}\frac{\partial \tilde{X}^\beta}{\partial X^i}\tilde{g}_{\alpha\beta}(\tilde{X}) \\
&= \frac{\partial \tilde{X}^0}{\partial \tau}\left[\frac{\partial \tilde{X}^\beta}{\partial X^i}\tilde{g}_{0\beta}(\tilde{X})\right] + \frac{\partial \tilde{X}^j}{\partial \tau}\left[\frac{\partial \tilde{X}^\beta}{\partial X^i}\tilde{g}_{j\beta}(\tilde{X})\right] \\
&= \big\{1+T'\big\}\left[\frac{\partial \tilde{X}^0}{\partial X^i}\tilde{g}_{00}(\tilde{X}) + \frac{\partial \tilde{X}^k}{\partial X^i}\tilde{g}_{0k}(\tilde{X})\right] + S'^j\left[\frac{\partial \tilde{X}^0}{\partial X^i}\tilde{g}_{j0}(\tilde{X}) + \frac{\partial \tilde{X}^k}{\partial X^i}\tilde{g}_{jk}(\tilde{X})\right] \\
&= \big\{1+T'\big\}\Big[\partial_i T a^2(\tau+T)\big\{1+2\tilde{\phi}\big\} + \big\{\delta_{ik}+\partial_i S^k\big\}\big\{-a^2(\tau+T)\tilde{B}_k\big\}\Big] \\
&\quad + S'^j\Big[\partial_i T\big\{-a^2(\tau+T)\tilde{B}_j\big\} + \big\{\delta_{ik}+\partial_i S^k\big\}\big\{-a^2(\tau+T)\big(\delta_{jk}+\tilde{H}_{jk}\big)\big\}\Big] \\
\overset{1^{st}\text{order}}{\Rightarrow} -a^2(\tau)B_i &= a^2(\tau)\Big[\partial_i T - \tilde{B}_i - S_i'\Big] \quad ,
\end{aligned} \tag{B.1.8}$$

which means that B_i transforms as

$$\boxed{B_i \to \tilde{B}_i = B_i + \partial_i T - S_i'} \quad . \tag{B.1.9}$$

Finally the (ij) component leads to

$$\begin{aligned}
g_{ij}(X) &= \frac{\partial \tilde{X}^\alpha}{\partial X^i}\frac{\partial \tilde{X}^\beta}{\partial X^j}\tilde{g}_{\alpha\beta}(\tilde{X}) \\
&= \frac{\partial \tilde{X}^0}{\partial X^i}\left[\frac{\partial \tilde{X}^\beta}{\partial X^j}\tilde{g}_{0\beta}(\tilde{X})\right] + \frac{\partial \tilde{X}^k}{\partial X^i}\left[\frac{\partial \tilde{X}^\beta}{\partial X^j}\tilde{g}_{k\beta}(\tilde{X})\right] \\
&= \partial_i T\left[\frac{\partial \tilde{X}^0}{\partial X^j}\tilde{g}_{00}(\tilde{X}) + \frac{\partial \tilde{X}^k}{\partial X^j}\tilde{g}_{0k}(\tilde{X})\right] \\
&\quad + \big\{\delta_{ik}+\partial_i S^k\big\}\left[\frac{\partial \tilde{X}^0}{\partial X^j}\tilde{g}_{k0}(\tilde{X}) + \frac{\partial \tilde{X}^\ell}{\partial X^j}\tilde{g}_{kl}(\tilde{X})\right] \\
&= \partial_i T\Big[\partial_j T a^2(\tau+T)\big\{1+2\tilde{\phi}\big\} + \big\{\delta_{jk}+\partial_j S^k\big\}\big\{-a^2(\tau+T)\tilde{B}_k\big\}\Big] \\
&\quad + \big\{\delta_{ik}+\partial_i S^k\big\}\Big[\partial_j T\big\{-a^2(\tau+T)\tilde{B}_k\big\} + \big\{\delta_{jl}+\partial_j S^\ell\big\} \\
&\quad \times\big\{-a^2(\tau+T)\big(\delta_{kl}+\tilde{H}_{kl}\big)\big\}\Big]
\end{aligned} \tag{B.1.10}$$

$$\overset{1^{st}\text{order}}{\Rightarrow} -a^2(\tau)(\delta_{ij}+H_{ij}) = -a^2(\tau)\Big[\delta_{ij}\big\{1+2\mathcal{H}T\big\} + \partial_i S_j + \partial_j S_i + \tilde{H}_{ij}\Big], \tag{B.1.11}$$

which finally means that H_{ij} transforms as

$$\boxed{H_{ij} \to \tilde{H}_{ij} = H_{ij} - 2\mathcal{H}T - \big\{\partial_i S_j + \partial_j S_i\big\}.} \tag{B.1.12}$$

B.1.2 *Technical details related to the perturbation of the stress-energy tensor*

B.1.2.1 *Scalar degrees of freedom in $T_{\mu\nu}$*

We derive here the expression of the relevant scalar degrees of freedom in $T_{\mu\nu}$.
Using the notation $\rho = \bar{\rho} + \delta\rho$, $P = \bar{P} + \delta P$, $U^\mu = \bar{U}^\mu + \delta U^\mu$ and introducing the anisotropic stress tensor $\Pi^\mu_{\ \nu}$, we have already written the perturbed part of the stress-energy tensor at first order as

$$\delta T^\mu_{\ \nu} = (\delta\rho + \delta P)\bar{U}^\mu\bar{U}_\nu + (\bar{\rho} + \bar{P})(\delta U^\mu\bar{U}_\nu + \bar{U}^\mu\delta U_\nu) - \delta P\delta^\mu_{\ \nu} - \Pi^\mu_{\ \nu}\,. \tag{B.1.13}$$

Without loss of generality, the spatial part of the anisotropic stress tensor is taken to be traceless $H^i_{\ i} = 0$, as it can be absorped in a redefinition of the isotropic pressure P. Furthemore, $\Pi^\mu_{\ \nu}$ is chosen to be orthogonal to U^μ, i.e $U^\mu\Pi_{\mu\nu} = 0$ and $\Pi^0_{\ 0} = \Pi^0_{\ i} = 0$.
We now introduced small velocities $\delta U^i = v^i/a$, considered as first order perturbations and use $g_{\mu\nu}\delta U^\mu\delta U^\nu = \bar{g}_{\mu\nu}\bar{U}^\mu\bar{U}^\nu = 1$ to obtain at linear order :

$$\begin{aligned} 1 = g_{\mu\nu}\delta U^\mu\delta U^\nu &= \{g_{\mu\nu} + \delta g_{\mu\nu}\}\{\bar{U}^\mu + \delta U^\mu\}\{\bar{U}^\nu + \delta U^\nu\} \\ \overset{1^{st}\text{ order}}{\Rightarrow}\ \delta g_{\mu\nu}\bar{U}^\mu\bar{U}^\nu + 2\bar{U}_\mu\delta U^\mu &= 0 \quad . \end{aligned} \tag{B.1.14}$$

We already have the (i) components of δU^μ, we only need its (0) one. Using the definition of $\bar{U}^\mu$ in conformal time $\bar{U}^\mu = a^{-1}\delta^0_{\ \mu}$, implying that only the (00) term of previous equations is non-zero and $\delta g_{00} = 2a^2\phi$, we have :

$$\begin{aligned} \delta g_{\mu\nu}\bar{U}^\mu\bar{U}^\nu + 2\bar{U}_\mu\delta U^\mu &= 0 \\ \Leftrightarrow \delta g_{00}\bar{U}^0\bar{U}^0 + 2\bar{U}_0\delta U^0 &= 0 \\ \Leftrightarrow 2a^2\phi a^{-2} + 2a^{-1}\delta U^0 = 0 & \\ \Leftrightarrow \delta U^0 = -\phi a^{-1}\,. & \end{aligned} \tag{B.1.15}$$

So in conformal time we have, $\delta U^\mu = a^{-1}\big[1 - \phi, v^i\big]$.
Using $U_\mu = g_{\mu\nu}U^\nu$, we obtain

$$U_0 = g_{00}U^0 + \overbrace{g_{0i}U^i}^{\mathcal{O}(2)} = a^2(1+2\phi)a^{-1}(1-\phi) = a(1+\phi)\ , \tag{B.1.16}$$

$$U_i = g_{i0}U^i + g_{ij}U^j = -a^2B_ia^{-1} - a^2(\delta_{ij} + H_{ij})a^{-1}v^j = -a(B_i + v_i)\,, \tag{B.1.17}$$

i.e. $U_\mu = a\big[1 + \phi, -(v_i + B_i)\big]$.
At the end of the day, the tensor $\delta T^\mu_{\ \nu}$ is given by

$$\begin{aligned} \delta T^0_{\ 0} &= (\delta\rho + \delta P)\bar{U}^0\bar{U}_0 + (\bar{\rho} + \bar{P})(\delta U^0\bar{U}_0 + \bar{U}^0\delta U_0) - \delta P \\ &= (\delta\rho + \delta P) + (\bar{\rho} + \bar{P})(-\phi a^{-1}a + a^{-1}a\phi) - \delta P \\ &= \delta\rho\ , \end{aligned} \tag{B.1.18}$$

$$\begin{aligned} \delta T^i_{\ 0} &= (\delta\rho + \delta P)\bar{U}^i\bar{U}_0 + (\bar{\rho} + \bar{P})(\delta U^i\bar{U}_0 + \bar{U}^i\delta U_0) \\ &= (\bar{\rho} + \bar{P})(a^{-1}v^ia) \\ &= (\bar{\rho} + \bar{P})v^i\ , \end{aligned} \tag{B.1.19}$$

$$\begin{aligned}
\delta T^0{}_j &= (\delta\rho+\delta P)\bar{U}^0\bar{U}_j + (\bar\rho+\bar P)(\delta U^0\bar U_j + \bar U^0\delta U_j)\\
&= \{\bar\rho+\bar P\}\{a^{-1}(-a)(v_j+B_j)\}\\
&= -(\bar\rho+\bar P)(v_j+B_j)\,, \qquad \text{(B.1.20)}\\
\delta T^i{}_j &= (\delta\rho+\delta P)\bar{U}^i\bar{U}_j + (\bar\rho+\bar P)(\delta U^i\bar U_j + \bar U^i\delta U_j) - \delta P\delta^i{}_j - \Pi^i{}_j\\
&= -\delta P\delta^i{}_j - \Pi^i{}_j\,. \qquad \text{(B.1.21)}
\end{aligned}$$

We have already mentioned that only the longitudinal part of v_i will be involved in the scalar sector, which we usually write : $v_i^{\parallel} = \partial_i v$. It is traditional to introduce as scalar degrees of freedom the divergence θ:

$$\theta \equiv \partial^i v_i = \nabla^2 v\,, \qquad \text{(B.1.22)}$$

where the last equality holds since the orthogonal part is, by definition, divergenceless.
In the same way, instead of introducing a potential through the longitudinal part of Π^i_j as $\Pi^{i\parallel}_j = (\partial_i\partial_j - \frac{1}{3}\nabla^2\delta_{ij})\tilde\sigma$, it is common to define the scalar degrees of freedom σ (called *shear* or *anisotropic stress*) by

$$(\bar\rho+\bar P)\nabla^2\sigma = -(\partial_i\partial_j - \frac{1}{3}\nabla^2\delta_{ij})\Pi^i{}_j = -\partial_i\partial_j\Pi^i{}_j\,. \qquad \text{(B.1.23)}$$

So, together with $\delta \equiv \delta\rho/\bar\rho$, the scalar degrees of freedom of the stress-energy tensor are

$$\boxed{\begin{aligned}
T^0{}_0 &= \bar\rho(1+\delta) \quad , && \text{(B.1.24a)}\\
\partial_i T^i{}_0 &= (\bar\rho+\bar P)\theta \quad , && \text{(B.1.24b)}\\
T^i{}_i &= -3(\bar P+\delta P) \quad , && \text{(B.1.24c)}\\
(\partial_i\partial_j - \frac{1}{3}\nabla^2\delta_{ij})T^i{}_j &= (\bar\rho+\bar P)\nabla^2\sigma \quad . && \text{(B.1.24d)}
\end{aligned}}$$

B.1.2.2 *Gauge transformations and Gauge invariant variables*

We now need to now how to perform gauge transformation on the stress-energy tensor. As before, performing the transformation of eq. (B.1.2) leads for the stress-energy tensor to (this is common to any rank-2 tensor transforming under the Lorentz group)

$$T^\mu{}_\nu(X) = \frac{\partial X^\mu}{\partial\tilde X^\alpha}\frac{\partial\tilde X^\beta}{\partial X^\nu}\tilde T^\alpha{}_\beta(\tilde X)\,. \qquad \text{(B.1.25)}$$

We only need to evaluate this for every components to find the transformation laws. Recalling that $\tilde\tau \equiv \tau + T$ and $\tilde{X^i} \equiv X^i + S^i$, the (00) component is

$$\begin{aligned}
T^0{}_0(X) &= \frac{\partial\tau}{\partial\tilde X^\alpha}\frac{\partial\tilde X^\beta}{\partial\tau}\tilde T^\alpha{}_\beta(\tilde X)\\
&= \frac{\partial\tau}{\partial\tilde\tau}\left[\frac{\partial\tilde\tau}{\partial\tau}\tilde T^0{}_0(\tilde X) + \frac{\partial\tilde X^j}{\partial\tau}\tilde T^0{}_j(\tilde X)\right] + \frac{\partial\tau}{\partial\tilde X^i}\left[\frac{\partial\tilde\tau}{\partial\tau}\tilde T^i{}_0(\tilde X) + \frac{\partial\tilde X^j}{\partial\tau}\tilde T^i{}_j(\tilde X)\right]\\
&= \{1-T'\}\left[\{1+T'\}\{\bar\rho(\tilde X)(1+\tilde\delta)\} + S'^j\{\bar\rho(\tilde X)+\bar P\}\{\tilde v_j+\tilde B_j\}\right]\\
&\quad -S'\left[\{1+T'\}\{\bar\rho(\tilde X)+\bar P\}\tilde v^i + S'^j\{-(\delta\tilde P\delta^i{}_j + \tilde\Pi^i{}_j)\}\right]. \qquad \text{(B.1.26)}
\end{aligned}$$

The only first order term is the first term inside the big brackets. It yields

$$\begin{aligned} T^0_{\ 0}(X) &= \big\{1-T'\big\}\big\{1+T'\big\}\big\{\bar\rho(\tilde X)\big(1+\tilde\delta\big)\big\} \\ &= \big\{\bar\rho(X)+\frac{\partial\bar\rho}{\partial X^\mu}(\tilde X^\mu - X^\mu)\big\}\big\{1+\tilde\delta\big\} \\ \Rightarrow \bar\rho(1+\delta) &= \bar\rho(1+\tilde\delta)+\bar\rho' T \quad , \end{aligned} \tag{B.1.27}$$

where the last lines holds since $\bar\rho$ is uniform. Hence, we have

$$\boxed{\delta \to \tilde\delta = \delta - \frac{\bar\rho'}{\bar\rho}T.} \tag{B.1.28}$$

In a very similar vein one can show

$$\boxed{\delta P \to \delta\tilde P = \delta P - T\bar P'\,,} \tag{B.1.29}$$

$$\boxed{\begin{aligned} & q_i \to \tilde q_i = q_i + \big(\bar\rho+\bar P\big)S'_i \\ \Leftrightarrow\ & \theta \to \tilde\theta = \theta + \partial^i S'_i \\ \Leftrightarrow\ & \upsilon \to \tilde\upsilon = \upsilon + S'\,, \end{aligned}} \tag{B.1.30a}$$

$$\boxed{\Pi_{ij} \to \Pi_{ij}\,.} \tag{B.1.31}$$

We have introduced the *comoving-gauge density perturbation* Δ defined as

$$\Delta \equiv \delta + \frac{\bar\rho'}{\bar\rho}(\upsilon+\zeta) \quad . \tag{B.1.32}$$

We prove here that it is indeed gauge invariant. If we compute $\tilde\Delta$

$$\begin{aligned} \tilde\Delta &= \tilde\delta + \frac{\bar\rho(\tilde X)'}{\bar\rho(\tilde X)}(\tilde\upsilon+\tilde\zeta) \\ &= \delta - \frac{\bar\rho'}{\bar\rho}T + \frac{(\bar\rho(X)+\bar\rho' T)'}{(\bar\rho(X)+\bar\rho' T)}\big(\upsilon+S'+\zeta+T-S'\big) \\ &= \delta - \frac{\bar\rho'}{\bar\rho}T + \frac{(\bar\rho(X)+\bar\rho' T)'}{\bar\rho(X)}\left\{1-\frac{\bar\rho'}{\bar\rho}T\right\}\big(\upsilon+\zeta+T\big) \\ &\overset{1^{st}\text{order}}{=} \delta - \frac{\bar\rho'}{\bar\rho}T + \frac{\bar\rho'}{\bar\rho}\big(\upsilon+\zeta+T\big) \\ &= \Delta\,. \end{aligned} \tag{B.1.33}$$

which shows that Δ is gauge invariant.

B.1.3 *Relating both sides of Einstein equation*

In this section, we explicitely relate metric perturbations to matter ones by means of the Einstein equation (1.1.2). To do so, one needs to perturb the Christoffels $\Gamma^\mu_{\alpha\beta}$, the Ricci tensor $R_{\mu\nu}$ and Ricci scalar $\mathcal{R}$. The Christoffel tensor is symmetric in its two lower indices, as well as the Ricci tensor, so we don't need to compute all combinaisons. We will do this calculation at first order, in the newtonian

gauge restricted to scalar modes, and then form the Bardeen variables to be able to change gauge easily. In this gauge, the metric is given by eq. (2.1.14).
The Christoffels symbols are :

$$\begin{aligned}
\Gamma^0_{00} &= \frac{1}{2}g^{00}g_{00,0} \\
&= \mathcal{H}+\phi' && \text{(B.1.34)}\\
\Gamma^0_{0i} &= \frac{1}{2}g^{00}g_{00,i} \\
&= \partial_i\phi && \text{(B.1.35)}\\
\Gamma^i_{00} &= -\frac{1}{2}g^{ij}g_{00,j} \\
&= -\frac{1}{2}a^{-2}\delta^{ij}\big(1+2\psi\big)\big[-2a^2\partial_j\phi\big] && \text{(B.1.36)}\\
&= \partial^i\phi && \text{(B.1.37)}\\
\Gamma^0_{ij} &= -\frac{1}{2}g^{00}g_{ij,0} \\
&= \frac{1}{2}a^{-2}\delta^{ij}\big(1-2\phi\big)\big[2a'a\delta_{ij}(1-2\psi)+a^2\delta_{ij}(-2\psi')\big] \\
&= \mathcal{H}\delta_{ij}-\big[\psi'+2\mathcal{H}(\phi+\psi)\big]\delta_{ij} && \text{(B.1.38)}\\
\Gamma^i_{j0} &= \frac{1}{2}g^{ik}g_{kj,0} \\
&= \frac{1}{2}a^{-2}\delta^{ik}[1+2\psi][2a'a\delta_{kj}(1-2\psi)-2a\delta_{kj}\psi'] \\
&= \delta^i{}_j[\mathcal{H}-\psi'] && \text{(B.1.39)}\\
\Gamma^i_{jk} &= \frac{1}{2}g^{il}\big[g_{lj,k}+g_{lk,j}-g_{jk,l}\big] \\
&= -\frac{a^{-2}}{2}(1+2\psi)\delta^{il}\big[2\partial_k\psi a^2\delta_{lj}+2\partial_j\psi a^2\delta_{lk}-2\partial_l\psi a^2\delta_{jk}\big] \\
&= -\big[\delta^i_j\partial_k\psi+\delta^i_k\partial_j\psi-\delta_{jk}\partial^i\psi\big]\,. && \text{(B.1.40)}
\end{aligned}$$

Now, we can compute the Ricci tensor as it is given by eq. (1.1.4), keeping again only zeroth and first order term

$$\begin{aligned}
R_{00} &= \Gamma^\alpha_{00,\alpha}-\Gamma^\alpha_{0\alpha,0}+\Gamma^\alpha_{\beta\alpha}\Gamma^\beta_{00}-\Gamma^\alpha_{\beta0}\Gamma^\beta_{0\alpha} \\
&= (\mathcal{H}+\phi')'+\partial_i\partial^i\phi-(\mathcal{H}+\phi')'-3(\mathcal{H}-\psi')' \\
&\quad +(\mathcal{H}+\phi')^2+\partial_i\phi\partial^i\phi+3(\mathcal{H}-\psi')(\mathcal{H}+\phi')-(2\partial_j\psi)\partial^j\phi \\
&\quad -(\mathcal{H}+\phi')^2-\partial_i\phi\partial^i\phi-\partial_i\phi\partial^i\phi-3(\mathcal{H}-\psi')^2 \\
\Rightarrow R_{00} &= -3\mathcal{H}'+\partial_i\partial^i\phi+3\mathcal{H}(\phi'+\psi')+3\psi'' && \text{(B.1.41)}\\
R_{0i} &= \Gamma^\alpha_{0i,\alpha}-\Gamma^\alpha_{0\alpha,i}+\Gamma^\alpha_{\beta\alpha}\Gamma^\beta_{0i}-\Gamma^\alpha_{\beta0}\Gamma^\beta_{i\alpha} \\
&= \partial_i\phi'+\partial_i(\mathcal{H}-\psi')-\partial_i(\mathcal{H}+\phi')-3\partial_i(\mathcal{H}-\psi') \\
&\quad +(\mathcal{H}+\phi')\partial_i\phi+\partial_i\phi(\mathcal{H}-\psi')+3(\mathcal{H}-\psi')\partial_i\phi-(2\partial_i\psi)(\mathcal{H}-\psi') \\
&\quad -(\mathcal{H}+\phi')\partial_i\phi-\partial_i\phi(\mathcal{H}-\psi')-\partial_i\phi\big\{\mathcal{H}-\psi'-2\mathcal{H}(\phi+\psi)\big\} \\
&\quad +\delta^j_k(\mathcal{H}-\psi')\big[\delta^k_i\partial_j\psi+\delta^k_j\partial_i\psi-\delta_{ij}\partial^k\psi\big] \\
&= 2\partial_i\psi'+5\mathcal{H}\partial_i\phi-2\partial_i\psi'-3\mathcal{H}\partial_i\phi+2\mathcal{H}\partial_i\psi \\
\Rightarrow R_{0i} &= 2\partial_i\psi'+2\mathcal{H}\partial_i\phi && \text{(B.1.42)}
\end{aligned}$$

$$
\begin{aligned}
R_{ij} &= \Gamma^{\alpha}_{ij,\alpha} - \Gamma^{\alpha}_{i\alpha,j} + \Gamma^{\alpha}_{\beta\alpha}\Gamma^{\beta}_{ij} - \Gamma^{\alpha}_{\beta i}\Gamma^{\beta}_{j\alpha} \\
&= \delta_{ij}\big[\mathcal{H} - \big\{\psi' + 2\mathcal{H}\big(\phi+\psi\big)\big\}\big]' - \big[2\partial_i\partial_j\psi - \delta_{ij}\partial_k\partial^k\psi\big] - \partial_i\partial_j\phi + 3\partial_i\partial_j\psi \\
&\quad + \big(\mathcal{H}+\phi'\big)\delta_{ij}\big[\mathcal{H} - \big\{\psi' + 2\mathcal{H}\big(\phi+\psi\big)\big\}\big] + 3\big(\mathcal{H}-\psi'\big)\delta_{ij}\big[\mathcal{H} - \big\{\psi' + 2\mathcal{H}\big(\phi+\psi\big)\big\}\big] \\
&\quad - \big[\partial_i\phi\partial_j\psi + \partial_i\phi\partial_j\psi - \delta_{ij}\partial_k\phi\partial^k\psi\big] - \partial_j\phi\partial_i\phi - 2\delta_{ij}\big[\mathcal{H} - \big\{\psi' + 2\mathcal{H}\big(\phi+\psi\big)\big\}\big]\big(\mathcal{H}-\psi'\big) \\
&= \delta_{ij}[\mathcal{H}' - \psi'' - 2\mathcal{H}'(\phi+\psi) - 2\mathcal{H}(\phi'+\psi') + \partial_k\partial^k\psi] + \partial_i\partial_j(\psi-\phi) \\
&\quad + \delta_{ij}[4\mathcal{H}^2 - 7\mathcal{H}\psi' + \mathcal{H}\phi' - 8\mathcal{H}^2(\phi+\psi)] \\
&\quad + \delta_{ij}[\partial_k\partial^k\psi - 2\mathcal{H}^2 + 4\mathcal{H}\psi' + 4\mathcal{H}^2(\phi+\psi)] \\
\Rightarrow R_{ij} &= \partial_i\partial_j(\psi-\phi) \\
&\quad + \delta_{ij}\big[\mathcal{H}' - \psi'' - 2\mathcal{H}'(\phi+\psi) - \mathcal{H}\phi' - 5\mathcal{H}\psi' + 2\mathcal{H}^2 + \partial_k\partial^k\psi - 2(\mathcal{H}' + 2\mathcal{H}^2)(\phi+\psi)\big]\,.
\end{aligned}
\tag{B.1.43}
$$

From this lengthy computation, it is straightforward to compute the Ricci scalar

$$
\begin{aligned}
\mathcal{R} &= g^{00}R_{00} + 2\overbrace{g^{0i}R_{0i}}^{0} + g^{ij}R_{ij} \\
&= a^{-2}(1-2\phi)\mathcal{R}_{00} - a^{-2}(1+2\psi)\delta^{ij}\mathcal{R}_{ij} \\
&= a^{-2}(1-2\phi)\big[-3\mathcal{H}' + \partial_i\partial^i\phi + 3\mathcal{H}(\phi'+\psi') + 3\psi''\big] \\
&\quad -3a^{-2}(1+2\psi)\big[\mathcal{H}' - \psi'' - 2\mathcal{H}'(\phi+\psi) - \mathcal{H}\phi' - 5\mathcal{H}\psi' + 2\mathcal{H}^2 \\
&\quad + \partial_k\partial^k\psi - 2(\mathcal{H}' + 2\mathcal{H}^2)(\phi+\psi)\big] - a^{-2}(1+2\psi)\partial_i\partial^i(\psi-\phi) \\
\overset{1^{st}\text{order}}{\Rightarrow}\mathcal{R} &= a^{-2}\big[-6(\mathcal{H}' + \mathcal{H}^2) + 2\partial_i\partial^i\phi - 4\partial_i\partial^i\psi + 12(\mathcal{H}' + \mathcal{H}^2)\phi + 6\psi'' + 6\mathcal{H}(\phi' + 3\psi')\big]\quad .
\end{aligned}
\tag{B.1.44}
$$

We can now compute the Einstein tensor. It is

$$
\begin{aligned}
G_{00} &= R_{00} - \frac{1}{2}g_{00}\mathcal{R} \\
&= -(\mathcal{H}+\phi')^2 - \partial_i\phi\partial^i\phi - \partial_i\phi\partial^i\phi - 3(\mathcal{H}-\psi')^2 \\
&= -3\mathcal{H}' + \partial_i\partial^i\phi + 3\mathcal{H}(\phi'+\psi') + 3\psi'' \\
&\quad -\frac{1}{2}(1+2\phi)\big[-6(\mathcal{H}' + \mathcal{H}^2) + 2\partial_i\partial^i\phi - 4\partial_i\partial^i\psi + 12(\mathcal{H}' + \mathcal{H}^2)\phi + 6\psi'' + 6\mathcal{H}(\phi' + 3\psi')\big] \\
\Rightarrow G_{00} &= 3\mathcal{H}^2 + 2\partial_i\partial^i\psi - 6\mathcal{H}\psi'\quad .
\end{aligned}
\tag{B.1.45}
$$

$$
G_{0i} = R_{0i} - \overbrace{\frac{1}{2}g_{00}\mathcal{R}}^{0} = 2\partial_i\psi' + 2\mathcal{H}\partial_i\phi
\tag{B.1.46}
$$

$$
\begin{aligned}
G_{ij} &= R_{ij} - \frac{1}{2}g_{ij}\mathcal{R} \\
&= \partial_i\partial_j(\psi-\phi) \\
&\quad + \delta_{ij}\big[\mathcal{H}' - \psi'' - 2\mathcal{H}'(\phi+\psi) - \mathcal{H}\phi' - 5\mathcal{H}\psi' + 2\mathcal{H}^2 + \partial_k\partial^k\psi - 2(\mathcal{H}' + 2\mathcal{H}^2)(\phi+\psi)\big] \\
&\quad + \frac{1}{2}(1-2\psi)\delta_{ij}\big[-6(\mathcal{H}' + \mathcal{H}^2) + 2\partial_i\partial^i\phi - 4\partial_i\partial^i\psi + 12(\mathcal{H}' + \mathcal{H}^2)\phi + 6\psi'' + 6\mathcal{H}(\phi' + 3\psi')\big] \\
\Rightarrow G_{ij} &= -(2\mathcal{H}' + \mathcal{H}^2)\delta_{ij} + \big[\partial_i\partial^i(\phi-\psi) + 2\psi'' + 2(2\mathcal{H}' + \mathcal{H}^2)(\psi+\phi) + 2\mathcal{H}\phi' + 4\mathcal{H}\psi'\big]\delta_{ij} \\
&\quad + \partial_i\partial_j(\psi-\phi)\,.
\end{aligned}
\tag{B.1.47}
$$

The final part is to use Einstein equation (1.1.2) to relate metric and matter perturbations. The scalar degrees of freedom are contained in ϕ and ψ on the metric side, δ, δP, θ (or υ), and σ on the matter-

side - The einstein equation will provide us 4 relations. The other relations will be fixed by *equation of state* relating P and ρ or σ and θ. We first consider the (00) component

$$\begin{aligned} G_{00} &= 8\pi G T_{00} \\ &= 8\pi G g_{0\mu} T^{\mu}_{\ 0} \\ &= 8\pi G (g_{00} T^{0}_{\ 0} + g_{0i} T^{i}_{\ 0}) \\ \Leftrightarrow 3\mathcal{H}^2 + 2\partial_i \partial^i \psi - 6\mathcal{H}\psi' &= 8\pi G a^2 (1+2\phi)\bar{\rho}(1+\delta)\,. \end{aligned} \tag{B.1.48}$$

Splitting between zeroth and first orders, we have

$$3\mathcal{H}^2 = 8\pi G a^2 \bar{\rho} \qquad \text{at zeroth order}\,, \tag{B.1.49}$$

$$2\partial_i \partial^i \psi - 6\mathcal{H}\psi' = 8\pi G a^2 \bar{\rho}(\delta + 2\phi) \qquad \text{at first order}\,. \tag{B.1.50}$$

Inserting the zeroth order equation into the first one, dividing by two and going to Fourier space yields

$$\boxed{k^2\psi + 3\mathcal{H}(\mathcal{H}\phi + \psi') = -4\pi G a^2 \bar{\rho}\delta\,.} \tag{B.1.51}$$

We can move to the $(0i)$ component

$$\begin{aligned} G_{0i} &= 8\pi G T_{0i} \\ &= 8\pi G (g_{00} T^{0}_{\ i} + g_{0j} T^{j}_{\ i}) \\ \Leftrightarrow 2\partial_i \psi' + 2\mathcal{H}\partial_i \phi &= -8\pi G a^2 q_i\,. \end{aligned} \tag{B.1.52}$$

Using again the notation $q_i = (\bar{\rho} + \bar{P})\partial_i v$, we can integrate eq. (B.1.52) assuming that perturbations decay at infinity (or go into Fourier space and simplify by k) to obtain

$$\psi' + \mathcal{H}\phi = -4\pi G a^2 (\bar{\rho} + \bar{P}) v\,, \tag{B.1.53}$$

or as a function of $\theta = -k^2 v$

$$-k^2(\psi' + \mathcal{H}\phi) = 4\pi G a^2 (\bar{\rho} + \bar{P})\theta\,. \tag{B.1.54}$$

Before evaluating other component, we can insert eq. (B.1.53) in eq. (B.1.51) to obtain the "Poisson equation" for ψ in Fourier space

$$\boxed{k^2\psi = -4\pi G a^2 \left[\bar{\rho}\delta - 3\mathcal{H}(\bar{\rho} + \bar{P})v\right].} \tag{B.1.55}$$

The terms inside the brackets correspond, in the newtonian gauge, to the gauge-invariant variable Δ of eq. (B.1.32) ! We still need two equations for closing the system. The next one is usually obtained from the (ij) term, given by eq. (B.1.47). In this coefficient, a bunch of term is proportional to δ_{ij} that contribute to the trace of G_{ij}. To avoid dealing with them, we consider the *longitudinal, traceless* part of G_{ij}, that can be extracted by means of the projection operator in Fourier space $(k^i k^j - (1/3)k^2\delta^{ij})$. It basically kills all terms proportional to δ_{ij}, leaving only

$$(k^i k^j - (1/3)k^2\delta^{ij})G_{ij} = (k^i k^j - (1/3)k^2\delta^{ij})[k_i k_j(\psi - \phi)] = \frac{2k^4}{3}(\psi - \phi)\,. \tag{B.1.56}$$

Contracting also the matter side with this operator yields

$$(k^i k^j - (1/3)k^2\delta^{ij})T_{ij} = (k^i k^j - (1/3)k^2\delta^{ij})\Pi_{ij} \overset{eq.\ (B.1.23)}{=} -(\bar{\rho} + \bar{P})k^2\sigma\,. \tag{B.1.57}$$

Equating both sides leads to

$$\boxed{k^2(\phi-\psi) = 12\pi G a^2(\bar{\rho}+\bar{P})\sigma\,.} \tag{B.1.58}$$

Finally, we still need to evaluate the trace part of G_{ij} :

$$\begin{aligned}
G^i{}_i &= g^{i\mu}G_{\mu i} \qquad\qquad (B.1.59)\\
&= g^{ik}G_{ki}\\
&= -a^{-2}(1+2\psi)\delta^{ik}\big[-(2\mathcal{H}'+\mathcal{H}^2)\delta_{ki}+\big[\partial_i\partial^i(\phi-\psi)+2\psi''+2(2\mathcal{H}'+\mathcal{H}^2)(\psi+\phi)\\
&\quad +2\mathcal{H}\phi'+4\mathcal{H}\psi'\big]\delta_{ki}+\partial_k\partial_i(\psi-\phi)\big]\\
&= -3a^{-2}(1+2\psi)\big[-(2\mathcal{H}'+\mathcal{H}^2)+2\psi''+2(2\mathcal{H}'+\mathcal{H}^2)(\psi+\phi)+2\mathcal{H}\phi'+4\mathcal{H}\psi'\big]\\
&\quad -a^{-2}(1+2\psi)2\partial_i\partial^i(\phi-\psi)\\
&= -3a^{-2}\big[-(2\mathcal{H}'+\mathcal{H}^2)+2\psi''+2(2\mathcal{H}'+\mathcal{H}^2)\phi+2\mathcal{H}\phi'+4\mathcal{H}\psi'\big]-a^{-2}2\partial_i\partial^i(\phi-\psi)\,.
\end{aligned}$$

On the other side, we have $T^i{}_i = -3(\bar{P}+\delta P)$. At zeroth order, we find the second Friedmann equation

$$2\mathcal{H}'+\mathcal{H}^2 = -8\pi G a^2\bar{P} \quad , \tag{B.1.60}$$

and at first order

$$\boxed{\psi''+(2\mathcal{H}'+\mathcal{H}^2)\phi+\mathcal{H}\phi'+2\mathcal{H}\psi'+\frac{1}{3}\partial_i\partial^i(\phi-\psi) = 4\pi G a^2\delta P}\,. \tag{B.1.61}$$

B.1.4 *Continuity and Euler equation at first order*

Instead of relating metric and tensor perturbations through Einstein equations, it might be useful to make use of the stress-energy conservation implied by Bianchi identies

$$T^\mu_{\nu;\mu} = T^\mu_{\nu,\mu}+\Gamma^\mu_{\alpha\mu}T^\alpha_\nu-\Gamma^\alpha_{\nu\mu}T^\mu_\alpha = 0 \quad . \tag{B.1.62}$$

This, together with the equations we have derived, will form a redundant set of equations. However, depending on the problem at hand, one formulation might be more useful than another. Indeed, we will use these equations when dealing with the decaying DM.
We start by considering the $\nu=0$ component

$$\begin{aligned}
T^\mu_{0;\mu} &= T^0_{0,0}+T^i_{0,i}+\big(\Gamma^0_{00}+\Gamma^i{}_{i0}\big)T^0_0+\underbrace{\Gamma^\mu_{i\mu}T^i_0}_{\mathcal{O}(2)}-\Gamma^0{}_{00}T^0_0-\underbrace{\Gamma^0_{i0}T^i_0}_{\mathcal{O}(2)}-\underbrace{\Gamma^i{}_{00}T^0_i}_{\mathcal{O}(2)}-\Gamma^i{}_{j0}T^j_i\\
&= \partial_0\big(\bar{\rho}(1+\delta)\big)+(\bar{P}+\bar{\rho})\theta+(\mathcal{H}+\phi'+3\mathcal{H}-3\psi')\bar{\rho}(1+\delta)\\
&\quad -(\mathcal{H}+\phi')\bar{\rho}(1+\delta)-(\mathcal{H}-\psi')\delta^i{}_j[-(\bar{P}+\delta P)\delta^j{}_i]\\
&= \bar{\rho}'(1+\delta)+\bar{\rho}\delta'+(\bar{P}+\bar{\rho})\theta+3\mathcal{H}\bar{\rho}(1+\delta)-3\bar{\rho}\psi'+3\mathcal{H}(\bar{P}+\delta P)-3\bar{P}\psi'\\
&\overset{!}{=} 0\,.
\end{aligned} \tag{B.1.63}$$

If we introduce the equation of state $\bar{P}=\omega\bar{\rho}$, we have $\bar{P}+\delta P = \omega\bar{\rho}+\frac{\delta P}{\delta\rho}\bar{\rho}\delta$ and we can write the standard continuity equation

$$\begin{aligned}
\bar{\rho}' &= -3\mathcal{H}(\bar{\rho}+\bar{P})\\
\Leftrightarrow \frac{\bar{\rho}'}{\bar{\rho}} &= -3\mathcal{H}(1+\omega)\,.
\end{aligned} \tag{B.1.64}$$

At first order, we have

$$\delta' = -\delta\left(\frac{\bar\rho'}{\bar\rho}+3\mathcal{H}\right)+\frac{1}{\bar\rho}(3\psi'-\theta)(\bar P+\bar\rho)-3\mathcal{H}(\delta+\frac{\delta P}{\bar\rho})\,. \tag{B.1.65}$$

and finally using eq. (B.1.64), ω, and $\delta=\delta\rho/\bar\rho$ we find

$$\boxed{\delta' = 3\mathcal{H}\delta\big(\omega-\frac{\delta P}{\delta\rho}\big)+(3\psi'-\theta)(1+\omega)}\,. \tag{B.1.66}$$

It describes the evolution of the density perturbation. The first term on the rhs is the dilution due to the background expansion, the θ term accounts for the local fluid flow due to peculiar velocity, and the ψ' term is a purely relativistic effect corresponding to the density changed caused by perturbations to the local expansion rate (defined as $(1-\psi)a$ in newtonian gauge).
Next, we turn to the $\nu=i$ component

$$\begin{aligned}
T^\mu_{i;\mu} &= T^0_{i,0}+T^j_{i,j}+(\Gamma^0_{00}+\Gamma^i{}_{i0})T^0_i+(\Gamma^0_{j0}+\Gamma^k_{jk})T^j_i-\Gamma^0{}_{0i}T^0_0-\Gamma^0{}_{ji}T^j_0-\Gamma^j{}_{0i}T^0_j-\Gamma^j{}_{ki}T^k_j\\
&= -\partial_0\big((\bar\rho+\bar P)v_i\big)+\partial_j\big[-(\bar P+\delta P)\delta^j{}_i-\Pi^i{}_j\big]-4\mathcal{H}(\bar\rho+\bar P)v_i-(\partial_j\phi-3\partial_j\psi)\bar P\delta^j{}_i-\partial_i\phi\bar\rho\\
&\quad -\mathcal{H}\delta_{ji}(\bar\rho+\bar P)v^j+\mathcal{H}\delta^j{}_i(\bar\rho+\bar P)v_j+(-\big[\delta^j_k\partial_i\psi+\delta^j_i\partial_k\psi-\delta_{ki}\partial^j\psi\big])\bar P\delta^k{}_j\\
&= -(\bar\rho'+\bar P')v_i-(\bar\rho+\bar P)v_i'-\partial_i\delta P-\partial_j\Pi^i{}_j-4\mathcal{H}(\bar\rho+\bar P)v_i-(\partial_i\phi-3\partial_i\psi)\bar P-\partial_i\phi\bar\rho-3\partial_i\psi\bar P\\
&= -(\bar\rho'+\bar P')v_i-(\bar\rho+\bar P)v_i'-\partial_i\delta P-\partial_j\Pi^i{}_j-4\mathcal{H}(\bar\rho+\bar P)v_i-\partial_i\phi(\bar\rho+\bar P)\\
&\overset{!}{=} 0
\end{aligned} \tag{B.1.67}$$

We can now use eq. (B.1.64) and divide by $(\bar\rho+\bar P)$

$$v_i'+\left(\frac{\bar P'}{\bar\rho+\bar P}+\mathcal{H}\right)v_i=-\frac{\partial_i\delta P}{\bar\rho+\bar P}-\partial_i\phi-\frac{\partial_j\Pi^i{}_j}{\bar\rho+\bar P} \tag{B.1.68}$$

We would like now to express this relation as a function of ω, θ and σ defined by eq. (B.1.23). We need to compute $\bar P'$:

$$\begin{aligned}
\bar P' &= (\omega\bar\rho)'\\
&= \omega'\bar\rho+\omega\bar\rho'\\
&= \bar\rho\big[\omega'-3\omega\mathcal{H}(1+\omega)\big]\quad .
\end{aligned} \tag{B.1.69}$$

Taking the divergence of eq. (B.1.68) and going to Fourier space leads to

$$\theta'+\left(\frac{\omega'-3\omega\mathcal{H}(1+\omega)}{1+\omega}+\mathcal{H}\right)\theta = \frac{k^2}{1+\omega}\frac{\delta P}{\delta\rho}\delta+k^2\phi-k^2\sigma\,. \tag{B.1.70}$$

Reordering the terms yields the euler equation in the common variables

$$\boxed{\theta' = (3\omega-1)\mathcal{H}\theta-\left(\frac{\omega'}{1+\omega}\right)\theta+\frac{k^2}{1+\omega}\frac{\delta P}{\delta\rho}\delta+k^2\phi-k^2\sigma}\,. \tag{B.1.71}$$

All these relations can be rewritten in other gauges by means of the gauge invariant variables Φ, Ψ, δ^{gi}, θ^{gi}, δP^{gi} through the relations

$$\boxed{\Psi=\phi+\mathcal{H}(\zeta-\mu')+(\zeta-\mu')' \qquad \Phi=-\psi-\mathcal{H}(\zeta-\mu')+\frac{1}{3}\nabla^2} \tag{B.1.72a}$$

$$\boxed{\delta^{gi}=\delta-\frac{\bar\rho'}{\bar\rho}(\dot\mu-\zeta) \qquad \theta^{gi}=\theta+\nabla^2(\dot\mu-\zeta) \qquad \delta P^{gi}=\delta P-\bar P'(\dot\mu-\zeta)\,.} \tag{B.1.72b}$$

Recalling that the metric in the synchronous gauge has the form

$$ds^2 = a^2(\tau)\{d\tau^2 - (\delta_{ij} + H_{ij})dx^i dx^j\} \qquad \text{with} \qquad H_{ij} = \hat{k}_i\hat{k}_j h + (\hat{k}_i\hat{k}_j - \frac{1}{3}\delta_{ij})6\eta\,, \tag{B.1.73}$$

we have for the particular example of switching between newtonian and synchronous gauge gives, in Fourier space,

$$\boxed{\begin{aligned}
\phi &= \mathcal{H}\frac{(6\eta+h)'}{2k^2} + \frac{(6\eta+h)''}{2k^2} && \text{(B.1.74a)}\\
\psi &= \eta - \mathcal{H}\frac{(6\eta+h)'}{2k^2} && \text{(B.1.74b)}\\
\delta(new) &= \delta(syn) + \frac{\bar{\rho}'}{\bar{\rho}}\frac{6\eta'+h'}{2k^2} && \text{(B.1.74c)}\\
\theta(new) &= \theta(syn) + \frac{1}{2}(6\eta'+h') && \text{(B.1.74d)}\\
\delta P(new) &= \delta P(syn) + \bar{P}'\frac{6\eta'+h'}{2k^2}\,. && \text{(B.1.74e)}
\end{aligned}}$$

This enables us to obtain Einstein equations as well as Euler and continuity equations in the synchronous gauge:

$$\boxed{\begin{aligned}
k^2\eta - \frac{1}{2}\mathcal{H}h' &= -4\pi G a^2\bar{\rho}\delta \qquad (00) && \text{(B.1.75a)}\\
-k^2\eta' &= 4\pi G a^2(\bar{\rho}+\bar{P})\theta \qquad (0i) && \text{(B.1.75b)}\\
-\frac{1}{2}h'' - \mathcal{H}h' + k^2\eta &= 12\pi G a^2\delta P \qquad (ii) && \text{(B.1.75c)}\\
\frac{1}{2}(6\eta''+h'') + \mathcal{H}(6\eta'+h') - k^2\eta &= 12\pi G a^2(\bar{\rho}+\bar{P})\sigma \qquad (ij) && \text{(B.1.75d)}
\end{aligned}}$$

I will prove the most complicated one, the (ii) term, to show the spirit of the calculation. The lfs gives

$$\begin{aligned}
\psi'' + (2\mathcal{H}' + \mathcal{H}^2)\phi + \mathcal{H}\phi' + 2\mathcal{H}\psi' - \frac{1}{3}k^2(\phi-\psi) &= \eta'' + 2\mathcal{H}'\left\{\mathcal{H}\frac{(6\eta+h)'}{2k^2} + \frac{(6\eta+h)''}{2k^2}\right\}\\
&- \left\{\mathcal{H}''\frac{(6\eta+h)'}{2k^2} + 2\mathcal{H}'\frac{(6\eta+h)''}{2k^2} + \mathcal{H}\frac{(6\eta+h)'''}{2k^2}\right\}\\
&+ \mathcal{H}^2\left\{\mathcal{H}\frac{(6\eta+h)'}{2k^2} + \frac{(6\eta+h)''}{2k^2}\right\}\\
&+ \mathcal{H}^2\frac{(6\eta+h)''}{2k^2} + \mathcal{H}\mathcal{H}'\frac{(6\eta+h)'}{2k^2} + \mathcal{H}\frac{(6\eta+h)'''}{2k^2}\\
&+ 2\mathcal{H}\eta' - 2\mathcal{H}\mathcal{H}'\frac{(6\eta+h)}{2k^2} - 2\mathcal{H}^2\frac{(6\eta+h)''}{2k^2}\\
&- \frac{1}{3}k^2\left\{2\mathcal{H}\frac{(6\eta+h)'}{2k^2} + \frac{(6\eta+h)''}{2k^2} - \eta\right\}
\end{aligned} \tag{B.1.76}$$

A lot of terms cancel out, after equating to the rhs of (ii) leaving only,

$$-\mathcal{H}''\frac{(6\eta+h)'}{2k^2} + \mathcal{H}\mathcal{H}'\frac{(6\eta+h)'}{2k^2} + \mathcal{H}^3\frac{(6\eta+h)'}{2k^2} - \frac{\mathcal{H}h'}{3} + \frac{k^2\eta}{3} - \frac{h''}{6} = 4\pi G a^2\left\{\delta P + \bar{P}'\frac{(6\eta+h)'}{2k^2}\right\}. \tag{B.1.77}$$

We now need to use some tricks

$$\begin{aligned}
\mathcal{H}'' &= \Big\{-\frac{4\pi}{3}Ga^2\big(\bar{\rho}+3\bar{P}\big)\Big\}' \\
&= -\frac{4\pi}{3}Ga^2\big\{2a\mathcal{H}(\bar{\rho}+3\bar{P})+(\bar{\rho}'+3\bar{P}')\big\} \\
&= -\frac{4\pi}{3}Ga^2\big\{-2\mathcal{H}\bar{\rho}+3\bar{P}'\big\}\underbrace{-\frac{4\pi}{3}Ga^2\mathcal{H}(\bar{\rho}+3\bar{P})}_{\mathcal{H}\mathcal{H}'} \\
&= -\frac{4\pi}{3}Ga^2\big\{-2\mathcal{H}\bar{\rho}+3\bar{P}'\big\}+\mathcal{H}\mathcal{H}' \qquad \text{(B.1.78)} \\
\mathcal{H}^3 &= \mathcal{H}\times\mathcal{H}^2=\mathcal{H}\left\{\frac{8\pi Ga^2}{3}\bar{\rho}\right\}. \qquad \text{(B.1.79)}
\end{aligned}$$

We end up with

$$\begin{aligned}
\left[\frac{4\pi}{3}Ga^2\big\{-2\mathcal{H}\bar{\rho}+3\bar{P}'\big\}-\mathcal{H}\mathcal{H}'\right]\frac{\big(6\eta+h\big)'}{2k^2}+\mathcal{H}\mathcal{H}'\frac{\big(6\eta+h\big)'}{2k^2}+\mathcal{H}\left\{\frac{8\pi Ga^2}{3}\bar{\rho}\right\}\frac{\big(6\eta+h\big)'}{2k^2} \\
-\frac{\mathcal{H}h'}{3}+\frac{k^2\eta}{3}-\frac{h''}{6}=4\pi Ga^2\left\{\delta P+\bar{P}'\frac{\big(6\eta+h\big)'}{2k^2}\right\} \qquad \text{(B.1.80)}
\end{aligned}$$

which gives the final result

$$-\frac{1}{2}h''-\mathcal{H}h'+k^2\eta=12\pi Ga^2\delta P \qquad \text{(B.1.81)}$$

B.2 Technical details in the derivation of the perturbed Boltzmann equation

B.2.1 *The collisionless Boltzmann equation at first-order*

B.2.1.1 *General equation in the Newtonian gauge*

We wish in this section to prove the derivation of the colisionless Boltzmann equation B.2.15. The derivation is made in the Newtonian gauge *in cosmic time* (no more a^2 term in g_{00} and $\tau \to t$). The starting point is to use some constraints to reduce the 8-dimension of $f(x_\mu, P_\mu)$. As already mentionnend, imposing the mass-shell conditions $P^2 = g_{\mu\nu}P^\mu P^\nu = m^2$, where P^μ is define in eq. (1.1.16), allows to express one of the 4-momentum component as a function of the others. This condition yields

$$P^2=(1+2\phi)(P^0)^2-p^2=m^2 \qquad \text{with } -p^2=g_{ij}P^iP^j\,, \qquad \text{(B.2.1)}$$

which immediately gives

$$P^0=\pm\sqrt{\frac{p^2+m^2}{(1+2\phi)}}=\pm E(1-\phi)\,, \qquad \text{(B.2.2)}$$

where we will consider positive energy. We can also express P^i as a function of $p^i = pn^i$, where we have introduced the magnitude p and the direction n^i. P^i is proportional to n^i, we can introduce a proportionality constant C such that $P^i \equiv Cn^i$ and we can determine it since

$$-p^2=g_{ij}P^iP^j=g_{ij}n^in^jC^2=-a^2(1-2\psi)C^2 \quad . \qquad \text{(B.2.3)}$$

So we have

$$C=\frac{p(1+\psi)}{a} \quad . \qquad \text{(B.2.4)}$$

We then start by expanding the Liouville operator in term of the energy E

$$\frac{df}{dt} = \frac{\partial f}{\partial t} + \frac{\partial f}{\partial x^i}\frac{dx^i}{dt} + \frac{\partial f}{\partial E}\frac{dE}{dt} + \frac{\partial f}{\partial n^i}\frac{dn^i}{dt}\,. \tag{B.2.5}$$

The zero-order distribution is either a Fermi-Dirac or a Bose-Einstein distribution (1.3.9), which does not depend on the direction n^i, $\partial f/\partial n^i$ is therefore a first order term. But so is the term which multiplies it dn^i/dt since particles moves in straight lines in the absence of potentials. Hence, the last term vanishes at first order.
In general relativity $P^\mu = m dx^\mu/d\lambda$. Therefore,

$$\frac{dx^i}{dt} = \frac{dx^i}{d\lambda}\frac{d\lambda}{dt} = \frac{P^i}{P^0} = \frac{pn^i}{Ea}(1+\psi+\phi)\,. \tag{B.2.6}$$

Since f does not depend on the position at zero-order, $\partial f/\partial x^i$ is a first order term and we can neglect the potentials when multiplying it to dx^i/dt. Finally, we need the geodesic equation to compute dE/dt. It is given by

$$\frac{dP^\mu}{d\lambda} + \Gamma^\mu{}_{\alpha\beta}P^\alpha P^\beta = 0\,, \tag{B.2.7}$$

and the time component yields

$$\begin{aligned}
\frac{dP^0}{d\lambda} + \Gamma^0{}_{\alpha\beta}P^\alpha P^\beta &= 0 \\
\Leftrightarrow \frac{dP^0}{dt}\left\{\frac{dt}{d\lambda} = P^0\right\} &= -\Gamma^0{}_{\alpha\beta}P^\alpha P^\beta \\
\Leftrightarrow \frac{d}{dt}[E(1-\phi)] &= -\Gamma^0{}_{\alpha\beta}\frac{P^\alpha P^\beta}{E}(1+\phi) \\
\Leftrightarrow \frac{dE}{dt}(1-\phi) &= E\frac{d\phi}{dt} - \Gamma^0{}_{\alpha\beta}\frac{P^\alpha P^\beta}{E}(1+\phi)\,.
\end{aligned} \tag{B.2.8}$$

We now can evaluate $\Gamma^0{}_{\alpha\beta}\frac{P^\alpha P^\beta}{E}$, it is

$$\begin{aligned}
\Gamma^0{}_{\alpha\beta}\frac{P^\alpha P^\beta}{E} &= \frac{g^{0\nu}}{2}\Big[2g_{\nu\alpha,\beta} - g_{\alpha\beta,\nu}\Big]\frac{P^\alpha P^\beta}{E} \\
&= \left(\frac{1-2\phi}{2}\right)\Big[2g_{0\alpha,\beta} - g_{\alpha\beta,0}\Big]\frac{P^\alpha P^\beta}{E}\,.
\end{aligned} \tag{B.2.9}$$

The first term inside the brackets gives

$$\begin{aligned}
2g_{0\alpha,\beta}\frac{P^\alpha P^\beta}{E} &= 2\Bigg[g_{00,\beta}\frac{P^0P^\beta}{E} + \overbrace{g_{0i,\beta}\frac{P^iP^\beta}{E}}^{0}\Bigg] \\
&= 4\left[\frac{\partial\phi}{\partial t}E + \frac{\partial\phi}{\partial x^i}\frac{pn^i}{a}\right],
\end{aligned} \tag{B.2.10}$$

and the second term

$$\begin{aligned}
-g_{\alpha\beta,0}\frac{P^\alpha P^\beta}{E} &= -\left[g_{00,0}\frac{P^0P^0}{E} + g_{ij,0}\frac{P^iP^j}{E}\right] \\
&= -2\frac{\partial\phi}{\partial t}E + a^2\Big[-2\frac{\partial\psi}{\partial t} + 2H(1-2\psi)\Big]\delta_{ij}\frac{P^iP^j}{E}\quad,
\end{aligned} \tag{B.2.11}$$

we can use $\delta_{ij}P^iP^j = P^jP^j = p^2(1+2\psi)/a^2$ to obtain

$$\begin{aligned} -g_{\alpha\beta,0}\frac{P^\alpha P^\beta}{E} &= -2\frac{\partial\phi}{\partial t}E + a^2\left[-2\frac{\partial\psi}{\partial t} + 2H(1-2\psi)\right]\frac{p^2(1+2\psi)}{Ea^2} \\ &= -2\frac{\partial\phi}{\partial t}E - 2\left[\frac{\partial\psi}{\partial t} - H\right]\frac{p^2}{E} \quad . \end{aligned} \tag{B.2.12}$$

Collecting all terms we have

$$\begin{aligned} \Gamma^0{}_{\alpha\beta}\frac{P^\alpha P^\beta}{E} &= \left(\frac{1-2\phi}{2}\right)\left\{4\left[\frac{\partial\phi}{\partial t}E + \frac{\partial\phi}{\partial x^i}\frac{pn^i}{Ea}\right] - 2\frac{\partial\phi}{\partial t}E - 2\left[\frac{\partial\psi}{\partial t} - H\right]\frac{p^2}{E}\right\} \\ &= (1-2\phi)\left\{\frac{\partial\phi}{\partial t}E + 2\frac{\partial\phi}{\partial x^i}\frac{pn^i}{a} - \left[\frac{\partial\psi}{\partial t} - H\right]\frac{p^2}{E}\right\} \\ &= \frac{\partial\phi}{\partial t}E + 2\frac{\partial\phi}{\partial x^i}\frac{pn^i}{a} - \left[\frac{\partial\psi}{\partial t} - H(1-2\phi)\right]\frac{p^2}{E}\,, \end{aligned} \tag{B.2.13}$$

and multiplying eq. (B.2.8) by $(1+\phi)$ yields

$$\begin{aligned} \frac{dE}{dt} &= E\frac{d\phi}{dt} - \Gamma^0{}_{\alpha\beta}\frac{P^\alpha P^\beta}{E}(1+2\phi) \\ &= E\left\{\frac{\partial\phi}{\partial t} + \underbrace{\frac{\partial\phi}{\partial x^i}\frac{dx^i}{dt}}_{\frac{\partial\phi}{\partial x^i}\frac{pn^i}{Ea}}\right\} - \left\{\frac{\partial\phi}{\partial t}E + 2\frac{\partial\phi}{\partial x^i}\frac{n^i}{Ea} - \left[\frac{\partial\psi}{\partial t} - H(1-2\phi)\right]\frac{p^2}{E}\right\}(1+2\phi) \\ &= -\frac{\partial\phi}{\partial x^i}\frac{pn^i}{a} + \left[\frac{\partial\psi}{\partial t} - H\right]\frac{p^2}{E}\,. \end{aligned} \tag{B.2.14}$$

We can now express the total time derivative of f

$$\boxed{\begin{aligned} \frac{df}{dt} &= \frac{\partial f}{\partial t} + \frac{\partial f}{\partial x^i}\frac{p}{E}\frac{n^i}{a} - \frac{\partial f}{\partial E}\left[\frac{\partial\phi}{\partial x^i}\frac{pn^i}{a} + \left[H - \frac{\partial\psi}{\partial t}\right]\frac{p^2}{E}\right] && \text{(B.2.15a)} \\ &\stackrel{!}{=} 0 \quad \text{collisionless} && \text{(B.2.15b)} \end{aligned}}$$

B.2.1.2 *The case of collisionless relativistic-massless species*

We derive here the Boltzmann hierarchy for colisionless relativistic-massless species. Photons and massless neutrinos for instance enter this category. We start by expanding the photon distribution f about its zero-order value

$$f(\vec{x}, p, \vec{n}, t) = \left[\exp\left\{\frac{p}{T(t)[1+\Theta(\vec{x},\vec{n},t)]}\right\} - 1\right]^{-1} \quad . \tag{B.2.16}$$

The zero-order temperature T is a function of time only and neither of location nor of p and $\vec{n}$. $\Theta \equiv \delta T/T$ is a inhomogeneous and anistropic perturbation to the distribution function. We make the only assumption that it doesn't depend on the magnitude p of the momentum, which follows from the fact that the magnitude of the photon momentum is virtually unchanged during a Compton scatter. Expanding at first order we have

$$\begin{aligned} f &\simeq f^{(0)} + \frac{\partial f^{(0)}}{\partial T} \times \{\delta T = T\Theta\} \\ &= f^{(0)} - p\frac{\partial f^{(0)}}{\partial p}\Theta \quad . \end{aligned} \tag{B.2.17}$$

The last lines holds since for this function the derivative with respect to T yields

$$\begin{aligned}
\frac{\partial}{\partial T} f^{(0)} &= \frac{\partial}{\partial T}\left[\exp\left\{\frac{p}{T(t)}\right\} - 1\right]^{-1} \\
&= \left\{-\left[\exp\left\{\frac{p}{T(t)}\right\} - 1\right]^{-2}\right\}\left\{-\frac{p}{T^2}\right\}\left\{\exp\left[\frac{p}{T(t)}\right]\right\} \\
\Rightarrow T\frac{\partial}{\partial T} f^{(0)} &= \left[\exp\left\{\frac{p}{T(t)}\right\} - 1\right]^{-2}\frac{p}{T}\exp\left[\frac{p}{T(t)}\right].
\end{aligned} \tag{B.2.18}$$

and taking the derivative with respect to p

$$\begin{aligned}
\frac{\partial}{\partial p} f^{(0)} &= \frac{\partial}{\partial p}\left[\exp\left\{\frac{p}{T(t)}\right\} - 1\right]^{-1} \\
&= \left\{-\left[\exp\left\{\frac{p}{T(t)}\right\} - 1\right]^{-2}\right\}\left\{\frac{1}{T}\right\}\left\{\exp\left[\frac{p}{T(t)}\right]\right\} \\
\Rightarrow -p\frac{\partial}{\partial p} f^{(0)} &= \left[\exp\left\{\frac{p}{T(t)}\right\} - 1\right]^{-2}\frac{p}{T}\exp\left[\frac{p}{T(t)}\right] = T\frac{\partial}{\partial T} f^{(0)}.
\end{aligned} \tag{B.2.19}$$

Equation (B.2.15) simplifies in the massless case. Indeed, we can set $E = \sqrt{p^2 + m^2} = p$ and replace the derivative with respect to E to a derivative with respect to p. It becomes

$$\frac{df}{dt} = \frac{\partial f}{\partial t} + \frac{\partial f}{\partial x^i}\frac{n^i}{a} - p\frac{\partial f}{\partial p}\left[\frac{\partial \phi}{\partial x^i}\frac{n^i}{a} - \frac{\partial \psi}{\partial t} + H\right] \quad . \tag{B.2.20}$$

We can plug eq. (B.2.17) into the previous one and split between zero and first order. The zero-order equation is then

$$\boxed{\left.\frac{df}{dt}\right|_{\text{zero-order}} = \frac{\partial f^{(0)}}{\partial t} - Hp\frac{\partial f^{(0)}}{\partial p} \stackrel{!}{=} 0} \quad . \tag{B.2.21}$$

The zero-order equation is always zero, since collisions will introduce terms proportional to Θ and other perturbatively small quantities. Furthermore, the zero-order distribution function is defines by the requirement that the collision term vanishes, which means that the rate of a reaction and its inverse-reaction are equal at equilibrium. We can manipulate a bit previous equations to get the famous result

$$\begin{aligned}
\frac{\partial f^{(0)}}{\partial t} - Hp\frac{\partial f^{(0)}}{\partial p} &= 0 \\
\Leftrightarrow \left[-\frac{\partial f^{(0)}}{\partial T}\frac{dT}{dt}\right] - Hp\frac{\partial f^{(0)}}{\partial p} &= 0 \\
\Leftrightarrow \left[-\frac{p}{T}\frac{\partial f^{(0)}}{\partial p}\frac{dT}{dt}\right] - Hp\frac{\partial f^{(0)}}{\partial p} &= 0 \\
\Leftrightarrow \left[-\frac{dT/dt}{T} - \frac{da/dt}{a}\right]p\frac{\partial f^{(0)}}{\partial p} &= 0 \\
\Leftrightarrow \frac{dT}{T} &= -\frac{da}{a} \\
\Leftrightarrow T &\propto \frac{1}{a} \quad .
\end{aligned} \tag{B.2.22}$$

What we want is the first-order equation. It is

$$\left.\frac{df}{dt}\right|_{\rm first-order} = -p\frac{\partial}{\partial t}\left[\frac{\partial f^{(0)}}{\partial p}\Theta\right] - p\frac{\partial\Theta}{\partial x^i}\frac{\partial f^{(0)}}{\partial p}\frac{n^i}{a} + Hp\Theta\frac{\partial}{\partial p}\left[p\frac{\partial f^{(0)}}{\partial p}\right] -p\frac{\partial f^{(0)}}{\partial p}\left[\frac{\partial\phi}{\partial x^i}\frac{n^i}{a} - \frac{\partial\psi}{\partial t}\right]. \tag{B.2.23}$$

We can manipulate previous equations, for instance the first term is

$$\begin{aligned} -p\frac{\partial}{\partial t}\left[\frac{\partial f^{(0)}}{\partial p}\Theta\right] &= -p\frac{\partial f^{(0)}}{\partial p}\frac{\partial\Theta}{\partial t} - p\Theta\left\{\frac{\partial^2 f^{(0)}}{\partial t\partial p} = \frac{\partial^2 f^{(0)}}{\partial T\partial p}\frac{dT}{dt}\right\} \\ &= -p\frac{\partial f^{(0)}}{\partial p}\frac{\partial\Theta}{\partial t} + p\Theta\frac{dT/dt}{T}\frac{\partial}{\partial p}\left[\frac{\partial f^{(0)}}{\partial p}\right]. \end{aligned} \tag{B.2.24}$$

Using now the zero-order result

$$\frac{dT/dt}{T} = -\frac{da/dt}{a} = -H\,. \tag{B.2.25}$$

we plug this in eq. (B.2.23) to get the result

$$\boxed{\left.\frac{df}{dt}\right|_{\rm first-order} = -p\frac{\partial f^{(0)}}{\partial p}\left[\frac{\partial\Theta}{\partial t} + \frac{\partial\phi}{\partial x^i}\frac{n^i}{a} - \frac{\partial\psi}{\partial t} + \frac{\partial\Theta}{\partial x^i}\frac{n^i}{a}\right]}, \tag{B.2.26}$$

and assuming collisionless species

$$\boxed{\frac{\partial\Theta}{\partial t} + \frac{\partial\phi}{\partial x^i}\frac{n^i}{a} - \frac{\partial\psi}{\partial t} + \frac{\partial\Theta}{\partial x^i}\frac{n^i}{a} = 0}. \tag{B.2.27}$$

Using the definition of the stress-energy tensor (1.1.18) and that in the newtonian gauge $(-\det[g_{\alpha\beta}]^{-1/2}) = a^{-3}(1-\phi+3\psi)$ and $d^3P = a^3(1-3\psi)p^2dpd\Omega$, we can relate the distribution to the degrees of freedom we have defined previously :

$$T^0_{\ 0} = \bar\rho(1+\delta) = g_s\int\frac{p^2dpd\Omega}{(2\pi)^3}p\left[f^{(0)} - p\frac{\partial f^{(0)}}{\partial p}\Theta\right]\quad, \tag{B.2.28}$$

$$\partial^i T^0_{\ i} = -(\bar\rho+\bar P)\theta = \partial^i\left\{-g_s\int\frac{p^2dpd\Omega}{(2\pi)^3}pn_i\left[f^{(0)} - p\frac{\partial f^{(0)}}{\partial p}\Theta\right]\right\}\quad, \tag{B.2.29}$$

$$T^i_{\ i} = -3(\bar P+\delta P) = -g_s\int\frac{p^2dpd\Omega}{(2\pi)^3}p\left[f^{(0)} - p\frac{\partial f^{(0)}}{\partial p}\Theta\right]\quad, \tag{B.2.30}$$

$$(\partial_i\partial_j - \frac{1}{3}\nabla^2\delta_{ij})T^i_{\ j} = (\bar\rho+\bar P)\nabla^2\sigma = (\partial_i\partial_j - \frac{1}{3}\nabla^2\delta_{ij})\left\{-g_s\int\frac{p^2dpd\Omega}{(2\pi)^3}p^2n^in_j\left[f^{(0)} - p\frac{\partial f^{(0)}}{\partial p}\Theta\right]\right\}\quad. \tag{B.2.31}$$

To go further, it is common to reduce the number of variables by integrating out the $p-$dependance in the distribution and to expand the angular dependance of the perturbations in a series of Legendre polynomials $\mathcal{P}_\ell(\mu)$, with $\mu \equiv \vec k\cdot\vec n/\|\vec k\|$:

$$\Theta(\vec k,\mu,t) = \sum_\ell(-i)^\ell(2\ell+1)\Theta_\ell(t,\vec k)\mathcal{P}_\ell(\mu)\,, \tag{B.2.32}$$

$$\Theta_\ell(t,\vec k) = \frac{1}{(-i)^\ell}\int_{-1}^{1}\frac{d\mu}{2}\Theta(\vec k,\mu,t)\mathcal{P}_\ell(\mu)\,. \tag{B.2.33}$$

The Legendre Polynomial $\mathcal{P}_\ell(\mu)$ is an ℓth-order polynomial of μ. For $-1 \leq \mu \leq 1$, $\mathcal{P}_\ell$ has ℓ zeroes in this interval. Some interesting values are

$$\mathcal{P}_0(\mu) = 1 \quad ; \quad \mathcal{P}_1(\mu) = \mu \quad ; \quad \mathcal{P}_2(\mu) = \frac{3\mu^2 - 1}{2} \quad . \tag{B.2.34}$$

It is an even function of μ for ℓ even, and an odd function for ℓ odd. They are orthogonal so that

$$\int_{-1}^{1} d\mu P_\ell(\mu) P'_\ell(\mu) = \delta_{ll'} \frac{2}{2\ell+1} \quad . \tag{B.2.35}$$

They verify the recurrence relation

$$(\ell+1)\mathcal{P}_{\ell+1}(\mu) = (2\ell+1)\mu\mathcal{P}_\ell(\mu) - \ell\mathcal{P}_{\ell-1}(\mu) \quad . \tag{B.2.36}$$

From this formalism, the perturbations can now be described either by $\Theta(\vec{k}, \mu, t)$ or a whole hierarchy of moments $\Theta_\ell(\vec{k}, t)$. We can use these definitions to integrate equations (B.2.28-B.2.31) and relate our scalar degrees of freedom to the first moments of Θ. For instance

$$\begin{aligned} T^0_{\ 0} &= g_s \int \frac{p^2 dp d\Omega}{(2\pi)^3} p \left[f^{(0)} - p \frac{\partial f^{(0)}}{\partial p} \Theta \right] \\ &= \rho_s - g_s \int \frac{p^4 dp d\Omega}{(2\pi)^3} \frac{\partial f^{(0)}}{\partial p} \Theta \, . \end{aligned} \tag{B.2.37}$$

Here we have used eq. (1.3.13) and if we integrate by part

$$\begin{aligned} \int \frac{p^4 dp d\Omega}{(2\pi)^3} \frac{\partial f^{(0)}}{\partial p} &= -\int \frac{dp d\Omega}{(2\pi)^3} f^{(0)} \left\{ \frac{\partial p^4}{\partial p} = 4p^3 \right\} + \underbrace{\int dp \frac{\partial}{\partial p} \left(p^4 f^{(0)} \right)}_{0} \\ &= -4 \int \frac{p^2 dp d\Omega}{(2\pi)^3} p f^{(0)} \, . \end{aligned} \tag{B.2.38}$$

Since $f^{(0)}$ does not depend on the direction, we can integrate it separately using eq. (B.2.32) if we develop $d\Omega = d\mu d\varphi$. It yields

$$\int d\Omega \Theta = 2 \int_0^{2\pi} d\varphi \int_{-1}^{1} \frac{d\mu}{2} \Theta = 4\pi \Theta_0 \, . \tag{B.2.39}$$

We plug those two results back to get

$$\begin{aligned} T^0_{\ 0} &= \rho_s + 4 \times g_s \int \frac{4\pi p^2 dp d\Omega}{(2\pi)^3} p f^{(0)} \times \Theta_0 \\ &= \rho_s (1 + 4\Theta_0) \, . \end{aligned} \tag{B.2.40}$$

Identifying with the lhs of eq. (B.2.28) gives

$$\delta = 4\Theta_0 \, . \tag{B.2.41}$$

This factors of 4 was predictible since $\rho \propto T^4 \Rightarrow \delta\rho/\rho = 4\delta T/T$. We can play the same game with other variables. Equation (B.2.29) gives in Fourier space

$$\begin{aligned} ik^i T^0_i &= -ig_s \int \frac{p^2 dp d\Omega}{(2\pi)^3} p(k^i \cdot n_i = k\mu) \left[f^{(0)} - p\frac{\partial f^{(0)}}{\partial p}\Theta \right] \\ &= -ikg_s \int \frac{p^2 dp d\mu d\varphi}{(2\pi)^3} p\mu \left[f^{(0)} - p\frac{\partial f^{(0)}}{\partial p}\Theta \right] \\ &= -ikg_s \left\{ \underbrace{\int \mu d\mu d\varphi}_{0} \int \frac{p^2 dp}{(2\pi)^3} p f^{(0)} - \underbrace{\int \mu d\mu d\varphi \Theta}_{-i4\pi\Theta_1} \underbrace{\int \frac{p^2 dp}{(2\pi)^3} p^2 \frac{\partial f^{(0)}}{\partial p}}_{-\rho_s/(g_s\pi)} \right\} \\ &= -4k\Theta_1 \rho_s \,. \end{aligned} \tag{B.2.42}$$

For relativistic species, $\bar{P} = 1/3\bar{\rho}$. We therefore have by identification with the lhs of eq. (B.2.29)

$$\theta = 3k\Theta_1 \,. \tag{B.2.43}$$

Finally, the last equation (B.2.31) will relate σ to another moment of Θ. Again in Fourier space, we have

$$\begin{aligned} -(k_i k_j - \frac{1}{3}k^2\delta_{ij})T^i{}_j &= g_s \int \frac{p^2 dp d\Omega}{(2\pi)^3} p^2 (k_i k_j - \frac{1}{3}k^2\delta_{ij}) n^i n_j \left[f^{(0)} - p\frac{\partial f^{(0)}}{\partial p}\Theta \right] \\ &= g_s \int \frac{p^2 dp d\Omega}{(2\pi)^3} p^2 (k^2\mu^2 - \frac{1}{3}k^2) \left[f^{(0)} - p\frac{\partial f^{(0)}}{\partial p}\Theta \right] \\ &= \underbrace{k^2 g_s \left[\left\{ \int \mu^2 d\mu d\varphi = \frac{4\pi}{3} \right\} \int \frac{p^4 dp}{(2\pi)^3} f^{(0)} - \frac{4\pi}{3} \int \frac{p^4 dp}{(2\pi)^3} f^{(0)} \right]}_{0} \\ &\quad -k^2 g_s \int \frac{p^4 dp d\Omega}{(2\pi)^3} \underbrace{(\mu^2 - \frac{1}{3})}_{\frac{2}{3}\mathcal{P}_2(\mu)} \left[p\frac{\partial f^{(0)}}{\partial p}\Theta \right] \\ &= -k^2 \frac{2}{3} g_s \underbrace{\int d\Omega \mathcal{P}_2(\mu)\Theta}_{-4\pi\Theta - 2} \underbrace{\int \frac{p^4 dp d\Omega}{(2\pi)^3} \frac{\partial f^{(0)}}{\partial p}}_{-\rho_s/(g_s\pi)} \\ &= -k^2 \frac{8}{3} \rho_s \Theta_2 \,. \end{aligned} \tag{B.2.44}$$

Again we identify this with the lhs of eq. (B.2.31) to obtain

$$\sigma = 2\Theta_2 \,. \tag{B.2.45}$$

We are now ready to reexpress the Boltzmann equation as an infinite hierarchy of coupled equations for the multipole moments of Θ. We insert eq. (B.2.32) in eq. (B.2.27). It yields in Fourier space

$$\begin{aligned} \dot{\Theta} + \frac{ik\mu}{a}\phi - \dot{\psi} + \frac{ik\mu}{a}\Theta &= \sum_\ell (-i)^\ell (2\ell+1) \dot{\Theta}_\ell(t, \vec{k}) \mathcal{P}_\ell(\mu) - \frac{ik\mu}{a}\phi + \dot{\psi} \\ &\quad + \frac{ik\mu}{a} \sum_{\ell'} (-i)^\ell (2\ell'+1) \Theta_{\ell'}(t, \vec{k}) \mathcal{P}_{\ell'}(\mu) \,. \end{aligned} \tag{B.2.46}$$

We now integrate over $\int d\mu \mathcal{P}_{\ell''}(\mu)$ to picks out every moments separately using the orthonormality of $\mathcal{P}'_\ell s$ (B.2.35)

$$\begin{aligned}
&\sum_\ell (-i)^\ell (2\ell+1)\dot{\Theta}_\ell(t,\vec{k}) \int d\mu \mathcal{P}_\ell(\mu)\mathcal{P}_{\ell"} + \frac{ik}{a}\phi \int d\mu \mu \mathcal{P}_{\ell"}(\mu) \\
&- \int d\mu \dot{\psi}\mathcal{P}_{\ell''}(\mu) + \frac{ik}{a}\sum_{\ell'}(-i)^{\ell'}(2\ell'+1)\Theta_{\ell'}(t,\vec{k}) \int d\mu \underbrace{\mu\mathcal{P}_{\ell'}(\mu)}_{eq.\ (B.2.36)} \mathcal{P}_{\ell''}(\mu) \\
= \;& (-i)^\ell(2\ell+1)\dot{\Theta}_\ell \delta_{ll''}\frac{2}{2\ell+1} + \frac{2ik}{3a}\phi\delta_{1\ell''} - 2\dot{\psi}\delta_{0\ell''} \\
&+ \frac{ik}{a}\sum_{\ell'}(-i)^{\ell'}(2\ell'+1)\Theta_{\ell'}(t,\vec{k})\left\{\frac{\ell'+1}{2\ell'+1}\delta_{(\ell'+1)\ell''}\frac{2}{2\ell'+3} + \frac{\ell'}{2\ell'+1}\delta_{(\ell'-1)\ell''}\frac{2}{2\ell'-1}\right\} \\
= \;& 2(-i)^\ell\dot{\Theta}_\ell\delta_{ll''} + \frac{2ik}{3a}\phi\delta_{1\ell''} - 2\dot{\psi}\delta_{0\ell''} + \frac{ik}{a}\sum_{\ell'}(-i)^{\ell'}\Theta_{\ell'}(t,\vec{k})\left\{\delta_{(\ell'+1)\ell''}\frac{2(\ell'+1)}{2\ell'+3} + \delta_{(\ell'-1)\ell''}\frac{2\ell'}{2\ell'-1}\right\} \\
\stackrel{!}{=} \;& 0\,.
\end{aligned} \tag{B.2.47}$$

For instance $\ell" = 0$ imposes $\ell = 0$ and $\ell" = 1$ and therefore

$$2\dot{\Theta}_0 - 2\dot{\psi} + 2\frac{ik}{a}(-i)\Theta_1 = 0\,. \tag{B.2.48}$$

More generally, splitting between $\ell'' = 0$, $\ell" = 1$ and $\ell" \geq 2$ gives the following hierarchy of moments of Θ

$$\dot{\Theta}_0 = -k\Theta_1 + \dot{\psi} \tag{B.2.49a}$$

$$\dot{\Theta}_1 = \frac{k}{3a}\left[\Theta_0 - 2\Theta_2 + \phi\right] \tag{B.2.49b}$$

$$\dot{\Theta}_\ell = \frac{k}{(2\ell+1)a}\left[\ell\Theta_{\ell-1} - (\ell+1)\Theta_{\ell+1}\right], \tag{B.2.49c}$$

which we can immediately relate to the Einstein equations using the relations we found just before. The equations now in conformal time $dt = ad\tau$ read

$$\boxed{\begin{aligned}
\delta' &= -\frac{4}{3}\theta + 4\psi' && \text{(B.2.50a)}\\
\theta' &= k^2\left[\frac{\delta}{4} - \sigma + \phi\right] && \text{(B.2.50b)}\\
\Theta'_\ell &= \frac{k}{(2\ell+1)}\left[\ell\Theta_{\ell-1} - (\ell+1)\Theta_{\ell+1}\right]. && \text{(B.2.50c)}
\end{aligned}}$$

It is straight forward to transform to the synchronous gauge thanks to eqs. 2.1.56, which gives

$$\boxed{\begin{aligned}
\delta' &= -\frac{4}{3}\theta - \frac{2}{3}h' && \text{(B.2.51a)}\\
\theta' &= k^2\left[\frac{\delta}{4} - \sigma\right] && \text{(B.2.51b)}\\
2\sigma' &= \frac{8}{15}\theta - \frac{3}{5}k\Theta_3 + \frac{4}{15}h' + \frac{8}{5}\eta' && \text{(B.2.51c)}\\
\Theta'_\ell &= \frac{k}{(2\ell+1)}\left[\ell\Theta_{\ell-1} - (\ell+1)\Theta_{\ell+1}\right] \qquad \ell \geq 3\,. && \text{(B.2.51d)}
\end{aligned}}$$

B.2.2 *The Thomson scattering term*

In this section, we wish to derive the Thomson scattering collision term to add in the Boltzmann equation for photons. In general, the collision term for a photon with momentum $\vec{p}$ can be written as [217]

$$\begin{aligned}\mathcal{C}[f(\vec{p})] &= \frac{1}{p}\int \frac{d^3q}{(2\pi)^3 E_e(q)}\frac{d^3q'}{(2\pi)^3 E_e(q')}\frac{d^3p'}{(2\pi)^3 E_\gamma(p')}|\mathcal{M}|^2(2\pi)^4 \\ &\times \delta^3[\vec{p}+\vec{q}-\vec{p}'-\vec{q}']\delta[E_\gamma(p)+E_e(q)-E_\gamma(p')-E_e(q')] \\ &\times \{f_e(\vec{q}')f_\gamma(\vec{p}')-f_e(\vec{q})f_\gamma(\vec{p})\} \end{aligned} \tag{B.2.52}$$

where the delta functions enfore energy momentum conservation and we neglect the effect of stimulated emission and Pauli blocking, valid at first order. Thomson scattering is nothing but the low-energy limit of a Compton event, i.e. $E_\gamma(p) \ll m_e$ and $E_e(q) = m_e + q^2/(2m_e)$ with $q \ll m_e$. Furthermore, there's little momentum transfer in the scattering i.e. $p' \simeq p$ and $q' \simeq q$, hence Thomson scattering mostly change photon direction. The first step is to "kill" one integral over momentum thanks to the delta function. Typically, one can integrate trivially over q' to get

$$\begin{aligned}\mathcal{C}[f(\vec{p})] &= \frac{\pi}{4m_e^2 p}\int \frac{d^3q}{(2\pi)^3}\frac{d^3p'}{(2\pi)^3 p'}|\mathcal{M}|^2\delta[E_\gamma(p)+E_e(q)-E_\gamma(p')-E_e(\vec{q}'=\vec{q}+\vec{p}-\vec{p}')] \\ &\times \times\{f_e(\vec{q}'=\vec{q}+\vec{p}-\vec{p}')f_\gamma(\vec{p}')-f_e(\vec{q})f_\gamma(\vec{p})\}\,. \end{aligned} \tag{B.2.53}$$

To perform the next integral we need to consider the kinematic. The condition that little energy is transfered to the outgoing electron translates as

$$\begin{aligned} E_e(q)-E_e(\vec{q}+\vec{p}-\vec{p}') &= \frac{q^2}{2m_e}-\frac{q^2+2(\vec{p}'-\vec{p})\vec{q}+(p'-p)^2}{2m_e}\,, \\ &\simeq \frac{(\vec{p}'-\vec{p})\cdot\vec{q}}{m_e} \end{aligned} \tag{B.2.54}$$

where the last hypothesis holds since $\vec{p}'-\vec{p} \simeq 0$. Note also that, although $E_e > E_\gamma$, the differences $E_e(q)-E(q') \ll E_\gamma(p)-E_\gamma(p')$ as $E_e(q)-E(q')$ gets an extra $1/m_e$ suppression. This allows to write the δ function as an expansion

$$\begin{aligned}\delta[E_\gamma(p)-E_\gamma(p')+E_e(q)-E_e(q')] &= \delta[E_\gamma(p)-E_\gamma(p')] \\ &+ (E_e(q')-E_e(q))\frac{\partial\delta(E_\gamma(p)-E_\gamma(p')+E_e(q)-E_e(q'))}{\partial E_\gamma(p)}\Big|_{E_e(q)=E_e(q')} \\ &= \delta[p-p'] - \frac{(\vec{p}'-\vec{p})\cdot\vec{q}}{m_e}\frac{\partial\delta(p'-p)}{\partial p} \\ &= \delta[p-p'] + \frac{(\vec{p}'-\vec{p})\cdot\vec{q}}{m_e}\frac{\partial\delta(p-p')}{\partial p'}\,. \end{aligned} \tag{B.2.55}$$

and finally, using that $f_e(\vec{q}+\vec{p}-\vec{p}') \simeq f_e(\vec{q})$, we can integrate over q which gives a factor n_e and $n_e\vec{v}_b$ for the q/m_e. We can thus reexpress the collision term as

$$\mathcal{C}[f(\vec{p})] = \frac{\pi n_e}{4m_e^2 p}\int \frac{d^3p'}{(2\pi)^3 p'}|\mathcal{M}|^2\left\{\delta[p-p'] + (\vec{p}'-\vec{p})\cdot\vec{v}_b\frac{\partial\delta(p-p')}{\partial p'}\right\}\{f(\vec{p}')-f(\vec{p})\}\,. \tag{B.2.56}$$

To perform the final integral, we need to express the matrix element of the Thomson scattering event [347]

$$|\mathcal{M}|^2 = 6\pi\sigma_T m_e^2(1+\cos^2[\hat{p}\cdot\hat{p}'])\,. \tag{B.2.57}$$

In reality the matrix element has a polarization dependance which is neglected because we focus on temperature anisotropies here. We now expand the photon distribution around the equilibrium distribution using eq. (B.2.17) to explicit make our variable Θ appear.

$$\begin{aligned}
\mathcal{C}[f(\vec{p})] &= \frac{3\pi^2 n_e}{2p}\sigma_T \int \frac{d^3p'}{(2\pi)^3 p'}\left\{\delta[p-p'] + (\vec{p}'-\vec{p})\cdot\vec{v}_b\frac{\partial\delta[p-p']}{\partial p'}\right\} \\
&\times \left\{f^{(0)}(\vec{p}') - f^{(0)}(\vec{p}) - p'\frac{\partial f^{(0)}}{\partial p'}\Theta(\hat{p}') + p\frac{\partial f^{(0)}}{\partial p}\Theta(\hat{p})\right\}\left\{1+\cos^2[\hat{p}\cdot\hat{p}']\right\} \\
&= \frac{3n_e}{16\pi p}\sigma_T \int dp'p' \int d\Omega'\left[\delta(p-p')\left\{-p'\frac{\partial f^{(0)}}{\partial p'}\Theta(\hat{p}') + p\frac{\partial f^{(0)}}{\partial p}\Theta(\hat{p})\right\}\right. \\
&+ \left.(\vec{p}-\vec{p}')\cdot\vec{v}_b\frac{\partial\delta(p-p')}{\partial p'}\left(f^{(0)}(\vec{p}') - f^{(0)}(\vec{p})\right)\right]\left\{1+\cos^2[\hat{p}\cdot\hat{p}']\right\}.
\end{aligned} \tag{B.2.58}$$

The last line is obtained by i) integrating the zero-order distribution over p', the delta functions ensures that it vanishes; ii) keeping only first order term. To integrate over $d\Omega'$ we first remark that

$$\cos^2(\hat{p}\cdot\hat{p}') + 1 = \frac{2\mathcal{P}_2(\cos(\hat{p}\cdot\hat{p}')) + 4}{3} = \frac{8\pi}{15}\sum_{m=-\ell}^{m=+\ell} Y_{2m}(\hat{p})Y^*_{lm}(\hat{p}') + \frac{4}{3} \tag{B.2.59}$$

In practice however, the azimuthal integration of all Y_{2m} will yield 0, except for $m=0$ when it is integrated over $\Theta_T(\hat{p}')$. Indeed, using the definition of the multipole of Θ_T eq. (B.2.32) and the fact that $Y_{20} = -\sqrt{5}\mathcal{P}_2/\sqrt{4\pi}$, the integral over Θ_T will give

$$\int d\Omega'\Theta_T(\hat{p}')\left[\frac{10\mathcal{P}_2(\mu)\mathcal{P}_2(\hat{p}'\cdot\hat{k})}{15} + \frac{1}{3}\right] = -\frac{8\pi}{3}\mathcal{P}_2(\mu)\Theta_{T2} + \frac{4\pi}{3}\Theta_{T0} \tag{B.2.60}$$

Collecting all non-zero terms, we are simply left with

$$\begin{aligned}
\mathcal{C}[f(\vec{p})] &= \frac{n_e\sigma_T}{p}\int dp'p'\left\{\delta(p-p')\left[-p'\frac{\partial f^{(0)}}{\partial p'}\left(\Theta_{T0} - \frac{\mathcal{P}_2(\mu)\Theta_{T2}}{2}\right) + p\frac{\partial f^{(0)}}{\partial p}\Theta(\hat{p})\right]\right. \\
&+ \left.\vec{p}\cdot\vec{v}_b\frac{\partial\delta(p-p')}{\partial p'}\left(f^{(0)}(\vec{p}') - f^{(0)}(\vec{p})\right)\right\}
\end{aligned} \tag{B.2.61}$$

and we can perform the integral over momentum trivially for the first line, by part for the second to get the final result

$$\mathcal{C}[f(\vec{p})] = -p'\frac{\partial f^{(0)}}{\partial p}n_e\sigma_T\left[\Theta_{T0} - \frac{1}{2}\mathcal{P}_2(\mu)\Theta_{T2} - \Theta_T(\hat{p}) + \hat{p}\cdot\vec{v}_b\right] \tag{B.2.62}$$

This treatment does not yield the part coming from the polarization because we started from decoupled equation for Θ_T and Θ_P. In general however, one would need to treat the vector $\vec{T} = (\Theta_T, \Theta_P)$ (here assuming already vanishing U and V for Thomson scattering) and to generalize the Liouville and Collision operator to this vector. The full expression is given in Ref. [328] (eqs. (21) and (22) therein) while the detailed computation can be found in Ref. [378]. In the usual case of vanishing U term, it simplifies to our eq. (2.1.99) [353], [604].

B.3 Basics of Bayesian statistics and parameter extraction

In this appendix, we explain the standard tools used to compare theoretical observables with actual data, in order to extract information on the cosmological parameters. In the ΛCDM model, these parameters encode information on the initial condition (A_s, n_s), the energy content of the universe $(\omega_m, \omega_b, \Omega_\Lambda)$ and the late universe expansion and star formation $(H_0, \tau_{\rm reio})$. Our strategy in Cosmology is essentially to "shoot in the dark", i.e. to start from random values of these parameters and through subsequent iterations, try to find their most likely ones, while taking into account instrumental noise or foreground contamination. We work in the widely used Bayesian framework, which allows to deal with these issues, and that we will now introduce briefly following Refs. [67], [226], [312].

B.3.1 *Fundamental definition and Bayes theorem*

All our knowledges *today* in Bayesian analysis is call the *data*, $\mathcal{D}$. One can describe the data $\mathcal{D}$ with a given *model* or *context* $\mathcal{I}$, that contains a certain number N of *parameters* grouped in a vector $\theta \in \mathbb{R}^N$. The Bayesian framework allows to answer two fundamental questions: i) is the model $\mathcal{I}$ better than another one; ii) in this model, what are the *best values* and the *credible intervals* for the parameters. However, there are big caveats associated to this framework. First, it will only allow to perform model comparaison, not to get the absolute "true" model. Furthermore, within a model, it does not provide an absolute credible interval for the parameter. It might be that in another model, degeneracies appear enlarging its credible value. Therefore, all credible intervals are model dependant. Parameters within a models are often extended to include *nuisance parameters*, which parametrize our ignorance of some phenomenon a priori not-related to the physics we want to learn about. It can be for instance the amplitude of a foreground or some experimental noise.
The rules of prability calculus applies to our case so that

- The probability "pr" of a given vector parameters θ must be positive-definite, i.e. $pr(\theta) \equiv pr(\theta|\mathcal{I}) \geq 0$.
- The integral over the whole volume must be normalized to 1, $\int pr(\theta) d\theta = 1$. The integral runs over the *prior volume*, which can be restricted for some parameters to ranges smaller than the whole real axis.
- The probability must satisfy the product rule, i.e. $pr(\phi, \theta) = pr(\phi|\theta) pr(\theta)$, where the joint probability of having ϕ *and* θ is nothing but the probability of having ϕ given that we have already θ, times the probability of having θ.

We can now come to the famous *Bayes theorem* applied to Cosmology. Given a context $\mathcal{I}$[1], it will relate our known input (the model and the data) to a desired unknown output (the credible intervals of the parameters and the relative merit of the model). It states

$$pr(\theta) pr(\mathcal{D}|\theta) = pr(\theta, \mathcal{D}) = pr(\mathcal{D}) pr(\theta|\mathcal{D})\,. \tag{B.3.1}$$

. Let us describe what it means with more standard notation:

1 Although we do not make it explicitely appear, all probabilities are in fact of the type $pr(X) = pr(X|\mathcal{I})$.

- The *Prior* $\pi = pr(\theta)$ is a probability assigned to the parameters *a priori* within a model, given the knowledges on preceeding experimental data or some theoretical preference. It has an important impact on the output credible intervals. Often, it is chosen to be flat, i.e. that no particular region in the prior volume is highlighted, in order for the results to reflect the data.

- The *Likelihood* $\mathcal{L} = pr(\mathcal{D}|\theta)$ is the probability of measuring the data $\mathcal{D}$ given a set of parameters θ, within a model. To get this information requires *calibration* of the instrument, such that for a given ouput, it corresponds to a reliable input (up to the precision of the machine). Then, we can play the converse game and ask, given an input θ, what is the probability to observe $\mathcal{D}$. The goal will be to maximize this function to determine the best parameters.

- The *Bayesian Evidence* $\mathcal{E} = pr(\mathcal{D})$ gives a number describing how likely it is that our context $\mathcal{I}$ produce the data $\mathcal{D}$. By taking ratio of this quantity computed for two models, one can compare the odds of those models and decide whether one is favored by the data. However, we emphasize again that it does not tell whether the given model $\mathcal{I}$ is the "true" model.

- Finally the *Posterior* $\mathcal{P}(\theta) = pr(\theta|\mathcal{D})$ represents our infered distribution of probability for the parameters (or credible intervals) within a model. It is also a probability so it sums to 1.

We can express the two output terms as a function of the input

$$\mathcal{E} = \int \mathcal{L}(\theta)\pi(\theta)d\theta\,, \tag{B.3.2}$$

$$\mathcal{P}(\theta) = \frac{\mathcal{L}(\theta)\pi(\theta)}{\mathcal{E}}\,. \tag{B.3.3}$$

It brings two remarks: i) The evidence $\mathcal{E}$ is a N-dimensional integral of a potentially complicated functions of the parameters. It can thus be very tough to compute and the most commonly used algorithm for parameter extraction (the Metropolis-Hasting) *does not* gives this information. ii) The evidence enters in the posterior distribution as a normalization constant. Someone interested in credible intervals and not in model comparaison, as we are, can therefore safely ignore it.
Finally, we can define 1D and 2D *marginalised* distributions as

$$\mathcal{P}(\theta_1, \theta_2|\mathcal{D}) = \int P(\theta|\mathcal{D}) \prod_{i\neq 1,2} d\theta_i\,. \tag{B.3.4}$$

B.3.2 *Parameter extraction and the Fisher matrix*

Comparing a model to observations is usually done in two steps. One first select a given set of parameters θ (including nuisance parameters) and compute the relevant observables with a Boltzmann code (e.g. CMB TT, TE, EE and matter power spectrum). Then, one compares the output of the code with the data using the likelihood, and aim at maximizing the likelihood in order to get an estimate of the "true" parameters and their associated errors. The most common likelihood functions is the so-called *Gaussian likelihood*. For N Gaussian random variables d_i with errors σ_i and correlation function C_{ij}, it is given by

$$\mathcal{L}(\{d_i, \sigma_i\}) = \frac{1}{\sqrt{\det C (2\pi)^N}} \exp\left(-\frac{d_i C_{ij}^{-1} d_j}{2}\right) \tag{B.3.5}$$

The best fitting model with parameters $\bar{\theta}$ corresponds to the maximum of the likelihood function

$$\left.\frac{d\mathcal{L}(\theta)}{d\theta}\right|_{\theta=\bar{\theta}} = 0\,. \tag{B.3.6}$$

We are also interested in the credible intervals associated to the parameters, which can be obtained via the approximate derivative of $d\ln\mathcal{L}/d\theta_i$ to first order

$$\frac{\partial \ln\mathcal{L}}{\partial\theta_i}(\bar{\theta}) \simeq \frac{\partial \ln\mathcal{L}}{\partial\theta_i}(\theta) + (\bar{\theta}_j - \theta_j)\frac{\partial^2 \ln\mathcal{L}}{\partial\theta_i\partial\theta_j}(\theta) \tag{B.3.7}$$

The *Fisher matrix* or curvature matrix is defined as the expectation value

$$F_{ij} \equiv \left\langle \frac{\partial^2 \ln\mathcal{L}}{\partial\theta_i\partial\theta_j} \right\rangle, \tag{B.3.8}$$

and one can show (e.g. ref [226])

$$F_{ij} = \frac{1}{2}\mathrm{Tr}\big(\mathrm{C}^{-1}(\partial_\mathrm{j}\mathrm{C})\mathrm{C}^{-1}(\partial_\mathrm{i}\mathrm{C})\big)\,. \tag{B.3.9}$$

Assuming that the posterior distributions of the parameters are Gaussian, then this matrix encodes the covariance of the parameters and the marginalized error of θ_i is given by $\sqrt{F^{-1}_{ii}}$.
For more involved distributions, however, this simple estimate would not work as it relies on the hypothesis of gaussian posteriors. The simplest strategy to get the posterior distribution and its maximum would then be to span an equally spaced grid in parameter space. However, if the parameter space is too large, this becomes very soon way too time consuming. However, if an experiment is precise enough, most of the parameters space is irrelevant and more clever methods are available.
One needs to go to *Monte Carlo* methods, which we used in this work.

B.3.3 *Monte Carlo Markov Chains*

The idea is that instead of deciding on an *a priori* exploration of the parameter space, we explore it randomly starting from some initial position. One possibility is to make use of a *Markov Chain*: starting from a given position with known likelihood, one proposed a new point and computes the associated likelihood. It it then decided with a given algorithm, whether the point should be accepted or not *independantly of previous points in the chain*. A good proposal algorithm does not accept point only when the likelihood is higher, otherwise it would quickly converge to the maximum of likelihood and stay there. To explore the parameter space, the algorithm should accept point with smaller likelihood at smaller rate, so that it traces the underlying distribution. The most commonly used algorithm is the so-called Metropolis-Hastings (MH) algorithm.

B.3.3.1 *The Metropolis-Hastings algorithm*

It is described by the following list of steps for the n-th iteration:

1. Propose a random point in the parameter space around the last point in some chain drawn from a "proposal density" $\mathcal{Q}(\theta^n, \theta^{n-1})$.

2. Compute the likelihood at this point n, $\mathcal{L}(n)$, and the ratio

$$r = \frac{\mathcal{L}(n)\mathcal{Q}(\theta^n, \theta^{n-1})}{\mathcal{L}(n-1)\mathcal{Q}(\theta^{n-1}, \theta^n)} \tag{B.3.10}$$

3. If $r \geq 1$, we accept the point as a next member of our chain .

4. Otherwise, we accept the point with probability r or simply increment the "weight" of the $n-1$ with probability $1-r$.

Often, the proposal density is chosen to be Gaussian centered around the current point such that it does not enter the ratio r. It is only necessary to propose the new point. The covariance matrix of the parameters can be used in the Gaussian proposal in order to improve the proposal. However, when one starts a chain the covariance matrix is not always known. Several ways are possible: i) one can start by "guessing" simple errors without correlations; ii) One can estimate the correlation matrix with the Fischer formalism; iii) One can start from the covariance matrix of a former run if the covariance matrix of the new run is believed to be close to it. In this work, it is often the third strategy that has been used.
The beginning of the MH algorithm is associated with a *burn in* until the "hill" of the likelihood is found, it is therefere necessary to remove the first n points (where n can be choosen arbitrarily by looking at the chains, often a few hundred is used). Several improvements are possible to decrease runtime, which are adopted in this work

- One can start an ensemble of N chains from different initial positions and analyze the chains together. This allows a faster sampling of the likelihood.

- While running, one can update the covariance matrix to improve the proposal distribution and increase *acceptance rate*. It is however necessary to throw away points that are not drawn from the same proposal density. Therefore the covariance matrix shouldn't be updated after some time, in order to gather enough points within a chain.

- Nuisance parameters does not require to re-run the full Boltzmann code. We therefore can decompose the covariance matrix into *fast* and *slow* parameters using the so-called Cholesky decomposition which allows to decorrelate fast/slow parameters. Then one can simply compute the part of likelihood related to these parameters, leaving the cosmological part unchanged. Usually, it is efficient to perform "oversampling" of the fast parameter with respect to the slow ones. This method has been introduced in the context of Cosmology in Ref. [403].

The MH can however show limitations, especially for multimodal posterior distributions. The algorithm is not well suited to go far away from a local maximum, and it can lead to difficulties if several local maxima are present in a distribution. Furthermore, with this algorithm, one samples the likelihood and not the prior, therefore it is not possible to get an estimate of the bayesian evidence from a MH. In the case this is needed, one needs to go for *Nested Sampling* algorithm such as MultiNest [241] or PolyChord [290]. We won't develop them here as it was never needed to use it.
In this work, we make use of the MontePython code [68] which incorporates both MH and MultiNest algorithms.

B.3.3.2 *Convergence diagnostics*

In order to determine the convergence of chains, several diagnostics are possible. First of all, one can look *by eye*, whether the chains looks "nice", i.e. whether they do not show too many holes or awkward shapes which would indicate that a longer sampling is needed. One can cut a chain in sub-chains and compare them to each others, to check the stationarity and assess whether a favorite region has indeed been found. However, the most used criterion is the so-called Gelman and Rubin diagnostic [265], based on the comparaison of the *variances within each chain* and the *variance between chains*. Large deviation between these two variances indicates nonconvergence. In practice, one calculates first the mean $\bar{x}_i$ and the variance σ_i from each chains, as well as the total mean from all chains $\bar{x}$. Then, one can calculate the variance of the chain means $\sigma(\bar{x}_i)^2 = \sum_i (\bar{x}_i^2 - \bar{x}^2)/(n-1)$ and the mean of the chain variances $\bar{\sigma}_i = \sum_i \sigma_i/(n-1)$. The ratio $R \equiv \sigma(\bar{x}_i)/\bar{\sigma}_i$ should be very close to 1 if the chains are converged. Usually, one uses the criterion $R - 1 < 0.1$ as a threshold for good convergence. The issue with this criterion is that a lower number of chains tend to give a lower value of R, and therefore it should also be used with caution.

C

APPENDIX TO CHAPTER 4

C.1 Decay terms in the Boltzmann equation

In this study, we consider a decaying cold dark matter (dcdm) and its daugther dark radiation (dr). Both have no interactions with other species in the Universe, hence we only need to add a decay term to the Boltzmann equations of the cold dark matter and relativistic massless particles to get our full system of equations. In the synchronous gauge comoving with the dcdm, *and only in this gauge*, it is possible to cast the decay term in a very useful form (in conformal time)

$$D \equiv a\Gamma f_{dcdm}\,, \tag{C.1.1}$$

where the Γ term contains all information about the matrix element and the phase space of both parent and daugther particles. From now on, we will work in this gauge, and we therefore need to recompute the general equation (B.2.15), adding this new term on the rhs with either a minus sign when considering the DM or a plus sign when considering its daugther particle. We will change here notation, so that we stick with [70], [412].

Our synchronous gauge will now be defined as

$$ds^2 = a^2(\tau)\Big\{ -d\tau^2 + (\delta_{ij} + H_{ij})dx^i dx^j \Big\}\,, \tag{C.1.2}$$

and our newtonian one by

$$ds^2 = a^2(\tau)\Big\{ -(1+2\psi)d\tau^2 + (1-2\phi)dx^i dx^j \Big\}\,. \tag{C.1.3}$$

Be careful, the gauge transformation will be the same but with renamed potentials $\phi \leftrightarrow \psi$. In this gauge, the 4-momentum P^μ can be related to the proper momentum p^i and energy E using the relations

$$P^2 = g_{\mu\nu}P^\mu P^\nu = -m^2\,, \qquad p^2 = g_{ij}P^i P^j\,, \tag{C.1.4}$$

which differed for a sign with our new notations. It is also standard to introduced the comoving momentum $q^i = ap^i$ and comoving energy $\epsilon = aE \Rightarrow \epsilon^2 = q^2 + am^2$.
Thus, we have

$$\begin{aligned} -a^2(\tau)(P^0)^2 + p^2 &= -m^2 \\ \Rightarrow P^0 = \frac{E}{a} &= \frac{\epsilon}{a^2}\,, \end{aligned} \tag{C.1.5}$$

and if we again set $P^i \equiv Cn^i$ we find

$$\begin{aligned} p^2 &= a^2(\delta_{ij}+H_{ij})C^2 \\ \Rightarrow C &= \frac{p}{a}(\delta_{ij}-\frac{1}{2}H_{ij}) \\ \Rightarrow P^i &= \frac{p^j}{a}(\delta_{ij}-\frac{1}{2}H_{ij})\,, \qquad \text{with } p^i = pn^i\,. \end{aligned} \tag{C.1.6}$$

Let's now go back to the full boltzmann equation, with decay term, written in terms of conformal time and momentum

$$\frac{df}{d\tau} = \frac{\partial f}{\partial \tau} + \frac{\partial f}{\partial x^i}\frac{dx^i}{d\tau} + \frac{\partial f}{\partial q}\frac{dq}{d\tau} + \frac{\partial f}{\partial n^i}\frac{dn^i}{dt} = \pm D\,. \tag{C.1.7}$$

Just as we already did, we can rewrite this equation more explicitely. Again, the fourth term is second order, therefore will be neglected. The second term can be recast since

$$\frac{dx^i}{d\tau} = \frac{dx^i}{d\lambda}\frac{d\lambda}{d\tau} = \frac{P^i}{P^0} = \frac{q^j}{\epsilon}(\delta_{ij}-\frac{1}{2}H_{ij})\,. \tag{C.1.8}$$

Then, using the geodesic equation like before, we can reexpress the $dq/d\tau$ term

$$P^0\frac{dP^0}{d\tau} = -\Gamma^0{}_{\alpha\beta}P^\alpha P^\beta\,. \tag{C.1.9}$$

We need the perturbed Christoffels in synchronous gauge. It is easy to compute following the development we made to derive eq. (B.1.34). The three Christoffels we need are

$$\Gamma^0{}_{00} = \frac{1}{2}g^{00}g_{00,0} = \mathcal{H}\,, \tag{C.1.10}$$

$$\Gamma^0{}_{i0} = \frac{1}{2}g^{00}g_{00,i} = 0\,, \tag{C.1.11}$$

$$\begin{aligned} \Gamma^0{}_{ij} &= -\frac{1}{2}g^{00}g_{ij,0} \\ &= \frac{1}{2}a^{-2}\Big[2a^2\mathcal{H}(\delta_{ij}+H_{ij}) + a^2H'_{ij}\Big] \\ &= \frac{1}{2}H'_{ij} + \mathcal{H}(\delta_{ij}+H_{ij})\,. \end{aligned} \tag{C.1.12}$$

Now we can compute $dP^0/d\tau$ since

$$\begin{aligned} a^4\big(P^0\big)^2 &= q^2 + a^2m^2 \\ \Rightarrow 4a^3da\big(P^0\big)^2 + 2a^4P^0dP^0 &= 2qdq + (2ada)m^2 \\ \Rightarrow P^0\frac{dP^0}{d\tau} &= -\frac{2}{a^4}\mathcal{H}q^2 - \frac{2}{a^2}m^2\mathcal{H} + \frac{q}{a^4}\frac{dq}{d\tau} + \frac{m^2}{a^2}\mathcal{H} \\ &= -\frac{2}{a^4}\mathcal{H}q^2 - \frac{m^2}{a^2}\mathcal{H} + \frac{q}{a^4}\frac{dq}{d\tau}\,, \end{aligned} \tag{C.1.13}$$

and the rhs of eq. (C.1.9) is

$$\begin{aligned} -\Gamma^0{}_{\alpha\beta}P^\alpha P^\beta &= -\Gamma^0{}_{00}\big(P^0\big)^2 - \Gamma^0{}_{ij}P^iP^j \\ &= -\frac{\mathcal{H}}{a^4}\big[q^2+m^2a^2\big] - \big[\frac{1}{2}H'_{ij} + \mathcal{H}(\delta_{ij}+H_{ij})\big]\frac{1}{a^4}\big[\delta_{ik}-\frac{1}{2}H_{ik}\big]q^k\big[\delta_{jl}-\frac{1}{2}H_{jl}\big]q^l \\ &= -\frac{\mathcal{H}}{a^4}\big[q^2+m^2a^2\big] - \frac{1}{2a^4}H'_{ij}q^iq^j - \frac{\mathcal{H}}{a^4}q^2 \\ &= -2\frac{\mathcal{H}}{a^4}q^2 - \frac{\mathcal{H}}{a^4}m^2a^2 - \frac{1}{2a^4}H'_{ij}q^iq^j\,. \end{aligned} \tag{C.1.14}$$

Equating both sides leaves the result

$$\begin{aligned} -\frac{2}{a^4}\mathcal{H}q^2 - \frac{m^2}{a^2}\mathcal{H} + \frac{q}{a^4}\frac{dq}{d\tau} &= -2\frac{\mathcal{H}}{a^4}q^2 - \frac{\mathcal{H}}{a^4}m^2a^2 - \frac{1}{2a^4}H'_{ij}q^iq^j \\ \Rightarrow \frac{q}{a^4}\frac{dq}{d\tau} &= -\frac{1}{2a^4}H'_{ij}q^iq^j \\ \Rightarrow \frac{dq}{d\tau} &= -\frac{1}{2}H'_{ij}qn^in^j\,. \end{aligned} \tag{C.1.15}$$

We can slightly rewrite this relation in fourier space since $H_{ij} = \hat{k}_i\hat{k}_j h + (\hat{k}_i\hat{k}_j - \frac{1}{3}\delta_{ij})6\eta$. Hence we have

$$\begin{aligned} \frac{dq}{d\tau} &= -\frac{1}{2}\big[\hat{k}_i\hat{k}_j h + (\hat{k}_i\hat{k}_j - \frac{1}{3}\delta_{ij})6\eta\big]'qn^in^j \\ &= q\eta' - \frac{1}{2}q\big(h' + 6\eta'\big)\big(\hat{k}\cdot n\big)^2\,. \end{aligned} \tag{C.1.16}$$

Therefore, the Boltzmann equation for decaying particle and its radiation in this gauge, at first order, takes the form

$$\frac{\partial f}{\partial\tau} + \frac{\partial f}{\partial x^i}\frac{q^i}{\epsilon} + \frac{\partial f}{\partial q}\left[q\eta' - \frac{1}{2}q\big(h' + 6\eta'\big)\big(\hat{k}\cdot n\big)^2\right] = \pm D\,. \tag{C.1.17}$$

We can also express it in term of the proper momentum p^i and energy E to make the cosmic expansion term appear,

$$\frac{dq}{d\tau} = \frac{d}{d\tau}[ap] = a\mathcal{H}p + a\frac{dp}{d\tau} \quad . \tag{C.1.18}$$

Hence we get

$$\frac{\partial f}{\partial\tau} + \frac{\partial f}{\partial x^i}\frac{p^i}{E} + p\frac{\partial f}{\partial p}\left[\eta' - \frac{1}{2}\big(h' + 6\eta'\big)\big(\hat{k}\cdot n\big)^2 - \mathcal{H}\right] = \pm D\,. \tag{C.1.19}$$

C.1.1 *Boltzmann equation for the decaying Dark Matter*

Starting with the decaying CDM, we have

$$\frac{\partial f_{dcdm}}{\partial\tau} + \frac{\partial f_{dcdm}}{\partial x^i}\frac{p^i}{E} + p\frac{\partial f_{dcdm}}{\partial p}\left[\eta' - \frac{1}{2}\big(h' + 6\eta'\big)\big(\hat{k}\cdot n\big)^2 - \mathcal{H}\right] = -D\,. \tag{C.1.20}$$

We now integrate over $\int d^3pE/(2\pi)^3$ and use the definition of ρ (1.3.13), as well as the one for v^i

$$\rho \equiv \int \frac{d^3p}{(2\pi)^3}Ef\,, \tag{C.1.21}$$

$$v^i \equiv \frac{1}{\rho}\int \frac{d^3p}{(2\pi)^3}fp^i\,. \tag{C.1.22}$$

Furthermore, we introduce here also the notation $\hat{k}\cdot n \equiv \mu$. It gives

$$\begin{aligned} \int \frac{d^3p}{(2\pi)^3}E\frac{\partial f_{dcdm}}{\partial\tau} + \int \frac{d^3p}{(2\pi)^3}\frac{\partial f_{dcdm}}{\partial x^i}p^i + \int \frac{d^3p}{(2\pi)^3}Ep\frac{\partial f_{dcdm}}{\partial p}\left[\eta' - \frac{1}{2}\big(h' + 6\eta'\big)\mu^2 - \mathcal{H}\right] \\ = -a\Gamma\int \frac{d^3p}{(2\pi)^3}Ef_{dcdm}\,. \end{aligned} \tag{C.1.23}$$

Here we can use the trick $\mu^2 = (2\mathcal{P}_2(\mu)+1)/3$, and furthermore we know that the integral over $d\Omega\mathcal{P}_2(\mu)$ will pick out the second moment of the distribution, which is negligible for the dcdm. Integrating the third term by part gives

$$\int \frac{d^3p}{2\pi^3} Ep \frac{\partial f}{\partial p} = \int \frac{d^3p}{(2\pi)^3} f\left[\frac{p^2}{E} + E\right] = \frac{3(\rho_{dcdm} + P_{dcdm})}{g_s}\,. \tag{C.1.24}$$

Therefore, setting $P_{dcdm} = 0$ we get

$$\rho'_{dcdm} + \frac{\partial(\rho_{dcdm} v^i_{dcdm})}{\partial x^i} + \frac{1}{2}h'\rho_{dcdm} + 3\mathcal{H}\rho_{dcdm} = -a\Gamma\rho_{dcdm}\,. \tag{C.1.25}$$

We introduce the usual notation $\rho_{dcdm} = \bar{\rho}_{dcdm}[1 + \delta_{dcdm}]$ and set in our gauge $v^i_{dcdm} = 0$ and $\theta_{dcdm} = \partial_i v^i_{dcdm} = 0$. We collect all zero-order term to get the modified background equation for the mass density $\bar{\rho}_{dcdm}$ in conformal time

$$\bar{\rho}'_{dcdm} = -3\mathcal{H}\rho_{dcdm} - a\Gamma\bar{\rho}_{dcdm}\,. \tag{C.1.26}$$

If we now turn to the first-order terms and divide by $\bar{\rho}_{dcdm}$ we get

$$\delta'_{dcdm} = -\frac{h'}{2}\,. \tag{C.1.27}$$

We now take the first moment of the distribution

$$\int \frac{d^3p}{(2\pi)^3} p^j \frac{\partial f_{dcdm}}{\partial \tau} + \underbrace{\int \frac{d^3p}{(2\pi)^3} \frac{\partial f_{dcdm}}{\partial x^i} p^2 n^i n^j}_{\mathcal{O}(2)} - \int \frac{d^3p}{(2\pi)^3} \frac{\partial f_{dcdm}}{\partial p} p^2 n^j \left[\eta' - \frac{1}{2}(h' + 6\eta')\mu^2 - \mathcal{H}\right] = -a\Gamma \int \frac{d^3p}{(2\pi)^3} p^j f_{dcdm}\,. \tag{C.1.28}$$

We can integrate by parts the fourth term, which makes the velocity appears, and hence at first order we can neglect all products with metric perturbations, leaving only

$$\frac{\partial(\rho_{dcdm} v^j_{dcdm})}{\partial t} + 4\mathcal{H}\rho_{dcdm} v^j_{dcdm} = -a\Gamma(\rho_{dcdm} v^j_{dcdm}). \tag{C.1.29}$$

It has no zero-order parts, since the velocity is a first order quantity. We take the divergence to get

$$\begin{aligned} (\bar{\rho}_{dcdm}\theta_{dcdm})' + 4\mathcal{H}\bar{\rho}_{dcdm}\theta_{dcdm} &= -a\Gamma\bar{\rho}_{dcdm}\theta_{dcdm} \\ \Leftrightarrow (-3\mathcal{H}\rho_{dcdm} - a\Gamma\bar{\rho}_{dcdm})\theta - \theta'\bar{\rho}_{dcdm} + 4\mathcal{H}\bar{\rho}_{dcdm} &= -a\Gamma\bar{\rho}_{dcdm}\theta_{dcdm} \\ \Leftrightarrow \theta'_{dcdm} &= -\mathcal{H}\theta_{dcdm} \stackrel{!}{=} 0\,. \end{aligned} \tag{C.1.30}$$

We now want to rewrite this two equations in the newtonian gauge. Indeed, This will allow us to cross-check that our derivation was right since the physical result shouldn't depend on the gauge. We use eq. (2.1.56) and introduce the parameter $\alpha \equiv (h' + 6\eta')/2k^2$.

It yields

$$\begin{aligned}
\delta^{(s)}_{dcdm} = -\frac{h'}{2} &= \delta^{(n)'}_{dcdm} + (3\mathcal{H}' + a\mathcal{H}\Gamma)\alpha + (3\mathcal{H} + a\Gamma)\alpha' \\
&= \delta^{(n)'}_{dcdm} + 3\mathcal{H}\alpha' + a\mathcal{H}\Gamma\alpha + 3\mathcal{H}\alpha' + a\Gamma\alpha' \\
&= \delta^{(n)'}_{dcdm} + 3\mathcal{H}\alpha' + a\mathcal{H}\Gamma\alpha + 3\mathcal{H}\left\{\frac{-\psi'}{\mathcal{H}} - \frac{\mathcal{H}'}{\mathcal{H}}\alpha + \frac{\eta'}{\mathcal{H}}\right\} + a\Gamma\{\phi - \mathcal{H}\alpha\} \\
&= \delta^{(n)'}_{dcdm} + a\Gamma\phi - 3\psi' + 3\eta' \\
\Leftrightarrow k^2\alpha &= \underbrace{\theta^{(s)}_{dcdm}}_{0} - \theta^{(n)}_{dcdm} = \delta^{(n)'}_{dcdm} + a\Gamma\phi - 3\psi' \\
\Leftrightarrow \delta^{(n)'}_{dcdm} &= -a\Gamma\phi + 3\psi - \theta^{(n)}_{dcdm}\,. \qquad \text{(C.1.31)}
\end{aligned}$$

$$\begin{aligned}
\theta^{(s)'}_{dcdm} = -\mathcal{H}\theta^{(s)}_{dcdm} &= \theta^{(n)'}_{dcdm} - k^2\alpha' \\
\Leftrightarrow -\mathcal{H}\{\theta^{(n)}_{dcdm} - k^2\alpha\} &= \theta^{(n)'}_{dcdm} - k^2\alpha' \\
\Leftrightarrow \theta^{(n)'}_{dcdm} &= -\mathcal{H}\theta^{(n)}_{dcdm} + \mathcal{H}k^2\alpha + k^2\alpha' \\
\Leftrightarrow \theta^{(n)'}_{dcdm} &= -\mathcal{H}\theta^{(n)}_{dcdm} + k^2\phi\,. \qquad \text{(C.1.32)}
\end{aligned}$$

From then, it is useful to introduce new sources variables that allow to write these equations in *both* gauges as

$$\boxed{\begin{aligned}
\delta'_{dcdm} &= -\theta_{dcdm} - \mathfrak{m}_{\rm cont} - a\Gamma\mathfrak{m}_\psi \qquad \text{(C.1.33a)} \\
\theta'_{dcdm} &= -\mathcal{H}\theta_{dcdm} + k^2\mathfrak{m}_\psi\,, \qquad \text{(C.1.33b)}
\end{aligned}}$$

where $\mathfrak{m}_{\rm cont}$ and $\mathfrak{m}_\psi$ are given by

	Synchronous	Newtonian
$\mathfrak{m}_{\rm cont}$	$h'/2$	$-3\phi'$
$\mathfrak{m}_\psi$	0	ψ

Table 10: Continuity and euler type of metric source terms for scalar perturbations in synchronous and Newtonian gauge.

C.1.2 *Boltzmann hierarchy for the daugther dark radiation*

From now on, to study perturbations of the dr and the dcdm, we used our formal definition for the perturbed phase-space distribution :

$$\begin{aligned}
f_{dr}(\vec{x}, p, \vec{n}, \tau) &= f^{(0)}_{dr}(p,\tau)(1 + \Psi_{dr}(\vec{x}, p, \vec{n}, \tau))\,, \\
f_{dcdm}(\vec{x}, p, \vec{n}, \tau) &= f^{(0)}_{dcdm}(p,\tau)(1 + \Psi_{dcdm}(\vec{x}, p, \vec{n}, \tau))\,. \qquad \text{(C.1.34)}
\end{aligned}$$

Then, we take the linearized Boltzmann equation in synchronous gauge and add the decay term (C.1.1) with now a plus sign on the rhs

$$\frac{\partial f_{dr}}{\partial\tau} + \frac{\partial f_{dr}}{\partial x^i}\frac{p^i}{E} + p\frac{\partial f_{dr}}{\partial p}\left[\eta' - \frac{1}{2}\left(h' + 6\eta'\right)\left(\hat{k}\cdot n\right)^2 - \mathcal{H}\right] = +D \qquad \text{(C.1.35)}$$

We can plug eq. (C.1.34) inside the previous one and follow the same step as for the dcdm, but with the equation of state $\bar{P}_{dr} = \bar{\rho}_{dr}/3$, to get the zero-order background density evolution

$$\bar{\rho}'_{dr} + 4H\bar{\rho}_{dr} = a\Gamma\bar{\rho}_{dcdm} \quad . \tag{C.1.36}$$

Having obtained the background equation, we switch our variables $p \to q$ and $E \to \epsilon$ to avoid dealing with extra $\mathcal{H}$ terms (which hence also disappear in previous equation),

$$\frac{\partial f_{dr}}{\partial\tau} + \frac{\partial f_{dr}}{\partial x^i}\frac{q^i}{\epsilon} + q\frac{\partial f_{dr}}{\partial q}\left[\eta' - \frac{1}{2}\left(h' + 6\eta'\right)\left(\hat{k}\cdot n\right)^2\right] = +D\,, \tag{C.1.37}$$

and introduced a similar notation as before to describe the perturbation of the integrated phase-space distribution

$$F_{dr} \equiv \frac{\int dqq^3 f^{(0)}_{dr}\Psi_{dr}}{\int dqq^3 f^{(0)}_{dr}} r_{dr} \equiv \sum_\ell (-i)^\ell (2\ell+1) F_{dr,\ell}(t,\vec{k})\mathcal{P}_\ell(\mu)\,, \tag{C.1.38}$$

with r_{dr} defined as

$$r_{dr} \equiv \frac{\bar{\rho}_{dr}a^4}{\rho_{cr,0}}\,, \tag{C.1.39}$$

where the critical energy density today, $\rho_{cr,0}$ has been introduced to make r_{dr} dimensionless. The introduction of this factor will help us to cancel the time-dependence of F_{dr} due to the background distribution function f^0_{dr} in the denominator of eq. (C.1.38). If follows that

$$r'_{dr} \;=\; \frac{1}{\rho_{cr,0}}[\bar{\rho}'_{dr}a^4 + 4a^4\mathcal{H}\bar{\rho}_{dr}] = \frac{\Gamma\bar{\rho}_{dcdm}a^5}{\rho_{cr,0}} = a\Gamma\frac{\bar{\rho}_{dcdm}}{\bar{\rho}_{dr}}r_{dr}\,. \tag{C.1.40}$$

From this, we want to establish the Boltzmann hierarchy as in the collisionless case. We now consider the first-order part of eq. (C.1.37)

$$\frac{\partial(f^{(0)}\Psi_{dr})}{\partial\tau} + \frac{\partial(f^{(0)}\Psi_{dr})}{\partial x^i}\frac{q^i}{\epsilon} + q\frac{\partial f^{(0)}_{dr}}{\partial q}\left[\eta' - \frac{1}{2}\left(h' + 6\eta'\right)\mu^2\right] = a\Gamma f^{(0)}_{dcdm}\Psi_{dcdm}\,. \tag{C.1.41}$$

We then move to Fourier space, integrate over q^2dqEr_{dr} (with $E = q$ for the dr but not for the dcdm) and divide by $\int dqq^3 f^{(0)}_{dr} \equiv \bar{\rho}_{dr}$. One has to be careful about the chain rules when taking the derivative of F_{dr} with respect to times. It is

$$\begin{aligned}
\frac{\partial}{\partial\tau}F_{dr} \;&=\; \frac{\partial}{\partial\tau}\frac{\int dqq^3 f^{(0)}_{dr}\Psi_{dr}}{\int dqq^3 f^{(0)}_{dr}} r_{dr} + \frac{\int dqq^3 f^{(0)}_{dr}\Psi_{dr}}{\int dqq^3 f^{(0)}_{dr}} r'_{dr} \\
&=\; r_{dr}\frac{\int dqq^3 \frac{\partial}{\partial\tau}(f^{(0)}_{dr}\Psi_{dr})}{\int dqq^3 f^{(0)}_{dr}} + F_{dr}\underbrace{\left[-\frac{\frac{\partial}{\partial\tau}\int dqq^3 f^{(0)}_{dr}}{\int dqq^3 f^{(0)}_{dr}} + a\Gamma\frac{\bar{\rho}_{dcdm}}{\bar{\rho}_{dr}}\right]}_{0} \\
&=\; r_{dr}\frac{\int dqq^3 \frac{\partial}{\partial\tau}(f^{(0)}_{dr}\Psi_{dr})}{\int dqq^3 f^{(0)}_{dr}}\,,
\end{aligned} \tag{C.1.42}$$

whereas the integration (by parts) and division for the last term on the lhs simply yields a factor of -4. Hence we get

$$\frac{\partial}{\partial\tau}F_{dr} + ik\mu F_{dr} + r_{dr}\left[\frac{2}{3}h' + \frac{4}{3}(h' + 6\eta')P_2(\mu)\right] = r'_{dr}\delta_{dcdm} \quad , \tag{C.1.43}$$

where we have used

$$\int q^2 dq E(f^{(0)}_{dcdm}\Psi_{dcdm}) = \delta_{dcdm}\bar{\rho}_{dcdm} \quad . \tag{C.1.44}$$

Then, we plug in it the Legendre multipoles expansion as it is defined in eq. (C.1.38) and we integrate over $d\mu P_m(\mu)$ to picks out every moments separately

$$\begin{aligned}
&\sum_\ell (-i)^\ell (2\ell+1) F'_{dr,\ell}(t,\vec{k}) \int d\mu P_m(\mu)\mathcal{P}_\ell(\mu) + ik\sum_{\ell'}(-i)^{\ell'}(2\ell'+1)F_{dr,\ell'}(t,\vec{k})\int d\mu\mu P_m(\mu)\mathcal{P}_{\ell'}(\mu)\\
&+r_{dr}\left[\frac{2}{3}h'\int d\mu P_m(\mu) + \frac{4}{3}(h'+6\eta')\int d\mu P_m(\mu)P_2(\mu)\right] = r'_{dr}\delta_{dcdm}\int d\mu P_m(\mu)\\
\Leftrightarrow\quad &(-i)^\ell(2\ell+1)F'_{dr,\ell}(t,\vec{k})\delta_{lm}\frac{2}{2\ell+1} + ik(-i)^{\ell'}F_{dr,\ell'}\left[(\ell'+1)\delta_{(\ell'+1)m}\frac{2}{2(\ell'+1)+1} + \ell'\delta_{(\ell'-1)m}\frac{2}{2(\ell'-1)+1}\right]\\
&+r_{dr}\left[\frac{2}{3}h'\delta_{0m} + \frac{4}{3}(h+6\eta')\delta_{2m}\frac{2}{5}\right] = r'_{dr}\delta_{dcdm}\delta_{0m}\,.
\end{aligned} \tag{C.1.45}$$

Splitting between $m = 0, 1, 2$ and $m > 2$ leads to the following hierarchy in synchronous gauge

$$\boxed{\begin{aligned}
F'_{dr,0} &= -kF_{dr,1} - \frac{2}{3}r_{dr}h' + r'_{dr}\delta_{dcdm} && \text{(C.1.46a)}\\
F'_{dr,1} &= \frac{k}{3}F_{dr,0} - \frac{2k}{3}F_{dr,2} && \text{(C.1.46b)}\\
F'_{dr,2} &= \frac{2k}{5}F_{dr,1} - \frac{3k}{5}F_{dr,3} + \frac{8}{15}r_{dr}\frac{(h'+6\eta')}{2} && \text{(C.1.46c)}\\
F'_{dr,\ell} &= \frac{k}{2\ell+1}\big(lF_{dr,\ell-1} - (\ell+1)F_{dr,\ell+1}\big) \qquad \ell > 2. && \text{(C.1.46d)}
\end{aligned}}$$

We now again want to rewrite this set of equations in the newtonian gauge for a cross-check. First of all, all $F_{dr,\ell}$ are gauge-invariant for $\ell > 1$. To know how the other multipole moments transform, we can use their relations to the standard variables δ and θ, as well as the gauge-invariant variable σ for consistency. Indeed, we have shown in section 2.1.2 all relations of interest up to the factor r_{dr} that we now need to add. They are

$$F_{dr,0} = r_{dr}\delta\,, \qquad F_{dr,1} = \frac{4r_{dr}}{3k}\theta\,, \qquad F_{dr,2} = 2\sigma\,. \tag{C.1.47}$$

Eq. (2.1.56) then immediately gives the way in which these moments change under a transformation from the synchronous to newtonian gauge

$$F^{(s)}_{dr,0} = F^{(n)}_{dr,0} - r_{dr}\frac{\bar{\rho}'_{dr}}{\bar{\rho}_{dr}}\alpha\,, \qquad F^{(s)}_{dr,1} = F^{(n)}_{dr,1} - \frac{4r_{dr}k}{3}\alpha\,, \tag{C.1.48}$$

where we have again introduced the parameter $\alpha = (h' + 6\eta')/2k^2$.
We recall that the metric potentials transform under our new notation as

$$\psi = \mathcal{H}\frac{(6\eta+h)'}{2k^2} + \frac{(6\eta+h)''}{2k^2}\,, \qquad \phi = \eta - \mathcal{H}\frac{(6\eta+h)'}{2k^2}\,. \tag{C.1.49}$$

These are the same transformation as before but with the potential name exchanged to stick with more standard notation.

Let start with the $\ell = 0$ multipole moment. In this case, we need to compute $F^{(s)'}_{dr,0}$ and hence $(\bar{\rho}'_{dr}/\bar{\rho}_{dr})'$. It is given by

$$\left(\frac{\bar{\rho}'_{dr}}{\bar{\rho}_{dr}}\right)' = \frac{\bar{\rho}''_{dr}}{\bar{\rho}_{dr}} - \left(\frac{\bar{\rho}'_{dr}}{\bar{\rho}_{dr}}\right)^2 , \tag{C.1.50}$$

with

$$\begin{aligned}
\bar{\rho}''_{dr} &= (-4\mathcal{H}\bar{\rho}_{dr} + a\Gamma\bar{\rho}_{dcdm})' \\
&= -4\mathcal{H}'\bar{\rho}_{dr} - 4\mathcal{H}[-4\mathcal{H}\bar{\rho}_{dr} + a\Gamma\bar{\rho}_{dcdm}] + aH\Gamma\bar{\rho}_{dcdm} + a\Gamma[-3H\bar{\rho}_{dcdm} - a\Gamma\bar{\rho}_{dcdm}] \\
&= -4\mathcal{H}'\bar{\rho}_{dr} + 16\mathcal{H}^2\bar{\rho}_{dr} - 6\mathcal{H}a\Gamma\bar{\rho}_{dcdm} - (a\Gamma)^2\bar{\rho}_{dcdm} \\
\Rightarrow \frac{\bar{\rho}''_{dr}}{\bar{\rho}_{dr}} &= -4\mathcal{H}' + 16\mathcal{H}^2 - 6\mathcal{H}\frac{r'_{dr}}{r_{dr}} - a\Gamma\frac{r'_{dr}}{r_{dr}} ,
\end{aligned} \tag{C.1.51}$$

and

$$\left(\frac{\bar{\rho}'_{dr}}{\bar{\rho}_{dr}}\right)^2 = \left(-4\mathcal{H} + \frac{r'_{dr}}{r_{dr}}\right)^2 = 16\mathcal{H}^2 + \left(\frac{r'_{dr}}{r_{dr}}\right)^2 - 8\mathcal{H}\frac{r'_{dr}}{r_{dr}} . \tag{C.1.52}$$

Collecting terms yields

$$\left(\frac{\bar{\rho}'_{dr}}{\bar{\rho}_{dr}}\right)' = -4\mathcal{H}' + 2\mathcal{H}\frac{r'_{dr}}{r_{dr}} - a\Gamma\frac{r'_{dr}}{r_{dr}} - \left(\frac{r'_{dr}}{r_{dr}}\right)^2 . \tag{C.1.53}$$

We can now develop the gauge transformation of the $\ell = 0$ equation

$$\begin{aligned}
& F^{(n)'}_{dr,0} - r'_{dr}\frac{\bar{\rho}'_{dr}}{\bar{\rho}_{dr}}\alpha - r_{dr}\left(\frac{\bar{\rho}'_{dr}}{\bar{\rho}_{dr}}\right)'\alpha - r_{dr}\frac{\bar{\rho}'_{dr}}{\bar{\rho}_{dr}}\alpha' = -k\left[F^{(n)}_{dr,1} - \frac{4r_{dr}k}{3}\alpha\right] - \frac{2r_{dr}}{3}h' + r'_{dr}\left[\delta^{(n)}_{dcdm} - \frac{\bar{\rho}'_{dcdm}}{\bar{\rho}_{dcdm}}\alpha\right] \\
\Leftrightarrow\ & F^{(n)'}_{dr,0} - r'_{dr}\left[-4\mathcal{H} + \frac{r'_{dr}}{r_{dr}}\right]\alpha - r_{dr}\left[-4\mathcal{H}' + 2\mathcal{H}\frac{r'_{dr}}{r_{dr}} - a\Gamma\frac{r'_{dr}}{r_{dr}} - \left(\frac{r'_{dr}}{r_{dr}}\right)^2\right]\alpha - r_{dr}\left[-4\mathcal{H} + \frac{r'_{dr}}{r_{dr}}\right]\alpha' \\
& = -kF^{(n)}_{dr,1} + \underbrace{k^2\frac{4r_{dr}k}{3}\alpha - \frac{2r_{dr}}{3}h'}_{4r_{dr}\eta' = 4r_{dr}[\phi' + \mathcal{H}'\alpha + \mathcal{H}\alpha']} + r'_{dr}\left[\delta^{(n)}_{dcdm} - (-3\mathcal{H} - a\Gamma)\alpha\right] \\
\Leftrightarrow\ & F^{(n)'}_{dr,0} + 2\mathcal{H}r'_{dr}\alpha + 4\mathcal{H}'r_{dr}\alpha + 4\mathcal{H}r_{dr}\alpha' - r'_{dr}\alpha' - a\Gamma r'_{dr}\alpha \\
& = -kF^{(n)}_{dr,1} + 4r_{dr}\phi' + 4\mathcal{H}'r_{dr}\alpha + 4\mathcal{H}r_{dr}\alpha' + r'_{dr}\delta^{(n)}_{dcdm} + 3\mathcal{H}r'_{dr}\alpha + a\Gamma r'_{dr}\alpha \\
\Leftrightarrow\ & F^{(n)'}_{dr,0} = -kF^{(n)}_{dr,1} - 4r_{dr}\phi' + r'_{dr}\left[\delta^{(n)}_{dcdm}\underbrace{-H\alpha + \alpha'}_{\psi}\right] \\
\Leftrightarrow\ & F^{(n)'}_{dr,0} = -kF^{(n)}_{dr,1} - 4r_{dr}\phi' + r'_{dr}\left[\delta^{(n)}_{dcdm} + \psi\right] ,
\end{aligned} \tag{C.1.54}$$

whereas the $\ell = 1$ equation yields

$$\begin{aligned}
F^{(n)'}_{dr,1} &- \frac{4r'_{dr}k}{3}\alpha - \frac{4r_{dr}k}{3}\alpha' = \frac{k}{3}\left[F^{(n)}_{dr,0} - r_{dr}\frac{\bar{\rho}'_{dr}}{\bar{\rho}_{dr}}\alpha\right] - \frac{2k}{3}F^{(n)}_{dr,2} \\
\Leftrightarrow F^{(n)'}_{dr,1} &= \frac{k}{3}F^{(n)}_{dr,0} + \frac{4k}{3}\left[r'_{dr}\alpha + r_{dr}\alpha'\right] - \frac{2k}{3}F^{(n)}_{dr,2} - \frac{kr_{dr}}{3}\left[-4\mathcal{H} + \frac{r'_{dr}}{r_{dr}}\right]\alpha \\
\Leftrightarrow F^{(n)'}_{dr,1} &= \frac{k}{3}F^{(n)}_{dr,0} - \frac{2k}{3}F^{(n)}_{dr,2} + \frac{4kr_{dr}}{3}\left[\psi - \mathcal{H}\alpha\right] - \frac{4kr_{dr}}{3}\mathcal{H}\alpha - kr'_{dr}\alpha \\
\Leftrightarrow F^{(n)'}_{dr,1} &= \frac{k}{3}F^{(n)}_{dr,0} - \frac{2k}{3}F^{(n)}_{dr,2} + \frac{4kr_{dr}}{3}\psi + \frac{r'_{dr}}{k}\theta^{(n)}_{dcdm} ,
\end{aligned} \tag{C.1.55}$$

where we have used in the last line the fact that $k^2\alpha = \theta^{(n)}_{dcdm} - \{\theta^{(s)}_{dcdm} = 0\} = \theta^{(n)}_{dcdm}$.
Finally, the $\ell = 2$ equation gives

$$\begin{aligned} F^{(n)}_{dr,2} &= \frac{2k}{5}\left[F^{(n)}_{dr,1} - \frac{4r_{dr}k}{3}\alpha\right] - \frac{3k}{5}F^{(n)}_{dr,3} + \frac{8r_{dr}k^2}{15}\alpha \\ &= \frac{2k}{5}F^{(n)}_{dr,1} - \frac{3k}{5}F^{(n)}_{dr,3}\,. \end{aligned} \tag{C.1.56}$$

Like for the dcdm, it is common to introduce the sources variables $\mathfrak{m}_{\rm cont}$ and $\mathfrak{m}_\psi$, already defined in table 10, and $\mathfrak{m}_{\rm shear}$, defined in table 11.

	Synchronous	Newtonian
$\mathfrak{m}_{\rm shear}$	$(h' + 6\eta')/2$	0

Table 11: Shear type of metric source terms for scalar perturbations in synchronous and Newtonian gauge.

The final set of equations for the dr written in both gauges reads

$$F'_{dr,0} = -kF_{dr,1} - \frac{4}{3}r_{dr}\mathfrak{m}_{\rm cont} + r'_{dr}(\delta_{dcdm} + \mathfrak{m}_\psi) \tag{C.1.57a}$$

$$F'_{dr,1} = \frac{k}{3}F_{dr,0} - \frac{2k}{3}F_{dr,2} + \frac{4k}{3}r_{dr}\mathfrak{m}_\psi + \frac{r'_{dr}}{k}\theta_{dcdm} \tag{C.1.57b}$$

$$F'_{dr,2} = \frac{2k}{5}F_{dr,1} - \frac{3k}{5}F_{dr,3} + \frac{8}{15}r_{dr}\mathfrak{m}_{\rm shear} \tag{C.1.57c}$$

$$F'_{dr,\ell} = \frac{k}{2\ell+1}\big(lF_{dr,\ell-1} - (\ell+1)F_{dr,\ell+1}\big) \qquad \ell > 2. \tag{C.1.57d}$$

This set of equations needs to be truncated at some maximum multipole order $\ell_{\rm max}$. To do so, we will use the improved truncation scheme from [412]. It is based on the solution of these equations when there is no cosmic shear, i.e. $\partial_\tau(\phi+\psi) = 0$. In this case, the time dependence of the analytical solution of the Boltzmann hierarchy is given by a bessel function $j_\ell(k\tau)$ for all ℓ's (only two being non-zero). From this, we assume that the solution still approximately holds even if the condition $\partial_\tau(\phi+\psi) = 0$ is not fulfilled anymore and make use of the recurrence relation for spherical Bessel functions to get

$$F_{(\ell_{\rm max}+1)} \simeq \frac{(2\ell_{\rm max}+1)}{k\tau}F_{\ell_{\rm max}} - F_{(\ell_{\rm max}-1)}\,. \tag{C.1.58}$$

C.2 Modifiying the stress-energy tensor conservation

Instead of using the Bolzmann equation, it is possible to use their integrated form through the stress-energy tensor conservation to derive equations of motion for δ and θ, not for the others moments of the distribution though. We can write the continuity and Euler equation in form

$$T^{\mu 0}_{dcdm;\mu} = -C\,, \qquad T^{\mu 0}_{dr;\mu} = C\,, \tag{C.2.1}$$

$$\partial_i T^{\mu i}_{dcdm;\mu} = -D\,, \qquad \partial_i T^{\mu i}_{dr;\mu} = D\,. \tag{C.2.2}$$

By identification with the term in the last section, we know that the C and D terms (careful here D is different than the one we expressed above), take a trivial form in the synchronous gauge comoving with the decaying species

$$C^{(s)} = a\Gamma\bar{\rho}_{dcdm}(1+\delta_{dcdm}) \ , \qquad D^{(s)} = 0 \ . \tag{C.2.3}$$

It is in this gauge, and only in this gauge, that C and D take so simple forms. It is then trivial to generalize the result at first-order for non-decaying, non-interacting species, as it is given by eq. (2.1.58). Indeed, the continuity and euler equations for the dcdm don't change at all, whereas the ones for the daugther radiation only have one further term. We had made the derivation in the newtonian gauge. All we would have to do is to start from eq. (B.1.63), proceed again by a gauge transformation to go in the synchronous gauge, and add $C^{(s)}$ on the rhs. For radiation, we recall $\omega = \delta P/\delta\rho = 1/3$. Splitting it between zero and first order, we find

$$\bar{\rho}'_{dr} = -4\mathcal{H} + a\Gamma\bar{\rho}_{dcdm} \qquad \text{zero} - \text{order} \tag{C.2.4}$$

$$\delta'_{dr} = \frac{2}{3}h' - \frac{4}{3}\theta + a\Gamma\frac{\bar{\rho}_{dcdm}}{\bar{\rho}_{dr}}(\delta_{dcdm} - \delta_{dr}) \qquad \text{first} - \text{order} \tag{C.2.5}$$

The euler equations are very simple to obtain in this gauge, since $D^{(s)} = 0$. Furthermore, we have chosen to set

$$\theta'_{dcdm} = -\mathcal{H}\theta_{dcdm} = 0 \, , \tag{C.2.6}$$

with our choice of gauge. We only need to slightly modify the equation for the θ_{dr}. The only difference from the standard derivation appears when computing $\bar{P}'$ as given by eq. (B.1.69). One here needs to add a term $a\Gamma\bar{\rho}_{dcdm}$ as it is indicated by eq. (C.2.4). Setting again $\omega = \delta P/\delta\rho = 1/3$ and $\omega' = 0$ yields

$$\theta'_{dr} = -\frac{k^2}{4}\delta_{dr} - k^2\sigma - a\Gamma\frac{\bar{\rho}_{dcdm}}{\bar{\rho}_{dr}} \, . \tag{C.2.7}$$

We cannot recover the full hierarchy, since $T_{\mu\nu}$ make use only of the integrated distribution, but still this is enough for the dcdm, and constitutes a cross-check for the dr.

D

APPENDIX TO CHAPTER 7

D.1 Comparison of the energy deposition treatments

We wish here to compare our formalism to the analytical treatment used by some authors to implement the energy deposition from DM annihilations. Instead of parametrizing the energy deposition history through the $f(z)$ functions, the authors of [96], [189], [270], [447] have used a more explicit method, which has however some caveats. Following notations of [189], equivalent to other articles, one can write after a few manipulations the energy deposition as:

$$\left.\frac{dE}{dVdt}\right|_{\rm dep}(z) = \tag{D.1.1}$$
$$\int_z^\infty \frac{dz'}{(1+z')H(z')}\frac{(1+z)^3}{(1+z')^3}\frac{n_A(z)\langle\sigma_{\rm ann}v\rangle}{2m_{\rm DM}^2}\rho^2(z')\int_0^{m_{\rm DM}} dE_\gamma E_\gamma \frac{dN_\gamma}{dE'_\gamma}(E'_\gamma)e^{-\kappa(z',z;E'_\gamma)}\sigma(E_\gamma)$$

where $\sigma(E'_\gamma)$ is obtained by summing $\sigma_{\gamma A\to e^-A+}$, $\sigma_{\gamma e^-\to\gamma e^-}$ and $\sigma_{\gamma A\to e^\pm A}$ (the index A refers to H and He atoms), $n_A(z)$ scales as $(1+z)^3$, $\frac{dN_\gamma}{dE'_\gamma}(E'_\gamma)$ is the spectrum of photons produced by the DM annihilations (both prompt and from inverse Compton scattering), E'_γ is the energy at the time of injection and E_γ is the energy at the time of deposition, and $\kappa(z',z;E'_\gamma)$ plays the role of an absorption coefficient defined as:

$$\kappa(z,z',E_\gamma) \simeq \int_{z'}^{z} dz''\frac{dt}{dz''}n_A(z'')\sigma(E''_\gamma) \quad . \tag{D.1.2}$$

Three comments can be made about this formula.

- First of all, a mistake is made in eq. (4) of Ref. [447] (the equivalent of our eq. (D.1.1)) and that mistake propagated to Ref. [270]. Indeed, in eq. (4) of Ref. [447], the last integral is performed over E'_γ (the energy at the time of injection) instead of E_γ (the energy at the time of deposition). Since the two are related by $E'_\gamma = E_\gamma(1+z')/(1+z)$, the final result differs by a factor $(1+z)^2/(1+z')^2$ in the last integral over dz'. This can be seen explicitely in eq. (4.21) of Ref. [270], where the exponent[1] 6 should in fact be 8.

- Secondly, in order to perform the integral analytically, Refs. [270], [447] assume that it is possible to consider that all interactions between injected photons and matter are due to Compton scattering in the Thomson limit. This approximation works well enough for the smooth background, that is not sensitive too much to the full deposition history, but it is inaccurate compared to the approach of Slatyer et al. [554] in the context of annihilation in halos.

1 Ref. [39] argue that this exponent should in fact be 7. This comes from a possible mistake in Refs. [96], [189], [270], [447] which considered that the photon energy density per energy interval $\frac{d^2N_\gamma}{dVdE_\gamma} \propto a^{-3}$ instead of a^{-2}.

- To further compare the approach of Refs. [96], [189], [270], [447] with that of Ref. [554], it is possible to manipulate eq. (D.1.1) in such way to absorb all the energy and redshift dependance. Then, the equivalent of the energy deposition function $f(z)$ appears, defined as:

$$\left.\frac{dE}{dV\,dt}\right|_{\rm dep}(z) = \tilde{f}(z)\rho^2(z)\frac{\langle\sigma_{\rm ann}v\rangle}{m_{\rm DM}}\,, \tag{D.1.3}$$

where

$$\tilde{f}(z) = \int_z^\infty \frac{dz'(1+z)^5}{H(z')(1+z')^6}\frac{n_A(z)\rho^2(z')}{2\,m_{\rm DM}\rho^2(z)}\int_0^{m_{\rm DM}} dE'_\gamma E'_\gamma \frac{dN_\gamma}{dE'_\gamma}(E'_\gamma)e^{-\kappa(z',z;E'_\gamma)}\sigma(E_\gamma)\,. \tag{D.1.4}$$

Even if this formalism goes one step beyond the "on-the-spot" approximation thanks to the integral over z', the complexity of the cascade evolution is not taken into account. The two approaches do not give significantly different results when considering only the smooth background, since the CMB experiments are not sensitive to the shape of $f(z)$ at low z, but using eq. (D.1.4) can lead to wrong results when halos are turned on.

D.2 The boost function $\mathcal{B}(z)$

Generally, it is possible to re-write the energy deposition rate in halos by introducing an enhanced dark matter density $\rho^2(z) = (1+\mathcal{B}(z))\bar{\rho}^2(z)$. One now has:

$$\left.\frac{dE}{dV\,dt}\right|_{\rm inj,\ halos} = \rho_c^2 c^2 \Omega_{\rm DM}^2 (1+z)^6 \frac{\langle\sigma_{\rm ann}v\rangle}{m_{\rm DM}}(1+\mathcal{B}(z)) \tag{D.2.1}$$

To compute this "boost" of the density, several ways have been introduced. In the so-called "Halo model" (HM) framework, it is assumed that all the mass in the Universe is contained in virialized objects (the halos), fully characterized by their mass. The key ingredients are the spatial distribution of matter inside a halo (usually called the *density profile*) and the number of halos per unit mass (namely, the *mass function*, that can evolve with the redshift). This allows one to express the boost $\mathcal{B}(z)$ as :

$$\mathcal{B}(z) = \frac{1}{\rho_c^2\Omega_{\rm DM}}(1+z)^3\int_{M_{\rm min}}^\infty dM\frac{dn}{dM}(z)\left(\int_0^{r_{200}} dr 4\pi r^2 \rho_{\rm h}^2(r)\right) \tag{D.2.2}$$

where $M_{\rm min}$ is the minimal mass of DM halos and r_{200} the radius of a sphere enclosing a mean density equal to 200 times the background density (some authors prefer to use the virial radius $r_{\rm v}$, but they are strictly equivalent). The last integral is usually recast in terms of the concentration function $F(c_{\rm h})$, which depends on the concentration parameter $c_{\rm h} \equiv r_{200}/r_s$ with r_s the scale radius of the given profile:

$$\int_0^{r_{200}} dr 4\pi r^2 \rho_{\rm h}^2(r) = \frac{M\bar{\rho}(z_F)}{3}\left(\frac{\Omega_{\rm DM}}{\Omega_{\rm M}}\right)^2 F(c_{\rm h}) \tag{D.2.3}$$

where z_F is the redshift of halo formation (not yet well known) and $\bar{\rho}(z_F) = 200\rho_c\Omega_{\rm M}(1+z_F)^3$ the average matter density within a sphere of radius r_{200}.

One now needs to relate the concentration function to the halo profile, and several types of profile have been proposed in the litterature. We presented the most commonly used one in section 3.3.1: those are the Navarro-Frenk-White (NFW) profile [448], Einasto profile [282], [449] and isothermal-like Burkert profile [135], the former two showing a more peaked distribution than the latter. The last key quantity

– the mass function – which in this framework also encodes how the density evolves with the redshift, can be calculated analytically in the Press-Schechter formalism [497], leading to :

$$\frac{dn}{dM} = \frac{\rho_c \Omega_{\rm M}}{M} \frac{d \ln \sigma^{-1}}{dM} f(\sigma) \tag{D.2.4}$$

where the variance of the density field σ and the differential mass function $f(\sigma)$ have been introduced. We shall not develop further the HM and the Press-Schechter formalism and refer to [270] for more details. Following their development, one can show that, in the frame of the HM with the Press-Schechter prescription for the mass function, the boost from halos is given by:

$$\mathcal{B}(z) = \frac{f_{\rm h}}{(1+z)^3} \mathrm{erfc}\left(\frac{1+z}{1+z_{\rm h}} \right) \tag{D.2.5}$$

where $f_{\rm h} = \frac{200}{3}(1+z_F)^3 F(c_{\rm h})$ and $z_{\rm h}$ is the characteristic redshift at which halos start to contribute (we typically have $z_F \simeq 2 z_{\rm h}$). It could be possible to use more advanced prescription for the halo mass function, such as the Sheth-Tormen formula [542] or the one from Tinker et al. [579], but this would not lead to major differences for the problem we are dealing with. Indeed, as it appears in this framework, the mass function mainly dictates the evolution of the distribution with z and is only known for very small redshifts compared to the range we want to span. The error function is merely a prescription inspired by a simple model to describe the transition from a smooth distribution of matter to structures of virialized objects, whose normalization at low redshift is encoded in the function $f_{\rm h}$. To learn how structure formation precisely happens, especially at high z, is one ingredient that would allow one to improve over the present study. Here, we will limit ourselves to vary $z_{\rm h}$ in the interval [20,30] to ease the comparison with existing literature. Concerning the additional parameter $f_{\rm h}$, we deduce a reasonable range for it from the range of $\mathcal{B}(z=0)$ computed in [533], [535]. In those references, an alternative method is used to compute the boost factor, by direct integration of the power-spectrum down to very small scales (where a cutoff is induced by WIMP dark matter free-streaming or kinetic decoupling) calibrated directly on simulations. The large uncertainties in dealing with the power-spectrum in the deeply non-linear range explain the broad interval $\mathcal{B}(z=0) \in [10^4, 10^8]$ inferred for typical WIMP candidates, although more recent simulations tend to narrow it down to $[5 \times 10^4, 10^6]$.

D.3 Discussion on $\tau_{\rm reio}$ as it is measured by Planck

The Planck collaboration explains in sec 3.4 of Ref. [19] how they proceed to obtain a measurement of the optical depth to reionization $\tau_{\rm reio}$. Let us recall briefly how this is done, and why this might be problematic when one modifies the reionization history in a non-trivial way and wants to compare the new $\tau_{\rm reio}$ to the Planck results.

In general, the optical depth at redhift z is defined as

$$\tau(z) \equiv \int_0^z n_H(z) x_e(z) \sigma_T \frac{dt}{dz'} dz' \ . \tag{D.3.1}$$

Planck obtains an estimate of the reionization optical depth by: (i) assuming single-step reionization where $x_e(z)$ is described by a postulated function centered on an adjustable redshift $z_{\rm reio}$; (ii) computing the corresponding CMB temperature and polarization power spectra using the Bolztmann codes CAMB [402] (or CLASS [109], [390] for cross-checks); (iii) comparing these spectra with those extracted from observed maps. The fit directly gives some bounds on the reionization redshift $z_{\rm reio}$.

At the same time, for each model, the codes also compute the integrated parameter $\tau_{\rm reio}^{\rm camb} \equiv \tau(z_{\rm c})$, where the cut-off redshift $z_{\rm c}$ takes an arbitrary default value $z_{\rm c} = 40$ in both CAMB and CLASS, and reports bounds on this $\tau_{\rm reio}^{\rm camb}$. Actually, since there is a one-to-one correspondance between $\tau_{\rm reio}^{\rm camb}$ and $z_{\rm reio}$ (valid for the postulated category of reionization models), the Bayesian parameter extraction can even be done with a flat prior on $\tau_{\rm reio}^{\rm camb}$ rather than $z_{\rm reio}$.

In such models, reionization affects:

- the low-ℓ part of the polarization spectra, creating the so-called reionization bump,
- the high-ℓ part of the temperature and polarization spectra, which are step-like suppressed, with a suppression factor saturating above $\ell \sim 70$ at a value very close to $e^{-2\tau_{\rm reio}^{\rm camb}}$.

The first impact is very challenging to detect because of the smallness of the signal, which requires a very good control of instrumental systematics and polarized foreground emissions. Even if theoretically, the signature of reionization on the CMB polarization spectra is very clear, the actual measurement of the E-mode low-ℓ spectrum still has quite large uncertainties, and that of the B-mode spectrum is not sensitive enough to probe any reionization bump. Hence, current sensitivity to reionization comes mainly from the second of the two effects. The data probe mainly the integrated parameter $\tau_{\rm reio}^{\rm camb}$, and the bounds reported on this parameter are often thought to be model-indepent (i.e., valid for any reionization history).

However, some of the above statements are only true for models such that the ionization fraction $x_e(z)$ only starts raising at low redshift. For more complicated models like those involving DM annihilation, the fact that there is a step-like suppression of the C_ℓ's, and that the suppression factor asymptotes to $e^{-2\tau_{\rm reio}^{\rm camb}}$, are not necessarily accurate. For instance, Figure 95 shows that in presence of DM annihilation in halos, the reionization effect is not exactly step-like. It has superimposed oscillations, and the suppression factor drifts significantly between $\ell \sim 100$ and $\ell \sim 2500$.

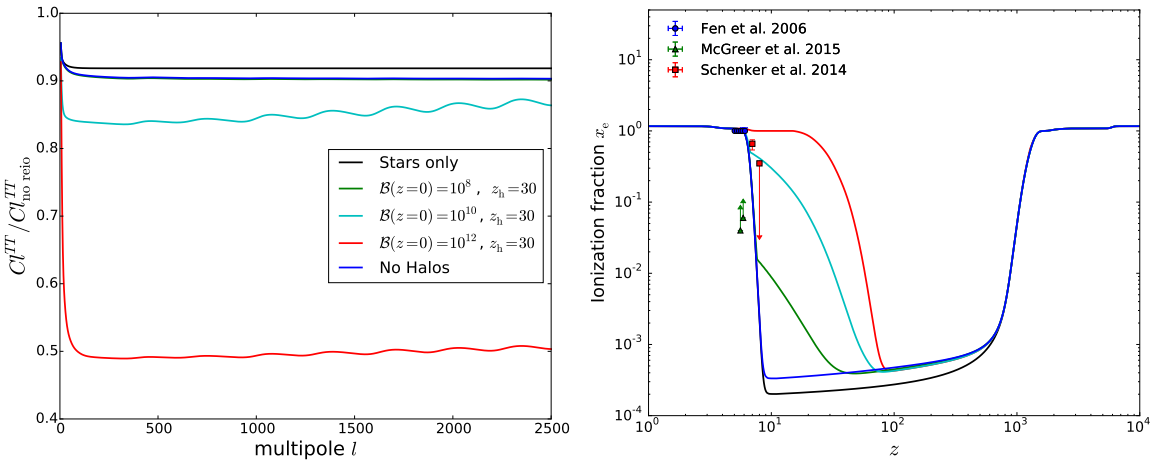

Figure 95: Left pannel - Comparison of the CMB temperature power spectrum for several mixed star-DM reionization models, with $z_{\rm reio} = 6.5$ and a DM particle of 1 GeV annihilating into electrons, normalized to the CMB power spectrum in a universe without reionization. Right pannel - The corresponding ionization histories.

This can easily be understood using the line-of-sight integral formalism [534] introduced in sec. 2.2.3.2, which shows that the Sachs-Wolfe and Dopper terms in the CMB transfer functions are given by an

integral over time of a product of cosmological perturbations, Bessel functions, and finally the visibility function $g \equiv \tau' e^{-\tau}$ (as well as its time derivative in the Doppler term). The visibility function $g(z)$ gives the probability of last scattering, and is normalised to one by construction: $\int g(z)\, dz = 1$. In absence of reionization, $g(z)$ has a single peak at recombination, and it could be approximated by zero for $z \ll z_{\rm dec}$ without changing the result (physically, this means that all observed photons last scattered near $z = z_{\rm dec}$). With conventional single-step reionization model (black line in fig. (96)), a second peak centered near $z = z_{\rm reio}$ is visible. For high ℓ's, the integral over time still only picks up contributions near $z = z_{\rm dec}$. However, the normalization of $g(z)$ implies that the amplitude of the recombination peak in $g(z)$ is reduced by exactly $e^{-\tau(z)}$, where z can be choosen anywhere in the range $z_{\rm reio} \ll z \ll z_{\rm dec}$ (e.g. $z = 40$, as taken by default in CAMB and CLASS). Hence the high-ℓ temperature and polarization power spectra are supressed by exactly $e^{-2\tau_{\rm reio}^{\rm camb}}$.

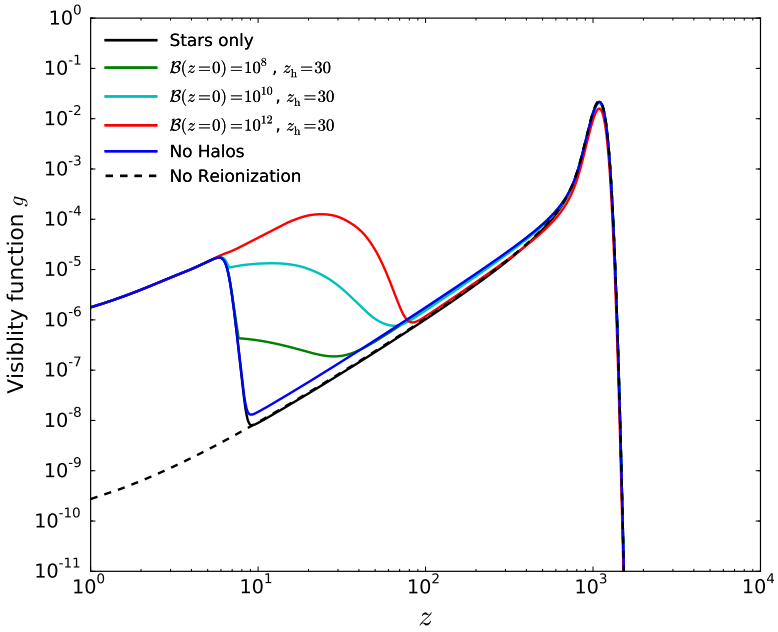

Figure 96: Visibility function for the reionization history from fig. 95, compared to the visibility function in the absence of reionization.

This conclusion is almost unspoiled by the introduction of DM annihilation in the smooth background, or for relatively small halo contribution (blue and green curves in fig. (96)). However, the non-standard shape of g in the case where reionization in DM halos is very strong and starts early (cyan and red curves in fig. (96)) produces non-trivial effects, because the line-of-sight integral starts to pick up sizeable contributions coming from the second reionization bump. Physically, this comes from extra small-scale anisotropies generated by CMB photons re-scattering at medium redshift, for instance between $z \sim 40$ and $z \sim 100$.

Since Planck measures the optical depth mainly through its suppression effects on the C_ℓ's at high ℓ, it is possible to say that what Planck really measures is an effective parameter

$$\tau_{\rm eff} \equiv -\frac{1}{2} \log(C_\ell^{TT}/C_\ell^{TT,\ \text{no reio}})\,, \tag{D.3.2}$$

where ℓ is some effective multipole value in the region where the data has maximum sensitivity, and we are assuming that most of the sensitivity comes from temperature. For usual single-step reionization

models, $\tau_{\rm eff}$ coincides both with $\tau_{\rm reio}^{\rm camb}$, computed up to $z_{\rm c} = 40$, and with a more sensible and robust definition that one could give of the reionization optical depth, where the integral would run up to the redshift at which the ionization fraction is minimal:

$$\tau_{\rm reio}^{\rm min} \equiv \tau(z_*) \ , \qquad x_e'(z_*) = 0 \ . \tag{D.3.3}$$

For models with a raise in $x_e(z)$ at high redshift, it is obvious that $\tau_{\rm eff}$ and $\tau_{\rm reio}^{\rm camb}$ can be very different, because integrating up to $z_{\rm c} = 40$ is not sufficient. We also checked this numerically and found a significant mismatch. A more interesting question is whether $\tau_{\rm eff}$ and $\tau_{\rm reio}^{\rm min}$ are close to each other. In other words, can we still say that the total effect on the CMB spectra at high ℓ is related to the optical depth computed up to the very beginning of reionization? We tested this Ansatz explicitly, and found that the difference between these two quantities is small, being of the order of 10% in the worst cases, i.e., still within the error bars of Planck. In summary:

- for usual single-step reionization:

$$\tau_{\rm reio}^{\rm camb} = \tau_{\rm eff} = \tau_{\rm reio}^{\rm min} \ .$$

- in more general cases with an early enhancement of the ionization fraction:

$$\tau_{\rm reio}^{\rm camb} \neq \tau_{\rm eff} \simeq \tau_{\rm reio}^{\rm min} \ .$$

Therefore, as a first approximation, it is safe to define everywhere in our analysis $\tau_{\rm reio}$ as $\tau_{\rm reio}^{\rm min}$, and to compare it with the value of $\tau_{\rm reio}$ reported by Planck. This conclusion legitimates the analysis performed in section 7.3. For even better accuracy, the next step would be to perform a full parameter extraction in which exact power spectra are fitted to the data, and to derive new bounds on $\tau_{\rm reio}$ valid in all cases, but this is not necessary for reaching the main conclusions of this work.

BIBLIOGRAPHY

[1] G. Aad *et al.*, "Observation of a new particle in the search for the standard model higgs boson with the atlas detector at the lhc," *Phys. Lett.*, vol. B716, pp. 1–29, 2012. DOI: 10.1016/j.physletb.2012.08.020. arXiv: 1207.7214 [hep-ex].

[2] M. G. Aartsen *et al.*, "Evidence for high-energy extraterrestrial neutrinos at the icecube detector," *Science*, vol. 342, p. 1 242 856, 2013. DOI: 10.1126/science.1242856. arXiv: 1311.5238 [astro-ph.HE].

[3] ——, "Search for dark matter annihilations in the sun with the 79-string icecube detector," *Phys. Rev. Lett.*, vol. 110, no. 13, p. 131 302, 2013. DOI: 10.1103/PhysRevLett.110.131302. arXiv: 1212.4097 [astro-ph.HE].

[4] K. Abazajian, M. Acero, S. Agarwalla, A. Aguilar-Arevalo, C. Albright, *et al.*, "Light sterile neutrinos: a white paper," 2012. arXiv: 1204.5379 [hep-ph].

[5] K. Abazajian, G. M. Fuller, and M. Patel, "Sterile neutrino hot, warm, and cold dark matter," *Phys. Rev.*, vol. D64, p. 023 501, 2001. DOI: 10.1103/PhysRevD.64.023501. arXiv: astro-ph/0101524 [astro-ph].

[6] B. P. Abbott *et al.*, "Gw151226: observation of gravitational waves from a 22-solar-mass binary black hole coalescence," *Phys. Rev. Lett.*, vol. 116, no. 24, p. 241 103, 2016. DOI: 10.1103/PhysRevLett.116.241103. arXiv: 1606.04855 [gr-qc].

[7] ——, "Observation of gravitational waves from a binary black hole merger," *Phys. Rev. Lett.*, vol. 116, no. 6, p. 061 102, 2016. DOI: 10.1103/PhysRevLett.116.061102. arXiv: 1602.03837 [gr-qc].

[8] B. P. Abbott *et al.*, "Gw170104: observation of a 50-solar-mass binary black hole coalescence at redshift 0.2," *Phys. Rev. Lett.*, vol. 118, no. 22, p. 221 101, 2017. DOI: 10.1103/PhysRevLett.118.221101. arXiv: 1706.01812 [gr-qc].

[9] P. A. Abell *et al.*, "Lsst science book, version 2.0," 2009. arXiv: 0912.0201 [astro-ph.IM].

[10] L. Ackerman, M. R. Buckley, S. M. Carroll, and M. Kamionkowski, "Dark matter and dark radiation," *Phys.Rev.*, vol. D79, p. 023 519, 2009. DOI: 10.1103/PhysRevD.79.023519,10.1142/9789814293792_0021. arXiv: 0810.5126 [hep-ph].

[11] M. Ackermann *et al.*, "Measurement of separate cosmic-ray electron and positron spectra with the fermi large area telescope," *Phys. Rev. Lett.*, vol. 108, p. 011 103, 2012. DOI: 10.1103/PhysRevLett.108.011103. arXiv: 1109.0521 [astro-ph.HE].

[12] ——, "Limits on dark matter annihilation signals from the fermi lat 4-year measurement of the isotropic gamma-ray background," 2015. arXiv: 1501.05464 [astro-ph.CO].

[13] ——, "Searching for dark matter annihilation from milky way dwarf spheroidal galaxies with six years of fermi large area telescope data," *Phys. Rev. Lett.*, vol. 115, no. 23, p. 231 301, 2015. DOI: 10.1103/PhysRevLett.115.231301. arXiv: 1503.02641 [astro-ph.HE].

[14] ——, "The spectrum of isotropic diffuse gamma-ray emission between 100 mev and 820 gev," *Astrophys. J.*, vol. 799, p. 86, 2015. DOI: 10.1088/0004-637X/799/1/86. arXiv: 1410.3696 [astro-ph.HE].

[15] R. Adam *et al.*, "Planck intermediate results. xlvii. planck constraints on reionization history," 2016. DOI: 10.1051/0004-6361/201628897. arXiv: 1605.03507 [astro-ph.CO].

[16] J. Adamek, D. Daverio, R. Durrer, and M. Kunz, "Gevolution: a cosmological n-body code based on general relativity," *JCAP*, vol. 1607, no. 07, p. 053, 2016. DOI: 10.1088/1475-7516/2016/07/053. arXiv: 1604.06065 [astro-ph.CO].

[17] P. A. R. Ade *et al.*, "Planck 2013 results. xvi. cosmological parameters," *Astron. Astrophys.*, vol. 571, A16, 2014. DOI: 10.1051/0004-6361/201321591. arXiv: 1303.5076 [astro-ph.CO].

[18] ——, "Planck 2015 results. xxiv. cosmology from sunyaev-zeldovich cluster counts," 2015. arXiv: 1502.01597 [astro-ph.CO].

[19] ——, "Planck 2015 results. xiii. cosmological parameters," *Astron. Astrophys.*, vol. 594, A13, 2016. DOI: 10.1051/0004-6361/201525830. arXiv: 1502.01589 [astro-ph.CO].

[20] ——, "Planck 2015 results. xv. gravitational lensing," *Astron. Astrophys.*, vol. 594, A15, 2016. DOI: 10.1051/0004-6361/201525941. arXiv: 1502.01591 [astro-ph.CO].

[21] P. Ade *et al.*, "Planck 2013 results. xvi. cosmological parameters," 2013. arXiv: 1303.5076 [astro-ph.CO].

[22] R. Adhikari *et al.*, "A white paper on kev sterile neutrino dark matter," *Submitted to: White paper*, M. Drewes, T. Lasserre, A. Merle, and S. Mertens, Eds., 2016. arXiv: 1602.04816 [hep-ph].

[23] S. Adrian-Martinez *et al.*, "First results on dark matter annihilation in the sun using the antares neutrino telescope," *JCAP*, vol. 1311, p. 032, 2013. DOI: 10.1088/1475-7516/2013/11/032. arXiv: 1302.6516 [astro-ph.HE].

[24] O. Adriani *et al.*, "An anomalous positron abundance in cosmic rays with energies 1.5-100 gev," *Nature*, vol. 458, pp. 607–609, 2009. DOI: 10.1038/nature07942. arXiv: 0810.4995 [astro-ph].

[25] N. Afshordi, P. McDonald, and D. N. Spergel, "Primordial black holes as dark matter: the power spectrum and evaporation of early structures," *Astrophys. J.*, vol. 594, pp. L71–L74, 2003. DOI: 10.1086/378763. arXiv: astro-ph/0302035 [astro-ph].

[26] N. Aghanim *et al.*, "Planck 2015 results. xi. cmb power spectra, likelihoods, and robustness of parameters," *Submitted to: Astron. Astrophys.*, 2015. arXiv: 1507.02704 [astro-ph.CO].

[27] ——, "Planck intermediate results. xlvi. reduction of large-scale systematic effects in hfi polarization maps and estimation of the reionization optical depth," 2016. arXiv: 1605.02985 [astro-ph.CO].

[28] E. Agol and M. Kamionkowski, "X-rays from isolated black holes in the milky way," *Mon. Not. Roy. Astron. Soc.*, vol. 334, pp. 553–562, Aug. 2002. DOI: 10.1046/j.1365-8711.2002.05523.x. eprint: astro-ph/0109539.

[29] M. Aguilar *et al.*, "Cosmic-ray positron fraction measurement from 1 to 30-gev with ams-01," *Phys. Lett.*, vol. B646, pp. 145–154, 2007. DOI: 10.1016/j.physletb.2007.01.024. arXiv: astro-ph/0703154 [ASTRO-PH].

[30] ——, "First result from the alpha magnetic spectrometer on the international space station: precision measurement of the positron fraction in primary cosmic rays of 0.5-350 gev," *Phys. Rev. Lett.*, vol. 110, p. 141 102, 2013. DOI: 10.1103/PhysRevLett.110.141102.

[31] ——, "Antiproton flux, antiproton-to-proton flux ratio, and properties of elementary particle fluxes in primary cosmic rays measured with the alpha magnetic spectrometer on the international space station," *Phys. Rev. Lett.*, vol. 117, no. 9, p. 091 103, 2016. DOI: 10.1103/PhysRevLett.117.091103.

[32] E. K. Akhmedov, V. A. Rubakov, and A. Yu. Smirnov, "Baryogenesis via neutrino oscillations," *Phys. Rev. Lett.*, vol. 81, pp. 1359–1362, 1998. DOI: 10.1103/PhysRevLett.81.1359. arXiv: hep-ph/9803255 [hep-ph].

[33] C. Alcock *et al.*, "The macho project: microlensing results from 5.7 years of lmc observations," *Astrophys. J.*, vol. 542, pp. 281–307, 2000. DOI: 10.1086/309512. arXiv: astro-ph/0001272 [astro-ph].

[34] S. Alekhin *et al.*, "A facility to search for hidden particles at the cern sps: the ship physics case," 2015. arXiv: 1504.04855 [hep-ph].

[35] Y. Ali-Haïmoud and C. M. Hirata, "Hyrec: a fast and highly accurate primordial hydrogen and helium recombination code," *Phys. Rev. D*, vol. 83, no. 4, 043513, p. 043 513, Feb. 2011. DOI: 10.1103/PhysRevD.83.043513. arXiv: 1011.3758.

[36] Y. Ali-Haïmoud and S. Bird, "An efficient implementation of massive neutrinos in non-linear structure formation simulations," *Mon. Not. Roy. Astron. Soc.*, vol. 428, pp. 3375–3389, 2012. DOI: 10.1093/mnras/sts286. arXiv: 1209.0461 [astro-ph.CO].

[37] Y. Ali-Haïmoud and C. M. Hirata, "Ultrafast effective multi-level atom method for primordial hydrogen recombination," *Phys. Rev.*, vol. D82, p. 063 521, 2010. DOI: 10.1103/PhysRevD.82.063521. arXiv: 1006.1355 [astro-ph.CO].

[38] ——, "Hyrec: a fast and highly accurate primordial hydrogen and helium recombination code," *Phys.Rev.*, vol. D83, p. 043 513, 2011. DOI: 10.1103/PhysRevD.83.043513. arXiv: 1011.3758 [astro-ph.CO].

[39] Y. Ali-Haïmoud and M. Kamionkowski, "Cosmic microwave background limits on accreting primordial black holes," *Phys. Rev.*, vol. D95, no. 4, p. 043 534, 2017. DOI: 10.1103/PhysRevD.95.043534. arXiv: 1612.05644 [astro-ph.CO].

[40] Z. S. Ali *et al.*, "Paper-64 constraints on reionization: the 21cm power spectrum at z =8.4," *Astrophys. J.*, vol. 809, no. 1, p. 61, 2015. DOI: 10.1088/0004-637X/809/1/61. arXiv: 1502.06016 [astro-ph.CO].

[41] R. Allahverdi, B. Dutta, F. S. Queiroz, L. E. Strigari, and M.-Y. Wang, "Dark matter from late invisible decays to/of gravitinos," *Phys. Rev.*, vol. D91, no. 5, p. 055 033, 2015. DOI: 10.1103/PhysRevD.91.055033. arXiv: 1412.4391 [hep-ph].

[42] R. Allison, P. Caucal, E. Calabrese, J. Dunkley, and T. Louis, "Towards a cosmological neutrino mass detection," *Phys. Rev.*, vol. D92, p. 123 535, 2015. arXiv: 1509.07471 [astro-ph].

[43] D. Aloni, K. Blum, and R. Flauger, "Cosmic microwave background constraints on primordial black hole dark matter," *JCAP*, vol. 1705, no. 05, p. 017, 2017. DOI: 10.1088/1475-7516/2017/05/017. arXiv: 1612.06811 [astro-ph.CO].

[44] R. A. Alpher, H. Bethe, and G. Gamow, "The origin of chemical elements," *Phys. Rev.*, vol. 73, pp. 803–804, 1948. DOI: 10.1103/PhysRev.73.803.

[45] R. A. Alpher and R. Herman, "Evolution of the universe," *Nature*, vol. 162, pp. 774–775, Nov. 1948. DOI: 10.1038/162774b0.

[46] L. A. Anchordoqui, H. Goldberg, X. Huang, and B. J. Vlcek, "Reconciling bicep2 and planck results with right-handed dirac neutrinos in the fundamental representation of grand unified e_6," *JCAP*, vol. 1406, p. 042, 2014. DOI: 10.1088/1475-7516/2014/06/042. arXiv: 1404.1825 [hep-ph].

[47] L. Anderson *et al.*, "The clustering of galaxies in the sdss-iii baryon oscillation spectroscopic survey: baryon acoustic oscillations in the data release 10 and 11 galaxy samples," *Mon.Not.Roy.Astron.Soc.*, vol. 441, pp. 24–62, 2014. arXiv: 1312.4877 [astro-ph.CO].

[48] P. e. a. André, "Prism (polarized radiation imaging and spectroscopy mission): an extended white paper," *JCAP*, vol. 2, 006, p. 006, Feb. 2014. DOI: 10.1088/1475-7516/2014/02/006. arXiv: 1310.1554.

[49] S. Aoyama, T. Sekiguchi, K. Ichiki, and N. Sugiyama, "Evolution of perturbations and cosmological constraints in decaying dark matter models with arbitrary decay mass products," *JCAP*, vol. 1407, p. 021, 2014. DOI: 10.1088/1475-7516/2014/07/021. arXiv: 1402.2972 [astro-ph.CO].

[50] T. Appelquist, H.-C. Cheng, and B. A. Dobrescu, "Bounds on universal extra dimensions," *Phys. Rev.*, vol. D64, p. 035 002, 2001. DOI: 10.1103/PhysRevD.64.035002. arXiv: hep-ph/0012100 [hep-ph].

[51] I. J. Araya and N. D. Padilla, "Dark matter annihilation energy output and its effects on the high-z igm," *Mon. Not. Roy. Astron. Soc.*, vol. 445, no. 1, pp. 850–868, 2014. DOI: 10.1093/mnras/stu1780. arXiv: 1302.5462 [astro-ph.CO].

[52] M. Archidiacono, T. Basse, J. Hamann, S. Hannestad, G. Raffelt, and Y. Y. Y. Wong, "Future cosmological sensitivity for hot dark matter axions," *JCAP*, vol. 1505, no. 05, p. 050, 2015. DOI: 10.1088/1475-7516/2015/05/050. arXiv: 1502.03325 [astro-ph.CO].

[53] M. Archidiacono, T. Brinckmann, J. Lesgourgues, and V. Poulin, "Physical effects involved in the measurements of neutrino masses with future cosmological data," *JCAP*, vol. 1702, no. 02, p. 052, 2017. DOI: 10.1088/1475-7516/2017/02/052. arXiv: 1610.09852 [astro-ph.CO].

[54] M. Archidiacono, E. Calabrese, and A. Melchiorri, "The case for dark radiation," *Phys.Rev.*, vol. D84, p. 123 008, 2011. DOI: 10.1103/PhysRevD.84.123008. arXiv: 1109.2767 [astro-ph.CO].

[55] M. Archidiacono, E. Giusarma, S. Hannestad, and O. Mena, "Cosmic dark radiation and neutrinos," *Adv.High Energy Phys.*, vol. 2013, p. 191 047, 2013. DOI: 10.1155/2013/191047. arXiv: 1307.0637 [astro-ph.CO].

[56] M. Archidiacono, E. Giusarma, A. Melchiorri, and O. Mena, "Dark radiation in extended cosmological scenarios," *Phys.Rev.*, vol. D86, p. 043 509, 2012. DOI: 10.1103/PhysRevD.86.043509. arXiv: 1206.0109 [astro-ph.CO].

[57] ——, "Neutrino and dark radiation properties in light of recent cmb observations," *Phys.Rev.*, vol. D87, no. 10, p. 103 519, 2013. DOI: 10.1103/PhysRevD.87.103519. arXiv: 1303.0143 [astro-ph.CO].

[58] M. Archidiacono and S. Hannestad, "Efficient calculation of cosmological neutrino clustering in the non-linear regime," *JCAP*, vol. 1606, no. 06, p. 018, 2016. DOI: 10.1088/1475-7516/2016/06/018. arXiv: 1510.02907 [astro-ph.CO].

[59] M. Archidiacono, S. Hannestad, R. S. Hansen, and T. Tram, "Cosmology with self-interacting sterile neutrinos and dark matter - a pseudoscalar model," 2014. arXiv: 1404.5915 [astro-ph.CO].

[60] ——, "Sterile neutrinos with pseudoscalar self-interactions and cosmology," *Phys. Rev.*, vol. D93, no. 4, p. 045 004, 2016. DOI: 10.1103/PhysRevD.93.045004. arXiv: 1508.02504 [astro-ph.CO].

[61] N. Arkani-Hamed, S. Dimopoulos, and G. R. Dvali, "The hierarchy problem and new dimensions at a millimeter," *Phys. Lett.*, vol. B429, pp. 263–272, 1998. DOI: 10.1016/S0370-2693(98)00466-3. arXiv: hep-ph/9803315 [hep-ph].

[62] N. Arkani-Hamed, D. P. Finkbeiner, T. R. Slatyer, and N. Weiner, "A theory of dark matter," *Phys. Rev.*, vol. D79, p. 015 014, 2009. DOI: 10.1103/PhysRevD.79.015014. arXiv: 0810.0713 [hep-ph].

[63] T. Asaka, S. Blanchet, and M. Shaposhnikov, "The numsm, dark matter and neutrino masses," *Phys. Lett.*, vol. B631, pp. 151–156, 2005. DOI: 10.1016/j.physletb.2005.09.070. arXiv: hep-ph/0503065 [hep-ph].

[64] T. Asaka and M. Shaposhnikov, "The numsm, dark matter and baryon asymmetry of the universe," *Phys. Lett.*, vol. B620, pp. 17–26, 2005. DOI: 10.1016/j.physletb.2005.06.020. arXiv: hep-ph/0505013 [hep-ph].

[65] A. Askew, S. Chauhan, B. Penning, W. Shepherd, and M. Tripathi, "Searching for dark matter at hadron colliders," *Int. J. Mod. Phys.*, vol. A29, p. 1 430 041, 2014. DOI: 10.1142/S0217751X14300415. arXiv: 1406.5662 [hep-ph].

[66] M. Asplund, D. L. Lambert, P. E. Nissen, F. Primas, and V. V. Smith, "Lithium isotopic abundances in metal-poor halo stars," *Apj*, vol. 644, pp. 229–259, Jun. 2006. DOI: 10.1086/503538. eprint: astro-ph/0510636.

[67] B. Audren, "Neutrino and Dark Matter Properties from Cosmological Observations," PhD thesis, Lausanne, 2014. DOI: 10.5075/epfl-thesis-6351.

[68] B. Audren, J. Lesgourgues, K. Benabed, and S. Prunet, "Conservative constraints on early cosmology: an illustration of the monte python cosmological parameter inference code," *JCAP*, vol. 1302, p. 001, 2013. DOI: 10.1088/1475-7516/2013/02/001. arXiv: 1210.7183 [astro-ph.CO].

[69] B. Audren, J. Lesgourgues, S. Bird, M. G. Haehnelt, and M. Viel, "Neutrino masses and cosmological parameters from a euclid-like survey: markov chain monte carlo forecasts including theoretical errors," *JCAP*, vol. 1301, p. 026, 2013. DOI: 10.1088/1475-7516/2013/01/026. arXiv: 1210.2194 [astro-ph.CO].

[70] B. Audren, J. Lesgourgues, G. Mangano, P. D. Serpico, and T. Tram, "Strongest model-independent bound on the lifetime of dark matter," *JCAP*, vol. 1412, no. 12, p. 028, 2014. DOI: 10.1088/1475-7516/2014/12/028. arXiv: 1407.2418 [astro-ph.CO].

[71] B. Audren *et al.*, "Robustness of cosmic neutrino background detection in the cosmic microwave background," *JCAP*, vol. 1503, p. 036, 2015. DOI: 10.1088/1475-7516/2015/03/036. arXiv: 1412.5948 [astro-ph.CO].

[72] P. P. Avelino, S. Esposito, G. Mangano, C. J. A. P. Martins, A. Melchiorri, G. Miele, O. Pisanti, G. Rocha, and P. T. P. Viana, "Early universe constraints on a time varying fine structure constant," *Phys. Rev.*, vol. D64, p. 103 505, 2001. DOI: 10.1103/PhysRevD.64.103505. arXiv: astro-ph/0102144 [astro-ph].

[73] E. Aver, K. A. Olive, and E. D. Skillman, "A new approach to systematic uncertainties and self-consistency in helium abundance determinations," *JCAP*, vol. 5, 003, p. 003, May 2010. DOI: 10.1088/1475-7516/2010/05/003. arXiv: 1001.5218.

[74] E. Aver, K. A. Olive, and E. D. Skillman, "An mcmc determination of the primordial helium abundance," *JCAP*, vol. 1204, p. 004, 2012. DOI: 10.1088/1475-7516/2012/04/004. arXiv: 1112.3713 [astro-ph.CO].

[75] H. Baer, K.-Y. Choi, J. E. Kim, and L. Roszkowski, "Dark matter production in the early universe: beyond the thermal wimp paradigm," *Phys. Rept.*, vol. 555, pp. 1–60, 2015. DOI: 10.1016/j.physrep.2014.10.002. arXiv: 1407.0017 [hep-ph].

[76] T. Baldauf, M. Mirbabayi, M. SimonoviÃĎÂĞ, and M. Zaldarriaga, "Lss constraints with controlled theoretical uncertainties," 2016. arXiv: 1602.00674 [astro-ph.CO].

[77] S. Banerjee, G. Bï£¡langer, B. Mukhopadhyaya, and P. D. Serpico, "Signatures of sneutrino dark matter in an extension of the cmssm," 2016. arXiv: 1603.08834 [hep-ph].

[78] T. M. Bania, R. T. Rood, and D. S. Balser, "The cosmological density of baryons from observations of 3he+ in the milky way," *Nature*, vol. 415, pp. 54–57, 2002. DOI: 10.1038/415054a.

[79] J. M. Bardeen, "Gauge invariant cosmological perturbations," *Phys. Rev.*, vol. D22, pp. 1882–1905, 1980. DOI: 10.1103/PhysRevD.22.1882.

[80] A. Barnacka, J.-F. Glicenstein, and R. Moderski, "New constraints on primordial black holes abundance from femtolensing of gamma-ray bursts," *Phys. Rev. D*, vol. 86, no. 4, 043001, p. 043 001, Aug. 2012. DOI: 10.1103/PhysRevD.86.043001. arXiv: 1204.2056.

[81] ——, "New constraints on primordial black holes abundance from femtolensing of gamma-ray bursts," *Phys. Rev.*, vol. D86, p. 043 001, 2012. DOI: 10.1103/PhysRevD.86.043001.

[82] A. Barrau, G. Boudoul, F. Donato, D. Maurin, P. Salati, and R. Taillet, "Anti-protons from primordial black holes," *Astron. Astrophys.*, vol. 388, p. 676, 2002. DOI: 10.1051/0004-6361:20020313. arXiv: astro-ph/0112486 [astro-ph].

[83] S. W. Barwick *et al.*, "Measurements of the cosmic ray positron fraction from 1-gev to 50-gev," *Astrophys. J.*, vol. 482, pp. L191–L194, 1997. DOI: 10.1086/310706. arXiv: astro-ph/9703192 [astro-ph].

[84] S. Bashinsky and U. Seljak, "Neutrino perturbations in cmb anisotropy and matter clustering," *Phys. Rev.*, vol. D69, p. 083 002, 2004. DOI: 10.1103/PhysRevD.69.083002. arXiv: astro-ph/0310198 [astro-ph].

[85] T. Basse, O. E. Bjaelde, J. Hamann, S. Hannestad, and Y. Y. Y. Wong, "Dark energy properties from large future galaxy surveys," *JCAP*, vol. 1405, p. 021, 2014. DOI: 10.1088/1475-7516/2014/05/021. arXiv: 1304.2321 [astro-ph.CO].

[86] T. Basse, J. Hamann, S. Hannestad, and Y. Y. Y. Wong, "Getting leverage on inflation with a large photometric redshift survey," *JCAP*, vol. 1506, no. 06, p. 042, 2015. DOI: 10.1088/1475-7516/2015/06/042. arXiv: 1409.3469 [astro-ph.CO].

[87] B. A. Bassett, S. Tsujikawa, and D. Wands, "Inflation dynamics and reheating," *Rev. Mod. Phys.*, vol. 78, pp. 537–589, 2006. DOI: 10.1103/RevModPhys.78.537. arXiv: astro-ph/0507632 [astro-ph].

[88] R. A. Battye, R. Crittenden, and J. Weller, "Cosmic concordance and the fine structure constant," *Phys. Rev.*, vol. D63, p. 043 505, 2001. DOI: 10.1103/PhysRevD.63.043505. arXiv: astro-ph/0008265 [astro-ph].

[89] D. Baumann, "Inflation," in *Physics of the large and the small, TASI 09, proceedings of the Theoretical Advanced Study Institute in Elementary Particle Physics, Boulder, Colorado, USA, 1-26 June 2009*, 2011, pp. 523–686. DOI: 10.1142/9789814327183_0010. arXiv: 0907.5424 [hep-th]. [Online]. Available: https://inspirehep.net/record/827549/files/arXiv:0907.5424.pdf.

[90] ——, "Cosmology," 2013.

[91] G. D. Becker, J. S. Bolton, M. G. Haehnelt, and W. L. Sargent, "Detection of extended he ii reionization in the temperature evolution of the intergalactic medium," *Mon.Not.Roy.Astron.Soc.*, vol. 410, p. 1096, 2011. DOI: 10.1111/j.1365-2966.2010.17507.x. arXiv: 1008.2622 [astro-ph.CO].

[92] G. D. Becker, J. S. Bolton, and A. Lidz, "Reionization and high-redshift galaxies: the view from quasar absorption lines," *Publ. Astron. Soc. Austral.*, vol. 32, p. 45, 2015. DOI: 10.1017/pasa.2015.45. arXiv: 1510.03368 [astro-ph.CO].

[93] G. D. Becker, M. Rauch, and W. L. W. Sargent, "The evolution of optical depth in the ly-alpha forest: evidence against reionization at z 6," *Astrophys. J.*, vol. 662, pp. 72–93, 2007. DOI: 10.1086/517866. arXiv: astro-ph/0607633 [astro-ph].

[94] R. H. Becker *et al.*, "Evidence for reionization at z=6: detection of a gunn-peterson trough in a z = 6.28 quasar," *Astron. J.*, vol. 122, p. 2850, 2001. DOI: 10.1086/324231. arXiv: astro-ph/0108097 [astro-ph].

[95] K. G. Begeman, A. H. Broeils, and R. H. Sanders, "Extended rotation curves of spiral galaxies: dark haloes and modified dynamics," *Mon. Not. Roy. Astron. Soc.*, vol. 249, p. 523, 1991.

[96] A. V. Belikov and D. Hooper, "How dark matter reionized the universe," *Phys.Rev.*, vol. D80, p. 035 007, 2009. DOI: 10.1103/PhysRevD.80.035007. arXiv: 0904.1210 [hep-ph].

[97] K. M. Belotsky and A. A. Kirillov, "Primordial black holes with mass 1016−1017 g and reionization of the universe," *JCAP*, vol. 1501, no. 01, p. 041, 2015. DOI: 10.1088/1475-7516/2015/01/041. arXiv: 1409.8601 [astro-ph.CO].

[98] C. Bennett *et al.*, "Nine-year wilkinson microwave anisotropy probe (wmap) observations: final maps and results," *Astrophys.J.Suppl.*, vol. 208, p. 20, 2013. DOI: 10.1088/0067-0049/208/2/20. arXiv: 1212.5225 [astro-ph.CO].

[99] Z. Berezhiani, A. D. Dolgov, and I. I. Tkachev, "Reconciling planck results with low redshift astronomical measurements," *Phys. Rev.*, vol. D92, no. 6, p. 061 303, 2015. DOI: 10.1103/PhysRevD.92.061303. arXiv: 1505.03644 [astro-ph.CO].

[100] F. Bernardeau, S. Colombi, E. Gaztanaga, and R. Scoccimarro, "Large scale structure of the universe and cosmological perturbation theory," *Phys. Rept.*, vol. 367, pp. 1–248, 2002. DOI: 10.1016/S0370-1573(02)00135-7. arXiv: astro-ph/0112551 [astro-ph].

[101] F. Beutler, C. Blake, M. Colless, D. H. Jones, L. Staveley-Smith, *et al.*, "The 6df galaxy survey: baryon acoustic oscillations and the local hubble constant," *Mon.Not.Roy.Astron.Soc.*, vol. 416, pp. 3017–3032, 2011. DOI: 10.1111/j.1365-2966.2011.19250.x. arXiv: 1106.3366 [astro-ph.CO].

[102] F. Bezrukov, H. Hettmansperger, and M. Lindner, "Kev sterile neutrino dark matter in gauge extensions of the standard model," *Phys. Rev.*, vol. D81, p. 085 032, 2010. DOI: 10.1103/PhysRevD.81.085032. arXiv: 0912.4415 [hep-ph].

[103] F. L. Bezrukov and M. Shaposhnikov, "The standard model higgs boson as the inflaton," *Phys. Lett.*, vol. B659, pp. 703–706, 2008. DOI: 10.1016/j.physletb.2007.11.072. arXiv: 0710.3755 [hep-th].

[104] S. Bird, I. Cholis, J. B. Muñoz, Y. Ali-Haïmoud, M. Kamionkowski, E. D. Kovetz, A. Raccanelli, and A. G. Riess, "Did ligo detect dark matter?" *Phys. Rev. Lett.*, vol. 116, no. 20, p. 201 301, 2016. DOI: 10.1103/PhysRevLett.116.201301. arXiv: 1603.00464 [astro-ph.CO].

[105] S. Bird, M. Viel, and M. G. Haehnelt, "Massive neutrinos and the non-linear matter power spectrum," *Mon. Not. Roy. Astron. Soc.*, vol. 420, pp. 2551–2561, 2012. DOI: 10.1111/j.1365-2966.2011.20222.x. arXiv: 1109.4416 [astro-ph.CO].

[106] G. Blackadder and S. M. Koushiappas, "Dark matter with two- and many-body decays and supernovae type ia," *Phys. Rev.*, vol. D90, no. 10, p. 103 527, 2014. DOI: 10.1103/PhysRevD.90.103527. arXiv: 1410.0683 [astro-ph.CO].

[107] R. D. Blandford and M. C. Begelman, "On the fate of gas accreting at a low rate onto a black hole," *Mon. Not. Roy. Astron. Soc.*, vol. 303, p. L1, 1999. DOI: 10.1046/j.1365-8711.1999.02358.x. arXiv: astro-ph/9809083 [astro-ph].

[108] D. Blas, M. Garny, M. M. Ivanov, and S. Sibiryakov, "Time-sliced perturbation theory for large scale structure i: general formalism," *JCAP*, vol. 1607, no. 07, p. 052, 2016. DOI: 10.1088/1475-7516/2016/07/052. arXiv: 1512.05807 [astro-ph.CO].

[109] D. Blas, J. Lesgourgues, and T. Tram, "The cosmic linear anisotropy solving system (class) ii: approximation schemes," *JCAP*, vol. 1107, p. 034, 2011. DOI: 10.1088/1475-7516/2011/07/034. arXiv: 1104.2933 [astro-ph.CO].

[110] C. Boehm, M. J. Dolan, and C. McCabe, "Increasing neff with particles in thermal equilibrium with neutrinos," *JCAP*, vol. 1212, p. 027, 2012. DOI: 10.1088/1475-7516/2012/12/027. arXiv: 1207.0497 [astro-ph.CO].

[111] J. R. Bond and G. Efstathiou, "Cosmic background radiation anisotropies in universes dominated by nonbaryonic dark matter," *Astrophys. J.*, vol. 285, pp. L45–L48, 1984. DOI: 10.1086/184362.

[112] H. Bondi, "On spherically symmetrical accretion," *Mon. Not. Roy. Astron. Soc.*, vol. 112, p. 195, 1952.

[113] H. Bondi and T. Gold, "The steady-state theory of the expanding universe," *Mon. Not. Roy. Astron. Soc.*, vol. 108, p. 252, 1948. DOI: 10.1093/mnras/108.3.252.

[114] H. Bondi and F. Hoyle, "On the mechanism of accretion by stars," *Mon. Not. Roy. Astron. Soc.*, vol. 104, p. 273, 1944. DOI: 10.1093/mnras/104.5.273.

[115] J. Bonn *et al.*, "The mainz neutrino mass experiment," *Nucl. Phys. Proc. Suppl.*, vol. 91, pp. 273–279, 2001, [PoShep2001,192(2001)]. DOI: 10.1016/S0920-5632(00)00951-8.

[116] V. Bonnivard *et al.*, "Dark matter annihilation and decay in dwarf spheroidal galaxies: the classical and ultrafaint dsphs," *Mon. Not. Roy. Astron. Soc.*, vol. 453, no. 1, pp. 849–867, 2015. DOI: 10.1093/mnras/stv1601. arXiv: 1504.02048 [astro-ph.HE].

[117] F. R. Bouchet *et al.*, "Core (cosmic origins explorer) a white paper," 2011. arXiv: 1102.2181 [astro-ph.CO].

[118] M. Boudaud, E. F. Bueno, S. Caroff, Y. Genolini, V. Poulin, V. Poireau, A. Putze, S. Rosier, P. Salati, and M. Vecchi, "The pinching method for galactic cosmic ray positrons: implications in the light of precision measurements," 2016. arXiv: 1612.03924 [astro-ph.HE].

[119] M. Boudaud *et al.*, "A new look at the cosmic ray positron fraction," *Astron. Astrophys.*, vol. 575, A67, 2015. DOI: 10.1051/0004-6361/201425197. arXiv: 1410.3799 [astro-ph.HE].

[120] A. Bouquet and P. Salati, "R parity breaking and cosmological consequences," *Nucl. Phys.*, vol. B284, p. 557, 1987. DOI: 10.1016/0550-3213(87)90050-2.

[121] R. Bouwens, G. Illingworth, P. Oesch, J. Caruana, B. Holwerda, *et al.*, "Cosmic reionization after planck: the derived growth of the ionizing background now matches the growth of the galaxy uv luminosity density," 2015. arXiv: 1503.08228 [astro-ph.CO].

[122] A. Boyarsky, J. Franse, D. Iakubovskyi, and O. Ruchayskiy, "Checking the dark matter origin of a 3.53 kev line with the milky way center," *Phys. Rev. Lett.*, vol. 115, p. 161 301, 2015. DOI: 10.1103/PhysRevLett.115.161301. arXiv: 1408.2503 [astro-ph.CO].

[123] A. Boyarsky, O. Ruchayskiy, D. Iakubovskyi, and J. Franse, "Unidentified line in x-ray spectra of the andromeda galaxy and perseus galaxy cluster," *Phys. Rev. Lett.*, vol. 113, p. 251 301, 2014. DOI: 10.1103/PhysRevLett.113.251301. arXiv: 1402.4119 [astro-ph.CO].

[124] J. Brandbyge, S. Hannestad, T. HaugbÃČÅ¿lle, and B. Thomsen, "The effect of thermal neutrino motion on the non-linear cosmological matter power spectrum," *JCAP*, vol. 0808, p. 020, 2008. DOI: 10.1088/1475-7516/2008/08/020. arXiv: 0802.3700 [astro-ph].

[125] J. Brandbyge, S. Hannestad, T. HaugbÃČÅ¿lle, and Y. Y. Y. Wong, "Neutrinos in non-linear structure formation - the effect on halo properties," *JCAP*, vol. 1009, p. 014, 2010. DOI: 10.1088/1475-7516/2010/09/014. arXiv: 1004.4105 [astro-ph.CO].

[126] T. D. Brandt, "Constraints on macho dark matter from compact stellar systems in ultra-faint dwarf galaxies," *Astrophys. J.*, vol. 824, no. 2, p. L31, 2016. DOI: 10.3847/2041-8205/824/2/L31. arXiv: 1605.03665 [astro-ph.GA].

[127] T. Bringmann, X. Huang, A. Ibarra, S. Vogl, and C. Weniger, "Fermi lat search for internal bremsstrahlung signatures from dark matter annihilation," *JCAP*, vol. 1207, p. 054, 2012. DOI: 10.1088/1475-7516/2012/07/054. arXiv: 1203.1312 [hep-ph].

[128] D. I. Britton *et al.*, "Improved search for massive neutrinos in pi+ —> e+ neutrino decay," *Phys. Rev.*, vol. D46, R885–R887, 1992. DOI: 10.1103/PhysRevD.46.R885.

[129] T. A. D. Brown, C. Bordeanu, K. A. Snover, D. W. Storm, D. Melconian, A. L. Sallaska, S. K. L. Sjue, and S. Triambak, "He3+he4 going to be7 astrophysical s factor," *Phys. Rev. C*, vol. 76, no. 5, 055801, p. 055 801, Nov. 2007. DOI: 10.1103/PhysRevC.76.055801. arXiv: 0710.1279 [nucl-ex].

[130] T. Buchert, "Dark energy from structure: a status report," *Gen. Rel. Grav.*, vol. 40, pp. 467–527, 2008. DOI: 10.1007/s10714-007-0554-8. arXiv: 0707.2153 [gr-qc].

[131] E. Bugaev and P. Klimai, "Formation of primordial black holes from non-gaussian perturbations produced in a waterfall transition," *Phys. Rev.*, vol. D85, p. 103 504, 2012. DOI: 10.1103/PhysRevD.85.103504. arXiv: 1112.5601 [astro-ph.CO].

[132] E. Bulbul, M. Markevitch, A. Foster, R. K. Smith, M. Loewenstein, and S. W. Randall, "Detection of an unidentified emission line in the stacked x-ray spectrum of galaxy clusters," *Astrophys. J.*, vol. 789, p. 13, 2014. DOI: 10.1088/0004-637X/789/1/13. arXiv: 1402.2301 [astro-ph.CO].

[133] A. Burgess, "Tables of hydrogenic photoionization cross-sections and recombination coefficients," *"Mem. Roy. Astron. Soc."*, vol. 69, p. 1, 1965.

[134] C. P. Burgess, H. M. Lee, and M. Trott, "Power-counting and the validity of the classical approximation during inflation," *JHEP*, vol. 09, p. 103, 2009. DOI: 10.1088/1126-6708/2009/09/103. arXiv: 0902.4465 [hep-ph].

[135] A. Burkert, "The structure of dark matter halos in dwarf galaxies," *IAU Symp.*, vol. 171, p. 175, 1996. DOI: 10.1086/309560. arXiv: astro-ph/9504041 [astro-ph].

[136] G. Cabass, A. Melchiorri, and E. Pajer, "μ distortions or running: a guaranteed discovery from cmb spectrometry," *Phys. Rev.*, vol. D93, no. 8, p. 083 515, 2016. DOI: 10.1103/PhysRevD.93.083515. arXiv: 1602.05578 [astro-ph.CO].

[137] N. Cabibbo, G. R. Farrar, and L. Maiani, "Massive photinos: unstable and interesting," *Phys. Lett.*, vol. B105, pp. 155–158, 1981. DOI: 10.1016/0370-2693(81)91010-8.

[138] F. Calore, I. Cholis, and C. Weniger, "Background model systematics for the fermi gev excess," *JCAP*, vol. 1503, p. 038, 2015. DOI: 10.1088/1475-7516/2015/03/038. arXiv: 1409.0042 [astro-ph.CO].

[139] A. G. W. Cameron and W. A. Fowler, "Lithium and the s-process in red-giant stars," *Apj*, vol. 164, p. 111, Feb. 1971. DOI: 10.1086/150821.

[140] F. Capela, M. Pshirkov, and P. Tinyakov, "Constraints on primordial black holes as dark matter candidates from star formation," *Phys. Rev.*, vol. D87, no. 2, p. 023 507, 2013. DOI: 10.1103/PhysRevD.87.023507. arXiv: 1209.6021 [astro-ph.CO].

[141] ——, "Constraints on primordial black holes as dark matter candidates from capture by neutron stars," *Phys. Rev.*, vol. D87, no. 12, p. 123 524, 2013. DOI: 10.1103/PhysRevD.87.123524. arXiv: 1301.4984 [astro-ph.CO].

[142] C. Carbone, M. Petkova, and K. Dolag, "Demnuni: isw, rees-sciama, and weak-lensing in the presence of massive neutrinos," *JCAP*, vol. 1607, no. 07, p. 034, 2016. DOI: 10.1088/1475-7516/2016/07/034. arXiv: 1605.02024 [astro-ph.CO].

[143] C. Carbone, L. Verde, Y. Wang, and A. Cimatti, "Neutrino constraints from future nearly all-sky spectroscopic galaxy surveys," *JCAP*, vol. 1103, p. 030, 2011. DOI: 10.1088/1475-7516/2011/03/030. arXiv: 1012.2868 [astro-ph.CO].

[144] B. J. Carr, K. Kohri, Y. Sendouda, and J. Yokoyama, "New cosmological constraints on primordial black holes," *Phys. Rev.*, vol. D81, p. 104 019, 2010. DOI: 10.1103/PhysRevD.81.104019. arXiv: 0912.5297 [astro-ph.CO].

[145] ——, "Constraints on primordial black holes from the galactic gamma-ray background," *Phys. Rev.*, vol. D94, no. 4, p. 044 029, 2016. DOI: 10.1103/PhysRevD.94.044029. arXiv: 1604.05349 [astro-ph.CO].

[146] B. J. Carr, "The primordial black hole mass spectrum," *Astrophys. J.*, vol. 201, pp. 1–19, 1975. DOI: 10.1086/153853.

[147] B. J. Carr and S. W. Hawking, "Black holes in the early universe," *Mon. Not. Roy. Astron. Soc.*, vol. 168, pp. 399–415, 1974.

[148] B. Carr, F. Kuhnel, and M. Sandstad, "Primordial black holes as dark matter," *Phys. Rev.*, vol. D94, no. 8, p. 083 504, 2016. DOI: 10.1103/PhysRevD.94.083504. arXiv: 1607.06077 [astro-ph.CO].

[149] B. Carr, M. Raidal, T. Tenkanen, V. Vaskonen, and H. Veermäe, "Primordial black hole constraints for extended mass functions," 2017. arXiv: 1705.05567 [astro-ph.CO].

[150] E. Castorina, C. Carbone, J. Bel, E. Sefusatti, and K. Dolag, "Demnuni: the clustering of large-scale structures in the presence of massive neutrinos," *JCAP*, vol. 1507, no. 07, p. 043, 2015. DOI: 10.1088/1475-7516/2015/07/043. arXiv: 1505.07148 [astro-ph.CO].

[151] J. A. R. Cembranos, "Dark matter from r2-gravity," *Phys. Rev. Lett.*, vol. 102, p. 141 301, 2009. DOI: 10.1103/PhysRevLett.102.141301. arXiv: 0809.1653 [hep-ph].

[152] J. A. R. Cembranos, J. L. Feng, A. Rajaraman, and F. Takayama, "Superwimp solutions to small scale structure problems," *Phys. Rev. Lett.*, vol. 95, p. 181 301, 2005. DOI: 10.1103/PhysRevLett.95.181301. arXiv: hep-ph/0507150 [hep-ph].

[153] R. Cen, "The universe was reionized twice," *Astrophys. J.*, vol. 591, pp. 12–37, 2003. DOI: 10.1086/375217. arXiv: astro-ph/0210473 [astro-ph].

[154] S. Chatrchyan *et al.*, "Observation of a new boson at a mass of 125 gev with the cms experiment at the lhc," *Phys. Lett.*, vol. B716, pp. 30–61, 2012. DOI: 10.1016/j.physletb.2012.08.021. arXiv: 1207.7235 [hep-ex].

[155] X.-L. Chen and M. Kamionkowski, "Particle decays during the cosmic dark ages," *Phys.Rev.*, vol. D70, p. 043 502, 2004. DOI: 10.1103/PhysRevD.70.043502. arXiv: astro-ph/0310473 [astro-ph].

[156] D. Cheng, M. C. Chu, and J. Tang, "Cosmological structure formation in decaying dark matter models," *JCAP*, vol. 1507, no. 07, p. 009, 2015. DOI: 10.1088/1475-7516/2015/07/009. arXiv: 1503.05682 [astro-ph.CO].

[157] J. R. Chisholm, "Clustering of primordial black holes: basic results," *Phys. Rev.*, vol. D73, p. 083 504, 2006. DOI: 10.1103/PhysRevD.73.083504. arXiv: astro-ph/0509141 [astro-ph].

[158] ——, "Clustering of primordial black holes. ii. evolution of bound systems," *Phys. Rev.*, vol. D84, p. 124 031, 2011. DOI: 10.1103/PhysRevD.84.124031. arXiv: 1110.4402 [astro-ph.CO].

[159] J. Chluba and R. A. Sunyaev, "Is there need and another way to measure the cosmic microwave background temperature more accurately?" *Astron. Astrophys.*, 2007, [Astron. Astrophys.478,L27(2008)]. DOI: 10.1051/0004-6361:20078200. arXiv: 0707.0188 [astro-ph].

[160] J. Chluba and R. A. Sunyaev, "Two-photon transitions in hydrogen and cosmological recombination," *Astron. Astrophys.*, vol. 480, pp. 629–645, Mar. 2008. DOI: 10.1051/0004-6361:20077921. arXiv: 0705.3033.

[161] ——, "Cosmological hydrogen recombination: influence of resonance and electron scattering," *Astron. Astrophys.*, vol. 503, pp. 345–355, Aug. 2009. DOI: 10.1051/0004-6361/200912335. arXiv: 0904.2220.

[162] ——, "Time-dependent corrections to the ly α escape probability during cosmological recombination," *Astron. Astrophys.*, vol. 496, pp. 619–635, Mar. 2009. DOI: 10.1051/0004-6361/200811100. arXiv: 0810.1045.

[163] ——, "Cosmological recombination: feedback of helium photons and its effect on the recombination spectrum," *Mon. Not. Roy. Astron. Soc.*, vol. 402, pp. 1221–1248, Feb. 2010. DOI: 10.1111/j.1365-2966.2009.15959.x. arXiv: 0909.2378.

[164] J. Chluba and R. A. Sunyaev, "The evolution of cmb spectral distortions in the early universe," *Mon. Not. Roy. Astron. Soc.*, vol. 419, pp. 1294–1314, 2012. DOI: 10.1111/j.1365-2966.2011.19786.x. arXiv: 1109.6552 [astro-ph.CO].

[165] J. Chluba and R. M. Thomas, "Towards a complete treatment of the cosmological recombination problem," *Mon. Not. Roy. Astron. Soc.*, vol. 412, p. 748, 2011. DOI: 10.1111/j.1365-2966.2010.17940.x. arXiv: 1010.3631 [astro-ph.CO].

[166] J. Chluba and R. M. Thomas, "Towards a complete treatment of the cosmological recombination problem," *MNRAS*, vol. 412, pp. 748–764, Apr. 2011. DOI: 10.1111/j.1365-2966.2010.17940.x. arXiv: 1010.3631.

[167] J. Chluba, G. Vasil, and L. Dursi, "Recombinations to the rydberg states of hydrogen and their effect during the cosmological recombination epoch," *Mon.Not.Roy.Astron.Soc.*, vol. 407, p. 599, 2010. DOI: 10.1111/j.1365-2966.2010.16940.x. arXiv: 1003.4928 [astro-ph.CO].

[168] J. Chluba, "Science with spectral distortions of the cosmic microwave background," *CUSO Lectures 2014*,

[169] ——, "Distinguishing different scenarios of early energy release with spectral distortions of the cosmic microwave background," *Mon. Not. Roy. Astron. Soc.*, vol. 436, pp. 2232–2243, 2013. DOI: 10.1093/mnras/stt1733. arXiv: 1304.6121 [astro-ph.CO].

[170] ——, "Green's function of the cosmological thermalization problem," *Mon. Not. Roy. Astron. Soc.*, vol. 434, p. 352, 2013. DOI: 10.1093/mnras/stt1025. arXiv: 1304.6120 [astro-ph.CO].

[171] ——, "Refined approximations for the distortion visibility function and îij-type spectral distortions," *Mon. Not. Roy. Astron. Soc.*, vol. 440, no. 3, pp. 2544–2563, 2014. DOI: 10.1093/mnras/stu414. arXiv: 1312.6030 [astro-ph.CO].

[172] ——, "Which spectral distortions does Λcdm actually predict?" *Mon. Not. Roy. Astron. Soc.*, vol. 460, no. 1, pp. 227–239, 2016. DOI: 10.1093/mnras/stw945. arXiv: 1603.02496 [astro-ph.CO].

[173] J. Chluba and Y. Ali-Haïmoud, "Cosmospec: fast and detailed computation of the cosmological recombination radiation from hydrogen and helium," *Mon. Not. Roy. Astron. Soc.*, vol. 456, no. 4, pp. 3494–3508, 2016. DOI: 10.1093/mnras/stv2691. arXiv: 1510.03877 [astro-ph.CO].

[174] J. Chluba, J. Fung, and E. R. Switzer, "Radiative transfer effects during primordial helium recombination," *Mon. Not. Roy. Astron. Soc.*, vol. 423, p. 3227, 2012. DOI: 10.1111/j.1365-2966.2012.21110.x. arXiv: 1110.0247 [astro-ph.CO].

[175] J. Chluba and D. Jeong, "Teasing bits of information out of the cmb energy spectrum," *Mon. Not. Roy. Astron. Soc.*, vol. 438, no. 3, pp. 2065–2082, 2014. DOI: 10.1093/mnras/stt2327. arXiv: 1306.5751 [astro-ph.CO].

[176] J. Chluba, R. Khatri, and R. A. Sunyaev, "Cmb at 2x2 order: the dissipation of primordial acoustic waves and the observable part of the associated energy release," *Mon. Not. Roy. Astron. Soc.*, vol. 425, pp. 1129–1169, 2012. DOI: 10.1111/j.1365-2966.2012.21474.x. arXiv: 1202.0057 [astro-ph.CO].

[177] J. Chluba, D. Paoletti, F. Finelli, and J.-A. Rubino-Martin, "Effect of primordial magnetic fields on the ionization history," *Mon. Not. Roy. Astron. Soc.*, vol. 451, no. 2, pp. 2244–2250, 2015. DOI: 10.1093/mnras/stv1096. arXiv: 1503.04827 [astro-ph.CO].

[178] J. Chluba, J. A. Rubino-Martin, and R. A. Sunyaev, "Cosmological hydrogen recombination: populations of the high level sub-states," *Mon. Not. Roy. Astron. Soc.*, vol. 374, pp. 1310–1320, 2007. DOI: 10.1111/j.1365-2966.2006.11239.x. arXiv: astro-ph/0608242 [astro-ph].

[179] J. Chluba and R. A. Sunyaev, "Free-bound emission from cosmological hydrogen recombination," *Astron. Astrophys.*, vol. 458, no. 2, pp. L29–L32, 2006. DOI: 10.1051/0004-6361:20066191. arXiv: astro-ph/0608120 [astro-ph].

[180] ——, "Induced two-photon decay of the 2s level and the rate of cosmological hydrogen recombination," *Astron. Astrophys.*, vol. 446, pp. 39–42, 2006. DOI: 10.1051/0004-6361:20053988. arXiv: astro-ph/0508144 [astro-ph].

[181] ——, "Cosmological hydrogen recombination: ly-n line feedback and continuum escape," *Astron. Astrophys.*, 2007, [Astron. Astrophys.475,109(2007)]. DOI: 10.1051/0004-6361:20077333. arXiv: astro-ph/0702531 [astro-ph].

[182] K. Choi *et al.*, "Search for neutrinos from annihilation of captured low-mass dark matter particles in the sun by super-kamiokande," *Phys. Rev. Lett.*, vol. 114, no. 14, p. 141 301, 2015. DOI: 10.1103/PhysRevLett.114.141301. arXiv: 1503.04858 [hep-ex].

[183] K. Choi, E. J. Chun, and J. E. Kim, "Cosmological implications of radiatively generated axion scale," *Phys. Lett.*, vol. B403, pp. 209–217, 1997. DOI: 10.1016/S0370-2693(97)00465-6. arXiv: hep-ph/9608222 [hep-ph].

[184] I. Cholis, "On the gravitational wave background from black hole binaries after the first ligo detections," *JCAP*, vol. 1706, no. 06, p. 037, 2017. DOI: 10.1088/1475-7516/2017/06/037. arXiv: 1609.03565 [astro-ph.HE].

[185] R. Chornock, E. Berger, D. B. Fox, W. Fong, T. Laskar, and K. C. Roth, "Grb 140515a at z=6.33: constraints on the end of reionization from a gamma-ray burst in a low hydrogen column density environment," May 2014. arXiv: 1405.7400.

[186] A. Chudaykin, D. Gorbunov, and I. Tkachev, "A dark matter component decaying after recombination: lensing constraints with planck data," 2016. arXiv: 1602.08121 [astro-ph.CO].

[187] M. Cirelli, "Status of (direct and) indirect dark matter searches," *PoS*, vol. CORFU2015, p. 026, 2016.

[188] M. Cirelli, G. Corcella, A. Hektor, G. Hutsi, M. Kadastik, P. Panci, M. Raidal, F. Sala, and A. Strumia, "Pppc 4 dm id: a poor particle physicist cookbook for dark matter indirect detection," *JCAP*, vol. 1103, p. 051, 2011, [Erratum: JCAP1210,E01(2012)]. DOI: 10.1088/1475-7516/2012/10/E01,10.1088/1475-7516/2011/03/051. arXiv: 1012.4515 [hep-ph].

[189] M. Cirelli, F. Iocco, and P. Panci, "Constraints on dark matter annihilations from reionization and heating of the intergalactic gas," *JCAP*, vol. 0910, p. 009, 2009. DOI: 10.1088/1475-7516/2009/10/009. arXiv: 0907.0719 [astro-ph.CO].

[190] M. Cirelli, E. Moulin, P. Panci, P. D. Serpico, and A. Viana, "Gamma ray constraints on decaying dark matter," *Phys. Rev.*, vol. D86, p. 083 506, 2012. DOI: 10.1103/PhysRevD.86.083506,10.1103/PhysRevD.86.109901. arXiv: 1205.5283 [astro-ph.CO].

[191] S. Clark, B. Dutta, Y. Gao, L. E. Strigari, and S. Watson, "Planck constraint on relic primordial black holes," 2016. arXiv: 1612.07738 [astro-ph.CO].

[192] S. Clesse and J. Garciŋa-Bellido, "Massive primordial black holes from hybrid inflation as dark matter and the seeds of galaxies," *Phys. Rev.*, vol. D92, no. 2, p. 023 524, 2015. DOI: 10.1103/PhysRevD.92.023524. arXiv: 1501.07565 [astro-ph.CO].

[193] S. Clesse and J. García-Bellido, "Detecting the gravitational wave background from primordial black hole dark matter," 2016. arXiv: 1610.08479 [astro-ph.CO].

[194] ——, "The clustering of massive primordial black holes as dark matter: measuring their mass distribution with advanced ligo," *Phys. Dark Univ.*, vol. 15, pp. 142–147, 2017. DOI: 10.1016/j.dark.2016.10.002. arXiv: 1603.05234 [astro-ph.CO].

[195] D. Clowe, M. Bradač, A. H. Gonzalez, M. Markevitch, S. W. Randall, C. Jones, and D. Zaritsky, "A direct empirical proof of the existence of dark matter," *Apj. let.*, vol. 648, pp. L109–L113, Sep. 2006. DOI: 10.1086/508162. eprint: astro-ph/0608407.

[196] A. Coc, J.-P. Uzan, and E. Vangioni, "Standard big bang nucleosynthesis and primordial cno abundances after planck," *JCAP*, vol. 1410, p. 050, 2014. DOI: 10.1088/1475-7516/2014/10/050. arXiv: 1403.6694 [astro-ph.CO].

[197] R. Cooke, M. Pettini, R. A. Jorgenson, M. T. Murphy, and C. C. Steidel, "Precision measures of the primordial abundance of deuterium," *Astrophys. J.*, vol. 781, no. 1, p. 31, 2014. DOI: 10.1088/0004-637X/781/1/31. arXiv: 1308.3240 [astro-ph.CO].

[198] R. Cowsik and J. McClelland, "An upper limit on the neutrino rest mass," *Phys. Rev. Lett.*, vol. 29, pp. 669–670, 1972. DOI: 10.1103/PhysRevLett.29.669.

[199] A. J. Cuesta, V. Niro, and L. Verde, "Neutrino mass limits: robust information from the power spectrum of galaxy surveys," *Phys. Dark Univ.*, vol. 13, pp. 77–86, 2016. DOI: 10.1016/j.dark.2016.04.005. arXiv: 1511.05983 [astro-ph.CO].

[200] A. Cuoco, M. Krämer, and M. Korsmeier, "Novel dark matter constraints from antiprotons in the light of ams-02," 2016. arXiv: 1610.03071 [astro-ph.HE].

[201] P. Cushman *et al.*, "Working group report: wimp dark matter direct detection," in *Proceedings, 2013 Community Summer Study on the Future of U.S. Particle Physics: Snowmass on the Mississippi (CSS2013): Minneapolis, MN, USA, July 29-August 6, 2013*, 2013. arXiv: 1310.8327 [hep-ex]. [Online]. Available: https://inspirehep.net/record/1262767/files/arXiv:1310.8327.pdf.

[202] R. H. Cyburt, J. R. Ellis, B. D. Fields, and K. A. Olive, "Updated nucleosynthesis constraints on unstable relic particles," *Phys. Rev.*, vol. D67, p. 103 521, 2003. DOI: 10.1103/PhysRevD.67.103521. arXiv: astro-ph/0211258 [astro-ph].

[203] R. H. Cyburt, B. D. Fields, K. A. Olive, and T.-H. Yeh, "Big bang nucleosynthesis: 2015," *Rev. Mod. Phys.*, vol. 88, p. 015 004, 2016. DOI: 10.1103/RevModPhys.88.015004. arXiv: 1505.01076 [astro-ph.CO].

[204] F.-Y. Cyr-Racine and K. Sigurdson, "Limits on neutrino-neutrino scattering in the early universe," 2013. arXiv: 1306.1536 [astro-ph.CO].

[205] S. De Lope Amigo, W. M.-Y. Cheung, Z. Huang, and S.-P. Ng, "Cosmological constraints on decaying dark matter," *JCAP*, vol. 0906, p. 005, 2009. DOI: 10.1088/1475-7516/2009/06/005. arXiv: 0812.4016 [hep-ph].

[206] E. De Valentino and others [CORE collaboration], *In preparation*,

[207] G. De Zotti *et al.*, "Exploring cosmic origins with core: extragalactic sources in cosmic microwave background maps," 2016. arXiv: 1609.07263 [astro-ph.GA].

[208] J. Delabrouille and others [CORE collaboration], *In preparation*,

[209] V. Desjacques, J. Chluba, J. Silk, F. de Bernardis, and O. Doré, "Detecting the cosmological recombination signal from space," 2015. arXiv: 1503.05589 [astro-ph.CO].

[210] P. Di Bari, S. F. King, and A. Merle, "Dark radiation or warm dark matter from long lived particle decays in the light of planck," *Phys.Lett.*, vol. B724, pp. 77–83, 2013. DOI: 10.1016/j.physletb.2013.06.003. arXiv: 1303.6267 [hep-ph].

[211] E. Di Dio, F. Montanari, R. Durrer, and J. Lesgourgues, "Cosmological parameter estimation with large scale structure observations," *JCAP*, vol. 1401, p. 042, 2014. DOI: 10.1088/1475-7516/2014/01/042. arXiv: 1308.6186 [astro-ph.CO].

[212] E. Di Dio, F. Montanari, J. Lesgourgues, and R. Durrer, "The classgal code for relativistic cosmological large scale structure," *JCAP*, vol. 1311, p. 044, 2013. DOI: 10.1088/1475-7516/2013/11/044. arXiv: 1307.1459 [astro-ph.CO].

[213] R. Diamanti, E. Giusarma, O. Mena, M. Archidiacono, and A. Melchiorri, "Dark radiation and interacting scenarios," *Phys.Rev.*, vol. D87, no. 6, p. 063 509, 2013. DOI: 10.1103/PhysRevD.87.063509. arXiv: 1212.6007 [astro-ph.CO].

[214] R. Diamanti, L. Lopez-Honorez, O. Mena, S. Palomares-Ruiz, and A. C. Vincent, "Constraining dark matter late-time energy injection: decays and p-wave annihilations," *JCAP*, vol. 1402, p. 017, 2014. DOI: 10.1088/1475-7516/2014/02/017. arXiv: 1308.2578 [astro-ph.CO].

[215] J. Diemand, B. Moore, and J. Stadel, "Convergence and scatter of cluster density profiles," *Mon. Not. Roy. Astron. Soc.*, vol. 353, p. 624, 2004. DOI: 10.1111/j.1365-2966.2004.08094.x. arXiv: astro-ph/0402267 [astro-ph].

[216] M. Dijkstra, M. Gilfanov, A. Loeb, and R. Sunyaev, "Constraints on the redshift evolution of the lX-sfr relation from the cosmic x-ray backgrounds," *Mon. Not. Roy. Astron. Soc.*, vol. 421, pp. 213–223, Mar. 2012. DOI: 10.1111/j.1365-2966.2011.20292.x. arXiv: 1108.4420.

[217] S. Dodelson, "Modern cosmology," 2003.

[218] V. A. Dogiel, V. S. Berezinsky, S. V. Bulanov, and V. S. Ptuskin, *Astrophysics of cosmic rays*, V. L. Ginzburg, Ed. 1990.

[219] V. Domcke, F. Muia, M. Pieroni, and L. T. Witkowski, "Pbh dark matter from axion inflation," 2017. arXiv: 1704.03464 [astro-ph.CO].

[220] M. Douspis, N. Aghanim, S. Ilic, and M. Langer, "A new parameterization of the reionisation history," *Astron. Astrophys.*, vol. 580, p. L4, 2015. DOI: 10.1051/0004-6361/201526543. arXiv: 1509.02785 [astro-ph.CO].

[221] V. K. Dubrovich and S. I. Grachev, "Dynamics of the primordial hydrogen and helium (hei) recombination in the universe," *Submitted to: Astron. Lett.*, 2005. arXiv: astro-ph/0501672 [astro-ph].

[222] V. K. Dubrovich and V. A. Stolyarov, "Fossil radio lines of hydrogen in the cosmic background radiation at decimeter and meter wavelengths.," *Astron. Astrop.*, vol. 302, p. 635, Oct. 1995.

[223] ——, "The spectrum of fossil he i and he ii recombination lines," *Astronomy Letters*, vol. 23, pp. 565–572, Sep. 1997.

[224] J. Dunkley *et al.*, "Five-year wilkinson microwave anisotropy probe (wmap) observations: likelihoods and parameters from the wmap data," *Astrophys.J.Suppl.*, vol. 180, pp. 306–329, 2009. DOI: 10.1088/0067-0049/180/2/306. arXiv: 0803.0586 [astro-ph].

[225] H. Dupuy and F. Bernardeau, "On the importance of nonlinear couplings in large-scale neutrino streams," *JCAP*, vol. 1508, no. 08, p. 053, 2015. DOI: 10.1088/1475-7516/2015/08/053. arXiv: 1503.05707 [astro-ph.CO].

[226] R. Durrer, *The Cosmic Microwave Background*. Cambridge University Press, Aug. 2008.

[227] C. Dvorkin, K. Blum, and M. Kamionkowski, "Constraining dark matter-baryon scattering with linear cosmology," *Phys. Rev.*, vol. D89, no. 2, p. 023 519, 2014. DOI: 10.1103/PhysRevD.89.023519. arXiv: 1311.2937 [astro-ph.CO].

[228] A. Einstein, "The foundation of the general theory of relativity," *Annalen Phys.*, vol. 49, pp. 769–822, 1916. DOI: 10.1002/andp.200590044,10.1002/andp.19163540702.

[229] D. J. Eisenstein *et al.*, "Detection of the baryon acoustic peak in the large-scale correlation function of sdss luminous red galaxies," *Astrophys. J.*, vol. 633, pp. 560–574, 2005. DOI: 10.1086/466512. arXiv: astro-ph/0501171 [astro-ph].

[230] I. El Mellah and F. Casse, "Numerical simulations of axisymmetric hydrodynamical bondi?hoyle accretion on to a compact object," *Mon. Not. Roy. Astron. Soc.*, vol. 454, no. 3, pp. 2657–2667, 2015. DOI: 10.1093/mnras/stv2184. arXiv: 1509.07700 [astro-ph.HE].

[231] J. R. Ellis, G. B. Gelmini, J. L. Lopez, D. V. Nanopoulos, and S. Sarkar, "Astrophysical constraints on massive unstable neutral relic particles," *Nucl. Phys.*, vol. B373, pp. 399–437, 1992. DOI: 10.1016/0550-3213(92)90438-H.

[232] K. Enqvist, S. Nadathur, T. Sekiguchi, and T. Takahashi, "Decaying dark matter and the tension in σ_8," *JCAP*, vol. 1509, no. 09, p. 067, 2015. DOI: 10.1088/1475-7516/2015/09/067. arXiv: 1505.05511 [astro-ph.CO].

[233] C. Evoli, M. Valdes, A. Ferrara, and N. Yoshida, "Energy deposition by weakly interacting massive particles: a comprehensiv e study," *Mon.Not.Roy.Astron.Soc.*, vol. 422, pp. 420–433, 2012. DOI: 10.1111/j.1365-2966.2012.20624.x.

[234] C. Evoli, A. Mesinger, and A. Ferrara, "Unveiling the nature of dark matter with high redshift 21 cm line experiments," *JCAP*, vol. 1411, no. 11, p. 024, 2014. DOI: 10.1088/1475-7516/2014/11/024. arXiv: 1408.1109 [astro-ph.HE].

[235] C. Evoli, M. Valdes, and A. Ferrara, "Particle energy cascade in the intergalactic medium," *PoS*, vol. CRF2010, p. 036, 2010.

[236] J. M. Ezquiaga, J. Garcia-Bellido, and E. Ruiz Morales, "Primordial black hole production in critical higgs inflation," 2017. arXiv: 1705.04861 [astro-ph.CO].

[237] A. L. Faisst, P. Capak, C. M. Carollo, C. Scarlata, and N. Scoville, "Spectroscopic observation of lyα emitters at z $\tilde{7}$.7 and implications on re-ionization," *Apj*, vol. 788, 87, p. 87, Jun. 2014. DOI: 10.1088/0004-637X/788/1/87. arXiv: 1402.3604.

[238] X.-H. Fan, M. A. Strauss, R. H. Becker, R. L. White, J. E. Gunn, *et al.*, "Constraining the evolution of the ionizing background and the epoch of reionization with z = 6 quasars. 2. a sample of 19 quasars," *Astron.J.*, vol. 132, pp. 117–136, 2006. DOI: 10.1086/504836. arXiv: astro-ph/0512082 [astro-ph].

[239] X.-H. Fan *et al.*, "A survey of z > 5.7 quasars in the sloan digital sky survey. 4. discovery of seven additional quasars," *Astron. J.*, vol. 131, pp. 1203–1209, 2006. DOI: 10.1086/500296. arXiv: astro-ph/0512080 [astro-ph].

[240] J. L. Feng, S.-f. Su, and F. Takayama, "Superwimp gravitino dark matter from slepton and sneutrino decays," *Phys. Rev.*, vol. D70, p. 063 514, 2004. DOI: 10.1103/PhysRevD.70.063514. arXiv: hep-ph/0404198 [hep-ph].

[241] F. Feroz, M. P. Hobson, and M. Bridges, "Multinest: an efficient and robust bayesian inference tool for cosmology and particle physics," *Mon. Not. Roy. Astron. Soc.*, vol. 398, pp. 1601–1614, 2009. DOI: 10.1111/j.1365-2966.2009.14548.x. arXiv: 0809.3437 [astro-ph].

[242] B. D. Fields, "The primordial lithium problem," *Annual Review of Nuclear and Particle Science*, vol. 61, pp. 47–68, Nov. 2011. DOI: 10.1146/annurev-nucl-102010-130445. arXiv: 1203.3551 [astro-ph.CO].

[243] B. D. Fields and K. A. Olive, "The revival of galactic cosmic-ray nucleosynthesis?" *Apj*, vol. 516, pp. 797–810, May 1999. DOI: 10.1086/307145. eprint: astro-ph/9809277.

[244] D. P. Finkbeiner, S. Galli, T. Lin, and T. R. Slatyer, "Searching for dark matter in the cmb: a compact parameterization of energy injection from new physics," *Phys.Rev.*, vol. D85, p. 043 522, 2012. DOI: 10.1103/PhysRevD.85.043522. arXiv: 1109.6322 [astro-ph.CO].

[245] D. P. Finkbeiner and N. Weiner, "Exciting dark matter and the integral/spi 511 kev signal," *Phys. Rev.*, vol. D76, p. 083 519, 2007. DOI: 10.1103/PhysRevD.76.083519. arXiv: astro-ph/0702587 [astro-ph].

[246] D. J. Fixsen, E. S. Cheng, J. M. Gales, J. C. Mather, R. A. Shafer, and E. L. Wright, "The cosmic microwave background spectrum from the full cobe firas data set," *Astrophys. J.*, vol. 473, p. 576, 1996. DOI: 10.1086/178173. arXiv: astro-ph/9605054 [astro-ph].

[247] G. L. Fogli, E. Lisi, A. Marrone, D. Montanino, A. Palazzo, and A. M. Rotunno, "Global analysis of neutrino masses, mixings and phases: entering the era of leptonic cp violation searches," *Phys. Rev.*, vol. D86, p. 013 012, 2012. DOI: 10.1103/PhysRevD.86.013012. arXiv: 1205.5254 [hep-ph].

[248] B. Follin, L. Knox, M. Millea, and Z. Pan, *In preparation*,

[249] A. Font-Ribera *et al.*, "Quasar-lyman α forest cross-correlation from boss dr11 : baryon acoustic oscillations," *JCAP*, 2013. arXiv: 1311.1767 [astro-ph.CO].

[250] ——, "Desi and other dark energy experiments in the era of neutrino mass measurements," *JCAP*, vol. 1405, p. 023, 2014. arXiv: 1308.4164 [astro-ph].

[251] A. Fradette, M. Pospelov, J. Pradler, and A. Ritz, "Cosmological constraints on very dark photons," *Phys. Rev.*, vol. D90, no. 3, p. 035 022, 2014. DOI: 10.1103/PhysRevD.90.035022. arXiv: 1407.0993 [hep-ph].

[252] T. Fragos, B. Lehmer, M. Tremmel, *et al.*, "X-ray binary evolution across cosmic time," *Apj*, vol. 764, 41, p. 41, Feb. 2013. DOI: 10.1088/0004-637X/764/1/41. arXiv: 1206.2395 [astro-ph.HE].

[253] K. Freese, M. Lisanti, and C. Savage, "Colloquium: annual modulation of dark matter," *Rev. Mod. Phys.*, vol. 85, pp. 1561–1581, 2013. DOI: 10.1103/RevModPhys.85.1561. arXiv: 1209.3339 [astro-ph.CO].

[254] F. Fuhrer and Y. Y. Y. Wong, "Higher-order massive neutrino perturbations in large-scale structure," *JCAP*, vol. 1503, no. 03, p. 046, 2015. DOI: 10.1088/1475-7516/2015/03/046. arXiv: 1412.2764 [astro-ph.CO].

[255] S. R. Furlanetto, S. P. Oh, and E. Pierpaoli, "The effects of dark matter decay and annihilation on the high-redshift 21 cm background," *Phys. Rev.*, vol. D74, p. 103 502, 2006. DOI: 10.1103/PhysRevD.74.103502. arXiv: astro-ph/0608385 [astro-ph].

[256] S. Furlanetto, S. P. Oh, and F. Briggs, "Cosmology at low frequencies: the 21 cm transition and the high-redshift universe," *Phys. Rept.*, vol. 433, pp. 181–301, 2006. DOI: 10.1016/j.physrep.2006.08.002. arXiv: astro-ph/0608032 [astro-ph].

[257] D. Gaggero, G. Bertone, F. Calore, R. M. T. Connors, M. Lovell, S. Markoff, and E. Storm, "Searching for primordial black holes in the radio and x-ray sky," *Phys. Rev. Lett.*, vol. 118, no. 24, p. 241 101, 2017. DOI: 10.1103/PhysRevLett.118.241101. arXiv: 1612.00457 [astro-ph.HE].

[258] S. Galli, K. Benabed, F. Bouchet, J.-F. Cardoso, F. Elsner, E. Hivon, A. Mangilli, S. Prunet, and B. Wandelt, "Cmb polarization can constrain cosmology better than cmb temperature," *Phys. Rev.*, vol. D90, no. 6, p. 063 504, 2014. DOI: 10.1103/PhysRevD.90.063504. arXiv: 1403.5271 [astro-ph.CO].

[259] S. Galli, F. Iocco, G. Bertone, and A. Melchiorri, "Cmb constraints on dark matter models with large annihilation cross-section," *Phys.Rev.*, vol. D80, p. 023 505, 2009. DOI: 10.1103/PhysRevD.80.023505. arXiv: 0905.0003 [astro-ph.CO].

[260] S. Galli, A. Melchiorri, G. F. Smoot, and O. Zahn, "From cavendish to planck: constraining newton's gravitational constant with cmb temperature and polarization anisotropy," *Phys. Rev.*, vol. D80, p. 023 508, 2009. DOI: 10.1103/PhysRevD.80.023508. arXiv: 0905.1808 [astro-ph.CO].

[261] S. Galli, T. R. Slatyer, M. Valdes, and F. Iocco, "Systematic uncertainties in constraining dark matter annihilation from the cosmic microwave background," *Phys.Rev.*, vol. D88, p. 063 502, 2013. DOI: 10.1103/PhysRevD.88.063502. arXiv: 1306.0563 [astro-ph.CO].

[262] J. Garcia-Bellido and E. Ruiz Morales, "Primordial black holes from single field models of inflation," *ArXiv e-prints*, Feb. 2017. arXiv: 1702.03901.

[263] J. Garcia-Bellido, A. D. Linde, and D. Wands, "Density perturbations and black hole formation in hybrid inflation," *Phys. Rev.*, vol. D54, pp. 6040–6058, 1996. DOI: 10.1103/PhysRevD.54.6040. arXiv: astro-ph/9605094 [astro-ph].

[264] J. Garcia-Bellido, M. Peloso, and C. Unal, "Gravitational waves at interferometer scales and primordial black holes in axion inflation," *JCAP*, vol. 1612, no. 12, p. 031, 2016. DOI: 10.1088/1475-7516/2016/12/031. arXiv: 1610.03763 [astro-ph.CO].

[265] A. Gelman and D. B. Rubin, "Inference from iterative simulation using multiple sequences," *Statist. Sci.*, vol. 7, pp. 457–472, 1992. DOI: 10.1214/ss/1177011136.

[266] G. Gelmini, E. Osoba, S. Palomares-Ruiz, and S. Pascoli, "Mev sterile neutrinos in low reheating temperature cosmological scenarios," *JCAP*, vol. 0810, p. 029, 2008. DOI: 10.1088/1475-7516/2008/10/029. arXiv: 0803.2735 [astro-ph].

[267] M. Gerbino, E. Di Valentino, and N. Said, "Neutrino anisotropies after planck," *Phys.Rev.*, vol. D88, no. 6, p. 063 538, 2013. DOI: 10.1103/PhysRevD.88.063538. arXiv: 1304.7400 [astro-ph.CO].

[268] M. Gerbino, K. Freese, S. Vagnozzi, M. Lattanzi, O. Mena, E. Giusarma, and S. Ho, "Impact of neutrino properties on the estimation of inflationary parameters from current and future observations," 2016. arXiv: 1610.08830 [astro-ph.CO].

[269] C. Germani and T. Prokopec, "On primordial black holes from an inflection point," 2017. arXiv: 1706.04226 [astro-ph.CO].

[270] G. Giesen, J. Lesgourgues, B. Audren, and Y. Ali-Ha
imoud, "Cmb photons shedding light on dark matter," *JCAP*, vol. 1212, p. 008, 2012. DOI: 10.1088/1475-7516/2012/12/008. arXiv: 1209.0247 [astro-ph.CO].

[271] G. Giesen, M. Boudaud, Y. Génolini, V. Poulin, M. Cirelli, P. Salati, and P. D. Serpico, "Ams-02 antiprotons, at last! secondary astrophysical component and immediate implications for dark matter," *JCAP*, vol. 1509, no. 09, p. 023, 2015. DOI: 10.1088/1475-7516/2015/09/023,10.1088/1475-7516/2015/9/023. arXiv: 1504.04276 [astro-ph.HE].

[272] E. Giusarma, M. Gerbino, O. Mena, S. Vagnozzi, S. Ho, and K. Freese, "On the improvement of cosmological neutrino mass bounds," 2016. arXiv: 1605.04320 [astro-ph.CO].

[273] G. Gloeckler and J. Geiss, "Deuterium and helium-3 in the protosolar cloud (invited paper)," in *The Light Elements and their Evolution*, L. da Silva, R. de Medeiros, and M. Spite, Eds., ser. IAU Symposium, vol. 198, 2000, p. 224.

[274] J.-O. Gong and N. Kitajima, "Small-scale structure and 21cm fluctuations by primordial black holes," 2017. arXiv: 1704.04132 [astro-ph.CO].

[275] M. C. Gonzalez-Garcia, M. Maltoni, and T. Schwetz, "Global analyses of neutrino oscillation experiments," *Nucl. Phys.*, vol. B908, pp. 199–217, 2016. DOI: 10.1016/j.nuclphysb.2016.02.033. arXiv: 1512.06856 [hep-ph].

[276] M. Gonzalez-Garcia, V. Niro, and J. Salvado, "Dark radiation and decaying matter," *JHEP*, vol. 1304, p. 052, 2013. DOI: 10.1007/JHEP04(2013)052. arXiv: 1212.1472 [hep-ph].

[277] J. Goodman, M. Ibe, A. Rajaraman, W. Shepherd, T. M. P. Tait, and H.-B. Yu, "Constraints on dark matter from colliders," *Phys. Rev.*, vol. D82, p. 116 010, 2010. DOI: 10.1103/PhysRevD.82.116010. arXiv: 1008.1783 [hep-ph].

[278] D. Gorbunov and M. Shaposhnikov, "How to find neutral leptons of the νmsm?" *JHEP*, vol. 10, p. 015, 2007, [Erratum: JHEP11,101(2013)]. DOI: 10.1007/JHEP11(2013)101,10.1088/1126-6708/2007/10/015. arXiv: 0705.1729 [hep-ph].

[279] R. J. Gould, "Energy loss of relativistic electrons and positrons traversing cosmic matter," *ApJ*, vol. 196, pp. 689–694, Mar. 1975. DOI: 10.1086/153457.

[280] A. de Gouvea and A. Kobach, "Global constraints on a heavy neutrino," *Phys. Rev.*, vol. D93, no. 3, p. 033 005, 2016. DOI: 10.1103/PhysRevD.93.033005. arXiv: 1511.00683 [hep-ph].

[281] S. I. Grachev and V. K. Dubrovich, "Dynamics of primordial hydrogen recombination with allowance for a recoil for scattering in the ly-alpha line," *Astron. Lett.*, vol. 34, p. 439, 2008. DOI: 10.1134/S1063773708070013. arXiv: 0801.3347 [astro-ph].

[282] A. W. Graham, D. Merritt, B. Moore, J. Diemand, and B. Terzic, "Empirical models for dark matter halos. i. nonparametric construction of density profiles and comparison with parametric models," *Astron.J.*, vol. 132, pp. 2685–2700, 2006. DOI: 10.1086/508988. arXiv: astro-ph/0509417 [astro-ph].

[283] A. M. Green, "Microlensing and dynamical constraints on primordial black hole dark matter with an extended mass function," *Phys. Rev.*, vol. D94, no. 6, p. 063 530, 2016. DOI: 10.1103/PhysRevD.94.063530. arXiv: 1609.01143 [astro-ph.CO].

[284] A. M. Green, "Astrophysical uncertainties on stellar microlensing constraints on multi-solar mass primordial black hole dark matter," 2017. arXiv: 1705.10818 [astro-ph.CO].

[285] D. Grin and C. M. Hirata, "Cosmological hydrogen recombination: the effect of extremely high-n states," *Phys. Rev. D*, vol. 81, no. 8, 083005, p. 083 005, Apr. 2010. DOI: 10.1103/PhysRevD.81.083005. arXiv: 0911.1359 [astro-ph.CO].

[286] J. E. Gunn and B. A. Peterson, "On the density of neutral hydrogen in intergalactic space," *Astrophys. J.*, vol. 142, p. 1633, 1965. DOI: 10.1086/148444.

[287] J. Hamann, S. Hannestad, J. Lesgourgues, C. Rampf, and Y. Y. Y. Wong, "Cosmological parameters from large scale structure - geometric versus shape information," *JCAP*, vol. 1007, p. 022, 2010. DOI: 10.1088/1475-7516/2010/07/022. arXiv: 1003.3999 [astro-ph.CO].

[288] J. Hamann, S. Hannestad, and Y. Y. Y. Wong, "Measuring neutrino masses with a future galaxy survey," *JCAP*, vol. 1211, p. 052, 2012. DOI: 10.1088/1475-7516/2012/11/052. arXiv: 1209.1043 [astro-ph.CO].

[289] S. Hanany *et al.*, "Maxima-1: a measurement of the cosmic microwave background anisotropy on angular scales of 10 arcminutes to 5 degrees," *Astrophys. J.*, vol. 545, p. L5, 2000. DOI: 10.1086/317322. arXiv: astro-ph/0005123 [astro-ph].

[290] W. J. Handley, M. P. Hobson, and A. N. Lasenby, "Polychord: nested sampling for cosmology," *Mon. Not. Roy. Astron. Soc.*, vol. 450, no. 1, pp. L61–L65, 2015. DOI: 10.1093/mnrasl/slv047. arXiv: 1502.01856 [astro-ph.CO].

[291] D. Hanneke, S. Fogwell Hoogerheide, and G. Gabrielse, "Cavity control of a single-electron quantum cyclotron: measuring the electron magnetic moment," *Phys. Rev. A*, vol. 83, no. 5, 052122, p. 052 122, May 2011. DOI: 10.1103/PhysRevA.83.052122. arXiv: 1009.4831 [physics.atom-ph].

[292] S. Hannestad, "Possible constraints on the time variation of the fine structure constant from cosmic microwave background data," *Phys. Rev.*, vol. D60, p. 023 515, 1999. DOI: 10.1103/PhysRevD.60.023515. arXiv: astro-ph/9810102 [astro-ph].

[293] ——, "Neutrino physics from precision cosmology," *Prog. Part. Nucl. Phys.*, vol. 65, pp. 185–208, 2010. DOI: 10.1016/j.ppnp.2010.07.001. arXiv: 1007.0658 [hep-ph].

[294] S. H. Hansen and Z. Haiman, "Do we need stars to reionize the universe at high redshifts? early reionization by decaying heavy sterile neutrinos," *Astrophys. J.*, vol. 600, pp. 26–31, 2004. DOI: 10.1086/379636. arXiv: astro-ph/0305126 [astro-ph].

[295] D. Hanson *et al.*, "Detection of b-mode polarization in the cosmic microwave background with data from the south pole telescope," *Phys. Rev. Lett.*, vol. 111, no. 14, p. 141 301, 2013. DOI: 10.1103/PhysRevLett.111.141301. arXiv: 1307.5830 [astro-ph.CO].

[296] T. Harada, C.-M. Yoo, and K. Kohri, "Threshold of primordial black hole formation," *Phys. Rev.*, vol. D88, no. 8, p. 084 051, 2013, [Erratum: Phys. Rev.D89,no.2,029903(2014)]. DOI: 10.1103/PhysRevD.88.084051,10.1103/PhysRevD.89.029903. arXiv: 1309.4201 [astro-ph.CO].

[297] J. Hasenkamp and J. Kersten, "Dark radiation from particle decay: cosmological constraints and opportunities," *JCAP*, vol. 1308, p. 024, 2013. DOI: 10.1088/1475-7516/2013/08/024. arXiv: 1212.4160 [hep-ph].

[298] S. W. Hawking, "Black hole explosions," *Nature*, vol. 248, pp. 30–31, 1974. DOI: 10.1038/248030a0.

[299] ——, "Particle creation by black holes," *Commun. Math. Phys.*, vol. 43, pp. 199–220, 1975, [,167(1975)]. DOI: 10.1007/BF02345020.

[300] M. R. S. Hawkins, "The case for primordial black holes as dark matter," *Mon. Not. Roy. Astron. Soc.*, vol. 415, p. 2744, 2011. DOI: 10.1111/j.1365-2966.2011.18890.x. arXiv: 1106.3875 [astro-ph.CO].

[301] A. Heger, E. Kolbe, W. C. Haxton, K. Langanke, G. Martínez-Pinedo, and S. E. Woosley, "Neutrino nucleosynthesis," *Physics Letters B*, vol. 606, pp. 258–264, Jan. 2005. DOI: 10.1016/j.physletb.2004.12.017. eprint: astro-ph/0307546.

[302] C. Heymans *et al.*, "Cfhtlens tomographic weak lensing cosmological parameter constraints: mitigating the impact of intrinsic galaxy alignments," *Mon. Not. Roy. Astron. Soc.*, vol. 432, p. 2433, 2013. DOI: 10.1093/mnras/stt601. arXiv: 1303.1808 [astro-ph.CO].

[303] J. C. Hill, N. Battaglia, J. Chluba, S. Ferraro, E. Schaan, and D. N. Spergel, "Taking the universe's temperature with spectral distortions of the cosmic microwave background," *Phys. Rev. Lett.*, vol. 115, no. 26, p. 261 301, 2015. DOI: 10.1103/PhysRevLett.115.261301. arXiv: 1507.01583 [astro-ph.CO].

[304] G. Hinshaw *et al.*, "Nine-year wilkinson microwave anisotropy probe (wmap) observations: cosmological parameter results," *Astrophys.J.Suppl.*, vol. 208, p. 19, 2013. DOI: 10.1088/0067-0049/208/2/19. arXiv: 1212.5226 [astro-ph.CO].

[305] ——, "Nine-year wilkinson microwave anisotropy probe (wmap) observations: cosmological parameter results," *Astrophys. J. Suppl.*, vol. 208, p. 19, 2013. DOI: 10.1088/0067-0049/208/2/19. arXiv: 1212.5226 [astro-ph.CO].

[306] C. M. Hirata, "Two-photon transitions in primordial hydrogen recombination," *Phys. Rev. D*, vol. 78, no. 2, 023001, p. 023 001, Jul. 2008. DOI: 10.1103/PhysRevD.78.023001. arXiv: 0803.0808.

[307] C. M. Hirata and J. Forbes, "Lyman-α transfer in primordial hydrogen recombination," *Phys. Rev. D*, vol. 80, no. 2, 023001, p. 023 001, Jul. 2009. DOI: 10.1103/PhysRevD.80.023001. arXiv: 0903.4925.

[308] C. Hirata, "Lecture on recombination," eprint: www.tapir.caltech.edu/\~{}chirata/ph217/lec06.pdf.

[309] C. M. Hirata, "Two-photon transitions in primordial hydrogen recombination," *Phys.Rev.*, vol. D78, p. 023 001, 2008. DOI: 10.1103/PhysRevD.78.023001. arXiv: 0803.0808 [astro-ph].

[310] C. M. Hirata and E. R. Switzer, "Primordial helium recombination. 2. two-photon processes," *Phys. Rev.*, vol. D77, p. 083 007, 2008. DOI: 10.1103/PhysRevD.77.083007. arXiv: astro-ph/0702144 [ASTRO-PH].

[311] R. Hlozek, D. J. E. Marsh, D. Grin, R. Allison, J. Dunkley, and E. Calabrese, "Future cmb tests of dark matter: ultra-light axions and massive neutrinos," 2016. arXiv: 1607.08208 [astro-ph.CO].

[312] M. P. Hobson, A. H. Jaffe, A. R. Liddle, P. Mukherjee, and D. Parkinson, *Bayesian Methods in Cosmology*. Feb. 2014.

[313] D. Hooper, P. Blasi, and P. D. Serpico, "Pulsars as the sources of high energy cosmic ray positrons," *JCAP*, vol. 0901, p. 025, 2009. DOI: 10.1088/1475-7516/2009/01/025. arXiv: 0810.1527 [astro-ph].

[314] B. Horowitz, "Revisiting primordial black holes constraints from ionization history," 2016. arXiv: 1612.07264 [astro-ph.CO].

[315] Z. Hou *et al.*, "Constraints on cosmology from the cosmic microwave background power spectrum of the 2500 deg^2 spt-sz survey," *Astrophys. J.*, vol. 782, p. 74, 2014. DOI: 10.1088/0004-637X/782/2/74. arXiv: 1212.6267 [astro-ph.CO].

[316] Z. Hou, R. Keisler, L. Knox, M. Millea, and C. Reichardt, "How additional massless neutrinos affect the cosmic microwave background damping tail," 2011. arXiv: 1104.2333 [astro-ph.CO].

[317] C. Howlett, A. Lewis, A. Hall, and A. Challinor, "Cmb power spectrum parameter degeneracies in the era of precision cosmology," *JCAP*, vol. 1204, p. 027, 2012. DOI: 10.1088/1475-7516/2012/04/027. arXiv: 1201.3654 [astro-ph.CO].

[318] F. Hoyle, "A new model for the expanding universe," *Mon. Not. Roy. Astron. Soc.*, vol. 108, p. 372, 1948. DOI: 10.1093/mnras/108.5.372.

[319] F. Hoyle and R. A. Lyttleton, "The effect of interstellar matter on climatic variation," *Proceedings of the Cambridge Philosophical Society*, vol. 35, p. 405, 1939. DOI: 10.1017/S0305004100021150.

[320] ——, "On the accretion of interstellar matter by stars," *Proceedings of the Cambridge Philosophical Society*, vol. 36, p. 325, 1940. DOI: 10.1017/S0305004100017369.

[321] ——, "On the physical aspects of accretion by stars," *Proceedings of the Cambridge Philosophical Society*, vol. 36, p. 424, 1940. DOI: 10.1017/S0305004100017461.

[322] W. Hu and J. Silk, "Thermalization constraints and spectral distortions for massive unstable relic particles," *Phys. Rev. Lett.*, vol. 70, pp. 2661–2664, 1993. DOI: 10.1103/PhysRevLett.70.2661.

[323] W. T. Hu, "Wandering in the background: a cmb explorer," PhD thesis, UC, Berkeley, 1995. arXiv: astro-ph/9508126 [astro-ph]. [Online]. Available: http://alice.cern.ch/format/showfull?sysnb=0207836.

[324] W. Hu, "Structure formation with generalized dark matter," *Astrophys.J.*, vol. 506, pp. 485–494, 1998. DOI: 10.1086/306274. arXiv: astro-ph/9801234 [astro-ph].

[325] W. Hu, D. J. Eisenstein, M. Tegmark, and M. J. White, "Observationally determining the properties of dark matter," *Phys.Rev.*, vol. D59, p. 023 512, 1999. DOI: 10.1103/PhysRevD.59.023512. arXiv: astro-ph/9806362 [astro-ph].

[326] W. Hu and G. P. Holder, "Model - independent reionization observables in the cmb," *Phys. Rev.*, vol. D68, p. 023 001, 2003. DOI: 10.1103/PhysRevD.68.023001. arXiv: astro-ph/0303400 [astro-ph].

[327] W. Hu, D. Scott, N. Sugiyama, and M. J. White, "The effect of physical assumptions on the calculation of microwave background anisotropies," *Phys. Rev.*, vol. D52, pp. 5498–5515, 1995. DOI: 10.1103/PhysRevD.52.5498. arXiv: astro-ph/9505043 [astro-ph].

[328] W. Hu, U. Seljak, M. J. White, and M. Zaldarriaga, "A complete treatment of cmb anisotropies in a frw universe," *Phys. Rev.*, vol. D57, pp. 3290–3301, 1998. DOI: 10.1103/PhysRevD.57.3290. arXiv: astro-ph/9709066 [astro-ph].

[329] W. Hu and J. Silk, "Thermalization and spectral distortions of the cosmic background radiation," *Phys. Rev.*, vol. D48, pp. 485–502, 1993. DOI: 10.1103/PhysRevD.48.485.

[330] W. Hu and M. J. White, "A cmb polarization primer," *New Astron.*, vol. 2, p. 323, 1997. DOI: 10.1016/S1384-1076(97)00022-5. arXiv: astro-ph/9706147 [astro-ph].

[331] ——, "Cmb anisotropies: total angular momentum method," *Phys. Rev.*, vol. D56, pp. 596–615, 1997. DOI: 10.1103/PhysRevD.56.596. arXiv: astro-ph/9702170 [astro-ph].

[332] G. Huetsi, A. Hektor, and M. Raidal, "Constraints on leptonically annihilating dark matter from reionization and extragalactic gamma background," *Astron. Astrophys.*, vol. 505, pp. 999–1005, 2009. DOI: 10.1051/0004-6361/200912760. arXiv: 0906.4550 [astro-ph.CO].

[333] G. Hutsi, J. Chluba, A. Hektor, and M. Raidal, "Wmap7 and future cmb constraints on annihilating dark matter: implications on gev-scale wimps," *Astron. Astrophys.*, vol. 535, A26, 2011. DOI: 10.1051/0004-6361/201116914. arXiv: 1103.2766 [astro-ph.CO].

[334] A. Ibarra, D. Tran, and C. Weniger, "Indirect searches for decaying dark matter," *Int. J. Mod. Phys.*, vol. A28, p. 1 330 040, 2013. DOI: 10.1142/S0217751X13300408. arXiv: 1307.6434 [hep-ph].

[335] K. Ichiki, M. Oguri, and K. Takahashi, "Wmap constraints on decaying cold dark matter," *Phys.Rev.Lett.*, vol. 93, p. 071 302, 2004. DOI: 10.1103/PhysRevLett.93.071302. arXiv: astro-ph/0403164 [astro-ph].

[336] S. Ichimaru, "Bimodal behavior of accretion disks - theory and application to cygnus x-1 transitions," *Astrophys. J.*, vol. 214, pp. 840–855, 1977. DOI: 10.1086/155314.

[337] Y. Inoue and A. Kusenko, "A new x-ray bound on primordial black holes density," 2017. arXiv: 1705.00791 [astro-ph.CO].

[338] F. Iocco, "The lithium problem, a phenomenologist's perspective," *Mem. Soc. Astron. Ital. Suppl.*, vol. 22, p. 19, 2012. arXiv: 1206.2396 [astro-ph.GA].

[339] F. Iocco, G. Mangano, G. Miele, O. Pisanti, and P. D. Serpico, "Primordial nucleosynthesis: from precision cosmology to fundamental physics," *Phys. Rept.*, vol. 472, pp. 1–76, 2009. DOI: 10.1016/j.physrep.2009.02.002. arXiv: 0809.0631 [astro-ph].

[340] J. R. Ipser and R. H. Price, "Accretion onto pregalactic black holes," *Apj.*, vol. 216, pp. 578–590, Sep. 1977. DOI: 10.1086/155499.

[341] H. Ishida, M. Kusakabe, and H. Okada, "Effects of long-lived 10 mev-scale sterile neutrinos on primordial elemental abundances and the effective neutrino number," *Phys. Rev.*, vol. D90, no. 8, p. 083 519, 2014. DOI: 10.1103/PhysRevD.90.083519. arXiv: 1403.5995 [astro-ph.CO].

[342] M. Ishigaki, R. Kawamata, M. Ouchi, M. Oguri, and K. Shimasaku, "Full-data results of hubble frontier fields: uv luminosity functions at $z \sim 6 - 10$ and a consistent picture of cosmic reionization," Feb. 2017. arXiv: 1702.04867.

[343] Y. I. Izotov and T. X. Thuan, "Heavy element abundances in blue compact galaxies," *Astrophys. J.*, vol. 511, pp. 639–659, 1999. DOI: 10.1086/306708. arXiv: astro-ph/9811387 [astro-ph].

[344] Y. I. Izotov and T. X. Thuan, "The primordial abundance of 4-he: evidence for non-standard big bang nucleosynthesis," *Apj Letters*, vol. 710, pp. L67–L71, Feb. 2010. DOI: 10.1088/2041-8205/710/1/L67. arXiv: 1001.4440.

[345] Y. I. Izotov, T. X. Thuan, and N. G. Guseva, "A new determination of the primordial he abundance using the he-λ10830 a emission line: cosmological implications," *Mon. Not. Roy. Astron. Soc.*, vol. 445, no. 1, pp. 778–793, 2014. DOI: 10.1093/mnras/stu1771. arXiv: 1408.6953 [astro-ph.CO].

[346] Y. I. Izotov and T. X. Thuan, "The primordial abundance of 4-he revisited," *Astrophys. J.*, vol. 500, p. 188, 1998. DOI: 10.1086/305698.

[347] J. D. Jackson, *Classical electrodynamics*. 1975.

[348] K. Jedamzik and J. C. Niemeyer, "Primordial black hole formation during first order phase transitions," *Phys. Rev.*, vol. D59, p. 124 014, 1999. DOI: 10.1103/PhysRevD.59.124014. arXiv: astro-ph/9901293 [astro-ph].

[349] K. Jedamzik, "Big bang nucleosynthesis constraints on hadronically and electromagnetically decaying relic neutral particles," *Phys. Rev.*, vol. D74, p. 103 509, 2006. DOI: 10.1103/PhysRevD.74.103509. arXiv: hep-ph/0604251 [hep-ph].

[350] T. E. Jeltema and S. Profumo, "Discovery of a 3.5 kev line in the galactic centre and a critical look at the origin of the line across astronomical targets," *Mon. Not. Roy. Astron. Soc.*, vol. 450, no. 2, pp. 2143–2152, 2015. DOI: 10.1093/mnras/stv768. arXiv: 1408.1699 [astro-ph.HE].

[351] L. M. Johnson, D. W. McKay, and T. Bolton, "Extending sensitivity for low mass neutral heavy lepton searches," *Phys. Rev.*, vol. D56, pp. 2970–2981, 1997. DOI: 10.1103/PhysRevD.56.2970. arXiv: hep-ph/9703333 [hep-ph].

[352] T. Kaluza, "On the problem of unity in physics," *Sitzungsber. Preuss. Akad. Wiss. Berlin (Math. Phys.)*, vol. 1921, pp. 966–972, 1921.

[353] M. Kamionkowski, A. Kosowsky, and A. Stebbins, "Statistics of cosmic microwave background polarization," *Phys. Rev.*, vol. D55, pp. 7368–7388, 1997. DOI: 10.1103/PhysRevD.55.7368. arXiv: astro-ph/9611125 [astro-ph].

[354] H.-S. Kang, M. Kawasaki, and G. Steigman, "Cosmological evolution of generic early decaying particles and their daughters," *Nucl. Phys.*, vol. B402, pp. 323–348, 1993. DOI: 10.1016/0550-3213(93)90645-6.

[355] K. Kannike, L. Marzola, M. Raidal, and H. Veermäe, "Single field double inflation and primordial black holes," 2017. arXiv: 1705.06225 [astro-ph.CO].

[356] M. Kaplinghat, M. Chu, Z. Haiman, G. Holder, L. Knox, and C. Skordis, "Probing the reionization history of the universe using the cosmic microwave background polarization," *Astrophys. J.*, vol. 583, pp. 24–32, 2003. DOI: 10.1086/344927. arXiv: astro-ph/0207591 [astro-ph].

[357] M. Kaplinghat, R. E. Lopez, S. Dodelson, and R. J. Scherrer, "Improved treatment of cosmic microwave background fluctuations induced by a late decaying massive neutrino," *Phys.Rev.*, vol. D60, p. 123508, 1999. DOI: 10.1103/PhysRevD.60.123508. arXiv: astro-ph/9907388 [astro-ph].

[358] M. Kaplinghat, R. J. Scherrer, and M. S. Turner, "Constraining variations in the fine structure constant with the cosmic microwave background," *Phys. Rev.*, vol. D60, p. 023516, 1999. DOI: 10.1103/PhysRevD.60.023516. arXiv: astro-ph/9810133 [astro-ph].

[359] J. C. Kapteyn, "First attempt at a theory of the arrangement and motion of the sidereal system," *Astrophys. J.*, vol. 55, pp. 302–328, 1922. DOI: 10.1086/142670.

[360] W. J. Karzas and R. Latter, "Electron radiative transitions in a coulomb field.," *ApJS*, vol. 6, p. 167, May 1961. DOI: 10.1086/190063.

[361] S. Kasuya and M. Kawasaki, "Early reionization by decaying particles in light of three year wmap data," *JCAP*, vol. 0702, p. 010, 2007. DOI: 10.1088/1475-7516/2007/02/010. arXiv: astro-ph/0608283 [astro-ph].

[362] M. Kawasaki and T. Moroi, "Electromagnetic cascade in the early universe and its application to the big bang nucleosynthesis," *Astrophys. J.*, vol. 452, p. 506, 1995. DOI: 10.1086/176324. arXiv: astro-ph/9412055 [astro-ph].

[363] M. Kawasaki, N. Kitajima, and T. T. Yanagida, "Primordial black hole formation from an axionlike curvaton model," *Phys. Rev.*, vol. D87, no. 6, p. 063519, 2013. DOI: 10.1103/PhysRevD.87.063519. arXiv: 1207.2550 [hep-ph].

[364] M. Kawasaki, K. Kohri, and T. Moroi, "Big-bang nucleosynthesis and hadronic decay of long-lived massive particles," *Phys. Rev.*, vol. D71, p. 083502, 2005. DOI: 10.1103/PhysRevD.71.083502. arXiv: astro-ph/0408426 [astro-ph].

[365] M. Kawasaki, A. Kusenko, Y. Tada, and T. T. Yanagida, "Primordial black holes as dark matter in supergravity inflation models," *Phys. Rev.*, vol. D94, no. 8, p. 083523, 2016. DOI: 10.1103/PhysRevD.94.083523. arXiv: 1606.07631 [astro-ph.CO].

[366] C. Kelso, S. Profumo, and F. S. Queiroz, "Nonthermal wimps as "dark radiation" in light of atacama, spt, wmap9 and planck," *Phys.Rev.*, vol. D88, no. 2, p. 023511, 2013. DOI: 10.1103/PhysRevD.88.023511. arXiv: 1304.5243 [hep-ph].

[367] R. Khatri and R. A. Sunyaev, "Time of primordial be-7 conversion into li-7, energy release and doublet of narrow cosmological neutrino lines," *Astron. Lett.*, vol. 37, p. 367, 2011. DOI: 10.1134/S1063773711060041. arXiv: 1009.3932 [astro-ph.CO].

[368] E. E. Kholupenko, A. V. Ivanchik, and D. A. Varshalovich, "Cmbr distortion concerned with recombination of the primordial hydrogen plasma," *Gravitation and Cosmology*, vol. 11, pp. 161–165, Jun. 2005. eprint: astro-ph/0509807.

[369] E. E. Kholupenko and A. V. Ivanchik, "Two-photon 2s<->1s transitions during recombination of hydrogen in the universe," *Astron. Lett.*, vol. 32, pp. 795–803, 2006. DOI: 10.1134/S1063773706120012. arXiv: astro-ph/0611395 [astro-ph].

[370] E. E. Kholupenko, A. V. Ivanchik, and D. A. Varshalovich, "Rapid heii->hei recombination and radiation concerned with this process," *Mon. Not. Roy. Astron. Soc.*, vol. 378, p. 39, 2007. DOI: 10.1111/j.1745-3933.2007.00316.x. arXiv: astro-ph/0703438 [ASTRO-PH].

[371] C. Kiefer, J. Lesgourgues, D. Polarski, and A. A. Starobinsky, "The coherence of primordial fluctuations produced during inflation," *Class. Quant. Grav.*, vol. 15, pp. L67–L72, 1998. DOI: 10.1088/0264-9381/15/10/002. arXiv: gr-qc/9806066 [gr-qc].

[372] O. Klein, "Quantentheorie und fünfdimensionale relativitätstheorie," *Zeitschrift fur Physik*, vol. 37, pp. 895–906, Dec. 1926. DOI: 10.1007/BF01397481.

[373] A. Kogut *et al.*, "Wilkinson microwave anisotropy probe (wmap) first year observations: te polarization," *Astrophys. J. Suppl.*, vol. 148, p. 161, 2003. DOI: 10.1086/377219. arXiv: astro-ph/0302213 [astro-ph].

[374] ——, "The primordial inflation explorer (pixie): a nulling polarimeter for cosmic microwave background observations," *JCAP*, vol. 1107, p. 025, 2011. DOI: 10.1088/1475-7516/2011/07/025. arXiv: 1105.2044 [astro-ph.CO].

[375] K. Kohri, C.-M. Lin, and T. Matsuda, "Primordial black holes from the inflating curvaton," *Phys. Rev.*, vol. D87, no. 10, p. 103 527, 2013. DOI: 10.1103/PhysRevD.87.103527. arXiv: 1211.2371 [hep-ph].

[376] E. Komatsu *et al.*, "Five-year wilkinson microwave anisotropy probe (wmap) observations: cosmological interpretation," *Astrophys.J.Suppl.*, vol. 180, pp. 330–376, 2009. DOI: 10.1088/0067-0049/180/2/330. arXiv: 0803.0547 [astro-ph].

[377] L. V. E. Koopmans *et al.*, "The cosmic dawn and epoch of reionization with the square kilometre array," *PoS*, vol. AASKA14, p. 001, 2015. arXiv: 1505.07568 [astro-ph.CO].

[378] A. Kosowsky, "Cosmic microwave background polarization," *Annals Phys.*, vol. 246, pp. 49–85, 1996. DOI: 10.1006/aphy.1996.0020. arXiv: astro-ph/9501045 [astro-ph].

[379] S. M. Koushiappas and A. Loeb, "Dynamics of dwarf galaxies disfavor stellar-mass black hole dark matter," 2017. arXiv: 1704.01668 [astro-ph.GA].

[380] M. R. Krumholz, C. F. McKee, and R. I. Klein, "Bondi accretion in the presence of vorticity," *Astrophys. J.*, vol. 618, pp. 757–768, 2005. DOI: 10.1086/426051. arXiv: astro-ph/0409454 [astro-ph].

[381] ——, "Bondi-hoyle accretion in a turbulent medium," *Astrophys. J.*, vol. 638, pp. 369–381, 2006. DOI: 10.1086/498844. arXiv: astro-ph/0510410 [astro-ph].

[382] M. Kusakabe, A. B. Balantekin, T. Kajino, and Y. Pehlivan, "Big-bang nucleosynthesis limit on the neutral fermion decays into neutrinos," *Phys. Rev.*, vol. D87, no. 8, p. 085 045, 2013. DOI: 10.1103/PhysRevD.87.085045. arXiv: 1303.2291 [astro-ph.CO].

[383] M. Kusakabe, M.-K. Cheoun, and K. S. Kim, "General limit on the relation between abundances of d and ^{7}li in big bang nucleosynthesis with nucleon injections," *Phys. Rev.*, vol. D90, no. 4, p. 045 009, 2014. DOI: 10.1103/PhysRevD.90.045009. arXiv: 1404.3090 [astro-ph.CO].

[384] T. Lacroix, "Phenomenology of dark matter particles at the centers of galaxies," Theses, Université Pierre et Marie Curie - Paris VI, Jul. 2016. [Online]. Available: https://tel.archives-ouvertes.fr/tel-01369006.

[385] M. Lattanzi and J. W. F. Valle, "Decaying warm dark matter and neutrino masses," *Phys. Rev. Lett.*, vol. 99, p. 121 301, 2007. DOI: 10.1103/PhysRevLett.99.121301. arXiv: 0705.2406 [astro-ph].

[386] R. Laureijs *et al.*, "Euclid definition study report," 2011. arXiv: 1110.3193 [astro-ph.CO].

[387] S. K. Lee, M. Lisanti, B. R. Safdi, T. R. Slatyer, and W. Xue, "Evidence for unresolved γ-ray point sources in the inner galaxy," *Phys. Rev. Lett.*, vol. 116, no. 5, p. 051 103, 2016. DOI: 10.1103/PhysRevLett.116.051103. arXiv: 1506.05124 [astro-ph.HE].

[388] B. D. Lehmer, D. M. Alexander, F. E. Bauer, W. N. Brandt, A. D. Goulding, L. P. Jenkins, A. Ptak, and T. P. Roberts, "A chandra perspective on galaxy-wide x-ray binary emission and its correlation with star formation rate and stellar mass: new results from luminous infrared galaxies," *Apj.*, vol. 724, pp. 559–571, Nov. 2010. DOI: 10.1088/0004-637X/724/1/559. arXiv: 1009.3943.

[389] J. Lesgourgues, "Ens lyon, m2 ăijchamps, particules et matière condensée, module de cosmologie," 2009.

[390] ——, "The cosmic linear anisotropy solving system (class) i: overview," 2011. arXiv: 1104.2932 [astro-ph.IM].

[391] ——, "Tasi lectures on cosmological perturbations," 2013. arXiv: 1302.4640 [astro-ph.CO].

[392] J. Lesgourgues, G. Mangano, G. Miele, and S. Pastor, *Neutrino cosmology*. Cambridge: Cambridge Univ. Press, 2013. [Online]. Available: http://cds.cern.ch/record/1519137.

[393] J. Lesgourgues, G. Marques-Tavares, and M. Schmaltz, "Evidence for dark matter interactions in cosmological precision data?" *JCAP*, vol. 1602, no. 02, p. 037, 2016. DOI: 10.1088/1475-7516/2016/02/037. arXiv: 1507.04351 [astro-ph.CO].

[394] J. Lesgourgues and S. Pastor, "Massive neutrinos and cosmology," *Phys. Rept.*, vol. 429, pp. 307–379, 2006. DOI: 10.1016/j.physrep.2006.04.001. arXiv: astro-ph/0603494 [astro-ph].

[395] ——, "Neutrino mass from cosmology," *Adv. High Energy Phys.*, vol. 2012, p. 608 515, 2012. DOI: 10.1155/2012/608515. arXiv: 1212.6154 [hep-ph].

[396] J. Lesgourgues and T. Tram, "The cosmic linear anisotropy solving system (class) iv: efficient implementation of non-cold relics," *JCAP*, vol. 1109, p. 032, 2011. DOI: 10.1088/1475-7516/2011/09/032. arXiv: 1104.2935 [astro-ph.CO].

[397] ——, "Fast and accurate cmb computations in non-flat flrw universes," *JCAP*, vol. 1409, no. 09, p. 032, 2014. DOI: 10.1088/1475-7516/2014/09/032. arXiv: 1312.2697 [astro-ph.CO].

[398] A. Lewis, "Cosmological parameters from wmap 5-year temperature maps," *Phys. Rev. D*, vol. 78, no. 2, 023002, p. 023 002, Jul. 2008. DOI: 10.1103/PhysRevD.78.023002. arXiv: 0804.3865.

[399] A. Lewis, "Efficient sampling of fast and slow cosmological parameters," *Phys. Rev.*, vol. D87, no. 10, p. 103 529, 2013. DOI: 10.1103/PhysRevD.87.103529. arXiv: 1304.4473 [astro-ph.CO].

[400] A. Lewis and S. Bridle, "Cosmological parameters from cmb and other data: a monte carlo approach," *Phys.Rev.*, vol. D66, p. 103 511, 2002. DOI: 10.1103/PhysRevD.66.103511. arXiv: astro-ph/0205436 [astro-ph].

[401] A. Lewis and A. Challinor, "Weak gravitational lensing of the cmb," *Phys. Rept.*, vol. 429, pp. 1–65, 2006. DOI: 10.1016/j.physrep.2006.03.002. arXiv: astro-ph/0601594 [astro-ph].

[402] A. Lewis, A. Challinor, and A. Lasenby, "Efficient computation of cmb anisotropies in closed frw models," *Astrophys.J.*, vol. 538, pp. 473–476, 2000. DOI: 10.1086/309179. arXiv: astro-ph/9911177 [astro-ph].

[403] A. Lewis, J. Weller, and R. Battye, "The cosmic microwave background and the ionization history of the universe," *Mon. Not. Roy. Astron. Soc.*, vol. 373, pp. 561–570, 2006. DOI: 10.1111/j.1365-2966.2006.10983.x. arXiv: astro-ph/0606552 [astro-ph].

[404] T. S. Li *et al.*, "Farthest neighbor: the distant milky way satellite eridanus ii," *Astrophys. J.*, vol. 838, no. 1, p. 8, 2017. DOI: 10.3847/1538-4357/aa6113. arXiv: 1611.05052 [astro-ph.GA].

[405] E. M. Lifshitz, "On the gravitational stability of the expanding universe," *Zhurnal Eksperimentalnoi i Teoreticheskoi Fiziki*, vol. 16, pp. 587–602, 1946.

[406] K. Lind, J. Melendez, M. Asplund, R. Collet, and Z. Magic, "The lithium isotopic ratio in very metal-poor stars," *Astron. and Astroph.*, vol. 554, A96, A96, Jun. 2013. DOI: 10.1051/0004-6361/201321406. arXiv: 1305.6564 [astro-ph.SR].

[407] A. Liu, J. R. Pritchard, R. Allison, A. R. Parsons, U. Seljak, and B. D. Sherwin, "Eliminating the optical depth nuisance from the cmb with 21 cm cosmology," *Phys. Rev.*, vol. D93, no. 4, p. 043 013, 2016. DOI: 10.1103/PhysRevD.93.043013. arXiv: 1509.08463 [astro-ph.CO].

[408] H. Liu, T. R. Slatyer, and J. Zavala, "The darkest hour before dawn: contributions to cosmic reionization from dark matter annihilation and decay," *Phys. Rev.*, vol. D94, no. 6, p. 063 507, 2016. DOI: 10.1103/PhysRevD.94.063507. arXiv: 1604.02457 [astro-ph.CO].

[409] L. Lopez-Honorez, O. Mena, A. Moliné, S. Palomares-Ruiz, and A. C. Vincent, "The 21 cm signal and the interplay between dark matter annihilations and astrophysical processes," *JCAP*, vol. 1608, no. 08, p. 004, 2016. DOI: 10.1088/1475-7516/2016/08/004. arXiv: 1603.06795 [astro-ph.CO].

[410] L. Lopez-Honorez, O. Mena, S. Palomares-Ruiz, and A. C. Vincent, "Constraints on dark matter annihilation from cmb observationsbefore planck," *JCAP*, vol. 1307, p. 046, 2013. DOI: 10.1088/1475-7516/2013/07/046. arXiv: 1303.5094 [astro-ph.CO].

[411] D. H. Lyth, "Primordial black hole formation and hybrid inflation," Jul. 2011. arXiv: 1107.1681 [astro-ph.CO].

[412] C.-P. Ma and E. Bertschinger, "Cosmological perturbation theory in the synchronous and conformal newtonian gauges," *Astrophys.J.*, vol. 455, pp. 7–25, 1995. DOI: 10.1086/176550. arXiv: astro-ph/9506072 [astro-ph].

[413] J. H. MacGibbon, "Quark and gluon jet emission from primordial black holes. 2. the lifetime emission," *Phys. Rev.*, vol. D44, pp. 376–392, 1991. DOI: 10.1103/PhysRevD.44.376.

[414] K. J. Mack and D. H. Wesley, "Primordial black holes in the dark ages: observational prospects for future 21cm surveys," 2008. arXiv: 0805.1531 [astro-ph].

[415] P. R. Mahaffy, T. M. Donahue, S. K. Atreya, T. C. Owen, and H. B. Niemann, "Galileo probe measurements of d/h and 3he/4he in jupiter's atmosphere," *Space Sci. Rev.*, vol. 84, pp. 251–263, Apr. 1998.

[416] G. Mangano, G. Miele, S. Pastor, T. Pinto, O. Pisanti, *et al.*, "Relic neutrino decoupling including flavor oscillations," *Nucl.Phys.*, vol. B729, pp. 221–234, 2005. DOI: 10.1016/j.nuclphysb.2005.09.041. arXiv: hep-ph/0506164 [hep-ph].

[417] S. P. Martin, "A supersymmetry primer," 1997, [Adv. Ser. Direct. High Energy Phys.18,1(1998)]. DOI: 10.1142/9789812839657_0001,10.1142/9789814307505_0001. arXiv: hep-ph/9709356 [hep-ph].

[418] J. Mastache and A. de la Macorra, "Extra relativistic degrees of freedom without extra particles using planck data," *Phys.Rev.*, vol. D88, p. 043 506, 2013. DOI: 10.1103/PhysRevD.88.043506. arXiv: 1303.7038 [gr-qc].

[419] T. Matsumura *et al.*, "Litebird: mission overview and focal plane layout," *J. Low. Temp. Phys.*, vol. 184, no. 3-4, pp. 824–831, 2016. DOI: 10.1007/s10909-016-1542-8.

[420] F. Mayet *et al.*, "A review of the discovery reach of directional dark matter detection," *Phys. Rept.*, vol. 627, pp. 1–49, 2016. DOI: 10.1016/j.physrep.2016.02.007. arXiv: 1602.03781 [astro-ph.CO].

[421] I. D. McGreer, A. Mesinger, and X. Fan, "The first (nearly) model-independent constraint on the neutral hydrogen fraction at z$\sim 5-6$," *Mon. Not. Roy. Astron. Soc.*, vol. 415, pp. 3237–3246, 2011. DOI: 10.1111/j.1365-2966.2011.18935.x. arXiv: 1101.3314 [astro-ph.CO].

[422] I. McGreer, A. Mesinger, and V. D'Odorico, "Model-independent evidence in favour of an end to reionization by $z \approx 6$," *Mon.Not.Roy.Astron.Soc.*, vol. 447, no. 1, pp. 499–505, 2015. DOI: 10.1093/mnras/stu2449. arXiv: 1411.5375 [astro-ph.CO].

[423] G. Mellema *et al.*, "Reionization and the cosmic dawn with the square kilometre array," *Exper. Astron.*, vol. 36, pp. 235–318, 2013. DOI: 10.1007/s10686-013-9334-5. arXiv: 1210.0197 [astro-ph.CO].

[424] E. Menegoni, S. Galli, J. G. Bartlett, C. J. A. P. Martins, and A. Melchiorri, "New constraints on variations of the fine structure constant from cmb anisotropies," *Phys. Rev.*, vol. D80, p. 087 302, 2009. DOI: 10.1103/PhysRevD.80.087302. arXiv: 0909.3584 [astro-ph.CO].

[425] A. Mesinger, Ed., *Understanding the Epoch of Cosmic Reionization*, vol. 423, ser. Astrophysics and Space Science Library, 2016. DOI: 10.1007/978-3-319-21957-8.

[426] A. Mesinger, S. Furlanetto, and R. Cen, "21cmfast: a fast, semi-numerical simulation of the high-redshift 21-cm signal," *Mon.Not.Roy.Astron.Soc.*, vol. 411, p. 955, 2011. DOI: 10.1111/j.1365-2966.2010.17731.x. arXiv: 1003.3878 [astro-ph.CO].

[427] S. P. Mikheyev and A. Y. Smirnov, "Resonance enhancement of oscillations in matter and solar neutrino spectroscopy," *Yadernaya Fizika*, vol. 42, pp. 1441–1448, 1985.

[428] S. Mineo, M. Gilfanov, and R. Sunyaev, "The collective x-ray luminosity of hmxb as a sfr indicator," *Astronomische Nachrichten*, vol. 332, p. 349, May 2011. DOI: 10.1002/asna.201011497. arXiv: 1009.4873 [astro-ph.HE].

[429] ——, "Vizier online data catalog: hmxbs in nearby galaxies (mineo+, 2012)," *VizieR Online Data Catalog*, vol. 741, Sep. 2011.

[430] ——, "X-ray emission from star-forming galaxies - ii. hot interstellarmedium," *Mon. Not. Roy. Astron. Soc.*, vol. 426, pp. 1870–1883, Nov. 2012. DOI: 10.1111/j.1365-2966.2012.21831.x. arXiv: 1205.3715 [astro-ph.HE].

[431] J. Mirocha, G. J. A. Harker, and J. O. Burns, "Interpreting the global 21-cm signal from high redshifts. ii. parameter estimation for models of galaxy formation," *Astrophys. J.*, vol. 813, no. 1, p. 11, 2015. DOI: 10.1088/0004-637X/813/1/11. arXiv: 1509.07868 [astro-ph.CO].

[432] P. J. Mohr, B. N. Taylor, and D. B. Newell, "Codata recommended values of the fundamental physical constants: 2010," *Rev. Mod. Phys.*, vol. 84, pp. 1527–1605, 2012. DOI: 10.1103/RevModPhys.84.1527. arXiv: 1203.5425 [physics.atom-ph].

[433] M. A. Monroy-Rodríguez and C. Allen, "The end of the macho era, revisited: new limits on macho masses from halo wide binaries," *Apj.*, vol. 790, 159, p. 159, Aug. 2014. DOI: 10.1088/0004-637X/790/2/159. arXiv: 1406.5169.

[434] M. Moresco, R. Jimenez, L. Verde, A. Cimatti, L. Pozzetti, C. Maraston, and D. Thomas, "Constraining the time evolution of dark energy, curvature and neutrino properties with cosmic chronometers," 2016. arXiv: 1604.00183 [astro-ph.CO].

[435] M. J. Mortonson and W. Hu, "Model-independent constraints on reionization from large-scale cmb polarization," *Astrophys. J.*, vol. 672, pp. 737–751, 2008. DOI: 10.1086/523958. arXiv: 0705.1132 [astro-ph].

[436] H. Motohashi and W. Hu, "Primordial black holes and slow-roll violation," 2017. arXiv: 1706.06784 [astro-ph.CO].

[437] J. W. Motz, H. A. Olsen, and H. W. Koch, "Pair production by photons," *Reviews of Modern Physics*, vol. 41, pp. 581–639, Oct. 1969. DOI: 10.1103/RevModPhys.41.581.

[438] V. Mukhanov, "Physical foundations of cosmology," 2005.

[439] K. Murase, R. Laha, S. Ando, and M. Ahlers, "Testing the dark matter scenario for pev neutrinos observed in icecube," *Phys. Rev. Lett.*, vol. 115, no. 7, p. 071 301, 2015. DOI: 10.1103/PhysRevLett.115.071301. arXiv: 1503.04663 [hep-ph].

[440] T. Nakama, J. Silk, and M. Kamionkowski, "Stochastic gravitational waves associated with the formation of primordial black holes," *Phys. Rev.*, vol. D95, no. 4, p. 043 511, 2017. DOI: 10.1103/PhysRevD.95.043511. arXiv: 1612.06264 [astro-ph.CO].

[441] T. Namikawa, S. Saito, and A. Taruya, "Probing dark energy and neutrino mass from upcoming lensing experiments of cmb and galaxies," *JCAP*, vol. 1012, p. 027, 2010. DOI: 10.1088/1475-7516/2010/12/027. arXiv: 1009.3204 [astro-ph.CO].

[442] R. Narayan, "Why do agn lighthouses switch off?," 2002. DOI: 10.1007/10856495_60. arXiv: astro-ph/0201260 [astro-ph].

[443] R. Narayan and I.-s. Yi, "Advection dominated accretion: a selfsimilar solution," *Astrophys. J.*, vol. 428, p. L13, 1994. DOI: 10.1086/187381. arXiv: astro-ph/9403052 [astro-ph].

[444] A. Natarajan, N. Battaglia, H. Trac, U.-L. Pen, and A. Loeb, "Reionization on large scales ii: detecting patchy reionization through cross correlation of the cosmic microwave background," *Astrophys. J.*, vol. 776, p. 82, 2013. DOI: 10.1088/0004-637X/776/2/82. arXiv: 1211.2822 [astro-ph.CO].

[445] A. Natarajan and D. J. Schwarz, "The effect of early dark matter halos on reionization," *Phys.Rev.*, vol. D78, p. 103 524, 2008. DOI: 10.1103/PhysRevD.78.103524,10.1103/PhysRevD.81.089905. arXiv: 0805.3945 [astro-ph].

[446] ——, "Dark matter annihilation and its effect on cmb and hydrogen 21 cm observations," *Phys.Rev.*, vol. D80, p. 043 529, 2009. DOI: 10.1103/PhysRevD.80.043529. arXiv: 0903.4485 [astro-ph.CO].

[447] ——, "Distinguishing standard reionization from dark matter models," *Phys.Rev.*, vol. D81, p. 123 510, 2010. DOI: 10.1103/PhysRevD.81.123510. arXiv: 1002.4405 [astro-ph.CO].

[448] J. F. Navarro, C. S. Frenk, and S. D. White, "The structure of cold dark matter halos," *Astrophys.J.*, vol. 462, pp. 563–575, 1996. DOI: 10.1086/177173. arXiv: astro-ph/9508025 [astro-ph].

[449] J. F. Navarro, A. Ludlow, V. Springel, J. Wang, M. Vogelsberger, *et al.*, "The diversity and similarity of cold dark matter halos," *Mon.Not.Roy.Astron.Soc.*, vol. 402, p. 21, 2010. DOI: 10.1111/j.1365-2966.2009.15878.x. arXiv: 0810.1522 [astro-ph].

[450] C. B. Netterfield *et al.*, "A measurement by boomerang of multiple peaks in the angular power spectrum of the cosmic microwave background," *Astrophys. J.*, vol. 571, pp. 604–614, 2002. DOI: 10.1086/340118. arXiv: astro-ph/0104460 [astro-ph].

[451] H. Niikura, M. Takada, N. Yasuda, R. H. Lupton, T. Sumi, S. More, A. More, M. Oguri, and M. Chiba, "Microlensing constraints on $10-10m\odot$-scale primordial black holes from high-cadence observation of m31 with hyper suprime-cam," 2017. arXiv: 1701.02151 [astro-ph.CO].

[452] T. Okamoto and W. Hu, "Cmb lensing reconstruction on the full sky," *Phys. Rev.*, vol. D67, p. 083 002, 2003. DOI: 10.1103/PhysRevD.67.083002. arXiv: astro-ph/0301031 [astro-ph].

[453] I. M. Oldengott, D. Boriero, and D. J. Schwarz, "Reionization and dark matter decay," 2016. arXiv: 1605.03928 [astro-ph.CO].

[454] I. M. Oldengott, C. Rampf, and Y. Y. Y. Wong, "Boltzmann hierarchy for interacting neutrinos i: formalism," 2014. arXiv: 1409.1577 [astro-ph.CO].

[455] K. A. Olive, P. Petitjean, E. Vangioni, and J. Silk, "Higher d or li: probes of physics beyond the standard model," *Mon. Not. Roy. Astron. Soc.*, vol. 426, p. 1427, 2012. DOI: 10.1111/j.1365-2966.2012.21703.x. arXiv: 1203.5701 [astro-ph.CO].

[456] J. Orloff, A. N. Rozanov, and C. Santoni, "Limits on the mixing of tau neutrino to heavy neutrinos," *Phys. Lett.*, vol. B550, pp. 8–15, 2002. DOI: 10.1016/S0370-2693(02)02769-7. arXiv: hep-ph/0208075 [hep-ph].

[457] A. Osipowicz *et al.*, "Katrin: a next generation tritium beta decay experiment with sub-ev sensitivity for the electron neutrino mass. letter of intent," 2001. arXiv: hep-ex/0109033 [hep-ex].

[458] Y. Oyama, K. Kohri, and M. Hazumi, "Constraints on the neutrino parameters by future cosmological 21 cm line and precise cmb polarization observations," *JCAP*, vol. 1602, no. 02, p. 008, 2016. DOI: 10.1088/1475-7516/2016/02/008. arXiv: 1510.03806 [astro-ph.CO].

[459] Y. Oyama, A. Shimizu, and K. Kohri, "Determination of neutrino mass hierarchy by 21 cm line and cmb b-mode polarization observations," *Phys. Lett.*, vol. B718, pp. 1186–1193, 2013. DOI: 10.1016/j.physletb.2012.12.053. arXiv: 1205.5223 [astro-ph.CO].

[460] N. Padmanabhan and D. P. Finkbeiner, "Detecting dark matter annihilation with cmb polarization: signatures and experimental prospects," *Phys.Rev.*, vol. D72, p. 023 508, 2005. DOI: 10.1103/PhysRevD.72.023508. arXiv: astro-ph/0503486 [astro-ph].

[461] D. N. Page, "Particle emission rates from a black hole: massless particles from an uncharged, nonrotating hole," *Phys. Rev.*, vol. D13, pp. 198–206, 1976. DOI: 10.1103/PhysRevD.13.198.

[462] P. B. Pal and L. Wolfenstein, "Radiative decays of massive neutrinos," *Phys. Rev.*, vol. D25, p. 766, 1982. DOI: 10.1103/PhysRevD.25.766.

[463] N. Palanque-Delabrouille, "Microlensing towards the small magellanic cloud. eros 2 first year survey," *Astron. Astrophys.*, vol. 332, p. 1, 1998. arXiv: astro-ph/9710194 [astro-ph].

[464] N. Palanque-Delabrouille, C. Yéche, A. Borde, J.-M. L. Goff, G. Rossi, *et al.*, "The one-dimensional ly-alpha forest power spectrum from boss," *A&A 559,*, vol. A85, 2013. DOI: 10.1051/0004-6361/201322130. arXiv: 1306.5896 [astro-ph.CO].

[465] N. Palanque-Delabrouille, C. Yéche, J. Lesgourgues, G. Rossi, A. Borde, *et al.*, "Constraint on neutrino masses from sdss-iii/boss lyα forest and other cosmological probes," 2014. arXiv: 1410.7244 [astro-ph.CO].

[466] N. Palanque-Delabrouille *et al.*, "Neutrino masses and cosmology with lyman-alpha forest power spectrum," *JCAP*, vol. 1511, no. 11, p. 011, 2015. DOI: 10.1088/1475-7516/2015/11/011. arXiv: 1506.05976 [astro-ph.CO].

[467] Z. Pan, L. Knox, and M. White, "Dependence of the cosmic microwave background lensing power spectrum on the matter density," *Mon. Not. Roy. Astron. Soc.*, vol. 445, no. 3, pp. 2941–2945, 2014. DOI: 10.1093/mnras/stu1971. arXiv: 1406.5459 [astro-ph.CO].

[468] D. Parkinson *et al.*, "The wigglez dark energy survey: final data release and cosmological results," *Phys. Rev.*, vol. D86, p. 103 518, 2012. DOI: 10.1103/PhysRevD.86.103518. arXiv: 1210.2130 [astro-ph.CO].

[469] C. Patrignani *et al.*, "Review of particle physics," *Chin. Phys.*, vol. C40, no. 10, p. 100 001, 2016. DOI: 10.1088/1674-1137/40/10/100001.

[470] R. D. Peccei and H. R. Quinn, "Cp conservation in the presence of instantons," *Phys. Rev. Lett.*, vol. 38, pp. 1440–1443, 1977. DOI: 10.1103/PhysRevLett.38.1440.

[471] ——, "Constraints imposed by cp conservation in the presence of instantons," *Phys. Rev.*, vol. D16, pp. 1791–1797, 1977. DOI: 10.1103/PhysRevD.16.1791.

[472] P. Peebles, "Recombination of the primeval plasma," *Astrophys.J.*, vol. 153, p. 1, 1968. DOI: 10.1086/149628.

[473] M. Peimbert and S. Torres-Peimbert, "Chemical composition of h ii regions in the large magellanic cloud and its cosmological implications," *Apj*, vol. 193, pp. 327–333, Oct. 1974. DOI: 10.1086/153166.

[474] ——, "Chemical composition of h ii regions in the small magellanic cloud and the pregalactic helium abundance," *Apj*, vol. 203, pp. 581–586, Feb. 1976. DOI: 10.1086/154114.

[475] S. Pellegrini, "Nuclear accretion in galaxies of the local universe: clues from chandra observations," *Astrophys. J.*, vol. 624, pp. 155–161, 2005, [Erratum: Astrophys. J.636,564(2005)]. DOI: 10.1086/429267. arXiv: astro-ph/0502035 [astro-ph].

[476] A. A. Penzias and R. W. Wilson, "A measurement of excess antenna temperature at 4080 mc/s.," *Apj*, vol. 142, pp. 419–421, Jul. 1965. DOI: 10.1086/148307.

[477] L. Perotto, J. Lesgourgues, S. Hannestad, H. Tu, and Y. Y. Y. Wong, "Probing cosmological parameters with the cmb: forecasts from full monte carlo simulations," *JCAP*, vol. 0610, p. 013, 2006. DOI: 10.1088/1475-7516/2006/10/013. arXiv: astro-ph/0606227 [astro-ph].

[478] M. A. C. Perryman, K. S. de Boer, G. Gilmore, E. Hog, M. G. Lattanzi, L. Lindegren, X. Luri, F. Mignard, O. Pace, and P. T. de Zeeuw, "Gaia: composition, formation and evolution of the galaxy," *Astron. Astrophys.*, vol. 369, pp. 339–363, 2001. DOI: 10.1051/0004-6361:20010085. arXiv: astro-ph/0101235 [astro-ph].

[479] P. Peter and J.-P. Uzan, *Primordial Cosmology*. Oxford: Oxford Univ. Press, 2009.

[480] M. Pettini, B. J. Zych, M. T. Murphy, A. Lewis, and C. C. Steidel, "Deuterium abundance in the most metal-poor damped lyman alpha system: converging on baryons density," *Mon. Not. Roy. Astron. Soc.*, vol. 391, pp. 1499–1510, 2008. DOI: 10.1111/j.1365-2966.2008.13921.x. arXiv: 0805.0594 [astro-ph].

[481] O. Pisanti, A. Cirillo, S. Esposito, F. Iocco, G. Mangano, G. Miele, and P. D. Serpico, "Parthenope: public algorithm evaluating the nucleosynthesis of primordial elements," *Comput. Phys. Commun.*, vol. 178, pp. 956–971, 2008. DOI: 10.1016/j.cpc.2008.02.015. arXiv: 0705.0290 [astro-ph].

[482] Planck Collaboration, P. A. R. Ade, N. Aghanim, *et al.*, "Planck early results. i. the planck mission," *A&A*, vol. 536, A1, A1, Dec. 2011. arXiv: 1101.2022 [astro-ph.IM].

[483] Planck Collaboration, P. A. R. Ade, N. Aghanim, *et al.*, "Planck 2013 results. xv. cmb power spectra and likelihood," *A&A*, vol. 571, A15, Nov. 2014. arXiv: 1303.5075.

[484] ——, "Planck 2013 results. xvii. gravitational lensing by large-scale structure," *A&A*, vol. 571, A17, Nov. 2014. arXiv: 1303.5077.

[485] J. C. Pober *et al.*, "Paper-64 constraints on reionization ii: the temperature of the z=8.4 intergalactic medium," 2015. arXiv: 1503.00045 [astro-ph.CO].

[486] A. G. Polnarev, "Polarization and anisotropy induced in the microwave background by cosmological gravitational waves," *Soviet Astronomy*, vol. 29, pp. 607–613, Dec. 1985.

[487] B. Pontecorvo, "Inverse beta processes and nonconservation of lepton charge," *Sov. Phys. JETP*, vol. 7, pp. 172–173, 1958, [Zh. Eksp. Teor. Fiz.34,247(1957)].

[488] ——, "Neutrino experiments and the problem of conservation of leptonic charge," *Sov. Phys. JETP*, vol. 26, pp. 984–988, 1968, [Zh. Eksp. Teor. Fiz.53,1717(1967)].

[489] M. Pospelov and J. Pradler, "Big bang nucleosynthesis as a probe of new physics," *Ann. Rev. Nucl. Part. Sci.*, vol. 60, pp. 539–568, 2010. DOI: 10.1146/annurev.nucl.012809.104521. arXiv: 1011.1054 [hep-ph].

[490] V. Poulin, J. Lesgourgues, and P. D. Serpico, "Cosmological constraints on exotic injection of electromagnetic energy," *JCAP*, vol. 1703, no. 03, p. 043, 2017. DOI: 10.1088/1475-7516/2017/03/043. arXiv: 1610.10051 [astro-ph.CO].

[491] V. Poulin and P. D. Serpico, "Loophole to the universal photon spectrum in electromagnetic cascades and application to the cosmological lithium problem," *Phys. Rev. Lett.*, vol. 114, no. 9, p. 091 101, 2015. DOI: 10.1103/PhysRevLett.114.091101. arXiv: 1502.01250 [astro-ph.CO].

[492] V. Poulin, P. D. Serpico, F. Calore, S. Clesse, and K. Kohri, "Squeezing spherical cows: cmb bounds on disk-accreting massive primordial black holes," 2017. arXiv: 1707.04206 [astro-ph.CO].

[493] V. Poulin, P. D. Serpico, and J. Lesgourgues, "Dark matter annihilations in halos and high-redshift sources of reionization of the universe," *JCAP*, vol. 1512, no. 12, p. 041, 2015. DOI: 10.1088/1475-7516/2015/12/041. arXiv: 1508.01370 [astro-ph.CO].

[494] ——, "A fresh look at linear cosmological constraints on a decaying dark matter component," *JCAP*, vol. 1608, no. 08, p. 036, 2016. DOI: 10.1088/1475-7516/2016/08/036. arXiv: 1606.02073 [astro-ph.CO].

[495] V. Poulin and P. D. Serpico, "Nonuniversal bbn bounds on electromagnetically decaying particles," *Phys. Rev.*, vol. D91, no. 10, p. 103 007, 2015. DOI: 10.1103/PhysRevD.91.103007. arXiv: 1503.04852 [astro-ph.CO].

[496] A. Pourtsidou and T. Tram, "Reconciling cmb and structure growth measurements with dark energy interactions," 2016. arXiv: 1604.04222 [astro-ph.CO].

[497] W. H. Press and P. Schechter, "Formation of galaxies and clusters of galaxies by selfsimilar gravitational condensation," *Astrophys.J.*, vol. 187, pp. 425–438, 1974. DOI: 10.1086/152650.

[498] R. J. Protheroe, T. Stanev, and V. S. Berezinsky, "Electromagnetic cascades and cascade nucleosynthesis in the early universe," *Phys. Rev.*, vol. D51, pp. 4134–4144, 1995. DOI: 10.1103/PhysRevD.51.4134. arXiv: astro-ph/9409004 [astro-ph].

[499] M. Raidal, V. Vaskonen, and H. Veermäe, "Gravitational waves from primordial black hole mergers," 2017. arXiv: 1707.01480 [astro-ph.CO].

[500] S. W. Randall, M. Markevitch, D. Clowe, A. H. Gonzalez, and M. Bradac, "Constraints on the self-interaction cross-section of dark matter from numerical simulations of the merging galaxy cluster 1e 0657-56," *Astrophys. J.*, vol. 679, pp. 1173–1180, 2008. DOI: 10.1086/587859. arXiv: 0704.0261 [astro-ph].

[501] M. S. Rao, R. Subrahmanyan, N. U. Shankar, and J. Chluba, "On the detection of spectral ripples from the recombination epoch," 2015. arXiv: 1501.07191 [astro-ph.IM].

[502] A. Rassat, A. Amara, L. Amendola, F. J. Castander, T. Kitching, M. Kunz, A. Refregier, Y. Wang, and J. Weller, "Deconstructing baryon acoustic oscillations: a comparison of methods," 2008. arXiv: 0810.0003 [astro-ph].

[503] M. J. Rees, E. S. Phinney, M. C. Begelman, and R. D. Blandford, "Ion supported tori and the origin of radio jets," *Nature*, vol. 295, pp. 17–21, 1982. DOI: 10.1038/295017a0.

[504] C. Reichardt, L. Shaw, O. Zahn, K. Aird, B. Benson, *et al.*, "A measurement of secondary cosmic microwave background anisotropies with two years of south pole telescope observations," *Astrophys.J.*, vol. 755, p. 70, 2012. DOI: 10.1088/0004-637X/755/1/70. arXiv: 1111.0932 [astro-ph.CO].

[505] M. Ricotti, "Bondi accretion in the early universe," *Astrophys. J.*, vol. 662, pp. 53–61, 2007. DOI: 10.1086/516562. arXiv: 0706.0864 [astro-ph].

[506] M. Ricotti, J. P. Ostriker, and K. J. Mack, "Effect of primordial black holes on the cosmic microwave background and cosmological parameter estimates," *Astrophys. J.*, vol. 680, p. 829, 2008. DOI: 10.1086/587831. arXiv: 0709.0524 [astro-ph].

[507] S. Riemer-Sorensen, J. K. Webb, N. Crighton, V. Dumont, K. Ali, S. KotuÅą, M. Bainbridge, M. T. Murphy, and R. Carswell, "A robust deuterium abundance; re-measurement of the z=3.256 absorption system towards the quasar pks1937-1009," *Mon. Not. Roy. Astron. Soc.*, vol. 447, p. 2925, 2015. DOI: 10.1093/mnras/stu2599. arXiv: 1412.4043 [astro-ph.CO].

[508] A. G. Riess, L. Macri, S. Casertano, H. Lampeitl, H. C. Ferguson, A. V. Filippenko, S. W. Jha, W. Li, and R. Chornock, "A 3% solution: determination of the hubble constant with the hubble space telescope and wide field camera 3," *Astrophys. J.*, vol. 730, p. 119, 2011, [Erratum: Astrophys. J.732,129(2011)]. DOI: 10.1088/0004-637X/732/2/129,10.1088/0004-637X/730/2/119. arXiv: 1103.2976 [astro-ph.CO].

[509] A. G. Riess *et al.*, "A 2.4% determination of the local value of the hubble constant," 2016. arXiv: 1604.01424 [astro-ph.CO].

[510] B. E. Robertson and R. S. Ellis, "Connecting the gamma ray burst rate and the cosmic star formation history: implications for reionization and galaxy evolution," *Astrophys.J.*, vol. 744, p. 95, 2012. DOI: 10.1088/0004-637X/744/2/95. arXiv: 1109.0990 [astro-ph.CO].

[511] B. E. Robertson, R. S. Ellis, S. R. Furlanetto, and J. S. Dunlop, "Cosmic reionization and early star-forming galaxies: a joint analysis of new constraints from planck and hubble space telescope," *Astrophys.J.*, vol. 802, no. 2, p. L19, 2015. DOI: 10.1088/2041-8205/802/2/L19. arXiv: 1502.02024 [astro-ph.CO].

[512] B. E. Robertson *et al.*, "New constraints on cosmic reionization from the 2012 hubble ultra deep field campaign," *Astrophys. J.*, vol. 768, p. 71, 2013. DOI: 10.1088/0004-637X/768/1/71. arXiv: 1301.1228 [astro-ph.CO].

[513] G. Rocha, R. Trotta, C. J. A. P. Martins, A. Melchiorri, P. P. Avelino, R. Bean, and P. T. P. Viana, "Measuring alpha in the early universe: cmb polarization, reionization and the fisher matrix analysis," *Mon. Not. Roy. Astron. Soc.*, vol. 352, p. 20, 2004. DOI: 10.1111/j.1365-2966.2004.07832.x. arXiv: astro-ph/0309211 [astro-ph].

[514] A. J. Ross, L. Samushia, C. Howlett, W. J. Percival, A. Burden, *et al.*, "The clustering of the sdss dr7 main galaxy sample i: a 4 per cent distance measure at z=0.15," *Mon.Not.Roy.Astron.Soc.*, vol. 449, no. 1, pp. 835–847, 2015. DOI: 10.1093/mnras/stv154. arXiv: 1409.3242 [astro-ph.CO].

[515] J. A. Rubiño-Martín, J. Chluba, W. A. Fendt, and B. D. Wandelt, "Estimating the impact of recombination uncertainties on the cosmological parameter constraints from cosmic microwave background experiments," *Mon. Not. Roy. Astron. Soc.*, vol. 403, pp. 439–452, Mar. 2010. DOI: 10.1111/j.1365-2966.2009.16136.x. arXiv: 0910.4383.

[516] J. A. Rubiño-Martín, J. Chluba, and R. A. Sunyaev, "Lines in the cosmic microwave background spectrum from the epoch of cosmological hydrogen recombination," *Mon. Not. Roy. Astron. Soc.*, vol. 371, pp. 1939–1952, Oct. 2006. DOI: 10.1111/j.1365-2966.2006.10839.x. eprint: astro-ph/0607373.

[517] S. G. Rubin, A. S. Sakharov, and M. Khlopov, "The formation of primary galactic nuclei during phase transitions in the early universe," *J. Exp. Theor. Phys.*, vol. 91, pp. 921–929, 2001, [J. Exp. Theor. Phys.92,921(2001)]. DOI: 10.1134/1.1385631. arXiv: hep-ph/0106187 [hep-ph].

[518] V. C. Rubin, N. Thonnard, and W. K. Ford Jr., "Rotational properties of 21 sc galaxies with a large range of luminosities and radii, from ngc 4605 /r = 4kpc/ to ugc 2885 /r = 122 kpc/," *Astrophys. J.*, vol. 238, p. 471, 1980. DOI: 10.1086/158003.

[519] V. C. Rubin and W. K. Ford Jr., "Rotation of the andromeda nebula from a spectroscopic survey of emission regions," *Astrophys. J.*, vol. 159, pp. 379–403, 1970. DOI: 10.1086/150317.

[520] J. A. Rubino-Martin, J. Chluba, and R. A. Sunyaev, "Lines in the cosmic microwave background spectrum from the epoch of cosmological helium recombination," *Astron. Astrophys.*, vol. 485, p. 377, 2008. DOI: 10.1051/0004-6361:20078993. arXiv: 0711.0594 [astro-ph].

[521] M. Ruffert, "Non-axisymmetric wind-accretion simulations. 2. density gradients," *Astron. Astrophys.*, vol. 346, p. 861, 1999. arXiv: astro-ph/9903304 [astro-ph].

[522] G. B. Rybicki and I. P. dell'Antonio, "Spectral distortions in the cmb from recombination.," in *Observational Cosmology*, G. L. Chincarini, A. Iovino, T. Maccacaro, and D. Maccagni, Eds., ser. Astronomical Society of the Pacific Conference Series, vol. 51, Jan. 1993, p. 548.

[523] A. D. Sakharov, "Violation of cp invariance, c asymmetry, and baryon asymmetry of the universe," *Pisma Zh. Eksp. Teor. Fiz.*, vol. 5, pp. 32–35, 1967, [Usp. Fiz. Nauk161,61(1991)]. DOI: 10.1070/PU1991v034n05ABEH002497.

[524] P. Salati and J. C. Wallet, "Recombination of the primeval plasma and light inos," *Phys. Lett.*, vol. B144, pp. 61–68, 1984. DOI: 10.1016/0370-2693(84)90176-X.

[525] M. G. Santos *et al.*, "Cosmology with a ska hi intensity mapping survey," 2015. arXiv: 1501.03989 [astro-ph.CO].

[526] M. Sasaki, T. Suyama, T. Tanaka, and S. Yokoyama, "Primordial black hole scenario for the gravitational-wave event gw150914," *Phys. Rev. Lett.*, vol. 117, no. 6, p. 061 101, 2016. DOI: 10.1103/PhysRevLett.117.061101. arXiv: 1603.08338 [astro-ph.CO].

[527] L. Sbordone, P. Bonifacio, E. Caffau, *et al.*, "The metal-poor end of the spite plateau. i. stellar parameters, metallicities, and lithium abundances," *Astron. and Astroph.*, vol. 522, A26, A26, Nov. 2010. DOI: 10.1051/0004-6361/200913282. arXiv: 1003.4510.

[528] M. A. Schenker, R. S. Ellis, N. P. Konidaris, and D. P. Stark, "Line emitting galaxies beyond a redshift of 7: an improved method for estimating the evolving neutrality of the intergalactic medium," *Astrophys.J.*, vol. 795, no. 1, p. 20, 2014. DOI: 10.1088/0004-637X/795/1/20. arXiv: 1404.4632 [astro-ph.CO].

[529] K. Schutz and A. Liu, "Pulsar timing can constrain primordial black holes in the ligo mass window," *Phys. Rev.*, vol. D95, no. 2, p. 023 002, 2017. DOI: 10.1103/PhysRevD.95.023002. arXiv: 1610.04234 [astro-ph.CO].

[530] C. G. Scoccola, S. J. Landau, and H. Vucetich, "Wmap 5-year constraints on α and m_e," *Mem. Soc. Ast. It.*, vol. 80, no. 4, pp. 814–819, 2009, [Highlights Astron.15,307(2010)]. DOI: 10.1017/S1743921310009476. arXiv: 0910.1083 [astro-ph.CO].

[531] S. Seager, D. D. Sasselov, and D. Scott, "A new calculation of the recombination epoch," *Astrophys. J.*, vol. 523, pp. L1–L5, 1999. DOI: 10.1086/312250. arXiv: astro-ph/9909275 [astro-ph].

[532] ——, "How exactly did the universe become neutral?" *Astrophys. J. Suppl.*, vol. 128, pp. 407–430, 2000. DOI: 10.1086/313388. arXiv: astro-ph/9912182 [astro-ph].

[533] E. Sefusatti, G. Zaharijas, P. D. Serpico, D. Theurel, and M. Gustafsson, "Extragalactic gamma-ray signal from dark matter annihilation: an appraisal," *Mon.Not.Roy.Astron.Soc.*, vol. 441, pp. 1861–1878, 2014. DOI: 10.1093/mnras/stu686. arXiv: 1401.2117 [astro-ph.CO].

[534] U. Seljak and M. Zaldarriaga, "A line of sight integration approach to cosmic microwave background anisotropies," *Astrophys. J.*, vol. 469, pp. 437–444, 1996. DOI: 10.1086/177793. arXiv: astro-ph/9603033 [astro-ph].

[535] P. D. Serpico, E. Sefusatti, M. Gustafsson, and G. Zaharijas, "Extragalactic gamma-ray signal from dark matter annihilation: a power spectrum based computation," *Mon.Not.Roy.Astron.Soc.*, vol. 421, pp. L87–L91, 2012. DOI: 10.1111/j.1745-3933.2011.01212.x. arXiv: 1109.0095 [astro-ph.CO].

[536] N. I. Shakura and R. A. Sunyaev, "Black holes in binary systems. observational appearance," *Astron. Astrophys.*, vol. 24, pp. 337–355, 1973.

[537] S. L. Shapiro, "Accretion onto black holes: the emergent radiation spectrum. ii. magnetic effects," *Apj.*, vol. 185, pp. 69–82, Oct. 1973. DOI: 10.1086/152396.

[538] ——, "Accretion onto black holes: the emergent radiation spectrum," *Apj.apj*, vol. 180, pp. 531–546, Mar. 1973. DOI: 10.1086/151982.

[539] ——, "Accretion onto black holes: the emergent radiation spectrum. iii. rotating (kerr) black holes," *Apj.*, vol. 189, pp. 343–352, Apr. 1974. DOI: 10.1086/152809.

[540] S. L. Shapiro and A. P. Lightman, "Black holes in x-ray binaries - marginal existence and rotation reversals of accretion disks," *Apj.*, vol. 204, pp. 555–560, Mar. 1976. DOI: 10.1086/154203.

[541] J. R. Shaw and J. Chluba, "Precise cosmological parameter estimation using cosmorec," *Mon. Not. Roy. Astron. Soc.*, vol. 415, p. 1343, 2011. DOI: 10.1111/j.1365-2966.2011.18782.x. arXiv: 1102.3683 [astro-ph.CO].

[542] R. K. Sheth and G. Tormen, "Large scale bias and the peak background split," *Mon. Not. Roy. Astron. Soc.*, vol. 308, p. 119, 1999. DOI: 10.1046/j.1365-8711.1999.02692.x. arXiv: astro-ph/9901122 [astro-ph].

[543] X.-D. Shi and G. M. Fuller, "A new dark matter candidate: nonthermal sterile neutrinos," *Phys. Rev. Lett.*, vol. 82, pp. 2832–2835, 1999. DOI: 10.1103/PhysRevLett.82.2832. arXiv: astro-ph/9810076 [astro-ph].

[544] E. Shima, T. Matsuda, H. Takeda, and K. Sawada, "Hydrodynamic calculations of axisymmetric accretion flow," *Mon. Not. Roy. Astron. Soc.*, vol. 217, pp. 367–386, Nov. 1985. DOI: 10.1093/mnras/217.2.367.

[545] M. Shoji and E. Komatsu, "Massive neutrinos in cosmology: analytic solutions and fluid approximation," *Phys.Rev.*, vol. D81, p. 123 516, 2010. DOI: 10.1103/PhysRevD.81.123516,10.1103/PhysRevD.82.089901. arXiv: 1003.0942 [astro-ph.CO].

[546] R. E. Shrock, "General theory of weak leptonic and semileptonic decays. 1. leptonic pseudoscalar meson decays, with associated tests for, and bounds on, neutrino masses and lepton mixing," *Phys. Rev.*, vol. D24, p. 1232, 1981. DOI: 10.1103/PhysRevD.24.1232.

[547] J. M. Shull and M. E. van Steenberg, "X-ray secondary heating and ionization in quasar emission-line clouds," *Apj*, vol. 298, pp. 268–274, Nov. 1985. DOI: 10.1086/163605.

[548] J. Shull and M. van Steenberg, "The ionization equilibrium of astrophysically abundant elements," *Astrophys.J.Suppl.*, vol. 48, pp. 95–107, 1982. DOI: 10.1086/190769.

[549] T. Siegert, R. Diehl, G. Khachatryan, M. G. H. Krause, F. Guglielmetti, J. Greiner, A. W. Strong, and X. Zhang, "Gamma-ray spectroscopy of positron annihilation in the milky way," *Astron. Astrophys.*, vol. 586, A84, 2016. DOI: 10.1051/0004-6361/201527510. arXiv: 1512.00325 [astro-ph.HE].

[550] J. L. Sievers *et al.*, "The atacama cosmology telescope: cosmological parameters from three seasons of data," *JCAP*, vol. 1310, p. 060, 2013. DOI: 10.1088/1475-7516/2013/10/060. arXiv: 1301.0824 [astro-ph.CO].

[551] T. R. Slatyer, "Energy injection and absorption in the cosmic dark ages," *Phys.Rev.*, vol. D87, no. 12, p. 123 513, 2013. DOI: 10.1103/PhysRevD.87.123513. arXiv: 1211.0283 [astro-ph.CO].

[552] ——, "Indirect dark matter signatures in the cosmic dark ages i. generalizing the bound on s-wave dark matter annihilation from planck," 2015. arXiv: 1506.03811 [hep-ph].

[553] ——, "Indirect dark matter signatures in the cosmic dark ages ii. ionization, heating and photon production from arbitrary energy injections," 2015. arXiv: 1506.03812 [astro-ph.CO].

[554] T. R. Slatyer, N. Padmanabhan, and D. P. Finkbeiner, "Cmb constraints on wimp annihilation: energy absorption during the recombination epoch," *Phys.Rev.*, vol. D80, p. 043 526, 2009. DOI: 10.1103/PhysRevD.80.043526. arXiv: 0906.1197 [astro-ph.CO].

[555] T. R. Slatyer and C.-L. Wu, "General constraints on dark matter decay from the cosmic microwave background," 2016. arXiv: 1610.06933 [astro-ph.CO].

[556] A. V. Smirnov, A. M. Baryshev, S. V. Pilipenko, N. V. Myshonkova, V. B. Bulanov, M. Y. Arkhipov, I. S. Vinogradov, S. F. Likhachev, and N. S. Kardashev, "Space mission millimetron for terahertz astronomy," in *Space Telescopes and Instrumentation 2012: Optical, Infrared, and Millimeter Wave*, ser. SPIE Conference Series, vol. 8442, Sep. 2012, p. 84424C. DOI: 10.1117/12.927184.

[557] K. M. Smith and S. Ferraro, "Detecting patchy reionization in the cmb," 2016. arXiv: 1607.01769 [astro-ph.CO].

[558] R. E. Smith, J. A. Peacock, A. Jenkins, S. D. M. White, C. S. Frenk, F. R. Pearce, P. A. Thomas, G. Efstathiou, and H. M. P. Couchmann, "Stable clustering, the halo model and nonlinear cosmological power spectra," *Mon. Not. Roy. Astron. Soc.*, vol. 341, p. 1311, 2003. DOI: 10.1046/j.1365-8711.2003.06503.x. arXiv: astro-ph/0207664 [astro-ph].

[559] T. L. Smith, S. Das, and O. Zahn, "Constraints on neutrino and dark radiation interactions using cosmological observations," *Phys.Rev.*, vol. D85, p. 023 001, 2012. DOI: 10.1103/PhysRevD.85.023001. arXiv: 1105.3246 [astro-ph.CO].

[560] V. V. Sobolev, *Moving envelopes of stars*. 1960.

[561] A. Solaguren-Beascoa and M. Gonzalez-Garcia, "Dark radiation confronting lhc in z' models," *Phys.Lett.*, vol. B719, pp. 121–125, 2013. DOI: 10.1016/j.physletb.2012.12.065. arXiv: 1210.6350 [hep-ph].

[562] D. N. Spergel *et al.*, "First year wilkinson microwave anisotropy probe (wmap) observations: determination of cosmological parameters," *Astrophys. J. Suppl.*, vol. 148, pp. 175–194, 2003. DOI: 10.1086/377226. arXiv: astro-ph/0302209 [astro-ph].

[563] ——, "Wilkinson microwave anisotropy probe (wmap) three year results: implications for cosmology," *Astrophys. J. Suppl.*, vol. 170, p. 377, 2007. DOI: 10.1086/513700. arXiv: astro-ph/0603449 [astro-ph].

[564] F. Spite and M. Spite, "Abundance of lithium in unevolved halo stars and old disk stars - interpretation and consequences," *Astronomy and Astrophysics*, vol. 115, pp. 357–366, Nov. 1982.

[565] M. Spite, F. Spite, and P. Bonifacio, "The cosmic lithium problem: an observer's perspective," 2012, [Mem. Soc. Astron. Ital. Suppl.22,9(2012)]. arXiv: 1208.1190 [astro-ph.CO].

[566] V. Springel, "The cosmological simulation code gadget-2," *Mon. Not. Roy. Astron. Soc.*, vol. 364, pp. 1105–1134, 2005. DOI: 10.1111/j.1365-2966.2005.09655.x. arXiv: astro-ph/0505010 [astro-ph].

[567] A. A. Starobinsky, "A new type of isotropic cosmological models without singularity," *Phys. Lett.*, vol. B91, pp. 99–102, 1980. DOI: 10.1016/0370-2693(80)90670-X.

[568] M. Su and D. P. Finkbeiner, "Strong evidence for gamma-ray line emission from the inner galaxy," 2012. arXiv: 1206.1616 [astro-ph.HE].

[569] M. Su, A. P. S. Yadav, M. McQuinn, J. Yoo, and M. Zaldarriaga, "An improved forecast of patchy reionization reconstruction with cmb," 2011. arXiv: 1106.4313 [astro-ph.CO].

[570] R. A. Sunyaev and Ya. B. Zeldovich, "Small scale fluctuations of relic radiation," *Astrophys. Space Sci.*, vol. 7, pp. 3–19, 1970.

[571] ——, "The interaction of matter and radiation in the hot model of the universe," *Astrophys. Space Sci.*, vol. 7, pp. 20–30, 1970.

[572] ——, "The observations of relic radiation as a test of the nature of x-ray radiation from the clusters of galaxies," *Comments Astrophys. Space Phys.*, vol. 4, pp. 173–178, 1972.

[573] R. Svensson and A. A. Zdziarski, "Photon-photon scattering of gamma rays at cosmological distances," *Astrophys. J.*, vol. 349, pp. 415–428, 1990. DOI: 10.1086/168325.

[574] E. R. Switzer and C. M. Hirata, "Primordial helium recombination. 1. feedback, line transfer, and continuum opacity," *Phys. Rev.*, vol. D77, p. 083 006, 2008. DOI: 10.1103/PhysRevD.77.083006. arXiv: astro-ph/0702143 [ASTRO-PH].

[575] ——, "Primordial helium recombination. 3. thomson scattering, isotope shifts, and cumulative results," *Phys. Rev.*, vol. D77, p. 083 008, 2008. DOI: 10.1103/PhysRevD.77.083008. arXiv: astro-ph/0702145 [ASTRO-PH].

[576] Y. Tada and S. Yokoyama, "Primordial black holes as biased tracers," *Phys. Rev.*, vol. D91, no. 12, p. 123 534, 2015. DOI: 10.1103/PhysRevD.91.123534. arXiv: 1502.01124 [astro-ph.CO].

[577] R. Takahashi, M. Sato, T. Nishimichi, A. Taruya, and M. Oguri, "Revising the halofit model for the nonlinear matter power spectrum," *Astrophys. J.*, vol. 761, p. 152, 2012. DOI: 10.1088/0004-637X/761/2/152. arXiv: 1208.2701 [astro-ph.CO].

[578] H. Tashiro and N. Sugiyama, "The effect of primordial black holes on 21-cm fluctuations," *"Mon. Not. Roy. Astron. Soc."*, vol. 435, pp. 3001–3008, Nov. 2013. DOI: 10.1093/mnras/stt1493. arXiv: 1207.6405.

[579] J. L. Tinker, A. V. Kravtsov, A. Klypin, K. Abazajian, M. S. Warren, *et al.*, "Toward a halo mass function for precision cosmology: the limits of universality," *Astrophys.J.*, vol. 688, pp. 709–728, 2008. DOI: 10.1086/591439. arXiv: 0803.2706 [astro-ph].

[580] P. Tisserand *et al.*, "Limits on the macho content of the galactic halo from the eros-2 survey of the magellanic clouds," *Astron. Astrophys.*, vol. 469, pp. 387–404, 2007. DOI: 10.1051/0004-6361:20066017. arXiv: astro-ph/0607207 [astro-ph].

[581] E. Tollet *et al.*, "Nihao iv: core creation and destruction in dark matter density profiles across cosmic time," *Mon. Not. Roy. Astron. Soc.*, vol. 456, no. 4, pp. 3542–3552, 2016. DOI: 10.1093/mnras/stv2856. arXiv: 1507.03590 [astro-ph.GA].

[582] R. Trotta and A. Melchiorri, "Indication for primordial anisotropies in the neutrino background from wmap and sdss," *Phys.Rev.Lett.*, vol. 95, p. 011 305, 2005. DOI: 10.1103/PhysRevLett.95.011305. arXiv: astro-ph/0412066 [astro-ph].

[583] D. Tseliakhovich and C. Hirata, "Relative velocity of dark matter and baryonic fluids and the formation of the first structures," *Phys. Rev.*, vol. D82, p. 083 520, 2010. DOI: 10.1103/PhysRevD.82.083520. arXiv: 1005.2416 [astro-ph.CO].

[584] M. Valdes, C. Evoli, A. Mesinger, A. Ferrara, and N. Yoshida, "The nature of dark matter from the global high redshift hi 21 cm signal," *Mon.Not.Roy.Astron.Soc.*, vol. 429, pp. 1705–1716, 2013. DOI: 10.1093/mnras/sts458. arXiv: 1209.2120 [astro-ph.CO].

[585] B. P. Venemans, J. R. Findlay, W. J. Sutherland, G. De Rosa, R. G. McMahon, R. Simcoe, E. A. Gonzalez-Solares, K. Kuijken, and J. R. Lewis, "Discovery of three z>6.5 quasars in the vista kilo-degree infrared galaxy (viking) survey," *Astrophys. J.*, vol. 779, p. 24, 2013. DOI: 10.1088/0004-637X/779/1/24. arXiv: 1311.3666 [astro-ph.CO].

[586] F. Villaescusa-Navarro, P. Bull, and M. Viel, "Weighing neutrinos with cosmic neutral hydrogen," *Astrophys. J.*, vol. 814, no. 2, p. 146, 2015. DOI: 10.1088/0004-637X/814/2/146. arXiv: 1507.05102 [astro-ph.CO].

[587] M.-Y. Wang, A. H. G. Peter, L. E. Strigari, A. R. Zentner, B. Arant, S. Garrison-Kimmel, and M. Rocha, "Cosmological simulations of decaying dark matter: implications for small-scale structure of dark matter haloes," *Mon. Not. Roy. Astron. Soc.*, vol. 445, no. 1, pp. 614–629, 2014. DOI: 10.1093/mnras/stu1747. arXiv: 1406.0527 [astro-ph.CO].

[588] S. Weinberg, "A new light boson?" *Phys. Rev. Lett.*, vol. 40, pp. 223–226, 1978. DOI: 10.1103/PhysRevLett.40.223.

[589] ——, "Cosmology," 2008.

[590] ——, "Goldstone bosons as fractional cosmic neutrinos," *Phys.Rev.Lett.*, vol. 110, no. 24, p. 241 301, 2013. DOI: 10.1103/PhysRevLett.110.241301. arXiv: 1305.1971 [astro-ph.CO].

[591] C. Weniger, "A tentative gamma-ray line from dark matter annihilation at the fermi large area telescope," *JCAP*, vol. 1208, p. 007, 2012. DOI: 10.1088/1475-7516/2012/08/007. arXiv: 1204.2797 [hep-ph].

[592] C. Weniger, P. D. Serpico, F. Iocco, and G. Bertone, "Cmb bounds on dark matter annihilation: nucleon energy-losses after recombination," *Phys.Rev.*, vol. D87, no. 12, p. 123 008, 2013. DOI: 10.1103/PhysRevD.87.123008. arXiv: 1303.0942 [astro-ph.CO].

[593] F. Wilczek, "Problem of strong p and t invariance in the presence of instantons," *Phys. Rev. Lett.*, vol. 40, pp. 279–282, 1978. DOI: 10.1103/PhysRevLett.40.279.

[594] R. J. Wilkinson, C. Boehm, and J. Lesgourgues, "Constraining dark matter-neutrino interactions using the cmb and large-scale structure," *JCAP*, vol. 1405, p. 011, 2014. DOI: 10.1088/1475-7516/2014/05/011. arXiv: 1401.7597 [astro-ph.CO].

[595] L. Wolfenstein, "Neutrino oscillations in matter," *Phys. Rev. D*, vol. 17, pp. 2369–2374, May 1978. DOI: 10.1103/PhysRevD.17.2369.

[596] W. Y. Wong, A. Moss, and D. Scott, "How well do we understand cosmological recombination?" *Mon. Not. Roy. Astron. Soc.*, vol. 386, pp. 1023–1028, 2008. DOI: 10.1111/j.1365-2966.2008.13092.x. arXiv: 0711.1357 [astro-ph].

[597] W. Y. Wong and D. Scott, "The effect of forbidden transitions on cosmological hydrogen and helium recombination," *Mon. Not. Roy. Astron. Soc.*, vol. 375, pp. 1441–1448, 2007. DOI: 10.1111/j.1365-2966.2006.11410.x. arXiv: astro-ph/0610691 [astro-ph].

[598] J. S. B. Wyithe and A. Loeb, "Reionization of hydrogen and helium by early stars and quasars," *Astrophys. J.*, vol. 586, pp. 693–708, 2003. DOI: 10.1086/367721. arXiv: astro-ph/0209056 [astro-ph].

[599] F.-G. Xie and F. Yuan, "Radiative efficiency of hot accretion flows," *Mon. Not. Roy. Astron. Soc.*, vol. 427, pp. 1580–1586, Dec. 2012. DOI: 10.1111/j.1365-2966.2012.22030.x. arXiv: 1207.3113 [astro-ph.HE].

[600] T. Yamazaki *et al.*, "Search for heavy neutrinos in kaon decay," p. I.262, 1984.

[601] S. Yeung, M. Chan, and M.-C. Chu, "Cosmic microwave background constraints of decaying dark matter particle properties," *Astrophys.J.*, vol. 755, p. 108, 2012. DOI: 10.1088/0004-637X/755/2/108. arXiv: 1206.4114 [astro-ph.CO].

[602] S. Young and C. T. Byrnes, "Signatures of non-gaussianity in the isocurvature modes of primordial black hole dark matter," *JCAP*, vol. 1504, no. 04, p. 034, 2015. DOI: 10.1088/1475-7516/2015/04/034. arXiv: 1503.01505 [astro-ph.CO].

[603] F. Yuan and R. Narayan, "Hot accretion flows around black holes," *Ann. Rev. Astron. Astrophys.*, vol. 52, pp. 529–588, 2014. DOI: 10.1146/annurev-astro-082812-141003. arXiv: 1401.0586 [astro-ph.HE].

[604] M. Zaldarriaga and U. Seljak, "An all sky analysis of polarization in the microwave background," *Phys. Rev.*, vol. D55, pp. 1830–1840, 1997. DOI: 10.1103/PhysRevD.55.1830. arXiv: astro-ph/9609170 [astro-ph].

[605] Ya. B. Zeldovich, V. G. Kurt, and R. A. Sunyaev, "Recombination of hydrogen in the hot model of the universe," *Sov. Phys. JETP*, vol. 28, p. 146, 1969, [Zh. Eksp. Teor. Fiz.55,278(1968)].

[606] Ya. B. Zeldovich and R. A. Sunyaev, "The interaction of matter and radiation in a hot-model universe," *Astrophys. Space Sci.*, vol. 4, pp. 301–316, 1969. DOI: 10.1007/BF00661821.

[607] Y. Zeldovich, V. Kurt, and R. Sunyaev, "Recombination of hydrogen in the hot model of the universe," *J.Exp.Theor.Phys.*, vol. 28, p. 146, 1969.

[608] L. Zhang, X. Chen, M. Kamionkowski, Z.-g. Si, and Z. Zheng, "Constraints on radiative dark-matter decay from the cosmic microwave background," *Phys.Rev.*, vol. D76, p. 061 301, 2007. DOI: 10.1103/PhysRevD.76.061301. arXiv: 0704.2444 [astro-ph].

[609] K. M. Zurek and C. J. Hogan, "White noise from dark matter: 21 cm observations of early baryon collapse," *Phys. Rev.*, vol. D76, p. 063 002, 2007. DOI: 10.1103/PhysRevD.76.063002. arXiv: astro-ph/0703624 [ASTRO-PH].

[610] F. Zwicky, "Die rotverschiebung von extragalaktischen nebeln," *Helvetica Physica Acta*, vol. 6, pp. 110–127, 1933.

[611] ——, "On the masses of nebulae and of clusters of nebulae," *Apj*, vol. 86, p. 217, Oct. 1937. DOI: 10.1086/143864.